Springer Series on Polymer and Composite Materials

Deepalekshmi Ponnamma
Kishor Kumar Sadasivuni
John-John Cabibihan
Mariam Al-Ali Al-Maadeed *Editors*

Smart Polymer Nanocomposites

Energy Harvesting, Self-Healing and Shape Memory Applications

Springer

Springer Series on Polymer and Composite Materials

Series editor

Susheel Kalia, Dehradun, India

More information about this series at http://www.springer.com/series/13173

Deepalekshmi Ponnamma
Kishor Kumar Sadasivuni
John-John Cabibihan
Mariam Al-Ali Al-Maadeed
Editors

Smart Polymer Nanocomposites

Energy Harvesting, Self-Healing and Shape Memory Applications

Springer

Editors
Deepalekshmi Ponnamma
Qatar University
Doha
Qatar

Kishor Kumar Sadasivuni
Department of Mechanical and Industrial Engineering
Qatar University
Doha
Qatar

John-John Cabibihan
Department of Mechanical and Industrial Engineering
Qatar University
Doha
Qatar

Mariam Al-Ali Al-Maadeed
Center for Advanced Materials
Qatar University
Doha
Qatar

ISSN 2364-1878 ISSN 2364-1886 (electronic)
Springer Series on Polymer and Composite Materials
ISBN 978-3-319-50423-0 ISBN 978-3-319-50424-7 (eBook)
DOI 10.1007/978-3-319-50424-7

Library of Congress Control Number: 2016959251

Printed on acid-free paper

This Springer imprint is published by Springer Nature
The registered company is Springer International Publishing AG
The registered company address is: Gewerbestrasse 11, 6330 Cham, Switzerland

Contents

Contributors

Zubair Ahmad Center for Advanced Materials (CAM), Qatar University, Doha, Qatar

Saquib Ahmed Portland Community College, Portland, OR, USA

Mariam Al-Ali Al-Maadeed Qatar University, Doha, Qatar; Materials Science and Technology Program, Qatar University, Doha, Qatar

Shaikh Faruque Ali Department of Applied Mechanics, Indian Institute of Technology Madras, Chennai, India

A. Arockiarajan Department of Applied Mechanics, Indian Institute of Technology Madras, Chennai, India

Muhammad Awais Department of Industrial Engineering, Faculty of Engineering, Taibah University, Medina, Saudi Arabia

Sankha Banerjee Mechanical Engineering, California State University, Fresno, CA, USA

M. Basheer Ahamed Department of Physics, B.S. Abdur Rahman University, Chennai, TN, India

K. Byrappa Center for Materials Science and Technology, Vijnana Bhavan, University of Mysore, Mysuru, India

John-John Cabibihan Mechanical and Industrial Engineering Department, Qatar University, Doha, Qatar

Mariem Mohamed Chamakh Center for Advanced Materials, Qatar University, Doha, Qatar

Bananakere Nanjegowda Chandrashekar Department of Materials Science and Engineering, Shenzhen Key Laboratory of Nanoimprint Technology, South University of Science and Technology, Shenzhen, People's Republic of China;

Center for Materials Science and Technology, Vijnana Bhavan, University of Mysore, Mysuru, India

Chun Cheng Department of Materials Science and Engineering, Shenzhen Key Laboratory of Nanoimprint Technology, South University of Science and Technology, Shenzhen, People's Republic of China

Kalim Deshmukh Department of Physics, B.S. Abdur Rahman University, Chennai, TN, India

S.R. Dhakate Physics and Engineering of Carbon, CSIR-National Physical Laboratory, New Delhi, India; Academy of Scientific and Innovative Research, New Delhi, India

Yara Mohamed Hany El-Gawady Center for Advanced Materials, Qatar University, Doha, Qatar

Alper Erturk George W. Woodruff School of Mechanical Engineering, Georgia Institute of Technology, Atlanta, GA, USA

Anil Ghule Department of Chemistry, Shivaji University, Kolhapur, Maharashtra, India

Solleti Goutham Centre for Nano Science and Technology, Institute of Science and Technology, Jawaharlal Nehru Technological University Hyderabad, Kukatpally, Hyderabad, India

M. Imran Khan Faculty of Materials Science and Chemical Engineering, GIK Institute of Science and Technology KPK, Topi, Swabi, Pakistan

K. Jagadish Center for Materials Science and Technology, Vijnana Bhavan, University of Mysore, Mysuru, India

Chunqian Ji Department of Mechanical Engineering, School of Engineering, University of Birmingham, Birmingham, UK

Jojo P. Joseph Institute of Nano Science and Technology, SAS Nagar, Punjab, India

S.K. Khadheer Pasha Sensors Laboratory, School of Advanced Sciences, VIT University, Vellore, Tamil Nadu, India

S. Krishnaveni Department of Studies in Physics, University of Mysore, Mysuru, India; Department of Electronics, Yuvaraja's College, University of Mysore, Mysuru, India

Aravind Kumar Department of Applied Mechanics, Indian Institute of Technology Madras, Chennai, India

Sanjeev Kumar Mechanical Engineering, California State University, Fresno, CA, USA

Sasi Kumar Chemistry Division, School of Advanced Sciences, VIT University, Vellore, Tamil Nadu, India

B.E. Kumara Swamy Department of P.G. Studies and Research in Industrial Chemistry, Kuvempu University, Shimoga, Karnataka, India

Meena Laad Symbiosis Institute of Technology (SIT), Symbiosis International University (SIU), Pune, Maharashtra, India

Dipankar Mandal Organic Nano-Piezoelectric Device Laboratory, Department of Physics, Jadavpur University, Kolkata, India

Payal Mazumdar Amity Institute of Applied Sciences, Amity University Uttar Pradesh, Noida, India

Mansoor Ani Najeeb Center for Advanced Materials (CAM), Qatar University, Doha, Qatar

Namratha Center for Materials Science and Technology, Vijnana Bhavan, University of Mysore, Mysuru, India

Asish Pal Institute of Nano Science and Technology, SAS Nagar, Punjab, India

Santwana Pati Physics and Engineering of Carbon, CSIR-National Physical Laboratory, New Delhi, India; Academy of Scientific and Innovative Research, New Delhi, India

S.I. Patil Department of Physics, University of Pune, Pune-7, India

Duc Truong Pham Department of Mechanical Engineering, School of Engineering, University of Birmingham, Birmingham, UK

Deepalekshmi Ponnamma Center for Advanced Materials, Qatar University, Doha, Qatar

Fabrizio Quadrini Department of Industrial Engineering, University of Rome "Tor Vergata", Rome, Italy

Mariappan Rajan Biomaterials in Medicinal Chemistry Laboratory, Department of Natural Products Chemistry, School of Chemistry, Madurai Kamaraj University, Madurai, Tamil Nadu, India

Sunita Rattan Amity Institute of Applied Sciences, Amity University Uttar Pradesh, Noida, India

Hector Ruiz Mechanical Engineering, California State University, Fresno, CA, USA

Kishor Kumar Sadasivuni Department of Mechanical and Industrial Engineering, Qatar University, Doha, Qatar

Avneet Saini Department of Biophysics, Panjab University, Chandigarh, India

Loredana Santo Department of Industrial Engineering, University of Rome "Tor Vergata", Rome, Italy

R.A. Shakoor Center for Advanced Materials (CAM), Qatar University, Doha, Qatar

Pradeep Sharma Department of Mechanical Engineering, University of Houston, Houston, TX, USA

Pratibha Sharma Department of Biophysics, Panjab University, Chandigarh, India

Ashmeet Singh Institute of Nano Science and Technology, SAS Nagar, Punjab, India

Bhanu Pratap Singh Physics and Engineering of Carbon, CSIR-National Physical Laboratory, New Delhi, India; Academy of Scientific and Innovative Research, New Delhi, India

A.S. Smitha Department of Electronics, Yuvaraja's College, University of Mysore, Mysuru, India

S. Srikantaswamy Center for Materials Science and Technology, Vijnana Bhavan, University of Mysore, Mysuru, India

Venkatavijayan Subramanian School of Engineering & Applied Sciences, Ahmedabad University, Ahmedabad, Gujarat, India

Udhay Sundar Rutgers University, New Brunswick, NJ, USA

Deepu Thomas Research and Development Centre, Bharathiar University, Coimbatore, India

Farid Touati Department of Electrical Engineering, College of Engineering, Qatar University, Doha, Qatar

Ramna Tripathi Department of Physics, THDC-Institute of Hydropower Engineering and Technology, Tehri, Uttarakhand, India

Dharmesh Varade School of Engineering & Applied Sciences, Ahmedabad University, Ahmedabad, Gujarat, India

Kalagadda Venkateswara Rao Centre for Nano Science and Technology, Institute of Science and Technology, Jawaharlal Nehru Technological University Hyderabad, Kukatpally, Hyderabad, India

Gaurav Verma Dr. SS Bhatnagar University Institute of Chemical Engineering & Technology, Panjab University, Chandigarh, India; Centre for Nanoscience & Nanotechnology, Panjab University, Chandigarh, India

Yongjing Wang Department of Mechanical Engineering, School of Engineering, University of Birmingham, Birmingham, UK

Ajith Weerasinghe Mechanical Engineering, California State University, Fresno, CA, USA

Bal Chandra Yadav Nanomaterials and Sensors Research Laboratory, Department of Applied Physics, Babasaheb Bhimrao Ambedkar University, Lucknow, Uttar Pradesh, India

M.M. Zagho Center for Advanced Materials (CAM), Qatar University, Doha, Qatar

Energy Harvesting: Breakthrough Technologies Through Polymer Composites

Saquib Ahmed, Sankha Banerjee, Udhay Sundar, Hector Ruiz, Sanjeev Kumar and Ajith Weerasinghe

Abstract Polymer composites have been extensively studied in the last few years toward application in solar-, thermoelectric-, and vibration-based energy harvesting technologies. Of late, polymer nanocomposites are being investigated successfully in hybrid organic–inorganic devices, in bulk heterojunction devices incorporating all flavors of solar cells, and through the perovskite structures. In the thermoelectric power generation arena, abundance of raw materials, lack of toxicity, and the feasibility for large-area applications are all advantages that polymer nanocomposites boast over their inorganic predecessors. Within the vibration-based energy systems, polymer nanocomposites are being used as the magnets within the harvester devices; they offer low rigidity and easy processing (spin coating, drop casting, and molding). Also, recent work has focused on utilizing polymer ceramic nanocomposites as electrostatic energy storage materials. Lastly, polymer-based piezoelectric materials can be used directly as an active material in different transduction applications.

Keywords Polymer nanocomposite · Hybrid organic–inorganic solar cells · Thermoelectric power generation · Seebeck · Piezoelectric · Transduction · Dielectric storage · Piezocomposites · Energy harvesting

S. Ahmed (✉)
Portland Community College, Cascade Campus, PO Box 19000, Portland, OR 97229, USA
e-mail: saquib.ahmed@gmail.com

S. Banerjee · H. Ruiz · S. Kumar · A. Weerasinghe
Mechanical Engineering, California State University, Fresno, CA 93740, USA

U. Sundar
Rutgers University, New Brunswick, NJ, USA

D. Ponnamma et al. (eds.), *Smart Polymer Nanocomposites*,
Springer Series on Polymer and Composite Materials,
DOI 10.1007/978-3-319-50424-7_1

Contents

1 Introduction

The various modes of energy harvesting and the many arenas where such harvesting is critical to implement include:

1.1 Energy Harvesting for Alternatives to Fossil Fuel

An assessment of economically feasible renewable energy sources is essential toward creating a global sustainable society. The projection for the mean global energy consumption rate is 28 TW by the year 2050 [1, 2]. Besides fusion, solar energy has the largest potential to satisfy the future global need for renewable energy sources. From the 1.7×10^5 TW of solar energy that strikes the earth's surface, a practical terrestrial global solar potential value is estimated to be about 600 TW [3]. By making use of a mere 10% efficient solar farm, 60 TW of power could be produced. It is impactful to understand and absorb these figures to gain insight on how solar technologies could help meet the global energy demand. Production of solar cells has constantly gathered momentum by growing 30% in the last decade and a half. A selling price of $\$2/W_p$, corresponding to a production cost of $\$0.5/W_p$, would make PV in general competitive with electricity generated from fossil fuels [4]. The traditional solar cells of today, the first-generation solar cells are made from crystalline silicon (c-Si) technology, constituting 90% of the current PV market. The production cost is presently $\$3/W_p$ (peak Watt), but can vary based on the market for silicon material.

The solar industry has evolved tremendously in the past few years, and the leading technologies of first-generation silicon (Si) and second-generation cadmium telluride (CdTe) and copper indium gallium diselenide (CIGS) are seeing cost reductions in an effort to reach the DOE's SunShot goal of $0.06/kWh by 2020 [5–7]. However, it is critical to note that it is the solar-to-current conversion efficiency that is the key modulator in reaching this goal: the cost to install modules exceeds the cost to make them, and having fewer panels (meaning higher efficiency modules) will help us reach the desired power output [8].

It is imperative now more than ever to focus on the various third-generation technologies such as organic photovoltaics (OPVs), dye-sensitized solar cells (DSSCs), perovskite structures, and inorganic-organic hybrids to see how they can achieve higher efficiencies—not only through stand-alone structures, but also through tandem or multijunction stacked architectures with their first- or second-generation counterparts. The third-generation cells intrinsically offer tremendously lower processing costs (compared to their first- and second-generation peers), with a much more impactful scope to enhance upon efficiency by leveraging their nanoscale properties [9]. Theoretically, the third-generation cells—for a standalone cell—can go up to the Carnot limit of 94% energy conversion; the first- and second-generation cells are, by comparison, constrained to the 31% Carnot limit.

Beyond tackling the efficiency and cost aspects of the technology, the third-generation solar cells like OPVs have numerous advantages such as low cost of production, flexibility, light weight, short energy payback time, improved performance in non-ideal conditions (better than first- and second-generation solar cells working under diffuse light conditions and higher temperatures), and a variety of design opportunities [10].

Polymer nanocomposites, in particular, have a critical and powerful role to play in the third-generation photovoltaic domain. They had previously been explored solely in the area of OPVs; currently, they are being investigated successfully in hybrid organic–inorganic devices, bulk heterojunction devices incorporating all three flavors of cells, and through the perovskite structures. An enormous research thrust continues to exist to investigate and improve upon the implementation of polymer nanocomposites within the active layers of solar energy absorption and transport, while at the same time minimizing recombination losses.

1.2 Energy Harvesting for Powering Sensors and Electronics

There has recently been a tremendous growth in the area of personal and mobile electronics for applications in communication, health care, and environmental monitoring [11]. The individual power consumption of such devices may be low, but the sheer magnitude of the number of devices requires the search for affordable and sustainable energy sources that can be incorporated within the devices themselves. Rechargeable batteries are the current choice for powering the electronic

devices; however, there are tremendous challenges in the area of development of the batteries as there exist legitimate concerns regarding environmental side effects. Energy harvesting from our living environment provides a powerful alternative; such sources include photovoltaics, biofuels, thermoelectricity, and vibrational energy harnessing.

For the plausible future for electronics, integrating these conventional devices with specific characteristics into smart and self-powered systems is the key aim [12]. Nowadays, nanomaterials are of incredibly smaller dimensions and can be tweaked compositionally to great accuracy to create unique properties—their bulk counterparts cannot match these crucial properties. By the same token, nanomaterials can be utilized in situ to power the device. The ultimate aim of energy harnessing technologies for such sustainable micro- and nanosystems was to innovate power sources that function over a wide range of conditions, and for prolonged time periods with high consistency.

Third-generation solar cells are being researched extensively for implementation in electronic and sensor devices. This is in part because of the intrinsic advantages that dimension (nanoscale) and tunability that such solar cells offer and in part because of the cost-effectiveness and scalability options that can be utilized from a manufacturing standpoint. As an example, for OPVs, the ability to change—through molecular and/or electrochemical doping of polymers—the electrical conductivity of components, along with the integration of cheap and facile processing techniques, has bolstered the function of polymer solar cells in such devices.

Looking at thermoelectric energy conversion, there has been tremendous interest in the past two decades on thermoelectric materials for generating electricity through harnessing energy from heat sources and waste heat from engines [13–15]. Apart from the obvious gains in providing an alternative energy to fossil fuels, there has also been focus on harvesting heat dissipated from humans to power microsensors in body-area networks and biomedical monitoring [16, 17]. In general, in the area of thermoelectric applications over the past two decades, the transport properties of electrically conductive polymers (and their composites) have improved the figure of merit of organic materials by several orders of magnitude [18].

Mechanical energy through vibration is prevalent in the environment and can be tapped into more easily than its solar and thermal counterparts. Mechanical vibrations exist in many systems at different frequencies varying from a few hertz to several kilohertz with their energy density varying between hundreds of microwatts to a few milli-watts per given centimeter cube [19, 20]. Vibrational mechanical energy has great potential to provide the continuous and changing operational need of sensors/electronic devices [21, 22]. The various forms of such energy include electrostatic, electromagnetic, and piezoelectric sources of energy generation [23–25].

Looking at the electrostatic arena of energy harvesting, breakthrough research is happening for capacitors that can store up a large amount of energy and then almost instantaneously release it—a feat that is difficult to achieve with other energy storage technologies such as batteries or ultracapacitors. ‘Pulse power’—ability to store and deliver nearly instantaneously a large amount of power—can be applied to a plethora of commercial and military devices. These applications typically would

require increased energy and power densities, more power stored per less volume, as well as higher charge–discharge current capabilities [26, 27]. For a linear capacitor, the maximum energy density that can potentially be stored scales directly as the permittivity of the dielectric material and as the square of the breakdown strength of the dielectric material. Improvements in permittivity, dielectric film thickness, and breakdown strength are thus sought to increase energy storage density of dielectric capacitors. A low dielectric loss is preferred both to reduce dissipated energy and thermal sensitivity [28].

Inorganic ceramic materials can have very large permittivities but are limited by relatively small breakdown strengths, poor process ability, and mechanical properties due to high sintering temperature, volumetric shrinkage during sintering, dislocations, and residual porosity. On the other hand, organic-based polymers typically have higher breakdown strengths, viscoelastic mechanical properties, and excellent processability but suffer smaller permittivity.

By incorporating high-permittivity inorganic nanoparticles into a polymer matrix with low dielectric loss, and high breakdown strength, there is great potential to develop new composite materials that have improved dielectric properties, dielectric strength, permittivity, and dielectric losses, and retain unique attributes of polymers [29–32].

Electromagnetic harvesters are very popular in meso- and macroscale systems owing to ease of design and high reliability [33]. However, due to difficulty in fabricating the coils and incorporating a microscale permanent magnet, the miniaturization of electromagnetic harvesters has proven to be quite challenging. In most microscale electromagnetic energy harvesters, a discrete permanent magnet, affixed after the microfabrication process, serves as the flux source [34, 35]. This solution is non-viable; it cannot utilize key cost-saving mechanisms such as batch manufacturing. A solution to the permanent magnet integration issue that is elegant utilizes a permanent magnetic nanocomposite (soft polymer and magnetic metal nanowires) instead of a discrete permanent magnet. The composite accomplishes the need for a low-rigidity material with remnant magnetization. Further, it is cost-effective and viable as it can be easily processed by spin coating, drop casting, and molding [36–38].

Delving into the world of piezoelectric energy harnessing, we find that if mechanical stress is applied on a piezoelectric material, an induced electric field across its boundaries can be seen. Polymer-based microelectromechanical systems (MEMS) and microfluidic devices boast—over their silicon counterparts—crucial metrics such as mechanical flexibility and faster and cheaper fabrication [39]. Piezoelectric functional polymers (piezopolymers) are a valuable class of polymers for microfabricated devices. An optimal design for harnessing piezoelectric vibration energy will output the highest harvested power possible over the smallest area feasible, and at the ideal frequency of the vibration source harvested [40]. A device or application that leverages such a design requires a high coupling coefficient; inorganic materials provide this crucial quality. Critically, however, being flexible and having lower stiffness provide the crucial advantage of using polymers over ceramics. These characteristics not only help to prevent fatigue, but also increase the lifetime of the device [41].

2 Photovoltaic Technologies

2.1 Role of Nanostructured Materials and Conducting Polymers in Various PV Technologies

2.1.1 Organic Polymer Solar Cells

Device Physics and Active Layers Involved in Energy Conversion

Organic polymer-based PV devices (OPVs) provide an excellent alternative to harnessing sunlight in a cost-effective manner [42, 43]. By using simple molecular and/or electrochemical doping of polymers, the electrical conductivity of these devices can be modified. This feature, together with cheap processing methods, has significantly bolstered the application of polymer-based solar cells. The device physics concerning organic solar cells necessitate excitons; these are separated into free electron–hole pairs by the electric field applied across a heterogeneous junction in between two unlike organic materials (called donor and acceptor materials) [44]. Conventional device configurations for OPVs include—but are not limited to—single-layer, bilayer heterojunction, bulk heterojunction, and diffusive bilayer heterojunction configurations [45]. The conversion efficiencies for single-layer and bilayer organic solar cells are in the range of 1%, sometimes lower. Recent advances in solution-processed polymer-bulk-heterojunction (BHJ) solar cells have received attention, due to increased energy-conversion efficiencies of approximately 6–8% which were achieved by careful tweaking of the favorable properties of the polymer, its morphology, and the device structure [46–48].

Device Physics and Active Layers Involved in Energy Conversion

The optical absorption coefficient of organic molecules is sufficiently high, and the cost of developing OPVs with sufficient energy-conversion efficiencies could be much lower than the second-generation thin-film solar cells. Fabrication methods, such as roll-to-roll processing which is an emerging technique, facilitate the production of OPVs to be scaled up to a level at which such devices are feasible and viable for powering flexible microstructured devices such as MEMS and even consumer electronics [49].

BJH OPV Cells: Focus on (Poly(3-hexylthiophene) (P3HT)) and MDMO-PPV (Poly[2-methoxy-5-(3,7-dimethyloctyloxy)-1,4-phenylene]-alt-(vinylene)) Polymer Composites in OPVs

Focusing on bulk heterojunction (BHJ) solar cells, the active layer is a bicontinuous composite of donor and acceptor phases, thereby maximizing the all-important

interfacial area between the donors (polymers) and acceptors (fullerenes). Polymer-based photovoltaic systems which can be processed in solution, and which generally take the form of BHJ devices, most closely conform to the ultimate vision of organic solar cells as low-cost, lightweight, and flexible devices. The real advantage of these BHJ devices compared to vacuum deposition is the versatility to develop the composite active layer from solution in a single step. A variety of techniques can be utilized to that end: ranging from spin coating to inkjet printing and roller casting. One efficient way to design superior BHJ polymer solar cells is by fabricating alternating donor–acceptor (D–A) copolymers with electron-rich (donor) and electron-deficient (acceptor) moieties. This model can modulate the energy levels and absorption properties by controlling the intermolecular charge transfer from the donor to acceptor [44].

The current high-tech BHJ solar cells are based on poly(3-hexylthiophene) (P3HT) as the donor material and the fullerene derivative—[6,6]-phenyl-C61-butyric acid methyl ester (PCBM)—as its acceptor counterpart. MDMO-PPV (poly [2-methoxy-5-(3,7-dimethyloctyloxy)-1,4-phenylene]-alt-(vinylene)) has also been an effective donor polymer for this device. To attain efficiencies approaching 10% in such organic solar cells, much effort is required to understand the fundamental electronic interactions between the polymeric donors and the fullerene acceptors as well as the complex interplay of device architecture, morphology, processing, and the fundamental electronic processes.

(i) Photoenergy-conversion process in BJH cells

Scheme 1 [44] shows the four fundamental steps in the commonly accepted mechanism: 1. light absorption and generation of excitons; 2. diffusion of the excitons; 3. dissociation of excitons with the generation of charge; and 4. charge transport and charge collection.

The fundamental steps defining the pathway from photoexcitation to the generation of free charges are shown in Scheme 2 [44]. It is key to note that electron transfer must be feasible from an energetics point of view to form the geminate pair in the 3rd step. Also, there needs to be an energetic driving force to separate the coulombically bound electron–hole pair.

Absolutely essential to the operating principle of the above process are all aspects of the composite structure that makes up the active layer (donor and acceptor). Among the key elements in particular is the morphology of the composite structure: This feature will dictate the kinetics of interaction between the acceptor and the donor [50, 51].

(ii) Electronic donor–acceptor interactions

Polymer-based fullerene PV cells rely on the intimate optimization of electronic properties of the acceptor and donor constituents, enhancing light absorption, free charge generation, and efficient charge transport to corresponding electrodes. The fact that these devices leverage only the electronic characteristics is a disadvantage, since morphological characteristics are ignored. The latter are crucial for the performance of these devices.

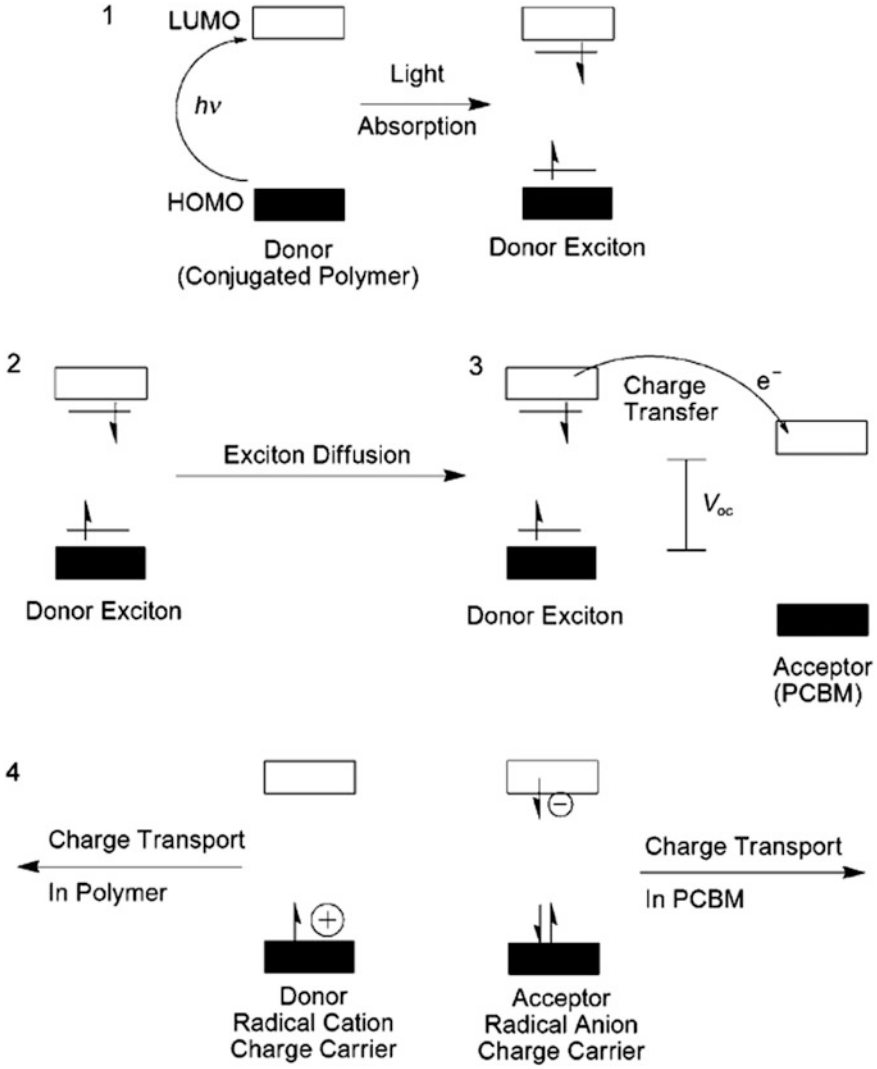

Scheme 1 Excitonic solar cells: operational physics [44]. Copyright 2016. Reproduced with permission from Wiley

The two components that are essential in devices such as these for optimal electronic performance include a fullerene—typically a C60 derivative—acceptor which is soluble, and a solution-processed polymeric donor.

Fullerenes exhibit a constant electronic structure irrespective of how they are made soluble. Most functionalized fullerenes exhibit a first reduction potential variation of ±100 mV compared to C60 [52, 53]. This fact enumerates the

$$D + A \xrightleftharpoons{h\nu} D^* + A \quad (1)$$

$$D^* + A \rightleftharpoons [D^*, A] \quad (2)$$

$$[D^*, A] \rightleftharpoons [D^{+\bullet}, A^{-\bullet}] \quad (3)$$

$$[D^{+\bullet}, A^{-\bullet}] \rightleftharpoons D^{+\bullet} + A^{-\bullet} \quad (4)$$

Scheme 2 Steps in photoinduced charge separation for a donor (D) and an acceptor (A): *1* photoexcitation of the donor; *2* diffusion of the exciton and formation of an encounter pair; *3* electron transfer within the encounter pair to form a geminate pair; and *4* charge separation [44] Copyright 2016. Reproduced with permission from Wiley

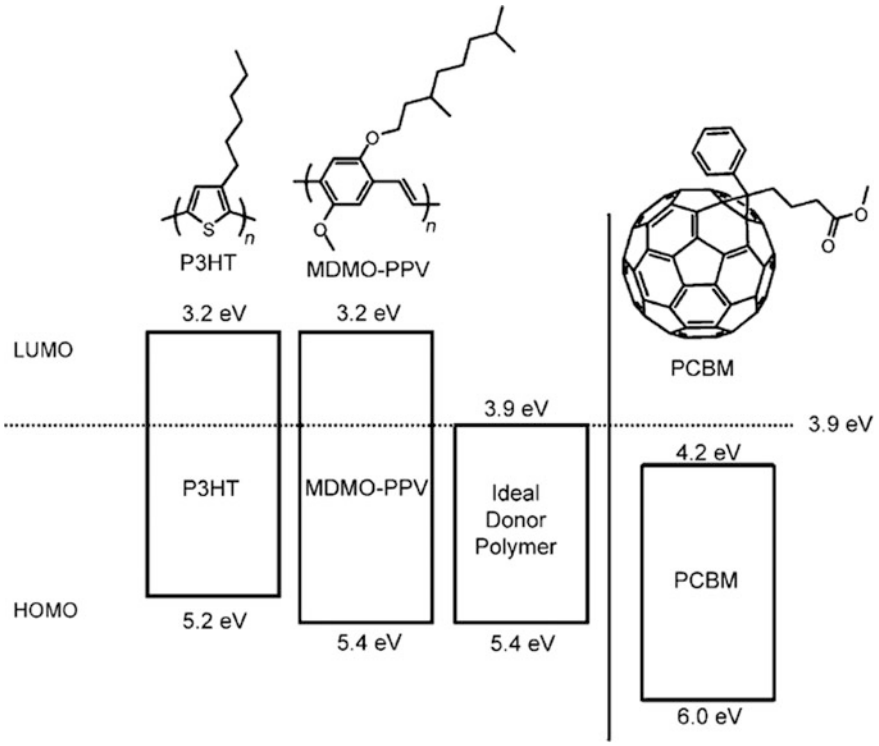

Fig. 1 Band structure diagram illustrating the HOMO and LUMO energies of donors P3HT and MDMO-PPV compared to the acceptor fullerene PCBM [44]. Copyright 2016. Reproduced with permission from Wiley

electronic bandgap requirement of the corresponding donor. Figure 1 captures the relative energies of the two constituents (as an example): MDMO-PPV (poly [2-methoxy-5-(3,7-dimethyloctyloxy)-1,4-phenylene]-alt-(vinylene)) and P3HT.

The first step is that upon excitation, the donor must be able to inject a charge into the fullerene (Scheme 1). A differential in the energy levels—manifesting as a driving force—is critical for this process to be viable; also, the driving force must overcome the exciton binding energy. Usual values for this binding energy between the electron–hole pair in the donor are approximately 0.4–0.5 eV [54]. The driving force impacts the exciton breakup by enabling the formation of a geminate pair (3rd step in Scheme 2). To generate free charges, an additional driving force is needed to separate this geminate pair (which is now held together by Columbic forces of attraction). Heat and the innate electric field in the device contribute to providing this additional force.

It is critical to note that the above reaction should be exogenic [51, 55]. An energy gradient has to exist between the LUMO levels to punch an electron from the donor to the acceptor. For the exciton to divide to respective charges, a minimum energy gradient of 0.3 eV is required [56, 57]. An energy gradient larger than this minimum value adds no value to the device performance [58]. Ideally, the polymer should have a minimum energy gradient that has a value between the LUMO levels; this would ensure that energy loss is minimized. Therefore, the ideal polymer would have its LUMO sit at 3.9 eV (given the LUMO energy for PCBM is 4.2 eV).

The HOMO level of the polymer can be easily calculated using the wavelength for the onset of light absorption; it can also be verified using a secondary method of looking at the open-circuit voltage. In looking at optimizing the HOMO level, there are opposing characteristics to consider. By lowering the HOMO level, we can increase the open-circuit voltage; on the flipside, that entails increasing the bandgap, which results in losing out quite a bit of the solar spectrum. An optimal value of 1.5 eV can be used [59]. Working backwards, we deduce a HOMO energy of 5.4 eV, which in turn correlates to an open-circuit voltage of 1.2 V. It is again, only through a careful balance of the open-circuit voltage and bandgap that we can attain an optimal value for the HOMO [60]. For an ideal system, also critical are the following items: a broad absorption band for the polymer with a high-absorption coefficient, and high charge carrier mobility for the polymer proportional to that of PCBM (10^{-3} cm^2 V^{-1} s^{-1} measured in a space–charge-restricted environment [61] or 10^{-1} cm^2 V^{-1} s^{-1} as measured in field-effect transistors [62]).

(iii) Morphology

A few key internal and external factors influence the morphology of the active layer components. The inherent properties are specific to the polymer and the fullerene and encompass the unique interaction between them: They include parameters such as relative miscibility and crystallinity. The external parameters include all the variables that have an impact on device fabrication: They include solvent type, concentration of constituent elements, and type of deposition technique used (roller casting vs. inkjet printing vs. spin coating, etc.).

(a) MDMO-PPV/PCBM solar cells

One of the most exhaustive studies done on BHJ cells are on the MDMO-PPV/PCBM cells [63, 64]. To start off, it is the solvent that is crucial in impacting the morphology of the active layer and the performance of the device. By deriving the active layer from toluene, and with a 1:4 weight ratio of polymer to fullerene, solar cell efficiencies of about 0.9% were obtained. With the solvent as chlorobenzene, however, the efficiency significantly improved to around 2.5% [65]. Using spectroscopy, it was shown that the difference between the active layers was purely structural. For the toluene-cast films, it was detected that micrometer-sized PCBM clusters are implanted in a polymer host [66]. This structure ultimately gave rise to a macroscale phase segregation in the system. By contrast, in the chlorobenzene-cast films, PCBM clusters with dimensions less than 100 nm are observed in a strikingly more homogenous composite.

The stark difference in performance of the two films can be attributed to the following: (a) For the chlorobenzene-cast film, the length scale of phase segregation is the same order of magnitude as the exciton diffusion length and (b) for the chlorobenzene-cast film, the more bicontinuous nature of the films expedite charge transport. The very obvious difference in morphology of the films resulted due to the greater solubility of PCBM in chlorobenzene compared to that in toluene [63]. The ultimate result of this is that the toluene solution contained already formed clusters, which in turn lead to large cluster size.

The inherent miscibility of the two active components played a key role in the film morphology as well. This goes to show that the ultimate device performance depended on an optimal composition. For the MDMO-PPV/PCBM system, it was in fact an inherent *immiscibility* that led toward phase segregation. The large amount of (by mass) fullerene required—compared to the polymer—to generate a percolated network shows proof of this. Thermal annealing enhances this immiscibility, leading to (macro) phase separation at temperatures even below the glass temperature (Tg) of the polymer [67]. An optimal morphology can be obtained only through controlling the solvent evaporation rate from a solvent in which both the components are highly soluble.

(b) P3HT/PCBM solar cells

With this flavor of cells, a few layers of iterations have already been made in terms of optimizing the performance. From a weight ratio standpoint of the two materials, results show that P3HT and PCBM exhibit greater miscibility than does MDMO-PPV and PCBM [68–70]. As the solvent, chlorobenzene is the typical choice [68–70]; also, 1,2-dichlorobenzene can be used for equivalent efficiencies [69, 71].

With regard to deposition, spin casting has been characteristically used to deposit P3HT/PCBM in fabricating the solar cell device [72]. When the two components are mixed, they appear much more homogenous in their outcome, compared to their MDMO-PPV/PCBM counterpart. Iterating on the obtained mixture, various methods have been probed to get the optimal morphology that outputs the best photovoltaic behavior. The most prevalently used methodology is

thermal annealing [56]. Thermal treatment of the active layer to a higher temperature than the glass temperature of P3HT allows the reorganization of the polymer chains and the free diffusion of the fullerene molecules into the composite layer for a thermodynamically advantageous reorganization.

(iv) Outlook, challenges, and future work for BJH OPVs

BHJ solar cells have overall seen tremendous improvements in the past years not only in active layer processing but also in device fabrication. The highest reported efficiencies are in the range of 6–8%. The probing of fundamental metrics including electronic properties and morphological properties has been key in elucidating device behavior. These learnings can be taken effectively for progressing into the next iteration of effective OPVs.

Investigating new materials for active layers is a promising field for the imminent future. An important material to investigate for enhancing device performance is one that has a low bandgap, high open-circuit voltage, and high charge carrier mobility. A second issue to look into is long-term stability of these devices under constant irradiance: To that end, cross-linking materials together with compatibilizing materials are critical areas of research. Lastly, the goal of OPVs as a feasible solar device is to be so not only in small cells, but across arrays and over real-time and real environmental conditions. An enormous amount of research and development awaits to happen in this sector.

Looking specifically at polymer–fullerene PVs, a few noteworthy endeavors are underway. In an effort to modulate morphology of the active laver, there has been effort to utilize block copolymers, in particular one that contains pendant fullerenes [73, 74]. There has been research to modify the entire architecture of the PV device while keeping the critical active layer components of the cell in place. In particular, a TiO_x layer has been utilized and has been inserted between a composite layer of P3HT and PCBM components and the back electrode to enhance light absorption. The result has been a tremendous increase in the photocurrent generated across the visible spectrum with a maximum IPCE or EQA value of 90% [75].

2.2 *The Bigger Picture: Maximizing Cell and Module Efficiency Through Inorganic-Organic Hybrid Structures*

Organic and inorganic materials boast a host of unique properties; hybrid (or tandem) structures are of great interest and of paramount importance to probe in an effort to leverage the best of both worlds. In particular, hybrid nanocomposites of organic conducting polymers and inorganic semiconductors hold tremendous potential for solar cells through enhanced light harvesting and transport [76]. Looking at organic conducting polymers, we find materials that can be easily processed, recycled and that are cheap and scalable: all the features that we need for

sustainability. As their complementary counterparts, inorganic semiconductors exhibit excellent electronic properties, including high dielectric constant, charge mobility, and thermal stability. The nanoparticles of such materials similarly showcase the desired attributes of superior electronic, photoconducting, and luminescent properties.

A variety of various inorganic materials and organic conducting polymers have been investigated for hybrid cells. A key phenomenon noted in these cells is that photoinduced charge separation predominantly occurs at the interfaces of the two materials. This is the junction where electron transfer from the conducting polymers into the inorganic semiconductors occurs; the holes remain back within the polymer matrix.

2.2.1 Charge Separation at the Organic–Inorganic Interface

From the previous discussion, it is evident that interfacial charge kinetics is critical to understand for optimizing hybrid PV devices. Previous works point out to an intermediate stage (a bound charge transfer complex) in the dissociation of a photogenerated exciton at the donor–acceptor heterojunction interface prior to fully separating into fully detached charge entities [77–79] as illustrated in Fig. 2. A successful charge separation depends on a rate that is faster than the complex recombination, as well as the energy transfer rate to multiple exciton flavors of either constituent. It is obvious that these interfacial charge kinetics depend intimately on a few pivotal parameters: the nature and size of the interfacial surface area, differences in energy levels across the interfaces, the morphology of the interfaces and domains, the interfacial layer constituents that include its molecular composition, the crystallinity and phase of the constituents, how homogeneous the mixture is and among others.

Figure 2 helps to enumerate the critical charge transfer process steps within a hybrid cell. The steps include, from the beginning, the photoexcitation that punches an electron from the HOMO to the LUMO level, leaving behind a hold; the electron and holes migrating to the interfaces; the electron/hole transfers at the interface; the migration of the charges to their respective electrodes; and the transfer of those charges into the electrodes. It is important to note that the effectiveness of each of these processes is dependent on how fast they occur: back recombination is a primary mode of loss in the final manifestation of solar cell efficiency.

As mentioned previously, a plethora of materials have been investigated to be candidates for the inorganic and organic components. For the inorganic semiconductors, the typical candidates include cadmium sulfide [80, 81], cadmium selenide [82, 83], cadmium telluride [84, 85], lead sulfide [86, 87], lead selenide [84, 88], zinc oxide [89, 90], and titanium dioxide [91, 92]. P3HT continues to be the organic polymer electron donor of choice.

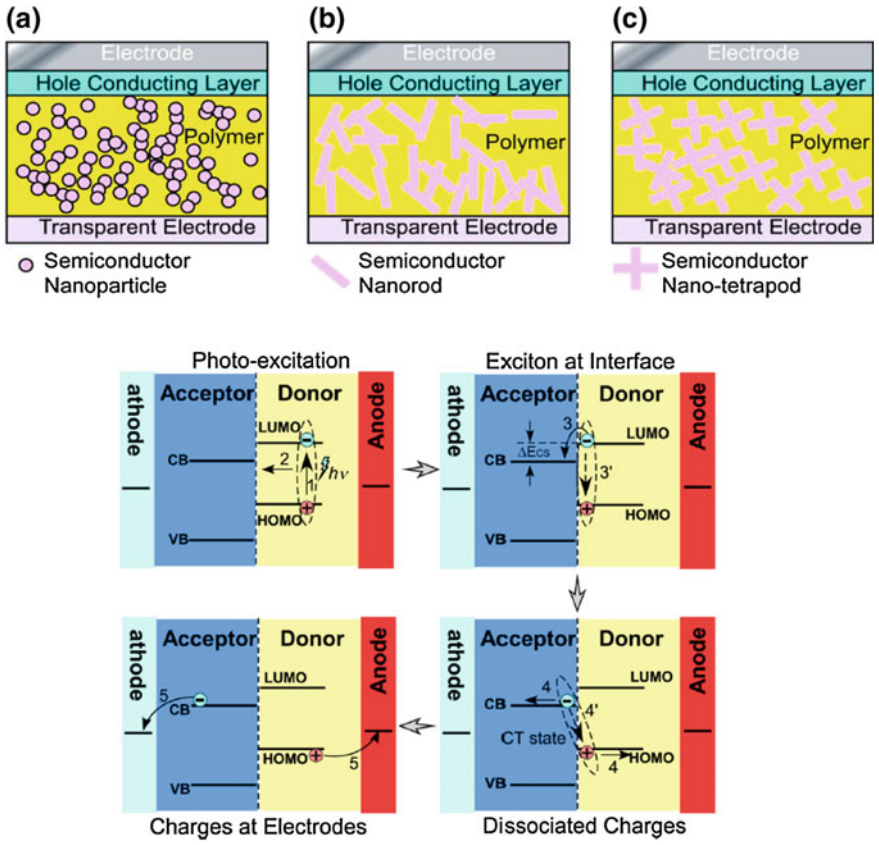

Fig. 2 Schematic of the interfacial charge transfer process for a hybrid PV device [76]. Open Access Journal. Reproduced with permission from MDPI

2.2.2 Nanostructured Architecture of Hybrid Cells

The above discussion has helped enumerate the critical nature of interfacial charge transfer kinetics in defining the efficiency of solar power conversion efficiency. With higher specific surface area for these interfaces, charges have a better scope to dissociate and get transported to their respective electrodes. Nanostructures provide such higher specific surface area and include shapes such as particles, rods, and host of other shapes and porous networks. These structures can be ordered and isotropic or tangled. Figure 3 illustrates these various structures [76].

Figure 3 helps to illustrate the various configurations of nanomaterials discussed for providing hybrid cells: (**a**) semiconductor nanoparticles and polymer films; (**b**) polymer films and semiconductor nanorods; (**c**) semiconductor polymer films and nanotetrapods; (**d**) porous semiconductor nanonetwork immersed in conducting

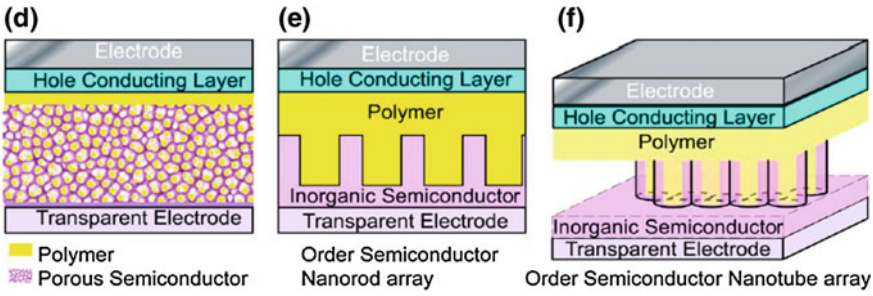

Fig. 3 Various configurations of nanomaterials [76]. Open Access Journal. Reproduced with permission from MDPI

polymer; (**e**) ordered semiconductor arrays (nanorods) and polymer films; and (**f**) ordered semiconductor arrays (nanotubes) and polymer films.

It is key to note here that the best photovoltaic performance attained is through a hybrid system of ordered TiO_2 nanotube arrays and P3HT [93]. Various other structures have also been reported to have comparable efficiencies [94, 95]. Overall, interfacial charge transfer kinetics together with charge transport through the cell are the critical parameters in impacting device efficiency. These parameters are further highlighted and discussed below, and we emphasize that hybrid systems can improve by optimizing on them.

2.2.3 Key Components and Optimization for Enhanced Device Performance

One of the key parameters influencing solar cell device efficiency is the short circuit current density. This value is heavily dependent on charge transport kinetics in both donor and acceptor components. In comparing nanoparticles versus nanorods and various branching networks of such nanorods, work has shown that the latter provides less recombination (through a more direct charge transfer as opposed to hopping as is the case with nanoparticles) and enhanced overall efficiency. This feature is especially critical in the polymer matrix component, and research shows the visible enhancement in device performance and efficiency with optimal nanostructures in place [94]. As a further iteration in optimizing this conducting array for efficient charge transport, nanotubes have been shown to provide higher garnering of photoelectrons (due to higher specific surface are) compared to nanorods. Three-dimensional network of porous-based systems also shows lower performance due to the fact that the interface between the organic–inorganic entities does not have good contact. As a final statement, it should be highlighted that the Fermi/HOMO/LUMO energy levels between interfacing components should be well matched to provide the driving force and directionality of electron and hole transport.

3 Thermoelectric Power Generation

3.1 The Physics of a Working Thermoelectric Energy Harvester

Thermoelectric devices offer a unique power generation solution because they convert thermal energy into electricity without requiring moving components [96, 97]. Thermoelectric devices offer a unique power generation solution because they convert thermal energy into electricity without requiring moving components. Thermoelectric energy harvesting has the reverse effect of a thermodynamic refrigerator. It has been studied extensively in the last few decades [98]. Joule first demonstrated that a current, I, flowing through a resistor, R, will produce a certain amount of heat Q

$$Q = I^2 R \tag{5}$$

The heat generated in a material is transported by a temperature gradient ∇T along the material, as described by the Fourier's law of heat transport material with area, A, and thermal conductivity, κ,

$$Q = -\kappa A \nabla T \tag{6}$$

Based on Joule heating and Fourier's law of heat transport described above, the thermoelectric effect can be described by a combination of the Peltier, Seebeck, and Thomson effects as shown in Figs. 4, 5, and 6, by the use of a thermocouple system [96, 97].

The Peltier effect as shown in Fig. 4 is a temperature difference created between two reservoirs by applying a voltage between the two electrodes connected to a

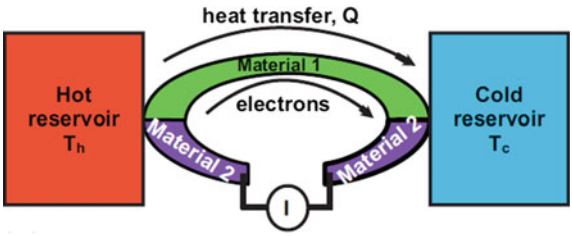

Fig. 4 The thermocouple system between two heat reservoirs required to demonstrate the Peltier effect [97]

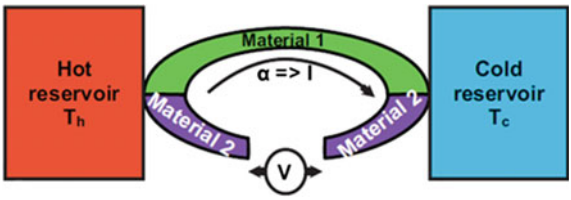

Fig. 5 The thermocouple system between two heat reservoirs required to demonstrate the Seebeck effect [97]

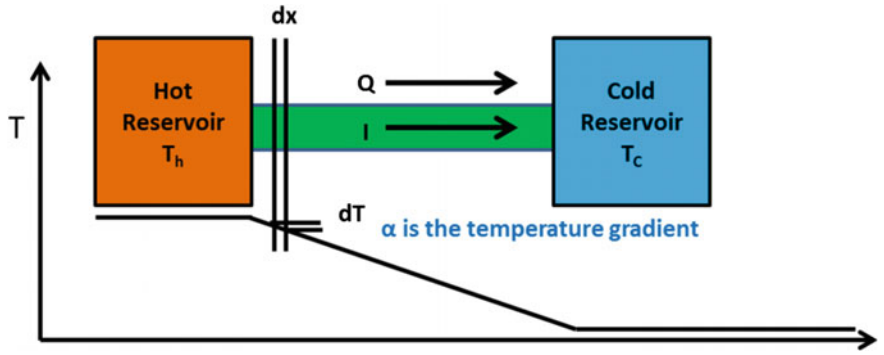

Fig. 6 The Thomson coefficient is required as there will be temperature dependence along any thermoelectric material connected to two heat reservoirs at different temperatures and this produces different Seebeck coefficients along the thermoelectric material. In this diagram, the Seebeck coefficient varies along the x-direction, i.e., $\alpha = \alpha\,(x)$ [97]

material. This phenomenon can be useful when it is necessary to transfer heat from one medium to another. The Peltier effect can be demonstrated by the following equation:

$$\prod = \frac{Q}{I} \tag{7}$$

π is the Peltier coefficient, which can be defined as the heat energy of each electron per unit charge and time from the hot reservoir to the cold reservoir.

The Seebeck effect requires a similar circuit to be constructed but this time, the gap in material two is left open circuit. The open-circuit voltage is proportional to the temperature difference between the reservoirs and can be defined as

$$\alpha = \frac{\mathrm{d}V}{\mathrm{d}T} \tag{8}$$

α is the Seebeck coefficient.

The Seebeck coefficient varies with temperature as shown in Fig. 6. So the heat is both generated and absorbed by the thermocouples. The heat flux gradient can be defined by the equation below:

$$\frac{\mathrm{d}Q}{\mathrm{d}x} = \beta I \frac{\mathrm{d}T}{\mathrm{d}x} \tag{9}$$

β is the Thomson coefficient. All these coefficients can be related to each other by the Kelvin's relationships:

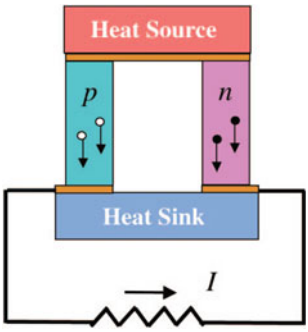

Fig. 7 A thermoelectric couple made of an *n*-type and a *p*-type thermoelectric material. Energy harvesting mode is possible, depending on the above configuration

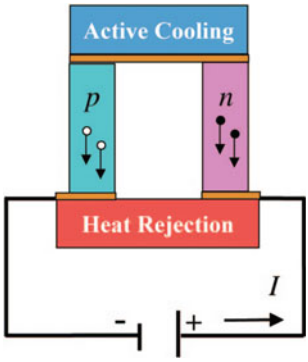

Fig. 8 A Peltier cooling device configuration based on an *n*-type and *p*-type thermoelectric material, as shown in Fig. 7

$$\prod = \alpha T \tag{10}$$

And,

$$\beta = T\frac{\mathrm{d}\alpha}{\mathrm{d}T} \tag{11}$$

Based on the thermoelectric effects described above, thermoelectric devices for energy harvesting (Fig. 7) and cooling system (Fig. 8) can be designed [38, 99]. The potential of the application of a material as a thermoelectric material depends on the figure of merit ZT which is based on several transport coefficients [99]:

$$\mathrm{ZT} = \frac{\alpha^2 T}{\rho\kappa} \tag{12}$$

where ρ is the electrical resistivity, and κ is the total thermal conductivity ($\kappa = \kappa_\mathrm{L} + \kappa_\mathrm{E}$, the lattice and electronic contributions, respectively).

3.2 Historical Implementation of Inorganic Materials: Evolution, Challenges Faced, and Limitations

Efficiency is a key driving factor in the history of thermoelectric materials. Metal thermocouples include some of the early applications of thermoelectric materials. These materials have been used as temperature and radiant energy sensors for many years [100, 101]. Semiconducting thermocouples have been used from the later part of the 1950s. Due to their competitive energy conversion compared with other forms of small-scale electric power generators, these devices have been applied in terrestrial cooling and power generation and later in space power generation [38, 96, 99, 100]. Commercialization of thermoelectric refrigerators started in the 1990s which was followed by the use of thermoelectrics to enhance the functions of automobiles such as thermoelectric cooled and heated seats in and around 2000 [38, 99, 100]. Thermoelectric devices have been largely limited in their applications due to the low efficiency (with ZT < 1). Many new opportunities have opened up due to the use of thermoelectric materials with ZT > 1. The area of energy harvesting has been an area of recent interest [99]. The variation of the figure of merit ZT as a function of the year is shown in Fig. 9 [97, 102–104].

3.3 Applications of Various Conductive Polymers for Organic Active Layers

3.3.1 Ease of Manufacturability

Over the last decade, thermoelectric materials has been investigated for energy harvesting from waste heat and other heat sources. There are commercially

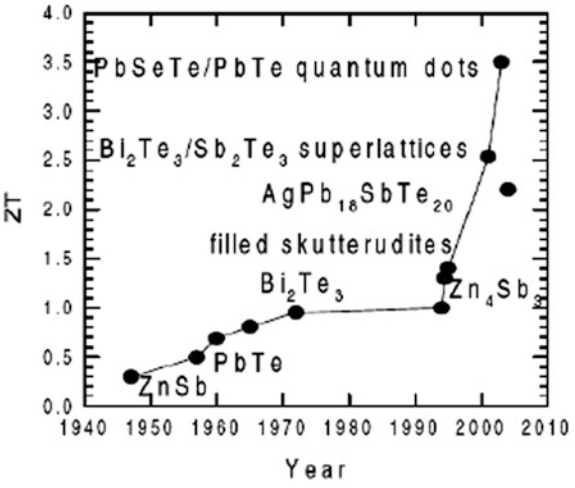

Fig. 9 Variation of the figure of merit ZT as a function of the year [97, 102–104]

Table 1 The electrical conductivity, Seebeck coefficient, thermal conductivity, and thermoelectric figure of merit of a few polymers [13–15, 17, 18, 38, 96–110, 112–115]

Polymer	Conductivity (S/cm)	Seebeck coefficient (μV/K)	Thermal conductivity (W/mK)	Thermoelectric figure of merit ZT at 300 K
Polyacetylene	11,110	28.4	0.7	3.8×10^{-1}
Polypyrrole	100	12	0.1–0.2	2.0×10^{-3}
PEDOT:PSS	55	13	–	1.4×10^{-3}
Polythiophene	100	21	–	6.6×10^{-3}
Poly (carbazolenevinylene) derivative	5×10^{-3}	230	–	8.0×10^{-5}
Polyaniline	7000	7	–	5.1×10^{-2}
Poly(paraphenylene)	10^{-5}	12	–	2.1×10^{-10}
Poly (*p*-phenylenevinylene)	10^{-5}	7	–	7.2×10^{-11}

available thermoelectric semiconductors bismuth telluride (Bi_2Te_3)-based alloys which possess a ZT value of ~ 1 [14, 17, 98]. Recently developed thermoelectrics with higher ZT values show low lattice thermal conductivities [104–106]. However, high ZT values are not the only driving factor in developing viable thermoelectric energy harvesting devices. For energy generation from heat exchangers, waste heat sources, and large volumes of fluids, the thermoelectric materials need to be integrated with these systems [17, 18, 97, 99]. The materials used for fabrication of thermoelectric devices should be easily synthesized, environmentally sustainable, air stable, and solution processable so that large patterns can be created [38, 100, 105]. To meet the above requirements, researchers have looked into polymer-based thermoelectric devices mainly with higher electrical conductivity and low intrinsic thermal conductivities [103, 106–117]. The electrical conductivities, Seebeck coefficients, thermal conductivities, and thermoelectric figure of merit of a few polymers are shown in Table 1.

3.3.2 Tunability: Effect of Doping Level on the Thermoelectric Properties of Conductive Polymers

Organic polymer displays interesting thermoelectric properties [102, 115]. It was shown that the oxidation level of poly(3,4-ethylenedioxythiophene) tosylate (PEDOTTos) was optimized to reach ZT values as high as 0.25 at room temperature. The low intrinsic thermal conductivities of conducting polymers typically range from 0.1 to 0.6 W m^{-1} K^{-1}. Such low thermal conductivity values can be reached with inorganic semiconductors only via complex strategies [14, 18, 96, 98, 106, 114]. One of the approaches to tune the ZT values of these thermoelectric devices is to control a few parameters: the value of the Seebeck coefficient, electrical conductivity of the polymers, the redox rate via chemical doping, and the doping level of these materials [106, 112, 116, 118].

Copolymers and Polymer Blends: Further Methods to Tune Properties

The properties of conductive polymer can be further tuned by the use of copolymers and their blends to modify and enhance the values of the figure of merit ZT [102, 110, 113, 114]. The thermodynamic efficiency of polymer chains can be enhanced by the use of molecular engineering [97, 100, 104, 107]. Copolymerization is a strong tool to introduce and arrange molecular segments in a polymer chain and allows to tailor the properties of polymer-based thermoelectric devices [14, 17, 103]. The values of power factors (power factor = Seebeck coefficient × conductivity) in the literature seen in oligophenylenevinylene-segmented block copolymers and their blends with MEH-PPV, 1.33 μW m^{-1} K^{-2} [119], polyselenophene and its copolymers with 3-methylthiophene via electropolymerization, 12 μW m^{-1} K^{-2} and a copolymer of 1,12-bis(carbazolyl)dodecane and thieno[3,2-b]thiophene, 0.32 μW m^{-1} K^{-2} [14, 38, 106, 107, 109]. Multilayer structuring of polymer films made with different layers of conductive polymers has also been observed [120]. The power factor (6.0 μW m^{-1} K^{-2}) was obtained for a PEDOT:PSS/P3HT bilayered nanofilm.

Ability to Utilize Additives and Their Respective Advantages

Additives and composite polymers have also been investigated to enhance the figure of merit, tune the electrical and thermal conductivities and enhance the Seebeck coefficient of conductive polymers. The final composites fabricated have been shown to maintain low thermal conductivities, ease of processability, mechanical flexibility, low-cost synthesis, and low density [13, 101, 105, 106, 110, 112, 115]. In thermoelectric polymer composites, percolation threshold has to be reached to achieve optimal electrical conductivity [13, 38, 97, 103]. The use of nanostructures also allows the selective blocking of phonons while allowing the transport of charge carriers [98, 113]. Tables 2 and 3 show the thermoelectric properties of some of the composite thermoelectric polymers with organic and inorganic additives.

Table 2 Thermoelectric parameters of conducting polymers composites with carbon materials at room temperature [18, 97, 102, 108, 112, 114]

Polymer composite	Power factor (μW m^{-1} K^{-2})	ZT
SWCNT/PEDOT:PSS, DMSO, GA	25	0.02
CNT/PEDOT stabilizer TCPP	500	–
CNT/PVAc	–	0.006
SWCNT/PEDOT:PSS PVAc	160	–
SWCNT/PEDOT:PSS-layered structure	21.1	–
SWCNT/PANI	0.2	0.004
3D-CNT/PANI	–	0.0022

(continued)

Table 2 (continued)

Polymer composite	Power factor ($\mu W\ m^{-1}\ K^{-2}$)	ZT
CNT-PANI nanofibers	0.16	0.0022
PANI-coated CNT/PANI	–	0.001
poly(3-hexylthiophene) SWCNTs	98	–
MWCNT/polithiophene	–	8.7×10^{-4}
PANI/graphite composites	4.18	1.37×10^{-3}
PANI/graphene nanosheets pellet	5.6	–
PANI/graphene nanosheets film	1.47	–
PANI/graphene nanoplatelets mechanical blending	14	–
PEDOT:PSS/expanded graphite	5.31	–
PEDOT:PSS/graphene fullerene	–	0.06

Table 3 Thermoelectric parameters of polymer composites with inorganic nanoparticles at room temperature [15, 38, 97, 100–102, 110, 112, 115, 119]

Polymer composite	Power factor ($\mu W\ m^{-1}\ K^{-2}$)	ZT
PEDOT:PSS PAA Bi_2Te_3	240	0.2
PEDOT:PSS Bi_2Te_3	131	0.08
PANI Bi_2Te_3 nanorods *p*-type	1.8	0.004
PANI Bi_2Te_3 nanorods *n*-type	10	–
PEDOT:PSS Bi_2Te_3 films	9.9	0.04
PEDOT:PSS Te	70.9	0.1
PEDOT:PSS Te nanowire	100	–
PEDOT:PSS Te nanowire	35	–
PEDOT:PSS gold nanorod	20	–
PH3T Bi_2Te_3	6.3	–

4 Mechanical Vibration-Based Energy Harvesting

Traditionally mechanical energy is transformed into electrical energy by means of a turbine generator. Today, however, we explore other exotic natural sources, large sources of wind and ocean motion, and small movement as in mechanical vibrations. These vibrations can extend from vehicular movement to ambient noise like in a factory [121, 122]. Vibrations and kinetic energy can even be scavenged from the human body as it was discussed in [22] allowing for human motion to be a potential source of energy.

These mechanical vibration-based energy harvesting devices have become a major topic for current research. These novel devices provide a source of energy that can assist in developing self-sustaining sensors [122–126]. The small wireless sensors today require very little energy [124], and maintenance can be cumbersome

with battery replacement, especially if there are numerous sensors to maintain. Currently, our common power supplies today are batteries. According to [124], Lithium-ion batteries have extended their life by a factor of 3 in the past 15 years, but devices have also evolved to use smaller amounts of energy, such that the power supply can be replaced with an energy harvester or in combination with rechargeable batteries.

These harvesters, as previously mentioned, can transform the energy in the environment and convert it into a usable source for sensors. When it comes to vibrations in particular, there are three common methods of transduction, namely electrostatic, electromagnetic, and piezoelectric. According to [123], the two favorite methods for harvesting energy are piezoelectric and electromagnetic because of their higher power densities.

4.1 Electromagnetic Energy Harvesters

In terms of electromagnetism, there are varies forms that energy can take. Electromagnetic waves are one form of electromagnetic energy that can be harvested. This is seen with standard solar panels but can also vary extensively to radio frequencies as well indoor lighting [121, 127]. But for our purposes, we will be discussing devices that operate on Faraday's principle for generating electricity like their macrogenerator counterparts.

4.1.1 Operating Principle and Challenges in Miniaturization of Device

As previously mentioned, the devices that we will cover in detail will be the ones that exploit Faraday's principle of a changing magnetic flux inducing a voltage in a coil. The principle is fairly simple as it is used extensively in the world of power generation. A material that is magnetic is made to move about a coil of conductive wire [128–130]. This movement by the magnet causes an alternating current in the material. In a turbine generator, permanent magnets move inside coils of wire, with the mechanical energy provided by the turbine. In terms of mechanical vibrations, these devices are displaced at a certain frequency providing the movement required for the magnet [130].

Traditionally, these harvesters can be developed using MEMS manufacturing methods (CMOS) in the miniaturization of the Faraday's principle. The mechanical beam or cantilever has a miniature permanent magnet affixed to it as it displaces over flat coils of wire [128–131]. This principle has work for others using silicon [125], but the rigidity of beam is not enough for the purposes of harvesting energy. In [125], the silicon beam is replaced with a type of polymer making the device more flexible. This, however, still uses the concept of a permanent magnet affixed to the cantilever which provides its own set of challenges. Batch manufacturing of devices becomes difficult for magnets fixed on beams [131].

Today's research in more cost-effective methods has lead toward the development and use of composite materials. The authors of [131] have developed an intriguing solution where instead of having a fixed permanent magnet, they use the properties of iron nanowires in a polymer matrix to create a flexible column that acts as permanent magnets. This work was inspired by biological structures called cilia.

4.1.2 Fabrication Using Polymer Nanocomposites

In the current research discussed electromagnetic energy harvesters, a common material has become the nanocomposite comprised of iron nanowires and polydimethylsiloxane (PDMS). This composite used in [37, 131, 132] exploits the flexible properties of the polymer while maintaining the magnetic properties of the iron nanowires.

The production of the iron nanowires has a series of steps outlined by [12–14]. The nanowires are said to be produced by an electrodeposition of iron onto aluminum oxide temples. First a clean aluminum disk is required to be subjected to 2 oxidation steps to give the pores a more uniform distribution on the alumina membrane [131]. This is then followed by the etching of aluminum on the backside to release the alumina membrane. The electrodeposition can commence in a $FeCl_3$ solution. The iron nanowires are then released by etching away the alumina temple in CrO_3 and phosphoric acid solution.

Once the nanowires have been freed, they can now be incorporated into the polymer matrix. The polymer used by [131] is PDMS, and it is first prepared with its curing agent in a 10:1 weight ratio. Once the polymer has been mixed, the nanowires can be added to the mixture in a specified volume fraction; note that [131] uses 4% while [132] uses 18%. The final mixture is mechanically stirred and then the nanocomposite is ready to be cast. Afterward, the PDMS will require a vacuum process to remove unnecessary bubbles in the polymer as well as to be cured at a specified temperature and period of time [131, 132].

Fabrication Methodologies

The fabrication of columns using polymer nanocomposites requires less steps than traditional MEMS, where different layers had to be constructed and then etched away. All that is required for the fabrication of the columns is the nanocomposite mixture and a cast used to shape it. Depending on the application and size, different approaches can be taken. In [131], the columns are developed by cutting holes into poly(methyl methacrylate) (PMMA) with a CO_2 laser cutter where the nanocomposite would be dropped cast. In [132], the nanocomposite is placed on the substrate followed by the PMMA mold cast on top of the nanocomposite. In [133], a silicon mold is used with an array of holes patterned into it. The nanowires are

dropped cast in acetone first with a permanent magnet at the bottom attracting the nanowires. Afterward, the PDMS is applied to the mold and is then peeled off.

Geometry of Harvesters

The principle harvester that was looked into was the one prepared by [131]. The design called for a 12 × 5 array of cilia, with each cilium being 250 μm wide and 2 mm long. The cilia were placed on a planar coil array. Each coil consisted of 14 turns and occupied an area of 600 × 600 μm^2.

Working Principles Behind Energy Capture

The working principle behind the cilia energy capture can be summed up by the electromagnetic principle that is Faraday's law. In [131], we see how the cilia will deflect depending on the force that is exerted on them. As the cilia deflect, they increase the magnetic flux, from the magnetized nanocomposite, as it approaches the coils. Since the neighboring cilia deflection is taken into account, we see that this flux effect is enhanced [131]. As the cilia vibrate over the planar coils, an alternating current will be induced in the coils. And since the coils are in series, the voltages of each coil can be summed up to obtain the total voltage output of the entire array [131].

4.1.3 Challenges and Work Underway

In [122], they discuss how vibration-based microgenerators have issues generating maximum power at any other environmental input other than its resonant frequency. There is a significant drop in power according to [121] and restricts their capability in real application. Therefore, in the review they provide a list of strategies to increase the operating frequency range of these energy harvesters. One typical strategy offered is the periodic tuning of the resonant frequency. Another is using a generator array to widen the bandwidth.

In [128], they add to the discussion that in macroelectromagnetic there is no problem with multiturn coils whereas MEMS systems have difficulties in fabrication due to the poor quality of planar magnets as well as with the number of turns a planar coil can have. Alignment still remains an issue with submillimeter electromagnetic systems.

In [130], the overarching issue remains to be the permanent magnet and its integration into the device, including the magnetization of the material and its use in lamination. This seems to be the prequel for what [131] tries to solve by using a nanocomposite.

4.2 Piezoelectric Energy Harvesters

Piezoelectricity can be defined as a linear electromechanical response between the mechanical and electrical energy states, which is driven by the microscale crystal structure of a material; with a unit cell, that has no center of symmetry [134]. Under application of a mechanical strain, certain classes of crystals become electrically polarized. This reversible phenomenon is called the direct piezoelectric effect. The displacement of ionic charges within a crystal structure is one of the reasons responsible for this effect. In the absence of an external strain, the charge distribution within the crystal is symmetric and the net electric dipole moment, i.e., polarization, is zero. However, when an external stress is applied, the charges are displaced and the charge distribution is no longer symmetric, thereby leading to a polarization. A net polarization develops and results in an electric field. Piezoelectric materials can be primarily subdivided into four major categories—bulk piezoceramics, piezopolymers, piezocomposites, and void charge polymers.

4.2.1 Operating Principal Utilizing Two Categories of Piezogenerators

Single-Phase Piezoceramics

Piezoelectricity as material property was discovered by the Curie Brothers in the early 1880s based on their study on the effects of pressure on tourmaline, quartz, and Rochelle salt [134]. The discovery of new piezoelectric materials in the early 1940s was spurred by the pressing need for high dielectric constant (ε) capacitors. During the mid-1940s, Barium titanate ($BaTiO_3$) was regarded as a new type of ceramic capacitor with high dielectric constant values of around 1100 [135]. This was around the same time that it was established that the domain within the crystallographic grains of the material can be oriented by means of an application of an applied external electric field [135, 136], which is known as the poling process. This produced an electromechanically active ceramic material that behaved similar to a single crystal and possessing piezoelectric properties. Lead zirconate titanate (PZT) was reported as a useful piezoceramic in the 1950s [135] and has been studied extensively in the last few decades and has been one of the most widely used piezoelectric materials for sensor/actuator applications [134, 137].

Single-phase piezoelectric ceramics, such as PZT and $BaTiO_3$, face challenges that limit their applications in energy harvesting devices. Piezoelectric ceramics exhibit poor mechanical properties and are prone to failure, which limits their applications in energy harvesting [138–141]. The brittle nature of piezoelectric ceramics makes these materials susceptible to premature failure when they subjected to static or frequency-dependent mechanical loading or mechanical shock [138–141]. Moreover, the single-phase ceramics exhibit a high stiffness constant and high density which make them mechanically less stable [137]. In addition to that, the piezoelectric ceramics encounter the problems in impedance match and

compatibility of mechanical properties that limit their application as structural health monitoring sensors [142–147]. Polymer-based piezoelectric composite materials increase the number of design degrees of freedom, which enable these materials to be tailored to meet the aforementioned applications [139, 148–150].

Piezocomposites

Piezocomposites comprised of piezoelectric ceramics and polymers are promising materials because of their excellent tailored properties. These materials have many advantages including high coupling factors, low acoustic impedance, mechanical flexibility, a broad bandwidth in combination with low mechanical quality factor [47, 134–137, 142, 143, 145, 151–180]. The mechanical and acoustic properties of these materials can also be tailored according to the nature of application of the composite material [137, 139, 140, 144, 148, 151, 153, 154, 156, 166, 168, 176, 181–194]. Inclusions of conductive filler within polymer matrixes has been demonstrated by several researchers [139, 140, 144, 148, 152, 153, 156, 157, 182–184, 186, 195–197]. All researchers have recorded that the polymer matrix conductivity was enhanced by the addition of electrically conductive fillers. Ma and Wang [166] compared the microstructure and dielectric properties of epoxy-based composites that contained carbon nanotubes (CNTs) and PMN PZT piezoelectric ceramic inclusions. They remarked that the composites exhibited a percolation threshold in the range of 1.0–1.5 g of CNTs per 100 g of epoxy. They also reported that in the region of the percolation threshold, a continuous electrically conductive network was formed and that beyond the percolation threshold, these materials exhibited dynamic loss factors that were superior to those below the percolation threshold and those without semiconductor inclusions. Tian and Wang [179] also investigated the performance of epoxy-MWCNT (multiwalled carbon nanotube) piezoelectric ceramic composites as rigid damping materials. Their results were similar to the results of Ma and Wang [166], where the percolation threshold was found to be in the range of 1.0–1.5 g CNTs per 100 g epoxy. They also concluded that loss factors were significantly higher with the introduction of CNT and (PZT), where the volume fraction of CNT was above the critical electrical percolation loading.

Piezopolymers

Piezoelectric nanogenerators based on oriented assembly of nanowires have been investigated for converting mechanical energy into electrical energy [139, 148–150]. Flexible piezoelectric generators have attracted considerable attention in recent years on account of their potential applications in mechanical energy scavenging devices using portable, wearable, and implantable electronics. Structural approaches propose to enhance the output power of the flexible piezoelectric generator using polyvinylidene fluoride (PVDF) [152, 173–175, 198–200], use of a

substrate and curved structure, and optimization of the aspect ratio of the generator responsible for maximizing output power density. Through these approaches, induced stress and output voltage of the generator are analyzed by finite element modeling and validated through experiments [173, 174, 200, 201].

PVDF is the most popular and most commonly cited piezoelectric polymer used in electromechanical devices. This is because it has large piezoelectric charge coefficient approximately between 20 and 28 pC/N [200], compared with other common polymers. As for fabrication, prepoled PVDF and PVDF–TrFE films of various thicknesses are commercially available [199, 200]. Such films have been used to develop MEMS pressure sensors and as energy harvesting devices [151]. Parylene-C is commonly used as an electrically insulating or encapsulation material in MEMS and microfabrication [151, 202]. This can be attributed to its biocompatibility, chemical inertness, and more importantly its distinctive vapor deposition technique. This deposition technique allows conformal coating over any surface, irrespective of its porosity. The physical deposition method for parylene consists of three steps: evaporation, pyrolysis, and deposition [151, 202]. The parylene-C molecular structure has a molecular dipole due to the single chlorine atom in the benzene ring [151]. Polyimide has been used in MEMS as a structural material. Its high glass-transition temperature (360–410 °C) permits it to be used in high-temperature applications [203].

Voided Charge Polymers

Voided charged polymers or cellular polymers are the materials that contain internal gas voids. When the polymer surfaces encompassing the voids are charged, these charged voids in the polymer behave like a piezoelectric material. This structure was first invented by Gerhard Sessler in the early 1960s [204] when he developed a microphone by making use of charged polymer devices, and hence, those were called ‘space-charged electrets.’ It was not until the late 1980s that researchers adopted the concept of treating the space-charged electrets as a ‘black box’ and studied the piezoelectricity and pyroelectricity of such materials [10, 205]. The concept of piezoelectricity in voided charged polymers is popularly known as ferroelectrets or piezoelectrets. Ferroelectric material possesses spontaneous polarization; that is, they can be reversed in a direction of the applied electric field over a specific temperature range. It usually involves a two-step fabrication procedure. The first one is the creation of air voids inside the polymer film. The second step is to resize the voids to permit higher charge density on the surfaces and hence generating higher piezoelectric response. The resulting fabricated film is typically in the range of 80–100 μm thick. The synthesis of cellular piezoelectric polymers (PP) essentially comprises of three steps: (a) generation of the voids by introducing micron-sized particles inside the polymers and by stretching, (b) causes the adjustment of the void size through the applied gas pressure and heating cycles, and (c) generation of dipoles through electrode or corona poling [205]. The resultant cellular polymer has anisotropic lens-like-shaped voids with crystallinity under

50%. Voids also can be formed by diffusion of supercritical CO_2 inside the polymer film (in this case, polyethylene naphthalate (PEN)) followed by heating to help expand the gas contained in the film and thereby causing voids [206]. To form multilayer-based VCP, it is fabricated to bond several layers with multiple porous surfaces, which introduces the voids in between the layers. This could be through bonding layers of different materials or properties such as porous polytetrafluoroethylene (PTFE) (Teflon-R) and non-porous fluoroethylenepropylene (FEP) [207, 208]. Cellular parylene is fabricated by vapor deposition of parylene on a silicon mold micromachined by reactive ion etching. The silicon is etched to release the parylene structure that is clamped to the silicon wafer. This structure is charged with the unique soft X-ray setup [209]. The piezoelectric coefficient in voided charge polymers is correlated with the density and shape of the voids which can affect the distribution of the formed dipoles. The type and pressure of gas inside the voids affects the amount of ionization occurring during the poling process [205, 206].

4.2.2 Comparison and Advantage of Piezoelectric Polymers Over Inorganic Piezoelectric Materials

Several researchers have studied two-phase piezoelectric polymer composites aimed at replacing the use of homogeneous piezoelectric ceramic material in practical conditions owing to the aforementioned mechanical limitations [137, 139] listed above. In two-phase composites, the individual materials combine to improve its overall applicability to several applications alike [182, 210]. Two-phase composites with uniformly distributed ferroelectric fillers within a continuous polymer matrix have been studied toward the development of materials for devices in energy harvesting with high stiffness [211] and structural health monitoring devices [181]. Despite these so-called two-phase composites exhibiting marked increase in mechanical properties compared to their homogeneous ceramic counterparts they show reduced electrical properties due to the insulating nature of the polymer matrix [186]. The overall piezoelectric and dielectric properties also show decreased values due to the low properties exhibited by the polymer matrix [212, 213]. The non-uniform dispersion of the ferroelectric ceramic fillers is caused due to formation of localized clusters leading to agglomerations in the composite microstructure, thereby further contributing to the insulating nature of the composite [148, 197]. The electrical properties of the matrix may be improved by introducing spherical electrically conducting metallic particle inclusions [139, 188] and/or high aspect ratio conductive inclusions such as carbon nanotubes (CNTs) [184, 214]; however, there is less literature about the mechanisms that govern the changes in properties such as electron tunneling, electron hopping [215], matrix cracking, and various interfacial effects [216] between the inclusions and the matrix. Also, more studies need to be carried out in interpreting their effects on the physical relationships between different phases and the measured properties by studying the microstructure of the material. The purpose of this study is to

investigate the influence of multiwalled carbon nanotubes (MWCNTs) as a third conducting phase on the dielectric and piezoelectric properties of PZT-epoxy-MWCNT three-phase piezoelectric composites.

Flexible thick-/thin-film piezoelectric composite materials have been investigated for applications ranging from micro-/nanogenerators, micro-/nanosensors, to meso-scale energy harvesters, and sensing devices [137, 139–148, 151, 157, 181, 187, 192, 211, 217, 218]. The electrode is influential in determining the sensitivity of the device and in the effectiveness of energy conversion [160, 202, 219]. Ideal electrodes ensure good lattice matching between itself and the piezoelectric material leading to enhanced mobility of charge carries owing to reduced contact resistance between the composite film surface and the electrode. Traditionally, metals such as silver, gold, copper, carbon, or aluminum have been used as electrode materials acting as points of contact for these flexible piezoelectric devices [160, 217, 220]. Graphene has emerged as an attractive alternative to these metal electrodes because of its high mechanical strength, superior flexibility, and high contact area in comparison with these traditional metal electrodes [47, 162, 172, 178, 191, 221–226].

4.2.3 Conclusions, Challenges, and Future Outlook

Two-phase composites that contain electrically conductive inclusions which are uniformly distributed have garnered a lot of attention due to their potential scalability, the ease of processing, and their overall flexibility [221, 227]. For the application of embedded capacitors, two-phase polymer–metal and two–phase ceramic–metal [176, 214] offer good choices. Two-phase composites with MWCNT conductive inclusions in PMMA show marked improvement in its electrical properties as the volume fraction increases [228, 229] with dramatic increase in electrical conductivity as the volume fraction goes above 0.1% of MWCNT [148, 188]. One functional difficulty with these kinds of percolative composites is the formation of continuous networks also known as conductive pathways either by direct contact of neighboring conductive particles or by electron tunneling causing a sharp increase in electrical conductivity leading to higher dielectric loss [152, 212]. In two-phase PZT-epoxy composites, researchers have shown a decrease in the dielectric constant from around 1000 for the single-phase PZT to values of around 50 [230] for two-phase PZT-epoxy composites. Even the values of the piezoelectric strain coefficients decrease from $\sim$20 pC/N for the single-phase to values <5 pC/N for the two-phase ferroelectric polymer composites [161, 212]. This can be attributed to the decrease in mobile charge carries as a result of the addition of the polymer matrix [231]. In order to tackle this problem, researchers have looked at introducing electrically conductive inclusions, as a third phase uniformly distributed within the polymer matrix [186, 188]. The conductive filler drives several physical properties such as the dielectric constant and electrical resistivity of the composite. Polymer matrix composites with piezoelectric inclusions have shown a lot of promise in applications as sensors and actuators, but a lot of areas need to be investigated. Some of them are described below.

The addition of electrically conductive inclusions improves the piezoelectric and dielectric properties of such composites as a result of mobilization of charge carriers which in turn increase the polarization. These improved material properties are directly correlated with the increasing content, i.e., volume fractions of the conductive inclusions as long as they are below the percolation threshold. Percolation is the formation of continuous clusters of the conductive inclusions when their volume fraction exceeds a critical value, this is usually associated with a sharp increase in overall conductivity of the composite. Further, the interfacial interaction also plays an important role in driving physical properties of the composite [63]. The electrode on the surface of the composite greatly influences the dielectric and piezoelectric properties as they contribute to mobilization of charge carriers which is dependent on the number of contact points between the surface of the film and the electrode [202]. Another contributing factor toward influencing the properties of the composite is the nature of the interactions between the different phases such as the conductive inclusions, the matrix material, and the active piezoelectric phase [153, 184].

A more profound understanding of the interaction of different phases within the composite is required in order to improve the charge storage capabilities of these materials. By studying the influence of different inclusions, we can improve the dielectric constant of such materials and hence store charge more effectively; this can, in turn, propel these materials to be further used in energy harvesting materials.

References

1. Service RF (2005) Is it time to shoot for the sun? Science 309(5734):548–551
2. Potočnik J (2007) Renewable energy sources and the realities of setting an energy agenda. Science 315(5813):810–811
3. Schiermeier Q, Tollefson J, Scully T, Witze A, Morton O (2008) Energy alternatives: electricity without carbon. Nature 454:816–823
4. International Energy Agency (2010) PV environmental, health and safety activities. Photovoltaic Power systems Programme
5. Metz A et al (2015) International technology roadmap for photovoltaic
6. Osborne M (2013) First solar hits cost reduction milestone. PV tech
7. Department of Energy. Sunshot initiative mission. Office of Energy Efficiency and Renewable Energy
8. Bailie CD, Christoforo MG, Mailoa JP, Bowring AR, Unger EL, Nguyen WH, Burschka J, Pellet N, Lee JZ, Gratzel M, Noufi R, Buonassisi T, Salleo A, McGehee MD (2015) Semi-transparent perovskite solar cells for tandems with silicon and CIGS. Energy Environ Sci 8(3):956–963
9. Green M (2003) Third generation photovoltaics: advanced solar energy conversion. Springer series in photonics. Springer, Berlin
10. Eriksson SK, Josefsson I, Ellis H, Amat A, Pastore M, Oscarsson J, Lindblad R, Eriksson AIK, Johansson EMJ, Boschloo G, Hagfeldt A, Fantacci S, Odelius M, Rensmo H (2016) Geometrical and energetical structural changes in organic dyes for dye-sensitized solar cells probed using photoelectron spectroscopy and DFT. Phys Chem Chem Phys 18 (1):252–260

11. Wang ZL, Wu W (2012) Nanotechnology-enabled energy harvesting for self-powered micro-/nanosystems. Angew Chem Int Ed 51(47):11700–11721
12. Wang ZL (2012) Progress in piezotronics and piezo-phototronics. Adv Mater 24(34): 4632–4646
13. Minnich AJ, Dresselhaus MS, Ren ZF, Chen G (2009) Bulk nanostructured thermoelectric materials: current research and future prospects. Energy Environ Sci 2(5):466–479
14. Liu W, Yan Z, Chen G, Ren Z (2012) Recent advances in thermoelectric nanocomposites. Nano Energy 1(1):42–56
15. Sootsman JR, Chung DY, Kanatzidis MG (2009) New and old concepts in thermoelectric materials. Angew Chem Int Ed 48(46):8616–8639
16. Chandrakasan AP, Verma N, Daly DC (2008) Ultralow-power electronics for biomedical applications. Annu Rev Biomed Eng 10(1):247–274
17. Leonov V (2011) Human machine and thermoelectric energy scavenging for wearable devices. ISRN Renew Energy 2011:11
18. Culebras M, Gómez CM, Cantarero A (2014) Review on polymers for thermoelectric applications. Materials 7(9):6701
19. Roundy S, Leland ES, Baker J, Carleton E, Reilly E, Lai E, Otis B, Rabaey JML, Wright PK, Sundararajan V (2005) Improving power output for vibration-based energy scavengers. IEEE Pervasive Comput 4(1):28–36
20. Wang X (2012) Piezoelectric nanogenerators—harvesting ambient mechanical energy at the nanometer scale. Nano Energy 1(1):13–24
21. Mathúna CÓ, Donnell TO, Martinez-Catala RV, Rohan J, O'Flynn B (2008) Energy scavenging for long-term deployable wireless sensor networks. Talanta 75(3):613–623
22. Mitcheson PD, Yeatman EM, Rao GK, Holmes AS, Green TC (2008) Energy harvesting from human and machine motion for wireless electronic devices. Proc IEEE 96(9): 1457–1486
23. Bouendeu E, Greiner A, Smith PJ, Korvink JG (2011) A low-cost electromagnetic generator for vibration energy harvesting. IEEE Sens J 11(1):107–113
24. Mitcheson PD, Miao P, Stark BH, Yeatman EM, Holmes AS, Green TC (2004) MEMS electrostatic micropower generator for low frequency operation. Sens Actuators, A 115 (2–3):523–529
25. Ramsay MJ, Clark WW (2001) Piezoelectric energy harvesting for bio-MEMS applications. In: SPIE Proceedings 4332
26. Chu B, Zhou X, Ren K, Neese B, Lin M, Wang Q, Bauer F, Zhang QM (2006) A dielectric polymer with high electric energy density and fast discharge speed. Science 313(5785): 334–336
27. Barber P, Balasubramanian S, Anguchamy J, Gong S, Wibowo A, Gao H, Ploehn HJ, Loye HZ (2009) Polymer composite and nanocomposite dielectric materials for pulse power energy storage. Materials 2(4):1697
28. Siddabattuni S, Schuman TP (2014) Polymer ceramic nanocomposite dielectrics for advanced energy storage, in polymer composites for energy harvesting, conversion, and storage. Am Chem Soc 1161:165–190
29. Wang Q, Zhu L (2011) Polymer nanocomposites for electrical energy storage. J Polym Sci Part B Polym Phys 49(20):1421–1429
30. Siddabattuni S, Schuman TP, Dogan F (2011) Improved polymer nanocomposite dielectric breakdown performance through barium titanate to epoxy interface control. Mater Sci Eng 176(18):1422–1429
31. Nayak S, Rahaman M, Pandey AK, Setua DK, Chaki TK, Kastgir D (2013) Development of poly (dimethylsiloxane)—titania nanocomposites with controlled dielectric properties: effect of heat treatment of titania on electrical properties. J Appl Polym Sci 127(1):784–796
32. Tang H, Ma Z, Zhong J, Yang J, Zhao R, Liu X (2011) Effect of surface modification on the dielectric properties of PEN nanocomposites based on double-layer core/shell-structured $BaTiO_3$ nanoparticles. Colloids Surf A 384(1–3):311–317

33. Arnold DP (2007) Review of microscale magnetic power generation. IEEE Trans Magn 43 (11):3940–3951
34. Wang P, Tanaka K, Sugiyama S, Dai X, Zhao X, Liu J (2009) A micro electromagnetic low level vibration energy harvester based on MEMS technology. Microsyst Technol 15(6): 941–951
35. Amirtharajah R, Chandrakasan AP (1998) Self-powered signal processing using vibration-based power generation. IEEE J Solid-State Circuits 33(5):687–695
36. Alfadhel A, Li B, Zaher A, Yassine O, Kosel J (2014) A magnetic nanocomposite for biomimetic flow sensing. Lab Chip 14(22):4362–4369
37. Alnassar M, Alfadhel A, Ivanov YP, Kosel J (2015) Magnetoelectric polymer nanocomposite for flexible electronics. J Appl Phys 117(17):17D711
38. Zheng JC (2008) Recent advances on thermoelectric materials. Front Phys China 3(3): 269–279
39. Khaled SR, Sameoto D, Evoy S (2014) A review of piezoelectric polymers as functional materials for electromechanical transducers. Smart Mater Struct 23(3):033001
40. Kim HS, Kim JH, Kim J (2011) A review of piezoelectric energy harvesting based on vibration. Int J Precis Eng Manuf 12(6):1129–1141
41. Saadon S, Sidek O (2011) A review of vibration-based MEMS piezoelectric energy harvesters. Energy Convers Manag 52(1):500–504
42. Tang CW (1986) Two-layer organic photovoltaic cell. Appl Phys Lett 48(2):183–185
43. Yu G, Gao J, Hummelen JC, Wudl F, Heeger AJ (1995) Polymer photovoltaic cells: enhanced efficiencies via a network of internal donor-acceptor heterojunctions. Science 270 (5243):1789–1791
44. Thompson BC, Frecher JMJ (2008) Polymer-fullerene composite solar cells. Angew Chem Int Ed 47(1):58–77
45. Hoppe H, Sariciftci NS (2004) Organic solar cells: an overview. J Mater Res 19(07): 1924–1945
46. Carsten D, Dyakonov V (2010) Polymer—fullerene bulk heterojunction solar cells. Rep Prog Phys 73(9):096401
47. Park SH, Roy A, Beaupré S, Cho S, Coates N, Moon JS, Moses D, Leclerc M, Lee K, Heeger AJ (2009) Bulk heterojunction solar cells with internal quantum efficiency approaching 100%. Nat Photonics 3(5):297–302
48. Liang Y, Xu Z, Xia J, Tsai ST, Wu Y, Li G, Ray C, Yu L (2010) For the bright future-bulk heterojunction polymer solar cells with power conversion efficiency of 7.4%. Adv Mater 22 (20):E135–E138
49. Krebs FC, Tromholt T, Jørgensen M (2010) Upscaling of polymer solar cell fabrication using full roll-to-roll processing. Nanoscale 2(6):873–886
50. Koeppe R, Sariciftci NS (2006) Photoinduced charge and energy transfer involving fullerene derivatives. Photochem Photobiol Sci 5(12):1122–1131
51. Kumar JSD, Das S (1997) Photoinduced electron transfer reactions of amines: synthetic applications and mechanistic studies. Res Chem Intermed 23(8):755–800
52. Brabec CJ, Cravino A, Meissner D, Sariciftci NS, Fromherz T, Rispens MT, Sanchez L, Hummelen JC (2001) Origin of the open circuit voltage of plastic solar cells. Adv Funct Mater 11(5):374–380
53. Hashiguchi M, Obata N, Maruyama M, Yeo KS, Ueno T, Ikebe T, Takahashi I, Matsuo Y (2012) $FeCl_3$-mediated synthesis of fullerenyl esters as low-LUMO acceptors for organic photovoltaic devices. Org Lett 14(13):3276–3279
54. Arkhipov VI, Bassler H (2004) Exciton dissociation and charge photogeneration in pristine and doped conjugated polymers. Phys Status Solidi A 201(6):1152–1187
55. Gaines GL, O'Neil MP, Svec WA, Niemczyk MP, Wasielewski MR (1991) Photoinduced electron transfer in the solid state: rate vs. free energy dependence in fixed-distance porphyrin-acceptor molecules. J Am Chem Soc 113(2):719–721

56. Brabec CJ, Winder C, Sariciftci NS, Hummelen JC, Dhanabalan A, Van Hal PA, Janssen RAJ (2002) A low-bandgap semiconducting polymer for photovoltaic devices and infrared emitting diodes. Adv Funct Mater 12(10):709–712
57. Winder C, Matt G, Hummelen JC, Janssen RAJ, Sariciftci NS, Brabec CJ (2002) Sensitization of low bandgap polymer bulk heterojunction solar cells. Thin Solid Films 403–404:373–379
58. Koster LJA, Kuo CY, Yuan MC, Jeng US, Su CJ, Wei KH (2006) Ultimate efficiency of polymer/fullerene bulk heterojunction solar cells. Appl Phys Lett 88(9):093511
59. Soci C, Huang IW, Moses D, Zhu Z, Waller D, Gaudiana R, Brabec CJ, Heeger AJ (2007) Photoconductivity of a low-bandgap conjugated polymer. Adv Funct Mater 17(4):632–636
60. Scharber MC, Dennler M, Ameri T, Denk P, Forberich K, Waldauf C, Brabec CJ (2006) Design rules for donors in bulk-heterojunction solar cells—towards 10% energy-conversion efficiency. Adv Mater 18(6):789–794
61. Mihailetchi VD, Mihailetchi, Van Duren JKJ, Blom PWM, Hummelen JC, Janssen RAJ, Kroon JM, Rispens MT, Verhees WJH, Wienk MM (2003) Electron transport in a methanofullerene. Adv Funct Mater 13(1):43–46
62. Singh TB, Marjanović N, Stadler P, Auinger M, Matt GJ, Günes S, Sariciftci NS, Schwödiauer R, Bauer S (2005) Fabrication and characterization of solution-processed methanofullerene-based organic field-effect transistors. J Appl Phys 97(8):083714
63. Hoppe H, Sariciftci NS (2006) Morphology of polymer/fullerene bulk heterojunction solar cells. J Mater Chem 16(1):45–61
64. Yang X, Loos J (2007) Toward high-performance polymer solar cells: the importance of morphology control. Macromolecules 40(5):1353–1362
65. Shaheen SE, Brabec CJ, Sariciftci NS, Padinger F, Fromherz T, Hummelen JC (2001) 2.5% efficient organic plastic solar cells. Appl Phys Lett 78(6):841–843
66. Hoppe H, Niggemann M, Winder C, Kraut J, Hiesgen R, Hinsch A, Meissner D, Sariciftci NS (2004) Nanoscale morphology of conjugated polymer/fullerene-based bulk-heterojunction solar cells. Adv Funct Mater 14(10):1005–1011
67. Yang X, van Duren JK, Janssen RA, Michels MA, Loos J (2004) Morphology and thermal stability of the active layer in poly(p-phenylenevinylene)/methanofullerene plastic photovoltaic devices. Macromolecules 37(6):2151–2158
68. Ma W, Yang C, Gong X, Lee K, Heeger AJ (2005) Thermally stable, efficient polymer solar cells with nanoscale control of the interpenetrating network morphology. Adv Funct Mater 15(10):1617–1622
69. Li G, Shrotriya V, Huang J, Yao Y, Moriarty T, Emery K, Yang Y (2005) High-efficiency solution processable polymer photovoltaic cells by self-organization of polymer blends. Nat Mater 4(11):864–868
70. Reyes R, Kim K, Carroll DL (2005) High-efficiency photovoltaic devices based on annealed poly(3-hexylthiophene) and 1-(3-methoxycarbonyl)-propyl-1-phenyl-(6,6)C61 blends. Appl Phys Lett 87(8):083506
71. Kim Y, Choulis SA, Nelson J, Bradley DDC, Cook S, Durrant JR (2005) Device annealing effect in organic solar cells with blends of regioregular poly(3-hexylthiophene) and soluble fullerene. Appl Phys Lett 86(6):063502
72. Padinger F, Rittberger RS, Sacriciftci NS (2003) Effects of postproduction treatment on plastic solar cells. Adv Funct Mater 13(1):85–88
73. Sivula K, Ball ZT, Watanabe N, Frecher JMJ (2006) Amphiphilic diblock copolymer compatibilizers and their effect on the morphology and performance of polythiophene: fullerene solar cells. Adv Mater 18(2):206–210
74. Stalmach U, Boer BD, Videlot C, Hutten PFV, Hadziioannou G (2000) Semiconducting diblock copolymers synthesized by means of controlled radical polymerization techniques. J Am Chem Soc 122(23):5464–5472
75. Kim JY, Kim SH, Lee HH, Lee K, Ma W, Gong X, Heeger AJ (2006) New architecture for high-efficiency polymer photovoltaic cells using solution-based titanium oxide as an optical spacer. Adv Mater 18(5):572–576

76. Liu R (2014) Hybrid organic/inorganic nanocomposites for photovoltaic cells. Materials 7 (4):2747
77. Silva C (2013) Organic photovoltaics: some like it hot. Nat Mater 12(1):5–6
78. Deibel C, Strobel T, Dyakonov V (2010) Role of the charge transfer state in organic donor-acceptor solar cells. Adv Mater 22(37):4097–4111
79. Bansal N, Reynolds LX, MacLachlan A, Lutz T, Ashraf RS, Zhang W, Nielsen CB, McCulloch I, Rebois DG, Kirchartz T, Hill MS, Molloy KC, Nelson J, Haque SA (2013) Influence of crystallinity and energetics on charge separation in polymer-inorganic nanocomposite films for solar cells. Sci Rep 3:1531
80. Bhardwaj RK, Kushwaha HS, Gaur J, Upreti T, Bharti V, Gupta V, Chaudhary N, Sharma GD, Banerjee K, Chand S (2012) A green approach for direct growth of CdS nanoparticles network in poly(3-hexylthiophene-2,5-diyl) polymer film for hybrid photovoltaic. Mater Lett 89:195–197
81. Xia C, Wang N, Kim X (2011) Mesoporous CdS spheres for high-performance hybrid solar cells. Electrochim Acta 56(25):9504–9507
82. Greaney MJ, Brutchey RL (2012) Improving open circuit potential in hybrid P3HT:CdSe bulk heterojunction solar cells via colloidal tert-butylthiol ligand exchange. ACS Nano 6 (5):4222–4230
83. Schierhorn M, Boettcher SW, Peet JH, Matioli E, Bazan GC, Stuck YGD, Moskovits M (2010) CdSe nanorods dominate photocurrent of hybrid CdSe–P3HT photovoltaic cell. ACS Nano 4(10):6132–6136
84. Tan ZN, Zhang WQ, Qian DP, Zheng H, Xiao SQ, Yang YP, Zhu T, Xu J (2011) Efficient hybrid infrared solar cells based on P3HT and PbSe nanocrystal quantum dots. Mater Sci Forum 685:38–43
85. Zhu T, Berger A, Tan Z, Cui D, Xu J, Khanchaitit P, Wang Q (2008) Composition-limited spectral response of hybrid photovoltaic cells containing infrared PbSe nanocrystals. J Appl Phys 104(4):044306
86. Jangwon S, Kim SJ, Kim WJ, Singh R, Samoc M, Cartwright AN, Prasad PN (2009) Enhancement of the photovoltaic performance in PbS nanocrystal: P3HT hybrid composite devices by post-treatment-driven ligand exchange. Nanotechnology 20(9):095202
87. Wang Z, Qu S, Zeng X, Zhang C, Shi M, Tan F, Wang Z, Liu J, Hou Y, Teng F, Feng Z (2008) Synthesis of MDMO-PPV capped PbS quantum dots and their application to solar cells. Polymer 49(21):4647–4651
88. Feng Y, Yun D, Zhang X, Feng W (2010) Solution-processed bulk heterojunction photovoltaic devices based on poly(2-methoxy,5-octoxy)-1,4-phenylenevinylene-multiwalled carbon nanotubes/PbSe quantum dots bilayer. Appl Phys Lett 96(9):093301
89. Baeten L, Conings B, Boyen HG, D'Haen J, Hardy A, D'Olieslaeger M, Manca JV, Van Bael MK (2011) Towards efficient hybrid solar cells based on fully polymer infiltrated ZnO nanorod arrays. Adv Mater 23(25):2802–2805
90. Noori K, Giustino F (2012) Ideal energy-level alignment at the ZnO/P3HT photovoltaic interface. Adv Funct Mater 22(24):5089–5095
91. Zhao J, He C, Yang R, Shi Z, Cheng M, Yang W, Xie G, Wang D, Shi D, Zhang G (2012) Ultra-sensitive strain sensors based on piezoresistive nanographene films. Appl Phys Lett 101(6):063112–063115
92. Zhu R, Jiang CY, Liu B, Ramakrishna S (2009) Highly efficient nanoporous TiO_2-polythiophene hybrid solar cells based on interfacial modification using a metal-free organic dye. Adv Mater 21(9):994–1000
93. Shankar K, Mor GK, Paulose M, Varghese OK, Grimes CA (2008) Effect of device geometry on the performance of TiO_2 nanotube array-organic semiconductor double heterojunction solar cells. J Non-Cryst Solids 354(19–25):2767–2771
94. Ren S, Chang LY, Lim SK, Zhao J, Smith M, Zhao N, Bulović V, Bawendi M, Gradečak S (2011) Inorganic–organic hybrid solar cell: bridging quantum dots to conjugated polymer nanowires. Nano Lett 11(9):3998–4002

95. Yun D, Xia X, Zhang S, Bian Z, Liu R, Huang C (2011) ZnO nanorod arrays with different densities in hybrid photovoltaic devices: fabrication and the density effect on performance. Chem Phys Lett 516(1–3):92–95
96. Li L (2015) Thermoelectric energy harvesting via piezoelectric material. arXiv.org
97. Paul D (2014) Thermoelectric energy harvesting. In: Fagas G (ed) ICT-energy-concepts towards zero-power information and communication technology
98. LeBlanc S (2014) Thermoelectric generators: linking material properties and systems engineering for waste heat recovery applications. Sustain Mater Technol 1–2:26–35
99. Tritt TM, Subramanian MA (2006) Thermoelectric materials, phenomena, and applications: a bird's eye view. MRS Bull 31(3):188–198
100. Wood C (1988) Materials for thermoelectric energy conversion. Rep Prog Phys 51(4):459
101. DiSalvo FJ (1999) Thermoelectric cooling and power generation. Science 285(5428): 703–706
102. Dubey N, Lecerc M (2011) Conducting polymers: efficient thermoelectric materials. J Polym Sci Part B Polym Phys 49(7):467–475
103. Meng C, Liu C, Fan S (2010) A promising approach to enhanced thermoelectric properties using carbon nanotube networks. Adv Mater 22(4):535–539
104. Snyder GJ, Toberer ES (2008) Complex thermoelectric materials. Nat Mater 7(2):105–114
105. Venkatasubramanian R, Siivola E, Colpitts T, O'Quinn B (2001) Thin-film thermoelectric devices with high room-temperature figures of merit. Nature 413(6856):597–602
106. Bubnova O, Khan ZU, Malti A, Braun S, Fahlman M, Berggren M, Crispin X (2011) Optimization of the thermoelectric figure of merit in the conducting polymer poly (3,4-ethylenedioxythiophene). Nat Mater 10(6):429–433
107. Yu C, Kim YS, Kim D, Grunlan JC (2008) Thermoelectric behavior of segregated-network polymer nanocomposites. Nano Lett 8(12):4428–4432
108. Kim D, Kim Y, Choi K, Grunlan JC, Yu C (2010) Improved thermoelectric behavior of nanotube-filled polymer composites with poly(3,4-ethylenedioxythiophene) poly(styrene-sulfonate). ACS Nano 4(1):513–523
109. Sun Y, Sheng P, Di C, Jiao F, Xu W, Qiu D, Zhu D (2012) Organic thermoelectric materials and devices based on p- and n-type poly(metal 1,1,2,2-ethenetetrathiolate)s. Adv Mater 24 (7):932–937
110. Abramson AR, Kim WC, Huxtable ST, Yan H, Wu Y, Majumdar A, Tien CL, Yang P (2004) Fabrication and characterization of a nanowire/polymer-based nanocomposite for a prototype thermoelectric device. J Microelectromech Syst 13(3):505–513
111. Xia Y, Sun K, Ouyang J (2012) Solution-processed metallic conducting polymer films as transparent electrode of optoelectronic devices. Adv Mater 24(18):2436–2440
112. Bubnova O, Krispin X (2012) Towards polymer-based organic thermoelectric generators. Energy Environ Sci 5(11):9345–9362
113. Kraemer D, Poudel B, Feng HP, Caylor JC, Yu B, Yan X, Ma Y, Wang X, Wang D, Muto A, McEnaney K, Chiesa M, Ren Z, Chen G (2011) High-performance flat-panel solar thermoelectric generators with high thermal concentration. Nat Mater 10(7):532–538
114. Du Y, Shen SZ, Cai K, Casey PS (2012) Research progress on polymer—inorganic thermoelectric nanocomposite materials. Prog Polym Sci 37(6):820–841
115. Zhang B, Sun J, Katz HE, Fang F, Opila RL (2010) Promising thermoelectric properties of commercial PEDOT:PSS materials and their Bi_2Te_3 powder composites. ACS Appl Mater Interfaces 2(11):3170–3178
116. Kaiser AB (2001) Electronic transport properties of conducting polymers and carbon nanotubes. Rep Prog Phys 64(1):1
117. Carpi F, De Rossi D (2005) Electroactive polymer-based devices for e-textiles in biomedicine. IEEE Trans Inf Technol Biomed 9(3):295–318
118. Jun T, Akio T, Kikuko K (1990) Structure and electrical properties of polyacetylene yielding a conductivity of 10 5 S/cm. Jpn J Appl Phys 29(1R):125

119. Taylor PS, Karasz LK, Wilusz E, Lahti PM, Karasz FE (2013) Thermoelectric studies of oligophenylenevinylene segmented block copolymers and their blends with MEH-PPV. Synth Met 185–186:109–114
120. Shi H, Liu C, Xu J, Song H, Lu B, Jiang F, Zhou W, Zhang G, Jiang Q (2013) Facile fabrication of PEDOT:PSS/polythiophenes bilayered nanofilms on pure organic electrodes and their thermoelectric performance. ACS Appl Mater Interfaces 5(24):12811–12819
121. Kazmierski TJ (2014) Energy harvesting systems. Springer, Berlin
122. Zhu D, Tudor MJ, Beeby SP (2009) Strategies for increasing the operating frequency range of vibration energy harvesters: a review. Meas Sci Technol 21(2):022001
123. Dallago E, Danioni A, Marchesi M, Nucita V, Venchi G (2011) A self-powered electronic interface for electromagnetic energy harvester. IEEE Trans Power Electron 26(11): 3174–3182
124. Vullers R, Doms I, Hoof CV, Mertens R (2009) Micropower energy harvesting. Solid-State Electron 53(7):684–693
125. Yang B, Lee C, Xiang W, Xie J, He JH, Kotlanka RK, SiewPingLow Feng H (2009) Electromagnetic energy harvesting from vibrations of multiple frequencies. J Micromech Microeng 19(3):035001
126. Foisal ARM, Hong C, Chung CS (2012) Multi-frequency electromagnetic energy harvester using a magnetic spring cantilever. Sens Actuators, A 182:106–113
127. Carvalho CMF, Manuel C, Paulino, Veríssimo NFS (2016) CMOS indoor light energy harvesting system for wireless sensing applications. Springer, Berlin
128. Arnold DP (2007) Review of microscale magnetic power generation. IEEE Trans Magn 43 (11):3940–3951
129. Beeby SPR, Torah N, Tudor MJ, Glynne-Jones P, Donnell TO, Saha CR, Roy S (2007) A micro electromagnetic generator for vibration energy harvesting. J Micromech Microeng 17 (7):1257
130. Cook-Chennault Thambi KN, Sastry AM (2008) Powering MEMS portable devices—a review of non-regenerative and regenerative power supplies systems with special emphasis on piezoelectric energy harvesting systems. Smart Mater Struct 17(4):043001
131. Khan MA, Alfadhel A, Kosel J (2016) Magnetic nanocomposite cilia energy harvester. IEEE Trans Magn: 1–4
132. Alfadhel A, Li B, Zaher A, Yassine O, Kosel J (2014) A magnetic nanocomposite for biomimetic flow sensing. Lab Chip 14(22):4362–4369
133. Zhou B, Xu W, Syed AA, Chau Y, Chen L, Chew B, Yassine O, Wu X, Gao Y, Zhang J, Xiao X, Kosel J, Zhang XX, Yao Z, Wen W (2015) Design and fabrication of magnetically functionalized flexible micropillar arrays for rapid and controllable microfluidic mixing. Lab Chip 15(9):2125–2132
134. Jordan OTL, Ounaies Z (2001) Piezoelectric ceramics characterization. Institute for Computer Applications in Science and Engineering (ICASE)
135. Haertling GH (1999) Ferroelectric ceramics: history and technology. J Am Ceram Soc 82 (4):797–818
136. Scala EP (1996) A brief history of composites in the U.S.—the dream and the success. JOM 48(2):45–48
137. Venkatragavaraj E, Satish B, Vinod PR, Vijaya MS (2001) Piezoelectric properties of ferroelectric PZT-polymer composites. J Phys D Appl Phys 34(4):487
138. Zhang TY, Kuo CM, Barnett DM, Willis JR (2002) Fracture of piezoelectric ceramics. In: Adv Appl Mech: 147–289
139. Banerjee S, Hennault KAC (2012) An investigation into the influence of electrically conductive particle size on electromechanical coupling and effective dielectric strain coefficients in three phase composite piezoelectric polymers. Compos Part A Appl Sci Manuf 43(9):1612–1619
140. Banerjee S, Hennault KAC (2013) Fabrication of dome-shaped PZT-epoxy actuator using modified solvent and spin coating technique. J Electroceram: 1–11

141. Banerjee S, Hennault KAC (2011) Influence of Al particle size and lead zirconate titanate (PZT) volume fraction on the dielectric properties of PZT-epoxy-aluminum composites. J Eng Mater Technol 133:041016
142. Rianyoi R, Potong R, Jaitanong N, Yimnirun R, Chaipanich A (2011) Dielectric, ferroelectric and piezoelectric properties of 0–3 barium titanate–Portland cement composites. Appl Phys A 104(2):661–666
143. Jaitanong N, Chaipanich A, Tunkasiri T (2008) Properties 0–3 PZT–Portland cement composites. Ceram Int 34(4):793–795
144. Chaipanich A, Jaitanong N, Yimnirun R (2009) Ferroelectric hysteresis behavior in 0–3 PZT-cement composites: effects of frequency and electric field. Ferroelectr Lett 36(3–4): 59–66
145. Huang S, Chang J, Xu R, Liu F, Lu L, Ye Z, Cheng X (2004) Piezoelectric properties of 0–3 PZT/sulfoaluminate cement composites. Smart Mater Struct 13(2):270
146. Li Z, Zhang D, Wu K (2002) Cement-based 0–3 piezoelectric composites. J Am Ceram Soc 85(2):305–313
147. Banerjee S, Chennault KC. Influence of Al inclusions and PZT volume fraction on the dielectric and piezoelectric characteristics of three phase PZT-cement-Al composites. In: Advances in Cement Research. Accepted for Publication
148. Banerjee S, Chennault KC (2011) Influence of Al particle size and lead zirconate titanate (PZT) volume fraction on the dielectric properties of PZT-epoxy-aluminum composites. J Eng Mater Technol 133(4):041016
149. Banerjee S, Du W, Wang L, Chennault KAC (2013) Fabrication of dome-shaped PZT-epoxy actuator using modified solvent and spin coating technique. J Electroceram 31(1–2):148–158
150. Banerjee S, Rajesh K, Chennault CAK, Manish C (2013) Multi-walled carbon-nanotube based flexible piezoelectric films with graphene monolayers. Energy Environ Focus 2 (3):195–202
151. Chennault CK, Thambi N, Sastry AM (2008) Powering MEMS portable devices—a review of non-regenerative and regenerative power supply systems with special emphasis on piezoelectric energy harvesting systems. Smart Mater Struct 17(4):043001
152. Dang ZM, Fan LZ, Shen Y, Nan CW (2003) Dielectric behavior of novel three-phase MWNTs/$BaTiO_3$/PVDF composites. Mater Sci Eng B 103(2):140–144
153. Dang ZM, Yao SH, Yuan JK, Bai J (2010) Tailored dielectric properties based on microstructure change in $BaTiO_3$-carbon nanotube/polyvinylidene fluoride three-phase nanocomposites. J Phys Chem C 114(31):13204–13209
154. Dong B, Li Z (2005) Cement-based piezoelectric ceramic smart composites. Compos Sci Technol 65(9):1363–1371
155. Frank S, Poncharal P, Wang ZL, De Hee WA (1998) Carbon nanotube quantum resistors. Science 280(5370):1744–1746
156. Gong H, Zhang Y, Quan J, Che S (2011) Preparation and properties of cement based piezoelectric composites modified by CNTs. Curr Appl Phys 11(3):653–656
157. Gullapalli H, Vemuru VSM, Kumar A, Mendez AB, Vajtai R, Terrones M, Nagarajaiah S, Ajayan PM (2010) Flexible piezoelectric ZnO–paper nanocomposite strain sensor. Small 6 (15):1641–1646
158. Hong SY, Glasser SP (1999) Alkali binding in cement pastes: part I. The C-S-H phase. Cem Concr Res 29(12):1893–1903
159. Hosseinzadegan H, Smith AD, Niklaus F, Paussa A, Vaziri S, Fischer AC, Sterner M, Forsberg F, Delin A, Esseni D, Palestri P, Östling M, Lemme MC (2012) Graphene has ultra high piezoresistive gauge factor. In: 2012 IEEE 25th international conference on micro electro mechanical systems (MEMS)
160. Kok SL, White NM, Harris NR (2008) Free-standing thick-film piezoelectric device. Electron Lett 44(4):280–281
161. Kuo DH, Chang CC, Su TY, Wang WK, Lin BY (2001) Dielectric behaviours of multi-doped $BaTiO_3$/epoxy composites. J Eur Ceram Soc 21(9):1171–1177

162. Kymakis E, Stratakis E, Stylianakis MM, Koudoumas E, Fotakis C (2011) Spin coated graphene films as the transparent electrode in organic photovoltaic devices. Thin Solid Films 520(4):1238–1241
163. Levy N, Burke SA, Meaker KL, Panlasigui M, Zettl A, Guinea F, Neto AHC, Crommie MF (2010) Strain-induced pseudo-magnetic fields greater than 300 Tesla in graphene nanobubbles. Science 329(5991):544–547
164. Li FX, Fang DN, Liu YM (2006) Domain switching anisotropy in poled lead titanate zirconate ceramics under orthogonal electromechanical loading. J Appl Phys 100 (8):084101–084106
165. Li X, Zhang RW, Wang K, Wei J, Wu D, Cao A, Li Z, Cheng Y, Quanshui Zheng Q, Ruoff RS, Zhu H (2012) Stretchable and highly sensitive graphene-on-polymer strain sensors. Sci Rep 2:1–6
166. Ma M, Wang X (2009) Preparation, microstructure and properties of epoxy-based composites containing carbon nanotubes and PMN-PZT piezoceramics as rigid piezo-damping materials. Mater Chem Phys 116(1):191–197
167. Maiti Suin S, Shrivastava NK, Khatua BB (2013) Low percolation threshold in melt-blended PC/MWCNT nanocomposites in the presence of styrene acrylonitrile (SAN) copolymer: preparation and characterizations. Synth Met 165:40–50
168. Miao X, Tongay S, Hebard AF (2012) Strain-induced suppression of weak localization in CVD-grown graphene. J Phys Condens Matter 24(47):475304
169. Nagarajan V, Ganpule CS, Nagaraj B, Aggarwal S, Alpay SP, Roytburd AL, Williams ED, Ramesh R (1999) Effect of mechanical constraint on the dielectric and piezoelectric behavior of epitaxial $Pb(Mg_{1/3}Nb_{2/3})O_3$(90%)–$PbTiO_3$(10%) relaxor thin films. Appl Phys Lett 75 (26):4183–4185
170. Romasanta L, Hernández M, Manchado ML, Verdejo R (2011) Functionalised graphene sheets as effective high dielectric constant fillers. Nanoscale Res Lett 6(1):1–6
171. Satish B, Sridevi K, Vijaya MS (2002) Study of piezoelectric and dielectric properties of ferroelectric PZT-polymer composites prepared by hot-press technique. J Phys D Appl Phys 35(16):2048
172. Schedin F, Geim AK, Morozov SV, Hill EW, Blake P, Katsnelson MI, Novoselov KS (2007) Detection of individual gas molecules adsorbed on graphene. Nat Mater 6(9): 652–655
173. Seema A, Dayas KR, Vargheze JM (2007) PVDF-PZT-5H composites prepared by hot press and tape casting techniques. J Appl Polym Sci 106(1):146–151
174. Sencadas V, Mendez SL, Filho RG, Chinaglia DL, Pouzada AS (2005) Influence of the processing conditions and corona poling on the morphology of β-PVDF. In: Proceedings of 12th International Symposium on Electrets (ISE-12)
175. Senthilkumar R, Sridevi K, Jambunathan V, Vijaya MS (2005) Investigations on ferroelectric PZT-PVDF composites of 0–3 connectivity. Ferroelectrics 325(1):121–130
176. Shen Y, Guan Y, Hu Y, Lei Y, Song Y, Lin Y, Nan CW (2013) Dielectric behavior of graphene/BaTiO[sub 3]/polyvinylidene fluoride nanocomposite under high electric field. Appl Phys Lett 103(7):072906-4
177. Song Y, ZhuDi Z, WenXue Y, Bo L, XinFang C (2007) Morphological structures of poly(vinylidene fluoride)/montmorillonite nanocomposites. Sci China Ser B Chem 50(6):790–796
178. Sordan R, Traversi F, Russo V (2009) Logic gates with a single graphene transistor. Appl Phys Lett 94(7):073305-3
179. Tian S, Wang X (2008) Fabrication and performances of epoxy/multi-walled carbon nanotubes/piezoelectric ceramic composites as rigid piezo-damping materials. J Mater Sci 43 (14):4979–4987
180. Topsakal M, Bagci VMK, Salim Ciraci S (2010) Current-voltage (I-V) characteristics of armchair graphene nanoribbons under uniaxial strain. Phys Rev B 81:205437

181. Akiyama M, Morofuji Y, Kamohara T, Nishikubo K, Tsubai M, Fukuda O, Ueno N (2006) Flexible piezoelectric pressure sensors using oriented aluminum nitride thin films prepared on polyethylene terephthalate films. J Appl Phys 100(11):114318-5
182. Banerjee S, Chennault CAK (2011) An analytical model for the effective dielectric constant of a 0–3–0 composite. J Eng Mater Technol 133(4):041005
183. Banerjee S, Chennault CAK, Capera R, Chowela M (2013) Influence of Al inclusions and PZT volume fraction on the dielectric and piezoelectric characteristics of three phase PZT-cement-Al composites. In: Advances in Cement Research. Accepted For Publication
184. Banerjee S, Chennault CAK (2013) Multi walled carbon nanotube based flexible multi-morph composite thick films with graphene electrodes. Energy Environ Focus
185. Biercuk MJ, Llaguno MC, Radosavljevic M, Hyun JK, Johnson AT, Fischer JE (2002) Carbon nanotube composites for thermal management. Appl Phys Lett 80(15):2767–2769
186. Choi HW, Heo YW, Lee JH, Kim JJ, Lee HY, Park ET, Chung YK (2006) Effects of $BaTiO_3$ on dielectric behavior of $BaTiO_3$-Ni-polymethyl methacrylate composites. Appl Phys Lett 89(13):132910-132910-3
187. Chennault CKA, Thambi N, Hameyie EB (2008) Piezoelectric energy harvesting: a green and clean alternative for sustained power production. Bull Sci Technol Soc 28(6):496–509
188. Dang ZM, Shen Y, Nan CW (2002) Dielectric behavior of three-phase percolative Ni–BaTiO[sub 3]/polyvinylidene fluoride composites. Appl Phys Lett 81(25):4814–4816
189. Gao G, Çagin T, Goddard WA (1998) Energetics, structure, mechanical and vibrational properties of single-walled carbon nanotubes. Nanotechnology 9(3):184
190. Li Z, Biqin Dong B, Zhang D (2005) Influence of polarization on properties of 0–3 cement-based PZT composites. Cement Concr Compos 27(1):27–32
191. Liang Y, Frisch J, Zhi L, Norouzi-Arasi H, Feng X, Rabe JP, Koch N, Müllen K (2009) Transparent, highly conductive graphene electrodes from acetylene-assisted thermolysis of graphite oxide sheets and nanographene molecules. Nanotechnology 20(43):434007
192. Nan CW, Liu L, Cai N, Zhai J, Ye J, Lin YH, Dong LJ, Xiong CX (2002) A three-phase magnetoelectric composite of piezoelectric ceramics, rare-earth iron alloys, and polymer. Appl Phys Lett 81(20):3831–3833
193. Thomas M, Folliard K, Drimalas T, Ramlochan T (2008) Diagnosing delayed ettringite formation in concrete structures. Cem Concr Res 38(6):841–847
194. Yadav K, Smelser CW, Jacob S, Blanchetiere C, Callender CL, Albert J (2011) Simultaneous corona poling of multiple glass layers for enhanced effective second-order optical nonlinearities. Appl Phys Lett 99(3):031109
195. Bao WS, Meguid SA, Zhu ZH, Pan Y, Weng GJ (2012) A novel approach to predict the electrical conductivity of multifunctional nanocomposites. Mech Mater 46:129–138
196. Blanas P, Gupta KD (1999) Composite piezoelectric materials for health monitoring of composite structures. In: MRS Proceedings
197. Yao SH, Dang ZM, Jiang MJ, Bai J (2008) BaTiO[sub 3]-carbon nanotube/polyvinylidene fluoride three-phase composites with high dielectric constant and low dielectric loss. Appl Phys Lett 93(18):182905-3
198. Arlt K, Wegener M (2010) Piezoelectric PZT/PVDF-copolymer 0–3 composites: aspects on film preparation and electrical poling. IEEE Trans Dielectr Electr Insul 17(4):1178–1184
199. Dietze M, Es-Souni M (2008) Structural and functional properties of screen-printed PZT–PVDF-TrFE composites. Sens Actuators, A 143(2):329–334
200. Oliveira F, Leterrier Y, Manson JA, Sereda O, Neels A, Dommann A, Damjanovic D (2014) Process influences on the structure, piezoelectric, and gas-barrier properties of PVDF-TrFE copolymer. J Polym Sci Part B Polym Phys 52(7):496–506
201. Son YH, Kweon SY, Kim SJ, Kim YM, Hong TW, Lee YG (2007) Fabrication and electrical properties of Pzt-Pvdf 0–3 type composite film. Integr Ferroelectr 88(1):44–50
202. Pedersen T, Hindrichsen CC, Thomsen EV (2007) Investigation of top/bottom electrode and diffusion barrier layer for PZT thick film MEMS Sensors. In: Sensors IEEE

203. Ounaies Z, Park C, Harrison J, Lillehei P (2008) Evidence of piezoelectricity in SWNT-polyimide and SWNT-PZT-polyimide composites. J Thermoplast Compos Mater 21(5):393–409
204. Sessler GM, West JE (1962) Self-biased condenser microphone with high capacitance. J Acoust Soc Am 34(11):1787–1788
205. Gerhard-Multhaupt R (2002) Less can be more. Holes in polymers lead to a new paradigm of piezoelectric materials for electret transducers. IEEE Trans Dielectr Electr Insul 9(5): 850–859
206. Fang P, Qiu X, Wirges W, Gerhard R (2010) Polyethylene-naphthalate (PEN) ferroelectrets: cellular structure, piezoelectricity and thermal stability. IEEE Trans Dielectr Electr Insul 17 (4):1079–1087
207. Zhang X, Huang J, Wang X, Xia Z (2010) Piezoelectricity and dynamic characteristics of laminated fluorocarbon films. IEEE Trans Dielectr Electr Insul 17(4):1001–1007
208. Hu Z, Seggern HV (2006) Breakdown-induced polarization buildup in porous fluoropolymer sandwiches: a thermally stable piezoelectret. J Appl Phys 99(2):024102
209. Feng Y, Hagiwara K, IguchiY Suzuki Y (2012) Trench-filled cellular parylene electret for piezoelectric transducer. Appl Phys Lett 100(26):262901
210. Banerjee S, Chennault KAC (2014) Influence of aluminium inclusions on dielectric properties of three-phase PZT–cement–aluminium composites. Adv Cement Res 26:63–76
211. Park KI (2010) Piezoelectric $BaTiO_3$ thin film nanogenerator on plastic substrates. Nano Lett 10(12):4939–4943
212. Qi L, Lee BI, Samuels WD, Exarhos GJ, Parler SG (2006) Three-phase percolative silver–$BaTiO_3$–epoxy nanocomposites with high dielectric constants. J Appl Polym Sci 102 (2):967–971
213. Zhao LY, Gu JG, Ma HR, Sun ZG (2010) Mechanical properties and curing kinetics of epoxy resins cured by various amino-terminated polyethers. Chin J Polym Sci 28(6): 961–969
214. Zepu W, Nelson JK, Miao J, Linhardt RJ, Schadler LS (2012) Effect of high aspect ratio filler on dielectric properties of polymer composites: a study on barium titanate fibers and graphene platelets. IEEE Trans Dielectr Electr Insul 19(3):960–967
215. Bao WS, Meguid SA, Zhu ZH, Weng GJ (2012) Tunneling resistance and its effect on the electrical conductivity of CNT nanocomposites. J Appl Phys 111:093726
216. Yang W, Pan Y, Pelegri AA (2013) Multiscale modeling of matrix cracking coupled with interfacial debonding in random glass fiber composites based on volume elements. J Compos Mater 47(27):3389–3399
217. Pan CT, Liu ZH, Chen YC, Liu CF (2010) Design and fabrication of flexible piezo-microgenerator by depositing ZnO thin films on PET substrates. Sens Actuators, A 159(1):96–104
218. Huang S, Chang J, Lu L, Liu F, Ye Z, Cheng X (2006) Preparation and polarization of 0–3 cement based piezoelectric composites. Mater Res Bull 41(2):291–297
219. Kok SL, White NM, Harris NR (2009) Fabrication and characterization of free-standing thick-film piezoelectric cantilevers for energy harvesting. Meas Sci Technol 20(12):124010
220. Chung SY, Kim S, Lee JH, Kim K, Kim SW, Kang SCY, Yoon SJ, Kim YS (2012) All-solution-processed flexible thin film piezoelectric nanogenerator. Adv Mater 24 (45):6022–6027
221. Park H, Brown PR, Bulović V, Kong J (2011) Graphene as transparent conducting electrodes in organic photovoltaics: studies in graphene morphology, hole transporting layers, and counter electrodes. Nano Lett 12(1):133–140
222. Eda G, Fanchini G, Chhowalla M (2008) Large-area ultrathin films of reduced graphene oxide as a transparent and flexible electronic material. Nat Nano 3(5):270–274
223. Wang X, Zhi L, Müllen K (2007) Transparent, conductive graphene electrodes for dye-sensitized solar cells. Nano Lett 8(1):323–327

224. Ren Y, Zhu C, Cai W, Li H, Ji H, Kholmanov I, Wu Y, Piner RD, Ruoff RS (2012) Detection of sulfur dioxide gas with graphene field effect transistor. Appl Phys Lett 100 (16):163114-4
225. Yavari F, Chen Z, Thomas AV, Ren W, Cheng HM, Koratkar N (2011) High sensitivity gas detection using a macroscopic three-dimensional. Sci Rep 1:1–5
226. Chen G, Paronyan TM, Harutyunyan AR (2012) Sub-ppt gas detection with pristine graphene. Appl Phys Lett 101(5):053119-4
227. Baughman RH, Zakhidov AA, Heer WA (2002) Carbon nanotubes—the route toward applications. Science 297(5582):787–792
228. Schmidt RH, Kinloch JA, Burgess AN, Windle AH (2007) The effect of aggregation on the electrical conductivity of spin-coated polymer/carbon nanotube composite films. Langmuir 23(10):5707–5712
229. Chen H, Muthuraman H, Stokes P, Zou J, Liu X, Wang J, Huo Q, Khondaker SI, Zhai L (2007) Dispersion of carbon nanotubes and polymer nanocomposite fabrication using trifluoroacetic acid as a co-solvent. Nanotechnology 18(41):415606
230. Pascariu V, Padurariu L, Avadanei O, Mitoseriu L (2013) Dielectric properties of PZT–epoxy composite thick films. J Alloy Compd 574:591–599
231. Bauhofer W, Kovacs JZ (2009) A review and analysis of electrical percolation in carbon nanotube polymer composites. Compos Sci Technol 69(10):1486–1498

Energy Harvesting from Crystalline and Conductive Polymer Composites

Aravind Kumar, Shaikh Faruque Ali and A. Arockiarajan

Abstract Modern electronic devices require less energy on-board and could be powered by energy harvested from the environment. Mechanical vibrations are attractive sources for energy harvesting due to their high availability in technical environments. Among the various mechanisms available to convert mechanical energy into electrical energy, piezoelectric transduction offers high power density at microenergy scales. In piezoelectric energy harvesters, the amount of electrical energy harvested directly depends on the strain undergone by the transducer. Commonly used piezoelectric transducers are made of perovskite ceramics such as PZT and are brittle. This limits the maximum allowable strain in the harvester and consequently the power harvested. In such cases, electroactive polymers act as viable alternatives due to their flexibility. Energy harvesting from conductive and crystalline electroactive polymers is explored in this chapter. Crystalline polymers such as polyurethane and semicrystalline polymers such as PVDF are commonly used in energy harvesting devices owing to their flexibility, affordability, and good electromechanical coupling properties. This chapter begins with a brief account on the material properties of PVDF and polyurethane. Subsequently, design of energy harvesters based on these materials is elucidated. A short note on energy harvesting from crystalline biopolymers such as cellulose nanocrystals is also included therein. Such harvesters are attractive as they are environment friendly and biocompatible. Among conductive polymer composites, harvesters based on polyaniline and carbon nanotubes are described. A comparison between the harvesting capabilities of different electroactive polymers and the challenges faced are discussed to draw an overall picture on energy harvesting from electroactive polymers.

Keywords Energy harvesting · Electroactive polymers · PVDF · Cellulose nanocrystals · Piezoelectricity · Polyurethane · Electrostriction · Conducting polymers · Thermogalvanic cells · Carbon nanotubes

A. Kumar · S.F. Ali (✉) · A. Arockiarajan
Department of Applied Mechanics, Indian Institute of Technology Madras, Chennai 600036, India
e-mail: sfali@iitm.ac.in

D. Ponnamma et al. (eds.), *Smart Polymer Nanocomposites*,
Springer Series on Polymer and Composite Materials,
DOI 10.1007/978-3-319-50424-7_2

Contents

1 Introduction

The realm of wireless devices is witnessing an exponential growth ever since its inception. But the extent of services offered by these devices is often limited by the lifetime of batteries powering them. A self-sustainable power source would thus thrust us forward to exploit the potential of such devices exhaustively. The current technological revolution is propelled by miniaturization, and as devices continue to shrink, less energy is required on-board. This has encouraged the researchers to explore the possibility of augmenting batteries with systems that continuously scavenge otherwise wasted energy from the environment [1–3]. This process of converting otherwise wasted ambient energy into a useful form is called *energy harvesting or scavenging*.

Energy harvesting would augment sustainable power supply to a wireless system network and might even offset the need to replace and to maintain the batteries in areas that are either inhospitable or difficult to reach. This includes applications such as safety monitoring devices, structure-embedded microsensors, and medical implants, to name a few. There are also environmental benefits associated with energy harvesting as it provides a 'battery-less' solution by scavenging energy from ambient energy sources such as vibrations, heat, light, and water and converting it into electrical power [4].

Mechanical energy harvesting converts energy from movement or vibration into electrical energy. The mechanical energy sources encompass vibrations and noise from industrial machinery and equipment, transportation, fluid flow such as air movements, biological locomotion such as walking, or in-body motion such as chest and heart movement. In general, there are two main ways of extracting energy from a mechanical source, *inertial* and *kinematic* [5].

Inertial energy harvesting relies on the resistance to acceleration of a mass. These systems consist of a spring-mass-damper system connected to the base at a single point. When the base moves, the mass vibrates due to its inertia, and these vibrations can be converted into electrical energy. Examples of harvester designs exploiting this principle of inertia include those based on cantilever beams [6, 7], pendulums [8, 9], and magnetoelastic oscillators [10–12].

In kinematic energy harvesting, the energy harvesting transducer is directly coupled to different parts of the source. The relative motion between these parts leads to a deformation in the transducer, which is then converted into electrical energy. Examples include harvesting energy from the bending of a tire wall to monitor pressure, or the flexing and extension of limbs to power mobile.

At present, mechanical-to-electricity energy conversion is mostly accomplished via electrostatic, electromagnetic, or piezoelectric transduction mechanisms [13]. Power density for piezoelectric transduction exceeds that for electromagnetic generators below 0.5 cm^3 [14], and consequently, they represent promising materials for electromechanical energy conversion technologies at smaller scales.

In piezoelectric energy harvesting, the power harvested is directly dependent on the strain and the electromechanical coupling coefficient of the material employed for electromechanical transduction. Piezoelectric ceramics such as lead zirconate titanate and barium titanate have very high electromechanical coupling coefficients, but they are very brittle, with the maximum strain that they can undergo being limited to 0.2% in case of polycrystalline materials and 1% in case of single-crystal piezoelectrics [15]. On the other hand, electroactive polymers (EAPs) generally undergo strains greater than 1%, and certain classes of EAPs can even go up to 50% [15]. But the electromechanical coefficient of EAPs is comparatively less than that of piezoceramics. Hence, in either case, the limitation of the material sets an upper bound to the power that can be harvested from the motion of the host structure. Hence, current research focuses on improving the ductility of piezoceramics and the coupling coefficient of electroactive polymers.

Knowledge of existing energy harvesting technologies, their advantages, and limitations would be essential in setting up the foundation for future research directions in the field. Hence, this chapter is dedicated to such a comprehensive review on energy harvesting technologies, particularly involving conductive and crystalline electroactive polymers. The properties of various electroactive polymers will be discussed initially, and further discussions will focus on the design and analysis of energy harvesters based on these polymers.

2 Electroactive Polymers (EAPs)

EAPs are polymers that undergo a change in shape and dimensions when subjected to an electric field [16]. EAPs are primarily used as actuators in aerospace [17–19], medical [20], and robotics [21] applications. They are also used as artificial muscles

in biomimetic applications [16, 22]. Recently, researchers have started to explore the power scavenging capabilities of EAPs. Most of the EAPs get electrically polarized when subjected to a mechanical strain. Since EAPs are flexible and can undergo large deformations, they are seen as potential alternatives for the conventional piezoceramics in the field of energy harvesting.

EAPs are classified into two families, namely electronic and ionic [16]. Electronic EAPs exhibit electromechanical coupling due to polarization based or electrostatic mechanisms [15]. Electronic EAPs are insulators and contain bound charges in the form of electric dipoles. Most of the electronic EAPs are either crystalline or semicrystalline. The crystal units within these polymers contain atoms with partial charges and generate dipole moments. For example, the electromechanical coupling in polyvinylidene fluoride (PVDF) is provided by a polar crystalline phase resulting from the spatially symmetric location of fluorine and hydrogen atoms along the polymer chain [23]. Thus, the inherent electromechanical coupling in polymers such as PVDF can be attributed to their crystalline nature. However, there are few amorphous polymers which exhibit electromechanical coupling. In such polymers, the electromechanical coupling is due to the freezing of electrical dipoles in the material below the glass transition temperature [23]. Examples of this type include polyimides.

Based on the relation between mechanical strain and electric polarization, the electronic EAPs can be further divided into ferroelectric and electrostrictive. Ferroelectric polymers exhibit a linear relationship between strain and polarization, whereas in electrostrictive polymers, strain is proportional to the square of polarization. PVDF is a classic example of ferroelectric polymer, while its co-polymers with trifluoroethylene (P(VDF-TrFE)) are electrostrictive. Another electrostrictive polymer, polyurethane, is also widely used for energy harvesting.

Ionic EAPs exhibit electromechanical coupling due to the diffusion of charged species within the polymer network. The diffusion of charged molecules or atoms gives rise to electrical conductivity in ionic EAPs. Such diffusion also leads to electromechanical coupling in these materials due to the accumulation of charges within the material [15].

Ionic EAPs are further subdivided into ionic polymer–metal composites (IPMCs) and conductive polymer composites [24]. IPMCs are based on ionic migration through a selective ionic membrane. Such selective ionic membranes allow only a particular species of ions (either anions or cations) to pass through them. Examples of this kind include Nafion and Flemion. Nafion is used in selective migration of hydrogen ions in proton exchange membrane fuel cells (PEMFCs). Conductive polymer composites undergo redox reactions in the presence of an electrolyte and, consequently, exhibit a change in volume. Polyaniline and polypyrrole are examples of this type. Electrical energy can be harvested from a conductive polymer composite kept in an electrolyte medium through the mechano-chemo-electric process, but the efficiency is very low [25]. However, composites made of conducting fillers such as carbon nanotubes and polymer materials such as PVDF and polydimethylsiloxane (PDMS) have better electromechanical coupling and are widely used in energy harvesting.

The energy harvesters based on ferroelectric, electrostrictive, and conductive polymers differ in their working principle. The material behavior plays an important role in the harvester design. Hence, a brief introduction to the properties of these materials is given, and energy harvesters based on these materials are discussed subsequently. Among crystalline polymers, the harvesters based on PVDF (ferroelectric semicrystalline polymer), cellulose nanocrystals (piezoelectric biopolymer), and polyurethane (electrostrictive polymer) are elucidated. Among polymers, harvesting energy using polyaniline, polypyrrole, and conducting polymer composites with carbon nanotube fillers is described to illustrate the principles involved.

3 Energy Harvesting from Ferroelectric Polymers

Ferroelectric materials are those which exhibit, at temperatures below Curie temperature (T_c), a domain structure and spontaneous polarization which can be reoriented by applied electric fields [23]. Common examples of ferroelectric materials are the perovskite ceramics such as barium titanate ($BaTiO_3$) and lead zirconate titanate (PZT) and polymers such as PVDF.

The domain morphology of ferroelectric materials results from the alignment of dipoles to minimize electrostatic and elastic energy, and materials with this structure will exhibit varying degrees of hysteresis at all drive levels. In the unpoled state (paraelectric phase), a positive strain is realized in these materials, whatever be the direction of application of electric field. To achieve bidirectional strains, these materials are poled and operated around this poled state. For low-to-moderate input fields, the response of the material around this poled state is approximately linear. Such materials operating in these linear regimes are designated as piezoelectric materials [23]. However, the terms ferroelectricity and piezoelectricity are interchangeably used in many literature, and this is a common misnomer.

Piezoelectricity is observed in a variety of synthetic polymers such as polypropylene, polystyrene, and nylon-11. Biopolymer substances such as cellulose with an asymmetric crystal structure also exhibit piezoelectricity. But the electromechanical coupling in these materials is very weak. Strong electromechanical coupling has been observed only in PVDF and its co-polymers. The piezoelectric properties of PVDF were discovered by Kawaii in 1969. PVDF is a semicrystalline polymer with approximately 50% crystallinity [26]. The molecular structure of PVDF consists of the repeated monomer unit **–CF_2–CH_2–**. The atoms are covalently bonded, forming long molecular chains. The hydrogen atoms are positively charged, and the fluorine atoms are negatively charged with respect to the carbon atoms, giving rise to electric dipoles within individual crystallites. Hence, PVDF is inherently polar. However, the average macroscopic polarization of the unpoled material is zero due to the random orientation of the individual crystallites. Permanent dipole polarization of PVDF is generally obtained by stretching and

polarizing extruded thin sheets of the polymer. A review of the various polarization methods is given by Sessler [27].

Typically, PVDF is produced in thin films whose thicknesses range from 9 to 800 μm (10^{-6} m). A thin layer of nickel, silver, or copper is deposited on both surfaces to provide electrical conductivity when an electric field is applied, or to allow measuring the charge induced by mechanical deformation [26].

3.1 Electromechanical Properties of PVDF

Typically, the piezoelectric properties of PVDF are determined within the framework of linear piezoelectric theory. The basic properties of a piezoelectric material are expressed mathematically as a relationship between two mechanical variables, stress σ and strain ε, and two electrical variables, electric field E and electric displacement D. Generally, applying stress to an elastic material will result in the deformation of the material. The ratio of change in dimension to the original dimension is called the strain. Assuming a uniaxial state of strain, the stress σ and strain ε along the direction of loading can be related by the Hooke's law:

$$\varepsilon = \frac{1}{Y}\sigma = S\sigma \tag{1}$$

where Y is the modulus of elasticity of the material and $S = 1/Y$ is the inverse of the modulus of elasticity known as compliance of the material.

For a piezoelectric material, the application of a mechanical stress also leads to accumulation of surface charges in the material, in addition to the mechanical strain. This is known as the direct piezoelectric effect. The surface charge accumulated per unit area is defined as the electric displacement D and is related to the stress as follows:

$$D = d\sigma \tag{2}$$

where d is known as the piezoelectric strain coefficient and is a measure of the coupling between mechanical and electrical domains. The piezoelectric strain coefficient d is equal to the eigenstrain developed in the piezoelectric material on application of unit electric field to the material. This definition is derived from the inverse piezoelectric effect which is elucidated by Eq. (3).

Just as the application of mechanical stress leads to an electric displacement, the application of an electric field also produces a mechanical strain in a piezoelectric material. This converse phenomenon is known as the inverse piezoelectric effect. The electric field and strain are related by:

$$\varepsilon = dE \tag{3}$$

All piezoelectric materials act as electrical insulators (dielectrics) and hence become polarized under the influence of an external electric field. The resulting electric displacement can be related to the applied electric field as follows:

$$D = \kappa E \tag{4}$$

Equations (1) to (4) can be combined together to give the linear constitutive relations for piezoelectric materials:

$$\varepsilon = S\sigma + dE \tag{5}$$

$$D = \kappa E + d\sigma \tag{6}$$

Equations (5) and (6) give the piezoelectric constitutive law with stress σ and electric field E as independent variables. The law can also be expressed by taking the fields (σ, D), (ε, D), and (ε, E) as independent variables to suit the modeling requirements. For a detailed discussion on the appropriate transformations that aid the conversion between one form and the other, please refer [15].

The piezoelectric constitutive relations can be extended to fit in a general three-dimensional scenario as follows:

$$\varepsilon_{ij} = s_{ijkl}\sigma_{kl} + d_{ijn}E_n \tag{7}$$

$$D_n = \kappa_{nm}E_m + d_{nij}\sigma_{ij} \tag{8}$$

The quantities stress σ and strain ε are second-order tensors, while electric field E and electric displacement D are first-order tensors. Mechanical compliance S is a fourth-order tensor, dielectric permittivity κ is a second-order tensor, and piezoelectric strain coefficient d is a third-order tensor.

Rewriting the above in Voigt notation, we obtained the following:

$$\begin{Bmatrix} \varepsilon_1 \\ \varepsilon_2 \\ \varepsilon_3 \\ \varepsilon_4 \\ \varepsilon_5 \\ \varepsilon_6 \\ D_1 \\ D_2 \\ D_3 \end{Bmatrix} = \begin{bmatrix} S_{11} & S_{12} & S_{13} & S_{14} & S_{15} & S_{16} & d_{11} & d_{21} & d_{31} \\ S_{12} & S_{22} & S_{23} & S_{24} & S_{25} & S_{26} & d_{12} & d_{22} & d_{32} \\ S_{13} & S_{23} & S_{33} & S_{34} & S_{35} & S_{36} & d_{13} & d_{23} & d_{33} \\ S_{14} & S_{24} & S_{34} & S_{44} & S_{45} & S_{46} & d_{14} & d_{24} & d_{34} \\ S_{15} & S_{25} & S_{35} & S_{45} & S_{55} & S_{56} & d_{15} & d_{25} & d_{35} \\ S_{16} & S_{26} & S_{36} & S_{46} & S_{56} & S_{66} & d_{16} & d_{26} & d_{36} \\ d_{11} & d_{12} & d_{13} & d_{14} & d_{15} & d_{16} & \kappa_{11} & \kappa_{12} & \kappa_{13} \\ d_{21} & d_{22} & d_{23} & d_{24} & d_{25} & d_{26} & \kappa_{12} & \kappa_{22} & \kappa_{23} \\ d_{31} & d_{32} & d_{33} & d_{34} & d_{35} & d_{36} & \kappa_{13} & \kappa_{23} & \kappa_{33} \end{bmatrix} \begin{Bmatrix} \sigma_1 \\ \sigma_2 \\ \sigma_3 \\ \sigma_4 \\ \sigma_5 \\ \sigma_6 \\ E_1 \\ E_2 \\ E_3 \end{Bmatrix} \tag{9}$$

where the subscripts 1, 2, and 3 denote the normal components and 4, 5, and 6 denote the shear components, respectively.

Most of the piezoelectric materials are transversely isotropic; hence, the compliance matrix will only have five independent constants as opposed to 21 as in Eq. (9). The electric field applied in a particular direction will not produce electrical displacements along orthogonal directions. Hence, the dielectric permittivity matrix will reduce to a diagonal matrix. Due to transverse isotropy, the dielectric permittivity along directions 1 and 2 will be equal, and hence, the dielectric permittivity matrix will have only two independent constants. Piezoelectric materials, when poled, exhibit cubic symmetry. If the poling is assumed to be along the 3-direction, then cubic symmetry implies that all the coefficients other than d_{31}, d_{32} d_{33}, d_{15}, and d_{24} vanish to zero [15]. Transverse isotropy leads to a further reduction in the piezoelectric strain matrix with $d_{31} = d_{32}$, $d_{15} = d_{24}$. Hence, the piezoelectric strain matrix will have only three independent constants. Reflecting all these changes in the material properties, Eq. (9) will reduce to:

$$\begin{Bmatrix} \varepsilon_1 \\ \varepsilon_2 \\ \varepsilon_3 \\ \varepsilon_4 \\ \varepsilon_5 \\ \varepsilon_6 \\ D_1 \\ D_2 \\ D_3 \end{Bmatrix} = \left[\begin{array}{cccccc:ccc} S_{11} & S_{12} & S_{11} & 0 & 0 & 0 & 0 & 0 & d_{31} \\ S_{12} & S_{11} & S_{13} & 0 & 0 & 0 & 0 & 0 & d_{31} \\ S_{13} & S_{13} & S_{33} & 0 & 0 & 0 & 0 & 0 & d_{33} \\ 0 & 0 & 0 & S_{44} & 0 & 0 & 0 & d_{15} & 0 \\ 0 & 0 & 0 & 0 & S_{55} & 0 & d_{15} & 0 & 0 \\ 0 & 0 & 0 & 0 & 0 & 2(S_{11}-S_{12}) & 0 & 0 & 0 \\ \hdashline 0 & 0 & 0 & 0 & d_{15} & 0 & \kappa_{11} & 0 & 0 \\ 0 & 0 & 0 & d_{15} & 0 & 0 & 0 & \kappa_{11} & 0 \\ d_{31} & d_{31} & d_{33} & 0 & 0 & 0 & 0 & 0 & \kappa_{33} \end{array}\right] \begin{Bmatrix} \sigma_1 \\ \sigma_2 \\ \sigma_3 \\ \sigma_4 \\ \sigma_5 \\ \sigma_6 \\ E_1 \\ E_2 \\ E_3 \end{Bmatrix} \tag{10}$$

The elastic, electrical, and piezoelectric properties of PVDF and the most commonly used piezoelectric ceramic PZT are compared in Table 1. From Table 1, it is observed that the piezoelectric strain coefficient d is comparatively small for PVDF than PZT. This implies that for the same external electric field applied, PZT would produce more strain than PVDF. This is concerned with the actuation capabilities of the two materials. However, we are interested in exploring the energy harvesting potential of the materials. To do so, we look at the piezoelectric stress coefficient g of the two materials. The piezoelectric stress coefficient g is a measure

Table 1 Elastic, dielectric, and piezoelectric properties of PVDF and PZT

Property	Symbol	PVDF	PZT-5A
Modulus of elasticity (N/mm^2)	Y	2×10^9	7.4×10^{10}
Poisson's ratio	v	0.34	0.35
Relative dielectric permittivity	κ_r	12	1800
Piezoelectric strain coefficient (pC/N)	d_{31}	22	−175
	d_{33}	−30	450
Piezoelectric stress coefficient (Vm/N)	g_{31}	0.216	−0.011
	g_{33}	−0.33	0.027
Piezoelectric coupling coefficient	k_{31}	0.14	0.34

of voltage developed per unit length of the material under the influence of an external mechanical stress. From Table 1, we see that the piezoelectric stress coefficient is about 10 times higher for PVDF than PZT. Hence, PVDF is an excellent candidate for energy harvesting applications and will provide higher voltage output than PZT for the same amount of mechanical stress applied. But, the elastic modulus of PVDF is very low compared to that of PZT, which means that PVDF will be subjected to a lower mechanical stress compared to that of PZT for the same amount of strain applied.

From the above argument, it is evident that the electromechanical conversion efficiency depends not only on the piezoelectric strain or stress coefficients but also on modulus of elasticity and dielectric permittivity. It would be helpful to express a quantity that takes into account the effect of all these material properties on electromechanical energy conversion. One such quantity is the piezoelectric coupling coefficient which is defined as [15],

$$k_{ij} = \frac{d_{ij}}{\sqrt{k_{ii}^{\sigma} S_{jj}^{E}}} \tag{11}$$

where the subscripts i and j indicate the components as in Voigt notation, and the superscripts σ and E denote that the properties are measured at constant stress and electric fields, respectively.

The piezoelectric coupling coefficient is related to the electromechanical conversion efficiency such that [24]:

$$k_{ij}^2 = \frac{\text{tranformed energy}}{\text{input energy}} \tag{12}$$

Hence, higher the coupling coefficient, higher the mechanical energy converted into electrical energy and vice versa.

For the commonly used 33- and 31-modes of transduction, the coupling coefficient can be defined as follows:

$$k_{33} = \frac{d_{33}}{\sqrt{\kappa_{33}^{\sigma} S_{33}^{\mathrm{E}}}} \tag{13}$$

$$k_{31} = \frac{d_{31}}{\sqrt{k_{33}^{\sigma} S_{11}^{\mathrm{E}}}} \tag{14}$$

The 31-mode coupling coefficients of PZT and PVDF are also shown in Table 1. Higher values of coupling coefficient for PZT show that it is more efficient than PVDF. Nevertheless, both the materials are extensively used in energy harvesting applications, as the ductility of PVDF provides an edge over PZT in certain cases.

3.2 *Energy Harvesting Using PVDF*

PVDF has a high piezoelectric strain coefficient compared to that of other polymers, and consequently, it is a suitable candidate for energy harvesting applications. The flexibility and the maneuverability of PVDF to form complex shapes augments the same. PVDF transducers can withstand high strains than their PZT counterparts. This justifies the use of PVDF in kinematic energy harvesters. Kinetic energy harvesters make use of both PZT and PVDF as transducer materials. The design of both kinematic and kinetic energy harvesters employing PVDF transducers is elucidated next.

3.2.1 Kinetic Energy Harvesters Using PVDF

In kinetic piezoelectric energy harvesters, the vibrations setup in a spring-mass-damper system is used to strain the piezoelectric material. One of the most common ways of achieving this is to connect a spring-mass-damper system to a vibrating source at a point. The mass oscillates due to excitation from the source. The kinetic energy from the oscillations is converted into electrical energy with the help of piezoelectric transducers.

As mentioned earlier, piezoelectric transducers used for commercial applications are generally poled. Poling the piezoelectric material causes all the dipoles to align along the axis parallel to the direction of the applied electric field. This axis is termed as the polar axis and is generally referred to as the 3-direction. The energy harvesting performance depends on the direction of the applied strain relative to this polar axis. By symmetry, all directions in the plane at right angles to the polar axis are equivalent and are referred to as the 1-direction. A stress can be applied either in the direction of the polar axis or at right angles to it, resulting in two configurations commonly used for piezoelectric generators, termed 33-mode and 31-mode.

The most common design of an inertial piezoelectric energy harvester is a cantilever beam oscillating under the influence of harmonic base acceleration as shown in Fig. 1. Piezoelectric patches can be pasted along the length of the beam,

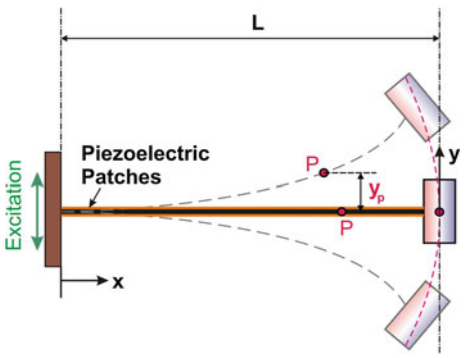

Fig. 1 Schematic representation of cantilever piezoelectric energy harvester

either in a unimorph or a bimorph configuration, to harvest electrical energy. The piezoelectric transducer, in this case, operates in 31-mode. The harvester can be modeled as a system of two coupled linear differential equations: one representing the mechanical domain and the other representing the electrical domain. The derivation of the governing differential equations is outlined here assuming a single degree-of-freedom (SDOF) approximation.

Consider a beam of length L, width b, thickness t, modulus of elasticity Y_b, and mass density ρ_b. Piezoelectric patches are pasted along the entire length of the beam as shown in Fig. 1. The width and thickness of the piezoelectric patches are b and t_p, respectively. Hence, the cross-sectional area of the composite harvester is given by $A = w(t + t_\mathrm{p})$. Let m_t be the mass of tip mass attached to the beam. Let $z = Z \sin \omega t$ be the base displacement. Let x denote the location of any point P along the length of the beam and $y_\mathrm{p}(x, t)$ denote the transverse displacement at the point P, at any time instant t. The transverse displacement of the tip mass is denoted by $y = y_\mathrm{p}(L, t)$. The beam deformation profile $\phi(x)$ relates the quantities y and y_p such that,

$$y_\mathrm{p}(x, t) = y(t) \cdot \phi(x) \tag{15}$$

Since we have assumed a single-mode approximation, we are only interested in the first mode of vibration of the beam. Hence, the beam deformation profile corresponds to the first mode of the solution of the eigenvalue problem,

$$Y_\mathrm{E} I \phi^{IV} + \rho A \phi = 0 \tag{16}$$

where Y_E, A, ρ, and I are the modulus of elasticity, area of cross section, density, and moment of inertia of the cross section of the composite beam.

The kinetic energy of the system is given as follows:

$$T = \frac{1}{2} m_t (\dot{y} + \dot{z})^2 + \frac{1}{2} \int_0^L \rho A (\dot{y}_p + \dot{z})^2 \mathrm{d}x \tag{17}$$

$$T = \frac{1}{2} \rho A \left[\dot{y}^2 \int_0^L (\phi(x))^2 \mathrm{d}x + \dot{z}^2 \int_0^L \mathrm{d}x + 2\dot{y}\dot{z} \int_0^L \phi(x) \mathrm{d}x \right] + \frac{1}{2} m_t \left[\dot{y}^2 + \dot{z}^2 + 2\dot{y}\dot{z} \right] \tag{18}$$

$$T = \frac{1}{2} (m\dot{y}^2 + M\dot{z}^2 + \mu \dot{y}\dot{z}) \tag{19}$$

where m, M, and μ are constants independent of time, such that

$$m = m_t + \rho A \int_0^L \phi^2 \mathrm{d}x \tag{20}$$

$$M = m_t + \rho A L \tag{21}$$

$$\mu = 2\left(m_t + \rho A \int_0^L \phi(x) \mathrm{d}x \right) \tag{22}$$

In the equations, overdot $(\cdot)$ denotes differentiation with respect to time.
The elastic potential energy of the system is given as follows:

$$\Pi_{\mathrm{E}} = \frac{1}{2} \int_0^L Y_{\mathrm{E}} I (\kappa(x,t))^2 \mathrm{d}x \tag{23}$$

where, $\kappa(x,t)$ is the curvature of the beam.
For the composite beam section, the moment of inertia is given as follows:

$$I = \frac{w(t+t_{\mathrm{p}})^3}{12} \tag{24}$$

The curvature of the beam is given as follows:

$$\kappa(x) = \frac{\mathrm{d}^2 y_{\mathrm{p}}}{\mathrm{d}x^2} \tag{25}$$

$$\kappa(x) = y \frac{\mathrm{d}^2 \phi}{\mathrm{d}x^2} \tag{26}$$

Substituting Eq. (26) into Eq. (23), we obtain the following:

$$\Pi_{\mathrm{E}} = \frac{1}{2} Y_{\mathrm{E}} I \left(y \int_0^L \frac{\mathrm{d}^2 \phi}{\mathrm{d}x^2} \mathrm{d}x \right)^2 \tag{27}$$

$$\Pi_{\mathrm{E}} = \frac{1}{2} Y_{\mathrm{E}} I y^2 (\phi'(L))^2 = \frac{1}{2} k y^2 \tag{28}$$

where $k = Y_{\mathrm{E}} I (\phi'(L))^2$ is the equivalent stiffness of the system.

The electrical work done in extracting the charges from the piezoelectric patches is given as follows:

$$W = \int_0^L M_\Lambda \kappa(x) \mathrm{d}x \tag{29}$$

where M_Λ is the moment due to the voltage developed across the piezoelectric patches and κ is the curvature of the beam.

Let v be the potential difference developed along the piezoelectric patches at any time instant t. For a bimorph configuration, the moment M_Λ produced due to this potential difference is given as follows:

$$M_\Lambda = Y_\mathrm{E} d_{31} w(t + t_\mathrm{p}) v \tag{30}$$

where d_{31} is the piezoelectric strain coefficient of piezoelectric patches.

On substituting Eqs. (26) and (30) into Eq. (29), we obtain the following:

$$W = Y_\mathrm{E} d_{31} w(t + t_\mathrm{p}) v \int_0^L y \frac{\mathrm{d}^2 \phi}{\mathrm{d}x^2} \mathrm{d}x \tag{31}$$

$$W = Y_\mathrm{E} d_{31} w(t + t_\mathrm{p}) v y \phi'(L) = Y_\mathrm{E} d_{31} \lambda v y \tag{32}$$

where

$$\lambda = w(t + t_\mathrm{p}) \phi'(L) \tag{33}$$

The total potential energy of the system is given as follows:

$$\Pi = \Pi_\mathrm{E} - W = \frac{1}{2} k y^2 - Y_\mathrm{E} d_{31} \lambda v y \tag{34}$$

Since the kinetic and potential energies of the system are known, the equation of motion can be derived using Euler–Lagrange equation:

$$\frac{\mathrm{d}}{\mathrm{d}t} \left(\frac{\partial L}{\partial \dot{y}} \right) - \frac{\partial L}{\partial y} = 0 \tag{35}$$

where $L = T - \Pi$ denotes the Lagrangian, which is the difference between kinetic and potential energies of the system.

On substituting Eqs. (19) and (34) into Eq. (35), the mechanical governing equation of the system can be obtained as follows:

$$m\ddot{y} + ky - Y_\mathrm{E} d_{31} \lambda v = -\mu \ddot{z} \tag{36}$$

Damping terms, such as viscous or material damping, can be added to the system defined in Eq. (36). On adding a viscous damping term, $c = 2\zeta\sqrt{km}$, the mechanical governing equation becomes:

$$m\ddot{y} + c\dot{y} + ky - Y_{\mathrm{E}} d_{31} \lambda v = -\mu\ddot{z} \tag{37}$$

The term $Y_{\mathrm{E}} d_{31} \lambda \dot{y}$ denotes the electromechanical coupling.

The electrical governing equation can be obtained by considering the piezoelectric patches to be a capacitor C_p connected across the load resistance R_{l}. Thus,

$$C_p \dot{v} + \frac{v}{R_{\mathrm{l}}} + Y_{\mathrm{E}} d_{31} \lambda \dot{y} = 0 \tag{38}$$

The term $Y_{\mathrm{E}} d_{31} \lambda \dot{y}$ arises due to the electromechanical coupling.

Equations (37) and (38) together represent the dynamics of a piezoelectric energy harvester based on a cantilever beam.

Assuming $y = Y\mathrm{e}^{i\omega t}$ and $v = V\mathrm{e}^{i\omega t}$ and performing a frequency-domain analysis on Eqs. (37) and (38) yield the following:

$$|V| = \left| \frac{\mu Y_{\mathrm{E}} d_{31} R_{\mathrm{l}} \lambda \omega^3 Z}{\sqrt{\left(k - m\omega^2 - C_p R_{\mathrm{l}} c\omega^2\right)^2 + \left(c\omega + R_{\mathrm{l}} \lambda^2 Y_{\mathrm{E}}^2 d_{31}^2 \omega - C_p R_{\mathrm{l}} m\omega^3 + C_p R_{\mathrm{l}} k\omega\right)^2}} \right| \tag{39}$$

The power harvested by the harvester over one cycle of excitation is given as follows:

$$P_{\mathrm{rms}} = \frac{\omega}{2\pi} \int_0^{2\pi/\omega} \frac{v^2}{R_{\mathrm{l}}} \mathrm{d}t = \frac{V^2}{2R_{\mathrm{l}}} \tag{40}$$

$$P_{\mathrm{rms}} = \frac{\left(\mu Y_{\mathrm{E}} d_{31} \lambda \omega^3 Z\right)^2 R_{\mathrm{l}}}{2\left[\left(k - m\omega^2 - C_p R_{\mathrm{l}} c\omega^2\right)^2 + \left(c\omega + R_{\mathrm{l}} \lambda^2 Y_{\mathrm{E}}^2 d_{31}^2 \omega - C_p R_{\mathrm{l}} m\omega^3 + C_p R_{\mathrm{l}} k\omega\right)^2\right]} \tag{41}$$

Equation (41) shows that the harvested power depends not only upon the material properties such as E and d_{31} but also on other factors such as load resistance R_{l} and capacitance of piezoelectric transducer C_{p}. However, we are only interested in a comparison of different materials for energy harvesting. Hence, we define a figure of merit F that depends only on the material properties as follows:

$$F = Y d_{31} \tag{42}$$

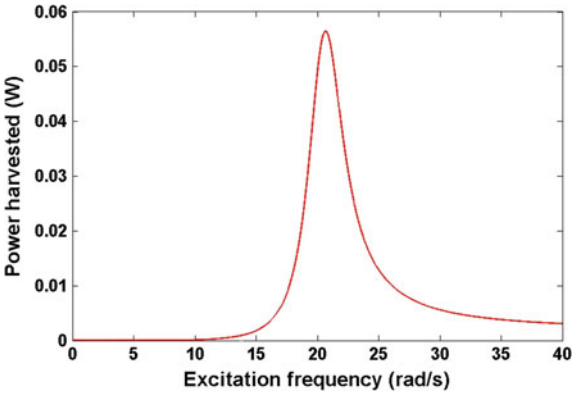

Fig. 2 Variation in harvested power with respect to frequency for a linear energy harvester employing a PVDF transducer

Thus, the power harvested can be related to the figure of merit as follows:

$$P_{\text{rms}} = \frac{(\mu F \lambda \omega^3 Z)^2 R_l}{2[(k - m\omega^2 - C_p R_l c\omega^2)^2 + (c\omega + R_l \lambda^2 F^2 \omega - C_p R_l m\omega^3 + C_p R_l k\omega)^2]} \tag{43}$$

The figure of merit defined in Eq. (42) is used to compare the harvesting properties of different electroactive polymers in Sect. 5.

Significant work has been done in the past in modeling cantilever-based linear piezoelectric energy harvesters (e.g., please refer [6, 13, 28, 29]). Such linear harvesters target a resonant design and suffer from poor efficiency at off-resonant frequencies as shown in Fig. 2.

To improve the operating bandwidth of kinetic vibration energy harvesters, techniques such as generator arrays, nonlinear oscillators, and active resonant tuning can be used [30]. Broadband piezoelectric energy harvesting techniques have been reviewed in [31]. Though the examples mentioned in [31] employ piezoelectric materials such as PZT, the design and analysis can be extended to harvesters employing PVDF or any other piezoelectric material by introducing appropriate changes in material properties.

3.2.2 Kinematic Energy Harvesters Using PVDF

While kinetic energy harvesters have a generic design in which there is a mass undergoing vibration, the design of kinematic energy harvesters is application specific. Kinematic energy harvesters are generally designed as an integral part of the host structure and deform along with the host structure. For example, a piezoelectric material can be coated on to the inner surface of a rubber tire. As the tire moves, the piezoelectric material deforms along with the tire and generates electrical energy. Generally, ductile piezoelectric materials such as PVDF are

employed in such applications. Modeling the dynamics of such harvesters, once again, would be application specific and hence not much research focus has been toward modeling such harvesters. But rather, modern research focuses on integrating kinematic energy harvesters as a part various commercial products such as tires, backpack straps [32], and footwear [33]. Significant efforts have also been made to harvest energy from biological processes such as respiration, walking, and squatting.

Another interesting area of application of kinematic energy harvesters is energy harvesting Eels. The design is based on bluff bodies and is intended to harvest energy from fluid–structure interaction [34, 35]. It converts the mechanical flow energy from oceans and rivers into electrical energy.

A comparison of various kinematic energy harvesters could be facilitated through a numerical model that takes into account the geometry, material properties, and other features of the harvester. However, since most of the kinematic energy harvesters are designed as an integral part of the structure and evaluated for their performance, not many studies related to modeling of such harvesters is available in the literature. Comparison of experimental data would not yield much information as the geometry and configuration of transducers used vary between different harvesters. Hence, a performance comparison between various transducer designs is not presented here per se, but a comparison of transducer materials based on their figure of merit is presented in Sect. 5.

3.2.3 Micro- and Nanogenerators Based on PVDF Composites

In addition to typical kinetic and kinematic energy harvesters, there is also significant opportunity to harvest the wasted energy from our daily activities, such as from walking, typing, speaking, and breathing. Energy harvested from such activities would range from few nanowatts to few microwatts, hence yielding such energy harvesters the name, micro- and nanogenerators.

Single-fiber PVDF nanowires [36], electrospun PVDF nanowebs, and nanowires made of semiconductive piezoelectric materials such as zinc oxide (ZnO) [37] are used as nanogenerators. ZnO nanowires have better electromechanical energy conversion efficiency than PVDF nanowires; but they are very brittle and are difficult to integrate with other most other materials. This has sparked the interest of researchers to develop a composite with PVDF matrix and ZnO nanoparticles to overcome the limitations associated with both the materials [38].

In such hybrid composites, PVDF nanowires provide the desired flexibility and the additive nanoparticles enhance the electromechanical coupling. Carbon nanotubes (CNTs) and piezoelectric ceramics such as $BaTiO_3$ and ZnO are some of the commonly used nanoparticles to improve the energy harvesting capabilities of PVDF nanogenerators. Figure 3 shows a nanogenerator that makes use of ZnO nanoparticles embedded in a PVDF nanofiber mat that is reported in [38].

Such flexible piezoelectric polymer–nanoparticle composites are generally manufactured using electro spinning process. The ingredients are dissolved in a

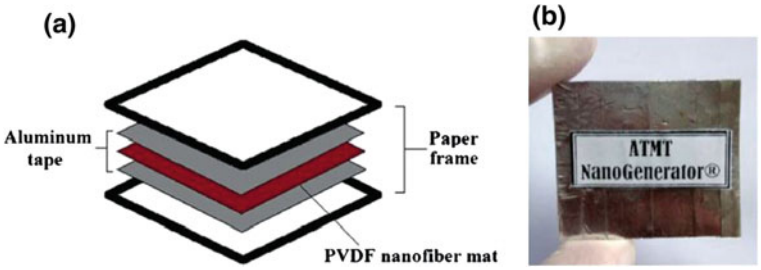

Fig. 3 Nanogenerator developed: **a** schematic diagram and **b** photograph of the actual device [38]. Copyright 2015. Reproduced with permission from Springer

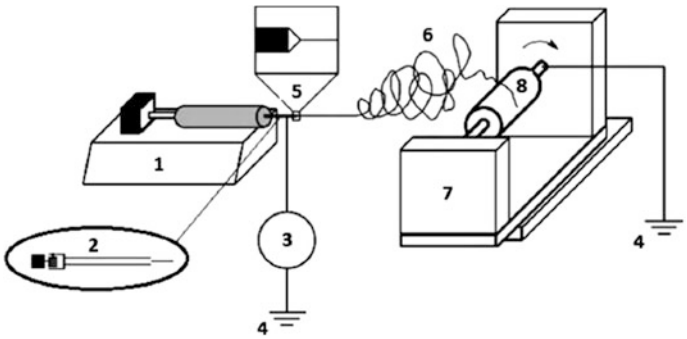

Fig. 4 Schematic diagram of the electrospinning process used for fabrication of PVDF nanofiber samples [38]. The numbers represent: (*1*) pump, (*2*) syringe, (*3*) high voltage supply, (*4*) ground, (*5*) Taylor cone, (*6*) draft zone, (*7*) frame of collector, and (*8*) rotary collector. Copyright 2015. Reproduced with permission from Springer

solvent such as acetone, and the solution is taken in a syringe pump. A high voltage is applied between the needle of the syringe and the collector. This would cause a fluid jet to be ejected from the needle. As the jet is accelerated, the solvent gets evaporated and the nanofibers get collected on the substrate. A schematic diagram describing the process is given by Fig. 4.

Apart from PVDF, polydimethylsiloxane (PDMS) and polyurethane (PU) are also used as matrix materials in such hybrid nanogenerators.

3.3 Energy Harvesting Using Cellulose Nanocrystals

Biopolymer electroactive materials such as cellulose nanocrystals are also explored for their energy harvesting capabilities owing to their low density, high mechanical strength, and most importantly their biocompatibility. The chemical resistance of cellulose ensures that it is not damaged by body fluids and its thermal stability

prevents fluctuating temperatures from altering its response. Hence, biocompatible composites made from cellulose nanocrystals have immense potential in the area of implantable energy harvesters. Such implantable energy harvesters would help to power cardiac pacemakers, enable targeted drug delivery through nanorobots, and aid in monitoring internal organs through biocompatible sensors.

Native cellulose, namely cellulose I, is the crystalline cellulose. The term, regenerated cellulose, is called cellulose II and usually needs a chemical treatment to prepare. The piezoelectric coupling constants depend on the crystallinity of the prepared cellulose. In general, the magnitude of the coupling constants increases with increase in crystallinity.

The network structure of cellulose consists of multiple OH groups in the glucose molecules from one chain forming hydrogen bonds with oxygen atoms in the same or neighboring chains. The hydrogen bonds hold the chains together side by side and are responsible for the spontaneous electric dipole formations in cellulose microfibrils inside the crystal lattice. The piezoelectric effect is produced by the displacement or reorientation of the dipoles in the crystal lattice under external stress [39].

In uniaxially oriented system of cellulose crystallites, relative movement between adjacent chains causes a reorientation of electric dipoles present in the crystal. The shear components predominantly contribute to relative movement between adjacent layers or chains. Hence, only the shear piezoelectric constants $-d_{14} = d_{25}$ are finite, while the other components are zero in a uniaxially oriented system of cellulose crystallites [40]. Hence, unlike the PVDF energy harvesters discussed so far which utilized either the 31- or 33-mode of coupling, energy harvesters based on cellulose nanocrystals make use of the shear mode of coupling.

In studies related to the piezoelectric behavior of cellulose fibers, different preparation and modification routes as well as characterization techniques have been considered. Corona-poled electroactive paper made from cellulose, cyanoethylated cellulose, and LiCl-DMAc-modified cotton (0.32 index of crystallinity) were reported to have shear piezoelectric constants of 0.0167, 0.01–0.02, and 0.016 nm/V, respectively.

Different designs of cellulose-based nanogenerators have been proposed in the past decade. The most prominent among such designs are described here. A nanogenerator based on cellulose-based electroactive paper was reported by [41]. In this design, the electromechanical coupling was enhanced through fiber functionalization that involves anchoring nanostructured $BaTiO_3$ into a stable matrix with wood cellulose fibers. The electroactive paper has the largest piezoelectric coefficient, $d_{33} = 4.8 \pm 0.4\ pC/N$, at the highest nanoparticle loading of 48% $BaTiO_3$ by weight [41].

A flexible nanogenerator based on native cellulose microfiber and polydimethylsiloxane embedded with multi-wall carbon nanotubes as filler was proposed by [42]. It delivers a high electrical throughput that is an open-circuit voltage of 30 V and power density of 9.0 $\mu W/cm^3$ under repeated hand punching. This design utilized naturally available cellulose fibers and avoided chemical post-processing treatment and electrical poling.

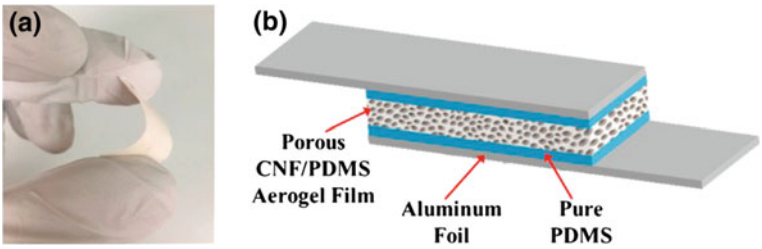

Fig. 5 **a** Photograph of the flexible porous CNF-PDMS aerogel film. **b** A schematic diagram of the CNF-PDMS aerogel film-based nanogenerator [43]. Copyright 2016. Reproduced with permission from Elsevier

Another flexible nanogenerator based on porous cellulose nanofibrils–polydimethylsiloxane (CNF–PDMS) aerogels was proposed by [43]. The design consists of three layers, namely the inner-most CNF-PDMS layer sandwiched between two thin PDMS films followed by two aluminum foils as shown in Fig. 5. The inner CNF-PDMS layer was produced by coating a layer of PDMS onto a compressed CNF aerogel film through a freeze–drying process. This nanogenerator exhibited very stable and high electrical output with an open-circuit voltage of 60.2 V, a short-circuit current of 10.1 μA, and a corresponding power density of 6.3 mW/cm^3.

Apart from the ones mentioned above, feasibility and performance studies on energy harvesting using ultra-thin cellulose nanocrystal films, hybrid cellulose–polydimethylsiloxane composites, etc., are underway.

4 Energy Harvesting from Electrostrictive Polymers

Electrostrictive materials are those in which the electromechanical coupling is represented by a quadratic relationship between strain and electric field [23]. In tensorial notation, the relation between strain and electric field is written as follows[44]:

$$\varepsilon_{ij} = S_{ijkl}\sigma_{kl} + M_{ijmn}E_mE_n \tag{44}$$

$$D_m = \kappa_{mn}E_n + 2M_{mnij}E_n\sigma_{ij} \tag{45}$$

where M_{ijmn} is a fourth rank tensor of electrostriction coefficients.

On considering only the 31 lateral vibration mode coupling, the constitutive equations reduce to [44]:

$$\varepsilon_1 = S_{11}\sigma_1 + M_{31}E_1^2 \tag{46}$$

$$D_3 = \kappa_{33}E_3 + 2M_{31}E_3\sigma_1 \tag{47}$$

where the input and response fields and associated material properties are expressed in Voigt notation.

In piezoelectric materials, linear coupling between strain and electric field produces a mechanical response that will change polarity when the polarity of the electric field is changed. On the other hand, electrostrictive materials, due to the quadratic dependence of strain on electric field relationship, always produce strain in only a single direction, irrespective of the polarity of the applied electric field.

Ceramics such as lead lanthanum zirconate titanate (PLZT), lead magnesium niobate (PMN) and a solid solution of lead magnesium niobate–lead titanate (PMN-PT) and polymers such as polyurethane (PU) and polymethyl dioxane are some common examples of electrostrictive materials.

4.1 Effect of Intrinsic Mechanisms

Analogous to electrostriction, there is another phenomenon observed widely in soft dielectric elastomers where the strain is proportional to the square of the electric field. This phenomenon is known as the Maxwell stress effect. The Maxwell stress is a result of the electrostatic forces between the free charges on the electrodes of a sample. Apart from Maxwell stress effect, other intrinsic mechanisms such as Joule's heating effect and space charge effect also contribute to the strain. To take into account all the intrinsic mechanisms that contribute to the strain, the true electrostrictive coefficient M_{31} must be replaced with the apparent electrostrictive coefficient M_{31}^*, which is defined as follows [45]:

$$M_{31}^* = M_{31} + M_{31}^M + M_{31}^T \tag{48}$$

where M_{31}^M and M_{31}^T denote the contributions from Maxwell stress effect and Joule's heating effect, respectively.

Now, the constitutive Eqs. (46) and (47) can be redefined as follows:

$$\varepsilon_1 = S_{11}\sigma_1 + M_{31}^*E_1^2 \tag{49}$$

$$D_3 = \kappa_{33}E_3 + 2M_{31}^*E_3\sigma_1. \tag{50}$$

4.2 Tackling Quadratic Dependence of Strain on Electric Field

The quadratic relationship between applied electric field and mechanical strain complicates the design of transducers based on electrostrictive materials. In an electrostrictive material, the spontaneous polarization is always zero. When the electrostrictive material is strained, some of the dipoles orient along a particular direction and the rest orient along the opposite direction, thus reducing the net polarization, as shown in Fig. 6.

One method of avoiding this is to apply a high dc bias voltage to the material along the desired direction of electrical response. The dc electric field will force the dipoles to orient in a direction parallel to it. Hence, to get a full cycle alternating current as output, electrostrictive energy harvesters require a dc bias field to be applied, while piezoelectric harvesters do not. This forms the essential difference between the operating principles of electrostrictive energy harvesters and their piezoelectric counterparts.

Continuing with our analysis, consider the electric field in the 3-direction to be the sum of a direct current (dc) bias field and an induced alternating current (ac) component:

$$E_3 = E_{\mathrm{dc}} + E_{\mathrm{ac}} \tag{51}$$

Substituting Eq. (51) into Eq. (49) yields

$$\varepsilon_1 = S_{11}\sigma_1 + M_{31}^{*}(E_{\mathrm{dc}} + E_{\mathrm{ac}})^2 \tag{52}$$

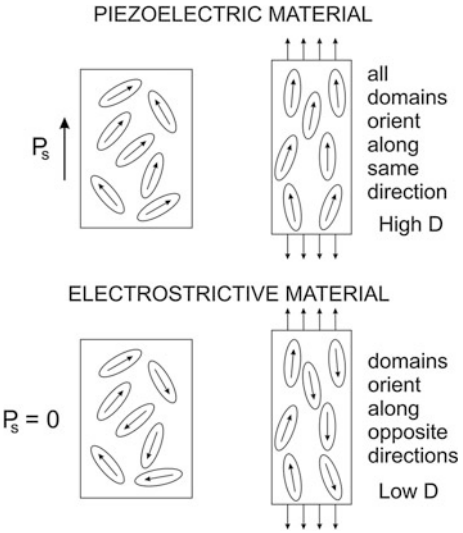

Fig. 6 Alignment of dipoles in response to applied strain in piezoelectric and electrostrictive materials

$$\varepsilon_1 = S_{11}\sigma_1 + M_{31}^*(E_{dc}^2 + 2E_{dc}E_{ac} + E_{ac}^2) \tag{53}$$

$$\varepsilon_1 - M_{31}^* E_{dc}^2 = S_{11}\sigma_1 + M_{31}^*(2E_{dc}E_{ac} + E_{ac}^2) \tag{54}$$

When $E_{ac}^2 \ll E_{dc}E_{ac}$, Eq. (54) can be approximated as follows:

$$\varepsilon_1 - M_{31}^* E_{dc}^2 \approx S_{11}\sigma_1 + 2M_{31}^* E_{dc}E_{ac} \tag{55}$$

The noteworthy fact in Eq. (55) is that the ac strain $(\varepsilon_1 - M_{31}^* E_{dc}^2)$ is a linear function of the ac field E_{ac} when a sufficiently large dc bias field E_{dc} is applied to the system. While the strain ε_1 can only be positive, the ac strain can be either positive or negative depending on the value of $M_{31}^* E_{dc}^2$. Thus, the relationship between ac strain and ac electric field in electrostrictive materials is similar to that of strain and electric field in piezoelectric materials.

Moreover, in Eq. (55), the coefficient $2M_{31}^* E_{dc}$ is constant as the applied dc field is constant with time. This leads to the notion of comparing Eq. (55) with that of the linear piezoelectric constitutive relations to express $d^* = 2M_{31}^* E_{dc}$ as the effective piezoelectric strain coefficient. This would be helpful in comparing the electromechanical transduction capability of electrostrictive materials with that of piezoelectric materials.

4.3 Energy Harvesting Using Polyurethane Transducers

Similar to piezoelectric transducers, electrostrictive transducers are widely used in kinetic energy harvesting. However, the requirement of a dc bias field limits the use of electrostrictive polymers in kinematic energy harvesting, as it is highly challenging to apply a uniform bias field over irregular membranes of electrostrictive materials pasted onto the surface of the host.

The modeling and analysis of kinetic electrostrictive energy harvesters also differ from their piezoelectric counterparts. Modeling of a cantilever-based electrostrictive energy harvester, similar to the one discussed for piezoelectric energy harvesting, is elucidated here.

Consider a cantilever beam of length L, cross-sectional area A, and modulus of elasticity E. Electrostrictive transducers are pasted in a bimorph configuration onto the beam as shown in Fig. 7. The transducer operates in 31-mode. A dc bias field of magnitude E_{dc} is applied to the transducer along the positive 3-direction. Due to the base excitation, the beam undergoes transverse vibrations along 1-direction.

The transducer equations are given as follows:

$$\varepsilon_1 = S_{11}\sigma_1 + M_{31}^*(E_{dc} + E_{ac})^2 \tag{56}$$

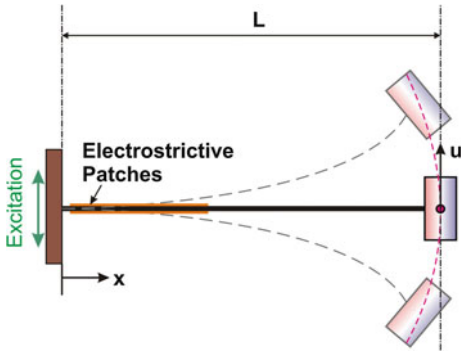

Fig. 7 Schematic representation of cantilever electrostrictive energy harvester

$$D_3 = \kappa_{33}(E_{dc} + E_{ac}) + 2M_{31}^{*}(E_{dc} + E_{ac})\sigma_1 \tag{57}$$

The harvested current I is the rate of change of total charge displaced. Hence,

$$I = \dot{q} \tag{58}$$

$$I = A_e D \tag{59}$$

$$I = A_e(\kappa_{33}E_{ac} + 2M_{31}^{*}E_{ac}\sigma_1 + 2M_{31}^{*}(E_{ac} + E_{dc})\dot{\sigma}_1) \tag{60}$$

$$I = A_e\left[[\kappa_{33} + 2M_{31}^{*}\sigma_1]E_{ac} + 2M_{31}^{*}(E_{ac} + E_{dc})\dot{\sigma}_1\right] \tag{61}$$

$$I = A_e\left[\left[\kappa_{33} - 6\frac{M_{31}^{*2}}{S_{11}}(E_{ac} + E_{dc})^2 + \frac{2M_{31}^{*2}}{S_{11}}\varepsilon_1\right]\dot{E}_{ac} + \frac{2M_{31}^{*2}}{S_{11}}(E_{ac} + E_{dc})\dot{\varepsilon}_1\right] \tag{62}$$

where A_e is the area of the electrode of the electrostrictive transducer.

For practically realizable values of current ($I < 100\,\mu A$), load resistance ($R_l < 10^7\,\Omega$), and electric field (1–100 MV/m), the ac component E_{ac} can be neglected when compared to the dc bias field. Hence, Eq. (62) becomes:

$$I = A_e\left[\left[\kappa_{33} - 6\frac{M_{31}^{*2}}{S_{11}}E_{dc}^2 + \frac{2M_{31}^{*2}}{S_{11}}\varepsilon_1\right]\dot{E}_{ac} + \frac{2M_{31}^{*2}}{S_{11}}E_{dc}\dot{\varepsilon}_1\right] \tag{63}$$

If t_p is the thickness of the electrostrictive transducer, then the potential difference across the transducer and the corresponding electric field are related by:

$$E_{ac} = \frac{v}{t_p} = \frac{IR_l}{t_p} \tag{64}$$

where R_l is the load resistance.

Substituting Eq. (64) into Eq. (63) yields

$$I = \frac{A_e R_l}{t_p}\left[\kappa_{33} - 6\frac{M_{31}^{*2}}{S_{11}}E_{dc}^2 + 2\frac{M_{31}^*}{S_{11}}\varepsilon_1\right]I + \frac{2M_{31}^* A_e}{S_{11}}E_{dc}\dot{\varepsilon}_1 \tag{65}$$

For small values of strain (a few percent), the terms $6\frac{M_{31}^{*2}}{S_{11}}E_{dc}^2$ and $2\frac{M_{31}^*}{S_{11}}\varepsilon_1$ are very small in magnitude compared to permittivity κ_{33} and can be neglected [46]. Thus,

$$I = \frac{A_e R_l}{t_p}\kappa_{33} I + \frac{2M_{31}^* A_e}{S_{11}}E_{dc}\dot{\varepsilon}_1 \tag{66}$$

On setting $\varepsilon_1 = \varepsilon_m e^{i\omega t}$ and $I = I_m e^{i\omega t}$, the frequency-domain analysis of Eq. (66) yields [46]:

$$|I_m| = \left|\frac{A_e M_{31}^* E_{dc} t_p}{S_{11}\sqrt{t_p^2 + (\omega\kappa_{33} R_l A_e)^2}}\varepsilon_m^2\right| \tag{67}$$

The power harvested over one cycle is then given as follows:

$$P_{rms} = \frac{1}{2}I_m^2 R_l \tag{68}$$

$$P_{rms} = \frac{(A_e M_{31}^* E_{dc} t_p)^2}{2S_{11}^2(t_p^2 + (\omega\kappa_{33} A_e R_l)^2)}\varepsilon_m^2 \tag{69}$$

Since the effective piezoelectric strain coefficient is defined as $d^* = 2M_{31}^* E_{dc}$, a figure of merit, equivalent to the one defined for piezoelectric materials, can also be defined for electrostrictive materials. In Eq. (42), replacing d_{31}^* with d_{31}, we obtained the following:

$$F = d_{31}^* Y \tag{70}$$

$$F = \frac{2M_{31}^* E_{dc}}{S_{11}} \tag{71}$$

From Eq. (71), we observe that the figure of merit for an electrostrictive material also depends on the dc bias field. This is expected because higher the dc bias field, higher will be the net polarization in the electrostrictive material. However, the net polarization will not increase beyond a certain limiting value of the dc bias field known as the saturation field E_s. Hence, the maximum permissible value of figure of merit is obtained when $E_{dc} = E_s$.

The power harvested and the figure of merit are related by:

$$P_{\text{rms}} = \frac{(FA_e t_p)^2 R_l}{8(t_p^2 + (\omega \kappa_{33} R_l A_e)^2)} \varepsilon_m^2 \tag{72}$$

The figure of merit defined in Eq. (71) is used to compare the harvesting properties of different electroactive polymers in Sect. 5.

The variation in harvested power with respect to load resistance R_l and strain amplitude ε_m for three different polyurethane composites is shown in Figs. 8 and 9, respectively. Pure polyurethane (PU), polyurethane embedded with 0.5% SiC nanowires (PU with 0.5% SiC), and polyurethane embedded with 1% carbon nanopowder (PU with 1% C) are the three materials chosen for study. The material properties used are given in Table 2. The excitation frequency, dc bias field,

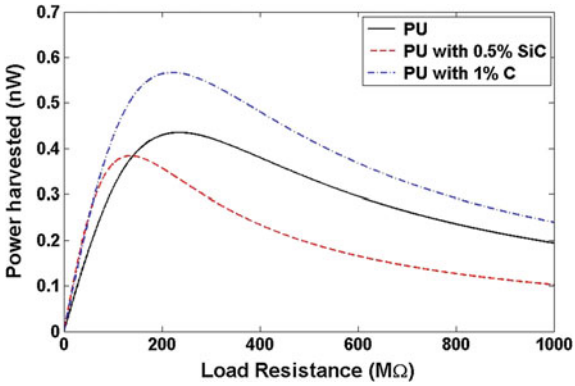

Fig. 8 Variation in harvested power with respect to load resistance for various polyurethane composites. The strain amplitude is taken to be 1%

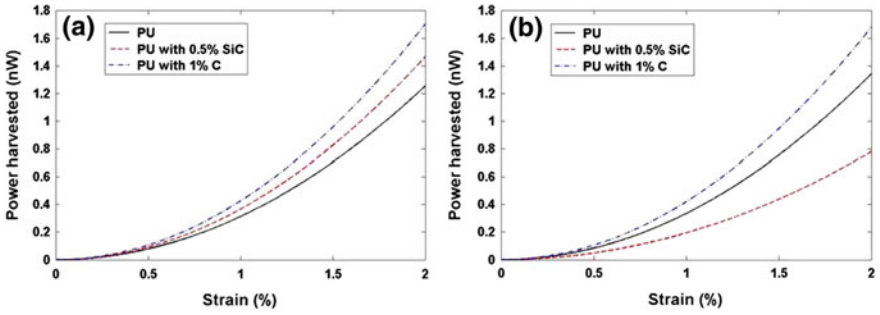

Fig. 9 Variation in harvested power with respect to strain for various polyurethane composites for a load resistance of **a** 100 MW and **b** 500 MW

Table 2 Comparison of electromechanical properties of various dielectric EAPs

Material	Modulus of elasticity (MPa)	Relative dielectric permittivity	Apparent electrostrictive coefficient (10^{-18} m^2/V^2)	Effective piezoelectric strain coefficient (10^{-12} pC/N)	Figure of merit (mC/m^2)
PU [47]	40	4.8	3.4	27.2	1.088
PU 0.5% SiC [47]	80	5.1	2.0	16	1.28
PU 1% C [47]	40	8.3	4.2	33.6	1.344
Polyethylene [47]	260	2.2	0.34	2.72	0.7072
Nylon [47]	2800	12	0.14	1.12	3.136
PVDF [48]	2600	12	–	37	96.2
PZT [23]	74000	1800	–	−175	−12950

The references are indicated in the first column

electrode surface area, and thickness of transducer are taken to be 10 rad/s, 4 MV/m, 5 cm^2, and 50 μm, respectively, for all the three cases.

As shown in Fig. 8, the power harvested is maximum corresponding to certain optimal load resistance. This optimal resistance is a function of material properties and is given by the expression $R_{opt} = (A_e \kappa_{33} \omega)^{-1}$ [46]. For more details on the optimization procedure and the corresponding maximum value of power harvested, please refer [46].

From Fig. 8, it is observed that the composite PU with 0.5% SiC performs better than PU in terms of power harvested for all load resistance levels. On the other hand, the composite PU with 1% C harvests more power than PU for lower resistances (<120 MΩ approx.) and harvests less power than PU for higher resistances. The same is reflected in Fig. 9. Figure 9 also shows that the harvested power varies quadratically with strain for all the three materials.

5 Comparison of Electromechanical Coupling in Various Dielectric EAPs

The apparent electrostrictive coefficient M_{31}^* is a measure of the mechanical-to-electrical energy conversion in electrostrictive materials. To increase the apparent electrostrictive coefficient of polyurethane, particles such as carbon black nanopowders or silicon carbide nanowires can be added to a polyurethane matrix [45, 47]. Co-polymerization of certain combination of monomers can also significantly improve the electromechanical coupling. For example, the co-polymer P (VDF-TrFE) has better electromechanical coupling properties than PVDF. However, a direct comparison cannot be made between the piezoelectric strain

coefficient of ferroelectric polymers and the apparent electrostrictive coefficient of electrostrictive polymers.

To facilitate the comparison between various dielectric EAPs, the notion of effective piezoelectric strain coefficient introduced in Sect. 4.2 can be used. Table 2 compares the effective piezoelectric strain coefficient of various electrostrictive polymers with that of the piezoelectric materials. To compare the energy harvesting efficiency of the materials, figure of merit defined in Eqs. (42) and (71) is used. To calculate the effective piezoelectric strain coefficient d_{31}^{*} and figure of merit F for electrostrictive materials, a dc bias field value of 4 MV/m is used.

Even though dielectric EAPs feature a very low figure of merit when compared to PZT, they are still used in energy harvesting applications due to their flexibility, maneuverability, and affordability.

6 Energy Harvesting from Conductive Polymer Composites

Conducting polymers are materials that exhibit a reversible volume change due to electrochemical reactions caused by the introduction and removal of ions into the polymer matrix [23]. A conductive polymer transducer consists of the conducting polymer material, an electrolyte that serves as a source of ions, and two electrodes that control the ionic diffusion. Polypyrrole, poly(p-phenylene), and several other polymers based on aromatic monomers such as thiopene and aniline when doped act as the conducting polymer material.

Application of a potential difference between the two electrodes causes an electrochemical redox reaction, which in turn causes a volume change inside the conducting polymer. The volume change in the conducting polymer results in its mechanical deformation. The deformation of the polymer film is used to provide the actuation strain. This phenomenon is called the electro-chemo-mechanical (ECM) deformation as it involves transformation of electrical energy to kinetic energy through a chemical reaction. The reversal process in which kinetic energy is transformed into electrical energy is observed experimentally toward the end of twentieth century by Takashima et al. [25]. The reversal effect, called the mechano-chemo-electrical (MCE) effect, can be utilized for sensing and energy harvesting applications. The kinetic-to-electrical energy conversion efficiency, as reported in [25], is less than 0.01%.

Owing to the very low MCE conversion efficiency of conducting polymers such as polyaniline and polypyrrole, they are not as such used in mechanical energy harvesting. Instead, they are used as electrodes in microbial fuel cells [49] and thermoelectric energy harvesters [50], and also as fillers in hybrid polymer-nanoparticle energy harvesters [51].

Apart from conducting polymers, composites consisting of conductive nanoparticles such as carbon nanotubes (CNTs) dispersed in a polymer matrix also fall under the category of conducting polymer composites.

Mechanical energy harvesting from such hybrid polymer–nanoparticle composites has been elucidated in Sect. 3.2.3. Apart from that, thermoelectric energy harvesters with carbon nanotube electrodes are one of the modern state-of-the-art technological devices where active research is going on. A brief review of latest advancements in their design and the perspectives is elucidated next.

6.1 Thermoelectric Energy Harvesters with Carbon Nanotube Electrodes

Carbon nanotubes (CNTs) were first discovered in 1953 through research in the Soviet Union, but the first accessible results were by Sumio Iijima in 1991 as a result of research into Buckminster fullerenes. CNTs have a cylindrical shape that can be considered as a grapheme sheet rolled up, either individually as a single-walled carbon nanotube (SWNT), or concentrically as a multi-walled carbon nanotube (MWNT) [52]. They exhibit remarkable electrical transport and mechanical properties, which is why interest and research into this material has increased over the last two decades.

The second law of thermodynamics dictates that a heat engine can never have perfect efficiency and will always produce surplus heat. This waste heat (or low-grade heat) is one of the world's most ubiquitous sources of untapped energy. For instance, nearly 70% of the energy produced by burning fuel in an IC engine ends up as waste heat energy in the form of hot exhaust gases and heated up engine components.

To convert such low-grade heat into electrical energy, a thermogalvanic cell, also known as a thermocell is used. A thermocell is an energy converter that utilizes electrochemical reactions to attain conversion of low-grade heat to electrical power. It operates based on the Seebeck effect. The two half cells of the system are held at different temperatures causing a difference in redox potentials of the mediator at the anode and cathode. This reaction can drive electrons through an external circuit that allows generation of current and power.

The thermal power flowing through the cell is largely controlled by cell design and electrolyte selection. When a reversible redox couple is used, no net consumption of the electrolyte occurs. Hence, typically, ferri/ferrocyanide redox couple is used as the electrolyte. The Seebeck coefficient of ferri/ferrocyanide redox couple is 1.4 mV/K. This implies that an open-circuit potential of 1.4 mV is attainable at a thermal gradient of 1 K. A schematic of a thermocell with a ferri/ferrocyanide redox couple is shown in Fig. 10. The redox reactions occurring at the electrodes are also indicated therein.

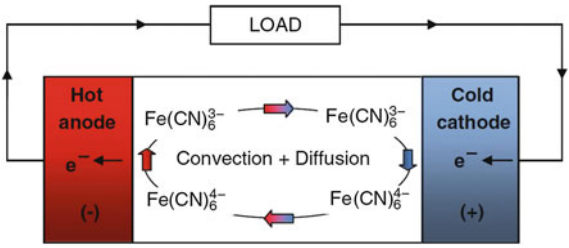

Fig. 10 Ferri/ferrocyanide redox couple thermogalvanic cell [53]. Copyright 2012. Reproduced with permission from Springer

Ferrocyanide is oxidized at the hot anode; the electron generated then travels through an external circuit and returns to the cell via the cold cathode where it is consumed in the reduction of ferricyanide. The accumulation of reaction products at half cell is prevented either by the diffusion or by the convection of the electrolyte that occurs naturally, thus eliminating the need for moving mechanical components.

The cell design should be such that it reduces the voltages losses occurring in the cell. Typically, voltage losses occur in the form of ohmic, mass transport, and activation overpotentials. Ohmic overpotential is the voltage loss due to resistance offered by the electrolyte, and mass transport overpotential is the loss incurred due to the time taken for the movement of ions within the electrolyte. Minimizing the distance between the electrodes would decrease the resistance and hence reduce the ohmic overpotential. Minimizing the distance would also reduce the time taken for ions to travel from one electrode to the other, thus reducing the mass transport overpotential. However, the distance between electrodes cannot be reduced beyond a certain limit as it would be hard to maintain the temperature gradient between the anode and the cathode. Hence, the electrode distance has to be fixed so as to achieve a balance between the two.

Activation overpotential is associated with the activation barrier needed to be overcome to start a reaction. For the same activation overpotential, larger current densities are realized when the exchange current density is increased. This increase is attained when the concentration of the redox couple in the electrolyte is maximized, the thermal gradient is increased, and the number of possible reaction sites is augmented. Porous electrodes have the advantage of increased electroactive surface area and will directly amplify the short-circuit current density.

This is where carbon nanotubes could play a significant role in improving the efficiency of thermogalvanic cells. The diameter of CNTs is of the range of few nanometers, and this gives rise to large gravimetric and volumetric specific surface areas (SSA). Their unique aspect ratios allow porous electrodes to be fabricated by a variety of methods. Also, CNT electrodes exhibit fast electron transfer kinetics with the redox couple ferri/ferrocyanide. This justifies the use of CNTs as electrodes in ferri/ferrocyanide thermo cells.

It has been demonstrated that the efficiency of thermocells with MWNT electrodes is high as 1.4% relative to the Carnot Cycle, which is three times higher than the efficiency of conventional thermocell devices with platinum electrodes [54]. This efficiency was raised to 2.6% by introducing a carbon SWNT/reduced

graphene oxide (rGO) composite electrode [55]. Improved mass transport due to enhanced porosity of the optimized SWNT/rGO composite was found responsible for the efficiency enhancement.

To improve this efficiency further to 3.95%, the following strategies have been deployed: the use of CNT aerogel sheets as electrodes, removal of low activity carbonaceous impurities that limit electron transfer kinetics, decoration of CNT sheets with catalytic platinum nanoparticles, mechanical compression of nanotube sheets to tune conductivity and porosity, and the utilization of a cylindrical cell geometry [56]. The use of aerogel sheets would increase the porosity, and the addition of catalytic particles and removal of low activity impurities would lower the activation overpotential, thereby leading to an increase in the overall efficiency.

Apart from CNT nanotube and aerogel electrodes, polymer electrodes embedded with CNTs have also been explored for the use in thermocells. A detailed review of such composite electrodes is presented in [57].

The prime challenge faced by the research community in thermoelectric energy harvesting is that the Carnot-relative efficiency should be around 5% for commercial viability of such harvesters. Hence, new methods of improving the efficiency of thermocells are under exploration.

7 Summary

Electroactive polymers offer the possibility of developing new high-performance, flexible energy harvesters. EAPs can be broadly classified into two categories: dielectric EAPs and ionic EAPs. Conductive polymer composites fall under the category of ionic EAPs, whereas most of the crystalline and semicrystalline polymers fall under the category of dielectric EAPs. The dielectric EAPs can be further classified into ferroelectric and electrostrictive based on their stain–electric field relationship.

As far as conductive polymer composites are concerned, their efficiency in terms of mechanical-to-electrical energy is very low. This is because, the energy conversion from mechanical to electrical is not direct but mediated through a chemical reaction. Hence, their use as transducers in mechanical energy harvesters is not efficient. However, conductive polymers with carbon nanotube fillers are excellent candidates for making electrodes of thermogalvanic cells owing to their low manufacturing cost, chemical and thermal stability, and fast electron transfer kinetics.

The Carnot-relative efficiency achieved so far in CNT-based thermocells is 3.95%. However, for commercial viability, the efficiently still needs to be improved, so as to achieve 5% Carnot-relative efficiency.

Crystalline and semicrystalline dielectric EAPs are widely used as transducers in mechanical energy harvesting. In the context of kinematic energy harvesting, wherein the harvesters could be designed as an integral part of the host structure, the use of ferroelectric PVDF transducers is highly promising. This can be

attributed to the fact that PVDF is very flexible and also possesses high piezoelectric strain coefficient than other polymers.

The use of electrostrictive polymers such as polyurethane and composites of polyurethane is highly encouraged in kinetic energy harvesting as they have high electromechanical coupling. However, the need for a dc bias field for operation is a limitation to electrostrictive transducers. In cases where application of a dc bias field is difficult, piezoelectric polymers such as PVDF could be employed.

Biopolymers such as cellulose nanocrystals are explored for their energy harvesting capabilities primarily because of their biocompatibility. They could be used to design implantable energy harvesters that could power pacemakers, targeted drug delivery systems, etc. Low density, high strength ease of availability, chemical resistance, and thermal stability of cellulose nanocrystals also contribute to their viability in mechanical energy harvesting.

The challenges facing the field of implantable energy harvesters are the legal issues concerned with performing in vitro experiments on living organisms. Though many prototypes have been designed and tested using laboratory equipment, the performance of such harvesters while being implanted into the host organism is yet to be explored.

To sum up, dielectric EAPs, both ferroelectric and electrostrictive, offer good performance levels in mechanical energy harvesting, whereas conductive polymer composites find more applications in the field of thermoelectric energy harvesting.

References

1. Kim H, Tadesse Y, Priya S (2009) Piezoelectric energy harvesting. Energy harvesting technologies. Springer, US, pp 3–39
2. Qi Y, Jafferis NT, Lyons K et al (2010) Piezoelectric ribbons printed onto rubber for flexible energy conversion. Nano Lett 10:524–528
3. Inman DJ, Erturk A, Inman DJ (2011) Piezoelectric energy harvesting. Wiley, USA
4. Mane P, Jingsi Xie J, Leang KK, Mossi K (2011) Cyclic energy harvesting from pyroelectric materials. IEEE Trans Ultrason Ferroelectr Freq Control 58:10–17
5. Bowen CR, Kim HA, Weaver PM, Dunn S (2014) Piezoelectric and ferroelectric materials and structures for energy harvesting applications. Energy Environ Sci 7:25
6. Erturk A, Inman DJ (2009) An experimentally validated bimorph cantilever model for piezoelectric energy harvesting from base excitations. Smart Mater Struct 18:025009
7. Friswell MI, Ali SF, Bilgen O et al (2012) Non-linear piezoelectric vibration energy harvesting from a vertical cantilever beam with tip mass. J Intell Mater Syst Struct 23:1505–1521
8. Ma TW, Zhang H, Xu NS (2012) A novel parametrically excited non-linear energy harvester. Mech Syst Signal Process 28:323–332
9. Malaji PV, Ali SF (2015) Analysis of energy harvesting from multiple pendulums with and without mechanical coupling. Eur Phys J Spec Top 224:2823–2838
10. Zhou S, Cao J, Inman DJ et al (2014) Broadband tristable energy harvester: modeling and experiment verification. Appl Energy 133:33–39

11. Aravind Kumar K, Ali SF, Arockiarajan A (2015) Piezomagnetoelastic broadband energy harvester: nonlinear modeling and characterization. Eur Phys J Spec Top. doi:10.1140/epjst/e2015-02590-8
12. Erturk A, Hoffmann J, Inman DJ (2009) A piezomagnetoelastic structure for broadband vibration energy harvesting. Appl Phys Lett 94:254102
13. Williams CB, Yates RB (1995) Analysis of a micro-electric generator for microsystems. Proc Int Solid-State Sens Actuators Conf TRANSDUCERS '95 1:8–11
14. Kim SG, Priya S, Kanno I (2012) Piezoelectric MEMS for energy harvesting. MRS Bull 37:1039–1050
15. Leo DJ (2007) Engineering analysis of smart material systems. Wiley, USA
16. Bar-Cohen Y (2004) Electroactive polymer (EAP) actuators as artificial muscles: reality, potential, and challenges. SPIE Press, USA
17. Kornbluh RD, Flamm DS, Prahlad H, et al (2003) Shape control of large lightweight mirrors with dielectric elastomer actuation. In: Bar-Cohen Y (ed) International society for optics and photonics, p 143
18. Krishen K (2009) Space applications for ionic polymer-metal composite sensors, actuators, and artificial muscles. Acta Astronaut 64:1160–1166
19. Menon C, Carpi F, De Rossi D (2009) Concept design of novel bio-inspired distributed actuators for space applications. Acta Astronaut 65:825–833
20. Shahinpoor M, Kim KJ, R BP, et al (2005) Ionic polymer–metal composites: IV. Industrial and medical applications. Smart Mater Struct 14:197–214
21. Wax SG, Sands RR (1999) Electroactive polymer actuators and devices. In: Bar-Cohen Y (ed) International society for optics and photonics, pp 2–10
22. Kovacs G, Lochmatter P, Wissler M et al (2007) An arm wrestling robot driven by dielectric elastomer actuators. Smart Mater Struct 16:S306–S317
23. Smith RC (2005) Smart material systems. Society for Industrial and Applied Mathematics
24. Jean-Mistral C, Basrour S, Chaillout J-J (2010) Comparison of electroactive polymers for energy scavenging applications. Smart Mater Struct 19:085012
25. Takashima W, Uesugi T, Fukui M et al (1997) Mechanochemoelectrical effect of polyaniline film. Synth Met 85:1395–1396
26. Vinogradov A (2002) Piezoelectricity in Polymers. In: Encyclopedia of smart materials. Wiley, USA
27. Sessler GM (1982) Chapter 6—polymeric electrets. In: electrical properties of polymers, pp 241–284
28. Erturk A, Inman DJ (2009) Electromechanical modeling of cantilevered piezoelectric energy harvesters for persistent base motions. Energ Harvesting Technol. Springer, US, pp 41–77
29. Roundy S, Wright PK, Rabaey J (2003) A study of low level vibrations as a power source for wireless sensor nodes. Comput Commun 26:1131–1144
30. Twiefel J, Westermann H (2013) Survey on broadband techniques for vibration energy harvesting. J Intell Mater Syst Struct 24:1291–1302
31. Tang L, Yang Y, Soh CK (2010) Toward broadband vibration-based energy harvesting. J Intell Mater Syst Struct 21:1867–1897
32. Granstrom J, Feenstra J, Sodano H, Farinholt K (2007) Energy harvesting from a backpack instrumented with piezoelectric shoulder straps. Smart Mater Struct 16:1810–1820
33. Rocha JG, Gonçalves LM, Rocha PF et al (2010) Energy harvesting from piezoelectric materials fully integrated in footwear. IEEE Trans Ind Electron 57:813–819
34. Taylor GW, Burns JR, Kammann SM et al (2001) The energy harvesting Eel: A small subsurface ocean/river power generator. IEEE J Ocean Eng 26:539–547
35. Allen JJ, Smits AJ (2001) Energ Harvesting Eel J Fluids Struct 15:629–640
36. Hansen BJ, Liu Y, Yang R, Wang ZL (2010) Hybrid nanogenerator for concurrently harvesting biomechanical and biochemical energy. ACS Nano 4:3647–3652
37. Yang R, Qin Y, Dai L, Wang ZL (2009) Power generation with laterally packaged piezoelectric fine wires. Nat Nanotechnol 4:34–39

38. Sorayani Bafqi MS, Bagherzadeh R, Latifi M (2015) Fabrication of composite PVDF-ZnO nanofiber mats by electrospinning for energy scavenging application with enhanced efficiency. J Polym Res 22:130
39. Fukada E (1968) Piezoelectricity as a fundamental property of wood. Wood Sci Technol 2:299–307
40. Csoka L, Hoeger IC, Rojas OJ et al (2012) Piezoelectric effect of cellulose nanocrystals thin films. ACS Macro Lett 1:867–870
41. Mahadeva SK, Walus K, Stoeber B (2014) Piezoelectric paper fabricated via nanostructured barium titanate functionalization of wood cellulose fibers. ACS Appl Mater Interfaces 6:7547–7553
42. Alam MM, Mandal D (2016) Native cellulose microfiber-based hybrid piezoelectric generator for mechanical energy harvesting utility. ACS Appl Mater Interfaces 8:1555–1558
43. Zheng Q, Zhang H, Mi H et al (2016) High-performance flexible piezoelectric nanogenerators consisting of porous cellulose nanofibril (CNF)/poly(dimethylsiloxane) (PDMS) aerogel films. Nano Energy 26:504–512
44. Liu Y, Member S, Ren KL, Hofmann HF (2005) Investigation electrostrictive polymers for energy harvesting. IEEE Trans Ultrason Ferroelectr Freq Control 52:2411–2417
45. Guyomar D, Lebrun L, Putson C et al (2009) Electrostrictive energy conversion in polyurethane nanocomposites. J Appl Phys 106:014910
46. Lallart M, Cottinet P-J, Lebrun L et al (2010) Evaluation of energy harvesting performance of electrostrictive polymer and carbon-filled terpolymer composites. J Appl Phys 108:034901
47. Lebrun L, Guyomar D, Guiffard B et al (2009) The characterisation of the harvesting capabilities of an electrostrictive polymer composite. Sens Actuators A Phys 153:251–257
48. Leaver P, Cunningham MJ, Jones BE (1987) Piezoelectric polymer pressure sensors. Sens Actuators 12:225–233
49. Yuan Y, Zhou S, Liu Y, Tang J (2013) Nanostructured macroporous bioanode based on polyaniline-modified natural loofah sponge for high-performance microbial fuel cells. Environ Sci Technol 47:14525–14532
50. Wang Y, Zhang SM, Deng Y et al (2016) Flexible low-grade energy utilization devices based on high-performance thermoelectric polyaniline/tellurium nanorod hybrid films. J Mater Chem A 4:3554–3559
51. Sultana A, Alam MM, Garain S et al (2015) An effective electrical throughput from PANI supplement ZnS nanorods and PDMS-based flexible piezoelectric nanogenerator for power up portable electronic devices: an alternative of MWCNT filler. ACS Appl Mater Interfaces 7:19091–19097
52. Antiohos D, Romano M, Chen J, Razal JM (2013) Carbon nanotubes for energy applications. In: Syntheses and applications of carbon nanotubes and their composites. InTech
53. Romano MS, Gambhir S, Razal JM et al (2012) Novel carbon materials for thermal energy harvesting. J Therm Anal Calorim 109:1229–1235
54. Hu R, Cola BA, Haram N et al (2010) Harvesting waste thermal energy using a carbon-nanotube-based thermo-electrochemical cell. Nano Lett 10:838–846
55. Romano MS, Li N, Antiohos D et al (2013) Carbon nanotube—reduced graphene oxide composites for thermal energy harvesting applications. Adv Mater 25:6602–6606
56. Im H, Kim T, Song H et al (2016) High-efficiency electrochemical thermal energy harvester using carbon nanotube aerogel sheet electrodes. Nat Commun 7:10600
57. Dey A, Bajpai OP, Sikder AK et al (2016) Recent advances in CNT/graphene based thermoelectric polymer nanocomposite: A proficient move towards waste energy harvesting. Renew Sustain Energy Rev 53:653–671

Ceramic-Based Polymer Nanocomposites as Piezoelectric Materials

Deepalekshmi Ponnamma, Mariem Mohamed Chamakh, Kalim Deshmukh, M. Basheer Ahamed, Alper Erturk, Pradeep Sharma and Mariam Al-Ali Al-Maadeed

Abstract Piezoelectric ceramics receive high interest due to their wide range of applications/usage in fabricating sensors, frequency filters, actuators, and many other electronic devices. Moreover, generating energy is the need of the hour. This chapter is written as a review of ceramic polymer composites that exhibit piezoelectric properties. A few synthesis methods for the ceramic particles as well as the polymer composites are discussed, followed by the core content of the chapter, the piezoelectric properties of the material.

Keywords Energy · Piezoelectric coefficient · Ceramics · Composites · Polymer

D. Ponnamma (✉) · M.M. Chamakh
Center for Advanced Materials, Qatar University, P.O. Box 2713, Doha, Qatar
e-mail: lekshmi_deepa@yahoo.com

K. Deshmukh · M.B. Ahamed
Department of Physics, B.S. Abdur Rahman University, Chennai 600048, TN, India

A. Erturk
George W. Woodruff School of Mechanical Engineering, Georgia Institute of Technology, Atlanta, GA, USA

P. Sharma
Department of Mechanical Engineering, University of Houston, Houston, TX 77204, USA

M.A.-A. Al-Maadeed
Qatar University, PO Box 2713, Doha, Qatar

M.A.-A. Al-Maadeed
Materials Science and Technology Program, Qatar University, PO Box 2713, Doha, Qatar

D. Ponnamma et al. (eds.), *Smart Polymer Nanocomposites*,
Springer Series on Polymer and Composite Materials,
DOI 10.1007/978-3-319-50424-7_3

Contents

1 Introduction

Ceramics are a widely explored form of materials due to their structural significance in terms of resistance to chemicals, high pressure and temperature, and wear [1–5]. These materials find vast number of applications in many areas of industry such as spacecrafts, nuclear power plants, mining equipment, and combustion engines, since its discovery [2–7]. Mainly the ceramic particles include oxides (silica, alumina, and zirconia), non-oxides (carbides, borides, nitrides, and silicides), and combinations of oxides and non-oxides. These materials are typically modified by adding primary and secondary phase materials (fibers and whiskers), and multiple phases (nanoparticles) in order to make it more durable and flaw resistant [5–8]. When nanoparticles are distributed within the large grains of ceramics, the stress is being transferred to these nanonetworks, because of their large surface area and aspect ratio [9–11].

An intermetallic compound, lead zirconate titanate (PZT), is one of the most significant ceramic materials, widely applied in piezoelectric devices [12, 13]. With the capability of changing mechanical deformations to electrical energy, such energy harvesters find potential applications in medical diagnostic devices, security systems, space vehicles, and other nondestructive testing [14–18]. This energy generation aspect has tremendous possibilities as it can be correlated with almost all dynamic movements in nature, including human motion. The typical piezoelectric coefficient of PZT is 220 pC/N. However, the conventional piezodevices based on ceramic materials are heavy, rigid, and in block form. So it is interesting to combine the higher dielectric and piezoelectric properties of ceramics with the soft, flexible, and low-cost polymers [14, 15]. A large number of polymers such as polyvinylidene fluoride (PVDF) and its copolymers, polypropylene (PP), polyamides, polyimides, polyurethane (PU), polyurea, Parylene-C, liquid crystal polymers, polydimethylsiloxanes (PDMS), and epoxy resin are used for fabricating different composites to harvest electrical energy [16, 17]. Combinations of crystalline and amorphous PVDF–PDMS polymers in fabricating piezoelectric nanogenerators are also reported [19] very recently.

This chapter particularly focuses on the polymer-based ceramic composites exhibiting piezoelectric responses. A brief introduction of the synthesis of ceramic particles and their polymer composites is provided, followed by the detailed investigation of the piezoelectric performance. The polymer/ceramic composites are explained under the two major classes—energy harvesters from crystalline and semicrystalline polymer composites and those from amorphous polymers.

2 Synthesis of Ceramic Particles and Their Polymer Composites

Ceramic particles are known to enhance the mechanical strength, elastic modulus, and wear resistance of matrices such as metals and polymers. A typical ceramic material is made of a metal, non-metal, or a metalloid bonded by means of ionic or covalent interactions. In general, the ceramic particles can be classified into crystalline and noncrystalline [10, 11]. The major examples of ceramic particles include compounds of boron (boron oxide and boron nitride), silicon (SiC, Si_3N_4, and silicon aluminum oxynitride), magnesium (magnesium diboride and magnesium silicate), titanium (titanium carbide, barium, and strontium titanate), and zirconium (lead zirconate titanate and zirconium dioxide). The usual synthesis methods of these materials include sintering, electrodeposition, cold spray coating, plasma chemical methods, combustion/flame synthesis, sol-emulsion-gel technique, spray pyrolysis, and aerosol synthesis. The process depends on the nature of ceramic particle to be synthesized, its particle size and the yield. Table 1 shows the synthesis of a few types of ceramic particles.

Many ceramic particles are established for their piezoelectric properties, capable of converting mechanical energy into electrical energy and vice versa. Such materials also show pyroelectric effect (converting thermal energy into electrical energy); all pyroelectric materials are piezoelectric. This property can also be related to the ferroelectricity, by which electric dipoles can be specifically oriented by electric field [20]. Examples of ferroelectric ceramics are lead titanate (PT), lead zirconate titanate (PZT), calcium-doped lead titanate (PTCa), and lead manganese niobate–lead titanate/barium titanate (PMN-PT/$BaTiO_3$). The piezoelectric properties of ceramic particles are used in designing actuators, transducers, high-frequency loudspeakers, etc. The most commonly used ceramic particles for these purposes are barium titanate and PZT.

A simple ceramic/polymer composite is defined as a material in which the ceramic phase is dispersed and reinforced with a polymer medium showing 0–3 connectivity [12]. The ceramic particles can be in micro- and nanodimensions based on which the polymer composites and nanocomposites are constructed. Most common synthesis method for such composites is melt mixing by extruder; however, other methods such as in situ polymerization and electrospinning are also practiced.

Table 1 Different methods of synthesis of ceramic particles

Ceramic particles	Synthesis technique	Method of preparation	References
CNT–CO–MgO CNT–Fe–Al_2O_3 CNT–Fe/CO–$MgAl_2O_3$	High-temperature extrusion technique	Mono-phased oxide solid solutions are chemically synthesized Transition metal particles are attached both inside and at the surface of each grain ZrO_2-based ceramics is first partially densified under 8.6 MPa load and then extruded under 43 MPa load Al_2O_3 and $MgAlO_4$—matrix materials are extruded in a graphite die at 1500 °C	[2, 4]
Al_2O_3/SiC system	Conventional powder route (hot pressing technique)	SiC powder dispersed ultrasonically in deionized water is added to an attritor mill containing zirconia media, dispersing agent and the alumina powder After milling for 2 h, at 500 rpm, the slurry is freeze dried, sieved, and hot pressed with a graphite die at 1700 °C for 1 h at 20 MPa	[1]
Al_2O_3–SiC–CNT	Sonication and ball milling	Al_2O_3 and SiC dispersion is magnetically stirred and sonicated In the next step, it is ball milled at 10:1 ball to powder weight ratio After adding CNT, the whole solution is sonicated	[6]
Ceramic–TiO_2	Mechanochemical synthesis (high-energy ball milling)	Waste glass powder and fly ash (70:30) is mechanically ground in ball mill for 6 h at 700 rpm TiO_2 nanoparticles (2, 4, 6, 8, and 16%) are added using a mixer The mixture is cylindrically pressed and heated up to 800 °C for 1 h in a box-type SiC furnace and cooled	[5]
Ceramic SiHfBCN	Mechanochemical synthesis (high-energy ball milling)	Polysilazane and borane dimethylsulfide are cross-linked on heating at 200–250 °C for 3 h and grounded Powder is pressed and pyrolyzed at 1100 °C and then annealed at 1300 °C	[3]

(continued)

Table 1 (continued)

Ceramic particles	Synthesis technique	Method of preparation	References
Zirconia-based ceramic nanocomposites	Mechanochemical synthesis (high-energy ball milling)	ZrO_2, Y_2O_3, and cordierite powders are grounded for 2 h by wet ball mixing, dried and again dry-milled for 12 h. After that, respectively, pressed uniaxially and isostatically under 29.4 and 196 MPa Composite is sintered in air at 1400, 1500, and 1600 °C with 10 °C/min for 4 h	[7]
SiOC–ZrO_2	Polymer precursor route	Polysilsesquioxanes-based materials modified with zirconia nanoparticles are cross-linked and pyrolyzed Then it is ball milled, warm pressed at 180 °C and 133 MPa for 30 min, and pyrolyzed at 1100 °C for 2 h in argon	[8]
$Bi_4Ti_3O_{12}$ ceramics	Coprecipitation technique	Ti^{4+} and Bi^{3+} precursors dissolved in acidic isopropyl alcohol solution are added to aqueous suspension of WO_3 Under pH control, aqueous NH_4OH is added to achieve complete hydroxide precipitation. This precipitate is washed and redispersed in isopropyl alcohol up to neutral pH The dried material is air calcined at 650 °C for 1 h, attrition milled in isopropyl alcohol for 2 h and uniaxially pressed and sintered at 800–1150 °C for 2 h	[9]
SiN_4–SiC	Vapor-phase reaction technique	$[Si(CH_3)_3]_2NH$ or $[Si(CH_3)_2NH]_3$ are mixed with NH_3 under N_2 used as carrier gas, and then passed into a reaction chamber at 1000 °C. The amorphous powder is collected and crystallized to Si_3N_4/SiC at 1500 °C for 6 h The C content and thus the SiC content in the crystallized powder can be adjusted by NH_3 content with a maximum value of 34 vol.% SiC in the final nanocomposite. The resulting highly reactive submicron powder can react with oxygen or water to generate heat and thus an immediate heat treatment at 1350 °C for 4 h under argon is done	[10]

(continued)

Table 1 (continued)

Ceramic particles	Synthesis technique	Method of preparation	References
TiN–SiC–Si_3N_4	Self-propagating high-temperature synthesis (SHS) and combustion synthesis (CS)	TiN–SiC–Si_3N_4 composites were synthesized from $TiSi_2$–SiC mixture by combustion under N_2 at 130 MPa and 1000–3000 °C under adiabatic conditions	[11]
ZrO_2–Al_2O_3	Sol-Gel technique	Stable (hydrous) boehmite and oxalate sols (zirconyl oxalate, cerium zirconyl oxalate, and yttrium zirconyl oxalate) were prepared prior to unstabilized, ceria-stabilized, or yttria-stabilized ZrO_2/Al_2O_3 composites The sols are then mixed in proper ratio and converted into a gel by stabilization and dried Then, it is calcined at different temperatures and sintered without pressure to obtain a homogeneous microstructure	[11]

3 Piezoelectric Energy from Ceramic Nanocomposites

3.1 Ceramic Composites of Semicrystalline and Crystalline Polymers

A very recent review by Ramadan et al. addresses significant parameters influencing the piezoelectric response of various polymers [21]. Other than the nature of the base polymers and fillers used to fabricate their composites, the method of fabrication, alignment of crystallites, poling conditions, etc., affect the piezoelectric performance of a typical sample. In a recent chapter, we have also reported the piezo- and thermoelectric properties of nanocomposites based on polymers [22]. Numerous polymers show this energy-generating property, and here, a classification of polymer nanocomposites based on the polymer crystallinity is provided for better understanding. Table 2 shows different ceramic polymer composites exhibiting piezoelectric property and their method of fabrication.

Annamalai et al. reviewed various ceramic polymer composites for their dielectric and piezoelectric properties in terms of their piezoelectric strain coefficient (d_{33}) and voltage coefficient (g_{33}). The g_{33} is directly proportional to d_{33}, whereas inversely proportional to the permittivity. It is also found that the d_{33} values depend on the volume fraction of the ceramic particles and the direction of polarization of the matrix. The ferroelectric ceramic, PZT, when mixed with PVDF

Table 2 Piezoelectric properties of a few ceramic particles and its polymer composites

Ceramic particle	Polymer	Fabrication method	Piezoelectric charge constant, d_{33} (pC/N)	Reference
PZT	Thermoplastic	Cold isostatic pressing	44	[23]
PZT	Epoxy	1–3 composite commercially available	593	[24]
PMNT	Epoxy	Dice-and-fill method	1200	[25]
PMNT	Epoxy	Modified dice-and-fill method	1256	[26]
PLZT	PVDF	Hot press	102	[27]
PLZT	PVDF	Solution mixing followed by hot press	17.8	[28]
PZT	Polyester resin	Spinning PZT in the resin in a centrifuge	29	[29]
PZT	PVDF	Brabender mixing	33	[30]
PZT	PVC	Calendering and tape casting	29	[31]
PZT	PU	Blending	28	[32]
PZT	P(VDF-TrFE)	Solution casting followed by hot pressing	410	[33]
PZT	PVC	Solution mixing	31	[34]
PZT and carbon black	PVC	Hot pressing	20	[35]
PZT	Poly (3-hydroxybutyrate)	Powder mixing and hot pressing	6.2	[36]

polymer in 0.5 volume fraction by hot pressing method exhibited reasonable d_{33} value, in addition to the stability and flexibility [13].

$BaTiO_3$ particles of various dimension 500 (tetragonal), 100 (cubic), and 10 nm (cubic) were filled with polyvinylidene fluoride-trifluoroethylene (PVDF-TrFE) and its piezoelectric performance was compared with that of pure PVDF. All samples were in the form of electrospun fibers. In the composite fibers, ceramic particles of lower size (<500 nm) were trapped inside the polymer fibers, and those particles with diameter 500 nm were randomly dispersed in and outside the fibers [14]. The electrically poled fibers were tested for the generated voltage, and the influence of frequency, time, and filler dimension on their performance is represented in Fig. 1.

Shin et al. [37] reported the piezoelectric response of $BaTiO_3$-reinforced polymer composite and its possible application in manufacturing nanogenerators. The PVDF copolymer poly(vinylidene fluoride-co-hexafluoropropylene) or P(VDF-HFP) was used as the base polymer, and a solvent-assisted film formation process was adopted for the composite fabrication. An excellent output performance was observed in the form of voltage and current, respectively, 110 V and 22 μA with corresponding

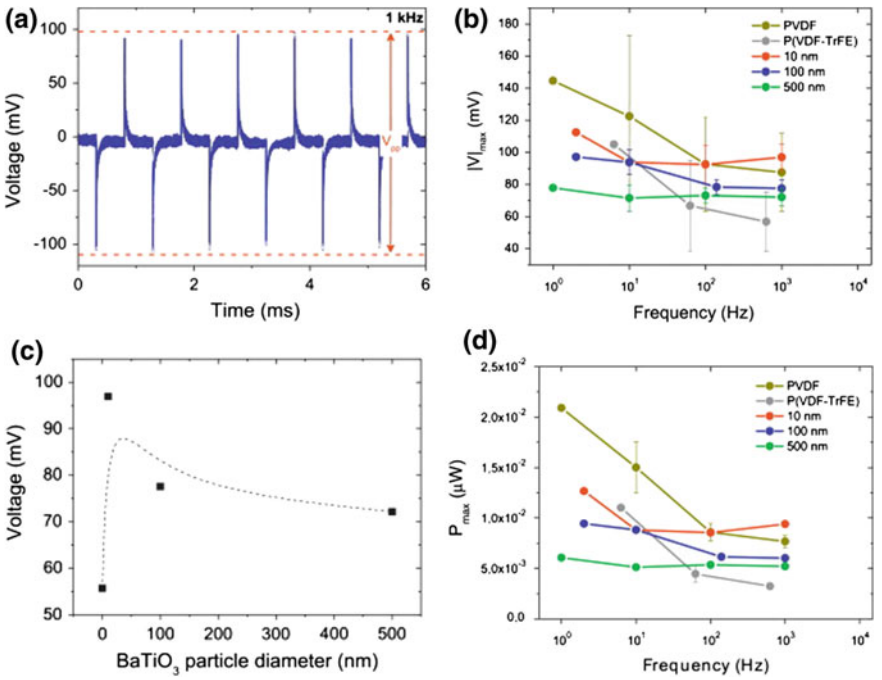

Fig. 1 **a** Voltage generated during 6 ms at a frequency of 1 kHz, of electrospun $BaTiO_3$/P(VDF-TrFE) at 20% filler; **b** maximum voltage generated at different frequencies for all samples; **c** piezopotential obtained at 1 kHz for P(VDF-TrFE) and $BaTiO_3$/P(VDF-TrFE) at 20% filler and **d** maximum power generated by the electrospun membranes [14]. Copyright 2013. Reproduced with the permission from Elsevier Ltd

output power density of 0.48 Wcm^{-3}. An optimal concentration of the $BaTiO_3$ was also found out by investigating the effect of solvent ratios on particle clustering.

Different sets of PVDF composites containing 50–90 vol.% of PLZT were made by hot pressing [27]. With PLZT volume fraction and its particle size, both d_{33} and relative permittivity values of the composites increased. The particular composite, containing 85% PLZT of 150 μm diameter, showed highest performance with a high d_{33} of 101 pC/N and relative permittivity of 299. The energy-harvesting efficiency of fibrous $BaTiO_3$/PVDF composites based on longitudinal stretch movement was investigated by Kakimoto et al. [38]. The fibrous ceramic particles of 800 nm diameter were dispersed in PVDF using the extruder. It is assumed that the piezoelectric system can behave like a parallel plate capacitor, and the energy output obtained under an electric load of 2 MΩ is demonstrated in Fig. 2.

Hybrid combination of PZT and polyaniline (PANI) in enhancing the properties of PVDF was reported by Sakamoto and coworkers [39]. A percolation at 20–30 vol.% was observed for the hybrid filler (PZT was coated with PANI) combination. At 30 vol.%, the composite showed best value for d_{33} constant. The enhancement in piezoelectricity is explained in terms of the conducting nature of

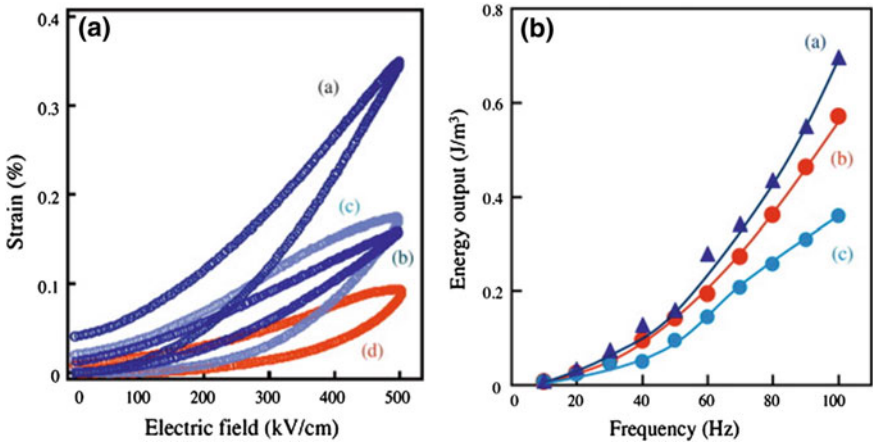

Fig. 2 **a** S–E curves for fibrous $BaTiO_3$-reinforced composite sheets ($BaTiO_3$/PVDF = 30/70 v/v %) having different $BaTiO_3$ orientation ratios of (*a*) 83% and (*b*) 38%, and two reference samples of (*c*) spherical $BaTiO_3$-reinforced composite sheets ($BaTiO_3$/PVDF = 30/70 v/v%) and (*d*) pure PVDF. **b** Generated power as a function of frequency applied to piezoelectric energy harvesting based on stretch movement [38]. Copyright 2013. Reproduced with the permission from Elsevier Ltd.

the sample and the poling process was employed (5 MV/m electric field for 15 min). This functional material is proposed for applications in structural health-monitoring systems.

PP is another polymer exhibiting piezoelectric response, specifically in its cellular form. The cellular PP is usually made by a modified extrusion process, in which voids of μm dimension are created in melt by gas blowing prior to foam blowing. The cooling in the subsequent step keeps the voids within the polymer. Corona charging is also employed to charge PP, other than the electrode charging and electron beam charging [15, 16]. Zhang et al. investigated the influence of fabrication on the piezoelectric d_{33} coefficient of cellular PP. The high-pressure exposure to long-time intervals increased the thickness and the d_{33} coefficient. Static pressures up to 10 kPa do not influence the value, whereas higher pressures cause a reversible decrease. The d_{33} constant is also correlated with the decrease in Young's modulus and the increase in chargeability of the material due to expansion [17].

Epoxy resins are also reported to exhibit piezoresponses, when ceramic particles are employed in it. Lead magnesium niobate titanate (PMNT)-filled epoxy composites of greater 1,3-piezoelectric coefficient was reported when compared to PZT/epoxy composite by Li et al. [40]. Wang et al. [26] also investigated the same system of PIMNT/epoxy 1–3 composite containing 60% filler by volume prepared by a modified dice-and-fill method and suggested the applicability in ultrasonic transducers. PZT/epoxy composites with good piezoresponse were fabricated by freeze-casting process by Xu and Wang [41]. The results obtained from their studies are represented in Fig. 3.

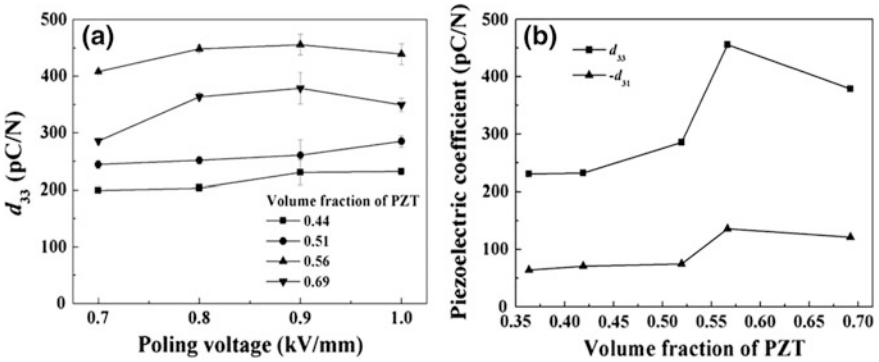

Fig. 3 **a** Effect of poling voltage on longitudinal piezoelectric strain coefficient, d_{33} of 3-1 type PZT/epoxy composites. **b** d_{33} and transverse piezoelectric strain coefficient (d_{31}) of 3-1 type PZT/epoxy composites as a function of PZT volume fraction

Both longitudinal and transverse piezoelectric strain coefficients (d_{33} and d_{31}) were studied for the PZT/epoxy 3-1 piezocomposites by Xu and Wang [41]. The composites were fabricated by tert-butyl alcohol (TBA)-based freeze casting of PZT followed by the infiltration of epoxy. The PZT volume fraction was varied from 0.36 to 0.69 by changing the initial solid loading in freeze-casting slurry. Figure 3 shows the variation of d_{33} with respect to the poling voltage and volume fraction of PZT. In general, the saturation polarization is achieved in PZT ceramics, when the poling voltage is >2 kV/mm. But, in this particular composite, saturation is attained at 0.9 kV/mm itself (Fig. 3a) which is due to the consistency of polarization direction and one-dimensional pore channel direction and the resultant easy deflection of electric domains along the polarization direction.

Figure 3b shows the change in d_{33} and d_{31} constant with PZT volume fraction at a poling voltage of 0.9 kV/mm. Both coefficients show an increase with PZT concentration with a highest value at 0.57 vol.%. This is attributed to the weak structural constitution of the composite above this particular filler volume fraction, pointing toward the fact that the d_{33} and d_{31} coefficients depend on the piezoelectric phase of the composite and interfacial connectivity. When the volume fraction becomes 0.69, the unidirectional porous structure loses its directionality and increases the disorder, thereby decreasing the piezoelectricity.

Figure 4 represents the influence of PZT volume fraction on the hydrostatic strain coefficient (d_h) and hydrostatic piezoelectric voltage coefficient (g_h) of epoxy/PZT composites. The d_h is calculated from the d_{33} and d_{31} constants as shown in Eq. 1.

$$d_h = d_{33} + 2d_{31} \tag{1}$$

The d_h value increased from 103 to 136 pC/N when PZT concentration was increased to 0.69 from 0.36. At 0.57 vol.%, the d_h is 184 pC/N, which is approximately three times higher than the neat PZT (56 pC/N). This behavior is

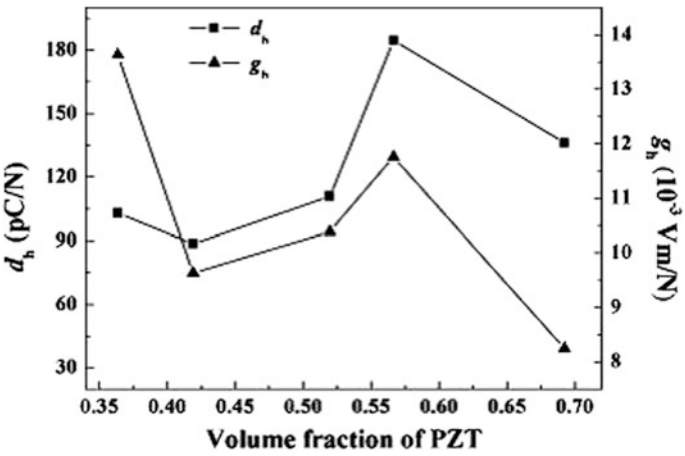

Fig. 4 Variation in hydrostatic strain coefficient (d_h) and hydrostatic piezoelectric voltage coefficient (g_h) with volume fraction of PZT

mainly attributed to the greater decrease observed in d_{31} compared to d_{33} and the porous structure of the particular sample containing 0.57 vol.% PZT. The hydrostatic piezoelectric voltage coefficient (g_h) defined as the hydrophone sensitivity in ultrasonic transducer application is calculated as

$$g_h = \frac{d_h}{\varepsilon_0 \varepsilon_r} \tag{2}$$

where ε_r is the relative permittivity of the sample.

The g_h changed from 13.6 to 8.2 $\times$ 10^{-3} V m/N in a similar way of d_h with increase in PZT volume fraction. Due to the high d_h and reduced ε_r, the g_h is bigger for the composite compared to the neat PZT (1.5 $\times$ 10^{-3} V m/N).

Jain et al. thoroughly investigated the correlation of dielectric properties with piezoelectricity in their recent review of PVDF/PZT composites [42]. They have done a good theoretical survey based on mathematical models and discussed the two models—Yamada model and Furukawa model—to predict the piezoelectric properties. According to Yamada model, the g_{33} can be explained by Eq. 3.

$$g_{33} = \frac{V_f n a d_{33_2}/\varepsilon_0}{\varepsilon 33_2 + (n-1)\varepsilon 33_1 \left\{1 + \frac{n V_f(\varepsilon 33_2 - \varepsilon 33_1)}{n\varepsilon 33_1 + (\varepsilon 33_2 - \varepsilon 33_1)(1-V_f)}\right\}} \tag{3}$$

where a is the poling ratio of ceramic inclusions, $\varepsilon 33_i$ is the dielectric constant of the inclusion at the ith direction of poling, V_f is the filler volume fraction, and n is a dimensionless parameter depending on the shape and orientation of ceramic inclusions.

The Furukawa model can also be defined by Eqs. 4 and 5.

$$d = V_f L_T L_E d_2 \tag{4}$$

and

$$g = V_f L_T L_D g_2 \tag{5}$$

where d and g represent the piezoelectric coefficients of the composites, and d_2 and g_2 denote the coefficients of the ceramic particles. L_T, $L_{D,}$ and L_E are the local field coefficients with respect to the stress, electrical displacement, and electric field.

3.2 Ceramic Composites of Amorphous Polymers

The investigation on flexible piezoelectric materials based on polymer composites has a long history starting from the reports of Kitayama and Sugawara in 1972 [43]. Piezoelectric flexible composites particularly applied in hydrophones are studied by Banno and Saito in 1983 [44]. The composites were based on synthetic rubbers and ceramic particles, lead titanate, and PZT. The rubber/ceramic composites made by hot rolling were poled in silicone oil by applying 100 kV/cm at 60 °C for 1 h. Out of all composites, the one made with pure lead titanate showed the best piezo-properties and established its use in making hydrophones. The experimental results were in good agreement with the theoretical 'modified cubes model' as well.

Mamada et al. investigated a set of pseudo-1-3 piezoelectric ceramic/polymer composites consisting of linearly ordered piezoelectric ceramic particles filled silicone gel, silicone rubber, urethane rubber, and poly-methyl-methacrylate, matrices for their piezoelectric responses [45]. The polymer matrices were classified into two sets—matrices Q and U not adhered to the electrodes (Q is the silicone rubber and U is the urethane rubber) and matrices A and G adhered to the electrodes (A represents PMMA and G represents silicone gel). Figure 5a shows the fabrication steps followed for the two sets of ceramic/polymer composites and 6b their d_{33} constant with respect to the filler volume fraction. At the same PZT concentration, the d_{33} values show a variation in the order of A < U < Q < G. When PZT concentration is 10 vol.%, the d_{33} for silicone gel composite was above 60 pC/N and at 40 vol.%, the value became 80 pC/N. However, for the PMMA composite, the d_{33} was 10 pC/N even at 40 vol.% PZT. This variation in piezoelectric coefficient is due to the difference in relative permittivity and Young's modulus of the samples. The difference in dielectric constant is due to the different area of exposure of each polymer matrix where PZT particle alignment is exposed out of the composite surface. In addition, the d_{33} values increase with decrease in Young's modulus of the matrix. This is due to the increase in force applied on the aligned PZT particles in the composites with lower Young's modulus and the increased force with the increased area of exposure.

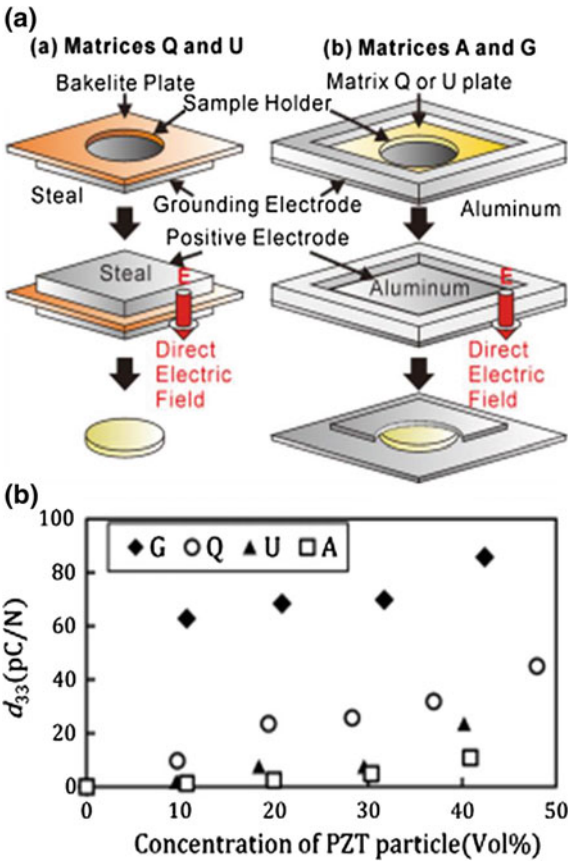

Fig. 5 **a** Fabrication process of aligned-type piezoelectric composite. (*a*) Matrices Q and U, (*b*) Matrices A and G. **b** Relationship between PZT particle concentration and d_{33} for aligned-type piezoelectric composite [45]

3.3 Miscellaneous

By the use of digital projection printing, Kim et al. [46] demonstrated the optical printing of barium titanate (BTO)-mixed polyethylene glycol diacrylate (PEGDA) polymer composite into three-dimensional microstructures. BTO particles of 85 ± 15 nm dimension were synthesized by hydrothermal method and the surface is modified with 3-trimethoxysilylpropyl methacrylate (TMSPM) linker molecule to enhance the C–C bond strength in BTO-PEGDA composite. A comparison of various combinations including the reported modification of BTO with CNTs [47] is represented in Fig. 6a. Under a constant load of 1.44 N, the piezoelectric output of PEDGA-BTO grafted with TMSPM was twice compared to the CNT composites and was 10 times higher than neat PEDGA-BTO composite. The unpolarized samples of PEDGA with and without TMSPM showed no response. The variation

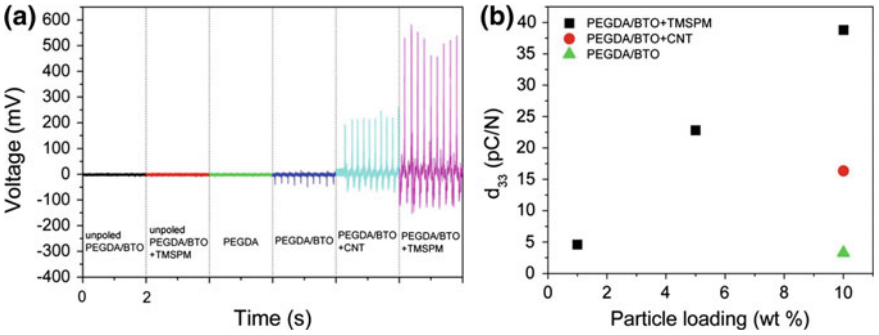

Fig. 6 **a** Voltage response of various unpoled and poled composite materials (neat films) cycled with a 1.44 N load applied perpendicular to the film surface. Cycling data were collected for a total of 2 s for each film. **b** Plot showing the effective piezoelectric modulus (d_{33}) of a grafted PEGDA/BTO composite material as a function of BTO mass loading. The piezoelectric moduli for the 10% loaded PEGDA/BTO with CNTs and PEGDA/BTO (no CNTs or TMSPM) composites are also included for comparison [46]. Copyright 2014. Reproduced with the permission from American Chemical Society

in d_{33} constant with respect to the filler concentration (Fig. 6b) shows almost 39 pC/N for the TMSPM-grafted BTO. This is attributed to the BTO-PEDGA mechanical interface, which allows an efficient mechanical to electrical energy conversion through the stress transfer from the polymer to piezoelectric crystals. In the case of CNT-modified composite, the mechanical response of the BTO nanoparticles increases as the CNTs stiffen the polymer, when the chains are strained.

4 Conclusion

The chapter reviewed the piezoelectric properties of ceramic polymer composites. The polymers (semicrystalline and amorphous) were investigated for their piezoelectric performance. In the beginning, a brief introduction of synthesis of ceramic particles and ceramic polymer composites is discussed. It is found that the piezoelectricity is influenced by the dielectric properties, Young's modulus of the matrix, poling conditions, filler orientation, etc.

Acknowledgment This chapter as well as the whole book was made possible by NPRP grant 6-282-2-119 from the Qatar National Research Fund (a member of Qatar Foundation). The statements made herein are solely the responsibility of the authors.

References

1. Carroll L, Sternitzke M, Derby B (1996) Silicon carbide particle size effects in alumina-based nanocomposites. Acta Mater 44(11):4543–4552
2. Peigney A, Flahaut E, Laurent C, Chastel F, Rousset A (2002) Aligned carbon nanotubes in ceramic-matrix nanocomposites prepared by high-temperature extrusion. Chem Phys Lett 352 (1–2):20–25
3. Yuan J, Galetz M, Luan X, Fasel C, Riedel R, Ionescu E (2016) High-temperature oxidation behavior of polymer-derived SiHfBCN ceramic nanocomposites. J Eur Ceram Soc 36 (12):3021–3028
4. Peigney A, Laurent C, Flahaut E, Rousset A (2000) Carbon nanotubes in novel ceramic matrix nanocomposites. Ceram Int 26(6):677–683
5. Yoon S, Byun H, Yun Y (2015) Characterization and photocatalytic properties of ceramics TiO_2 nanocomposites. Ceram Int 41(6):8241–8246
6. Saheb N, Mohammad K (2016) Microstructure and mechanical properties of spark plasma sintered Al_2O_3-SiC-CNTs hybrid nanocomposites. Ceram Int 42(10):12330–12340
7. Hirvonen A, Nowak R, Yamamoto Y, Sekino T, Niihara K (2006) Fabrication, structure, mechanical and thermal properties of zirconia-based ceramic nanocomposites. J Eur Ceram Soc 26(8):1497–1505
8. Ionescu E, Linck C, Fasel C, Mã¼Ller M, Kleebe H, Riedel R (2010) Polymer-derived $SiOC/ZrO_2$ ceramic nanocomposites with excellent high-temperature stability. J Am Ceram Soc 93(1):241–250
9. Villegas M, Caballero AC, Moure C, Durán P, Fernández JF (1999) Factors affecting the electrical conductivity of donor-doped $Bi_4Ti_3O_{12}$ piezoelectric ceramics. J Am Ceram Soc 82 (9):2411–2416
10. Sternitzke M (1997) Review: structural ceramic nanocomposites. J Eur Ceram Soc 17:1061–1082
11. Palmero P (2015) Structural ceramic nanocomposites: a review of properties and powders' synthesis methods. Nanomaterials 5(2):656–696
12. Sundaram S, Sampathkumar P, Gowdhaman P, Annamalai V (2014) Dielectric and piezoelectric properties of various ferroelectric ceramic-polymer composites. J Environ Nanotechnol 3(3):27–31
13. Venkatragavaraj E, Satish B, Vinod PR, Vijaya MS (2001) Piezoelectric properties of ferroelectric PZT-polymer composites. J Phys D Appl Phys 34:487
14. Nunes-Pereira J, Sencadas V, Correia V, Rocha JG, Lanceros-Méndez S (2013) Energy harvesting performance of piezoelectric electrospun polymer fibers and polymer/ceramic composites. Sens Actuators, A 196:55–62
15. Lindner M, Bauer-Gogonea S, Bauer S, Paajanen M, Raukola J (2002) Dielectric barrier microdischarges: Mechanism for the charging of cellular piezoelectric polymers. J Appl Phys 91:5283–5528
16. Patel I (2011) Ceramic based intelligent piezoelectric energy harvesting device. INTECH Open Access Publisher, Croatia
17. Zhang X, Hillenbrand J, Sessler GM (2004) Piezoelectric d33 coefficient of cellular polypropylene subjected to expansion by pressure treatment. Appl Phys Lett 85:1226–1228
18. Patel I, Siores E, Shah T (2010) Utilisation of smart polymers and ceramic based piezoelectric materials for scavenging wasted energy. Sens Actuators, A 159(2):213–218
19. Zhang Z, Yao C, Yu Y, Hong Z, Zhi M, Wang X (2016) Mesoporous piezoelectric polymer composite films with tunable mechanical modulus for harvesting energy from liquid pressure fluctuation. Adv Funct Mater 26(37):6760–6765
20. Pullar RC (2012) Hexagonal ferrites: a review of the synthesis, properties and applications of hexaferrite ceramics. Prog Mater Sci 57(7):1191–1334
21. Ramadan KS, Sameoto D, Evoy S (2014) A review of piezoelectric polymers as functional materials for electromechanical transducers. Smart Mater Struct 23:033001

22. Ponnamma D, Ogunleye GJ, Sharma P, AlMaadeed MA (2016) Piezo- and thermoelectric materials from biopolymer composites. In Biopolymer composites in electronics, Elsevier, Amsterdam
23. Almusallam A, Yang K, Cao Z, Zhu D, Tudor J, Beeby SP (2014) Improving the dielectric and piezoelectric properties of screen-printed low temperature PZT/polymer composite using cold isostatic pressing. J Phys Conf Ser 557:012083
24. Kim KB, Hsu DK, Ahn B, Kim YG, Barnard DJ (2010) Fabrication and comparison of PMN-PT single crystal, PZT and PZT-based 1-3 composite ultrasonic transducers for NDE applications. Ultrasonics 50:790–797
25. Zhang YY, Wang S, Liu DA, Zhang QH, Wang W, Ren B, Zhao XY, Luo HS (2011) Fabrication of angle beam two-element ultrasonic transducers with PMN-PT single crystal and PMN-PT/epoxy 1-3 composite for NDE applications. Sens Actuators, A 168:223–228
26. Wang W, Or SW, Yue Q, Zhang Y, Jiao J, Ren B, Luo H (2013) Cylindrically shaped ultrasonic linear array fabricated using PIMNT/epoxy 1-3 piezoelectric composite. Sens Actuators, A 192:69–75
27. Han P, Pang S, Fan J, Shen X, Pan T (2013) Highly enhanced piezoelectric properties of PLZT/PVDF composite by tailoring the ceramic Curie temperature, particle size and volume fraction. Sens Actuators, A 204:74–78
28. Senthilkumar R, Sridevi K, Venkatesan J, Annamalai V, Vijaya MS (2005) Investigations on ferroelectric PZT-PVDF composites of 0–3 connectivity. Ferroelectrics 325(1):121–130
29. Nhuapeng W, Tunkasiri T (2002) Properties of 0–3 lead zirconate titanate-polymer composites prepared in a centrifuge. J Am Ceram Soc 85(3):700–702
30. Cai X, Zhong C, Zhang S, Wang H (1997) A surface treating method for ceramic particles to improve the compatibility with PVDF polymer in 0-3 piezo-electric composites. J Mater Sci Lett 16:253–254
31. Fries R, Moulson AJ (1994) Fabricaton and properties of an anisotropic PZT/polymer 0–3 composite. J Mater Sci Mater Electron 5:238–243
32. Hanner KA, Safari A, Newnham RE, Runt J (1989) Thin film 0-3 polymer/piezoelectric ceramic composites: piezoelectric paints. Ferroelectrics 100:255
33. Ng KL, Chan HL, Choy W, Loong C (2000) Piezoelectric and pyroelectric properties of PZT/P(VDF-TrFE) composites with constituent phases poled in parallel or antiparallel directions, IEEE Trans Ultrason Ferroelectr Freq Control 47(6):1308–1315
34. Liu XF, Sun H J, Xiong CX, Zhang CY, Zheng H, Wei M (2009) Effect of volume fraction and molding temperature on the electric properties of PZT/PVC composites. IEEE International symposium on the applications of ferroelectrics, 1–4
35. Xiaofang L, Chuanxi X, Huajun S, Lijie D, Rui L, Yang L (2005) Characterization of PZT/PVC composites added with carbon black. J Wuhan Univ Technol Mater Sci Ed 20 (4):60–64
36. Malmonge JA, Malmonge LF, Fuzari GC Jr, Malmonge SM, Sakamoto WK (2008) Piezo and dielectric properties of PHB–PZT composite. Polym Compos 30(9):1333–1337
37. Shin SH, Kim YH, Jung JY, Lee MH, Nah J (2014) Solvent-assisted optimal BaTiO3 nanoparticles-polymer composite cluster formation for high performance piezoelectric nanogenerators. Nanotechnology 25(48):485401
38. Kakimoto K, Fukata K, Ogawa H (2013) Fabrication of fibrous BaTiO3-reinforced PVDF composite sheet for transducer application. Sens Actuators, A 200:21–25
39. FuzariJr GC, Arlindo EPS, Zaghete MA, Longo E, Sakamoto WK (2014) Poled polyaniline coated piezo composite using low electric field and reduced poling time: a functional material. J Mater Sci Eng B 4(4):109–115
40. Li G, Luan GD, Qu H (2014) Study on novel relaxor ferroelectric single crystal PMNT/epoxy composite. Appl Mech Mater 475–476:1257–1261
41. Xu T, Wang C (2014) Piezoelectric properties of a pioneering 3-1 type PZT/epoxy composites based on freeze-casting processing. J Am Ceram Soc 97(5):1511–1516
42. Jain A, Prashanth KJ, Sharma AK, Jain A, Rashmi PN (2015) Dielectric and piezoelectric properties of PVDF/PZT composites: a review. Polym Eng Sci 55(7):1589–1616

43. Kitayama T, Sugawara S (1972) Rept Prof. Gr Inst Elec Comm Eng Japan. CPM, 72–17
44. Banno H, Saito S (1983) Piezoelectric and Dielectric Properties of Composites of Synthetic Rubber and $PbTiO_3$ or PZT. Jpn J Appl Phy 22:67–69
45. Mamada S, Yaguchi N, Hansaka M, Yamato M, Yoshida H (2015) Matrix influence on the piezoelectric properties of piezoelectric ceramic/polymer composite exhibiting particle alignment. J. Appl. Polym. Sci. 132(15): doi:10.1002/APP.41817
46. Kim K, Zhu W, Qu X, Aaronson C, McCall WR, Chen S, Sirbuly DJ (2014) 3D optical printing of piezoelectric nanoparticle-polymer composite materials. ACS Nano 8(10):9799–9806
47. Park KI, Lee M, Liu Y, Moon S, Hwang GT, Zhu G, Kim JE, Kim SO, Kim DK, Wang ZL, Lee KJ (2012) Flexible nanocomposite generator made of $BaTiO_3$ nanoparticles and graphitic carbons. Adv Mater 24:2999–3004

Poly(3-Hexylthiophene) (P3HT), Poly (Gamma-Benzyl-L-Glutamate) (PBLG) and Poly(Methyl Methacrylate) (PMMA) as Energy Harvesting Materials

Zubair Ahmad, Muhammad Awais, Mansoor Ani Najeeb, R.A. Shakoor and Farid Touati

Abstract The average temperature of the earth is rising at an alarming rate. The rising symptoms of global warming led us to a situation where we have to find out an alternative way for energy harvesting without disconcerting the homeostasis of nature. Therefore, finding renewable and clean energy sources has become one of the foremost challenges of modern societies. Polymer composites have found considerable attention in energy harvesting, especially for but not limited to organic solar cells, transducers and energy storage applications. For example, poly(3-hexylthiophene) (P3HT) and [6,6]-phenyl C61 butyric acid methyl ester (PCBM) have proven among the best combination for organic solar cell application and have persisted prominent for a decade. Being a semicrystalline polymer, P3HT is well known as a donor material with a wide absorption range of the solar spectrum and comparable high conductivity. Similarly, poly(gamma-benzyl-L-glutamate) (PBLG) was found out to be an excellent choice in flexible transducer applications because of its stability and high piezoelectric coefficients. Finally, poly(methyl methacrylate) (PMMA) was proved to be an ideal polymeric material for energy storage applications because of its highly effective insulating properties. In this chapter, we review the recent progress in the field of energy harvesting and storage materials such as P3HT, PBLG and PMMA and their role in maximizing the efficiency of energy devices.

Keywords Nanogenerators · Acoustic energy harvesting · Regioregular polymers · Quantum dots

Z. Ahmad (✉) · M.A. Najeeb · R.A. Shakoor
Center for Advanced Materials (CAM), Qatar University, P.O. Box 2713, Doha, Qatar
e-mail: zubairtarar@qu.edu.qa

M. Awais (✉)
Department of Industrial Engineering, Faculty of Engineering, Taibah University, P.O. Box 344, Medina 41411, Saudi Arabia
e-mail: myounas@taibahu.edu.sa

F. Touati
Department of Electrical Engineering, College of Engineering, Qatar University, P.O. Box 2713, Doha, Qatar

D. Ponnamma et al. (eds.), *Smart Polymer Nanocomposites*,
Springer Series on Polymer and Composite Materials,
DOI 10.1007/978-3-319-50424-7_4

Contents

1 Regioregular Poly(3-Hexylthiophene-2,5-Diyl) (P3HT)

There has been a great deal of attraction for the semiconducting polymers during the last few decades mainly because of their exceptional optoelectric properties together with economical and simple solution process ability [1–3]. One of the most widely recognized conjugated polymers is poly(3-hexylthiophene) (P3HT), whose optoelectronic properties and device performance have been explored broadly in various reports. Akin to many other semiconductive polymers, P3HT is a polymorph which exhibit flexibility to form different crystal structures at varying processing conditions. Dynamic of charge mobility in P3HT has been widely investigated by means of adjusting its regioregularity, molecular weight and morphology that often lead to enhance hole mobility and in turn the resultant efficiency of P3HT:PCBM bulk heterojunction (BHJ) photovoltaic devices. For instance, in 2005, a research group has developed P3HT solar cells with power conversion efficiency (PCE) as high as 4.4% [4].

Despite being soluble in many solvents, P3HT also possesses rather inferior mechanical and electrical properties along with poor stability in extreme environmental conditions. Therefore, the presence of alkyl group within its structure plays somewhat a pivotal role in granting its applications in optoelectronic devices. P3HT is mainly incorporated in thiophene ring with two distinct regioregularities, head to head (HH) and head to tail (HT). Nonetheless, the HT regioregularity is much preferred over the HH one due to its better conductivity as well as magnetic properties and optical nonlinearity. One of the components in developing P3HT, 3-hexylthiophene, is an unsymmetrical monomer which contributes to regioregularities of its final product. In general, synthesis of polythiophenes group involves a careful management of its repeating monomers unit and especially the regioregularity behavior of the

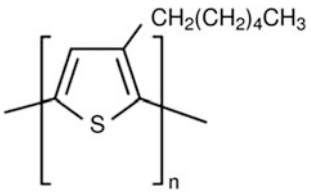

Fig. 1 Chemical structure of regioregular poly (3-hexylthiophene-2,5-diyl) (P3HT)

polymer. In addition, P3HT also commonly demonstrates decent photoluminescence by virtue of its highly tunable properties under multiple conditions of synthesizing [5–7]. Molecular structure of regioregular poly(3-hexylthiophene-2,5-diyl) (P3HT) is given in Fig. 1.

The first part of this chapter will reveal recent reports on the process of morphological control and regioregular properties P3HT in thin films. Thin-film properties and issues pertaining applications of P3HT-based solar cells are presented here.

1.1 P3HT-Based Thin-Film Devices

Due to its promising characteristics, P3HT has been widely investigated for organic electronic devices such as organic photovoltaics (OPV) [4, 8, 9], organic field-effect transistor (OFET) [10–12], mechanical and environmental organic sensors [13–15]. The significant effect of the morphological structure of P3HT on the resulting performance of the electronic device has been well acknowledged. The ability of P3HT to form a crystallized structure in thin-film form is very much favorable for its applications in organic electronic devices. The orderly intermolecular chains in P3HT thin films have granted much effective passage to enhanced charge mobility and strengthen its mechanical properties. In addition, by virtue of its highly conjugated and rigid backbone structure, P3HT offers efficient light absorption in the visible spectrum. Albeit, the presence of highly complex multi-phases structures has often been regarded as one major feature of its morphology once produced as blended film. This has been proven as one formidable challenge for researchers to gain deeper understanding, especially on its charge transports dynamic and crystalline properties in real applications. Likewise, the stringent requirement for highly efficient and cost-effective technique in producing highly uniform active film layer in large-scale applications has further slowed down progress in crystal formation methods of P3HT. Therefore, simple deposition techniques such as spin coating, dip coating, inject printing and doctor blading have been widely adopted instead [16], where imperfect crystal growth often occurs during the drying phase, right after the deposition process takes place. Apart from the conditioning during the deposition process, proper choice of solvents and substrates has been found to be another paramount factor that influences subsequent formation of the crystals structure to a certain extent.

Optical properties of P3HT in thin-film form can be observed by naked eyes through shades of color appeared depending on its regioregularity and molecular weight. Range of colors from as bright as orange to dark purple resembles degree of the two chosen parameters in any given solutions used. For instance, study was done by Zen et al. [17] to investigate the effect of molecular weight from annealing of P3HT film. A potent change in color has been observed from red to yellow as the film undergone annealing process at 210 °C which correlates with aggregation of its backbone due to the applied heat energy. For comparison, only little changes were noticed in P3HT films with either high or low molecular weight. Absorption spectroscopy is another technique often used to find out inter- and intra-molecular chain properties of P3HT layer. Low spectrum absorption energy can be attributed to the crystalline phase of the layer, while the high energy absorption was mostly correlated with the amorphous portion of the film [18].

In the next section, optimized parameters which mainly influence in the modification of morphological structure and alteration of molecular chains, for its application in OPV, will be discussed much in details.

1.2 P3HT in Solar Cells

Organic materials have been investigated for the fabrication of solar cells since the last few decades due to their flexibility and solution process-able nature. However, the efficiency of the organic solar cells is still low due to limited absorption of the solar spectrum and relatively poor charge mobility. Recent years have witnessed a swift increase in the efficiency of OPV devices to over 10%, which has been attained with a profound knowledge of the underlying photovoltaic mechanism and the advancement of device architectures and tailored materials.

In OPV devices, conjugated polymer matrix works as an active layer. Initially, among the major issues encountered by researchers was the fact that the organic conjugated materials develop a tightly bound excited state. Frequently, even under light illuminations, sufficient excitation does not occur to allow effective separation of charges. The recombination phenomenon befalls as fast as few picoseconds. This problem has been tentatively resolved through the introduction of the bulk heterojunction (BHJ) model. The bulk BHJ concept has been well thought out as a leading design for organic solar cells due to its better efficiency, tunable properties and processing costs [19–22]. By this approach, the splitting of the photoinduced excitons is significantly improved and the exciton diffusion length issue has been resolved up to some extent. However, in BHJ solar cells, the optimum value of the active layer is very crucial. Although the thicker active layer can increase the optical absorption, the efficiency starts to decline after a critical thickness due to series resistance and charge recombination effects. A number of BHJ composite-based photovoltaic schemes have been proposed so far. P3HT (poly(3-hexylthiophene)) and PCBM (phenyl-C61-butyric acid methyl ester) have proven themselves among the best combinations and persisted prominent for a decade [23]. P3HT exhibits a

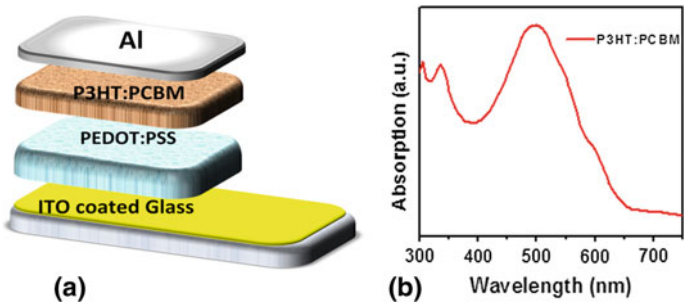

Fig. 2 **a** Typical device diagram of P3HT:PCBM-based BHJ solar cells, **b** optical absorption spectrum of the P3HT:PCBM BHJ film

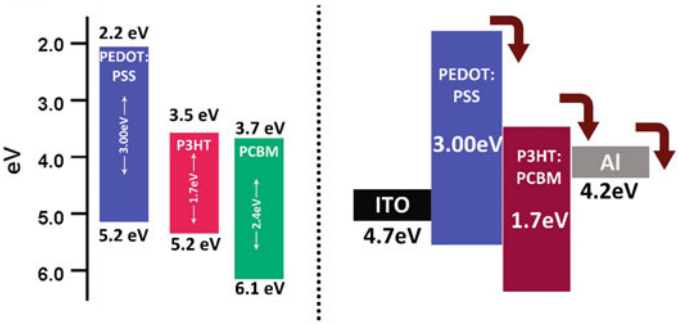

Fig. 3 Energy band diagram of a P3HT:PCBM-based BHJ solar cell

wide range of absorption in the visible region of the solar band. Figure 2a, b shows, respectively, the schematic diagram of P3HT:PCBM-based BHJ solar cells and optical absorption spectrum of the P3HT:PCBM BHJ film. The energy band diagram of P3HT:PCBM-based solar cells is given in Fig. 3. Until 2003, improvement had been reported by Padinger et al. [24], with new record of PCE at 3.5%, and they have broken the previous record (PCE ~ 2.5%) for OPV devices [25]. Also, morphological studies on the P3HT:PCBM film composite had been reported in 1993 by Ihn et al. [26] and by Bouman et al. in 1994 [27], just before the conceptual idea of BHJ-based OPV devices [28].

PV devices are commonly made by using semiconductor materials of the distinctive values of the optical band gap (E_g). E_g represents the minimum amount of electromagnetic energy needed to allow absorption of the light source within the semiconductive materials that subsequently excites the electron from the valance band up to the conduction band across the band gap. However, unlike the conventional PV devices, the organic ones mainly consist of multiple molecular species; thus, the term extended energy band does not apply. In this case, E_g simply means minimum energy required to promote an electron from its highest occupied molecular orbital (HOMO) to the lowest unoccupied molecular orbital (LUMO)

within the polymer molecules. Thus, electromagnetic radiations with quite less energy than the E_g can hardly contribute to any form of photocurrent generation. Ideally, the photoconversion efficiency (PCE) of a PV cell can be improved by harnessing more photons, thus increasing J_{sc} or by minimizing recombination of charges hence raising V_{oc} to approach E_g. The following formulas (here all the symbols have conventional meaning) describe the relationship between these parameters.

$$\mathrm{PCE} = \frac{J_{max} \times V_{max}}{P_{in}} = \frac{J_{sc} \times V_{oc} \times \mathrm{FF}}{P_{in}} \tag{1}$$

While the fill factor (FF) can be given by;

$$\mathrm{FF} = \frac{J_{max} \times V_{max}}{J_{sc} \times V_{oc}} \tag{2}$$

In addition, the efficiency can also be measured through the measurement of external quantum efficiency (EQE) of the fabricated device. This measurement directly conveys the quantum production of photocurrent by photons with a specific wavelength (λ). The obtained value of EQE, however, depends on two main components. The first step concerns the capacity of photonic absorption, and the second relates to the probability of photocurrent induction at a certain applied bias. Overall, EQE phenomenon can be expressed as;

$$\mathrm{EQE} = \eta_{abs} \times \eta_{el} \tag{3}$$

where η_{abs} is the probability of photonic absorption and η_{el} represents the probability of photocurrent generation.

1.2.1 Effect of Molecular Weight and Ratio

Polymeric materials are made up of long-chain macro-molecules without a well-determined value of molecular weight (M_w) [29]. Nonetheless, M_w often has enormous influence on subsequent solubility and miscibility of a polymer. Polymer with smaller M_w commonly is more readily soluble. However, the polymers with low M_w have tendency to rapidly undergo de-wetting process, thus forming undesirable surface voids, apart from the large-scale phase separations and inability to produce highly viscous solutions [30]. Studies reported in Ref. [31] have shown the influence of M_w on structure and crystallinity of P3HT, while Ref. [32] describes the dependency of morphological and charge mobility of P3HT on M_w. The former concluded that at lower values of M_w, pure P3HT tends to produce high crystallinity, but with lesser connected strands allowing hence more effective charge mobility. The latter, on the other hand, explained the adjoining crystalline domains in the case of higher M_w. In solar cell applications, studies have shown that the

Table 1 Photovoltaic performance of the fullerene multi-adduct acceptors in P3HT matrix

Donor/acceptor (weight ratio)	*J*sc (mA/cm^2)	V_{oc} (V)	FF	PCE (%)	Reference
P3HT/PC60BM(1:0.8)	10.9	0.62	0.62	4.18	[36]
P3HT/bisThC60BM(1:1.2)	5.91	0.72	0.41	1.73	[36]
P3HT/triThC60BM(1:1.4)	1.88	0.64	0.28	0.34	[36]
P3HT/bisPC60BM(1:1.2)	9.14	0.724	0.68	4.5	[37]
P3HT/PC60BM(1:1)	8.94	0.61	0.60	2.4	[38]
P3HT/bisPC60BM(1:1.2)	7.30	0.73	0.63	2.4	[38]
P3HT/bisPC70BM(1:1.2)	7.03	0.75	0.62	2.3	[38]
P3HT/bisThC60BM(1:1.2)	7.31	0.72	0.66	2.5	[38]

addition of P3HT components with regioregularity value of M_w (ranging from 2000 up to 75,000 KD) is much favorable for enhanced efficiency [33, 34].

Likewise, the weight ratio between the blended acceptor and donor materials film may also contribute enormously to the subsequent performances of the fabricated devices. Therefore, the goal has always been to come up with the finest ratio that would yield OPV devices with highest PCE. It follows that the studies have been aimed to refine the ratio between the two distinctive components of P3HT:PCBM BHJ. Moulé et al. have done an extensive study pertaining to the effects of adding P3HT:PCBM as active components at multi-compositions [35]. The finding revealed that in case of thicker active layer, higher amounts of PCBM are much favorable, while with thinner film, lesser amounts of PCBM produced much efficient charge motilities. In general, this study has suggested that the suitable composition ratio of the donor and acceptor materials is not necessarily fixed, but predictably depends more on the composite film thickness. Varying amount of PCBM composition in P3HT has made it possible the fabrication of well-functioned OPV devices, even with thicker active film thicker than 200 nm. Table 1 shows the photovoltaic performance of the fullerene multi-adduct acceptors in P3HT matrix.

1.2.2 Effect of Solvent

When it comes to solution preparation, often solvents that offer good solubility with the materials of choice have always generally been regarded as the better option. More soluble solutions can be made at much higher concentration. According to Moulé et al. [30], a minimal concentration of 10 mg/ml of P3HT:PCBM solutions is recommended to obtain highly planar defect-free spin-coated layer with thickness above 80 nm. P3HT:PCBM has also shown better solubility when polar aromatic solvents such as chlorobenzene are used. In addition, boiling points of the solvents must be taken into consideration as it determines the rate of solvent evaporation and thus affects subsequent formations of the polymer domains inside the film during the deposition process. Solvent with higher boiling point, for instance, commonly

leaves more traces of crystalline structures as the polymer equilibrates at much slower rates. On the other hand, solvents of lower boiling points tend to produce polymer film of more amorphous in nature. A higher crystalline P3HT structure is much favorable for OPV applications, as shown by Li et al. [4] in 2005 with their record breaking 4% of PCE at that time. Nonetheless, the realization on the importance of solvents has come about as early as 2001, through a study carried out by Shaheen et al. [25]. In this study, a dramatic change in PCE (from 1.1% up to 2.5%) has been successfully achieved by MDMO-PPV:PCBM solar cell prepared using chlorobenzene as solvent opposed to their previous choice, toluene. Few other researches have also been performed to investigate the effect of OPV solar cells fabricated using combinations of multiple solvents [39–41]. The mixed solvents commonly consist of combination between one primary soluble carrier and a nonsoluble additive, where the additive solvents often being the ones with higher boiling point [30, 42]. Ideally, during active film deposition processes, the primary solvents get evaporated, whereas the co-solvents remain, thereby changing the morphology and structure of the coated film at nanoscale [43]. One of the most commonly used solvent additives for OPV is 1,8-di-iodo-octane (DIO) [42, 44, 45].

1.2.3 Effect of Annealing

One of the most widely investigated OPV performance optimization techniques is thermal annealing process. This is a common method employed to induce phase separation between P3HT and PCBM domains within bounds of the active film composite. Ma et al. [46] developed spin-coated P3HT:PCBM OPV devices which thereafter thermally annealed at 150 °C for 5–30 min. Enhanced efficiency of up to 5% has been reported in regard to the annealing process at optimum temperature of 150 °C. However, the proper timing choice for heating must also be carefully considered. At longer heating period, diffusions of PCBM into P3HT domains are more likely to occur. The dominations of PCBM elements inside the film have been proven detrimental for the fabricated OPV. As discussed in the prior section, the need of maintaining compositional ratio for the two active elements is crucial in order to maintain well-balanced charge mobility. The apparent changes in morphological structure of P3HT:PCBM active film due to thermal annealing have been attributed to enhanced optical properties of the fabricated OPV cells, as reported in [47]. The samples have been annealed at higher temperatures, ranging from 50 to 180 °C for 10 min. Remarkably, enhanced J_{sc}, FF and spectral absorption at particularly red-shifted region have been observed from the samples annealed at higher temperatures. Among widely adapted techniques in determining changes in morphological structure due to annealing process is Raman spectroscopy analysis, which has been frequently used by researchers to uncover degree of crystallinity of developed P3HT:PCBM OPV active films [48–50]. Upon annealing, enlargements of P3HT crystallites within the blends become more obvious, in addition to improvements of intermolecular chains between the elemental domains.

Unlike the former thermal annealing technique, solvent annealing is much recently adopted as OPV performance optimizing method. This process allows the newly deposited active film to be put under exposure of solvent-rich atmosphere. It is commonly carried out by putting a cover on top of the film right after the deposition to prevent further evaporation of solvents from within. Apparent changes in samples' morphology have been reported as a result of the film undergoing solvent annealing [5, 51]. In the previous section, we have discussed that longer relaxation times gained by the virtue of using higher boiling point solvents ultimately produced much desirable crystalline P3HT films. Similarly, the process of solvents annealing has afforded formation of crystalline P3HT within the composite film. This further halts the emergence of much undesirable amorphous P3HT:PCBM phase.

1.2.4 Effect of Active Layer Modification

The thickness of the active layer has undoubtedly huge effects on the subsequent performance of the fabricated solar cells. While increasing the thickness of active film further intensifies its light-absorbing capacity, alas the travel distance of mobile charges in the active cell layer toward the electrode may be lengthened too. Therefore, a higher BHJ film thickness is not necessary to produce a much efficient OPV device. Furthermore, scholars have also noticed nonlinear photonic absorption as a result of increased BHJ layer, due to the interference of incident and reflected light source [9, 52]. For instance, only at optimized thickness layer, 70–100 nm, does the capacity of photon captured maximize. For layers thicker than 120 nm, the interference phenomenon permitted rather less photonic energy absorption. A comparative study has been done by Moulé et al. [35] between layer thickness and resulting J_{sc} of their fabricated P3HT:PCBM and OC_1C_{10}-PPV:PCBM OPV solar cells. It was found that an optimized film thickness of 70 nm yielded higher J_{sc} than its thicker counterpart, suggesting a drop in performance as thickness increases above 70 nm. Interestingly, however, for the former sample with the presence of P3HT, higher optimized thickness was observed particularly at 210 nm, as opposed to its thinner equivalents. With enhanced J_{sc}, and thus PCE, the P3HT:PCBM cells have been proven to be the better combination with much well-matched electron and hole mobility. Apart from the thickness factor, the PCE certainly depends heavily on the refractive index (n) and other properties of the materials. Indeed, Peumans et al. [53] have outlined that in BHJ layer of $\lambda/4n$ thickness, constructive interferences can be observed more frequently, whereby at thickness $\lambda/2n$, destructive interferences instead dominate. Also, processes such as thermally annealing and solvent annealing have each been shown to influence spectrum of light absorption for the fabricated P3HT:PCBM sample film at 1:1 ratio, due to the apparent altered morphology [40, 52].

Another popular method involving physical modifications of the active film is the addition of pre-formed polymer additives [54]. A BHJ layer made up from P3HT nanofibers coated with PCBM layer has been developed by a research team

with the motivation to reduce defects in P3HT domains, a well-known peculiarity for OPV devices [55, 56]. The aim was well fulfilled, and P3HT fibers did exhibit much vibronic behavior as compared to the one produced in thin-film form. However, further investigations that were later done have shown a much poorer performance of the nanofiber composite film in OPV applications. Enhanced activation barrier that impedes hole mobility in between the gap of unattached fibers has been identified to be among contributing factors in this regard, whereas formations of exciton between the unattached boundaries due to charge recombination phenomena further reduced charge density. To overcome this, addition of amorphous P3HT additives among the fibers has been proposed [8]. As expected, the newly fabricated device has shown enhanced FF and J_{sc}, mainly from the re-established connection between the domains. Other researchers [57] have also introduced the elements of nanoparticle additives to serve a similar purpose. In order to overcome these apparent flaws encountered, the proposed counteract mechanism has always been to create a more crystalline structure of P3HT domains, proper control of their sizes and to provide connections among the entangled fibers.

1.2.5 Effect of Quantum Dots (QDs)

Ideal solar cells were mainly made up of semiconducting organic materials as electron donors, while fullerene derivatives that act as electron acceptors have reported to achieve PCEs as high as 5 or 6% [58]. Similarly, inorganic semiconductive nanocrystals along with the QDs like ZnSe, ZnSTe, CdSe and CdTe, have the advantages of highly tunable band gaps along with excellent intrinsic charge carrier mobility. Therefore, being potent electron acceptors QDs can also be incorporated into conjugated polymers like P3HT to form BHJ hybrid PV devices [59]. Numerous works have been carried out pertaining to the synthesis of various morphological properties of QDs and their applications in the hybrid BHJ PV devices. Interestingly, with the addition of the elongated QDs, more extended and directed electrical pathways are established within the OPV films, leading hence to dramatic reduction of the interparticle hopping events, which is critically necessary for the extraction of electrons toward the electrode. However, it is noteworthy that the subsequent device efficiency does not solely depend on the shape of the QDs themselves, but also hang on their solubility and surficial alteration. These combined factors indeed influence the resultant charge transport behavior of the fabricated devices significantly. Mostly, the surfactants are used to aim to avoid further aggregation during growth of the QDs containing long alkyl chains. Therefore, to further improve charge mobility within the QDs polymer film, proper modifications of its morphological surface structure have been previously reported by employing the technique of ligand exchange using various capping ligands. For instance, pyridine treatment of the QDs has been commonly utilized as an effective procedure that leads to enhanced PCE for the developed OPV devices. Recently, structural, morphological and optical properties of the nanocomposite of poly(3,4-ethylenedioxythiophene) polystyrene sulfonate (PEDOT:PSS), ZnSe and CdSe QDs have been investigated by Najeeb et al. [60, 61].

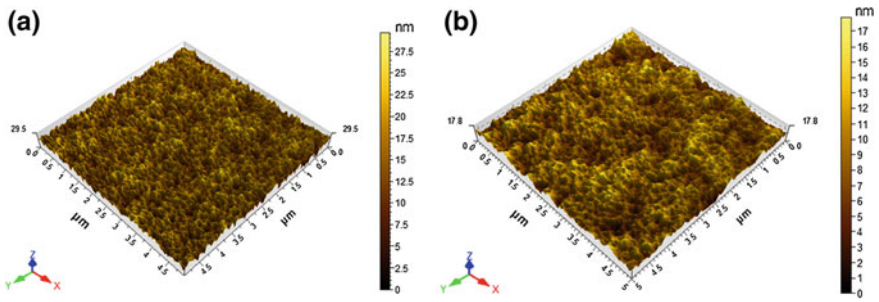

Fig. 4 3D AFM images of **a** P3HT, **b** QDs in P3HT

The ZnSe and CdSe QDs have been synthesized, with the aid of mercaptoacetic acid (MAA), by a colloidal method with an average size of 5–7 nm. QDs have been embedded in PEDOT:PSS using a simple solution-processing approach and have been deposited as thin films by spin-coating technique. The QDs have shown a significant effect on the performance of the P3HT:PCBM BHJ solar cells. Figure 4 shows the AFM images of pristine P3HT and QD-embedded P3HT.

In addition, Olson et al. [62] reported a CdSe/P3HT-blended device with the best efficiency of 1.77% using butylamine as a shorter capping ligand for CdSe QDs. Investigations also revealed that the shortening of the insulating ligands has improved the PCEs of CdSe/P3HT-based OPV devices. On the other hand, ZnSe due to its wider band gap and hence poor absorption of sunlight within the visible and infrared ranges poses several limitations toward its applications in OPV devices. However, QDs have been found to play an important role in preventing recombination of electrons. Regardless of many advantages offered by the QD-sensitized organic solar cells, the efficiency of QD-sensitized solar cells is still considered as low compared to state-of-the-art PV devices. Hence, more rigorous efforts in carefully tailoring and exploiting state-of-the-art fabrication techniques have to be adopted to bring them similar to current OPV devices standard.

2 Poly(Gamma-Benzyl-L-Glutamate) (PBLG)

2.1 Poly(Glutamate)s or Poly(α-Amino Acid)s

Poly(glutamate)s or poly(α-amino acid)s are one of the most investigated biopolymers due to their polar helical structure and well-established chemical composition [63]. They exhibit a strict α-helical structural arrangement in solution, as well as in solid state [64]. Their axial rise per residue (amino acid) is estimated to be 1.5 Å for 3.5 residues per turn helix. The internal hydrogen bonds in helical axis direction between amide hydrogen donor and carbonyl oxygen acceptor stabilize alpha-helix [63]. The identical orientation of all hydrogen bonds increases the

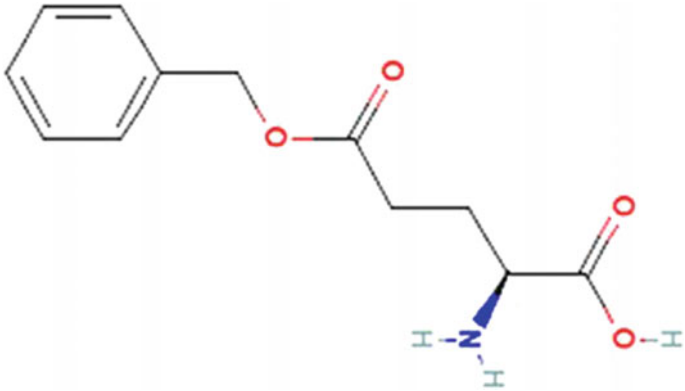

Fig. 5 Chemical structure of PBLG

permanent polarity of rod-like α-helix [65]. The amino acid residues can create dipoles of high electric density on applying a permanent dipole force that changes permanent polarity of fibers, exhibiting piezoelectric characteristics [66]. Poly (gamma-benzyl-L-glutamate) (PBLG) is one of the well-known poly(α-amino acid)s and a synthetic polymer with molecular weight of 237.2518 g/mol. Its molecular formula is ($C_{12}H_{15}NO_4$), and the chemical structure of PBLG is shown in Fig. 5. PBLG is one of the most common poly(α-amino acid) which is utilized in many biomedical applications [63] such as in tissue engineering [67, 68] and drug delivery carrier [69, 70]. In order to improve their degradation property and to control their hydrophobic nature, second components [71–74] and functional groups [63, 75] are attached into PBLG, for increasing their applications in biomedical engineering [63]. In addition, it is frequently used in energy harvesting applications due to its tunable orientation and piezoelectric properties [76].

2.2 *Energy Harvesting Applications of PBLG*

The examination of piezoelectric property in organic materials such as woods and bones was initiated in mid-1950s [77, 78]. Afterward, many researchers started to investigate the piezoelectricity in proteins, polysaccharides and polynucleotides biopolymers [79–81]. Later, synthetic polymers having piezoelectric property were discovered and since then investigation was largely focused on the piezoelectricity in poled polyvinylidene difluoride (PVDF) [82, 83].

However, in early 1970s, Fakuda and his group confirmed the piezoelectric property in helical poly-α-amino acids such as poly-γ-alkyl glutamate derivatives and especially in PBLG [84–87]. They demonstrated that by applying mechanical force or magnetic field in PBLG films, a strong piezoelectric property in shear mode can be

produced in uniaxial direction of the polymer chains, with piezoelectric coefficient d14 in the range of 1–2 pC/N [84–87]. The piezoelectric coefficient d14 of PBLG can be increased up to 26 pC/N [88], when polymers are allied by strong magnetic field. The dipole density of PVDF is greater than PBLG; however, PVDF conformation in solution is random coil, needing increased energy by an electric field for poling compared to PBLG; thus, effectiveness of PBLG in energy harvesting applications is more than PVDF [89]. The use of piezoelectric materials in energy harvesting applications was investigated already by many researchers [65, 89–93].

2.3 *Fabrication of PBLG with Piezoelectric Properties*

In order to produce materials with piezoelectric properties, the molecular or atomic arrangement within that material is extremely important which is achieved by mechanical treatment such as mechanical drawing or by electrical treatment, e.g., poling under electrical field. According to the type of treatment, these piezoelectric materials are divided into two classes [88]. The electrically treated materials are known as class I material which normally show $C_{\infty v}$ symmetry. PVDF is one of the class I materials. The class II materials are macroscopically aligned biopolymers which are treated by magnetic field or mechanical stretching. Their structure has D_{∞} symmetry. PBLG is one of the class II piezoelectric materials [88]. The dipole orientation of the two classes of materials is shown schematically in Fig. 6.

Fukuda and coworkers determined the piezoelectricity only in the shear mode (d14); many researchers tried to find the piezoelectric coefficients in d33 and d31 mode; however, due to problem in fabricating films having all helical dipoles poled in one direction [88], it remained a challenge. The polymer main chain direction in a crystalline lattice is required to be perpendicular to the dipole direction in order to employ them for piezoelectric applications. Thus, electrospinning process has huge

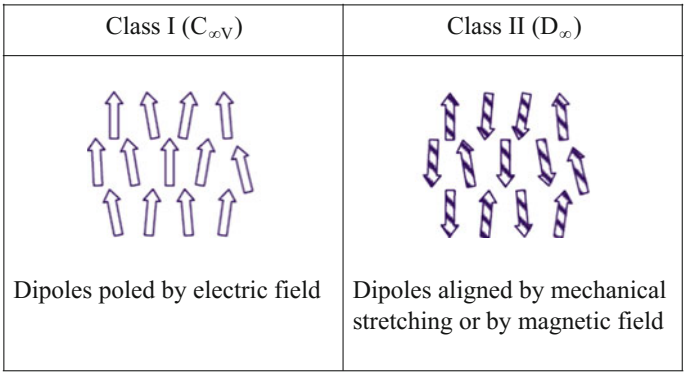

Fig. 6 Schematic description of class I and class II types of piezoelectric polymer system associated with molecular dipole orientation (modified from [65])

potential in arranging the diploes and the polymer chains parallel to each other by creating electric field and shear force in the same direction. However, electrostatic force in this process sometimes causes the fibers to bend due to stretching [89]. Ren et al. [65] used the combined electrospinning and hot pressing in order to successfully fabricate the PBLG film with stable and one-directional polarity having PBLG helices poled in parallel mode with C ∞ v symmetry. Firstly, the electrospinning was used to prepare polar nanofibers with all helical dipoles arranged in the same direction of polymer fiber axis. Later, hot pressing was utilized in order to fuse loosely adhered electrospun PBLG fibers together to form an adherent incessant film without losing the polar alignment. With the help of this combined technique, Ren et al. [65] were able to produce robust PBLG films with helical molecular structure steady in solid state even up to 130 °C [94]. Their fabricated PBLG film showed relatively high piezoelectric coefficient in d33 and d14 modes and was advantageous in terms of ease of fabrication and showed good thermal stability.

Near-field electrospinning (NFES) as an alternative to conventional electrospinning technique has also been utilized to prepare highly arranged fibers [89, 95]. NFES is an economic technique, to produce micro- or nanometer-thick homogeneous polymer fibers, since it runs at a relatively low voltage. Pan et al. [89] investigated the piezoelectric properties of PBLG, fabricated using cylindrical NFES. They were able to produce piezoelectric PBLG fibers having increased thermal stability, good flexibility and reasonable toughness.

2.4 Characterization of PBLG Films

Tinoco [96, 97] carried out a detailed investigation of electrical properties of PBLG films. Magnetic orientation of PBLG was studied by Go et al. [87]. A solid liquid crystal film of PBLG was firstly introduced by Samulski and Tobolsky in their breakout work in 1967 published in Nature [98]. Later on many researchers focused on the structural properties of cast films of PBLG [99–102]. Magnetic torque and electric conduction of PBLG films were also measured in order to investigate their applications in energy harvesting applications [103, 104].

Pan et al. [89] carried out an Fourier transform infrared (FTIR) spectroscopy of PBLG fibers, presenting a strong peak at 1655 cm^{-1} of α-helical structure. They examined the mechanical properties of the piezoelectric fibers of PBLG as well, and 60.54 MPa and 3.64 GPa values were calculated for the maximum ultimate tensile stress and Young's modulus, respectively. These values were very high when compared to PVDF fibers of similar specifications [89]. Finally, they investigated the potential of PBLG piezoelectric fiber for energy harvesting applications by generating voltage throughput on applying these PBLG fibers on cicada (an insect) wings.

3 Poly(Methyl Methacrylate) (PMMA)

Poly(methyl methacrylate), (PMMA), is an unbreakable, transparent polymer. It is commonly known as acrylates or acrylics [105]. PMMA is used in several applications as a substitute to conventional glass. However, it is more advantageous over glass especially when making thicker windows, because of its high-grade transparency [106]. Polycarbonate (PC) is another polymer used as an indestructible substitute to glass; however, PMMA is more economical. In addition to optical clarity PMMA has numerous exceptional properties, including excellent insulating properties, reasonable strength and stability. Besides, it provides comparatively better defense against external atmosphere [105, 107, 108]. Thus, it presents promising appliance in various fields, especially in biomedical and energy harvesting applications.

3.1 Synthesis of PMMA

PMMA is formed by solution [109], emulsion [110] and bulk [111] polymerizations from the monomer methyl methacrylate. Generally, during the formation of PMMA, living polymerization methods such as radical initiation [112] is used; however, anionic polymerization [113] of PMMA can also be utilized, as shown in below equation:

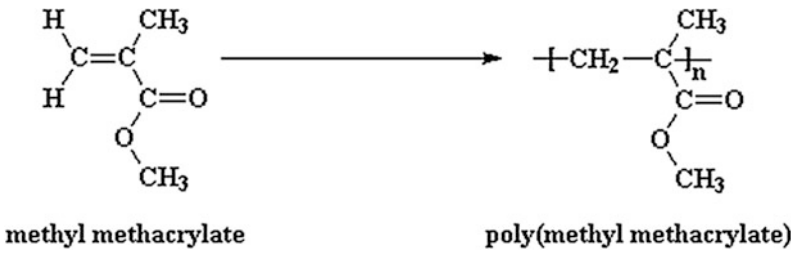

methyl methacrylate poly(methyl methacrylate)

3.2 Applications of PMMA in Energy Devices

3.2.1 Acoustic Energy Harvesting

Wu et al. [114] used PMMA as acoustic band gap crystals (sonic crystal) in conjunction with polyvinylidene fluoride (PVDF) piezoelectric material for energy harvesting application. Many researchers worked for some years on the transmission of acoustic waves in sonic crystals [115, 116]. The sonic crystals have shown

their potential usage in various applications including transducers and acoustic filters. For acoustic energy harvesting, a resonant cavity is created by rod removal in sonic crystal in order to investigate the localized wave mechanism of sonic crystal in point defect mode [114–116]. By doing so, when the incident acoustic wave reached at the significant frequency, it was contained in the cavity of the sonic crystal and by placing the right piezoelectric material inside the cavity of the sonic crystal; Wu et al. were able to convert the acoustic energy into electric energy at the cavity's resonant frequency. A maximum power was generated at 4.2 kHz frequency of the incident acoustic wave under 3.9 kΩ load resistance. Similarly, Mikoshiba et al. [117] used PMMA by exploiting a collection of multi-functional resonators based upon on the theory of locally resonant materials from structural vibrations in energy harvesting application.

3.2.2 Nanogenerator

The first nanogenerator (NG) was prepared by Wang et al. [118]. They were able to successfully generate current/voltage by sweeping an AFM tip on ZnO nanowires which were vertically grown. The generation of power was due to the combined effect of semiconducting and piezoelectric properties of the ZnO nanowires. From first NG to date there is a great improvement in the performance of NGs as shown in Fig. 7. A big jump in the produced voltage was observed in 2011 and 2012 when

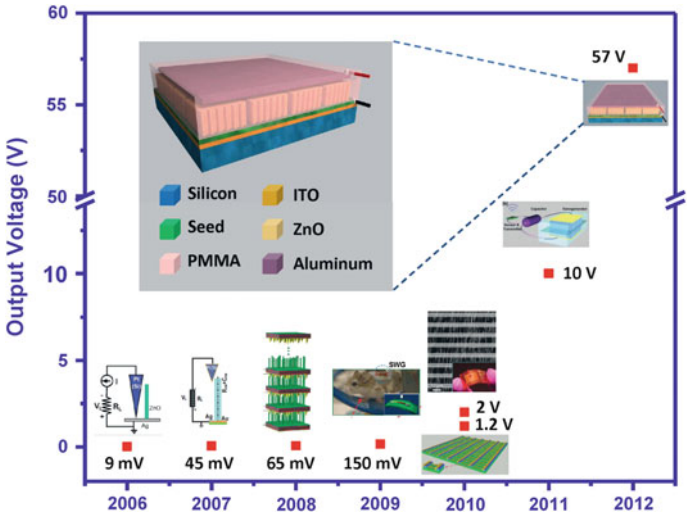

Fig. 7 A summary on the development of high-output piezoelectric nanogenerators ever since it was invented in 2006. *Inset* the schematic of the mostly recently developed integrated nanogenerator based on vertically aligned ZnO arrays [120] Copyright 2012. Reproduced with permission from Elsevier Ltd.

PMMA was used as the substrates. Zhu et al. used PMMA and Kapton (polyimide) together as contact materials to produce triboelectric nanogenerator (TENG) [119].

Lee et al. [121] prepared a low-cost superflexible nanogenerator (NG) by using very economical aluminum foil electrodes. Nanowire (NW) of ZnO was homogeneously deposited on Al electrodes, and a PMMA coating was applied on the Al electrodes as an insulation layer prior to the deposition of ZnO for the prevention of short circuits between the ZnO NWs (due to *n*-type semiconductivity of ZnO) and Al electrode. The spin-coated layer of PMMA applied on the Al electrode not only assists ZnO NWs to grow homogeneously along *c*-axis by reducing the process of chemical growth of Al into hydrated aluminum oxide due to boehmite phase effect, but also provides increased output of the process by fully insulation of Al electrode and ZnO NWs with no diminution in performance and flexibility of NG. In addition, due to its extreme sensitivity towards motion, Lee et al. [121] suggested a potential application of superflexible NG as a dynamic sensor to detect even minor movements of skin. In addition, the superflexible NG illustrates probable appliance as a dynamic sensor due to its extremely low resistance to motion that can detect even minor movements of skin. Gao et al. [122] applied 200-nm-thick PMMA coating on the plastic substrate after depositing ZnO NWs, in order to improve the adhesive properties of substrate and ZnO wires, in the fabrication of flexible nanogenerators.

Wang's group used PMMA as a substrate for applying Cu thin films in the fabrication of TENG for harvesting liquid wave energy [123]. They also used PMMA as a substrate in large-scale energy harvesting by preparing nanoparticulate-enhanced TENG and rotational mechanical energy harvesting by fabricating disk TENG [124]. PMMA is chosen as the substrate due to its high strength, flat surface and light weight properties.

3.2.3 Other Energy Harvesting Applications of PMMA

Bouendeu et al. [125] used PMMA for the encapsulation of electromagnetic generator prepared for micro-energy harvesting applications. Jo et al. [126] utilized PMMA as a mold for preparing polydimethylsiloxane (PDMS) film for body heat energy harvesting of human beings in construction of flexible thermoelectric generator. Al-Haik et al. [127] used PMMA as an insulating layer in the preparation of miniature turbine for harvesting energy produced from original organic capacitor. Meng et al. [128] utilized PMMA in PVDF solution to improve PVDF's energy storage and dielectric properties. The optimized film of mixing 40 wt% of PMMA and PVDF demonstrated a reduction in energy loss with energy storage density increased.

Phase change material (PCM) has attracted widespread attention for storing thermal energy since they have capability to alter their state during phase change process within a definite temperature range and can accumulate and discharge energy, when needed. PMMA has been used in PCM applications in different capacities [105, 107, 108]. Sari et al. [105] utilized PMMA as shell material in the preparation of micro-PCM materials by emulsion polymerization having

n-heptadecane as a core material. They were able to synthesize microcapsules of PMMA/heptadecane for thermal energy storage because of their improved thermal properties, excellent thermal reliability and large surface area.

4 Conclusion

In this chapter, state-of-the-art synthesis methods for P3HT, PBLG and PMMA and their application in energy harvesters, transducers and energy storage devices have been described. Further, device fabrication for the above-mentioned applications that developed over the years by many of esteemed fellow researchers with an aim to further increase their efficiency and reliability has also been discussed thoroughly. Till to date, many of the past shortcomings of these devices have been resolved by the collective efforts of the researchers. These findings have highlighted the importance of the fabrication parameters that often lead to new discoveries and better understanding of the mechanism behind such devices. Challenges have always been there, and of course over the years, it would be certainly possible for organic-based energy devices to find their room in commercial applications if the current trends are continued.

Acknowledgments This document was made possible by PDRA Grant # PDRA1-0117-14109 from the Qatar National Research Fund (a member of Qatar Foundation). The statements made herein are solely the responsibility of the authors.

References

1. He Z, Zhong C, Su S, Xu M, Wu H, Cao Y (2012) Enhanced power-conversion efficiency in polymer solar cells using an inverted device structure. Nat Photon 6(9):591–595
2. Aziz F, Sulaiman K, Karimov KS, Muhammad MR, Sayyad MH, Majlis BY (2012) Investigation of optical and humidity-sensing properties of vanadyl phthalocyanine-derivative thin films. Mol Cryst Liq Cryst 566(1):22–32
3. Ahmad Z, Zafar Q, Sulaiman K, Akram R, Karimov KS (2013) A humidity sensing organic-inorganic composite for environmental monitoring. Sensors 13(3):3615–3624
4. Li G, Shrotriya V, Huang J, Yao Y, Moriarty T, Emery K, Yang Y (2005) High-efficiency solution processable polymer photovoltaic cells by self-organization of polymer blends. Nat Mater 4(11):864–868
5. Chen LM, Hong Z, Li G, Yang Y (2009) Recent progress in polymer solar cells: manipulation of polymer: fullerene morphology and the formation of efficient inverted polymer solar cells. Adv Mater 21(14–15):1434–1449
6. Kuila BK, Malik S, Batabyal SK, Nandi AK (2007) In-situ synthesis of soluble poly (3-hexylthiophene)/multiwalled carbon nanotube composite: morphology, structure, and conductivity. Macromolecules 40(2):278–287
7. Kuila BK, Nandi AK (2004) Physical, mechanical, and conductivity properties of poly (3-hexylthiophene)-montmorillonite clay nanocomposites produced by the solvent casting method. Macromolecules 37(23):8577–8584

8. Berson S, De Bettignies R, Bailly S, Guillerez S (2007) Poly (3-hexylthiophene) fibers for photovoltaic applications. Adv Funct Mater 17(8):1377–1384
9. Pettersson LA, Roman LS, Inganäs O (1999) Modeling photocurrent action spectra of photovoltaic devices based on organic thin films. J Appl Phys 86(1):487
10. Tanase C, Meijer EJ, Blom PWM, De Leeuw DM (2003) Unification of the hole transport in polymeric field-effect transistors and light-emitting diodes. Phys Rev Lett 91(21):216601
11. Bao Z, Dodabalapur A, Lovinger AJ (1996) Soluble and processable regioregular poly (3-hexylthiophene) for thin film field-effect transistor applications with high mobility. Appl Phys Lett 69(26):4108–4110
12. Yang H, Shin TJ, Yang L, Cho K, Ryu CY, Bao Z (2005) Effect of mesoscale crystalline structure on the field-effect mobility of regioregular poly (3-hexyl thiophene) in thin-film transistors. Adv Funct Mater 15(4):671–676
13. Lin P, Yan F (2012) Organic thin-film transistors for chemical and biological sensing. Adv Mater 24(1):34–51
14. Azmer MI, Ahmad Z, Sulaiman K, Touati F (2016) Morphological and structural properties of VoPcPhO: P3HT composite thin films. Mater Lett 164:605–608
15. Hwang J, Jang J, Hong K, Kim KN, Han JH, Shin K, Park CE (2011) Poly (3-hexylthiophene) wrapped carbon nanotube/poly (dimethylsiloxane) composites for use in finger-sensing piezoresistive pressure sensors. Carbon 49(1):106–110
16. Tremel K, Ludwigs S (2014) Morphology of P3HT in thin films in relation to optical and electrical properties. In: P3HT revisited–from molecular scale to solar cell devices. Springer, Berlin, pp 39–82
17. Zen A, Pflaum J, Hirschmann S, Zhuang W, Jaiser F, Asawapirom U, Rabe JP, Scherf U, Neher D (2004) Effect of molecular weight and annealing of poly (3-hexylthiophene) s on the performance of organic field-effect transistors. Adv Funct Mater 14(8):757–764
18. Spano FC (2005) Modeling disorder in polymer aggregates: the optical spectroscopy of regioregular poly (3-hexylthiophene) thin films. J Chem Phys 122(23):234701
19. Cai W, Gong X, Cao Y (2010) Polymer solar cells: recent development and possible routes for improvement in the performance. Sol Energy Mater Sol Cells 94(2):114–127
20. Lilliu S, Böberl M, Sramek M, Tedde SF, Macdonald JE, Hayden O (2011) Inkjet-printed organic photodiodes. Thin Solid Films 520(1):610–615
21. Ichikawa M, Takeuchi T, Jeon HG, Jin Y, Lee S, Kim KS (2012) Organic photodiode with high infrared light sensitivity based on tin phthalocyanine/C_{60} bulk heterojunction and optical interference effect. Jpn J Appl Phys 51(3):034103
22. Guvenc AB, Ozkan C, Ozkan M (2012) Early-effect like behavior in space charge regions of organic bulk-heterojunction photodiodes. Cambridge University Press, Cambridge
23. Mihailetchi VD, Xie HX, de Boer B, Koster LA, Blom PW (2006) Charge transport and photocurrent generation in poly (3-hexylthiophene): methanofullerene bulk-heterojunction solar cells. Adv Funct Mater 16(5):699–708
24. Padinger F, Rittberger RS, Sariciftci NS (2003) Effects of postproduction treatment on plastic solar cells. Adv Funct Mater 13(1):85–88
25. Shaheen SE, Brabec CJ, Sariciftci NS, Padinger F, Fromherz T, Hummelen JC (2001) 2.5% efficient organic plastic solar cells. Appl Phys Lett 78(6):841–843
26. Ihn KJ, Moulton J, Smith P (1993) Whiskers of poly (3-alkylthiophene)s. J Polym Sci, Part B Polym Phys 31(6):735–742
27. Bouman M, Havinga EE, Janssen RAJ, Meijer EW (1994) Chiroptical properties of regioregular chiral polythiophenes. Mol Cryst Liq Cryst 256(1):439–448
28. Halls JJM, Walsh CA, Greenham NC, Marseglia EA, Friend RH, Moratti SC, Holmes AB (1995) Efficient photodiodes from interpenetrating polymer networks. Nature 376:498–500
29. Ludwigs S (2014) P3HT revisited: from molecular scale to solar cell devices, vol 265. Springer, Berlin
30. Moulé AJ, Neher D, Turner ST (2014) P3HT-based solar cells: structural properties and photovoltaic performance. In: P3HT revisited–from molecular scale to solar cell devices. Springer, Berlin, pp 181–232

31. Zen A, Saphiannikova M, Neher D, Grenzer J, Grigorian S, Pietsch U, Asawapirom U, Janietz S, Scherf U, Lieberwirth I, Wegner G (2006) Effect of molecular weight on the structure and crystallinity of poly (3-hexylthiophene). Macromolecules 39(6):2162–2171
32. Kline RJ, McGehee MD, Kadnikova EN, Liu J, Fréchet JM, Toney MF (2005) Dependence of regioregular poly (3-hexylthiophene) film morphology and field-effect mobility on molecular weight. Macromolecules 38(8):3312–3319
33. Kim Y, Cook S, Tuladhar SM, Choulis SA, Nelson J, Durrant JR, Bradley DD, Giles M, McCulloch I, Ha CS, Ree M (2006) A strong regioregularity effect in self-organizing conjugated polymer films and high-efficiency polythiophene: fullerene solar cells. Nat Mater 5(3):197–203
34. Hoth CN, Choulis SA, Schilinsky P, Brabec CJ (2009) On the effect of poly (3-hexylthiophene) regioregularity on inkjet printed organic solar cells. J Mater Chem 19 (30):5398–5404
35. Moulé AJ, Bonekamp JB, Meerholz K (2006) The effect of active layer thickness and composition on the performance of bulk-heterojunction solar cells. J Appl Phys 100(9):094503
36. Lenes M, Shelton SW, Sieval AB, Kronholm DF, Hummelen JCK, Blom PW (2009) Electron trapping in higher adduct fullerene-based solar cells. Adv Funct Mater 19 (18):3002–3007
37. Lenes M, Wetzelaer GJA, Kooistra FB, Veenstra SC, Hummelen JC, Blom PW (2008) Fullerene bisadducts for enhanced open-circuit voltages and efficiencies in polymer solar cells. Adv Mater 20(11):2116–2119
38. Choi JH, Son KI, Kim T, Kim K, Ohkubo K, Fukuzumi S (2010) Thienyl-substituted methanofullerene derivatives for organic photovoltaic cells. J Mater Chem 20(3):475–482
39. Zhang F, Jespersen KG, Björström C, Svensson M, Andersson MR, Sundström V, Magnusson K, Moons E, Yartsev A, Inganäs O (2006) Influence of solvent mixing on the morphology and performance of solar cells based on polyfluorene copolymer/fullerene blends. Adv Funct Mater 16:667–674
40. Moulé AJ, Meerholz K (2008) Controlling morphology in polymer–fullerene mixtures. Adv Mater 20(2):240–245
41. Guo X, Cui C, Zhang M, Huo L, Huang Y, Hou J, Li Y (2012) High efficiency polymer solar cells based on poly (3-hexylthiophene)/indene-C 70 bisadduct with solvent additive. Energy Environ Sci 5(7):7943–7949
42. van Franeker JJ, Turbiez M, Li W, Wienk MM, Janssen RA (2015) A real-time study of the benefits of co-solvents in polymer solar cell processing. Nat Commun 6
43. Aïch BR, Beaupré S, Leclerc M, Tao Y (2014) Highly efficient thieno [3, 4-c] pyrrole-4, 6-dione-based solar cells processed from non-chlorinated solvent. Org Electron 15(2):543–548
44. Aïch BR, Lu J, Beaupré S, Leclerc M, Tao Y (2012) Control of the active layer nanomorphology by using co-additives towards high-performance bulk heterojunction solar cells. Org Electron 13(9):1736–1741
45. Ye L, Zhang S, Ma W, Fan B, Guo X, Huang Y, Ade H, Hou J (2012) From binary to ternary solvent: morphology fine-tuning of D/A blends in PDPP3T-based polymer solar cells. Adv Mater 24(47):6335–6341
46. Ma W, Yang C, Gong X, Lee K, Heeger AJ (2005) Thermally stable, efficient polymer solar cells with nanoscale control of the interpenetrating network morphology. Adv Funct Mater 15(10):1617–1622
47. Turner ST, Pingel P, Steyrleuthner R, Crossland EJ, Ludwigs S, Neher D (2011) Quantitative analysis of bulk heterojunction films using linear absorption spectroscopy and solar cell performance. Adv Funct Mater 21(24):4640–4652
48. Tsoi WC, James DT, Kim JS, Nicholson PG, Murphy CE, Bradley DD, Nelson J, Kim JS (2011) The nature of in-plane skeleton Raman modes of P3HT and their correlation to the degree of molecular order in P3HT: PCBM blend thin films. J Am Chem Soc 133(25):9834–9843

49. Pascui OF, Lohwasser R, Sommer M, Thelakkat M, Thurn-Albrecht T, Saalwächter K (2010) High crystallinity and nature of crystal–crystal phase transformations in regioregular poly (3-hexylthiophene). Macromolecules 43(22):9401–9410
50. Scharsich C, Lohwasser RH, Sommer M, Asawapirom U, Scherf U, Thelakkat M, Neher D, Köhler A (2012) Control of aggregate formation in poly (3-hexylthiophene) by solvent, molecular weight, and synthetic method. J Polym Sci, Part B: Polym Phys 50(6):442–453
51. Li G, Yao Y, Yang H, Shrotriya V, Yang G, Yang Y (2007) "Solvent annealing" effect in polymer solar cells based on poly (3-hexylthiophene) and methanofullerenes. Adv Funct Mater 17(10):1636–1644
52. Moulé A, Meerholz K (2007) Minimizing optical losses in bulk heterojunction polymer solar cells. Appl Phys B 86(4):721–727
53. Yakimov PA, Forrest SR (2003) Small molecular weight organic thin-film photodetectors and solar cells. J Appl Phys 93(7):3693–3723
54. Moulé AJ, Meerholz K (2009) Morphology control in solution-processed bulk-heterojunction solar cell mixtures. Adv Funct Mater 19(19):3028–3036
55. Oosterbaan WD, Vrindts V, Berson S, Guillerez S, Douhéret O, Ruttens B, D'Haen J, Adriaensens P, Manca J, Lutsen L, Vanderzande D (2009) Efficient formation, isolation and characterization of poly (3-alkylthiophene) nanofibres: probing order as a function of side-chain length. J Mater Chem 19(30):5424–5435
56. Bertho S, Oosterbaan WD, Vrindts V, D'Haen J, Cleij TJ, Lutsen L, Manca J, Vanderzande D (2009) Controlling the morphology of nanofiber-P3HT: PCBM blends for organic bulk heterojunction solar cells. Org Electron 10(7):1248–1251
57. Xin H, Reid OG, Ren G, Kim FS, Ginger DS, Jenekhe SA (2010) Polymer nanowire/fullerene bulk heterojunction solar cells: how nanostructure determines photovoltaic properties. ACS Nano 4(4):1861–1872
58. Kim JY, Lee K, Coates NE, Moses D, Nguyen TQ, Dante M, Heeger AJ (2007) Efficient tandem polymer solar cells fabricated by all-solution processing. Science 317(5835):222–225
59. Greenham NC, Peng X, Alivisatos A (1996) Charge separation and transport in conjugated-polymer/semiconductor-nanocrystal composites studied by photoluminescence quenching and photoconductivity. Phys Rev B 54(24):17628–17637
60. Najeeb MA, Abdullah SM, Aziz F, Ahmad Z, Rafique S, Wageh S, Al-Ghamdi AA, Sulaiman K, Touati F, Shakoor RA, Al-Thani NJ (2016) Structural, morphological and optical properties of PEDOT: PSS/QDs nano-composite films prepared by spin-casting. Physica E 83:64–68
61. Najeeb MA, Abdullah SM, Aziz F, Azmer MI, Swelm W, Al-Ghamdi AA, Ahmad Z, Supangat A, Sulaiman K (2016) Improvement in the photovoltaic properties of hybrid solar cells by incorporating a QD-composite in the hole transport layer. RSC Adv 6(27):23048–23057
62. Olson JD, Gray G, Carter SA (2009) Optimizing hybrid photovoltaics through annealing and ligand choice. Sol Energy Mater Sol Cells 93(4):519–523
63. Guo J, Huang Y, Jing X, Chen X (2009) Synthesis and characterization of functional poly(gamma-benzyl-L-glutamate) (PBLG) as a hydrophobic precursor. Polymer 50(13):2847–2855
64. Block H (1983) Poly ([gamma]-benzyl-L-glutamate) and other glutamic acid containing polymers, vol 9. Gordon & Breach Science Publishers
65. Ren K, Wilson WL, West JE, Zhang QM, Yu SM (2012) Piezoelectric property of hot pressed electrospun poly (γ-benzyl-α, L-glutamate) fibers. Appl Phys A 107(3):639–646
66. Andrew J, Clarke D (2008) Effect of electrospinning on the ferroelectric phase content of polyvinylidene difluoride fibers. Langmuir 24(3):670–672
67. Qian J, Yong X, Xu W, Jin X (2013) Preparation and characterization of bimodal porous poly(gamma-benzyl-L-glutamate) scaffolds for bone tissue engineering. Mater Sci Eng C-Mater Biol Appl 33(8):4587–4593

68. Fang J, Yong Q, Zhang K, Sun W, Yan S, Cui L, Yin J (2015) Novel injectable porous poly (γ-benzyl-L-glutamate) microspheres for cartilage tissue engineering: preparation and evaluation. J Mater Chem B 3(6):1020–1031
69. Sugimoto H, Nakanishi E, Hanai T, Yasumura T, Inomata K (2004) Aggregate formation and release behaviour of hydrophobic drugs with graft copolypeptide-containing tryptophan. Polym Int 53(7):972–983
70. Cauchois O, Segura-Sanchez F, Ponchel G (2013) Molecular weight controls the elongation of oblate-shaped degradable poly(gamma-benzyl-L-glutamate) nanoparticles. Int J Pharm 452(1–2):292–299
71. de Miguel L, Cebrián-Torrejón G, Caudron E, Arpinati L, Doménech-Carbó A, Ponchel G (2015) Bone-targeted cisplatin-complexed poly(gamma-benzyl-L-glutamate)-poly(glutamic acid) block polymer nanoparticles: an electrochemical approach. ChemElectroChem 2 (5):748–754
72. Perdih P, Pahovnik D, Cegnar M, Miklavžin A, Kerč J, Žagar E (2014) Synthesis of chitosan-graft-poly(sodium-L-glutamate) for preparation of protein nanoparticles. Cellulose 21(5):3469–3485
73. Ravichandran R, Venugopal JR, Sundarrajan S, Mukherjee S, Ramakrishna S (2012) Precipitation of nanohydroxyapatite on PLIA/PBLG/Collagen nanofibrous structures for the differentiation of adipose derived stem cells to osteogenic lineage. Biomaterials 33(3):846–855
74. Huang W, Wang W, Wang P, Tian Q, Zhang C, Wang C, Yuan Z, Liu M, Wan H, Tang H (2010) Glycyrrhetinic acid-modified poly(ethylene glycol)-b-poly(gamma-benzyl L-glutamate) micelles for liver targeting therapy. Acta Biomater 6(10):3927–3935
75. Kuo SW, Chen CJ (2012) Functional polystyrene derivatives influence the miscibility and helical peptide secondary structures of poly(gamma-benzyl L-glutamate). Macromolecules 45(5):2442–2452
76. Konaga T, Fukada E (1971) Piezoelectricity in oriented films of poly (gamma-benzyl-l-glutamate). J Polym Sci Part A-2-Polym Phys 9(11):2023
77. Fukada E, Yasuda I (1957) On the piezoelectric effect of bone. J Phys Soc Jpn 12(10):1158–1162
78. Fukada E (1955) Piezoelectricity of wood. J Phys Soc Jpn 10(2):149–154
79. Ando Y, Fukada E (1976) Piezoelectric properties of oriented deoxyribonucleate films. J Polym Sci Polym Phys Ed 14(1):63–79
80. Bazhenov VA (1961) Piezoelectric properties of wood. Consultants Bureau, New York
81. Fukada E (1956) On the piezoelectric effect of silk fibers. J Phys Soc Jpn 11:1301
82. Ueberschlag P (2001) PVDF piezoelectric polymer. Sens Rev 21(2):118–126
83. Kawai H (1969) The piezoelectricity of poly (vinylidene fluoride). Jpn J Appl Phys 8(7):975
84. Nakiri T, Imoto K, Ishizuka M, Okamoto S, Date M, Uematsu Y, Fukada E, Tajitsu Y (2004) Piezoelectric characteristics of polymer film oriented under a strong magnetic field. Jpn J Appl Phys 43(9S):6769
85. Fukada E (1984) Piezoelectricity of natural biomaterials. Ferroelectrics 60(1):285–296
86. Fukada E, Furukawa T, Baer E, Hiltner A, Anderson JM (1973) Piezoelectric relaxations in homopolymers and copolymers of γ-Benzyl-L-glutamate and L-Leueine. J Macromol Sci Part B Phys 8(3–4):475–481
87. Go Y, Ejiri S, Fukada E (1969) Magnetic orientation of poly-γ-benzyl-l-glutamate. Biochim et Biophys Acta (BBA)-Protein Struct 175(2):454–456
88. Furukawa T (1989) Piezoelectricity and pyroelectricity in polymers. IEEE Trans Electr Insul 24(3):375–394
89. Pan CT, Yen CK, Lin L, Lu YS, Li HW, Huang JCC, Kuo SW (2014) Energy harvesting with piezoelectric poly (γ-benzyl-L-glutamate) fibers prepared through cylindrical near-field electrospinning. RSC Adv 4(41):21563–21570
90. Pan CT, Yen CK, Wu HC, Lin L, Lu YS, Huang JCC, Kuo SW (2015) Significant piezoelectric and energy harvesting enhancement of poly (vinylidene fluoride)/polypeptide fiber composites prepared through near-field electrospinning. J Mater Chem A 3(13):6835–6843

91. Guan MJ, Liao WH (2008) Characteristics of energy storage devices in piezoelectric energy harvesting systems. J Intell Mater Syst Struct 19(6):671–680
92. Steven RA, Henry AS (2007) A review of power harvesting using piezoelectric materials (2003–2006). Smart Mater Struct 16(3):R1
93. Beeby S, Tudor MJ, White NM (2006) Energy harvesting vibration sources for microsystems applications. Meas Sci Technol 17(12):R175
94. Farrar D, Ren K, Cheng D, Kim S, Moon W, Wilson WL, West JE, Yu SM (2011) Permanent polarity and piezoelectricity of electrospun α-helical poly (α-amino acid) fibers. Adv Mater 23(34):3954–3958
95. Sun D, Chang C, Li S, Lin L (2006) Near-field electrospinning. Nano Lett 6(4):839–842
96. Tinoco I (1957) Dynamic electrical birefringence studies of poly-gamma-benzyl-l-glutamate. J Am Chem Soc 79(16):4336–4338
97. Tinoco I (1957) The change of optical activity of poly-gamma-benzyl-l-glutamate in an electric field. J Am Chem Soc 79(15):4248–4249
98. Samulski ET, Tobolsky AV (1967) Solid liquid crystal films of poly-gamma-benzyl-l-glutamate. Nature 216(5119):997
99. Watanabe T, Tsujita Y, Uematsu I (1975) Influence of casting conditions on structure of poly (gamma-benzyl-l-glutamate). Polym J 7(2):181–185
100. Lio T (1971) Conformations of low-molecular-weight poly-gamma-benzyl-l-glutamate films. Bull Chem Soc Jpn 44(3):859–861
101. McKinnon AJ, Tobolsky AV (1968) Structure and properties of poly-gamma-benzyl-l-glutamate cast from dimethylformamide. J Phys Chem 72(4):1157–1161
102. Takenaka T, Harada K, Matsumoto M (1980) Structural studies of poly-gamma-benzyl-l-glutamate monolayers by infrared ATR and transmission spectra. J Colloid Interface Sci 73(2):569–577
103. Hikichi K, Tsutsumi A, Higuchi T, Saito J (1978) Electric conduction of poly(gamma-benzyl l-glutamate). Polym J 10(6):629–630
104. Tohyama K, Iizuka E (1974) Magnetic torque measurement of PBLG films. J Phys Soc Jpn 37(4):1172
105. Sari A, Alkan C, Karaipekli A (2010) Preparation, characterization and thermal properties of PMMA/n-heptadecane microcapsules as novel solid-liquid microPCM for thermal energy storage. Appl Energy 87(5):1529–1534
106. Blaga A (1978) Use of plastics in solar energy applications. Sol Energy 21(4):331–338
107. Alay S, Göde F, Alkan C (2010) Preparation and characterization of poly (methylmethacrylate-coglycidyl methacrylate)/n-hexadecane nanocapsules as a fiber additive for thermal energy storage. Fibers Polym 11(8):1089–1093
108. Alkan C, Sari A (2008) Fatty acid/poly(methyl methacrylate) (PMMA) blends as form-stable phase change materials for latent heat thermal energy storage. Sol Energy 82(2):118–124
109. Huskić M, Žigon M (2007) PMMA/MMT nanocomposites prepared by one-step in situ intercalative solution polymerization. Eur Polym J 43(12):4891–4897
110. Huang X, Brittain WJ (2001) Synthesis and characterization of PMMA nanocomposites by suspension and emulsion polymerization. Macromolecules 34(10):3255–3260
111. Park SJ, Cho MS, Lim ST, Choi HJ, Jhon MS (2003) Synthesis and dispersion characteristics of multi-walled carbon nanotube composites with poly (methyl methacrylate) prepared by in-situ bulk polymerization. Macromol Rapid Commun 24(18):1070–1073
112. Shen D, Huang Y (2004) The synthesis of CDA-g-PMMA copolymers through atom transfer radical polymerization. Polymer 45(21):7091–7097
113. Allen R, Long T, McGrath J (1986) Preparation of high purity, anionic polymerization grade alkyl methacrylate monomers. Polym Bull 15(2):127–134
114. Wu LY, Chen LW, Liu CM (2009) Acoustic energy harvesting using resonant cavity of a sonic crystal. Appl Phys Lett 95(1):013506
115. Wu F, Hou Z, Liu Z, Liu Y (2001) Point defect states in two-dimensional phononic crystals. Phys Lett A 292(3):198–202

116. Kushwaha MS, Djafari-Rouhani B (1998) Giant sonic stop bands in two-dimensional periodic system of fluids. J Appl Phys 84(9):4677–4683
117. Mikoshiba K, Manimala JM, Sun C (2013) Energy harvesting using an array of multifunctional resonators. J Intell Mater Syst Struct 24(2):168–179
118. Wang ZL, Song J (2006) Piezoelectric nanogenerators based on zinc oxide nanowire arrays. Science 312(5771):242–246
119. Zhu G, Pan C, Guo W, Chen CY, Zhou Y, Yu R, Wang ZL (2012) Triboelectric-generator-driven pulse electrodeposition for micropatterning. Nano Lett 12(9):4960–4965
120. Wang ZL, Zhu G, Yang Y, Wang S, Pan C (2012) Progress in nanogenerators for portable electronics. Mater Today 15(12):532–543
121. Lee S, Bae SH, Lin L, Yang Y, Park C, Kim SW, Cha SN, Kim H, Park YJ, Wang ZL (2013) Super-flexible nanogenerator for energy harvesting from gentle wind and as an active deformation sensor. Adv Funct Mater 23(19):2445–2449
122. Gao PX, Song J, Liu J, Wang ZL (2007) Nanowire piezoelectric nanogenerators on plastic substrates as flexible power sources for nanodevices. Adv Mater 19(1):67–72
123. Lin ZH, Cheng G, Lin L, Lee S, Wang ZL (2013) Water-solid surface contact electrification and its use for harvesting liquid-wave energy. Angew Chem Int Ed 52(48):12545–12549
124. Zhu G, Lin ZH, Jing Q, Bai P, Pan C, Yang Y, Zhou Y, Wang ZL (2013) Toward large-scale energy harvesting by a nanoparticle-enhanced triboelectric nanogenerator. Nano Lett 13(2):847–853
125. Bouendeu E, Greiner A, Smith PJ, Korvink JG (2011) A low-cost electromagnetic generator for vibration energy harvesting. IEEE Sens J 11(1):107–113
126. Jo SE, Kim MK, Kim MS, Kim YJ (2012) Flexible thermoelectric generator for human body heat energy harvesting. Electron Lett 48(16):1013–1015
127. Al-Haik MY, Zakaria MY, Hajj MR, Haik Y (2016) Storage of energy harvested from a miniature turbine in a novel organic capacitor. J Energy Storage 6:232–238
128. Meng Q, Li W, Zheng Y, Zhang Z (2010) Effect of poly (methyl methacrylate) addition on the dielectric and energy storage properties of poly (vinylidene fluoride). J Appl Polym Sci 116(5):2674–2684

Self-healing Polymer Composites Based on Graphene and Carbon Nanotubes

Santwana Pati, Bhanu Pratap Singh and S.R. Dhakate

Abstract Self-healing is a bioinspired concept as nature itself is filled with self-healable composites. For the last 15 years, immense curiosity has been developed in materials that can self-heal for real engineering applications such as aerospace and sporting goods, electronics, and robotics, as this property can improve the longevity of the materials, diminish replacement costs, and improve safety. In materials technology, structural polymer composites are vulnerable to damage, failure, and degradation. Cracks are formed deep within the structure, and hence, it is not easy to detect such cracks and their repair is unfeasible. Self-healing is a microscale bottom-up approach which provides the ability to repair degradation and heal these cracks while still achieving the structural strength requirement. All types of polymers, from thermosetting polymers to thermoplastics, have the potential for self-healing. Self-healing approach can be successfully applied using various approaches such as microencapsulation of the healing agent and vascular impregnation of self-healing materials in tubular networks, but all these extrinsic approaches result in a considerable loss of mechanical strength, while in intrinsic approach, the healing capability is latent in the material itself. The healing is achieved by reversible bonding in the matrix polymer. Carbon nanotubes (CNTs) and graphene have immense hope in this world of smart and multifunctional materials and can be used as nanofillers to obtain nanocomposites of extraordinary mechanical, electrical, thermal, and self-healing properties with the added advantage of lower weight. Their good compatibility with polymer resulting after surface modification of CNTs and graphene, achieving the desirable chemical stability added with outstanding thermal and electrical properties place them as the appropriate and the nascent research topic for self-healing polymer nanocomposites. This chapter initially gives a brief idea about the basic concepts and then examines the different approaches to self-healing techniques along with the various self-healing assessment terms and concepts.

S. Pati · B.P. Singh (✉) · S.R. Dhakate
Physics and Engineering of Carbon, CSIR-National Physical Laboratory,
Dr. K.S. Krishnan Road, New Delhi 110 012, India
e-mail: bps@nplindia.org; bpsingh2k4@yahoo.com

S. Pati · B.P. Singh · S.R. Dhakate
Academy of Scientific and Innovative Research, New Delhi, India

D. Ponnamma et al. (eds.), *Smart Polymer Nanocomposites*,
Springer Series on Polymer and Composite Materials,
DOI 10.1007/978-3-319-50424-7_5

This chapter then revolves around the different self-healing nanocomposites based on graphene using various polymers such as polyurethane and epoxy and even hydrogel composites. The characterization of the self-healing systems and analysis of the exact mechanism taking place using different triggering mechanisms is discussed. Then, the various CNT-based self-healing nanocomposites are encompassed. The efficient utilization of CNTs as reinforcement filler and as the healing agent in extrinsic approach is discussed. Then, the utilization of CNTs to fabricate self-healing nanocomposites for a variety of end applications is discussed. The various results on healable multifunctional CNTs and graphene-based polymer nanocomposites are summarized in a tabular form. Finally, the challenges and future research opportunities are highlighted in this chapter.

Keywords Self-healing · Polymer composites · Graphene · Carbon nanotubes · Polyurethanes · Epoxy · Multifunctional materials

Contents

1 Fundamentals and Basic Concept of Self-healing

1.1 Background

New age has come up with different kinds of smart and intelligent materials, but degradation and damage are inescapable. Every material in this universe is susceptible to natural or artificial degradation and has therefore limited lifetime. For example, muscles and bones can be damaged by excessive mechanical loading, but only the biological systems have the ability to self-repair. Biologic system can sense external stimuli, respond to it, redevelop, and heal in case of damage. Having

inspired from the natural systems, human race is trying to imitate the healing process into the man-made materials. In 1969, Malinskii et al. [1] presented the detailed analysis of the self-healing of the crack in polyvinyl alcohol (PVA) specimens and that marked the beginning of self-healing concept. Following that, self-healing became an attractive topic, and research began on self-healing in thermoplastic and cross-linked polymer systems [2, 3]. And in 1990s, Dry [4] also reported about self-healing concrete. In 2001, White et al. [5] published his work on the observation of self-healing behavior in polymer-based materials and that led to the beginning of the era of smart healable materials. Thereafter, self-healing materials became a huge focus worldwide.

1.2 Assessing the Self-healing Behavior

For the successful study of the performance of a material for self-healing applications, we need to quantify this characteristic. Therefore, healing efficiency calculations are done to estimate the behavior of the material. Healing efficiency is calculated based on various ratios of the physical properties of the material after healing and before damage [6]. The different parameters considered in calculating the mechanical healing efficiency are fracture toughness, fatigue life, tensile strength, etc., summarized in Fig. 1. Apart from mechanical efficiency, self-healing behavior in polymer composites is also analyzed based on electrical properties. The electrical self-healing is assessed by a simple circuit arrangement. A lamp is connected across the material using a circuit. After creating an artificial damage, the lamp extinguishes. But the healable material gains back its lost conductivity, and lamp glows again.

The various terms in Fig. 1 are as follows: K_{IC}^{healed} is the mode 1 fracture toughness of a healed specimen, and K_{IC}^{virgin} is that of a virgin specimen. P_C^{healed} and P_C^{virgin} are the critical loads at fracture for the healed and virgin specimens, respectively. G_{IC}^{virgin} and G_{IC}^{healed} are the critical energy release rate from testing the virgin and then the healed specimens, respectively. U_{healed} and U_{virgin} are the strain energy. b_n is the width of the crack surface created. W is the distance from the loading line to the end of the specimen. $a_{o_{healed}}$ and $a_{o_{virgin}}$ are the initial precrack lengths for the healed and virgin cases, respectively. σ_C^{virgin} and σ_C^{healed} are the tensile strengths of the virgin and the healed specimens, respectively. $\sigma_{C_{flexural}}^{healed}$ is the residual flexural strength of the material after it has been damaged and then allowed to heal, $\sigma_{C_{flexural}}^{damaged}$ is the residual flexural strength of the damaged specimen, and $\sigma_{C_{flexural}}^{virgin}$ is that of the virgin specimen. N_{healed} is the total number of cycles to failure for a self-healing sample, and $N_{control}$ is that of a similar sample without healing. Therefore, the self-healing mechanism is assessed using the various physical properties and comparing their values before and after healing. This assessment gives a quantitative measure to the process, and hence, it becomes more convenient to further modify the conditions to obtain the maximum healing.

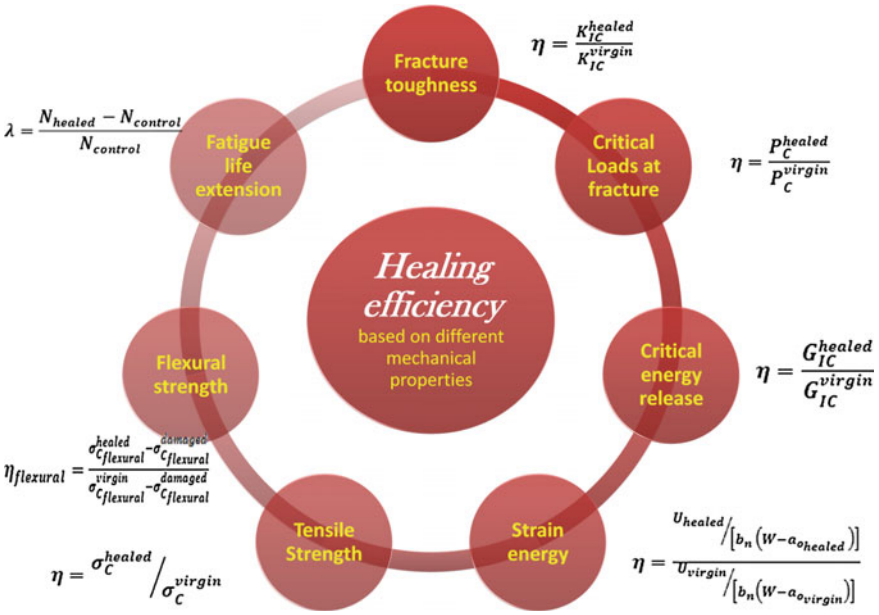

Fig. 1 The various modes of calculating healing efficiency

1.3 Different Mechanisms of Self-healing

Basically, there are three different categories of self-healable materials depending on the healing mechanism: capsule-based, vascular, and intrinsic [6–8].

1.3.1 Capsule Mechanism

Capsule-based mechanism basically works by the encapsulation of the healing agent inside capsules. A crack in the system triggers the bursting of the capsules and thereby causes the outward flow of the healing agent. The healing mechanism is explained by 4 steps: storage of the healing agent inside the capsules, outflow of the healing agent triggered by damage, transport of the healing agent to the site of the crack, and restoration. In the storage step, the healing agent is microencapsulated, and then, capsules are uniformly dispersed throughout the matrix of the material. The healing agent does not react during the storage process. The crack breaks the wall of the capsule that results in the release and hence sealing of the crack by the healing agent. This whole procedure is illustrated in Fig. 2a.

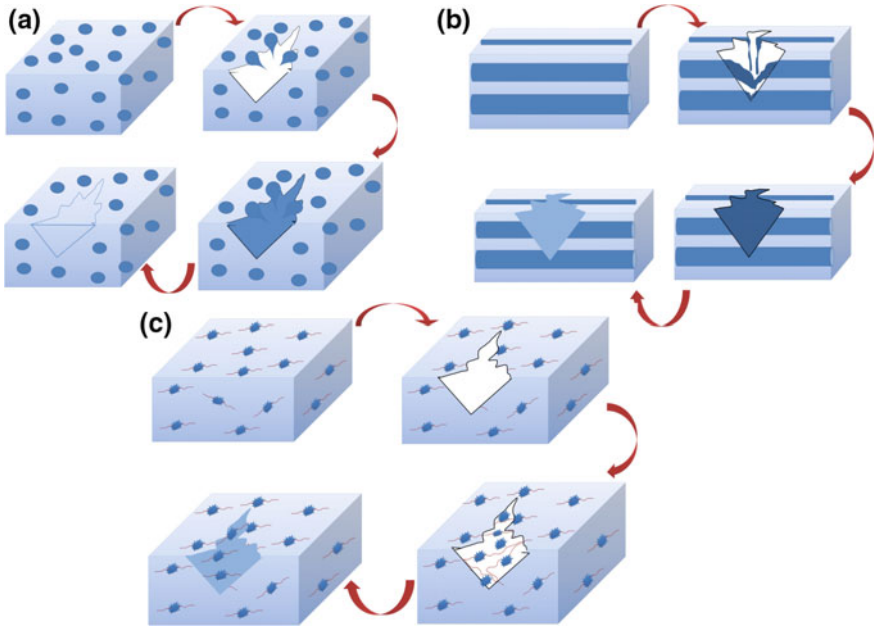

Fig. 2 Various approaches of crack healing: **a** capsule-based, **b** vascular, and **c** intrinsic

1.3.2 Vascular Mechanism

This mechanism is the closest replica of the biologic systems. In this approach, the material is designed with organized series of network channels as in the vascular network of plants and animals that circulates the required chemicals and healing substances in the body to the site of damage. Here, hollow tubes or systems with fiber-like structures are used to carry the healing agent as shown in Fig. 2b. This approach is better than the aforementioned capsule mechanism as it gives continuous supply of the healing agent at a particular place even for multiple damages. A much higher amount of the healing agent is transferred to the crack area using this technique as compared to the capsule mechanism. Although capsule-based approaches are easy to impregnate into any system, their functionality can be used just for a single damage event, but this vascular mechanism can be used multiple times.

1.3.3 Intrinsic Mechanism

Intrinsic technique is based on the specific property of the polymer or polymer composites that facilitates crack healing under certain conditions and application of a particular stimuli (like sunlight). This mechanism is much better than the

above-mentioned approaches as intrinsic self-healing polymers do not have impregnated capsules or vascular systems (hollow fibers). Therefore, the mechanical properties are not compromised in order to make the specimen self-healing. Figure 2c gives a brief illustration about the intrinsic mechanism.

Although all the three different mechanisms of healing have shown their own advantages for enhancing the self-healing behavior, this chapter basically discusses the self-healing polymers and polymer composite systems and most of them work on intrinsic mechanism.

Various polymer composites have shown self-healing property on the exposure to a particular stimulus like UV exposure and self-healing behavior in polydimethylsiloxane—PU cross-linked networks by repairing mechanical damage has been seen [9, 10]. Similarly, specific kinds of polymers with ligands attached via metal ion binding have shown healing property through exposure to light [11]. Another composite material consisting of an organic polymer group and nickel nanostructured microparticles shows self-healing properties at ambient conditions [12]. Therefore, various such polymers with ligands attached by hydrogen bonding, π–π interactions, ionomers, and coordinative bonds have been realized for self-healing applications [13]. Various ionomers have also shown self-healing property like Surlyn 8940 [14]. These ionomers have ionic cross-linkings which show response to thermal energy, and hence, Surlyn polymers [15, 16] show self-healing behavior. Carbon nanotubes (CNTs) and graphene with its high thermal and electrical conductivity [17, 18] can also impart self-healing property in polymers and can also contribute to additional mechanical properties in the polymer system, and hence, the material can be used in high end applications such as aerospace, body armor, and military equipments. Hence, this chapter further discusses CNTs and graphene-based self-healing polymer composites using various approaches.

2 Carbon Nanotubes and Graphene: A Brief Idea

Carbon has always been the most flexible and all fields applicable element that has various allotropes and forms which have enormous applications in materials world. There are different forms of carbon that exist, and out of them, CNTs and graphene have become the most interesting materials and have unlimited scope for research in every field of science and technology.

CNT has been the well-known term in science and technology since its discovery in 1991 by Iijima [19]. CNT can be envisioned as a rolled-up sheet of single-layer carbon atoms and can be formed in two different basic forms: single-walled and multiwalled (Fig. 3). The single-walled carbon nanotubes (SWCNTs) are formed by a single sheet of monolayered carbon atoms rolled up, while multiwalled carbon nanotubes (MWCNTs) have multiple walls. The diameter of CNTs is in the range of a few nanometers in the case of SWCNTs, and MWCNTs have in the range of tens of nanometers. CNTs generally have lengths in the range of micrometers.

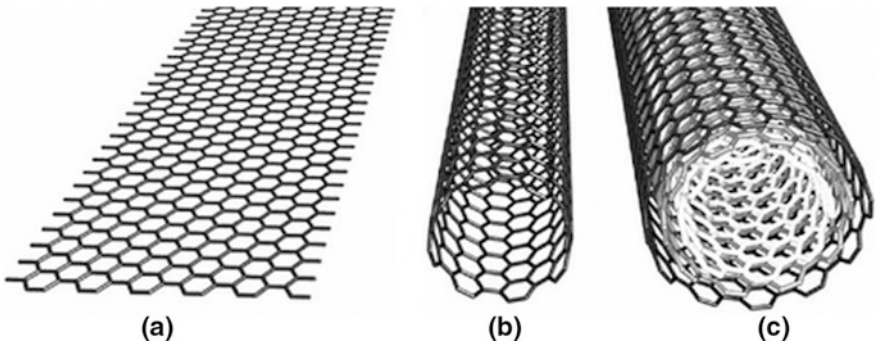

Fig. 3 Illustration of the structure of **a** graphene, **b** SWCNT, and **c** MWCNT [21]. Copyright 2005. Reprinted with the permission from Springer

CNTs show three different chiralities: armchair, zigzag, and chiral depending on the different lattice vectors and chiral angles [20]. CNTs with lattice vectors (*m*, *m*) and (*m*, 0) types are termed as "armchair" and "zigzag," respectively, else they are termed as "chiral." Based on the chirality, SWCNTs can be metallic or semiconducting. CNTs with its widespread applications from industry to nanoscale starting with modular electronics, energy storage to structural composites and conductive plastics has become the most awaited material in the society to be viewed as a trendsetter for transforming every technology to an advanced form.

Another form of carbon that has been recently explored for various applications is graphene, although graphene is very new in the world of materials but has shown extraordinary mechanical, thermal, and electronic properties owing to its unique structure. Graphene is the allotrope of carbon, consisting of a hexagonal arrangement of carbon atoms on a single plane giving it a two-dimensional structure. Although graphene is the building block of the other forms of carbon nanomaterials such as CNT and fullerene, graphene was practically realized most recently in 2004. After that, a sudden surge of research into the structure and properties of graphene started, and graphene did not disappoint. Detailed characterization of graphene yielded high values for the different properties, such as carrier mobility and tensile strength. With these groundbreaking properties, graphene is a potential candidate in various areas of applications such as thin and flexible displays, solar cells, electronics, medical, chemical, and industrial processes [17, 22, 23].

CNTs and graphene have been well explored in the various polymer systems including both thermoplastic and thermosetting in order to improve the electrical and mechanical properties of the polymer systems. Several researchers have presented various works by using different polymers such as polyurethane [24–26], polystyrene [27–30], polycarbonate [31–35], ABS [36–38], PMMA [27, 39–41], polyethylene [42–44], epoxy [45–48], and phenolic systems [49–51]. With high thermal conductivity and stability, CNT and graphene have also been used with

polymers to develop self-healing nanocomposites. The following sections discuss briefly the self-healing effect achieved using graphene along with the polymers subsequently using CNTs in a similar manner.

3 Graphene-Based Self-healing Polymer Composites

3.1 Intrinsic Defect Healing using Graphene

Graphene shows intrinsic defects' healing property. The healing effect consists of the reconstruction (knitting) of the graphene structure [52, 53]. In the event of a vacancy defect, carbon atoms jump out from the external regions and fill up the vacancies [53, 54]. Generally, impurities like hydrocarbon impurities serve as the source of these extra carbon atoms.

When graphene is etched out in the presence of metals, the carbon atoms are supplied from the nearby hydrocarbon impurities and fill up the hole created and hence show this peculiar reknitting of the holes of graphene process [55]. This is an intrinsic self-healing property seen in graphene, and this opens up possibilities for various applications of graphene using different techniques such as e-beam technique and etching process.

A molecular dynamics simulation analysis by creating a nanodamage in suspended graphene monolayer by a rigid C_{60} molecule shows the efficient self-healing procedure by appropriate heat treatment [56, 57]. The self-healing mechanism is explained as a two-step procedure:

(a) formation of local curvature around the defects created by the damage and
(b) defect reconstruction leading to smoothening of the curved surface created by the damage finally leading to the shrinking of the damage.

Effectively, the self-healing ability of the graphene depends on two factors:

1. Size of the damage created and
2. Thermal fluctuation.

Therefore, it is noteworthy that graphene being a monoatomic layer can retain the energy from the passing electrons and hence can heal the damage. In a similar way, graphene when incorporated with polymer composites can easily heal the damage in the microstructures. The main focus of this chapter is the self-healing in polymer composites by utilizing graphene and CNTs.

Another interesting application of graphene-based polymer composites is high-performance thermal interface materials owing to its planar structure and hence better thermal contraction. Many studies have reported that addition of graphene has resulted in enhanced thermal conductivity. This shall improve the heat transfer capability in the polymer matrix and hence improved self-healing with thermal or any other external stimuli. Various studies have been conducted on the

self-healing property analysis of the various polymers such as polyurethane and epoxy by incorporating graphene in it.

3.2 Polyurethane–Graphene Self-healing Systems

Most of the man-made materials are vulnerable to environmental impact, and hence, safety and lifetime are important aspects. Among all the polymers in the world, polyurethanes (PU) are the most versatile family. They are widely applied in every sector from industrial, transportation, and building to packaging, electronics, machine, and foundry. PU is the building block of most of the materials around us: coatings, adhesives, elastomers, insulation foam, footwear sole and flexible plastics. They form the inevitable choice in polymer materials. Researchers all around the world are working on healable PU polymer networks that can increase the lifetime of the materials, and also, incorporating healing property can widen the applications of the PU. Although researchers have reported various self-healing polymeric systems with embedded microcontainers or microvascular arrangements containing the healing agent, that results in poor mechanical strength as compared to the original polymer system. Graphene has been a well-utilized material for fabrication of polymer nanocomposites because of its compatibility with the polymer systems, easy availability of its precursor graphite, and dramatic enhancement of the various mechanical, electrical, physical, and barrier properties of polymer composites even at addition of quite lower amount of graphene [58]. Further, they possess excellent thermal conductivity [59] and IR response [60] due to the perfect sp^2 carbon network structures of the graphene materials. In this regard, graphene can be the promising candidate for absorbing energy from IR radiation [60] and transferring it to the damage site and healing the defect. Similarly, graphene has also shown good thermal and electrical conductivities [61] and microwave-absorbing capability. Therefore, efficient and repeatable self-healing can be obtained from graphene-based polymer materials using IR [62], microwave [63], and electrical energy [64] as the stimulus. Various researchers have reported graphene-based polyurethane nanocomposites with enhanced self-healing capabilities. Huang et al. [65] fabricated a nanocomposite of graphene and polyurethane using few-layer graphene (FG) and thermoplastic polyurethane (TPU), and this FG-TPU system could be healed. FG-TPU self-healing material was highly responsive toward all three different kinds of stimuli: infrared (IR) light, electricity, and electromagnetic wave, and they showed above 98% healing efficiency in all the three cases as shown in Fig. 4.

The actual mechanism of self-healing capability of graphene can be attributed to its energy-absorbing capability and very good thermal conductivity. Hence, it could transfer the absorbed energy from all the three sources into the TPU matrix, and this energy could help the interface TPU chains to diffuse and re-entangle and build back the TPU structure.

The different healing efficiency obtained with different loadings of graphene is shown in Fig. 5.

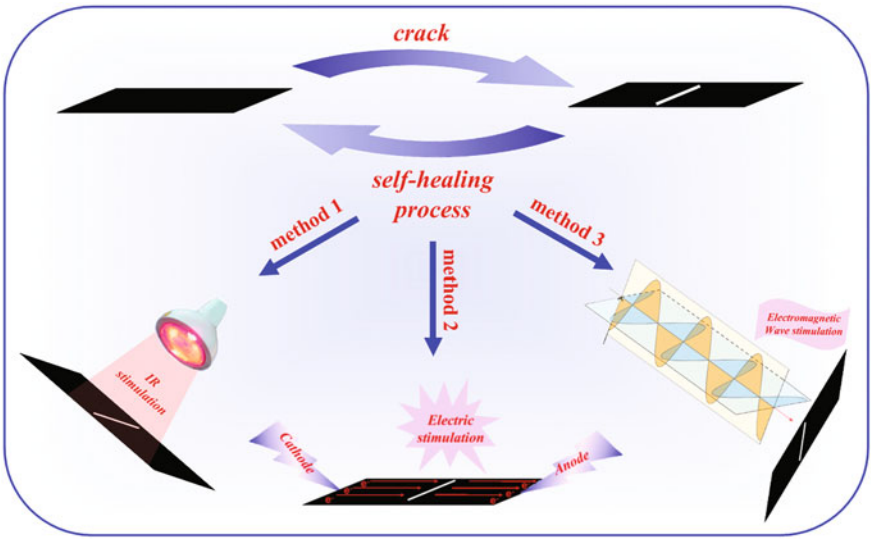

Fig. 4 The healing concept. The FG-TPU composites were healed by IR light, electricity, and electromagnetic wave with high healing efficiencies [65]. Copyright 2013. Reprinted with the permission from John Wiley and Sons

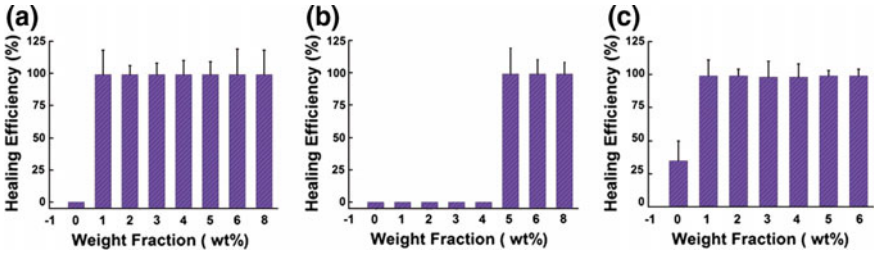

Fig. 5 The healing performances of the FG-TPU samples with different FG loadings under the three healing processes. **a** The IR light healing efficiencies. **b** The electrical healing efficiencies. **c** The electromagnetic wave healing efficiencies [65]. Copyright 2013. Reprinted with the permission from John Wiley and Sons

The above section showed the graphene-based PU composites showing excellent self-healing behavior. Similarly, other forms of graphene such as modified graphene (MG) and reduced graphene oxide (GO) have also been explored with polymers to obtain self-healing behavior.

Modified graphene (MG) has also similar self-healing properties, and hence, incorporating MG into PU leads to self-healing polymer composites. Chemically modified PU/MG nanocomposites have shown light-induced self-healing capability [66]. For quantitative healing test, the nanocomposite film was scratched to a depth of 50–60% or cut using a razor blade and healing was done by NIR absorption.

The healing efficiency was calculated using the modulus of toughness which is a measure of the strain energy required to break the material and corresponds to the area under the stress–strain curve [11, 67, 68]. The main contribution of MG was improving the NIR absorbance that increased the self-healing property of the PU/MG nanocomposite. And this effect is more pronounced on using MG075 (the sample with an optimized intermediate amount of MG added). However, at high MG content, interchain diffusion is disturbed which leads to the decrease of self-healing efficiency.

Similarly, reduced GO has also shown excellent sunlight-absorbing capacity like graphene and hence can be a self-healing material [69]. An elastomeric nanocomposite of hyperbranched polyurethane (HPU), iron oxide (IO) nanoparticles decorated reduced graphene oxide (RGO) nanohybrid has shown self-healing behavior [70]. IO nanoparticles are also known to possess good microwave-absorbing capacity and excellent thermal conductivity [71]. Hence, combining IO and RGO could enhance the self-healing effect in the polymer system. The nanocomposites were efficiently healed with 20–30 s of microwave power input (180–360 W) and by exposure to direct sunlight for 5–7.5 min, and the healing efficiency is demonstrated in Fig. 6 for both the stimuli [70].

Similarly, another nanocomposite of HPU with TiO_2 and RGO was synthesized which were effectively healed within 7.5–10 min under direct sunlight [72]. TiO_2 being a semiconductor photocatalyst, the TiO_2-RGO nanohybrid exhibited superior photocatalytic activity under visible light or sunlight [73]. TiO_2-RGO absorbed the solar energy, and with the help of this energy, the HPU matrix soft segment repairs the crack by molecular diffusion.

Therefore, graphene has been successfully used along with polyurethane to prepare self-healing composites that have shown nearly 100% healing efficiency. Graphene has become an efficient healable composite not only because of the intrinsic healing property but also because of the good dispersion, as well as the

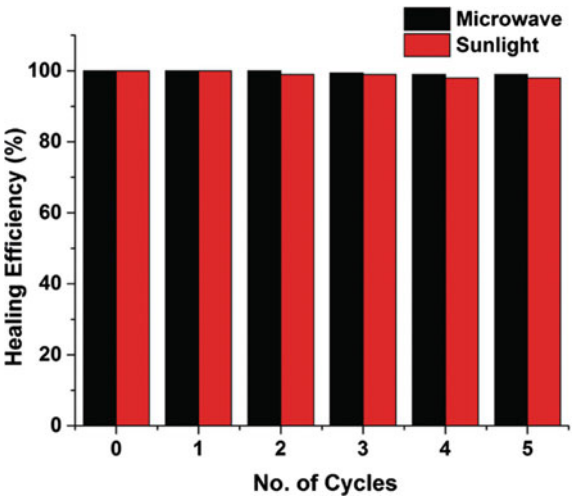

Fig. 6 Healing efficiency of HPU–IO–RGO (2 wt% of IO-RGO) nanocomposite for repeated cycles under MW (at 360 W) and sunlight stimuli [70]. Copyright 2015. Reprinted with the permission from Royal Society of Chemistry

effective interfacial interaction between the graphene and host PU polymer, which strengthens the polymer chains and is more resistant toward the external force [74].

PU is the widely used polymer in daily life. Therefore, the graphene-based self-healing PU composites have shown enhanced stability, flexibility, and lifetime and hence can be soon realized in practical appliances.

3.3 Epoxy–Graphene Healable Composites

The impressive mechanical, electrical, and thermal properties of epoxy make it suitable for various applications such as structural composites in aerospace and automobile, electrical and electronic laminates, and marine coating. The whole research world is searching for low-weight high-performance material particularly in automotive and aerospace sectors, and owing to this surge, the market demand of epoxy has taken an exponential increment and the global epoxy resin market is expected to reach USD 12.10 billion by 2022, according to the recent report by Grand View Research [75].

Although epoxy is a widely used polymer for various applications, it is vulnerable to damage. The high-end applications that are being envisioned today are in aerospace and automotives. Here, even a scratch can lead to damage. Hence, one important solution is to improve the crack resistance of the epoxy system by integrating the self-healing property in it. Various researchers have reported successful fabrication of self-healing epoxy composites with healing agents embedded inside the microcapsules [76, 77], but these systems lead to severe degradation of the mechanical strength of the system. Hence, for high-tech applications, no compromise can be made with the mechanical properties of the polymer. Therefore, intrinsic approach of self-healing is a more practical solution for crack-free epoxy systems.

Graphene is the most promising and most utilized reinforcing filler for imparting self-healing behavior and has already shown to be the successful self-healing imparting filler in PU-based systems. Therefore, graphene/epoxy composites are also the most ideal materials for self-healing analysis. A graphene-based epoxy composite using nanolayer graphene (NLG) was fabricated, and its self-healing behavior was tested using scratch test [78]. Addition of NLG (as shown in Fig. 7) in the epoxy system led to the improvement of fracture toughness of the system. G0, G1, and G2 were the samples with 0, 0.0025, and 0.0125 vol.% of NLG loaded in the epoxy, respectively. As very well demonstrated in Fig. 8, the unfilled epoxy (G0) developed many large cracks, whereas G1 showed no large cracks and G2 showed no visible cracks (neither large nor small).

The drastic enhancement in scratch resistance (thus the thermal healing capability) of the composites can be attributed to the exceptional in-plane fracture strength of the individual graphene sheets. The interlayer movements due to the NLG serve as a highly effective energy dissipation mechanism that reduces crack formation/propagation.

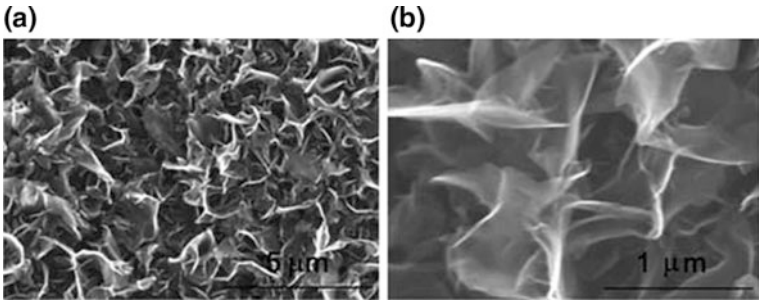

Fig. 7 SEM images of the NLG synthesized at different magnification [78]. Copyright 2010. Reprinted with the permission from the Royal Society of Chemistry

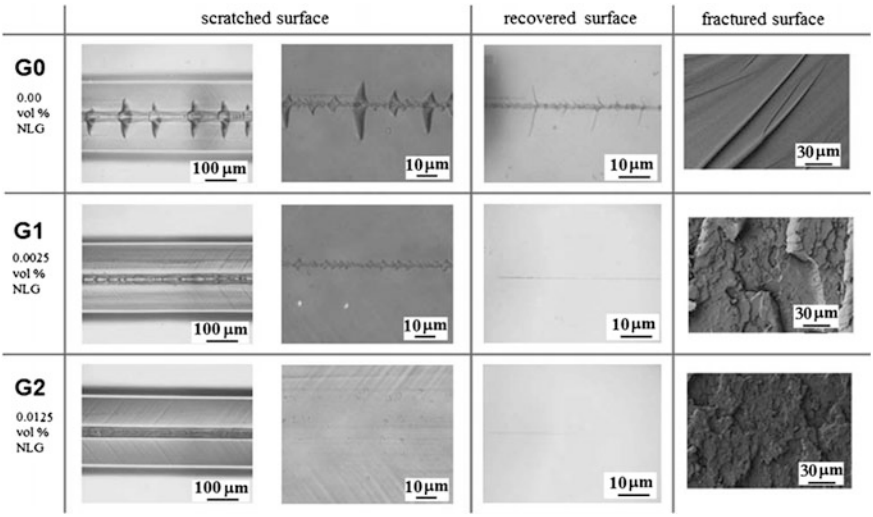

Fig. 8 The surface images of the as-scratched, recovered, and fractured polymer surfaces. The optical images in the *left two columns* represent samples after scratch testing. The optical images in the *third column* are the recovered samples after heating. The *fourth column* shows the SEM images of the fractured surfaces [78]. Copyright 2010. Reprinted with the permission from the Royal Society of Chemistry

Hence, graphene-based epoxy nanocomposites have shown immense crack resistance as analyzed from the above tests.

Graphene/epoxy nanocomposites have already shown advanced properties such as very high mechanical strength, improved electrical conductivity, and shielding effectiveness, and now, graphene has also imparted crack resistance leading to the fabrication of self-healing epoxy composites. Hence, from all these above findings, it can be concluded that graphene-based epoxy nanocomposites with intrinsic self-healing behavior can be realized in the near future which shall widen the

applications of epoxy and it can be used in various high-stress environments such as space missions and military applications.

3.4 Graphene-Based Healable Composites with Other Polymers

Apart from these well-known polymer systems such as PU and epoxy, graphene has also been utilized along with other polymer systems. An amine-terminated oligomer (HBN) incorporated with GO as both cross-linkers and fillers was developed as an efficient and rapid self-healing thermoreversible elastomer which self-healed without any external stimuli [79]. This healable elastomer can be used as a protecting barrier for electronic wires and devices, and when incorporated with additional electrical fillers, this elastomer can be a successful material for stretchable self-healing conducting wires.

Two common polymers poly(acrylamide) (PAM) and poly(acrylic acid) (PAA) were used to develop a graphene–poly(acrylamide-co-acrylic acid) hybrid material through hydrogen bonds [80]. The graphene-based composite showed impressive self-healing property with just 10% incorporated graphene. The cut samples healed in 20 min just by heating the sample to 37 °C. This property could be attributed to the enhanced π-interactions due to abundant π-electrons in graphene.

Multilayer polyelectrolyte film has also been explored to analyze self-healing behavior [81]. Polyelectrolyte film was incorporated with graphene to fabricate a hybrid using poly(acrylic acid) and branched poly(ethyleneimine) based on layer-by-layer self-assembly technique. This hybrid multilayer polyelectrolyte film shows impressive self-healing behavior as can be visualized in Fig. 9. The film was cut into a cross using a scalpel as in Fig. 9a which healed by injecting a drop of water on the cut surface. The process of the film rapidly absorbing water and swelling, and obvious healing process in 3 min are well demonstrated in Fig. 9.

Hence, various works have been reported on graphene-based polymer nanocomposites showing intrinsic self-healing behavior using various stimuli-like sunlight and heat energy.

3.5 Graphene-Based Healable Hydrogel Composites

Hydrogels are the most recent class of materials that are fabricated for specific end applications such as actuators, sustained drug release, biosensors, and drug delivery systems [82–84]. Hydrogels can be envisioned as a 3D network of polymer chains swollen with water. Silica, clay, and CNTs have already been used as nanofillers to improve the mechanical strength and toughness of the hydrogel. Graphene, having

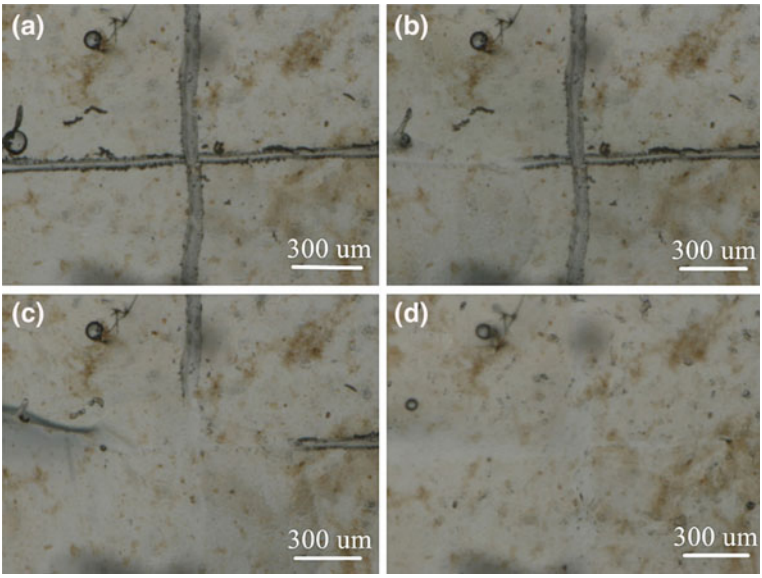

Fig. 9 Visual observation of the healing process of multilayer polyelectrolyte hybrid film using poly(acrylic acid), graphene, and branched poly(ethyleneimine) [81]. Copyright 2015. Reprinted with the permission from Elsevier

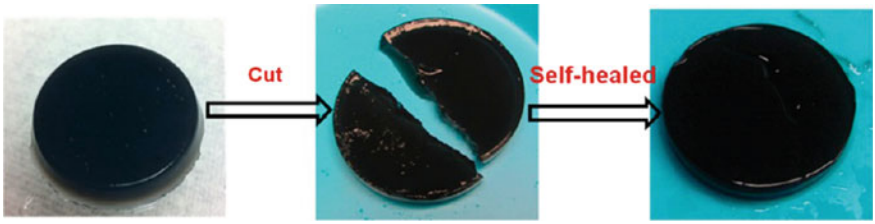

Fig. 10 Graphene-incorporated PAM hydrogel exhibiting self-healing property [85]. Copyright 2013. Reprinted with the permission from the American Chemical Society

inbuilt self-healing properties, can be used along with hydrogels to impart self-healing properties to the materials along with increasing the toughness of the hydrogel. Graphene was incorporated as a reinforcing filler in polyacrylamide (PAM) hydrogels that imparted successful self-healing properties as clearly demonstrated in Fig. 10 [85]. Similarly, a graphene–poly(*N*,*N*-dimethylacrylamide) (PDMAA) hydrogel that showed efficient near-infrared-triggered photothermal self-healing behavior due to the cross-linking structure was developed. This artificial self-healing material that is electroactive and bioapplicable can be used as an artificial tissue [86].

Graphene oxide (GO)-based hydrogels have shown impressive self-healing properties. Graphene oxide (GO)/poly(acryloyl-6-aminocaproic acid) (PAACA) composite hydrogels have shown interesting self-healing capability to pH stimulus [87]. Similarly, GO composite hydrogel fabricated by using graphene peroxide has shown 88% of mechanical healing efficiency [88]. GO was also utilized along with poly(*N*,*N*-dimethylacrylamide) (PDMAA) synthesizing a hybrid hydrogel [89] that showed fast self-healing by near-infrared (NIR) irradiation.

Graphene has been successfully tested as reinforcing filler imparting intrinsic self-healing property in polymer composites as well as in hydrogels as summarized in Table 1. Owing to the high thermal conductivity and appropriate availability of π-electrons along with the good-quality heat transfer ability, graphene has been reported to impart self-healing behavior. But at the same time, graphene has also shown to degrade the self-healing ability of the polymers. Incorporation of GO in PU composites has declined the healing efficiency of pristine PU composites developed by Diels–Alder technique [90]. Similarly, graphene oxide (GO)/polyacrylamide(PAM) composite hydrogels have lower healing efficiency as compared to the pure PAM hydrogels as GO confines the movability of the polymer chains [91]. Therefore, it cannot be taken for sure that graphene always significantly improves the healing capability. But it always depends on various factors such as (i) the matrix in which it is incorporated, (ii) the amount of graphene that is being incorporated, and (iii) the form of graphene being integrated into the polymer system. Apart from these, more intense work needs to be done on the synthesis of graphene-based polymer composites showing intrinsic self-healing behavior. Apart from graphene, various other forms of carbon can also be used to prepare nanocomposites with polymers, thereby producing self-healing materials. Among all the other carbon nanomaterials, CNTs are the superior nanofillers to modify the polymer materials due to extraordinary properties such as electrical conductivity, mechanical strength, and low density.

4 Carbon Nanotube-Based Self-healing Polymer Nanocomposites

CNTs have been the focus of material research since its discovery as they can impart high mechanical properties when used as a structural reinforcement and improve the electrical conductivity when used as fillers in polymers. These CNT-reinforced materials have wide applications in every sector. Apart from these mentioned applications, CNT has also been extensively studied to analyze the self-healing behavior of CNT-based polymer composites. Owing to its 1D tubular structure and high reinforcement qualities on one side and impressive thermal conductivity and heat transfer capability on the other side, CNT can be used in both extrinsic and intrinsic approaches of self-healing materials.

Table 5.1 Summary of various Graphene based self healing polymer composites

S. No.	Type of graphene	Type of polymer	Healing stimulus	Healing efficiency and mechanism	Remarks	Reference
1	Few layer graphene	Polyurethane	IR radiation electrical simulation Microwave radiations	Almost 98% Mechanical crack damage	Maximum repeatable healing efficiency obtained through IR radiation healing	(Huang, Yi et al. [65])
2	Modified graphene	Polyurethane	Near infra red radiation	Modulus of toughness, 40%	0.75 wt% MG (MG075) gave maximum healing efficiency up to 40%	(Kim, Kim et al. [66])
3	Reduced graphene oxide	Hyperbranched Polyurethane	Microwave power Direct sunlight	Almost 100%	Composite is also incorporated with iron oxide	(Thakur and Karak [72])
4	Reduced graphene oxide	Hyperbranched Polyurethane	Direct sunlight	–	Composite is also incorporated with TiO2	(Thakur and Karak [72])
5	Nanolayer graphene	Epoxy	Thermal healing	Scratch resistance is tested	Crack free epoxy polymer compsites	(Xiao, Xie et al. [78])
6	Graphene oxide	Amine terminated oligomer (HBN)	No external stimuli	60% of its original tensile strength	Protecting barrier for electronic wires and devices, sealing layer for gas systems	(Wang, Liu et al. [79])
7	Graphene	PAM and PAA	Thermal healing	Almost 100%	Above 10 wt% of graphene yields the self healing behavior	(Dong, Ding et al. [80])
8	Graphene	Polyelectrolyte film	Water enabled healing	–	Improved cyclic stability in battery, supercapacitor or hydrogen fuel cel	(Zhu, Yao et al. [81])

(continued)

Table 5.1 (continued)

S. No.	Type of graphene	Type of polymer	Healing stimulus	Healing efficiency and mechanism	Remarks	Reference
9	Graphene	Polyacrylamide hydrogel	Thermal healing	Crack is completely repaired	Actuators, biosensors, sustained drug-release	(Das, Irin et al. [85])
10	Graphene	Polydimethylacrylamide PDMAA hydrogel	Near infra red radiation	Repaired the damage in 2 hours	Promising artificial tissue material	(Hou, Duan et al. [86])
11	Graphene oxide	PAACA hydrogel	pH	Separated parts could be rejoined in acidic environment	Promising candidate for drug delivery, external coating	(Cong, Wang et al. [87]
12	Graphene oxide	Polyacrylamide (PAA)	No external stimulus	Mechanical efficiency: 88%	This tough self-healing hydrogel can be used in biomedical and engineering fileds	(Liu, Song et al. [88])
13	Graphene oxide	Polydimethylacrylamide (PDMAA) hydrogel	Near infra red radiation	96% of the original tensile strength	Self-healable surgical dressing,which can repair itself from physical damage is a potential application	(Zhang, Wang et al. [89]

4.1 CNTs in Extrinsic Self-healing Polymers

Extrinsic self-healing approach can be realized in two different ways: capsule-based and vascular-based. CNTs with its effective 1D nanotubular structure can be used as a nanoreservoir for the healing agent. Secondly, due to its structural enhancement property, it can be used as a healing agent along with other polymers in vascular-based self-healing. Thirdly, in microcapsule-based healable polymers, CNTs can be reinforced to regain the lost mechanical strength.

4.1.1 CNTs as Nanoreservoirs

Single-walled CNTs with its highly stable tube-like structure can be applied for microvascular self-healing approach in which SWCNTs can be used as nanoreservoirs of healing agents as shown briefly in Fig. 11 [92]. The detailed investigation of dynamics of fluid flow from the ruptured SWCNT upon damage where the fluid resembles a healing agent is done. The dynamics analysis concludes that the healing agent molecules and the catalytic trigger molecules chemically react to seal the crack. The use of SWCNTs as self-healing container provides mechanical reinforcement to the entire system. The following are the major factors which affect the amount of healing agent that needs to be stored in SWCNT reservoir for the efficient self-healing process:

(a) Diameter of the CNT being incorporated,
(b) Length of the CNT used,
(c) Type of the healing agent that is being used,
(d) The material that incorporates these healing agent-filled SWCNTs,
(e) Density of the CNTs in the hosting material and its distribution, and
(f) Orientation and the dispersion of the CNTs used.

While designing a practical CNT-based self-healing system, these factors will depend on the end applications of the material. Based on such theoretical

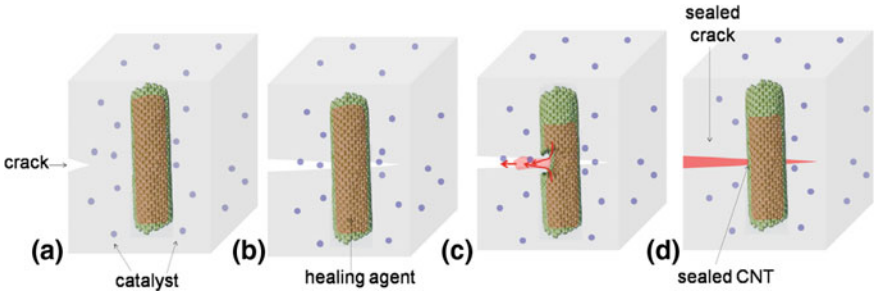

Fig. 11 Concept of the self-healing process using carbon nanotubes as nanoreservoirs [92]. Copyright 2009. Reprinted with the permission from IOP

investigations, encapsulation of the healing agents inside the CNTs is also being achieved practically. Liquid monomers used as healing agents were intercalated into the CNTs using the self-sustained diffusion technique [93]. Empty CNTs were first blended with a semisolid solution of the healing agent (dicyclopentadiene (DCPD) or isophorone diisocyanate) in benzene. Then, the solution was sonicated, and the benzene was evaporated out that resulted in the diffusion of the solutes into the CNTs. After the intercalation was over, fresh benzene was added and sonicated for 3–4 min to clean the outside of the CNTs. If such filling up of the CNTs with self-healing agents can be achieved practically in more convenient ways, then this can be the beginning of the production of smart composites with embedded self-healing agents on a mass scale.

4.1.2 CNTs as Reinforcing Filler in Capsule-Based Healable Polymers

Various capsule- and vascular-based self-healing polymer systems face three major limitations:

1. Degradation of the mechanical strength of the materials due to embedding of capsules and vascular.
2. Difficulty in embedding the capsules with healing agents inside the polymer systems.
3. Depletion of the healing agent after singular cracks.

CNTs are ideal as reinforcing conductive fillers due to their tremendous electrical conductivity and excellent mechanical properties as compared to pristine polymers.

Therefore, CNT reinforcement can gain back the strength lost due to capsule embedment. An electrically conducting self-healing epoxy-based coating reinforced with CNT fillers was developed in which the healing agent was microencapsulated within the polymer system [94, 95]. Although it is widely known that the use of microcapsules inside the polymer system degrades its mechanical strength, the degraded mechanical strength was regained by incorporating SWCNTs into the polymer system. Nanoindentation tests showed that elastic modulus and hardness of the samples were significantly improved by adding SWCNTs into the system. Hence, CNTs can easily enhance the physical properties of the composites that shall not only widen its applications but also help regain the lost mechanical properties due to capsule embedment.

4.1.3 CNTs as Efficient Healing Agents

Apart from capsule based mechanism, CNTs have also been used in vascular-based self-healing polymer systems as healing agents. A nanocomposite consisting of SWCNTs was prepared along with 5-ethylidene-2-norbornene (5E2N), reacted with

ruthenium Grubbs catalyst (RGC) [96] was injected inside the empty channels of the epoxy resin system to be used as healing agent. This is basically a kind of microvascular self-healing approach. In order to test the self-healing behavior, the damage in the form of an impact hole was created by dropping a mass. Then, the damaged sample was thermally healed by heating at 60 °C for 15 min, and the hole was filled by the 5E2N/SWCNT nanocomposite healing agent. Although mechanical healing efficiency was not quantifiably stated, the epoxy system regained its structure in 30 min. Similarly, in a capsule-based approach, 2.5% of CNT was mixed with ethyl phenylacetate (EPA) and used as a healing agent [94]. CNTs used along with the healing agents improve not only the mechanical healing efficiency but also electrical healing efficiency.

Hence, CNTs have been well explored in extrinsic self-healing materials in various methods. CNTs with its tubular structure can be used as a nanoreservoir of the healing agents, as a healing agent itself, and also in microcapsule-based healable polymers to regain the degraded mechanical properties. Apart from these studies, CNTs have also been used to prepare CNT-based polymer composites with intrinsic healing capability which is discussed in the following section.

4.2 CNTs in Intrinsic Self-healing Polymer Composites

CNTs are incorporated into the polymers to fabricate healable composites that can be used in various major applications which require enhanced crack resistance, longevity, and flexibility of the material. Some of the major applications are conductive healable polymers for new generation electronic skin to be used in robotics, shear stiffening (S-ST) materials for body armors, transparent electronics for smartwatches, supramolecular hydrogels for crack-free lenses and actuators, superhydrophobic surfaces for water proof electronics, syntactic foam structures for shock absorbing structures in military and submarines. All these various applications of CNT-based polymers with intrinsic healing capacity are discussed below.

4.2.1 Multifunctional Healable Conductive Polymer Composites

Multifunctional self-healing conductive materials can be effectively used in electric and electronic appliances to recover the conductivity of circuits, prevent fatal damage, and extend lifetime. Electrically conductive and healable materials are the class of functional materials that could be applied in many advanced electronics such as electronic skin and batteries and thereby improve the lifetime of these devices. CNTs have very high electrical conductivity and mechanical properties. Incorporation of CNTs into the elastomer system can create composites with good electrical conductivity, proximity sensitivity, humidity sensitivity, and intrinsic self-healing ability. A nanocomposite of poly(2-hydroxyethyl methacrylate) (PHEMA) and SWCNTs combined through host–guest interactions was prepared

that is found to be a conductive elastomer with autonomic healing ability [97]. Both electrical and mechanical healing efficiencies were calculated in the sample. The nanocomposite sample was connected in a circuit with a power source and LED lamp. The intensity of the light in the LED lamp varied with the amount of SWCNTs in the PHEMA–SWCNT composite (7 wt%). The LED went off immediately as the sample was cut into two pieces due to loss of connectivity. But the sample pieces when kept close to each other healed in 5 min under the ambient conditions and the LED lamp turned on again. The electrical healing efficiency was calculated for all the different kinds of samples, and it was nearly 95% with various amounts of SWCNTs. The mechanical healing efficiency increased with the increase in the mass fraction of SWCNTs. Hence, an electrically conducting and mechanically stronger elastomer was synthesized using SWCNTs that could be a potential material for building advanced sensing electronics. Another nanocomposite using hyperbranched poly(amido amine)s (HPAMAM) polymers layered with CNT films and rolled up in a sushi-like structure has also shown self-healing property with 100% recovery of electrical conductivity in nearly 18 min without any external stimuli as shown in Fig. 12 [98].

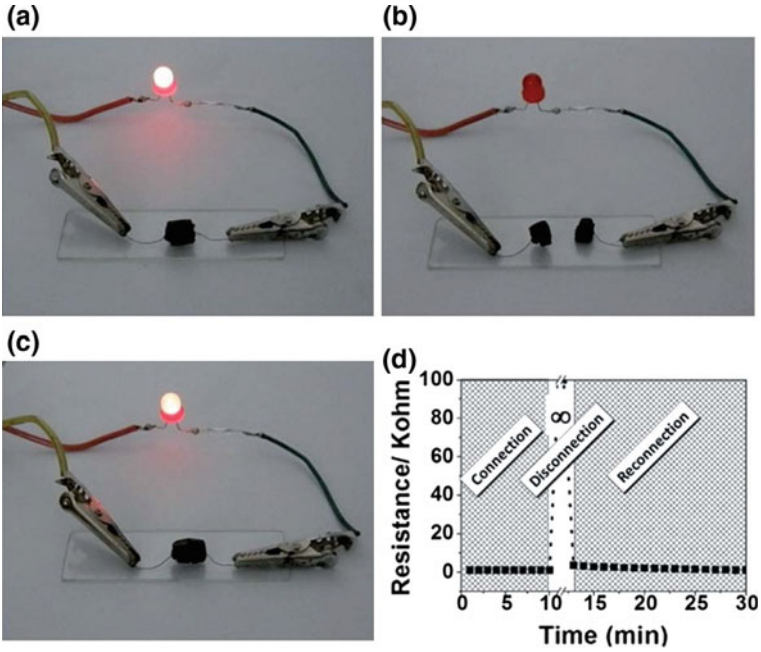

Fig. 12 **a** The light is on when the original sample was connected in circuit; **b** the light is off when being severed; **c** the light turned on again after recombined; **d** measured resistance before and after disconnection [98]. Copyright 2015. Reprinted with the permission from the Royal Society of Chemistry

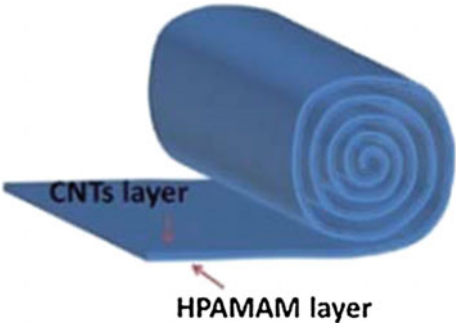

Fig. 13 Schematic structure of the sushi-like conductive HPAMAM/CNT composite disconnection [98]. Copyright 2015. Reprinted with the permission from the Royal Society of Chemistry

The self-healing conductive composite restored its structural integrity and conductivity due to the sushi-like assembly structure as shown in Fig. 13. The layers of CNT are spirally coiled, and hence, at the site of damage, the surfaces touch together and the conduction paths are reconnected.

The polymer matrix and the assembly structure are two very important factors to decide the healing capability of the multifunctional conductive CNT-based polymer composites. Further research can optimize the assembly structure and the polymer to synthesize the CNT-based healable smart materials for practical applications.

4.2.2 Shear Stiffening Self-healing Polymer Composites

Shear thickening (ST) material falls in the category of smart materials. The viscosity of these materials shows an interesting property that it sharply increases when the stress applied is more than the critical shear rate. S-ST polymer composites have recently become the major research area owing to their highly critical applications in military for body armors. The combination of S-ST with other functionalities together shall produce the most appropriate composites for high-performance body armors. MWCNTs, with excellent electrical conductivity, mechanical properties, and low density, are ideal nanofillers to reinforce the polymer materials. Owing to its better dispersity than SWCNTs, the MWCNTs can be easily mixed into the polymer matrix to form multifunctional nanocomposites. Several researchers have already reported on the improvement of the mechanical properties of the polymers by incorporating MWCNTs in them. The MWCNT-based S-ST polymer composite may be an interesting body armor material that can show high protective performance and compression rate-dependent conductivity. A MWCNT/S-ST polymer composite based on a derivative of polyborondimethylsiloxane (PBDMS) has shown impressive electrical self-healing capability [99]. An LED bulb was connected in a circuit using the MWCNT/S-ST-polymer composite on the other side. The LED shined with a power source of 9 V and suddenly extinguished when the composite was broken into two pieces. The broken pieces rejoined when brought in contact and the LED shone brightly again. This shows the self-healing property of the material and negligible

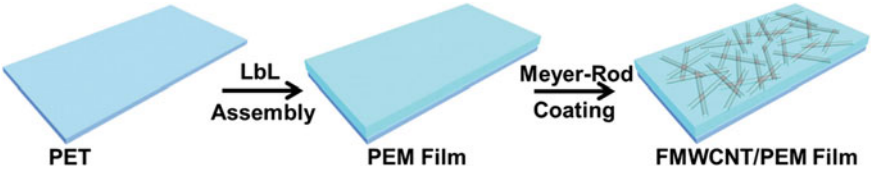

Fig. 14 Schematic illustration of the fabrication of CNT network-coated LbL-assembled transparent healable PEM films [100]. Copyright 2015. Reprinted with the permission from John Wiley and Sons

loss of conductivity of the healed specimen. Hence, the MWCNT/S-ST polymer composite exhibits impressive self-healing at room temperature.

4.2.3 Damage-Free Transparent Electronics

Self-healing concept has been a hot topic not only in body armors and protective coverings, but also in transparent electronics. The transparent electronic devices like transparent displays, touch screens, ultrasensitive sensors, and supercapacitors are incorporated with a self-healing coating that makes them highly resistant to mechanical degradations like fracture due to bending or mechanical degradation of the device over time. Ultimately this can help in reducing the consumption of raw materials and lead to sharp decrease in the electronic waste. Healable transparent chemical gas sensor device can be integrated into optoelectronic devices, such as transparent displays, touch screens, smart windows, and portable watches that can sense the chemical vapor analytes in room temperature operations. Polyelectrolyte multilayer (PEM) films could be the potential substrate for transparent chemical gas sensor device. A healable transparent chemical gas sensor device consisting of PEM with transparent CNT networks assembled from layer-by-layer method was developed as shown in Fig. 14 [100]. The as-produced material demonstrates impressive chemical sensing capability, vigorous healability, flexibility due to the 1D confined network structure, higher carrier mobility, and huge surface-to-volume ratio of the tubular structure of CNTs.

It is difficult to disperse the CNTs into a polymer matrix due to strong van der Waal force in CNTs, due to which they agglomerate. For the efficient reinforcement of the CNTs in the polymer, it is necessary to incorporate surface interactions between the CNTs and the polymer matrix. Then, the load can be efficiently transferred from the matrix to the CNTs. Intense studies on reinforcement have concluded that the chemically modified CNTs have shown better dispersion in the polymer matrix, and hence, it shall help to improve the physical properties of the nanocomposites [101]. Hence, MWCNTs attached with functional groups were used along with PEM to fabricate the FMWCNT/PEM films. A cut was created on the FMWCNT/PEM film which completely healed by dropping deionized water as illustrated in Fig. 15.

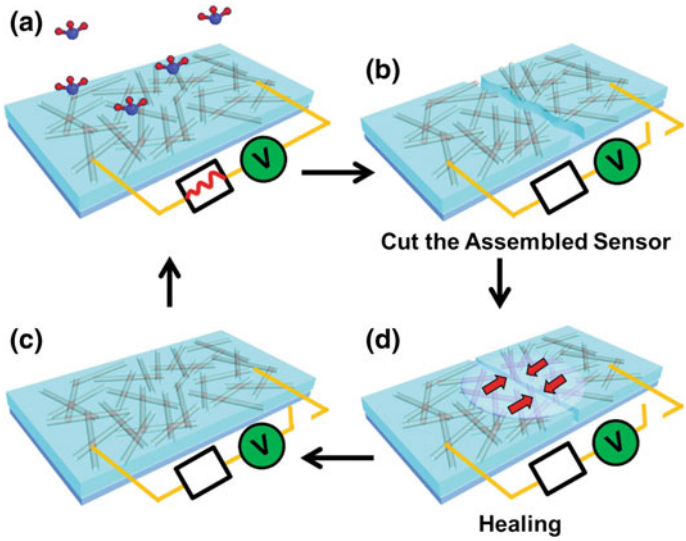

Fig. 15 Illustration of the fabrication of a healable transparent chemical gas sensor device assembled from CNT network-coated transparent healable PEM films. **a** The effective sensing from the assembled healable transparent chemical gas sensor; **b** cut the assembled sensor; **c** water-enabled healing; and **d** after healing [100]. Copyright 2015. Reprinted with the permission from John Wiley and Sons

Therefore, CNT-based PEM films show healability and therefore soon can be implemented in practical devices such as touch screens and damage-free electronics.

4.2.4 Supramolecular Healable Hydrogels

Hydrogels are a specialized class of polymers that have recently become a very attractive research topic due to its wide range of applications from biology to sensors and contact lenses. A supramolecular system consists of two or more molecular bodies held together by means of intermolecular non-covalent binding interactions [102]. Supramolecular hydrogels with healing capability have wide applications such as contact lenses, sensors, actuators, and various biomaterials. A healable supramolecular hydrogel/CNT hybrid is prepared by adding polyethylene polyamine (PPA) into oxidized CNTs aqueous [103]. The oxidized CNTs and PPA molecules develop strong hydrogen bonds from the interactions and show impressive self-healing ability even without any external stimuli due to these hydrogen bonds. The hybrid hydrogel healed within 2 min without any external stimuli. This successfully proved the instantaneous self-healing in the material. The detailed rheological test done to study the self-healing behavior also showed that when a deformation shear stress of 200 Pa was applied to the material through

continuous deformations and recovery cycles, the shear modulus of the hydrogel could be efficiently restored to 90% of its initial value in 90 s. And with extremely large stress of about 800 Pa, most of the mechanical properties could be recovered in extended time duration (35 min) to 80%. These PPA/CNT hydrogels maintained its self-repairing property even after being dried. Therefore, as-prepared physically cross-linked self-healing PPA/CNT hydrogels could be used as a kind of temperature-dependent, removable, and low-cost adhesives and have immense applications in sensors, biomaterials, and actuators. And like graphene, CNTs can also be used to prepare healable hydrogels for various applications.

4.2.5 Healable Superhydrophobic Surfaces

As technology and electronics have become more integrated with life, the need for protecting the electronic items from liquid hazards has become necessary. Therefore, the superhydrophobic coatings have become a focus of modern-day materials research. Surfaces with high water contact angle (CA ≥ 150°) and low sliding angle (SA) are called superhydrophobic surfaces. A superhydrophobic surface with self-healing properties can be prepared by combining organosilanes and MWCNTs by a spray-coating approach [104]. The polysiloxane/MWCNT nanocomposites produced by hydrolytic condensation were thoroughly tested for self-healing properties. Damage was created by water jetting and sand abrasion, and healing was done by cleaning the damaged surface by nitrogen flow and spray-coating with toluene and then drying. After repeated abrasion and healing cycles, the CA was stable, but the SA rose up to 10–13°. The sample was then soaked in toluene and then cured at 240 °C for 10 min to regain the original SA. The actual mechanism behind toluene directed healing is that by spraying toluene on the damaged surface the hydrophobic free polysiloxane remaining within the coating gets dissolved and the polysiloxane-modified MWCNTs were exposed to the solid/vapor surface. As a result, the damaged flattened polysiloxane/MWCNTs surface renovated its microstructure. Therefore, these durable, stable, and healable superhydrophobic surfaces using CNT-based polymer composites could be used in many areas such as maritime industries, vehicle windshields, and critical electronics as it shall be stable toward corrosive liquids, organic solvents, and UV irradiation also.

4.2.6 Self-healing Syntactic Foam

Syntactic foam is another class of structural materials in which microballoons are dispersed into a polymeric or metallic matrix. Recently, they are growing exponentially in composite sandwich structure studies and are basically used in submarines as thermoinsulation materials. Syntactic foams have wide applications in civil and military sectors. Syntactic foam based on CNTs can be fabricated by dispersing glass microballoons and MWCNTs into a shape memory polymer matrix

Table 5.2 Summary of various CNT based self healing polymer composites

S. No.	Type of carbon nanotube	Type of polymer	Type of healing approach	Healing mechanism	Applications	References
1	SWCNTs	Poly(2-hydroxyethyl methacrylate) (PHEMA)	Intrinsic	95% efficiency without any external stimulus	Multifunctional healable conducting polymers	(Guo, Zhang et al. [97])
2	CNT films	Hyperbranched poly(amido amines) (HPAMAM)	Intrinsic	100% electrical efficiency without any external stimulus	Self-healing conductive materials	(Yang, Song et al. [98])
3	MWCNTs	Polyborondimethylsiloxane (PBDMS)	Intrinsic	Almost 100% electrical & mechanical healing	Shear stiffening (S-ST) composites for body armor	(Wang, Xuan et al. [99])
4	Functionalized MWCNT networks	Polyectrolyte multilayer	Intrinsic	Water enabled healing	Healable chemical gas sensor to be used in portable watches and electronics	(Bai, Sun et al. [100])
5	Oxidized MWCNTs	Polyethylene polyamine	Intrinsic	90% efficiency without any external stimuli	Supramolecular hydrogel for contact lenses, sensors	(Du, Wu et al. [103])
6	MWCNTs	Polysiloxane	Intrinsic	Damage was healed by spraying toluene in N_2 environment	Healable superhydrophobic surfaces for electronics, windshields	(Li and Zhang [104])
7	MWCNTs	Polystyrene	Intrinsic	Almost 100% healable by thermal stimulus	Smart syntactic foam for thermo insulations in submarines and aircrafts	(Li and John [105])
8	–	Epoxy	Extrinsic	CNTs were used as healing agents and as reinforcing fillers, 81% healing efficiency	Electrically conducting healable coatings in microelectronics	(Bailey, Leterrier et al. [94])
9	SWCNTs	Epoxy	Extrinsic	CNTs used to reinforce the structure	Healable epoxy for automotive, aerospace and shipbuilding	(Ahangari and Fereidoon [95])
10	SWCNTs	Epoxy	Extrinsic	CNTs used as healing agent along with 5E2N could heal impact hole	Self-repair functionality in space environment	(Aissa, Haddad et al. [96])

[105]. Not only the incorporation of MWCNTs increased the mechanical properties, but also due to its good conductivity, it can serve as a medium for heating and triggering self-healing from stimuli-like IR radiation or electricity. Self-healing analysis shows that the impact damage was healable even after multiple damages. The residual strength and the tolerance to damage are recovered after healing the composites. In fact, after the 7th impact and healing cycle (heating at 100 °C for 3 h), the residual strength was more than the original yield strength.

Therefore, CNTs have been widely studied in self-healing polymer systems. For extrinsic self-healing materials, CNT has been visualized as a nanoreservoir of healing agent for a self-healing polymer system. In fact, practically successful intercalation of the healing agent inside the CNTs has been reported. CNTs have also been used as a healing agent itself and also as structural reinforcing fillers in capsule-based healable systems. As far as extrinsic approach is concerned, more detailed characterization has to be done to analyze the amount of healing agent inside the CNT and then practically visualize the crack healing process. Intrinsic self-healing behavior has also been realized by incorporating CNTs along with various kinds of polymers which has resulted in the fabrication of specific multi-functional smart materials for high-end applications. CNTs need to be vigorously tested in various other polymer systems to practically realize CNT-based intrinsic self-healing polymer composites. Hence, like graphene, CNTs also have equal contribution for imparting self-healing behavior in polymers.

CNTs have been found as a promising future self-healing material, and its contribution has been summarized in Table 2.

5 Conclusion and Future Scope

In this age of plastics and indispensible flexible electronics, the society is waiting for crack- and damage-free materials. Practically, industry-scale fabrication of self-healing materials shall take the technology era to a different advanced age, and especially, aerospace and military sector will be completely reformed. This shall enhance the lifetime of all the man-made materials and also reduce the maintenance cost and increase the flexibility. Incorporation of graphene and CNTs into the polymer systems has led to the production of healable composites with enhanced healing efficiency. Although graphene seems like a promising self-healing material, incorporating graphene in all the polymer systems is still a big challenge. Restacking of the graphene is a major limitation for production of graphene-based polymer composites at an industry scale. Similarly, CNT has very good conductivity and healing properties, but CNT shows agglomeration effect when mixed with the polymers. Therefore, both graphene and CNTs face major limitation while synthesizing polymer nanocomposites using various techniques. However, a hybrid of CNT and graphene can possibly solve these issues: graphene with better dispersibility than CNTs can help decrease the agglomeration effect, and CNTs with flexible, resilient tubular structure can help diminish the restacking effect of

graphene. Therefore, a hybrid of CNT and graphene incorporated into the polymer can have higher healing efficiency and healable by multiple stimuli such as IR, thermal, microwave, electrical, and pH. The effect of both CNTs and graphene in a polymer composite was analyzed for enhancing the intrinsic self-healing behavior. An amino acid-based hydrogel was incorporated with SWCNTs, graphene, and both pristine SWCNTs and graphene. The resulting hybrid hydrogel showed enhanced self-healing properties which can be attributed to the π–π interfacial interactions between the gelator and the graphene and/or Pr SWCNTs [106]. In another extrinsic approach, the use of CNT as a nanoreservoir should be applied practically and detailed self-healing tests should be conducted. Self-healing is still no more than an illusion, but we are not much far from the day when man-made materials can restore their structural integrity in case of a failure.

References

1. Malinskii YM, Prokopenko V, Ivanova N, Kargin V (1970) Investigation of self-healing of cracks in polymers. Polym Mech 6(2):240–244
2. Wool RP (1980) Crack healing in semicrystalline polymers, block copolymers and filled elastomers. In: Adhesion and adsorption of polymers. Springer, Berlin, pp 341–362
3. Wool R, O'connor K (1981) A theory crack healing in polymers. J Appl Phys 52(10):5953–5963
4. Dry C (1994) Matrix cracking repair and filling using active and passive modes for smart timed release of chemicals from fibers into cement matrices. Smart Mater Struct 3(2):118
5. White SR, Sottos N, Geubelle P, Moore J, Kessler MR, Sriram S, Brown E, Viswanathan S (2001) Autonomic healing of polymer composites. Nature 409(6822):794–797
6. Kessler M (2007) Self-healing: a new paradigm in materials design, proceedings of the institution of mechanical engineers. Part G. J Aerosp Eng 221(4):479–495
7. Blaiszik B, Kramer S, Olugebefola S, Moore JS, Sottos NR, White SR (2010) Self-healing polymers and composites. Annu Rev Mater Res 40:179–211
8. Yuan Y, Yin T, Rong M, Zhang M (2008) Self healing in polymers and polymer composites. Concepts, realization and outlook: a review. Polym Lett 2(4):238–250
9. Wang Z, Yang Y, Burtovyy R, Luzinov I, Urban MW (2014) UV-induced self-repairing polydimethylsiloxane–polyurethane (PDMS–PUR) and polyethylene glycol–polyurethane (PEG–PUR) Cu-catalyzed networks. J Mater Chem A 2(37):15527–15534
10. Ling J, Rong MZ, Zhang MQ (2012) Photo-stimulated self-healing polyurethane containing dihydroxyl coumarin derivatives. Polymer 53(13):2691–2698
11. Burnworth M, Tang L, Kumpfer JR, Duncan AJ, Beyer FL, Fiore GL, Rowan SJ, Weder C (2011) Optically healable supramolecular polymers. Nature 472(7343):334–337
12. Tee BC, Wang C, Allen R, Bao Z (2012) An electrically and mechanically self-healing composite with pressure-and flexion-sensitive properties for electronic skin applications. Nat Nanotechnol 7(12):825–832
13. Herbst F, Döhler D, Michael P, Binder WH (2013) Self-healing polymers via supramolecular forces. Macromol Rapid Commun 34(3):203–220
14. Bergman SD, Wudl F (2008) Mendable polymers. J Mater Chem 18(1):41–62
15. Fall RA (2001) Puncture reversal of polyethylene ionomers-mechanistic studies
16. Huber A, Hinkley JA (2005) Impression testing of self-healing polymers. NASA Tech Man 213532

17. Thostenson ET, Ren Z, Chou T-W (2001) Advances in the science and technology of carbon nanotubes and their composites: a review. Compos Sci Technol 61(13):1899–1912
18. Baughman RH, Zakhidov AA, de Heer WA (2002) Carbon nanotubes—the route toward applications. Science 297(5582):787–792
19. Iijima S (1991) Helical microtubules of graphitic carbon. Nature 354(6348):56–58
20. Prasek J, Drbohlavova J, Chomoucka J, Hubalek J, Jasek O, Adam V, Kizek R (2011) Methods for carbon nanotubes synthesis—review. J Mater Chem 21(40):15872–15884
21. Graham AP, Duesberg GS, Hoenlein W, Kreupl F, Liebau M, Martin R, Rajasekharan B, Pamler W, Seidel R, Steinhoegl W, Unger E (2005) How do carbon nanotubes fit into the semiconductor roadmap? Appl Phys A 80(6):1141–1151
22. Lee G-H, Cooper RC, An SJ, Lee S, van der Zande A, Petrone N, Hammerberg AG, Lee C, Crawford B, Oliver W, Kysar JW, Hone J (2013) High-strength chemical-vapor—deposited graphene and grain boundaries. Science 340(6136):1073–1076
23. Gómez-Navarro C, Burghard M, Kern K (2008) Elastic properties of chemically derived single graphene sheets. Nano Lett 8(7):2045–2049
24. Gupta TK, Singh BP, Dhakate SR, Singh VN, Mathur RB (2013) Improved nanoindentation and microwave shielding properties of modified MWCNT reinforced polyurethane composites. J Mater Chem A 1(32):9138–9149
25. Farukh M, Dhawan R, Singh BP, Dhawan S (2015) Sandwich composites of polyurethane reinforced with poly(3,4-ethylene dioxythiophene)-coated multiwalled carbon nanotubes with exceptional electromagnetic interference shielding properties. RSC Adv 5(92):75229–75238
26. Verma M, Verma P, Dhawan S, Choudhary V (2015) Tailored graphene based polyurethane composites for efficient electrostatic dissipation and electromagnetic interference shielding applications. RSC Adv 5(118):97349–97358
27. Mathur R, Pande S, Singh B, Dhami T (2008) Electrical and mechanical properties of multi-walled carbon nanotubes reinforced PMMA and PS composites. Polym Compos 29 (7):717–727
28. Saini P, Choudhary V, Singh B, Mathur R, Dhawan S (2011) Enhanced microwave absorption behavior of polyaniline-CNT/polystyrene blend in 12.4–18.0 GHz range. Synth Met 161(15):1522–1526
29. Shahzad F, Yu S, Kumar P, Lee J-W, Kim Y-H, Hong SM, Koo CM (2015) Sulfur doped graphene/polystyrene nanocomposites for electromagnetic interference shielding. Compos Struct 133:1267–1275
30. Han Y, Wang T, Gao X, Li T, Zhang Q (2016) Preparation of thermally reduced graphene oxide and the influence of its reduction temperature on the thermal, mechanical, flame retardant performances of PS nanocomposites. Compos A Appl Sci Manuf 84:336–343
31. Babal A, Gupta R, Singh B, Singh V, Mathur R, Dhakate S (2014) Mechanical and electrical properties of high performance MWCNT/polycarbonate composites prepared by industrial viable twin screw extruder with back flow channel. RSC Adv 4:64649–64658
32. Jindal P, Pande S, Sharma P, Mangla V, Chaudhury A, Patel D, Singh BP, Mathur RB, Goyal M (2013) High strain rate behavior of multi-walled carbon nanotubes-polycarbonate composites. Compos B Eng 45(1):417–422
33. Pande S, Singh BP, Mathur RB (2014) Processing and properties of carbon nanotube/polycarbonate composites, polymer nanotube nanocomposites: synthesis, properties, and applications, 2nd ed. Wiley, New Jersey, pp 333–364
34. Gedler G, Antunes M, Velasco J, Ozisik R (2016) Enhanced electromagnetic interference shielding effectiveness of polycarbonate/graphene nanocomposites foamed via 1-step supercritical carbon dioxide process. Mater Des 90:906–914
35. Shen B, Zhai W, Tao M, Lu D, Zheng W (2013) Enhanced interfacial interaction between polycarbonate and thermally reduced graphene induced by melt blending. Compos Sci Technol 86:109–116

36. Jyoti J, Basu S, Singh B, Dhakate S (2015) Superior mechanical and electrical properties of multiwall carbon nanotube reinforced acrylonitrile butadiene styrene high performance composites. Compos B Eng 83:58–65
37. Gao C, Zhang S, Wang F, Wen B, Han C, Ding Y, Yang M (2014) Graphene networks with low percolation threshold in ABS nanocomposites: selective localization and electrical and rheological properties. ACS Appl Mater Interfaces 6(15):12252–12260
38. Sharma S, Gupta V, Tandon R, Sachdev V (2016) Synergic effect of graphene and MWCNT fillers on electromagnetic shielding properties of graphene–MWCNT/ABS nanocomposites. RSC Adv 6(22):18257–18265
39. Pande S, Singh B, Mathur R, Dhami T, Saini P, Dhawan S (2009) Improved electromagnetic interference shielding properties of MWCNT–PMMA composites using layered structures. Nanoscale Res Lett 4(4):327–334
40. Li X, McKenna GB, Miquelard-Garnier G, Guinault A, Sollogoub C, Regnier G, Rozanski A (2014) Forced assembly by multilayer coextrusion to create oriented graphene reinforced polymer nanocomposites. Polymer 55(1):248–257
41. Zeng X, Yang J, Yuan W (2012) Preparation of a poly(methyl methacrylate)-reduced graphene oxide composite with enhanced properties by a solution blending method. Eur Polym J 48(10):1674–1682
42. Singh BP, Saini P, Gupta TK, Garg P, Kumar G, Pande I, Pande S, Seth RK, Dhawan SK, Mathur RB (2011) Designing of multiwalled carbon nanotubes reinforced low density polyethylene nanocomposites for suppression of electromagnetic radiation. J Nanopart Res 13(12):7065–7074
43. Fim FC, Basso NR, Graebin AP, Azambuja DS, Galland GB (2013) Thermal, electrical, and mechanical properties of polyethylene–graphene nanocomposites obtained by in situ polymerization. J Appl Polym Sci 128(5):2630–2637
44. Rajput S, Singh BP, Jyoti J, Dhakate SR (2015) Utilization of polymer wastes using multiwalled carbon nanotubes as a reinforcing filler to make strong value added products. Mater Focus 4(3):213–218
45. Garg P, Singh BP, Kumar G, Gupta T, Pandey I, Seth R, Tandon R, Mathur RB (2010) Effect of dispersion conditions on the mechanical properties of multi-walled carbon nanotubes based epoxy resin composites. J Polym Res 18(6):1397–1407
46. Singh BP, Saini K, Choudhary V, Teotia S, Pande S, Saini P, Mathur RB (2014) Effect of length of carbon nanotubes on electromagnetic interference shielding and mechanical properties of their reinforced epoxy composites. J Nanopart Res 16(1):1–11
47. Tang L-C, Wan Y-J, Yan D, Pei Y-B, Zhao L, Li Y-B, Wu L-B, Jiang J-X, Lai G-Q (2013) The effect of graphene dispersion on the mechanical properties of graphene/epoxy composites. Carbon 60:16–27
48. Park YT, Qian Y, Chan C, Suh T, Nejhad MG, Macosko CW, Stein A (2015) Epoxy toughening with low graphene loading. Adv Funct Mater 25(4):575–585
49. Mathur RB, Singh BP, Dhami T, Kalra Y, Lal N, Rao R, Rao AM (2010) Influence of carbon nanotube dispersion on the mechanical properties of phenolic resin composites. Polym Compos 31(2):321–327
50. Teotia S, Singh BP, Elizabeth I, Singh VN, Ravikumar R, Singh AP, Gopukumar S, Dhawan S, Srivastava A, Mathur R (2014) Multifunctional, robust, light-weight, free-standing MWCNT/phenolic composite paper as anodes for lithium ion batteries and EMI shielding material. RSC Adv 4(63):33168–33174
51. Liu Y-Z, Li Y-F, Yang Y-G, Wen Y-F, Wang M-Z (2013) Preparation and properties of graphene oxide–carbon fiber/phenolic resin composites. Carbon 52:624
52. Özçelik VO, Gurel HH, Ciraci S (2013) Self-healing of vacancy defects in single-layer graphene and silicene. Phys Rev B 88(4):045440
53. Botari T, Paupitz R, da Silva Autreto PA, Galvao DS (2016) Graphene healing mechanisms: a theoretical investigation. Carbon 99:302–309

54. Bangert U, Zan R, Ramasse Q, Novoselov K (2012) Graphene re-knits its holes. Nano Letters 12(8):3936–3940
55. Zan R, Ramasse QM, Bangert U, Novoselov KS (2012) Graphene reknits its holes. Nano Lett 12(8):3936–3940
56. Zhu J, Shi D (2013) A possible self-healing mechanism in damaged graphene by heat treatment. Comput Mater Sci 68:391–395
57. Xu Z-C, Zhong W-R (2014) Probability of self-healing in damaged graphene bombarded by fullerene. Appl Phys Lett 104(26):261907
58. Galpaya D, Wang M, Liu M, Motta N, Waclawik E, Yan C (2012) Recent advances in fabrication and characterization of graphene-polymer nanocomposites. Graphene 1(2). doi:10.4236/graphene.2012.12005
59. Balandin AA, Ghosh S, Bao W, Calizo I, Teweldebrhan D, Miao F, Lau CN (2008) Superior thermal conductivity of single-layer graphene. Nano Lett 8(3):902–907
60. Liang J, Xu Y, Huang Y, Zhang L, Wang Y, Ma Y, Li F, Guo T, Chen Y (2009) Infrared-triggered actuators from graphene-based nanocomposites. J Phys Chem C 113 (22):9921–9927
61. He Q, Wu S, Yin Z, Zhang H (2012) Graphene-based electronic sensors. Chem Sci 3 (6):1764–1772
62. Sun X, Liu Z, Welsher K, Robinson JT, Goodwin A, Zaric S, Dai H (2008) Nano-graphene oxide for cellular imaging and drug delivery. Nano Res 1(3):203–212
63. Fan Y, Yang H, Li M, Zou G (2009) Evaluation of the microwave absorption property of flake graphite. Mater Chem Phys 115(2):696–698
64. Huang X, Zeng Z, Fan Z, Liu J, Zhang H (2012) Graphene-based electrodes. Adv Mater 24 (45):5979–6004
65. Huang L, Yi N, Wu Y, Zhang Y, Zhang Q, Huang Y, Ma Y, Chen Y (2013) Multichannel and repeatable self-healing of mechanical enhanced graphene-thermoplastic polyurethane composites. Adv Mater 25(15):2224–2228
66. Kim JT, Kim BK, Kim EY, Kwon SH, Jeong HM (2013) Synthesis and properties of near IR induced self-healable polyurethane/graphene nanocomposites. Eur Polym J 49(12):3889–3896
67. Burattini S, Greenland BW, Merino DH, Weng W, Seppala J, Colquhoun HM, Hayes W, Mackay ME, Hamley IW, Rowan SJ (2010) A healable supramolecular polymer blend based on aromatic π–π stacking and hydrogen-bonding interactions. J Am Chem Soc 132 (34):12051–12058
68. Jastrzebski ZD (1977) The nature and properties of engineering materials. Wiley, New Jersey
69. Bernardi M, Palummo M, Grossman JC (2013) Extraordinary sunlight absorption and one nanometer thick photovoltaics using two-dimensional monolayer materials. Nano Lett 13 (8):3664–3670
70. Thakur S, Karak N (2015) A tough, smart elastomeric bio-based hyperbranched polyurethane nanocomposite. New J Chem 39(3):2146–2154
71. Chen Y, Gao P, Zhu C, Wang R, Wang L, Cao M, Fang X (2009) Synthesis, magnetic and electromagnetic wave absorption properties of porous Fe_3O_4/Fe/SiO_2 core/shell nanorods. J Appl Phys 106(5):054303
72. Thakur S, Karak N (2015) Tuning of sunlight-induced self-cleaning and self-healing attributes of an elastomeric nanocomposite by judicious compositional variation of the TiO_2–reduced graphene oxide nanohybrid. J Mater Chem A 3(23):12334–12342
73. Akhavan O, Abdolahad M, Esfandiar A, Mohatashamifar M (2010) Photodegradation of graphene oxide sheets by TiO_2 nanoparticles after a photocatalytic reduction. J Phys Chem C 114(30):12955–12959
74. Huang X, Yin Z, Wu S, Qi X, He Q, Zhang Q, Yan Q, Boey F, Zhang H (2011) Graphene-based materials: synthesis, characterization, properties, and applications. Small 7 (14):1876–1902
75. http://www.grandviewresearch.com/press-release/global-epoxy-resins-market (2015)

76. Yin T, Rong MZ, Zhang MQ, Yang GC (2007) Self-healing epoxy composites—preparation and effect of the healant consisting of microencapsulated epoxy and latent curing agent. Compos Sci Technol 67(2):201–212
77. Xiao DS, Yuan YC, Rong MZ, Zhang MQ (2009) Self-healing epoxy based on cationic chain polymerization. Polymer 50(13):2967–2975
78. Xiao X, Xie T, Cheng Y-T (2010) Self-healable graphene polymer composites. J Mater Chem 20(17):3508–3514
79. Wang C, Liu N, Allen R, Tok JBH, Wu Y, Zhang F, Chen Y, Bao Z (2013) A rapid and efficient self-healing thermo-reversible elastomer crosslinked with graphene oxide. Adv Mater 25(40):5785–5790
80. Dong J, Ding J, Weng J, Dai L (2013) Graphene enhances the shape memory of poly (acrylamide-co-acrylic acid) grafted on graphene. Macromol Rapid Commun 34(8):659–664
81. Zhu Y, Yao C, Ren J, Liu C, Ge L (2015) Graphene improved electrochemical property in self-healing multilayer polyelectrolyte film. Colloids Surf A 465:26–31
82. Peppas NA, Hilt JZ, Khademhosseini A, Langer R (2006) Hydrogels in biology and medicine: from molecular principles to bionanotechnology. Adv Mater 18(11):1345–1360
83. Qiu Y, Park K (2012) Environment-sensitive hydrogels for drug delivery. Adv Drug Deliv Rev 64:49–60
84. Satarkar NS, Biswal D, Hilt JZ (2010) Hydrogel nanocomposites: a review of applications as remote controlled biomaterials. Soft Matter 6(11):2364–2371
85. Das S, Irin F, Ma L, Bhattacharia SK, Hedden RC, Green MJ (2013) Rheology and morphology of pristine graphene/polyacrylamide gels. ACS Appl Mater Interf 5(17):8633–8640
86. Hou C, Duan Y, Zhang Q, Wang H, Li Y (2012) Bio-applicable and electroactive near-infrared laser-triggered self-healing hydrogels based on graphene networks. J Mater Chem 22(30):14991–14996
87. Cong H-P, Wang P, Yu S-H (2013) Stretchable and self-healing graphene oxide–polymer composite hydrogels: a dual-network design. Chem Mater 25(16):3357–3362
88. Liu J, Song G, He C, Wang H (2013) Self-healing in tough graphene oxide composite hydrogels. Macromol Rapid Commun 34(12):1002–1007
89. Zhang E, Wang T, Zhao L, Sun W, Liu X, Tong Z (2014) Fast self-healing of graphene oxide-hectorite clay-poly(N,N-dimethylacrylamide) hybrid hydrogels realized by near-infrared irradiation. ACS Appl Mater Interf 6(24):22855–22861
90. Li J, Zhang G, Deng L, Zhao S, Gao Y, Jiang K, Sun R, Wong C (2014) In situ polymerization of mechanically reinforced, thermally healable graphene oxide/polyurethane composites based on Diels-Alder chemistry. J Mater Chem A 2(48):20642–20649
91. Cui W, Ji J, Cai Y-F, Li H, Ran R, Robust (2015) Anti-fatigue, and self-healing graphene oxide/hydrophobically associated composite hydrogels and their use as recyclable adsorbents for dye wastewater treatment. J Mater Chem A 3(33):17445–17458
92. Lanzara G, Yoon Y, Liu H, Peng S, Lee W (2009) Carbon nanotube reservoirs for self-healing materials. Nanotechnology 20(33):335704
93. Sinha-Ray S, Pelot D, Zhou Z, Rahman A, Wu X-F, Yarin AL (2012) Encapsulation of self-healing materials by coelectrospinning, emulsion electrospinning, solution blowing and intercalation. J Mater Chem 22(18):9138–9146
94. Bailey BM, Leterrier Y, Garcia S, Van Der Zwaag S, Michaud V (2015) Electrically conductive self-healing polymer composite coatings. Prog Org Coat 85:189–198
95. Ahangari MG, Fereidoon A (2015) Micromechanical properties and morphologies of self-healing epoxy nanocomposites with microencapsulated healing agent. Mater Chem Phys 151:112–118
96. Aissa B, Haddad E, Jamroz W, Hassani S, Farahani R, Merle P, Therriault D (2012) Micromechanical characterization of single-walled carbon nanotube reinforced ethylidene norbornene nanocomposites for self-healing applications. Smart Mater Struct 21(10):105028
97. Guo K, Zhang DL, Zhang XM, Zhang J, Ding LS, Li BJ, Zhang S (2015) Conductive elastomers with autonomic self-healing properties. Angew Chem 127(41):12295–12301

98. Yang W, Song J, Wu X, Wang X, Liu W, Qiu L, Hao W (2015) High-efficiency self-healing conductive composites from HPAMAM and CNTs. J Mater Chem A 3(23):12154–12158
99. Wang S, Xuan S, Jiang W, Jiang W, Yan L, Mao Y, Liu M, Gong X (2015) Rate-dependent and self-healing conductive shear stiffening nanocomposite: a novel safe-guarding material with force sensitivity. J Mater Chem A 3(39):19790–19799
100. Bai S, Sun C, Yan H, Sun X, Zhang H, Luo L, Lei X, Wan P, Chen X (2015) Healable, transparent, room-temperature electronic sensors based on carbon nanotube network-coated polyelectrolyte multilayers. Small 11(43):5807–5813
101. Hsu S-H, Wu M-C, Chen S, Chuang C-M, Lin S-H, Su W-F (2012) Synthesis, morphology and physical properties of multi-walled carbon nanotube/biphenyl liquid crystalline epoxy composites. Carbon 50(3):896–905
102. Li J (2010) Self-assembled supramolecular hydrogels based on polymer–cyclodextrin inclusion complexes for drug delivery. NPG Asia Mater 2:112–118
103. Du R, Wu J, Chen L, Huang H, Zhang X, Zhang J (2014) Hierarchical hydrogen bonds directed multi-functional carbon nanotube-based supramolecular hydrogels. Small 10 (7):1387–1393
104. Li B, Zhang J (2015) Polysiloxane/multiwalled carbon nanotubes nanocomposites and their applications as ultrastable, healable and superhydrophobic coatings. Carbon 93:648–658
105. Li G, John M (2008) A self-healing smart syntactic foam under multiple impacts. Compos Sci Technol 68(15):3337–3343
106. Roy S, Baral A, Banerjee A (2013) An amino-acid-based self-healing hydrogel: modulation of the self-healing properties by incorporating carbon-based nanomaterials. Chem A Eur J 19 (44):14950–14957

Self-healed Materials from Thermoplastic Polymer Composites

Venkatavijayan Subramanian and Dharmesh Varade

Abstract The self-healing materials from thermoplastic polymer composites reveal outstanding properties. They impart distinctive advantages over traditional polymers with monotonous chain structures, and cure damage by itself (without human intervention) prompted by thermal (fatigue) and mechanical (fracture, corrosion) means with its intrinsic character of self-healing from injury as inspired from nature. This increases the lifetime and safety of materials with less maintenance. Moreover, it could be an interesting field of research for developing competitive materials with biomimetic properties whose opportunities include electronics, energy, armor, and space applications. This chapter addresses the various approaches of healing mechanism, brief discussion about critical issues and challenges during autonomic self-repair process and concludes with some significant work undergone in various thermoplastic polymer composites.

Keywords Thermoplastics · Polymer composites · Intrinsic approach · Autonomic self-healing mechanism

Contents

V. Subramanian · D. Varade (✉)
School of Engineering & Applied Sciences, Ahmedabad University, Navrangpura, Ahmedabad 380009, Gujarat, India
e-mail: dharmesh.varade@ahduni.edu.in

D. Ponnamma et al. (eds.), *Smart Polymer Nanocomposites*,
Springer Series on Polymer and Composite Materials,
DOI 10.1007/978-3-319-50424-7_6

1 Introduction

The dramatic escalation of growth rate, economic progress, and technological advancement contributes to the development of fascinating new generation of stimuli-responsive materials with wide range of functionalities which will foster the evolution of human welfare and security. One can adopt this stimuli-responsive behavior to different kinds of applications perhaps the most vital characteristics are to self-heal themselves in an autonomic way [1]. These are new classes of smart materials which have the ability to heal themselves through autonomic/non-autonomic way by imitating the spontaneous mode of self-healing from the biological systems to increase lifetime and also for its survival [1, 2]. The images of self-healing mechanism observed in plant stem and polymer composite materials with incorporated healing agent and krubb's catalyst are shown in Fig. 1.

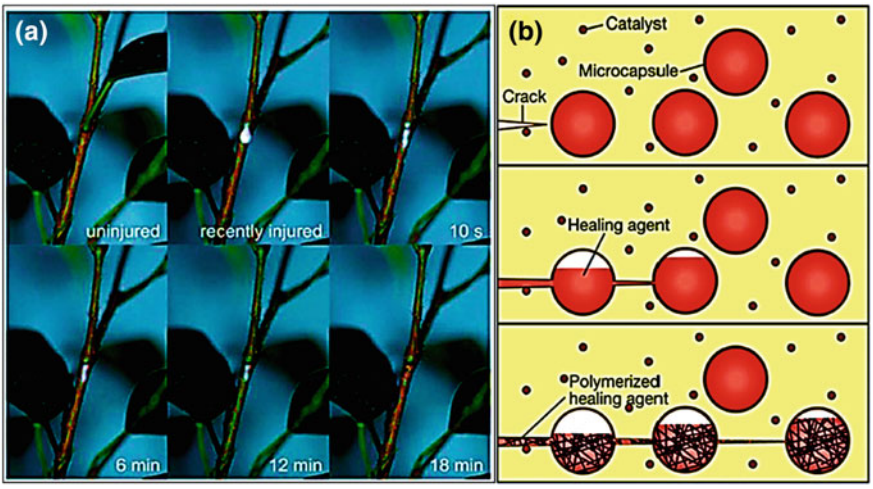

Fig. 1 Self-healing by **a** coagulation of latex after wound is created in plant stem [3]. Copyright 2010. Reproduced with permission from WIT press **b** polymer composites with microencapsulated healing agent along with catalyst in an autonomic way [4]. Copyright 2001. Reproduced with permission from Nature Publishing group

The polymer-based materials attracted great attention in large number of applications because of its intrinsic properties such as flexibility, ease of processing, and light weight, available from both fossil fuels and renewable resources such as starch, lignin, and cellulose, and able to customize according to the demand in the market [5]. The derivatives of thermoset, thermoplastic, polymer composites, polymer nanocomposites, supramolecular polymers, shape memory polymers, and elastomers can be used to make synthetic self-healing materials with multifunctional properties which is capable of recuperating its original properties such as conductivity, corrosion resistance, mechanical strength adhesion, color, hardness, and fracture toughness from failure [6–8]. However, the pristine polymer possesses poor mechanical properties (modulus, strength) as compared with ceramics and metals. These properties can be improved by making composites with other materials or adding nanomaterials to form nanocomposites. The interaction of nanomaterials with polymer in nanorange on account of incorporating nanomaterials in the host polymer matrix evolves novel homogeneous materials with exceptional properties. The damages in the form of cracks or failure caused by various impacts on material are depicted in Fig. 2. The formation of cracks/microcracks is common in polymer nanocomposites due to repeated impacts when it is used in application such as aerospace, armor, or ballistic protection. The self-healing of mesoscopic damages (cracks/microcracks and cavitation), surface scratches, and degradation associated with polymer nanocomposites was found to be the critical concern which obstructing its usage in large scale [5, 9, 10].

On broad classification, the healing mechanism was based on various stimulus such as mechanical (microencapsulation, hollow glass fiber, supramolecular,

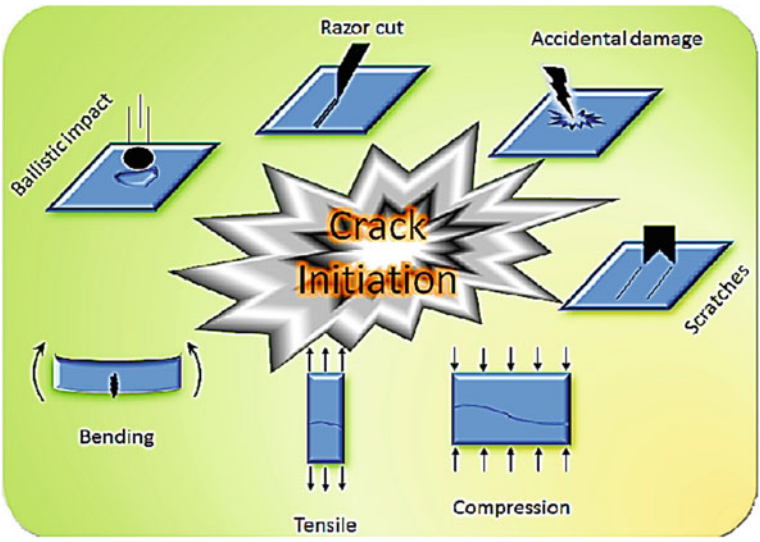

Fig. 2 Failure/crack types by different impacts [11]. Copyright 2015. Reproduced with permission from Elsevier Ltd.

microvascular networks), thermal (Diels-Alder, solid-state particles), electrical (carbon fiber, shape memory alloy, organometallic polymer), electromagnetic (ferrite particles), photo (cycloaddition), and ballistic (ionomer) [12]. The healing process of polymer and polymer composite materials can be understood by theoretical modeling and use of computational design tools. Currently, the techniques available for the polymer nanocomposites are very less. The understanding of self-healing in polymer nanocomposites needs great insights in terms of experimental and theoretical aspects. The use of skills in the form of computer (micromechanics) simulation and theoretical modeling provides substantial information about healing mechanisms which could easily validate the incorporation of nanoparticles in micro-/nanoscale cracks of polymer nanocomposites. This could possibly open the avenue for developing multifunctional materials with high performance. The composite materials possess good thermal stability, strength, stiffness, light weight, and low cost over pristine polymer materials, which clearly shows that it is capable of becoming an ideal and efficient candidate for sustainable potential applications. Moreover, the introduction of self-healing mechanism in polymer composites paves the way of research toward safer, long-lasting, and sustainable materials with wide range of properties and functionalities in the field of energy, transportation, armor, electronics, textiles, and coatings [5, 13].

2 Role of Polymer Architecture on Self-healing of Polymers/Polymer Composites

The development of present research toward healing based on damage types and sizes slightly varies from its earlier stages of research which mainly targets on recovery from drastic mechanical failure. The performance of a wide range of materials such as corrosion resistance, adhesion, wear resistance, electrical or thermal conductivity, hardness, color, hydrophobicity, liquid or gas barrier, and ion selection can be healable through restoring its original property (performance), thereby extending the lifetime of the system [6].

Figure 3 explains the performance of the material by the application of healing concepts. A traditional polymer can be made by interchanging the polymer architecture (e.g., crystallinity, cross-linking density, aromatic chains) or by adding external agents (e.g., graphene plates, exfoliated clays). The age of the traditional material shows a good improvement but very small developments from the original materials with less resistance and compatibility. But, the healing strategy provides an alternative path to overcome the damage or failure occurred in the materials. The curve a in Fig. 3 indicates virgin or original material and shows a very less service lifetime after damage occurs. The curve b represents traditionally improved material having extended lifetime than original materials. The curve c depicts self-healing material shows a significant service lifetime even after failure when it compared with original and traditional counterparts. The curve d corresponds to ideal

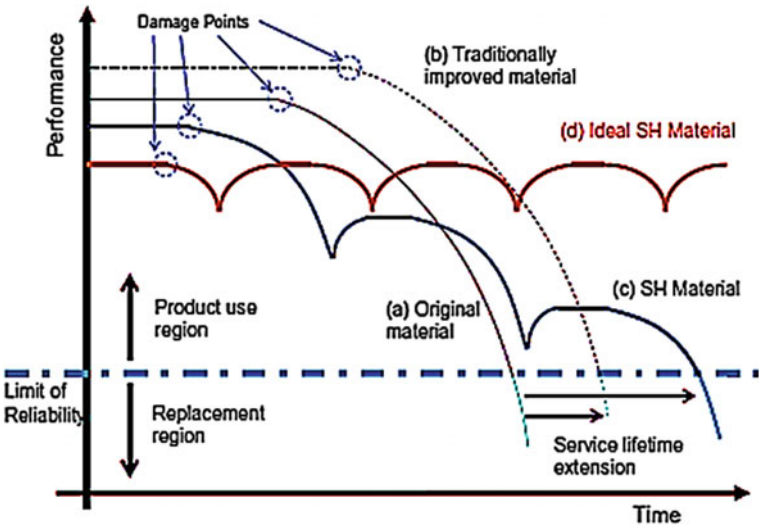

Fig. 3 Graph shows the extension of material age by adopting self-healing technique [6]. Copyright 2014. Reproduced with permission from Elsevier Ltd.

self-healing material has the capability to heal multiple times whose performance and lifetime remains extended when exposed to fracture. There is a possibility of healing the material on account of multiple failure events which improves the age in drastic manner as mentioned as curve d, but its primary mechanical property seems to be not enough for making potential applications. The development of materials having high mechanical performance with multiple healing capabilities was found to be interesting and challenging one for future in this field of research. Certainly, the ideal characteristics of typical self-healing materials for potential applications are as follows: The healing process should be autonomic, restore its original properties by multiple times, cure themselves for cracks/failure of any size, low maintenance cost, able to reveal good performance as compared to traditionally improved materials and feasible than the current materials which is commercially used in applications [6].

3 Healing Mechanisms

3.1 Autonomic and Non-autonomic Way

The polymer–polymer composites can be classified into two categories on the basis of chemistry of materials which is autonomic (the chemical potential discharged and immediately heal the rupture) and non-autonomic (heal with manual intervention) self-healing materials. The stability and durability of the final material can

be increased by repairing the damage in autonomic way. The healing agent is incorporated or phase-separated by mending with bulk polymer materials so that the healing of cracks/failure takes place without external intervention at ambient temperature. When the crack is initiated and tries to propagate, the healing agent discharged instantaneously into the planes due to capillary effect and reassemble to restore the damaged space. The self-healing process should take place in a rapid manner in order to achieve the required healing effectiveness. Generally, for high healing efficiency, the healing agent forms a homogeneous mixture as it is difficult to process in terms of large-scale production in industries [5].

3.2 Intrinsic/Extrinsic Approach

Depending on the chemistry and its applications, the materials are categorized into either intrinsic or extrinsic self-healing systems. The materials which have the ability to heal themselves through the sudden interchain mobility of polymer chains for molecular and macroscopic level of damages promoted by the driving force in the form of energy, i.e., heat or light (temperature, static load or UV), are known as intrinsic self-healing polymers. This is followed by the repairing of bond strength (either physical or chemical) even after removing the stimulus from the system. The ability to heal multiple times is possible in intrinsic healing process holds great advantage over extrinsic process.

The intrinsic self-healing properties of polymer materials inspired from biological systems from humans, animals, or plants entail identifying damages, time for rest, reunion of chain arrangements, integration of polymer materials during healing process, and critical size of impairment. As in the case of plants, the local impairment can be healed by flooding of liquid followed by hardening, together forms two-step repair process. For intrinsic healing process, the first step is the softening and movement of healing substance toward the damage and the second step found to be hardening process which restores its original properties through recovery of local viscosity by removing healing mode of trigger, e.g., temperature as described in Fig. 5. The intrinsic self-healing approach provides feasible solution to multiple healing concepts. Generally, the healing process occurred by the sequence of steps. First, the mobility of healing matters toward the cracks/failure followed by interaction and precipitation stimulated by varying ambient humidity [6, 11, 14] (Fig. 4).

Intrinsic process, a macroscale healing mechanism classified based on molecular principle, it can be either reversible covalent bonds, supramolecular interactions on the basis of chemistry and shape memory polymers or polymer blends on the basis of physical and chemical approaches. Based on the chemistry, the intrinsic self-healing materials can be classified into non-covalent (hydrogen bonding, Π–Π

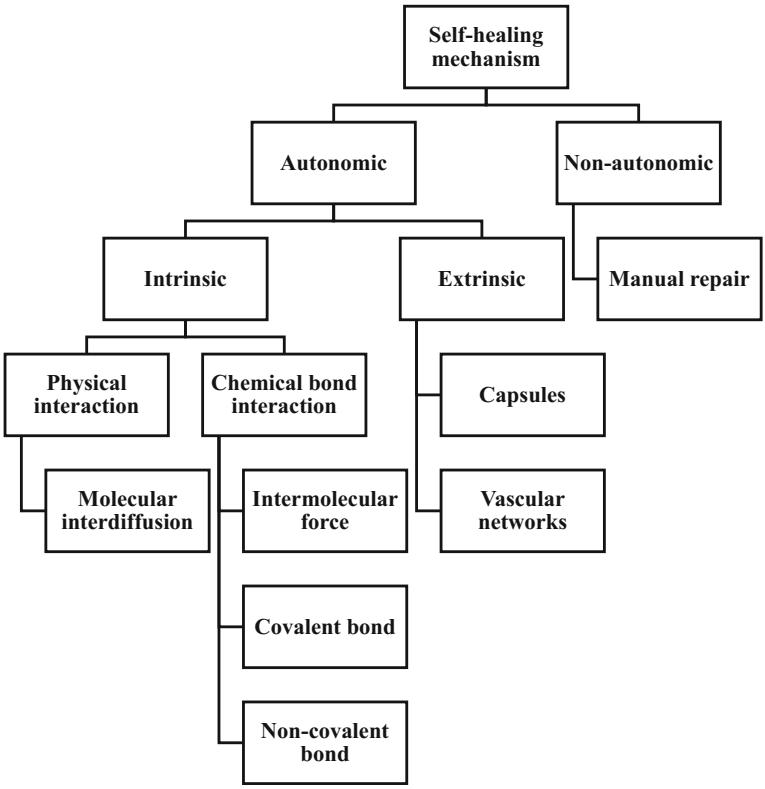

Fig. 4 Flowchart representing self-healing approach

stacking, host–guest interaction stacking, or ligand–metal bonding) and dynamic covalent (Diels-Alder reaction, dynamic urea bond, trans-esterification, and radical exchange). In extrinsic healing process, the two ideal steps which are mentioned in intrinsic approach also form a root cause for developing extrinsic self-healing approaches. Here, the healing agent is incorporated as discrete units in the polymer matrix in the form of capsules/microcapsules or vascular networks [6, 15–17].

The autonomic materials are designed in such a way that catalyst also embedded in a discrete manner along with healing agent in the polymer matrix. The extrinsic healing process can be performed by two approaches, namely microencapsulation and microvascular network. Then, the healing process is stimulated by internal or external rupture in capsules and vascular networks. The capsule shells were made up of polyurethane, poly (urea–formaldehyde), poly (melamine–formaldehyde), or poly (melamine–urea–formaldehyde) using different polymerization methods [5]. This is a catalyst-driven process, and its efficiency can be increased by encapsulating in wax

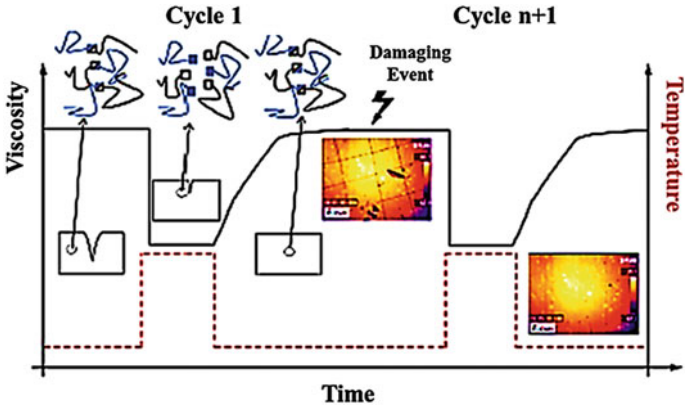

Fig. 5 Illustration of concepts behind intrinsic self-healing approach [6]. Copyright 2015. Reproduced with permission from Elsevier Ltd.

and recrystallized [18]. The limitations of microencapsulation techniques were as follows: Cost of catalyst (Grubbs Catalyst) is very high and healing can be done only once due to depletion of healing agents [5]. In addition, compatibility of healing agents with catalyst, stability and lifetime of the catalyst and healing agent for fabricating composite materials, viscous nature (preferably low), and wetting property of the healing agent to fill the cracks, dissolution of catalyst in healing agents, and kinetics were the critical issues concerned with microencapsulation-based repairing mechanism [19]. The intrinsic approach can be well applied in thermoplastic, thermoset, and elastomers materials provided that the perfect healing of the new interface may be possible only if the properties of new interface are identical with the bulk material. The damage can be eventually vanished by healing process due to chain entanglements through molecular interdiffusion and also chemical or physical cross-links as compared with the characteristics of bulk material [6]. The self-healing mechanisms based on the organizational structure of polymers were crack filling (healing agents in microencapsulation, in phase-separated, in hollow fibers, microvascular networks), diffusion (viscoelastic, dangling chain, thermoplastic or thermoset blends), reformation of chemical bonds (UV, heat, supramolecular arrangement, metal–ligand association or dissociation), strengthening of original properties (mechanophores) as shown in Fig. 6 [11, 19, 20]. For thermoplastic polymers, the type of healing may be either molecular (molecular interdiffusion—thermal or solvent, reversible bond formation, recombination of chain ends, photo-induced healing or living polymer) or structural (healing by nanoparticle) [21].

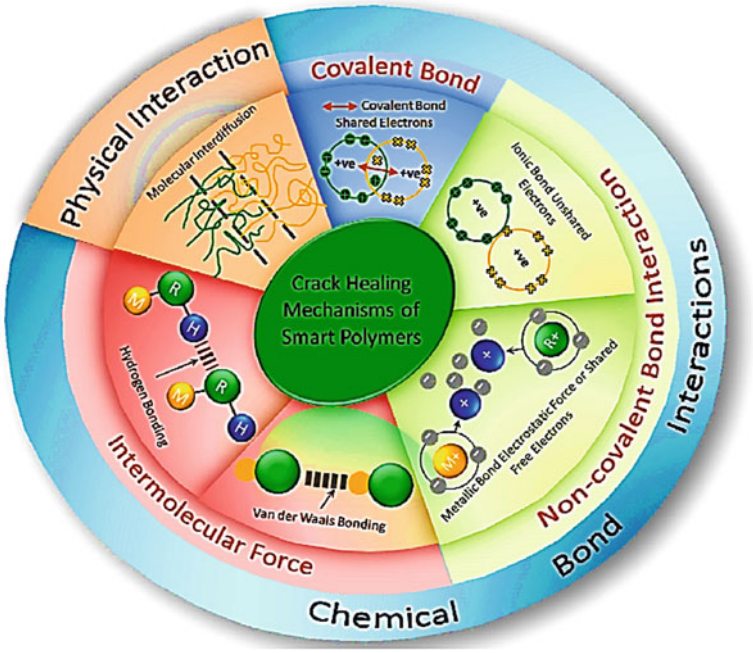

Fig. 6 Representation of various self-healing mechanisms [11]. Copyright 2015. Reproduced with permission from Elsevier Ltd.

4 Self-healing—Concepts, Controlling Factors, and Performance

Glass transition temperature, T_g, is the temperature at which the polymer transits from hard, glassy substance to soft, rubbery material and specifically for thermosets, and the intrinsic process occurs above this temperature. For thermoplastics, intrinsic healing process was found to be above the melting point stimulated by external trigger such as temperature or solvent. The gradient of glass transition temperature, T_g, between the bulk and the new interface (below glass transition temperature, T_g) stimulates the healing process through interdiffusion of chains [6]. The highly flexible polymer materials can be prepared by amalgamation of polymers with high glass transition temperature (less chain flexibility) and low glass transition temperature (high flexible) [22]. The prerequisite investigations to be enquired for intrinsic self-healing materials were the chemical reactions involved, the physical properties of the networks for those chemical reactions, the repairing mechanism from dislocated macromolecular segments. The detail analysis could give the clear picture for basic understanding of the concepts concealed behind the self-healing mechanisms. The two macroscopic concepts, thermodynamics and reaction kinetics which govern the chemical reactions (like other chemical

processes), were responsible for the establishment of physical networks to restore the original properties. For a chemical process to be proceed in spontaneous way, the total energy in terms of Gibbs free energy ($\Delta G = \Delta H - T\Delta S$) should be less than zero (<0). The formation of reactive groups due to chain cleavage and conformational changes due to slippage are the two consequences as a result of mechanical failure of a material. The interface of both chemical (chemical reactions) and physical (segmental/chain rearrangements) aspects is crucial to restore the ruptured networks in an autonomic way. The mechanisms of self-repair comprise five steps namely chain rearrangements, mobility of reactive surface, wetting, diffusion, and reestablishment of networks/bonds. The diffusion of chain segments was responsible for (acts as driving force) healing mechanism to occur and repairing to be accomplish only if the chain disengagement from the tube try to attain equilibrium within a certain time, T_r (Time for complete separation of chain from tube). The dependence of molecular weight to repair time is correlated as $T_r \alpha M^3$, which explains that the polymers with high molecular weight (long chains) take more time for self-repair, but lower chain polymers favor repairing mechanism. It is difficult for the intrinsic polymers system to heal by itself unless the physical and chemical compositions are changed. The ability of a polymer system to heal themselves is based on the intrinsic properties such as concentrations, elasticity, physical/chemical compositions, density, and specific energy and also it determines whether the healing agent is attached to polymer backbone (chemical way) or embedded in matrix (physical way). The reactive groups can be either cleaved chain ends or pendant groups such as formation of cyclic structures, $–NH_2$, –C=C–, –OH, –COOH, S–S, –C=O, –SH, –Si–O or free radicals which helps to make bonds (rebonding) again for self-healing. As previously mentioned, the self-healing process can be through either chemical way (hydrogen bonding, supramolecular chemistry, covalent bonding, Π–Π stacking, ionic interactions) or physical means (chemo-mechanical repair in terms of remote self-healing, encapsulation, and shape memory polymers) which targets to fabricate autonomic self-repair materials [1].

The process of self-healing and regeneration imitates from nature which is a systematic assembly of heterogeneous anatomy composed of complex metabolic, highly synchronized defense systems. The designing of self-healing process is highly challenging and even side reactions also happen, as it could possibly affect the main reaction. The sequence of repair mechanism by polymer chain due to failure caused by mechanical means is clearly depicted in Fig. 7. Due to damage, the networks got broken and subsequently the slippage of polymer chains happens. This leads to the formation of reactive groups and decides whether the reactive chain ends to restore itself without external intervention or react to form oxidative products with surrounding. As soon as the cleavage, the movement of segments due to conformational changes and diffusion of low molecular weight networks correlate to the reformation of bond due to chemical reactions, as it paves the way to self-healing which is also pertinent for physical approach. The healing efficiency, $R(\sigma)$ [ratio of initial fracture stress (before repair) to the healed fracture stress (after repair)], was found to be the extent of recovery from its failure state by assuming bond cleavage is not there during damage. Also, the relation between fracture stress with molecular

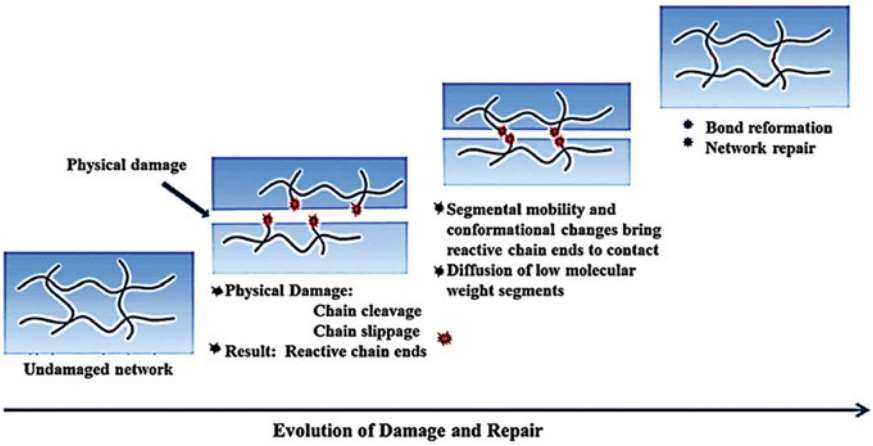

Fig. 7 Schematic representation shows the sequence of ideal self-healing process [1]. Copyright 2013. Reproduced with permission from Royal Society of Chemistry

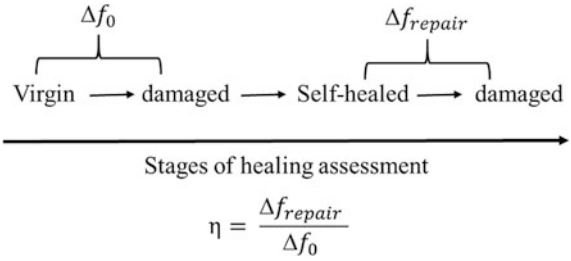

Fig. 8 Evaluation of healing efficiency [23]. Copyright 2015. Reproduced with permission from John Wiley & Sons, Inc

weight of the polymer, M, and repairing time, t, is generally described as $\sigma \alpha (t/M)^{1/4}$ and considering $t = T_r$ (happens when chain escapes at T_r during t) leads to rearrangements of conformation of chain proceeds to self-healing [1] (Figs. 7, 8).

$$R(\sigma) = \frac{\sigma_{\text{healed}}}{\sigma_{\text{initial}}} \tag{1}$$

5 Self-healing Approach in Selected Thermoplastic Polymer Composites

5.1 Poly(Methyl Methacrylate)–Glycidyl Methacrylate Composites (Through ATRP) Based

The polymers and composites repair themselves from cracks/failure independently by encapsulating healing agents in the matrix. Generally, the fluidic healant-loaded vessels for autonomic self-healing are not applicable to thermoplastic polymers, as

the polymerization of healant is unable to form covalent bond with polymer matrix [24]. The formation of covalent bond is highly desirable for crack healing which helps to make high-strength materials suitable for applications. The healing of polymers due to secondary forces (hydrogen, electrostatic, and van der Waals) is always weaker than the chemical bonds formed between the separated parts. The drawbacks for the existing approach are solved by living polymerization technique known as atom transfer radical polymerization (ATRP), in which polymers can be made with well-controlled molecular weight and distribution so that the polymerization (chain growth) continues till the monomers emptied out. Here [24], the healing happens as a result of chemical reaction between poly(methyl methacrylate)—PMMA matrix (crack surface)—and microencapsulated spheres of glycidyl methacrylate—GMA (healing agent). As soon as the crack initiation and propagation happens, polymerization reaction takes place once the healant (monomer) meets the PMMA matrix and blends completely to form covalent bond which helps to fill the interstitial fissures. However, this is not a catalyst-driven process, as it eventually quits the deactivation of catalyst. By using this living polymerization technique, i.e., ATRP, highly chain end-functionalized polymers adapting modification in post-polymerization stages can be obtained and also different kinds of monomers such as glycidyl methacrylate (GMA), benzyl methacrylate (BMA), and methyl methacrylate (MMA) were homopolymerized at room temperature.

GMA is less soluble, nonvolatile with high boiling point, and ease of wetting on the surface of PMMA matrix due to similarity in polar groups for the copolymerization to occur. Here, the polymer PMMA synthesized at ambient temperature by using initiator as ethyl 2-bromoisobutyrate and catalyst as cuprous bromide (CuBr)/*N*,*N*,*N*′,*N*′,*N*″-pentamethyldiethylenetriamine (PMDETA)/tetrabutylammonium bromide (Bu_4NBr). Bu_4NBr is added because of the low solubility of catalyst complex [Cu(II)/PMDETA] in MMA. The kinetic plot shows dependence of $\ln\left([M]_o/[M]\right)$ over time is linear (as shown in Fig. 9a) which clearly states that the disappearance of MMA monomer and constant increase in concentration of radicals seem to be first-order polymerization reaction.

The variations of polydispersity index (M_w/M_n) were observed to be very less in the range of 1.08–1.15. Also, there is a linear relationship between number average molecular weight (M_n) and monomer conversion using ATRP approach which is depicted in Fig. 9b clearly states that this polymerization reaction is a controlled or living process. A typical experiment was carried out by pouring ethyl methacrylate (EMA) with yellow dye, MMA, GMA with carbon black and then finally MMA monomers in a random manner after preparing PMMA from ATRP approach. An interesting multilayer sandwich structure in the shape of rod which is shown in Fig. 10 is due to polymerization reaction of healing monomers with matrix (by keeping PMMA as a base polymer). The copolymerization followed by monomer diffusion makes the polymer interface between layers in ambiguity.

The polymerization process continues to occur again and again once the monomer repeatedly contacts with PMMA from ATRP approach, and finally, the self-repairing PMMA composites embedded with GMA capsules were prepared

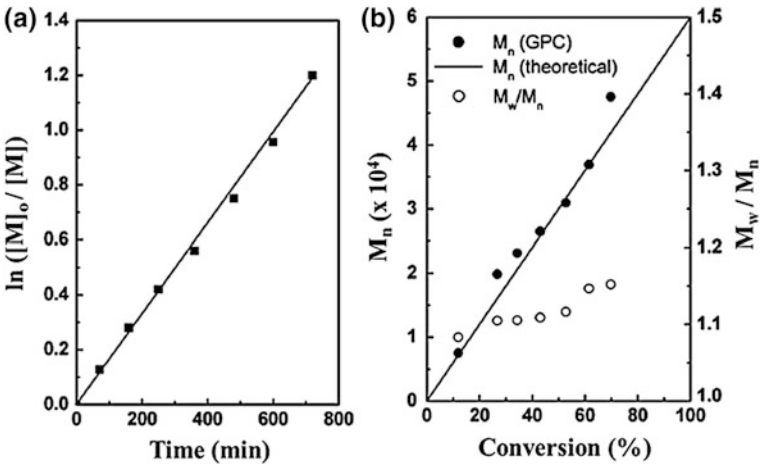

Fig. 9 **a** Polymerization kinetics of MMA monomer. **b** Number average molecular weight and polydispersity index against conversion of MMA monomer [24]. Copyright 2009. Reproduced with permission from American Chemical Society

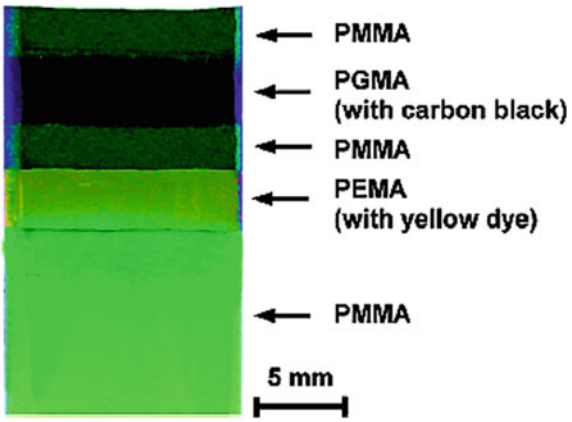

Fig. 10 Multilayer sandwich structure as a result of polymerization of monomer with matrix [24]. Copyright 2009. Reproduced with permission from American Chemical Society

(wall material—polymelamine formaldehyde (PMF); diameter—283 μm; core content—94.6%). The healing efficiency increases with increase in repairing time, and it is the ratio of the measure of impact strengths (based on Izod impact testing method which shows the resistance of materials when exposed to impact) of healed specimen to the pristine specimen. Here, the efficiency of the fabricated polymer composites reaches 89% after 12 h and attains 100% of healing (considered as equilibrium state) after 21 h as shown in Fig. 11.

The adhesion of microcapsules in the fractured surfaces of polymer matrix by viewing through scanning electron microscope (SEM) was shown in Fig. 12a. When the specimen is subjected to fracture, the microcapsules become cleaved and enclosed GMA was released to form a solid structure on the failure surface

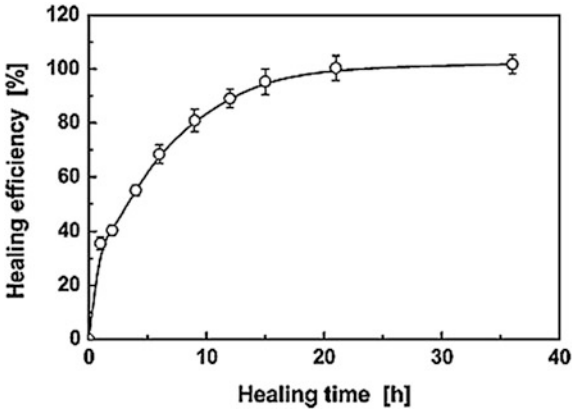

Fig. 11 Healing efficiency of PMMA with 15 wt% GMA-loaded microcapsules versus healing time at 25 °C [24]. Copyright 2009. Reproduced with permission from American Chemical Society

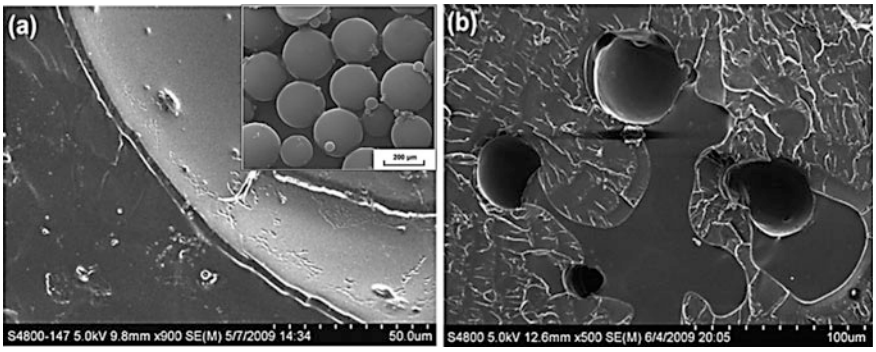

Fig. 12 SEM images of PMMA composites with 15 wt% GMA-loaded microcapsules (*inset*) **a** sample undergone first impact test and immediately solvent is used to remove released GMA. **b** After repairing for 24 h due to first impact test, sample is subjected to second impact test [24]. Copyright 2009. Reproduced with permission from American Chemical Society

(Fig. 12b). The evidence of surface polymerization reaction can be proved by Raman spectroscopy. From the graph (Fig. 13a), the intensity of peak for C=C at 1638 cm^{-1} decreases with time which represents the methacrylate group as the measure of kinetics of self-healing mechanism which states that GMA from capsules tries to heal the fractured surface through polymerization reaction.

By using solvent, chain entanglement can be possible to heal cracks in thermoplastics. The procedure was withdrawn because of the drawbacks associated with it, in which the healing efficiency is not as expected, the absorption of solvent leads to plasticization by thermoplastics, and possibly damage of property of the materials if desorption of solvent not takes place. In this, GMA acts as a solvent at

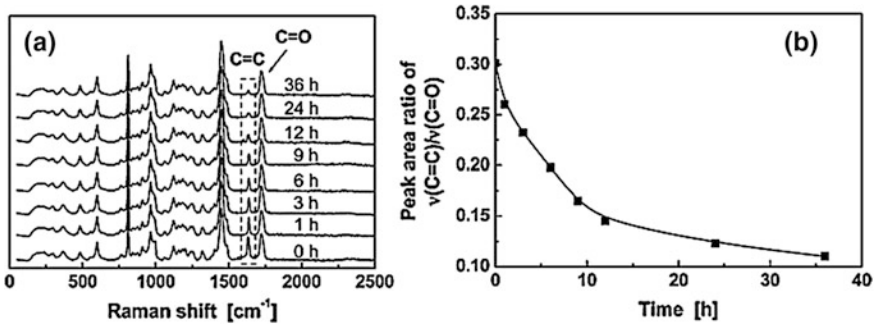

Fig. 13 **a** Raman spectra of fractured surface of the specimen. **b** Dependency of Raman peak area ratio over time [24]. Copyright 2009. Reproduced with permission from American Chemical Society

initial states and polymerization happens immediately. The living polymerization approaches have the ability to heal the thermoplastic polymer composites through chemical bonding without external intervention and addition of catalyst at ambient temperature itself. The specimen healed through this approach remains unchanged and has the ability to recover its full strength. This matrix can self-heal by recombining itself through macromolecular and new free radicals on the chain ends when it is exposed to degradation induced by radiation (electromagnetic radiation, UV etc.).

Limitations of ATRP process

1. Although the complete recovery of impact strength of the material is achieved by this process, there is a need for huge catalyst for the reaction to occur.
2. Even after reaction, it is very difficult to remove the remaining catalyst from the polymer matrix.
3. ATRP catalysts are made up of transition metal ions that are unstable when exposed to atmospheric air leads to aging of the polymer.
4. Polymerization process ceases due to oxidation of Cu(I) to Cu(II) in ATRP catalysts as the polymer matrix exposed to air even in short time. So, the repairing process stops when cracked surface contacts with air.
5. The catalysts used in ATRP are toxic, as it affects the fabrication and feasible usage of resultant polymers.

5.2 *Poly(Methyl Methacrylate)–Glycidyl Methacrylate Composites (Through RAFT) Based*

Reversible addition–fragmentation chain transfer (RAFT) reaction is an alternative and more versatile approach, in which thioester is used to perform living radical

polymerization to achieve resistance to aging of the end polymer matrix [25, 26]. Oxygen perhaps does not affect the polymer reactivity as it only inhibits the reaction. Polymerization continues to happen once oxygen is removed from the system. Eventually, the air only affects the top cracked surface of the monomer, but remending remains unaffected inside the fractured surface. The self-healing thermoplastics PMMA with GMA-loaded microcapsules through living polymerization RAFT expands its potential applications and can be thermally initiated through gamma, UV, or oxygen.

The PMMA matrix was prepared by mixing MMA, 2,2′-azoisobutyronitrile (AIBN), and cumylphenyldithioacetate (CPDA) through magnetic stirrer and the resulting solution purged with inert gas argon for 30 min to remove oxygen [25]. The experiment was carried out between 25 and 45 °C. The rate of polymerization is high such that the process was conducted at higher temperature, i.e., 45 °C. Then, the polymer was dissolved in tetrahydrofuran (THF) for three times and precipitates as yellow powder with methanol. The resultant polymer was subjected to drying at 40 °C for 24 h in vacuum oven. The GMA-loaded microcapsules were added into living polymer matrix PMMA in argon atmosphere under stirring for 22–24 h. The C=C bonds in GMA intrinsically react with PMMA matrix and carry the properties associated with both monomer and solvent. Then, the final specimen can be obtained by placing the GMA-incorporated PMMA mixture in closed moulds of silicone rubber at atmospheric temperature for 96 h. The sequential steps for repairing in thermoplastic polymer composites by living polymerization technique are shown in Fig. 14.

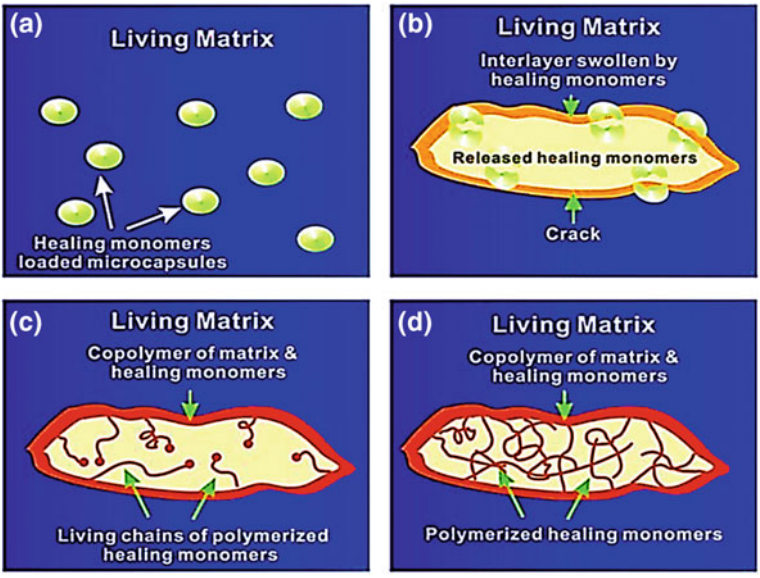

Fig. 14 Sequence of self-healing mechanism in thermoplastic polymer prepared from living polymerization [25]. Copyright 2011. Reproduced with permission from Royal Society of Chemistry

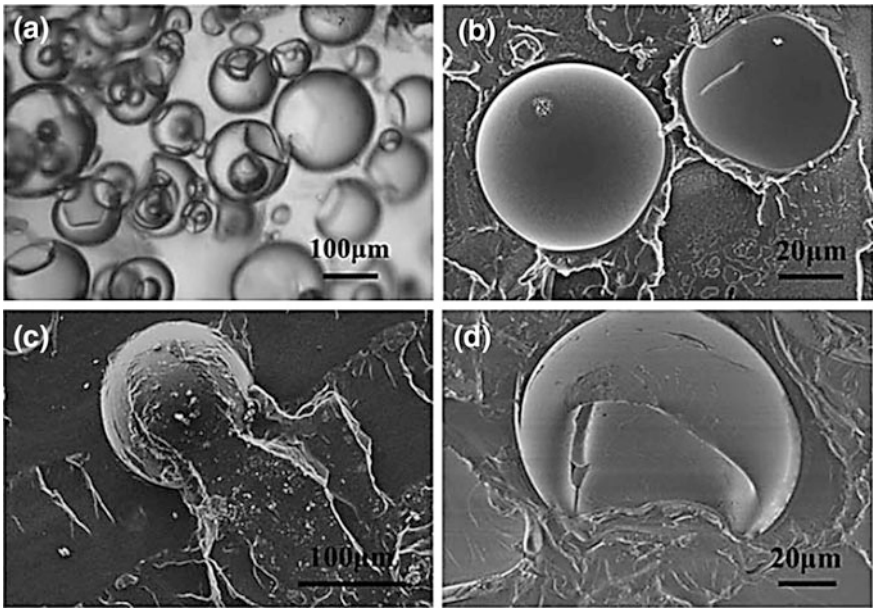

Fig. 15 **a** Images of PMMA specimen taken from optical microscope. SEM micrograph. **b** Cracked surface of pristine PMMA specimen after first impact test (GMA—10 wt% released was removed by using solvent). **c** Image of the specimen after 72 h from first impact test. **d** Cracked specimen after second impact test [25]. Copyright 2011. Reproduced with permission from Royal Society of Chemistry

The GMA-loaded microcapsules should be well dispersed in polymer matrix in order to achieve high efficiency. The images taken from optical microscopy show that the aggregation of microcapsules is not there, which ease the mobility of healing agent to the fractured surface. Also, the SEM images (Fig. 15a, b) show the adhesion of microcapsules due to the interaction between the matrix and capsules is strong enough for making composite materials. The amount of healing agent released from the microcapsules forms copolymerization reaction on the cracked surface to restore the full strength of the fractured materials.

The control tests were performed to find the sensitive nature of PMMA with GMA-loaded microcapsules specimen on exposure to air. The specimen undergoes impact test to form broken pieces followed by exposure to air for certain time period. Then, the broken pieces were sent to healing in the presence of argon for 72 h at 25 °C. The broken pieces interact with each other to heal themselves. The specimen was subjected to second impact tests to determine the efficiency of healing. It is found that chemical bonding due to living polymerization was responsible to repair cracks in PMMA composites instead of solvent effects. The healing efficiency (Fig. 16) initially increases by rise in healing time and attains the equilibrium, i.e., recovery of full (100%) impact strength after 72 h.

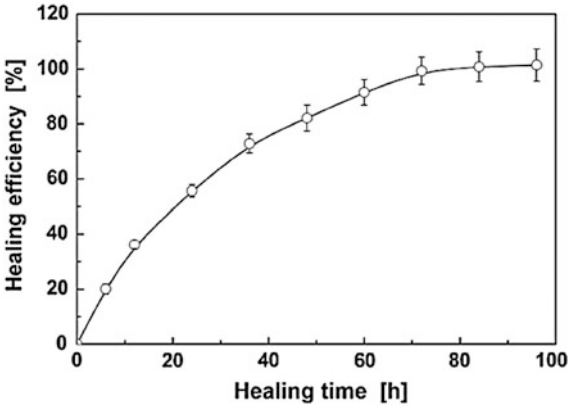

Fig. 16 Time dependence of healing efficiency for PMMA specimen with 15 wt% GMA-loaded microcapsules [25]. Copyright 2011. Reproduced with permission from Royal Society of Chemistry

5.3 Polystyrene–Glycidyl Methacrylate Composites Based

The polymer composite material is prepared by keeping polystyrene (PS) as living polymer matrix in which the sphere-shaped multilayer microreactors containing GMA-loaded microcapsules are incorporated in well-distributed manner [27]. The healant initially acts as a solvent and tries to polymerize with the matrix for the healing process to occur, thereby retaining the mechanical strength with the help of both physical and chemical interactions. The polymerization reaction happens when the healant in the interior portion contacts with the catalyst in microreactors as a result of matrix damage. The mobility and reformation of chain networks found to be primary cause for healing of fractures. The assimilation of plasticizers or encapsulated solvents in thermoplastic polymer helps to avoid external intervention. The microreactors (Fig. 17) can be prepared by three steps, which are (i) synthesis of GMA-loaded poly(melamine formaldehyde) (PMF) microcapsules, (ii) fabrication of second shell of microreactors, and (iii) incorporation of catalyst and formation of protection layer.

The PMF prepolymer can be prepared by missing melamine with formaldehyde and maintaining the pH of the solution at 8–9 with the help of triethanolamine. The emulsion of glycidyl methacrylate (GMA) along with surfactant solutions (sodium dodecyl benzene sulfonate and poly vinyl alcohol) was prepared, and the pH of the

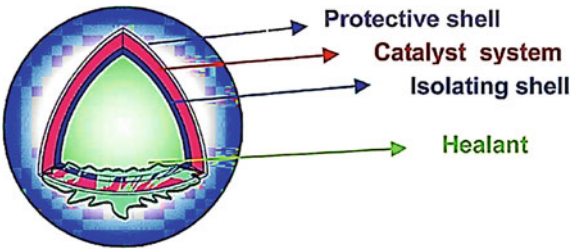

Fig. 17 Microreactor loaded with GMA microcapsules [27]. Copyright 2013. Reproduced with permission from Royal Society of Chemistry

emulsion was maintained at 3.5 by means of acetic acid solution. The prepolymer mixture along with emulsion was subjected to agitation at 65 °C for 3 h to obtain microcapsule deposits. Finally, GMA-loaded PMF microcapsules in the form of white powder were prepared by washing with water and drying the microcapsule deposit at ambient temperature. The microinitiator PMMA-Br prepared by adding MMA, tetrabutyl ammonium bromide (Bu_4NBr), cuprous bromide (CuBr), *N*,*N*,*N*′,*N*′,*N*″-pentamethyl diethylene triamine (PMDETA), and dichloromethane to undergoes atom transfer radical polymerization (ATRP) reaction for 4 h at 25 °C. The mixture was diluted with chloroform, and copper was removed by filtration in neutral alumina column. The microinitiator was obtained as white solid after drying in vacuum.

The second shell was made by means of emulsion solvent evaporation by dissolving living PMMA for 15 min in solution containing microcapsules with dichloromethane. The mixture was agitated for 6 h to remove dichloromethane by evaporation. Then, the mixture was washed, filtered, and dried at room temperature to fabricate double-walled microcapsules. The CuBr/PMDETA was added in second shell and also coating was done with paraffin wax in outer layer.

The microcapsules prepared were well dispersed in CuBr/PMDETA solution at ambient temperature in ethanol for 3 h and sent to filtration for removing volatile ethanol. At this point, the microcapsules in paraffin wax of cyclohexane were agitated and microreactors were prepared by drying followed by filtration under vacuum. The composite material can be prepared by dry blending of microreactors and PS at 150 °C though compression moulding process. The 3D image (Fig. 18) taken from microcomputed tomography (mCT scan) shows the proper dispersion of spherical-shaped microreactors in the polymer matrix. Due to plastification of healant, the glass transition temperature, T_g, becomes low with samples containing larger microreactors as compared with specimen with only PS or with smaller microreactors. The healing efficiency of composite specimen shows 86% in 12 h,

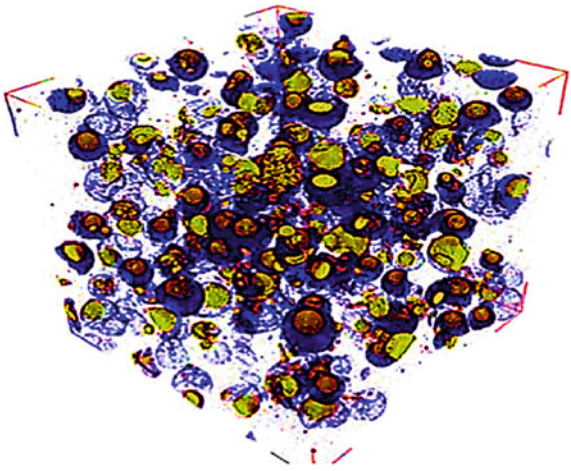

Fig. 18 Three-dimensional image taken from mCT showing arrangement of microreactors over PS polymer matrix [27]. Copyright 2013. Reproduced with permission from Royal Society of Chemistry

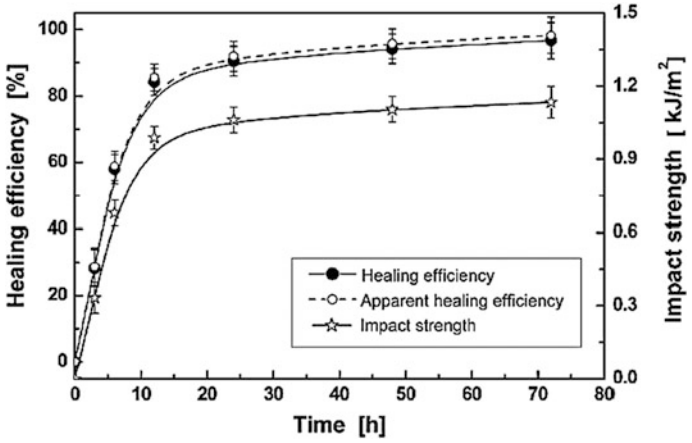

Fig. 19 Healing efficiency and impact strength versus time graph for composite specimen containing PS with 20 wt% GMA-loaded microreactors [27]. Copyright 2013. Reproduced with permission from Royal Society of Chemistry

when it subjected to impact test at 25 °C. After 24 h, the curve progresses very slightly, and at the end of 48 h, it attains 95% recovery of original strength, which is an equilibrium stage. From this, it is confirmed that minimum 48 h is required for the PS-GMA-loaded microcapsules composite to recover its maximum impact strength. The average healing efficiency (Fig. 19) of 95% can be increased by maintaining 20 wt% of microreactors content in polymer matrix, which shows the dependency of microreactors content over healing efficiency.

5.4 Chitosan–Cerium Nitrate Composite Based

The protection of aluminum alloys in aeronautical industries against corrosion remains a critical issue. Due to environmental regulations, the usage of chromium for surface coatings was reduced. Cerium salts can be alternative one, when doped in chitosan derivatives yields a significant result against corrosion. Chitosan, a biopolymer, possess distinct characteristics such as formation of film over surfaces, biodegradable, compatible, and antimicrobial activity [28]. The cerium nitrate was doped in chitosan derivatives, which were prepared from three different systems such as one unmodified (pure chitosan) and two functionalized chitosan (chitosan–glycidyl tetrafluoropropyl ether (GTFE), chitosan–vanillin). By subjecting chitosan to alkylation reaction using GTFE, the hydrophobic nature of chitosan increases. To examine the effect of large substituent on its surface characteristics, the chitosan was functionalized with vanillin. The behavior of corrosion on aluminum alloys by chitosan-based coatings doped with cerium nitrate was studied and characterized by FTIR and 1H-NMR analyses [28].

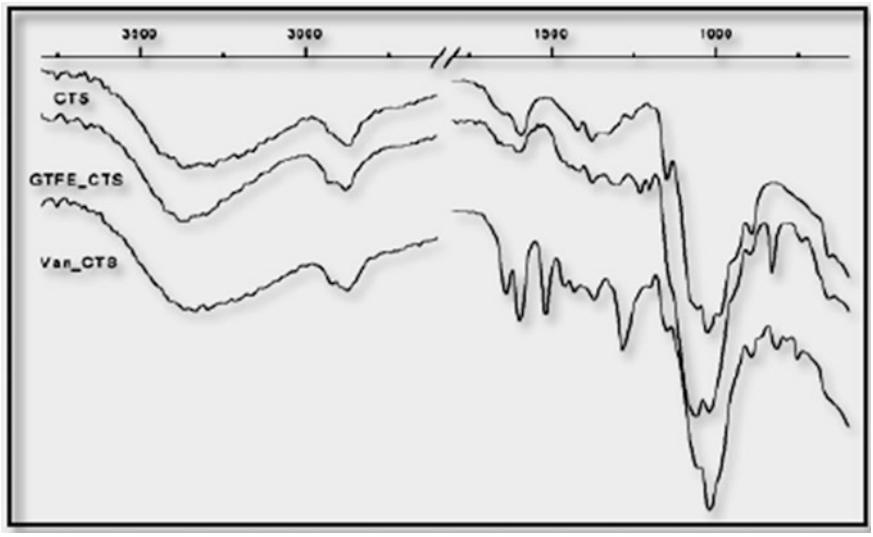

Fig. 20 FTIR image for pure chitosan, chitosan–GTFE, and chitosan–vanillin samples [28]. Copyright 2012. Reproduced with permissions from Elsevier Ltd.

The FTIR spectrum (Fig. 20) shows OH, NH_2 groups at 3500 and 3150 cm^{-1} for pure chitosan, respectively. For chitosan–GTFE, due to alkylation reaction, the aliphatic ether at 830 cm^{-1}, C-F bonds at 1202 and 1230 cm^{-1}, primary amine at 1590 cm^{-1}, and secondary amine at 1640 cm^{-1} were found. Regarding the FTIR characteristic band for chitosan–vanillin, the peaks at 1635, 1593, and 1515 cm^{-1} represents benzene ring and at 1283 cm^{-1} represents phenolic hydroxyl group. The protons of chitosan pyranoside ring at resonances between δ 3.3 and 4.6 ppm, triplet of H-5″ proton coupled with fluorine atoms, represent the 1H-NMR spectrum of chitosan–GTFE as shown in Fig. 21. The intensity of proton was compared with pure chitosan and chitosan–GTFE known to be degree of substation as 30%. The resonance of chitosan between δ 2.5–5.0 ppm, methoxy protons of vanillin at δ 3.7 ppm, aromatic protons at δ 6.8 and 7.3 ppm, imine protons at δ 9.5 ppm, and degree of substation of protons (H-3′ and H-1) as 30% for chitosan–vanillin were depicted.

The hydrophobic nature of surfaces for three samples was analyzed through water contact angle measurements, in which chitosan derivatives show contact angle of about 55° while chitosan doped with cationic inhibitor was increased to 90°. The reduction in migration of NH_2 and OH moieties on the surface is due to the addition of cerium salts on chitosan derivatives. Due to intramolecular complexation of cerium nitrate with amine groups, the viscosity of the solutions decreases. The anticorrosion properties in the presence of sodium chloride solutions were tested using the electrochemical impedance spectroscopy (EIS) technique. The chitosan derivatives with corrosion inhibitors show better impedance results over time compared with the undoped chitosan derivatives due to its strong hydrophobic nature and barrier toward the ingress of water molecules. The chitosan with 10 wt%

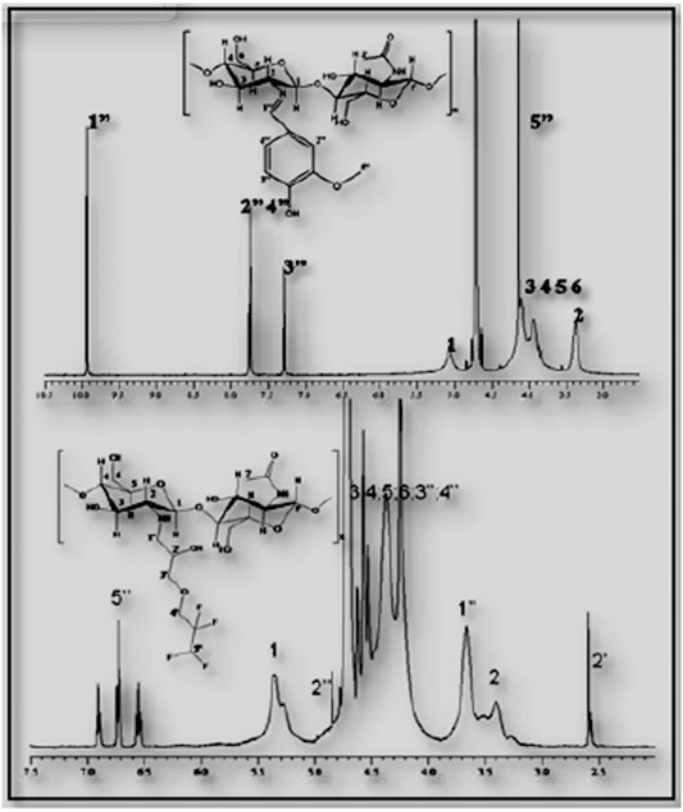

Fig. 21 1H-NMR images for chitosan–vanillin and chitosan–GTFE [28]. Copyright 2012. Reproduced with permissions from Elsevier Ltd.

of cerium nitrate found to be best as compared with the remaining three chitosan systems because of its fast self-recovery and stability against detrimental effect of corrosion of longer immersion duration (1 week). The reasons for the reduction in corrosion were the interchain interaction between cerium salts–chitosan derivative matrix and the dispersion level of corrosion inhibitors in matrix.

5.5 Polyurethane–Graphene Composite Based

The self-healing ability by integrating thermoplastic polyurethane (TPU) with few-layer graphene (FG) to form a composite material under infra red light (IR), electromagnetic wave, and electricity was described [29]. The Π-conjugated electrons of graphene facilitate compatible with different polymers and also acts as fillers in making composite materials with high strength, chemically stable and possess thermal and electrical conductivity.

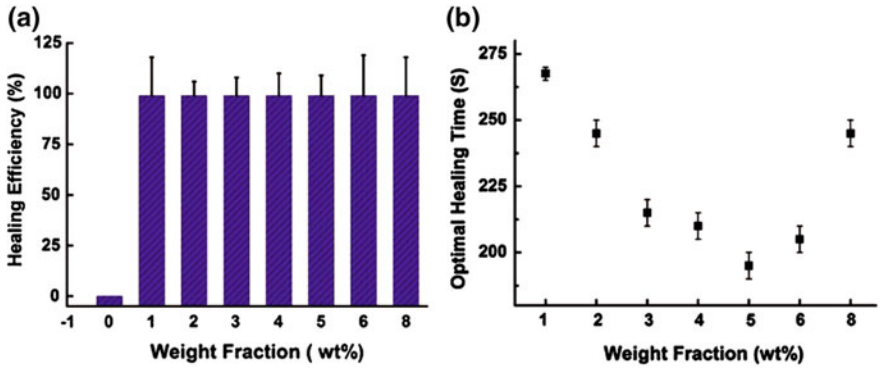

Fig. 22 **a** Healing efficiency by IR light versus weight fraction of samples. **b** Healing time versus weight fraction of pristine TPU and different compositions of FG-TPU composite [29]. Copyright 2013. Reprinted with permissions from John Wiley & Sons

FG-TPU composite strips were prepared by mixing FG and pristine TPU followed by the removal of solvent. A fracture was created in the middle of strips and it is subjected to healing process under electricity, IR light, and electromagnetic waves. The time of optimal healing (less time duration for achieving maximum efficiency), efficiency (ratio of tensile strength of the healed sample to the pristine sample), and the voltage required (lowest voltage to achieve high efficiency in 180 s) were used to evaluate the performance of healing process. First, the fractured sample is kept under IR light with power density less than 0.2 W/cm^2. The efficiency of healing for FG-TPU composites is almost same as 99%, but the pristine sample shows zero efficiency, which causes breaking down of samples even after extending the healing time. The doping of FG on TPU enhances the performances of healing. Also, graphene absorbs IR light and is a good conductor of heat, as it transfers energy throughout the TPU matrix. FG acts as nanoheater, heats the entire composite matrix evenly which could diffuse the TPU chains and joins together to repair the fractured parts. As shown in Fig. 22, the matrix composite with 5 wt% FG provides less time for healing. This composition provides optimum healing time, as the movement of matrix can possibly blocked by addition of graphene layer above 5 wt% of FG (Fig. 23).

The increase in FG concentration in composite matrix increases the electrical conductivity with less voltage in 3 min which helps to attain maximum healing efficiency. The concentration of FG up to 4 wt% shows zero efficiency even though the voltage of 220 V was given for an hour. The good efficiency is obtained at 175, 115, and 75 V in 3 min for respective samples with concentrations of 5, 6, and 8 wt% of FG. The wide range of samples require 8 wt% of FG for achieving complete healing. The sample has the ability to heal very efficiently at 75 V in 3 min for 8 wt% of FG concentration. The same sample took only 15 s to attain the maximum efficiency, when it is subjected to 110 V. For most samples, at the voltage of about 100 and 110 V, the better healing efficiency can be obtained. The fractured FG-TPU

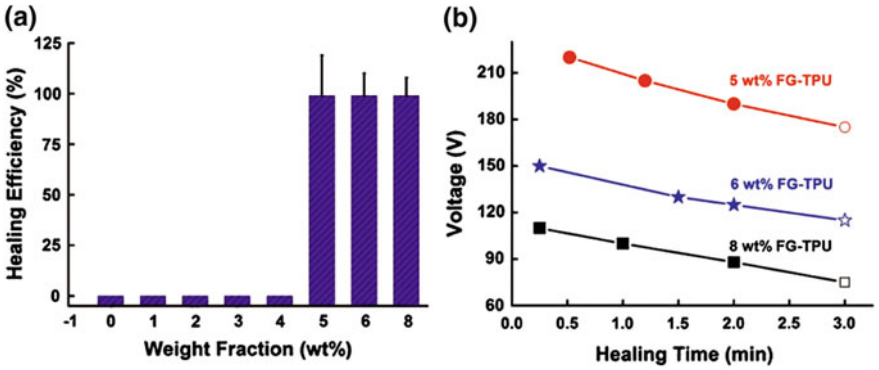

Fig. 23 **a** Healing efficiency by electricity versus weight fraction of samples. **b** Voltage versus healing time different compositions of FG-TPU composite [29]. Copyright 2013. Reprinted with permissions from John Wiley & Sons

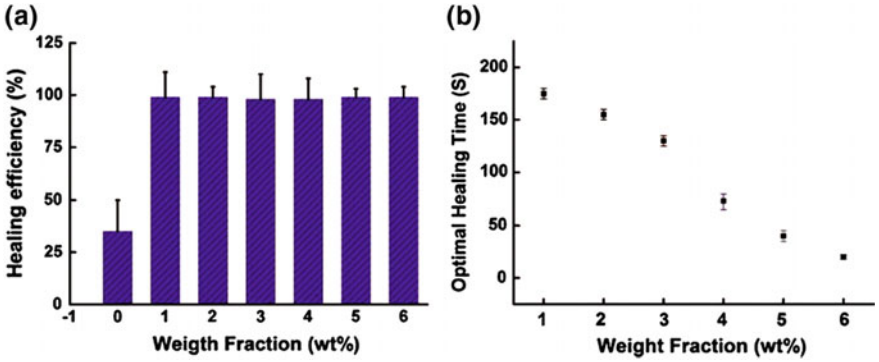

Fig. 24 **a** Healing efficiency by electromagnetic waves versus weight fraction of samples. **b** Optimal healing time versus weight fraction for different compositions of FG-TPU composite [29]. Copyright 2013. Reprinted with permissions from John Wiley & Sons

composite is exposed to electromagnetic wave from 800-W microwave oven at 2.45 GHz. The healing efficiency of about 98% can be obtained by varying the FG concentration in matrix. Due to high absorbing capacity of microwave radiation and thermal conductivity possessed by FG, the sample with 8 wt% FG took shortest time to attain the best healing efficiency (Fig. 24).

The healing behavior can be observed by using optical and SEM images before and after healing process taken place, when the composite sample is subjected to fracture. The healing process can be done using IR light, electricity and electromagnetic waves. The images in Fig. 25d–f show a clear evidence for repairing through three different healing processes by disappearance of fracture.

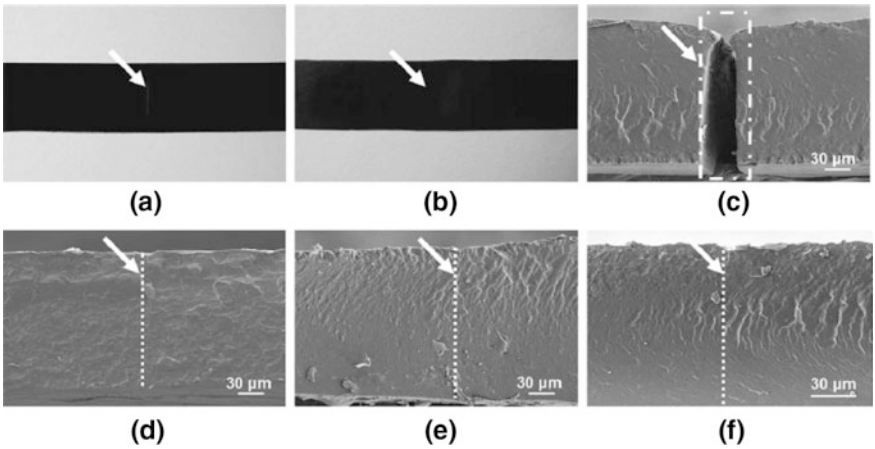

Fig. 25 Optical images **a** 6 wt% FG-doped FG-TPU fractured surface **b** composite surface after healing by IR light; SEM images **c** fractured surface **d** after healing by IR light **e** after healing by electricity **f** after healing by electromagnetic waves [29]. Copyright 2013. Reproduced with permissions from John Wiley & Sons

The self-healing of fractured surface by multiple times can be performed by using FG-TPU composites. The FG-TPU composite with 5 wt% FG composition is taken for this cycling test, due to its best healing performance through all three healing processes. The composite was subjected to fracture. The healing of sample can be achieved multiple times of about more than 20 times in terms of IR light, 2 times for electricity and 5 times through electromagnetic waves. In all three healing processes, the healing efficiency of about 99% can be observed. This clearly states that the materials possess long service life and reliable one for applications such as aerospace and microelectronics.

6 Challenges and Future Trends

The development and consumption of polymer and its composites materials acquired significant place in present technology such as automobiles, aerospace, textiles, electronics, and surface coatings [5, 30, 31]. The mechanical properties, thermal stress or impact as a consequence of continuous usage of materials, resulted in degradation of physical property. The emerging technique, self-healing, is an approach used to repair themselves which not only enhance the lifetime of the product but also it reduces the environmental impact. There are several critical issues faced by the current researchers for incorporating this technology to fabricate materials in bulk through industries. Even though nature is the benchmark for

developing self-healing mechanism, all the functional properties of the materials cannot be restored in an autonomic way. The existing process has the ability to recover only single functional property from damage can be replaced with advanced technique to restore multifunctional properties. The external intervention in the form of electricity and pumps to heat and circulate chemical for the fractured space was found in the current studies to be replaced by trying chemistry at ambient temperature. The healing should not be size centric, not only in the range of micro-/nanorange, but also strive to develop the concepts for large cracks. Due to mobility of polymer chains, the healing of soft materials is possible but for hard materials such as composites or metals, the healant reacts on surface of the specimen possibly produces a weak interface. The solution for strong adhesion to be found through various chemical healing process. The problem of fast ingress of water by damaged composite specimens can be solved by compartmentalization technique, which fills the gap exists between self-repairing and tolerance to failure possessed by traditional engineering design [32, 33]. Further, the time taken for chemical process is very high as the repairing process requires fast and efficient enough to restore the damage of the materials [1, 23]. Currently, the casting method using solvent is widely used to fabricate composite self-healing materials. But, living polymerization technique opens wide range of opportunities yet to be commercialized especially thermoplastic polymer and its composites [27].

7 Conclusion

The ability of the thermoplastic polymers and its composites to response upon internal or external stimulus was found to be one of the fascinating and emerging paths of the present research which is still unexplored. There are few challenges and risks, one can cross over to reveal the undisclosed notes concealed in nature, which serves as the inspiration for infinite discoveries. The objective of this present chapter is to discuss about the structure, architecture, functional properties, and performance required by the thermoplastic polymer composites to repair themselves without outside intervention in order to increase the lifetime as it exposed to physical damage. The polymer composites possess superior properties as it could possibly fill the limitations set by pristine/virgin polymer materials. The production of self-healing thermoplastic composites through living polymerization technique is yet to be commercialized on large scale. The new materials with high glass transition temperature (T_g), intrinsic autonomic approach with multiple times self-healing, serves as an better one for wide range of present commercial applications.

References

1. Yang Y, Urban MW (2013) Self-healing polymeric materials. Chem Soc Rev. doi:10.1039/c3cs60109a
2. Mackman N, Tilley RE et al (2007) Role of the extrinsic pathway of blood coagulation in hemostasis and thrombosis. Arterioscler Thromb Vasc Biol 27:1687–1693
3. Bauer G, Nellesen A, Speck T (2010) In: Brebbia CA, Carpi A (eds) Carpi design and nature V. WIT Press, Southampton, pp 453–459
4. White SR, Sottos NR et al (2001) Autonomic healing of polymer composites. Nature 409:794–797
5. Thakur VK, Kessler MR (2015) Self-healing polymer nanocomposite materials: a review. Polym J. doi:10.1016/j.polymer.2015.04.086
6. Garcia SJ (2014) Effect of polymer architecture on the intrinsic self-healing character of polymers. Eur Polym J 53:118–125
7. Bergman SD, Wudl F (2007) Mendable polymers. J Mater Chem 18:41–62
8. Chen Y, Kushner AM et al (2012) Multiphase design of autonomic self-healing thermoplastic elastomers. Nat Chem 4:467–472
9. vanGemert GML, Peeters JW et al (2012) Self-healing supramolecular polymers in action. Macromol Chem Phys 213:234–242
10. Folmer BJB, Sijbesma RP et al (2000) Supramolecular polymer materials: chain extension of telechelic polymers using a reactive hydrogen-bonding synthon. Adv Mater 12(12):874–878
11. Zhang P, Li G (2016) Advances in healing-on-demand polymers and polymer composites. Prog Polym Sci. doi:10.1016/j.progpolymsci.2015.11.005
12. Murphy EB, Wudl F (2010) The world of smart healable materials. Prog Polym Sci 35:223–251
13. Herbst F, Döhler D et al (2013) Self-healing polymers via supramolecular forces. Rapid Commun, Macromol. doi:10.1002/marc.201200675
14. Zhang MQ, Rong MZ (2013) Intrinsic self-healing of covalent polymers through bond reconnection towards strength restoration. Polym Chem. doi:10.1039/c3py00005b
15. Yan X, Wang F et al (2012) Stimuli-responsive supramolecular polymeric materials. Soc Rev, Chem. doi:10.1039/c2cs35091b
16. Botterhuis NE, van Beek DJM et al (2008) Self-assembly and morphology of polydimethyl siloxane supramolecular thermoplastic elastomers. J Polym Sci Part A: Polym Chem 46:3877–3885
17. Zhu D, Ye Q et al (2013) Self-healing polymers with PEG oligomer side chains based on multiple H-bonding and adhesion properties. Polym Chem. doi:10.1039/x0xx00000x
18. Jones AS, Rule JD (2007) Life extension of self-healing polymers with rapidly growing fatigue cracks. J R Soc Interface 4:395–403
19. Mauldin TC, Kessler MR (2010) Self-healing polymers and composites. Int Mater Rev 55 (6):317–346
20. Toohey KS, Sottos NR et al (2007) Self-healing materials with microvascular networks. Nat Mat 6:581–585
21. Wu DY, Meure S et al (2008) Self-healing polymeric materials: a review of recent developments. Prog Polym Sci. doi:10.1016/j.progpolymsci.2008.02.001
22. Binder WH, Bernstorff S et al (2005) Tunable materials from hydrogen-bonded pseudo block copolymers. Adv Mater 17:2824–2828
23. Diesendruck CE, Sottos NR (2015) Biomimetic self-healing. Angew Chem Int Ed 54:10428–10447
24. Wang HP, Yuan YC et al (2010) Self-healing of thermoplastics via living polymerization. Macromolecules 43:595–598
25. Yao L, Rong MZ (2011) Self-healing of thermoplastics via reversible addition—fragmentation chain transfer polymerization. J Mater Chem 21:9060–9065

26. Moad G, Rizzardo E et al (2008) Toward living radical polymerization. Acc Chem Res 41 (9):1133–1142
27. Zhu DY, Wetzel B (2013) Thermo-molded self-healing thermoplastics containing multilayer microreactors. J Mater Chem A 1:7191–7198
28. Carneiro J, Tedim J et al (2012) Chitosan-based self-healing protective coatings doped with cerium nitrate for corrosion protection of aluminum alloy 2024. Prog Org Coat. doi:10.1016/j.porgcoat.2012.02.012
29. Huang L, Yi N et al (2013) Multichannel and repeatable self-healing of mechanical enhanced graphene-thermoplastic polyurethane composites. Adv Mater 25:2224–2228
30. Colquhoun HM (2012) Materials that heal themselves. Nat Chem 4:435–436
31. Takeda K, Tanahashi M (2003) Self-repairing mechanism of plastics. Sci Technol Adv Mater 4:435–444
32. Trask RS, Williams HR et al (2007) Self-healing polymer composites: mimicking nature to enhance performance. Bioinsp Biomim 2:P1–P9
33. Sottos NR, Moore JS (2011) Spot-on healing. Nature 472:299–300 (Research news and views)

Molecular Design Approaches to Self-healing Materials from Polymer and its Nanocomposites

Jojo P. Joseph, Ashmeet Singh and Asish Pal

Abstract Recent years have seen an exponential growth in research activities on self-healing materials, with increasing number of research group being involved and new concepts being explored. These mendable materials belong to a class of stimuli-responsive materials that are designed to regain the functionality of the material once it is lost. In this chapter, we stress on the systematic understanding of these functional materials with respect to their mode of interactions, both covalent and non-covalent. We summarize the latest approaches to design self-healing systems, gathering different synthetic strategies and concepts and analyzing the main mechanisms for their functional behaviors. Based on the structural and functional units, we relate to variable healing properties of the materials and potent wider range of applications in designing protective coating, shape memory polymer, adhesives and self-healing for engineering and medical aspects.

Keywords Autonomic · Dynamic covalent chemistry · Graphene · Photodimerization · Nanoclay · Shape memory · Adhesion

Contents

J.P. Joseph · A. Singh · A. Pal (✉)
Institute of Nano Science and Technology,
SAS Nagar, Punjab 160062, India
e-mail: apal@inst.ac.in

D. Ponnamma et al. (eds.), *Smart Polymer Nanocomposites*,
Springer Series on Polymer and Composite Materials,
DOI 10.1007/978-3-319-50424-7_7

1 Introduction

Smart materials with the capability to repair mechanical damage over its duration are called self-healing materials [1]. The innate ability of living systems to self-rectify the damage caused by injuries inspires the concept of the aforementioned materials. Self-healing ability is highly desired for improving reliability for synthetic materials in view of lifetime and safety [2]. With many interesting examples of self-healing phenomenon in nature, translation of the living self-healing mechanism to engineered synthetic materials emerges as a greatest challenge for the material and organic chemists [3–5]. Fractures due to mechanical distortion, chemical corrosion and irradiation effects cause chemical bond dissociation and damages at the micro- and mesoscale structure of materials [6]. This normally leads to the formation of microcracks or microcavities which eventually can cause macroscale damage. Self-healing processes at the molecular dimension can suppress the escalation of further bond dissociation. Hence, the recently developed self-healing systems involve interactions at the molecular level with knowledge about the chemistry of the processes involving covalent (irreversible), non-covalent (reversible) bond formation, etc. Reversible covalent and non-covalent interactions are becoming increasingly significant due to their capability to heal damage repeatedly at the same spot (e.g., metal–ligand interactions, π–π interactions, ionic interactions, multiple hydrogen bonding interactions and dynamic covalent interactions). Thus, the current emphasis of self-healing material research dwells on the design of multifunctional materials that have the inherent capability to restore properties such as mechanical strength, fracture, conductivity and toughness that were disrupted due to damages caused by aforesaid effects [7].

2 Classifications

2.1 Autonomic and Non-autonomic Self-healing Systems

Generally, the self-healing materials are categorized as autonomic and non-autonomic on the basis of the essential chemistry of action. In autonomic

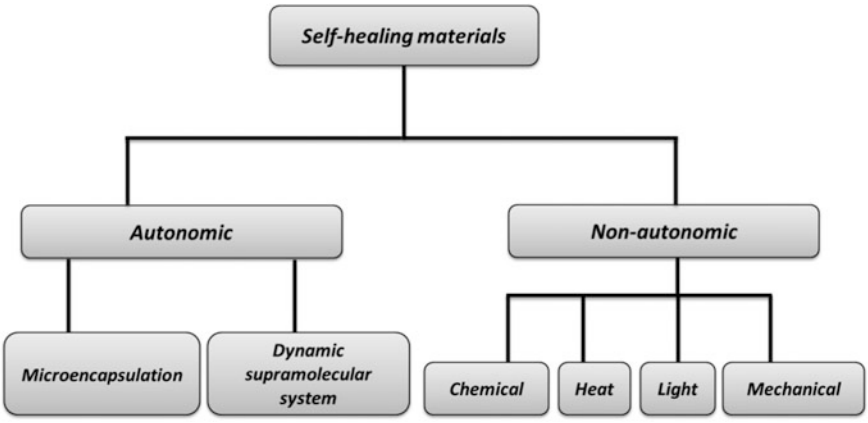

Fig. 1 Classification of self-healing materials on the basis of the chemistry involved in self-healing action [1]. Copyright 2015. Reproduced with permission from Elsevier Ltd

self-healing systems, automatic release of the harnessed chemical potential results in the healing of the damage whereas involvement of external stimuli heals the damage in non-autonomic self-healing systems. Heat [8], chemical environment [9], light [10] and mechanical forces [11] are common stimuli used in non-autonomic self-healing. In a detailed review, the mechanism behind autonomic and non-autonomic self-healing has been discussed by Williams et al. [12]. The autonomic self-healing system utilizes a microencapsulated healing agent and catalyst that are disseminated within a polymer matrix. The mechanism includes the rupture of the embedded microcapsules mediated by the propagation of the crack to eventually release the healing agent that is subsequently polymerized with or without the aid of catalyst [13, 14]. In some cases, dynamic supramolecular system shows autonomic self-healing action without external stimuli (Fig. 1). The non-autonomic self-healing exploits external stimuli-mediated chemistry based on either dynamic covalent bond or non-covalent interactions [15–17].

2.2 *Extrinsic and Intrinsic Self-healing Systems*

The self-healing material can also be classified into extrinsic and intrinsic based on the mechanism employed in the repair of the damage. Table 1 illustrates the key differences between them. Extrinsic self-healing system requires external healing agents, either encapsulated in microcapsule or embedded in matrix network, and the healing process is initiated in autonomic manner by the damage caused to the microcapsule or vascular network. The capsules or networks are made of polymer such as polyurethane (PU), poly(urea-formaldehyde) (PUF). However, there are also some shortcomings of the microcapsule-mediated extrinsic self-healing

Table 1 Salient features of extrinsic and intrinsic self-healing materials

Parameters	Extrinsic	Intrinsic
Healing system	An external healing agent dispersed in capsules or vascular networks	Non-covalent chemistry or dynamic covalent chemistry
Mechanism	Healing agent and a catalyst	Reformation of chemical bonds
Initiation	Triggered by external/internal damage/rupture	Triggered by external stimuli, e.g., pH change, light, temperature, pressure
Drawbacks	Expensive catalysts Multiple healing is not possible	Multiple healing is possible

approach as multiple times healing is not possible and catalysts are usually expensive. On the contrary, intrinsic self-healing system utilizes non-covalent interactions or dynamic covalent chemistry. The non-covalent interactions employed are hydrogen bonding, host–guest complex, metal–ligand interaction, etc. The reversible dynamic covalent chemistry (DCC) involve Diels–Alder reaction, imine chemistry, radical exchange and transesterification, etc. The healing mechanism may be triggered by some external stimuli. Due to the reversible nature of the supramolecular interactions or DCC employed in the intrinsic self-healing system, healing of damaged area is possible multiple times. Thus, the current research goal is focused toward designing next-generation materials capable of exhibiting intrinsic self-healing behavior.

2.3 Dynamic Polymer and Polymer Composite-Based Self-healing Systems

In the last decade, the science community has observed several publications in the self-healing field, showcasing synthesis, chemistry and applications of self-healing materials from polymers. Polymers gained significant attraction, due to the large variety of chemistry and healing mechanism available as compared to other group of materials. The development of novel self-healing polymers in the recent years has significantly improved the lifespan, efficiency and environmental influence of synthetic materials. Generally, self-healing systems are categorized into dynamic polymer and polymer composite on the basis of the type of constituents (Table 2)

Table 2 Salient features of dynamic polymer and polymer composite-based self-healing

Parameters	Dynamic polymer	Polymer composite
Mechanism	Reactive groups to expedite self-healing	Embedded healing microcapsule or nanomaterial-based composites
Polymer fate after self-healing	Change in original chemical structure	No change in original chemical structure
Efficiency	Can heal small volume cracks	Can heal large volume cracks

[18]. Dynamic polymer system employs the thermodynamics of self-healing reaction such as covalent bond formation, supramolecular chemistry, while self-healing polymer composite approach involves reactive embedded healing agents in microcapsules and incorporation of nanomaterials such as nanoclays, nanotubes and nanoparticles in the polymer matrices.

3 Designing Strategies for Self-healing Based on Interaction

In this section, we will discuss different strategies to design self-healing materials. We have categorized and discussed the strategies into different sections under the heading of non-covalent interaction, covalent interaction, dynamic covalent interactions and polymer nanocomposites.

3.1 Self-healing via Non-covalent Interactions

The design of self-healing polymers via non-covalent interactions is an interesting concept as it renders thermodynamically stable polymers with reversibility and tunability. The supramolecular system can be tuned by changing reaction conditions (e.g., temperature, polarity of solvent, concentration and pH) or by external stimulations. It utilizes reversible cooperative non-covalent interactions to generate novel materials with distinctive properties and functionalities. These interactions include hydrogen bonding, host–guest complex, metal–ligand complex, hydrophobic, π–π and ionic interactions.

3.1.1 Hydrogen Bonding Interactions

In natural plant and animal systems, hydrogen bonding interaction forms an important part of self-repair and inspires the material chemist to mimic this mechanism of self-healing in synthetic materials. Recently, the strategy to incorporate strong and reversible hydrogen bonding motifs into the polymeric structure to generate self-healing polymer has gained a lot of significance. Several studies have been reported demonstrating the design of self-healing materials exploiting some of the hydrogen bond-forming functionalities like ureido-pyrimidine [19], catechol-quinone moiety [20]. As shown in Fig. 2, a series of random copolymers were synthesized by Zeng et al. employing *n*-butyl acrylate (BA) backbones containing hydrogen bonding units of 2-ureido-4[1H]-pyrimidinone (UPy) by means of living polymerization method such as atom transfer radical polymerization (ATRP) [19].

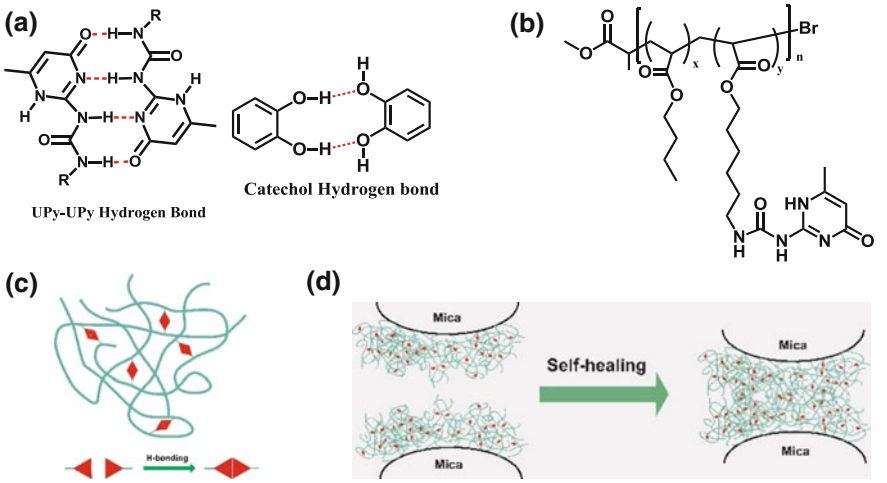

Fig. 2 **a** Hydrogen bonding interaction in UPy dimers and catechol dimers, **b** chemical structure of poly(BA-UPy) copolymer, **c** interchain hydrogen bonding among UPy groups and **d** self-healing mechanisms mediated by multiple hydrogen bonding polymers coated on mica surface [19]. Copyright 2014. Reproduced with permission from WILEY-VCH Verlag GmbH & Co. KGaA, Weinheim

Sijbesma et al. showed formation of UPy dimer mediated by strong quadruple hydrogen bonding for designing highly thermally responsive supramolecular polymers [21]. The poly(*n*-butyl acrylate) polymer with UPy units (PBA-UPy) was spin-coated on mica substrates to produce a uniform smooth polymer film with thickness of 100 nm. The surface energies of the UPy-grafted copolymers was studied using contact angle measurements and was found to be 45–56 mJ m^{-2}, which indicates a higher surface energy than that of poly(*n*-butyl-acrylate) (31–34 mJ m^{-2}). This is due to the strong intermolecular interaction among the strong hydrogen bonding UPy dimers. The adhesion properties of PBA-UPy copolymers were contributed by the surface density of the polymer chains that can traverse across the topological interface and the bulk viscoelasticity of the polymers and were sensitive to humidity and temperature. The UPy functional groups could significantly increase the polymer adhesion property due to multiple hydrogen bonding interaction at the interface. Thus, fractured PBA-UPy copolymer films can fully recover to 100% of their self-adhesion strength in about 2 days under almost zero external load.

3.1.2 Host–Guest Chemistry

Some highly non-specific interactions such as hydrogen bonding, ionic interactions may lead to passivized self-healing. This disadvantage prompted improvised strategy to design highly distinct and dynamic host–guest interactions that involve

binding of different guest molecules with cyclic macromolecules such as cyclodextrins (CD), crown ethers, calix[*n*]arenes, pillar[*n*]arenes and cucurbit[*n*]urils [22]. Consequently, these interactions have a significant role in the design of self-healing polymers through the interplay of supramolecular chemistry with a polymer. This chemistry has been utilized for designing self-healing materials employing various host–guest moieties, e.g., cyclodextrin-ferrocene [23], cyclodextrin-adamantane [24], crown ether-based cryptands [25], cucurbit[*n*]urils [26], calix[*n*]arenes [27] and pillar[*n*]arenes [28], grafted on polymer chains. Reversible electrochemically controlled formation of the inclusion complex of ferrocene (Fc) with the hydrophobic cavities of cyclodextrins is a unique example of this type (Fig. 3a).

The oxidation of ferrocene to charged group (Fc+) causes the dissociation of CD-Fc complexes rapidly, while reduction to neutral Fc species results reformation of the complex. Chuo et al. reported an electrically driven self-healing polymeric material based on ferrocene-grafted poly(glycidyl methacrylate) (PGMA-Fc) and a bifunctional β-cyclodextrin derivative (bis-CD) (Fig. 3b) [23]. Crosslinked PGMA-Fc/CD network was coated on a copper surface and was cut with a sharp knife to give a knife print of 80 µm in width which got reduced to 40 µm with an electrical treatment of 1.5 V × 6 for 24 h. Restricted chain mobility reduced the efficiency of healing process, that was further improved with thermal treatment at 85 °C for 24 h to the sample after electrochemical healing procedure (Fig. 4). Also, only annealing the sample without the redox stimuli did not show any healing

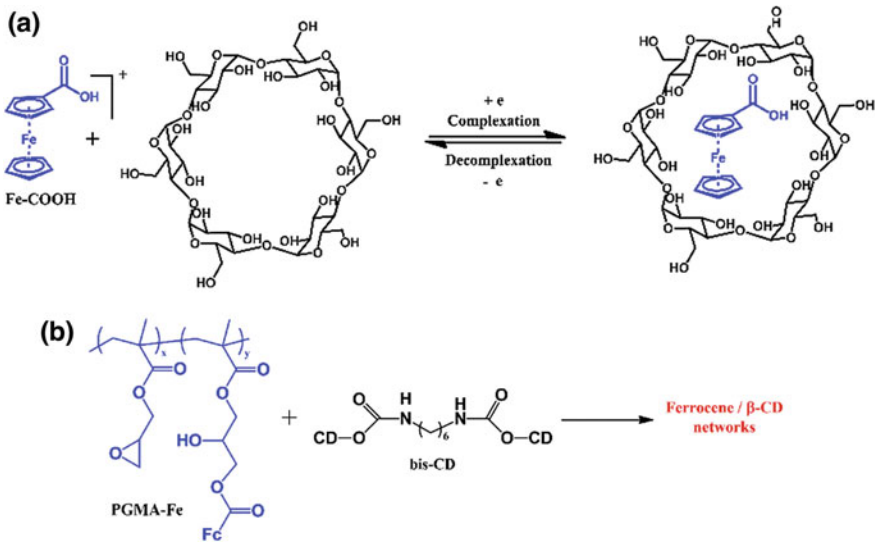

Fig. 3 **a** Redox-mediated reversible host–guest complex formation between β-cyclodextrins (CD) with ferrocene (Fc), **b** copolymer of Fc-grafted PGMA chains (PGMA-Fc) and difunctional β-cyclodextrins compound (bis-CD) for the construction of redox-responsive intrinsic self-healing material network [23]. Copyright 2013. Reproduced with permission from Wiley Periodicals, Inc

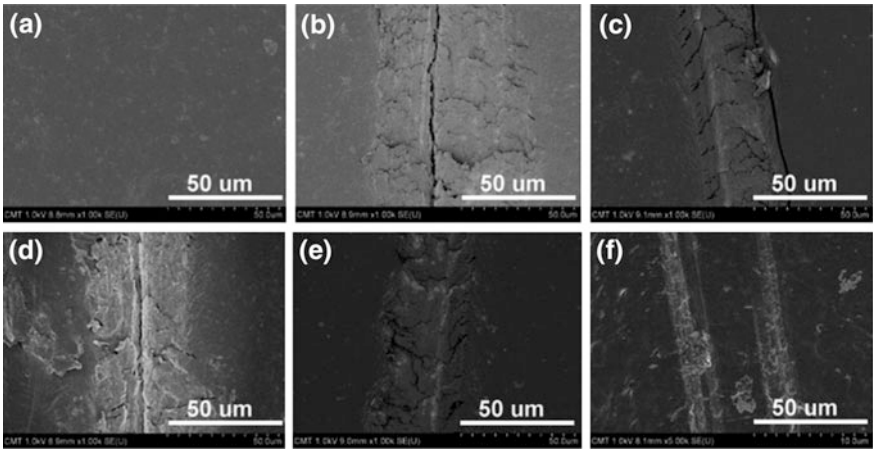

Fig. 4 SEM images demonstrating the self-healing behavior for crosslinked polymer of PGMA-Fc/CD. **a** Original sample surface before damage, **b** sample surface after cutting with knife, **c–f** electrochemically driven self-healed sample surface with different treatments: **c** 1.5 V × 6 for 24 h and at room temperature for 24 h, **d** 9 V × 1 for 24 h and at room temperature for 24 h, **e** 9 V × 1 for 24 h and at 85 °C for 24 h, and **f** 9 V × 1 for 24 h and at 85 °C for 24 h on wetted sample [23]. Copyright 2013. Reproduced with Permission from Wiley Periodicals, Inc

behavior with the sample. Thus, redox-triggered decomplexation reaction of the Fc/CD complexes was inevitable for the efficiency of self-healing behavior. Moreover, sample wetting along with increased electrical conductivity led to further improvement in the efficiency. Potentially, this type of material could serve as an excellent healing agent for commercial painting products.

3.2 Self-healing via Covalent Interactions

3.2.1 Thermosetting Polymers

Preparation of endurable microcapsules filled with a reactive material as part of a thermosetting polymeric matrix is an interesting approach explored in self-healing technology. A thermosetting polymer (also known as a thermoset) is a prepolymer material, which on curing with external stimuli, get transformed from soft malleable state to hardened polymeric network. The preparations of microcapsules are realized by employing different methods that adopts self-assembly, polymerization process, templated synthesis and phase separation. These different methods are specific and possess several advantages according to the intended applications. Thermosetting polymeric matrix, in which the microencapsulated reactive chemicals and catalysts are embedded, remains a very common strategy for several self-healing applications like polymeric coatings, adhesives. The healing process is

initiated by stimulation by an external agent and assisted by a catalyst. However, high cost of catalytic systems restricts the strategy within small-scale self-healing applications. Thus, recent research is driven toward introducing strategies to employ autonomic self-healing in thermosetting systems by removing the catalyst. Several thermosetting polymeric formulations had been realized for self-healing applications activated via mechanical, heat, electrical, light or other external stimuli rather than using catalytic systems [29, 30]. Recently, a concept of self-healing in an aqueous or moisture sensitive environment was reported by Barbara Di Credico et al. They demonstrated a catalyst-free thermosetting self-healing systems consisting of microcapsules filled with isocyanides [31]. They designed microcapsules incorporating liquid isophorone diisocyanate (IPDI) with different polymeric shells, i.e., polyurethane (PUT), poly(urea-formaldehyde (PUF) and bilayer polyurethane/poly(urea-formaldehyde) (PU/PUF) using oil-in-water emulsion and distributed in epoxy matrices.

The liquid IPDI was preserved within the double-walled shell that consists of a durable protection layer of PUF around the soft sticky surface layer of PU. Desmodur L-75 prepolymer was reacted with 1,4-butan-diol to create PU shell (Fig. 5a) with Gum Arabic as emulsifier in the encapsulation process followed by interfacial polymerization with formaldehyde to produce PU/PUF capsules. The microcapsules were chemically characterized by FTIR spectroscopy which showed the characterized bands of the corresponding chemical constituents. The TGA and DSC curves of the microcapsules confirmed their excellent thermal stability that is crucial for further applications in functional coating. The self-healing study was conducted on glass panel coated with epoxy resin matrix that is loaded with 15 wt% of microencapsulated catalyst-free healing agent (Fig. 5b). A scratch-induced crack in the coated panel led to rupture of the microcapsule and release of IPDI. Complete disappearance of the scratched area after 48 h immersion in aqueous solution confirmed self-healing ability by comparing damaged and healed coated glass samples. This precise and versatile method of preparation microcapsules can provide promising applications in storage and coating.

3.2.2 Thermoplastic Polymers

Nearly all strategies toward self-healing materials demand stimuli such as heat, light, healing agents, plasticizer or solvent for initiating the process. Nowadays, an increasing number of research are being directed toward designing thermoplastic polymer materials that show intrinsic self-healing capability. Thermoplastic elastomer consists of a soft rubbery matrix embedded with block or brush copolymers as hard crystalline domain. Thus, combination of high elastic modulus and toughness with spontaneous healing capability is a unique feature for supramolecular thermoplastic elastomers (TPEs). Utilizing a multiphase morphology that encompasses the elasticity of rubbers with stiffness of thermoplastic

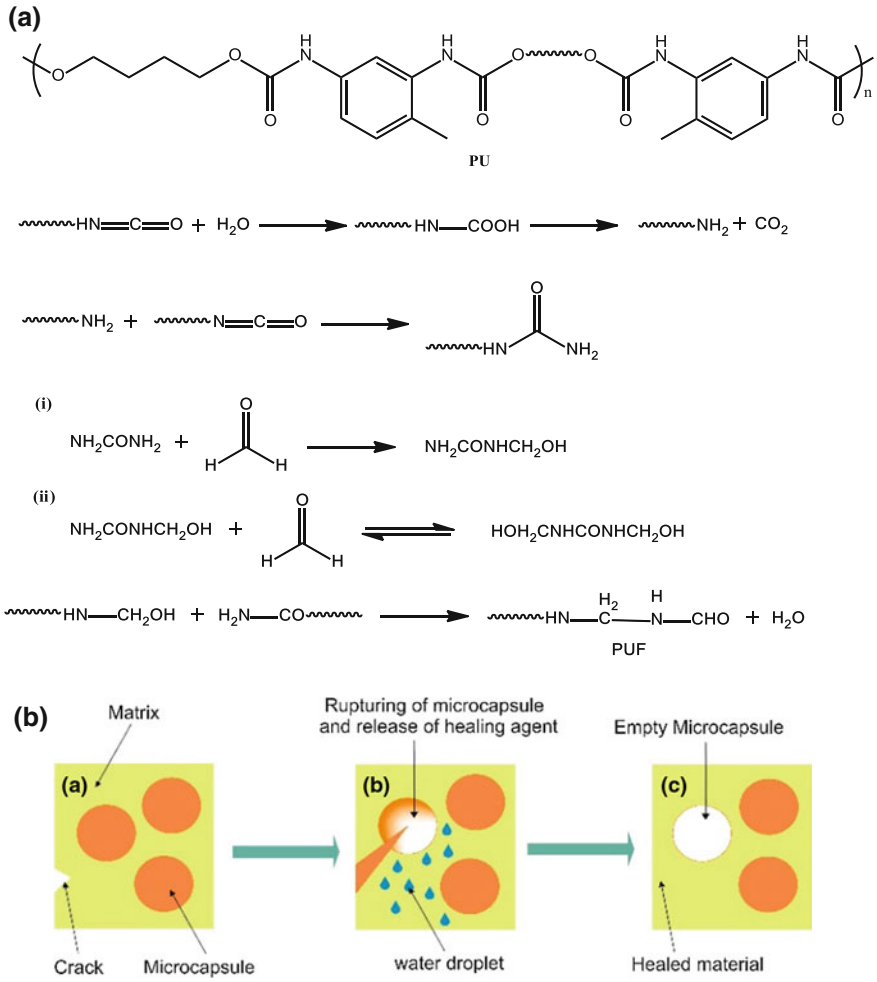

Fig. 5 **a** Reactions to synthesize PU and PU/PUF polymer for microcapsule shell formation, **b** demonstration of autonomic self-healing process mediated by the microcapsules [31]. Copyright 2013. Reproduced with permission from Elsevier Ltd

polymers widens its scope to engineering applications. Till date the multiphase morphology has been recognized through employment of various strategies for fusion of thermoplastic component into thermoset background with supramolecular brush polymers [32], diblock copolymers [33], etc. Zhibin Guan et al. demonstrated a novel multiphase design of a thermoplastic elastomer system that incorporates rigidity and spontaneous healing [32]. As shown in Fig. 6, a dynamic healing motif was integrated into the hard–soft multiphase thermoplastic elastomer. Self-healing

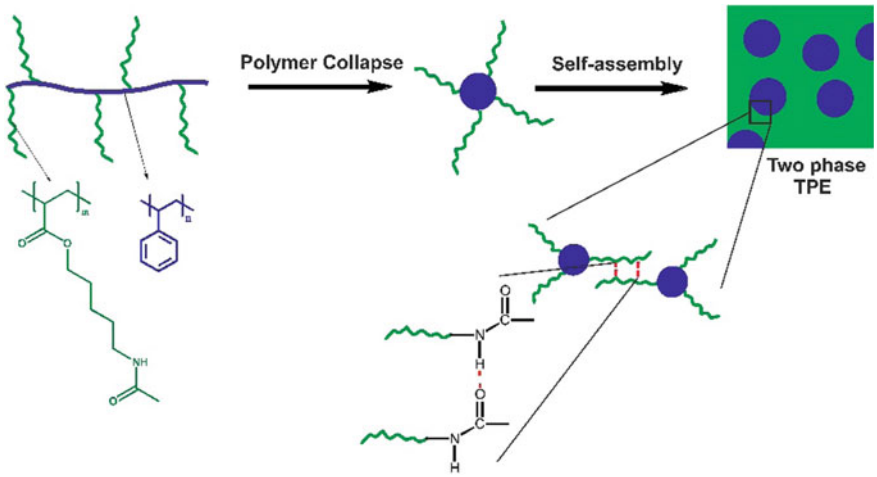

Fig. 6 Design of multiphase thermoplastic elastomeric self-healing brush polymer system. Polymer with polystyrene backbone and polyacrylate amide brush collapses into core-shell nanostructures that self-assemble into a biphasic morphology of thermoplastic elastomer. The dynamic hydrogen bonds among the amides form cluster of hydrogen bonding interactions to result in a *molecular velcro* [32]. Copyright 2012. Reproduced with permission from Nature Publishing Group

for TPEs was mediated by non-covalent supramolecular matrix in the soft segments at temperatures below the glass transition (T_g) of the hard phase. Polystyrene backbone (hard phase) and polyacrylate amide (PA-amide) (soft phase) were used to synthesize the multiphasic brush polymers via living polymerization such as atom transfer radical polymerization (ATRP). Polymers had varied polystyrene weight fraction, the brush length and functional brush density. They collapsed to form a core–shell nanostructure having a hard polystyrene core and a soft PA-amide shell on treatment with a polar solvent. Reversible hydrogen bonding interaction among the PA-amide brushes results in dynamic microphase-separated nanostructure with reduced glass transition temperature (T_g). The mechanical stability of the brush polymers was at par with the classical elastomers which was confirmed through static stress–strain and creep recovery test which displayed self-healing behavior at room temperature in the absence of any external agents or stimuli. Thus, a multiphase design integrates the mechanical properties of thermoplastic polymer (polystyrene) with thermoset (epoxy) and facilitates autonomic self-healing.

In another multiphase TPE design by Guan's group, a covalent block copolymer system of poly(*n*-butyl acrylate) and polystyrene was compared to supramolecular triblock copolymer with partial grafting of 2-ureido-4-pyrimidinone (UPy) as hydrogen bonding group (Fig. 7) [33]. While for the covalent TPE, mechanical breakage results in irreversible damage due to breakage of covalent bond, the combination of thermoplastic phase with supramolecular motif endows the polymer with interesting dynamics and self-healing capability as evident on stress–strain analysis.

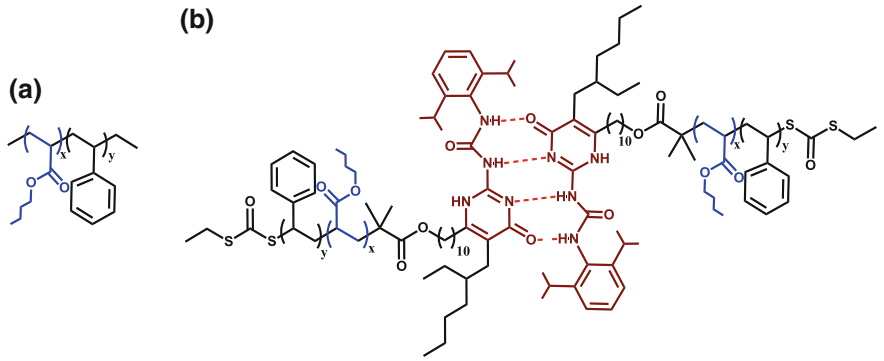

Fig. 7 Design of **a** conventional PS-PBA block copolymers and **b** supramolecular block copolymers PS-PBA-UPy to form a microphase-separated thermoplastic elastomer [33]. Copyright 2012. Reproduced with permission from WILEY-VCH Verlag GmbH & Co. KGaA, Weinheim

3.2.3 Metallopolymer

Inspired from the natural healing processes that take place within mussel byssus threads, metal complexation is explored as a prominent crosslinking approach for the assembly of polymeric materials. Owing to the reversibility, high stability and rates of formation of the coordination complexes, this strategy can be used to synthesize polymeric structures accustomed with stimulated self-assembly, self-healing capacity and mechanical tunability. Some of the metal–ligand complexes used for designing self-healing materials include catechol-iron [34], terpyridine-iron complexes [35]. Schubert's group demonstrated a crosslinked metallopolymeric system based on iron–bis-terpyridine (metal–ligand) complex chemistry [35]. The authors synthesized different polymers from terpyridine methacrylate monomers (6-(2, 2′:6′, 2″-terpyridin-4′-yloxy)-hexyl methacrylate) copolymerized with three different methacrylate monomers (i.e., methyl methacrylate, butyl methacrylate and lauryl methacrylate) via living polymerization technique. This approach renders control over the loading of crosslinking units and the resulting thermal, mechanical behavior of the networks. As shown in Fig. 8, the authors crosslinked the copolymers containing the terpyridine moiety with iron (II) sulfate resulting in the metallopolymers. The crosslinking mediated by metal–ligand interactions resulted in gel formation which on drying led to the formation of a polymer film. Differential scanning calorimetry (DSC) study showed melting temperature of 250 °C. The healing behavior was examined after making a small cut into the polymer film followed by performing heating cycle.

Based on the nature of copolymer present, the polymers showed different self-healing ability (Table 3). Thus, it was revealed that the polymer (**CP1**) having methyl methacrylate as comonomer manifested no healing behavior at 100 °C, while the copolymer network (**CP2**) having butyl methacrylate as comonomer repaired smaller scratches (length 180 μm; width 10 μm) over a short time period

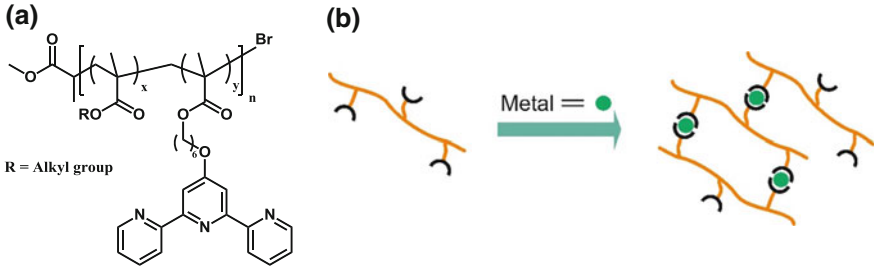

Fig. 8 **a** Chemical structure of copolymer having terpyridine moiety, a potential binding site of the Fe(II) ion, **b** metal ion-mediated formation of crosslinked polymer network [35]. Copyright 2012. Reproduced with permission from WILEY-VCH Verlag GmbH & Co. KGaA, Weinheim

Table 3 Summary of the self-healing behavior exhibited by the metallopolymer

Polymers	Alkyl groups	Glass transition temperature of non-crosslinked polymer (°C)	Healing temperature (°C)	Healed crack width (μm)	Healed crack length (μm)
CP1	Methyl	74	No healing	No healing	No healing
CP2	Butyl	−2	80	50	180
CP3	Lauryl	−65	80	35	250

Reproduced with permission from Ref. [35]. Copyright © 2012 WILEY-VCH Verlag GmbH & Co. KGaA, Weinheim

of 40 min at 100 °C. Furthermore, the copolymer (**CP3**) showed healing of larger and wider scratches that was attributed to the superior pliability of the polymer backbone due to the presence of lauryl methacrylate as comonomer.

The sustainability of the dark violet color of iron(II)-bis-terpyridine complex even during heating at 100 °C proved that metal–ligand complexation may not have significant impact on the self-healing behavior. Owing to this high stability of the ionic metal complexes, endorsed by Raman spectroscopic studies, the self-healing behavior was ascribed to generation of ionic clusters. From certain previous studies on ionomers by SAXS (small-angle X-ray scattering), it was confirmed that certain energy was required for attaining sufficient mobility/flexibility leading to reformation of ionic clusters. Thus, crosslinked metallopolymer networks with highlighted self-healing behavior were delineated by the authors and the mechanism behind the direct correlation of the self-repair with mobility/flexibility of the copolymer backbone was also unveiled.

3.3 Self-healing via Dynamic Covalent Chemistry

For organic and polymer chemists, dynamic covalent chemistry (DCC) is an increasingly interesting approach for synthesizing novel polymer materials eliciting

self-healing behavior. Dynamic covalent bond retains the intrinsic fundamental covalent nature and is capable of dissociating and reforming in the presence of external stimuli like pH, temperature, light, chemical agents. Flexible polymeric architectures synthesized through dynamic covalent chemistry provides an approach that is thermodynamically controlled and is different from kinetically controlled merely covalent approach. The following section describes the utilization of various dynamic covalent strategies in the synthesis of polymeric architectures that exhibit self-healing behavior.

3.3.1 Diels–Alder Reaction

One of the very adaptable and flexible [4+2]-cycloadditions is Diels–Alder (DA) reaction, which has characteristic dynamic equilibrium between the Diels–Alder and the retro Diels–Alder reaction. The equilibrium constant of this reaction between a diene and dienophile can be controlled thermally, which is applicable in material and polymer science to achieve novel polymeric architectures with intrinsic self-healing behavior. Diene-dienophile combinations, e.g., furan-maleimide [36], anthracene-maleimide [37] and cyclopentadiene-dicyclopentadiene moieties [38], have been employed in designing self-healing materials. Schubert et al. synthesized terpolymers functionalized with furan and maleimide groups and observed the effect of different polar and nonpolar comonomers on self-healing performance on the basis of DA reversible crosslinking reaction [36]. Terpolymers from maleimide methacrylates (MIMA1 and MIMA2), furan methacrylate (FMA) and different polar and nonpolar comonomers were designed (Fig. 9), which were capable of forming DA crosslinking via [4+2]-cycloaddition between furan and maleimide units. Hydroxyethyl methacrylate (HEMA), dimethylaminoethyl methacrylate (DMAEMA) and 2-(hydroxyethoxy) ethyl methacrylate (DEGMA) were used as polar comonomers, and butyl methacrylate (BMA) was employed as nonpolar comonomers. Synthesis of several terpolymers (**P1**–**P4**) was conducted by living

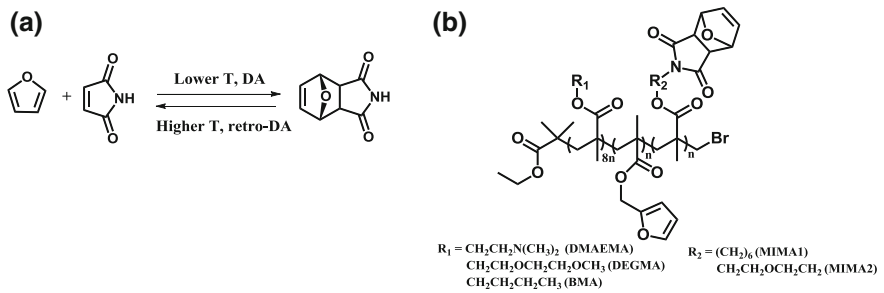

Fig. 9 **a** Classical DA and retro DA reactions between furan and maleimide moieties and **b** chemical structure of the terpolymers derived from maleimide methacrylate monomers copolymerized with different polar and nonpolar comonomers [36]. Copyright 2015. Reproduced with permission from Elsevier Ltd

Table 4 Composition, reaction conditions, SEC calculations, glass transition temperature and temperature of the retro DA for **P1**–**P4** polymers [36]

Polymer	Comonomer	Diene-MA	Dienophile-MA	M_n (SEC) [g/mol]	T_g (°C)	T_{rDA} (°C)
P1	BMA	FMA	MIMA1	4910	50	125–180
P2	BMA	FMA	MIMA2	4330	40	115–180
P3	DMAEMA	FMA	MIMA3	4440	35	120–180
P4	DEGMA	FMA	MIMA3	3100	−10	115–160

ATRP with CuBr (catalyst), HMTETA-1,1,4,7,10,10-hexamethyltriethylene tetramine (ligand) and ethyl-2-bromoisobutyrate (initiator). The terpolymers with different maleimide methacrylate monomers, polar and nonpolar comonomers, molecular weight obtained from SEC measurements, are shown in Table 4.

The DA reactions between furan and maleimide suffer from a drawback of using high temperature (120–180 °C) for retro DA. The authors tried different chain lengths, polar comonomers for decreasing the temperature of the reaction along with the variation of the maleimide methacrylate copolymer that enhanced the flexibility of the system to exhibit self-healing behavior at room temperature. With the information from DSC and TGA studies, self-healing behavior of the polymers was investigated by annealing process monitored with a microscope fitted with a camera. Copolymers **P1** and **P2** having BMA as comonomer and MIMA1, MIMA2 with the longer linker exhibited good self-healing behaviors.

Copolymer **P1** showed complete healing of scratch in a millimeter range at 140 °C after 3 min and also at 110 °C after 3 h. The self-healing studies of copolymer **P2** exhibited complete healing of the scratch at 80 °C after 48 h and at 140 °C after 5 min. **P2** and **P3** showed good self-healing properties compared on the basis of the healed scratch size and healing temperature. **P4** was displayed complete healing at 100 °C after 2 h for smaller scratches and after 4 h for the larger ones. Among all the synthesized polymers, the copolymer **P4** exhibited best self-healing behavior due to higher flexibility of the linker unit in addition to DEGMA as the comonomer leading to reduction of healing temperature. This self-healing system demonstrates the challenges for healing mechanism due to mechanical stiffness and film defects which hindered reflow of damaged parts for reversible reaction. Enhanced flexibility, nature of the linker unit had shown a profound impact on healing behavior as compared to polarity of the comonomer used in the polymer chain.

3.3.2 Thiol–Disulfide Chemistry

Thiol–disulfide exchange chemistry is one of the most significantly studied and utilized reactions in the area of dynamic covalent applications. In nature, this chemistry is utilized for making covalent connections in many biomolecules, especially proteins and small peptides. Therefore, researcher started utilizing this chemistry for the design and synthesis of novel self-healing materials.

Matyjaszewski et al. demonstrated controlled synthesis of star polymers containing reversible covalent disulfide bond through living ATRP [39]. As shown in Fig. 10a, poly(*n*-butyl acrylate)-anchored star polymers were synthesized from crosslinked cores made of poly(ethylene glycol acrylate) by chain extension ATRP and in the following step, the peripheral branch was further crosslinked with bis (2-methacryloyloxyethyl disulfide) (DSDMA) introducing disulfide reversible linkages at the branch peripheries to form crosslinked networks of star polymers. The peripheral SS linkages can be employed to introduce self-healing behavior utilizing reversible, dynamic covalent crosslinking mediated by thiol–disulfide redox exchange reactions (Fig. 10b). Crosslinked star polymer with disulfide was reduced to solutions of SH-functionalized polymers, and films were prepared by depositing it onto silicon wafers. Oxidative crosslinking of the films in the presence of an oxidant (e.g., I_2 or $FeCl_3$) made it insoluble in organic solvents such as $CHCl_3$ or THF, resulting in the crosslinked polymer gel. AFM tip was used for inducing scratches of millimeter to nanometer range on the film and also for simple characterization of topomechanical properties that help in assessing the degree of healing in the film.

Surface scratches range from nanometers to micrometers micromachined by commercial silicon probes in two different modes, i.e., tapping mode scanning and contact mode scanning. Scratch (0.4 μm wide and 17 nm deep) was formed by negative lift interleave tapping mode scanning on a 50-nm-thick crosslinked film with employed lift height and scan rate at 300 nm and 80 μm/s, respectively, and was monitored for healing by utilizing continuous tapping mode AFM imaging. The accessibility of the cut surfaces and bond reformation initiated the healing response and subsequently decreased the size of the cut area.

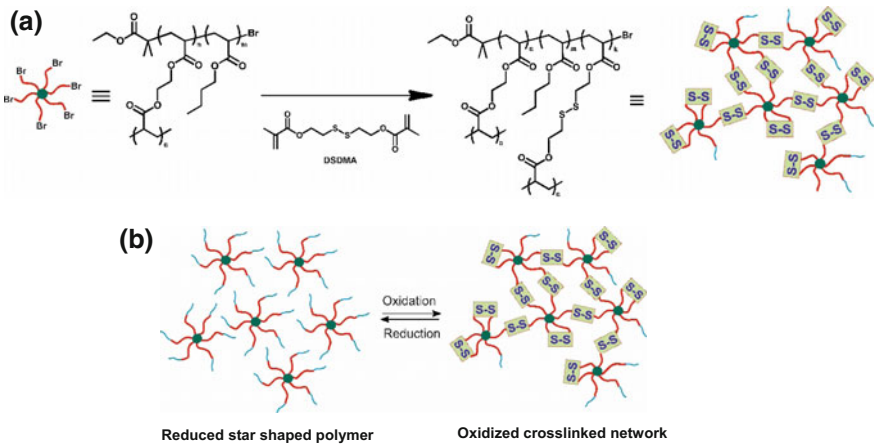

Fig. 10 **a** Strategy to design S–S-functionalized multi-arm polymer by living chain extension ATRP and **b** reduction to SH-functionalized star polymer and further oxidation to form permanently crosslinked polymer gel [39]. Copyright 2012. Reproduced with permission from American Chemical Society

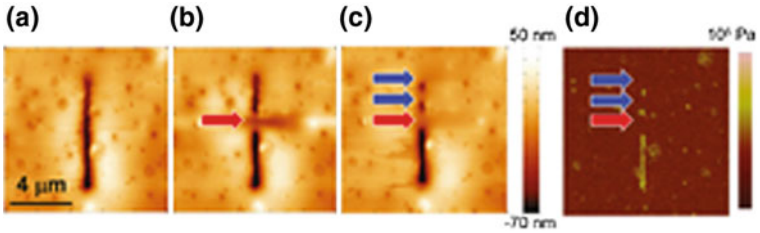

Fig. 11 Healing of the polymer film enhanced by AFM tip stroke with contact scanning mode: **a** original scratch, **b** after the first series of AFM tip strokes at the position indicated by a *red arrow* (+0.5 V), **c** after the second series of strokes at two positions indicated by *blue arrows* (0 V) and **d** HarmoniX tapping mode modulus map in a logarithmic scale [39]. Copyright 2012. Reprinted with permission from American Chemical Society

A gentle stroke was applied with the AFM tip under contact scanning mode in perpendicular direction to bring the two cut surfaces access each other. The results obtained as shown in Fig. 11 indicated that only stroked areas recovered the original smoothness of the original film following two series of AFM tip strokes, with deflections equal to +0.5 and 0 V respectively, HarmoniX tapping mode modulus mapping determines the extent of healing through effective monitoring of the mechanical properties of the resulting film. The moduli of repaired damaged areas were comparable with the intact area, indicating effective healing of the surfaces. Thus, the study envisaged the importance of grafted multi-arm polymeric architectures as a promising strategy for self-healing materials, highlighting the significance of low intrinsic viscosity and easy contact to functional groups.

3.3.3 Acylhydrazone Chemistry

The integration of acylhydrazones into polymeric materials can be envisaged as a bridge from supramolecular chemistry to adaptive chemistry that represents constitutional dynamic chemistry. This is because the acylhydrazone functionality combines both the supramolecular hydrogen bonding ability through the amide moiety and the molecular linkage ability as a result of the dynamic character of the imine bond. The overall imine chemistry approaches that attracted the attention of the scientific community for self-healing include motifs such as iminocarbohydrazides [40] and acylhydrazones [41]. Schubert's group reported self-healing behavior of a linear polymer covalently crosslinked with acylhydrazone moiety [41]. Acylhydrazone crosslinked copolymers were synthesized by copolymerization of acylhydrazone containing dimethacrylate monomer with triethyleneglycolmethyl ether methacrylate (TEGMEMA), 2-hydroxyethyl methacrylate (HEMA) and a 1:1 mixture of both (HEMA and TEGMEMA) as shown in Fig. 12 employing a radical polymerization procedure. The possibility to adjust the flexibility of the polymer backbone and the glass transition temperature (T_g) was studied by using different methacrylates as comonomer. Thus, the copolymer with TEGMEMA exhibited the

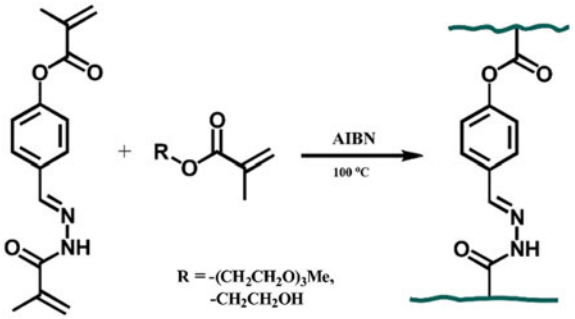

Fig. 12 Synthetic strategy toward acyl hydrazone crosslinked polymer via free radical polymerization [41]. Copyright 2015. Reproduced with permission from WILEY-VCH Verlag GmbH & Co. KGaA, Weinheim

Table 5 Composition and thermal properties of the crosslinked acylhydrazone polymers [41]

Crosslinked polymer	Acylhydrazone monomer	Comonomer	Acylhydrazone content (mol%)	Glass transition temperature (°C)	Decomposition temperature (°C)
AP1	M1	TEGMEMA	5	−33	289
AP2	M1	TEGMEMA/HEMA	10	45	303
AP3	M1	HEMA	10	101	321

Copyright 2015. Reproduced with permission from WILEY-VCH Verlag GmbH & Co. KGaA, Weinheim

lowest T_g (−33 °C) and the one with HEMA had shown the highest one (101 °C) as obtained from differential scanning calorimetry data (Table 5). Polymer films **AP1**–**AP3** obtained by performing polymerizations in bulk were investigated for their potential self-healing properties. Cut was made by a scalpel, and the damaged area was exposed to heating at a certain temperature to generate sufficient mobility for self-healing. The process was observed with an optical microscope. Copolymer **AP1** with TEGMEMA as comonomer and 5 mol% acylhydrazone content did not any self-healing. This can be ascribed to low acylhydrazone content in polymer film **AP1**. However, the expansion of the crack occurred on thermal treatment due to release of intrinsic stress of the polymer film. As delineated in Fig. 13a, the copolymer **AP2** with equal mixture of TEGMEMA and HEMA as comonomers and 10 mol% acylhydrazone content showed repair of cut as large as one centimeter length. The HEMA-based copolymer **(AP3)** on thermal process at 125 °C had shown repair of scratches of only smaller dimensions which was attributed to high T_g of the polymer.

The persistence of original structure of the polymer upon thermal treatment proved by temperature-dependent FTIR spectra and solid-state NMR experiments was an indication of exchange reaction as shown in Fig. 13b involved in the self-healing mechanism. Thus, the employment of methacrylate monomers along with other acylhydrazones may facilitate the refinement of self-healing properties such as the control of healing temperature, overseeing healing kinetics to the desired extent.

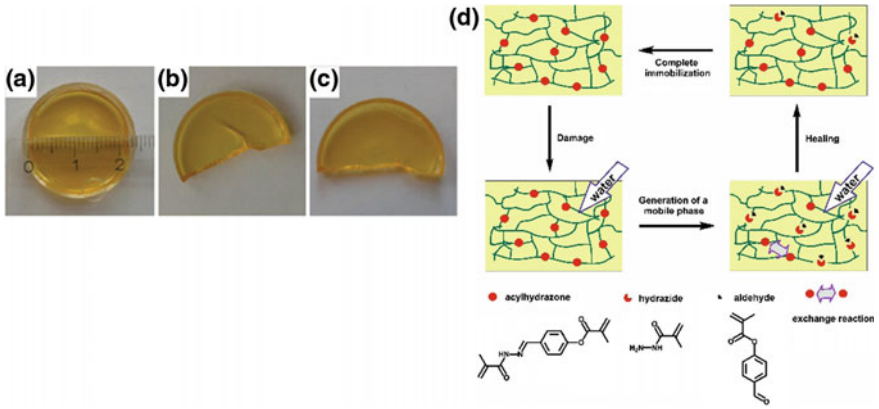

Fig. 13 Self-healing study of crosslinked polymer **AP2**: **a** polymer film, **b** scratch before heating and **c** healed scratch after annealing at 100 °C. **d** Schematic representation of self-healing mediated by reversible exchange reactions in acylhydrazones polymer [41]. Copyright 2015. Reproduced with permission from WILEY-VCH Verlag GmbH & Co. KGaA, Weinheim

3.3.4 Photodimerization

Photostimulated reversible cycloaddition is the most common type of dimerization reaction explored in the area of dynamic covalent chemistry. The molecules containing olefinic moieties, e.g., cinnamic acid, anthracene, thymine, coumarin, undergo dimerization reactions upon irradiation with longer ultraviolet (UV) light ($\lambda > 300$ nm) to produce cyclobutane adducts. However, reversibility of the adducts to the former monomer on exposure to shorter wavelength UV light makes this class of photosensitive polymers excellent candidate for designing self-healing materials with the advantages of reproducibility, affordability and environmental compatibility. Rudolf Faust et al. designed polyisobutylene (PIB)-based polymer network containing reversibly photocrosslinkable coumarin moieties and explored them for smart photovoltaic device coatings applications (Fig. 14) [42].

The photodimerization reaction of polymer films were performed by irradiating the samples with UVA ($\lambda_{max} = 365$ nm), while irradiation with UVC ($\lambda_{max} = 254$ nm) had resulted in the photocleavage. The change in the absorbance of the reactive coumarin moiety at 320 nm was monitored by UV-Vis spectroscopy. AFM was utilized for the study of self-healing behavior of photocrosslinked triarm star PIB network films. A range of cuts (from nm to μm) was micromachined using commercial AFM silica tips. Initial cut of 74 nm depth made in the crosslinked thin film of polymer was subjected to consecutive UVC and UVA irradiation for 5 min, which led to ~86% of healing as the depth of the cut diminished to 10 nm (Fig. 14iv). The depth of the cut again diminished to 5 nm on further exposure to UVC and UVA irradiation for 25 min. Further exploration of the sunlight-induced self-healing behavior of polymer film had given a healing efficiency that complied with the reported experiments with low-intensity UV lamp. Detailed examination of

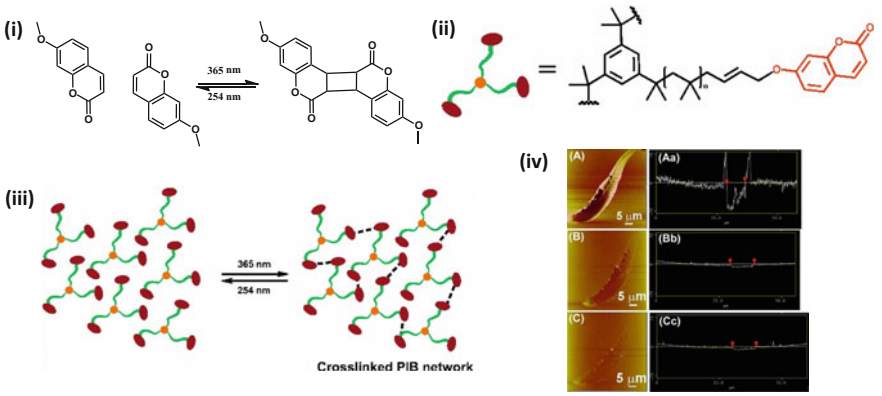

Fig. 14 **i** Reversible [2+2] photodimerization of coumarin moieties, **ii** triarm star coumarin-functionalized PIB polymer, **iii** reversible cyclodimerization of coumarin-functionalized triarm star PIB polymer leading to crosslinked network formation. **iv** AFM image for the time-dependent change for the scratch on the surface of the crosslinked PIB polymer film using an UV lamp, time = (*A*) 0, (*B*) 5, and (*C*) 30 min. (*Aa–Cc*) Corresponding depth profiles reveal the evolution of the damage depth [42]. Copyright 2015. Reprinted with Permission from American Chemical Society

the healing response had shown that the healing response was driven by initial photocleavage of the cyclobutane ring by UVC irradiation giving the polymer sufficient viscoelastic mobility. Thus, the PIB polymer with low glass transition temperature acquires sufficient mobility to flow at room temperature and facilitated the dimerization of the coumarin functionalities. The reformation of the cyclobutane ring via UVA-induced photodimerization at this stage led to the formation of the crosslinked network which eventually healed the damage. Complete macroscopic healing in the bulk state was obstructed due to the restricted chain mobility. The permeability analysis study of the films revealed that the crosslinked polymers had excellent barrier protection against oxygen and moisture which made them suitable as photovoltaic device coatings.

4 Polymer Nanocomposites

Polymeric self-healing materials have profound applications in various fields of material science due to their innate attributes like easy availability, pliability, easy processing, light weight and provision for tailor-made architecture. However, they are very poor in mechanical performance in comparison with metals and ceramics. The integration of nanomaterials into polymer network renders desired modifications in the properties of the polymer nanocomposites material and paves way for the design of novel polymeric self-healing materials with outstanding properties. A number of polymer nanocomposites doped with carbon nanomaterials, e.g.,

graphene, silica nanoparticles, gold nanoparticles, silver nanoparticles and nanocellulose, have been studied.

4.1 Polymer Nanocomposites from Nanoparticles

G. Kickelbick et al. reported self-healing polymer nanocomposites with varying thermal properties by doping surface-functionalized silica nanoparticles into polymers networks [43]. The diene or dienophile derivatives as the capping ligand on silica nanoparticles were crosslinked with functional poly(butyl methacrylates) or structurally diversified polysiloxane matrices via Diels–Alder reaction (Fig. 15). Spherical amorphous silica nanoparticles (~6 nm) with the surface derivatization of 2-furyl-(undecenyl)-11-triethoxysilane (FUTES) and *N*-((3-triethoxysilyl) propyl)maleimide (MPTES) were synthesized by modified Stöber process to produce FUTES@SiO_2 or MPTES@SiO_2. The cofunctionalized polybutylmethacrylates or polysiloxane polymers with maleimide and furan moieties and surface-modified silica nanoparticles were mixed with a molar ratio of 5:1 in terms of reactive groups and were crosslinked via DA reaction. Rheological measurements had shown that there was an increase in viscosity of polysiloxanes after incorporation of the nanoparticles which of 5:1 in terms of reactive groups and were crosslinked via DA reaction.

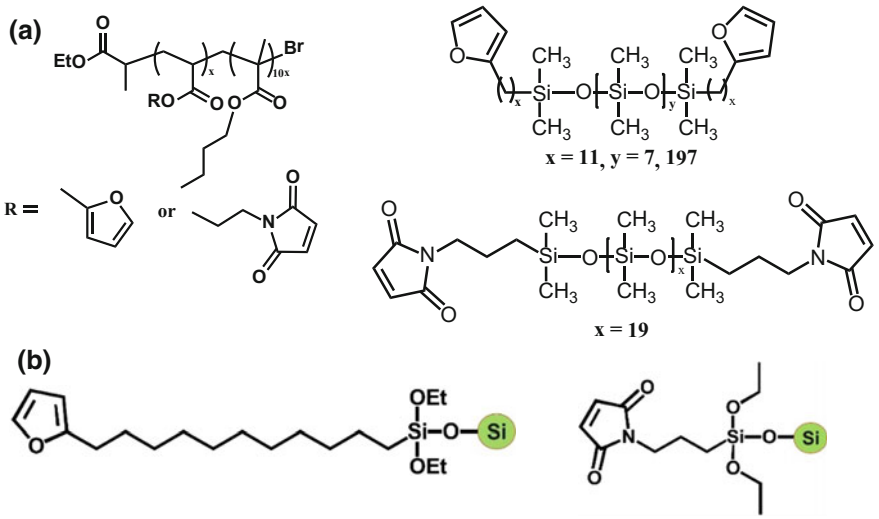

Fig. 15 **a** Poly(butyl methacrylate) and polysiloxane polymers with maleimide and furan moieties as the functional groups, **b** silica nanoparticles with maleimide and furan moieties for DA reactions [43]. Copyright 2015. Reproduced with permission from Elsevier Ltd

Rheological measurements had shown that there was an increase in viscosity of polysiloxanes after incorporation of the nanoparticles which was attributed to a filler effect and crosslinking of polymer chain with nanoparticles. The differential scanning calorimetry study shows that the spacer length between the functional groups had a significant impact on the DA/reverse DA reaction in the polymer nanocomposites. However, the extent of flexibility and mobility of the polymers in the nanocomposites plays important role in determining the self-healing ability. In comparison with the nanocomposites from butylmethacrylate system, self-healing was more efficient in the nanocomposites from polysiloxanes which was attributed to the deficient mobility of the polymer chain. Further explorations are needed in designing tailor-made self-healing nanocomposite with exploitation of their properties (e.g., magnetism, conductivity) as an integral part of stimuli-responsive system.

4.2 Polymer Nanocomposites from Carbon Nanotubes

Carbon nanotubes have been envisaged as one of the hardest synthetic materials known to scientific community till date. They also exhibit high electrical conductivity that makes it useful for applications in the electrical and communication field. The excellent properties of these materials were explored by dispersing them in soft polymer matrices. Non-covalent interactions to improve their chemical affinity toward the polymeric matrix introduce self-healing behavior with promising applications. Recently, Guo et al. reported such type of conducting nanocomposite with self-healing capability by conjoining poly(2-hydroxyethyl methacrylate) (PHEMA) and single-walled carbon nanotubes (SWCNTs) via β-cyclodextrin-adamantane host–guest chemistry [44]. β-Cyclodextrin-grafted pyrene stacked onto SWCNTs via non-covalent interaction and simultaneous host–guest chemistry-mediated crosslinking with adamantane-grafted 2-hydroxyethylmethacrylate resulted a ternary inclusion complex.

The subsequent free radical polymerization of the acrylate resulted in the desired polymer composites (Fig. 16). All the nanocomposites with variable doping of CNT showed rubber-like behavior with glass transition temperature (T_g) below room temperature. The presence of a large number of host–guest groups in the material ensured excellent self-healing properties as demonstrated in the electrical healing experiments. The nanocomposite sample was connected to a circuit with a LED lamp. Remarkably, the LED was shining for the circuit with nanocomposite doped with more than 7 wt% SWCNTs. The cut species of the sample turned the LED off; however, the cut pieces in contact for 5 min at room temperature showed recovery of electrical conductivity with glowing LED. Unlike hydrogen bonding-mediated self-healing, where the presence of moisture affects the healing efficiency during the waiting time with cut samples in contact, host–guest complexation-mediated self-healing benefits from humidity due to absorption of moisture by the PHEMA polymers. These materials showed change in resistance

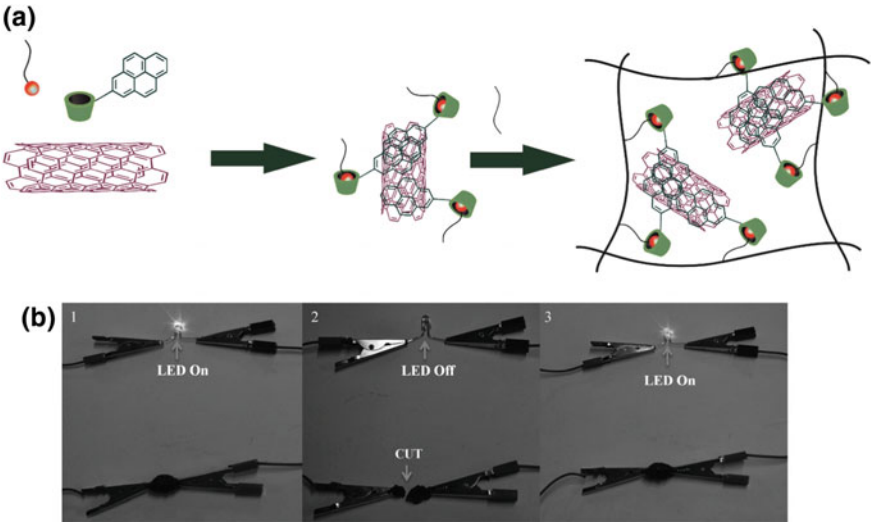

Fig. 16 **a** Ternary complex formation through host–guest and π–π interactions with subsequent polymerization to result SWCNT nanocomposites with electrical conductivity. **b** Electrical healing process for the nanocomposite: (*1*) polymer nanocomposite sample was connected in a circuit to glow, (*2*) the sample was cut to turn the LED off, (*3*) LED shined again after the sample had self-healed [44]. Copyright 2015. Reproduced with permission from WILEY-VCH Verlag GmbH & Co. KGaA, Weinheim

with relative humidity and human skin touch and can be used as humidity and proximity sensor. Wang et al. reported a strain-stiffening polymer nanocomposite with multiwalled CNTs by dispersing the nanotubes into polyborondimethylsiloxanes (PBDMS) polymer matrix via solvent etching method [45]. This material showed self-healing behavior via recovery of mechanical and electrical properties on damage and subsequent healing experiment and can have for potential application as force-sensitive body armor. However, further study on the properties of polymer composites containing CNTs as fillers with promising self-healing chemistry is necessary which can eventually pave way for smart robotics.

4.3 Polymer Nanocomposites from Graphene

Graphene is considered as the lightest material which consists of a 2D planar thin sheet of sp^2-hybridized carbon atoms arranged in a honey-comb crystal lattice. Excellent thermal, mechanical and electrical properties render graphene an interesting material as fillers in polymer composites for various applications in a numerous range of devices [46]. Incorporation of reversible non-covalent chemistry into polymer nanocomposites containing graphene adds to promising self-healing

applications. A number of polymeric hydrogel showed tough mechanical property in mimicking natural structural tissues. However, the mechanically rigid hydrogels usually do not exhibit good self-healing behavior and the self-healing hydrogels are mechanically weak in general. Only a few self-healing hydrogels with useful mechanical properties have been developed. Incorporation of graphene in polymeric hydrogels enhances the mechanical strength along with retention of self-healing behavior.

Additionally, the functionalized graphene oxide/peroxide (GO/GPO) provides sites for polyfunctional initiating and crosslinking centers (PFICC). Liu et al. reported a graphene-based polyacrylamide hydrogel nanocomposite which showed outstanding self-healing capability at ambient conditions [47]. Interestingly, variable percentage of GO doping in the hydrogel nanocomposites significantly influenced their self-healing ability. Thus, the cut surface of the GO composite gels autonomically self-healed within short span of time and with longer waiting period the mechanical property of the composites showed high degree of recovery with highest ever elongation and tensile strengths. As shown in Fig. 17, the authors had demonstrated the mechanism of repair of damaged polymer/graphene nanocomposite by related distribution of long polyacrylamide polymer chains at the interface of two damaged hydrogel samples. The mutual diffusion of the long polyacrylamide chains and GO sheets via reversible hydrogen bonding across the cut surfaces of 3D polymer network makes the interaction stronger with high degree of recovery and self-healing.

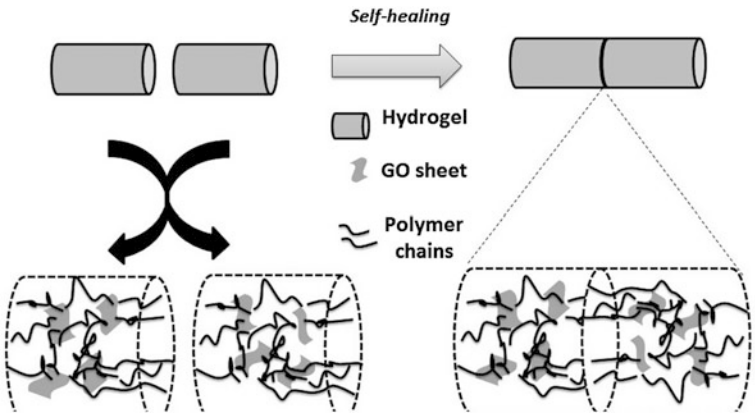

Fig. 17 Self-healing mechanism of the GO composite hydrogels [47]. Copyright 2013. Reproduced with permission from WILEY-VCH Verlag GmbH & Co. KGaA, Weinheim

4.4 Polymer Nanocomposites from Nanoclays

Nanoclays formed by layered mineral silicates are an excellent class of nanomaterials that have attracted the attention of the scientific community for the development of polymer nanocomposites with superior properties for specific applications [48]. The most commonly used nanoclay minerals for the preparation of nanocomposites are montmorillonite, hectorite and saponite with high surface area and reactivity. Even a very low amount of nanoclay loading in polymer matrices can provide interesting and superior properties to the nanocomposite through the intercalation of nanoclays in between the polymer chains [49]. Recently, Zhu et al. had reported that reinforcement of nanoclay materials into dynamic biocompatible polymers can result in the formation of autonomic self-healing synthetic polymer nanocomposites that will mimic biological composites, e.g., nacre, an organic–inorganic composite material found in some mollusks [50]. They designed a nacre mimetic polymeric nanocomposite using hydrogen bonding-mediated non-covalent interaction to develop a self-healing system for application in organo-electronics. The copolymer of water-soluble polyethyleneglycol methacrylate with UPy-functionalized acrylate polymer was reinforced with high-aspect-ratio synthetic sodium fluorohectorite (NHT) nanoclays (Fig. 18a). The mechanical strength of the nanocomposites was modulated with varying composition of polymer and nanoclays every stiff yet transparent films which could be applied for gas barrier application in organo-electronics.

Wang et al. reported a water-soluble polymeric gel-based clay nanosheet (CNS) composite material that showed excellent mechanical properties along with self-healing properties (Fig. 18b) [51]. The non-covalent electrostatic interaction between telechelic dendritic macromolecule with positively charged terminal groups and clay nanosheet covered with negatively charged sodium polyacrylate

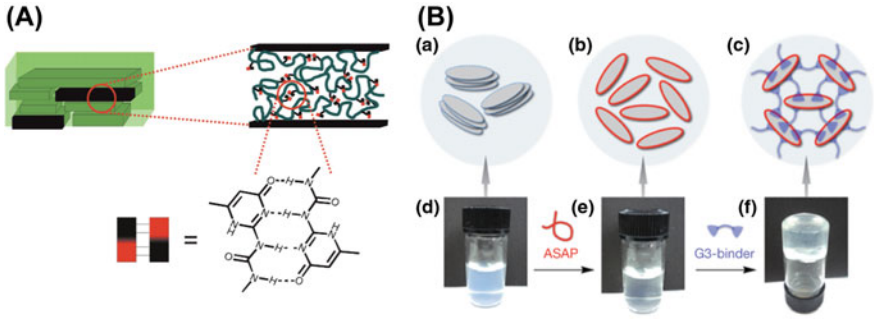

Fig. 18 **A** Nacre mimetic self-assembly of synthetic nanoclay and polyethyleneglycol methacrylate with UPy-functionalized acrylate polymer in brick-and-mortar mode [50]. Copyright 2015. Reproduced with permission from WILEY-VCH Verlag GmbH & Co. KGaA, Weinheim. **B** Formation of the nanoclay-hydrogel composites through electrostatic crosslinking of sodium polyacrylate covered nanoclays with dendritic molecular binder [51]. Copyright 2010. Reproduced with permission from Nature Publishing Group

resulted in a gel material showing autonomic self-healing behavior which is evident by very quick retrieval of its mechanical properties after a large-amplitude oscillatory mechanical collapse of the nanocomposite gel.

5 Applications

At the present stage, development of the self-healing materials for industrial usage is in the preliminary level and the use of these novel materials is expected to dominate industry in the near future. This section describes the potential utilization of the self-healing materials for different applications such as protective coating, shape recovery polymer, adhesive and self-healing hydrogel.

5.1 Protective Coating

Protective polymeric coatings have found increasing applications in industry such as corrosion prevention in metals, prevention of damage of walls by paints, semiconductor fabrication. Polymeric coatings are widely used to conceal the surfaces of numerous substrates for both functional and decorative purposes. However, most of the coating materials are vulnerable to the impairments caused by the environmental hazards and mechanical abrasion which eventually leads to compromised function and irreversible loss of the coating. Repair of the damage on ordinary coating is unaffordable in many cases and demands tedious effort with considerable labor. Thus, a protective coating that can self-heal without much cost escalation would be suitable as a next-generation coating material. The most prevalent approaches for designing self-healing coating is the polymerization of monomeric healing agents that are released by extrinsic damage to microcapsule dispersed in a matrix. However, owing to the limitation of microcapsule approach for the once-only release of the healing agents, processing difficulties and inhomogeneous distributions of the components, the alternative approaches using reversible chemistry such as non-covalent interactions and dynamic covalent interactions are also being translated toward industrial application. The work from Lei Gao et al. narrates a photo-absorbing hybrid microcapsule (PAHM) containing polymer coating material (Fig. 19i) in which the microcapsules are protected by polymeric shell [18]. This polymeric shell is designed via a hybrid strategy in which photo-absorbing TiO_2 nanoparticles and poly(urea-formaldehyde) (PUF) are combined to form a microcapsule. A mixture of EPON 828 epoxy (diglycidyl ether of bisphenol A) curing agent PAA (phenol-aldehyde amine) and diluent diisobutyl phthalate (DBP) gave the unfilled coatings. Addition of 15 wt% of microcapsules to the above mixture resulted in the polymer composite having self-healing coating capability. Upon mechanical damage and then exposure to light, the photoresponsive healing agents in the cracks would be solidified to allow for self-healing,

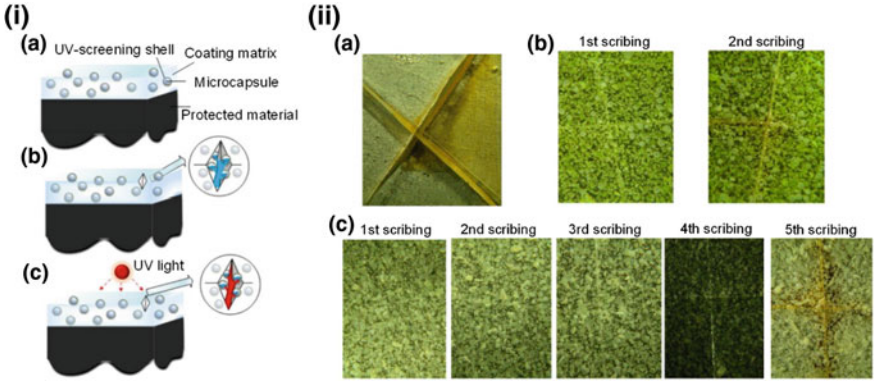

Fig. 19 Concept of self-healing as protective coating application. **i** (*a*) Material protected with coating matrix and microcapsule composite, (*b*) mechanical damage to generate the cracks and rupture of the microcapsules with subsequent release of the healing agent to fill the cracks, (*c*) cracks are healed by photopolymerization of the healing agent induced by UV light. **ii** Anticorrosion study by optical images after a 48-h immersion in salt water for control samples (*a*) C1, (*b*) C2, and (*c*) self-healing coatings sample [18]. Copyright 2015. Reprinted with permission from American Chemical Society

while the healing agents in the unbroken PAHM would be protected and remain unreacted. Anticorrosion testing was employed to study self-healing of the polymer composites. Mechanical damage was induced by scribing with razor blade through ~500-μm-thick coatings of the self-healing coating with PAHM, C1 control sample (without microcapsules) and C2 control sample (with PUF-shelled microcapsule fillers). The samples were placed in a dark room for an hour and subsequent exposure to UV light for 30 s for healing of the cracks followed by immersion in 10 wt% aqueous NaCl solution for 48 h.

As shown in Fig. 19ii, C1 sample without the microcapsule corroded but the C2 sample and PAHM-containing self-healing coating showed no proof of corrosion. The entire process was repeated and the C2 sample showed corrosion on the second cycle and the anticorrosion property was exhibited only by the self-healing samples which was sustained till fourth scribing cycle. C2 sample showed healing of the first scribed crack in a non-selective photopolymerization in both the scribing and non-ruptured region; hence, no further healing agent were available and this led to unhealed coating on second scribing. For the self-healing samples, exposure to light resulted in the solidification of healing agents in the crack, but for unruptured microcapsules, the shielding by the photo-absorbing shells keeps the healing agents unreacted. Furthermore, accumulative exposure time for every cycle resulted in the polymerization of the healing agents even in the unexposed area leading to loss in healing behavior for the fifth cycle of scribing. Thus, a one-component photo-stimulated extrinsic self-healing system that contains photo-absorbing hybrid microcapsules has been designed and can be utilized in due course for protective shielding of outdoor applications.

5.2 Shape Memory Polymers (SMPs)

In the last several years, a new strategy that utilizes self-healing concept for designing shape memory materials had been evolved. This class of stimuli-responsive materials can be programmed to a temporary shape and can be triggered to revert back to their original shape [52]. As compared to shape memory alloys (SMAs), shape memory polymers (SMPs) possess some important advantages, viz. easy processibility, high elastic deformation, low cost, low density, tunable stiffness, biocompatibility and biodegradability with tunable and broad range of working temperatures. The mechanism of shape memory effect in the polymer exploits the reversible thermal transition such as glass transition temperature (T_g), melting temperature (T_m) as molecular switch components. Most of the SMPs with one temporary shape in a cycle are dual-shape materials having a single T_{trans} in the switching domain. Of late, multiple shape memory polymers (MSMPs) with single or multiple T_{trans} are being investigated to meet increasing requirements and promising applications. Yuzhong Wang et al. had reported a triple shape memory polymer mediated by self-complementary quadruple hydrogen bonding based on the dynamic non-covalent network of UPy-telechelic poly(tetramethylene ether) glycol (PTMEG) and four-arm PCL precursors (Fig. 20a) [53]. The strategy to combine two semicrystalline polymers with different melting transitions serves as the switching domains ensuring triple shape memory (TSM). The dimerization of Upy followed by subsequent aggregation of the UPy dimers strengthens the dynamic network providing reversibility, reprocessability and self-healing features. The triple shape memory of this material is shown in Fig. 20b. Programming of the SMP was obtained by deforming the permanently shaped flat sample (shape A) at 60 °C (more than the T_m of both the PTMEG and PCL segments) and followed by cooling to 35 °C to ensure the crystallinity of PCL segment. Removal of the external stress rendered shape B. Further, deformation of the specimen performed at

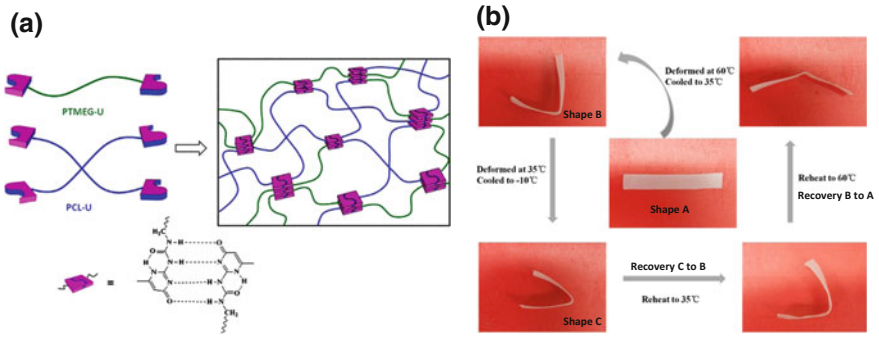

Fig. 20 **a** Quadruple hydrogen bonding in the PCL-PTMEG network and **b** shape memory effect of a strip made from PCL–PTMEG polymer sample based on the heating transitions of semicrystalline polymers [52]. Copyright 2015. Reprinted with permission from American Chemical Society

35 °C and subsequent cooling below −10 °C rendered shape C. Reheating to 35 °C resulted in good recovery ratios from shapes C to B (83.9% while recovery from shape C to A did not vary much (71–75%) over a wide range of PCL content (36–80%) in the composites. An increasing PTMEG content resulted in improved efficiency of self-healing due to decrease in the concentration of crystalline PCL phase in the overall polymer.

5.3 Adhesion Application

Over the last several decades the scientists were trying to synthesize novel materials including polymers which promote adhesiveness in wet conditions. However, one of the major challenges was that these synthetic materials that set in the water environment were prone to reaction with water itself rather than reaction with the targeted substrate. Recently, exploration of the chemistry of waterlogged adherence of the sea animals such as mussels, barnacles and oysters to rock and other hard surfaces in sea unveiled a new approach to design novel wet adhesives. Mussels have a special type of protein matrix functionalized with 3,4-dihydroxyphenylalanine (DOPA) amino acid that is responsible for the wet adhesiveness making DOPA-based polymers attractive for adhesion. The catechol side chain of DOPA polymer and hydrogels exploits the coordination bond formation via metal chelation. The reversible non-covalent nature of metal–ligand bonds rendered self-healing behavior to the polymer or hydrogel. However, toxicity of the metal can make the system incompatible for biological applications. Recently, Herbert Waite et al. put forth a metal-free strategy to realize the self-healing of polymers in wet condition mediated via hydrogen bonding between catechol moieties. The authors synthesized two polymers with different elastic moduli, i.e., semirigid with low modulus and rigid polymer rods with high modulus from triethyl silane-blocked catechol acrylate and catechol methacrylate monomers, as shown in Fig. 21a, b, using free radical ultraviolet polymerization. Bisected halves of the rod-shaped polymer were immersed in different buffers with increasing pH ranging from 3 to 10 for 20 min, followed by healing study, i.e., rejoining the cut ends of the rods at light compression (6–104 Pa) kept in the above aqueous solution (pH 3, 7 and 10) for 2 min.

At pH 3, deprotection of triethylsilyl groups led to activation of the catechol functionalities on the surfaces, while the triethylsilyl catechols at pH 7 and 10 remained unreacted. The high quinone reduction potential ($E_o \sim 0.38$) at pH 3 ensured catechol stability preventing its oxidation and ring coupling reactions. When surface treatments were carried out at pH 3, the semirigid rods didn't break up at the contact region after damage and healing whereas rigid rods got ruptured on applying tension after healing. Tensile test showed retention of the mechanical properties of the healed part in comparison with the undamaged portions of the rigid polymer rods at pH 3 (Fig. 21c), but at pH 7 and 10 both the rigid and semirigid polymer rods failed to self-heal at the contact area due to blocked catechol groups. The interfacial mechanism of adhesion mediated by reversible hydrogen bonding

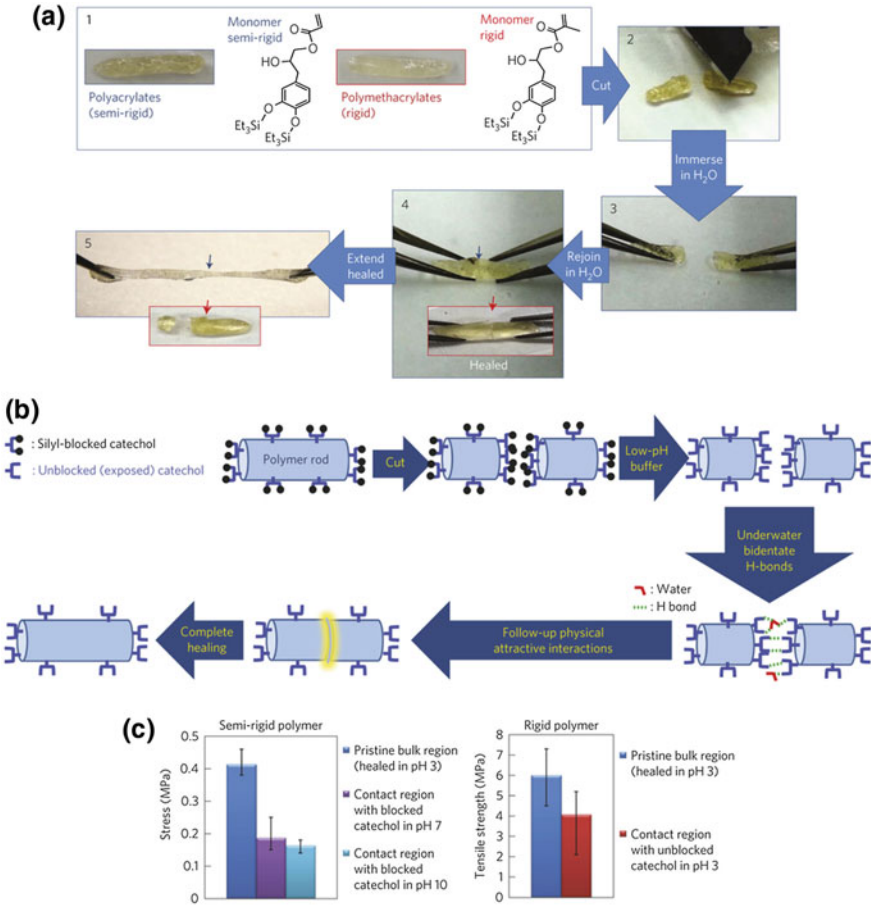

Fig. 21 **a** Self-healing studies on adhesive polymer rods with the following process. Rigid and semirigid polymer rods (*1*), bisection (*2*), immersion in H_2O (pH 3 buffer) at room temperature (*3*), contact (*4*) and mechanical tension with pull (*5*). The *blue* (semirigid) and *red* (rigid) *arrows* denote the location of the healed incisions. **b** Schematic representation of the self-healing. **c** Average tensile strength for the healed semirigid and rigid polymer rods [20]. Copyright 2014. Reproduced with permission from Nature Publishing Group

interactions between the pendant catechol groups of the polymers resulted in self-healing and was elucidated with the aid of surface force apparatus which monitored the time-dependent adhesion at the self-healing (contact) surface (Fig. 22a). Adhesion force, F_{ad} of semirigid polymers with both the blocked and exposed catechol groups as delineated in Fig. 20b displayed a low value of 50–70 mN till a critical contact time, t_c value of 30–120 s after which there was a constant elevation to 820 mN at a t_c of 120 s for exposed one, whereas blocked catechols F_{ad} showed elevation only up to 230 mN at a t_c of 3600 s. Additionally, no damage occurred to contact surface of blocked polymer on detachment up to

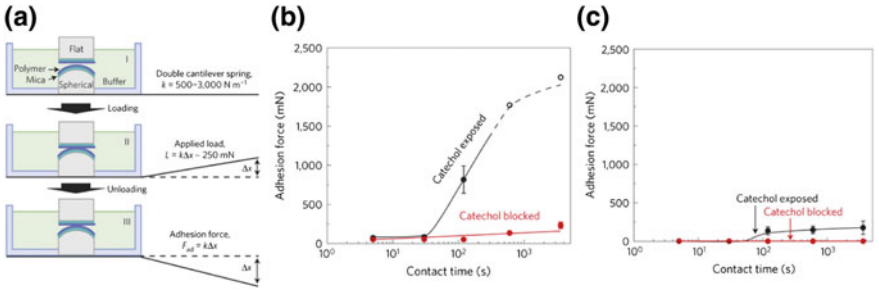

Fig. 22 Adhesion between polymer films grafted with exposed and blocked catechol moieties as estimated by the surface force apparatus. **a** Scheme of the symmetric surface geometry. **b**, **c** Graph showing adhesion force (F_{ad}) versus contact time (t_c) between two **b** semirigid and **c** rigid polymeric surfaces under an applied load of 250 mN [20]. Copyright 2014. Reproduced with permission from Nature Publishing Group

3600 s (Fig. 22b). The rigid polymers (Fig. 22c) with low molecular mobility showed no elevation in F_{ad} for the blocked catecholic polymer till a t_c of 3600 s and for exposed catecholic polymers up to a critical t_c of 50 s. This elevation was only up to 180 mN. This made the authors to propose that the adhesion in the catechol-functionalized polymers and proteins depends on both bidentate hydrogen bonding of catechols and hydrophobic contributions. Here the semirigid polymers had shown larger adhesiveness and self-healing capacity that indicated the significance of molecular mobility within the polymer for promoting the self-repair. The time taken for the rearrangement of polymer chains and molecular groups was indicated by t_c that facilitated extensive interfacial hydrogen bonding. Also, the hydrogen bonding was a prerequisite to speed up other interactions, viz. van der Waals, hydrophobic, polymer interdigitation, interpenetration and interdiffusion required for self-healing. The significance of hydrogen bonding was further highlighted by experiments in which the catechol rings were oxidized to quinones with periodate, which further decreased adhesive forces between the soft polymer films. Proposed bidentate mode of hydrogen bonding between catechols is thermodynamically more favorable than the hydrogen bonding in water-catechol paving way for hydrogen bonding attraction between the catechol moieties even in the aqueous environment. Thus, the precise reorientation of the surfaces of polymer-based biomaterials provides excellent and promising self-mending properties.

5.4 Self-healing Hydrogel

Hydrogels are three-dimensional complex systems that consist of hydrophilic polymers which are fashioned through covalent or non-covalent interactions between the polymer chains [54]. The versatile and biocompatible nature of hydrogels led to their widespread application in drug delivery, regenerative tissue

engineering, biomaterials synthesis and fabrication of functional devices [55–59]. As compared to covalent hydrogels, the reversible interactions and extensive stimuli-responsive endow dynamic and self-healing properties to the supramolecular hydrogel. A number of supramolecular chemistry have been explored for the design of efficient and fast self-healing hydrogels in the past few decades including hydrogen bonding [60], host–guest interactions [61–63], electrostatic interactions

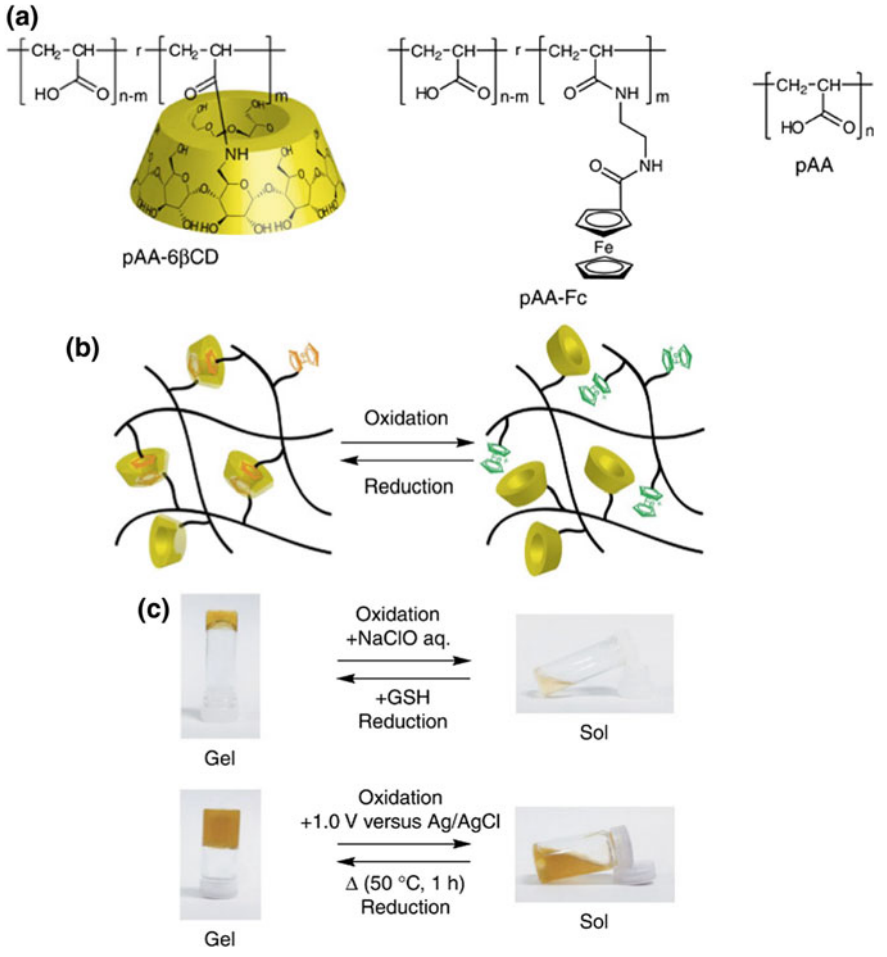

Fig. 23 Self-healing hydrogel mediated by redox-responsive sol–gel transition. **a** Chemical structures of the host polymers, pAA-6βCD and the guest polymers, pAA-Fc, **b** schematic illustration of redox-mediated inclusion complex to result pAA-6βCD/pAA-Fc hydrogel, **c** sol–gel reversible transition experiment using oxidation–reduction. Addition of NaClO solution to the pAA-6βCD/pAA-Fc hydrogel makes it to the sol state, and addition of GSH to the sol reverts back into hydrogel. Electrochemical oxidation (+1.0 V vs. Ag/AgCl) transformed the hydrogel into the sol, whereas chemical reduction reverting it back to the hydrogel [66]. Copyright 2011. Reproduced with permission from Nature Publishing Group

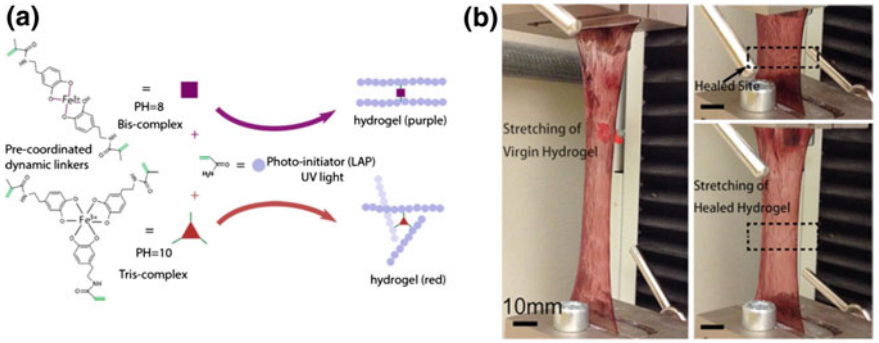

Fig. 24 **a** Photopolymerized hydrogels using precoordinated catechol–Fe^{3+} complexes as dynamic crosslinkers, **b** high extensibility and fast self-healing property of the hydrogel prepared using the precoordination method [34]. Copyright 2015. Reprinted with permission from American Chemical Society

[51] and metal–ligand coordination [64, 65]. As mentioned earlier in this chapter pertaining to host–guest interactions, Harada et al. reported durable self-healing hydrogels based on the interactions between hydrophilic host and hydrophobic guest molecules [66]. The authors synthesized reversible hydrogels exploiting the interaction between β-cyclodextrin and ferrocene moieties grafted on the poly-acrylic acid polymer chains (pAA-6βCD/pAA-Fc interaction) as shown in Fig. 23a. A redox reaction-induced reversible formation of the inclusion complex assisted the gel-to-sol reversible transition in the system (Fig. 23b, c). The suitability of that system to undergo self-healing processes such as rejoining of cut surfaces was demonstrated and was envisaged for applications, e.g., stimuli-responsive-targeted drug delivery and design of peripheral vascular embolization material.

In another work, Ma et al. reported a novel approach to synthesize extensible and fast self-healing supramolecular hydrogels via precoordinated mussel-inspired catechol-Fe^{3+} dynamic crosslinking complexation (Fig. 24a) [34]. The hydrogels exhibit high extensibility by 10 times of the original length and fast recovery (within 20 min) as delineated in Fig. 24b.

6 Discussion and Future Perspectives

We have discussed different approaches to design self-healing materials in the previous sections. The scientific community had succeeded in exploiting various approaches to comprehend self-healing mechanisms. They are summarized in Table 6. The physical and chemical mechanisms of the process that lead to self-repair of the cracks, damaged surfaces, adhesion of cut surfaces, etc., can be easily manipulated to render materials with desired properties.

Table 6 Strategies employed to design self-healing material based on different chemistry

Design strategies	Chemistry involved	Stimuli	Healing agent
Supramolecular polymer	Hydrogen bonding (PBA-UPy dimer) [19]	Non-autonomic; heat, moisture	Intrinsic
	Host–guest chemistry (Ferrocene-β-CD) [23]	Non-autonomic; redox, heat, moisture	Intrinsic
Covalent polymer	Thermosetting polymers (PU/PUF) [31]	Non-autonomic; moisture	Extrinsic; isophorone diisocyanate
	Thermoplastic polymers (PS-PA-amide) [32]	Autonomic	Intrinsic
	Metallopolymer (TerPy-iron) [35]	Non-autonomic; heat	Intrinsic
Dynamic covalent polymer (dynamer)	Diels–Alder reaction (furan-maleimide) [36]	Non-autonomic; heat	Intrinsic
	Thiol–disulfide chemistry (PBA-DSDMA) [39]	Non-autonomic; mechanical force	Intrinsic
	Acylhydrazone chemistry (HEMA-TEGMEMA) [41]	Non-autonomic; heat	Intrinsic
	Photodimerization (PIB-coumarin dimer) [42]	Non-autonomic; UV light	Intrinsic
Polymer composites	Microcapsules (PU/PUF with TiO_2) [18]	Non-autonomic; UV light	Extrinsic; PAA, epoxy
	Composites from nanoparticles (PBA–PSO–SiO_2) [43]	Non-autonomic; UV light	Intrinsic
	Composites from carbon nanotubes [44]	Autonomic	Intrinsic
	Composites from graphene [47]	Autonomic	Intrinsic
	Composites from nanoclays [51]	Autonomic	Intrinsic

Note The nature of self-healing is specific for the examples listed in the table and discussed in the chapter

Discovery and application of novel supramolecular chemistry offer facile, quick and controlled formation of innovative materials that undergo efficient self-healing. Thus, it is apparent that most of the methods are non-autonomic in nature with heat being one of the important stimuli, which affects the self-healing behavior profoundly based on the glass transition temperature of the polymers. Recent research is being driven toward modifying the materials toward autonomic self-healing materials. Also, extrinsic self-healing approach is found to be restricted with covalent thermoset/thermoplastic polymers and its composites due to reusability and localization of the embedded microcapsules. Many recent approaches, especially supramolecular polymer, dynamic covalent polymer, employ intrinsic self-healing which does not require external healing agent. However, it is a challenge to translate the self-healing repair from micron scale to larger scale. Weak mechanical strength of the polymer initially restricted the practical use of the self-healing concept. With recent development of many polymer composites from nanoclays, graphene, etc., produced much robust self-healing materials with improved mechanical properties due to the filler effect associated with the

nanomaterials. For example, the polymer composite with SWCNT or graphene utilizes high elasticity of the polymer network and the conductivity of the SWCNT/graphene demonstrated excellent autonomic healing ability and can be instrumental in developing advanced sensing electronics, e.g., passive resistors-capacitors and electro-active sensor devices. In addition, other functional nanomaterials, e.g., magnetic fluid particles, could also be useful dopant to design a wide range of self-healing material using the design concept developed so far. The self-healing research in the area of polymer composites put forward an array of smart materials that has versatile applications in various fields ranging from household to industrial level that are still in the experimental stage and deserves commercial attention. Thus, further optimization of the healing process is necessary for attaining the aforementioned goal. Although some of them have been commercialized, still the technique is in need of robust strategies for the less explored areas such as polymer nanocomposites, supramolecular polymers, hydrogels. Moreover, further insight into the underlying chemistry of the self-healing materials is inevitable and may drive toward a new direction for future research into this field. Research into further improvement in reproducibility of the system is another concern that still remains a barrier for their functional applications.

References

1. Thakur VK, Kessler MR (2015) Self-healing polymer nano-composite materials: a review. Polymer 69:369–383
2. Yuan YC, Yin T, Rang MZ, Zhang MQ (2008) Self-healing in polymers and polymer composites. Concepts, realization and outlook. Express Polym Lett 2(4):238–250
3. Bergman SD, Wudl F (2008) Mendable polymer. J Mater Chem 18:41–62
4. Wu DY, Meure S, Solomon D (2008) Self-healing polymeric materials: a review of recent developments. Prog Polym Sci 33(5):479–522
5. Wool RP (2008) Self-healing materials: a review. Soft Matter 4:400–418
6. An SY, Noh SM, Nam JH, Oh JK (2015) Dual sulfide–disulfide cross-linked networks with rapid and room temperature self-healability. Macromol Rapid Commun 36:1255–1260
7. Zhang Y, Broekhuis A, Picchioni F (2009) Thermally self-healing polymeric materials: the next step to recycling thermoset polymers? Macromolecules 42(6):1906–1912
8. Liu YL, Chuoa TW (2013) Self-healing polymers based on thermally reversible Diels-Alder chemistry. Polym Chem 4:2194–2205
9. Varnoosfaderani MV, Hashmi S, Nejad AG, Stadler FJ (2014) Rapid self-healing and triple stimuli responsiveness of a supramolecular polymer gel based on boron–catechol interactions in a novel water-soluble mussel-inspired copolymer. Polym Chem 5:512–523
10. Bag M, Banerjee S, Faust R, Venkataraman D (2016) Self-healing polymer sealant for encapsulating flexible solar cells. Sol Energy Mater Sol Cells 145:418–422
11. Shchukin DG (2013) Container-based multifunctional self-healing polymer coatings. Polym Chem 4:4871–4877
12. Williams KA, Dreyer DR, Bielawski CW (2008) The underlying chemistry of self-healing materials. MRS Bull 33(8):759–765
13. White SR, Sottos NR, Geubelle PH, Moore JS, Kessler MR, Sriram SR, Brown EN, Viswanathan S (2001) Autonomic healing of polymer composites. Nature 409:794–797

14. Toohey KS, Sottos NR, Lewis JA, Moore JS, White SR (2007) Self-healing materials with microvascular networks. Nat Mater 6:581–585
15. Chen X, Dam MA, Ono K, Mal A, Shen H, Nutt SR, Sheran K, Wudl F (2002) A thermally re-mendable cross-linked polymeric material. Science 295(5560):1698–1702
16. Chen X, Wudl F, Mal A, Shen H, Nutt SR (2003) New thermally remendable highly cross-linked polymeric materials. Macromolecules 36(6):1802–1807
17. Cordier P, Tournilhac F, Soulié-Ziakovic C, Leibler L (2008) Self-healing and thermoreversible rubber from supramolecular assembly. Nature 451:977–980
18. Gao L, He J, Hu J, Wang C (2015) Photo-responsive self-healing polymer composite with photo-absorbing hybrid microcapsules. ACS Appl Mater Interfaces 7:25546–25552
19. Faghihnejad A, Feldman KE, Yu J, Tirrell MV, Israelachvili JN, Hawker CJ, Kramer EJ, Zeng H (2014) Adhesion and surface interactions of a self-healing polymer with multiple hydrogen-bonding groups. Adv Funct Mater 24:2322–2333
20. Ahn BK, Lee DW, Israelachvili JN, Waite JH (2014) Surface-initiated self-healing of polymers in aqueous media. Nat Mater 13:867–872
21. ten Cate AT, Sijbesma RP (2003) Coils, rods and rings in hydrogen-bonded supramolecular polymers. Macromol Rapid Commun 23(18):1094–1112
22. Yang X, Yu H, Wang L, Tong R, Akram M, Chen Y, Zhai X (2015) Self-healing polymer materials constructed by macrocycle-based host–guest interactions. Soft Matter 11: 1242–1252
23. Chuo TW, Wei TC, Liu YL (2013) Electrically driven self-healing polymers based on reversible guest-host complexation of β-cyclo-dextrin and ferrocene. J Polym Sci, Part A: Polym Chem 51:3395–3403
24. Kakuta T, Takashima Y, Nakahata M, Otsubo M, Yamaguchi H, Harada A (2013) Pre-organized hydrogel: self-healing properties of supramolecular hydrogels formed by polymerization of host–guest-monomers that contain cyclodextrins and hydrophobic guest groups. Adv Mater 25:2849–2853
25. Zhang M, Xu D, Yan X, Chen J, Dong S, Zheng B, Huang F (2012) Self-healing supramolecular gels formed by crown ether based host-guest interactions. Angew Chem Int Ed 51(28):7011–7015
26. McKee JR, Appel EA, Seitsonen J, Kontturi E, Scherman OA, Ikkala O (2014) Healable, stable and stiff hydrogels: combining conflicting properties using dynamic and selective three-component recognition with reinforcing cellulose nanorods. Adv Funct Mater 24 (18):2706–2713
27. Guo DS, Liu Y (2012) Calixarene-based supramolecular polymerization in solution. Chem Soc Rev 41:5907–5921
28. Zhang H, Zhao Y (2013) Pillararene-based assemblies: design principle, preparation and applications. Eur J Chem 19(50):16862–16879
29. Gil ES, Hudson SM (2004) Stimuli-responsive polymers and their bioconjugates. Prog Polym Sci 29:1173–1222
30. Lutz JF (2011) Thermo-switchable materials prepared using the OEGMA-platform. Adv Mater 23(19):2237–2243
31. Credico BD, Levi M, Turri S (2013) An efficient method for the output of new self-repairing materials through a reactive isocyanate encapsulation. Eur Polymer J 49(9):2467–2476
32. Chen Y, Kushner AM, Williams GA, Guan Z (2012) Multiphase design of autonomic self-healing thermoplastic elastomers. Nat Chem 4:467–472
33. Hentschel J, Kushner AM, Ziller J, Guan Z (2012) Self-healing supramolecular block copolymers. Angew Chem Int Ed 51(42):10561–10565
34. Hou S, Ma PX (2015) Stimuli-responsive supramolecular hydrogels with high extensibility and fast self-healing via precoordinated mussel-inspired chemistry. Chem Mater 27 (22):7627–7635
35. Bode S, Zedler L, Schacher FH, Dietzek B, Schmitt M, Popp J, Hager MD, Schubert US (2013) Self-healing polymer coatings based on cross-linked metallosupramolecular copolymers. Adv Mater 25(11):1634–1638

36. Kotteritzsch J, Hager MD, Schubert US (2015) Tuning the self-healing behavior of one-component intrinsic polymers. Polymer 69:321–329
37. Syrett JA, Mantovani G, Barton WRS, Price D, Haddleton DM (2010) Self-healing polymers prepared via living radical polymerisation. Polymer Chemistry 1:102–106
38. Kennedy JP, Castner KF (1979) Thermally reversible polymer systems by cyclopentadienylation. II. The synthesis of cyclopentadiene-containing polymers. J Polym Sci, Part A: Polym Chem 17(7):2055–2070
39. Yoon JA, Kamada J, Koynov K, Mohin J, Nicolay R, Zhang Y, Balazs AC, Kowalewski T, Matyjaszewski K (2012) Self-healing polymer films based on thiol-disulfide exchange reactions and self-healing kinetics measured using atomic force microscopy. Macromolecules 45:142–149
40. Roy N, Buhler E, Lehn JM (2014) Double dynamic self-healing polymers: supramolecular and covalent dynamic polymers based on the bis-iminocarbohydrazide motif. Polym Int 63 (8):1400–1405
41. Kuhl N, Bode S, Bose RK, Vitz J, Seifert A, Hoeppener S, Garcia SJ, Spange S, Zwaag S, Hager MD, Schubert US (2015) Acylhydrazones as reversible covalent cross linkers for self-healing polymers. Adv Funct Mater 25:3295–3301
42. Banerjee S, Tripathy R, Cozzens D, Nagy T, Keki S, Zsuga M, Faust R (2015) Photo-induced smart, self-healing polymer sealant for photovoltaics. ACS Appl Mater Interfaces 7: 2064–2072
43. Schafer S, Kickelbick G (2015) Self-healing polymer nano-composites based on Diels-Alder reactions with silica nanoparticles: the role of the polymer matrix. Polymer 69:357–368
44. Guo K, Zhang DL, Zhang XM, Zhang J, Ding LS, Li BJ, Zhang S (2015) Conductive elastomers with autonomic self-healing properties. Angew Chem Int Ed 54:12127–12133
45. Wang S, Xuan S, Jiang W, Jiang W, Yan L, Mao Y, Liua M, Gong X (2015) Rate-dependent and self-healing conductive shear stiffening nanocomposite: a novel safe-guarding material with force sensitivity. J Mater Chem A 3:19790–19799
46. Potts JR, Dreyer DR, Bielawski CW, Ruoff RS (2011) Graphene-based polymer nanocomposites. Polymer 52:5–25
47. Liu J, Song G, He C, Wang H (2013) Self-healing in tough graphene oxide composite hydrogels. Macromol Rapid Commun 34:1002–1007
48. Giannelis EP (1996) Polymer layered silicate nanocomposites. Adv Mater 8:29–35
49. Hussain F, Hojjati M, Okamoto M, Gorga RE (2006) Polymer-matrix nanocomposites, processing, manufacturing, and application: an overview. J Compos Mater 40:1511–1575
50. Zhu B, Jasinski N, Benitez A, Noack M, Park D, Goldmann AS, Barner-Kowollik C, Walther A (2015) Hierarchical nacre mimetics with synergistic mechanical properties by control of molecular interactions in self-healing polymers. Angew Chem Int Ed 54: 8653–8657
51. Wang Q, Mynar JL, Yoshida M, Lee E, Lee M, Okuro K, Kinbara K, Aida T (2010) High-water-content mouldable hydrogels by mixing clay and a dendritic molecular binder. Nature 463:339–343
52. Lewis CL, Dell EM (2016) A review of shape memory polymers bearing reversible binding groups. J Polym Sci, Part B: Polym Phys 54(14):1340–1364
53. Wei M, Zhan M, Yu D, Xie H, He M, Yang K, Wang Y (2014) Novel poly(tetramethylene ether)glycol and poly(ε-caprolactone) based dynamic network via quadruple hydrogen bonding with triple-shape effect and self-healing capacity. ACS Appl Mater Interfaces 7 (4):2585–2596
54. Hennink WE, Nostrum CF (2002) Novel crosslinking methods to design hydrogels. Adv Drug Deliv Rev 54(1):13–36
55. Wang Y, Ameer GA, Sheppard BJ, Langer R (2002) A tough biodegradable elastomer. Nat Biotechnol 20:602–606
56. Engelmayr GC, Cheng M, Bettinger CJ, Borenstein JT, Langer R, Freed LE (2008) Accordion-like honeycombs for tissue engineering of cardiac anisotropy. Nat Mater 7: 1003–1010

57. Chen Q, Liang S, Thouas GA (2013) Elastomeric biomaterials for tissue engineering. Prog Polym Sci 38:584–671
58. Najafabadi AH, Tamayol A, Annabi N, Ochoa M, Mostafalu P, Akbari M, Nikkhah M, Rahimi R, Dokmeci MR, Sonkusale S, Ziaie B, Khademhosseini A (2014) Biodegradable nanofibrous polymeric substrates for generating elastic and flexible electronics. Adv Mater 26 (33):5823–5830
59. White MS, Kaltenbrunner M, Głowacki ED, Gutnichenko K, Kettlgruber G, Graz I, Aazou S, Ulbricht C, Egbe DAM, Miron MC, Major Z, Scharber MC, Sekitani T, Someya T, Bauer S, Sariciftci NS (2013) Ultrathin, highly flexible and stretchable PLEDs. Nat Photonics 7: 811–816
60. Dankers PYW, Hermans TM, Baughman TW, Kamikawa Y, Kieltyka RE, Bastings MMC, Janssen HM, Sommerdijk NAJM, Larsen A, Luyn MJA, Bosman AW, Popa ER, Fytas G, Meijer EW (2012) Hierarchical formation of supramolecular transient networks in water: a modular injectable delivery system. Adv Mater 24(20):2703–2709
61. Chen Y, Pang XH, Dong CM (2010) Dual stimuli-responsive supramolecular polypeptide-based hydrogel and reverse micellar hydrogel mediated by host-guest chemistry. Adv Funct Mater 20(4):579–586
62. Yan X, Xu D, Chi X, Chen J, Dong S, Ding X, Yu Y, Huang F (2012) A multi-responsive, shape-persistent, and elastic supramolecular polymer network gel constructed by orthogonal self-assembly. Adv Mater 24(3):362–369
63. Jia YG, Zhu XX (2015) Self-healing supramolecular hydrogel made of polymers bearing cholic acid and β-cyclodextrin pendants. Chem Mater 27(1):387–393
64. Ceylan H, Urel M, Erkal TS, Tekinay AB, Dana A, Guler MO (2013) Mussel inspired dynamic cross-linking of self-healing peptide nanofiber network. Adv Funct Mater 23 (16):2081–2090
65. Park JP, Song IT, Lee J, Ryu JH, Lee Y, Lee H (2015) Vanadyl-catecholamine hydrogels inspired by ascidians and mussels. Chem Mater 27(1):105–111
66. Nakahata M, Takashima Y, Yamaguchi H, Harada A (2011) Redox-responsive self-healing materials formed from host–guest polymers. Nat Commun 2:511

Self-healed Materials from Elastomeric Composites: Concepts, Strategies and Developments

Ramna Tripathi, Pratibha Sharma, Avneet Saini and Gaurav Verma

Abstract Self-healing materials have been inspired by the ability of human/animal skins and plant tissues to self-repair their minor damages. Self-healing polymers and fibre-reinforced polymer composites acquire the ability to heal small ruptures and cracks during their service life. Presence of microscopic cracks and other types of damage depletes thermal, electrical, mechanical and acoustical properties, and seriously impairs performance of the material. This can ultimately lead to complete failure. Self-healing materials are imbibed with huge quantities of inorganic conducting fillers to trigger self-healing behaviours which are influenced by external forces, such as temperature, change in light intensity and spectrum, pH, or ambient chemistry. Three conceptual approaches of healing system exists which are based upon encapsulation, arterial network and intrinsic capabilities. Self-healing can be generated intrinsically by auto-response mode without manual intervention or requiring external stimulus. Primarily self-healing mechanisms entail resuming mechanical integration lost during cracking and crazing. As polymers are critical products used in coatings, electronics, transportation and energy industries, it is important to induce them with self-repairing mechanisms. Self-healing materials possess remarkable potential in enhancing the longevity of load bearing and tribological materials. Consequently, a large number of academic and industrial research organizations have come forward to explore new concepts in design and synthesis of such materials like thermosets, thermoplastic, elastomers, polymer composites, supramolecular gels, nanostructure conductive hydrogels. These

R. Tripathi
Department of Physics, THDC-Institute of Hydropower Engineering and Technology, Tehri, Uttarakhand, India

P. Sharma · A. Saini
Department of Biophysics, Panjab University, Chandigarh, India

G. Verma (✉)
Dr. SS Bhatnagar University Institute of Chemical Engineering & Technology, Panjab University, Chandigarh, India
e-mail: gauravvermas@gmail.com; gauravverma@pu.ac.in

G. Verma
Centre for Nanoscience & Nanotechnology, Panjab University, Chandigarh, India

D. Ponnamma et al. (eds.), *Smart Polymer Nanocomposites*,
Springer Series on Polymer and Composite Materials,
DOI 10.1007/978-3-319-50424-7_8

materials can be easily processed, re-used and recycled. Their unique self-repairing properties, the simplicity of their synthesis, their availability from renewable resources and the low cost of raw ingredients augur well for futuristic applications.

Keywords Responsive polymers · Elastomeric composites · Intrinsic · Extrinsic and supramolecular approaches

Contents

1 Physics of Polymers and Elastomers

An elastomer or "elastic polymer" is characterized by its typical mechanical response "they bounce", i.e. they can be stretched to many times their original length and can bounce back into their original shape without permanent deformation. Elastomers comprise an incredibly versatile range of chemical structures although they have weak intermolecular forces. An elastomer will undergo an immediate, linear and reversible response, i.e. an elastic response in which the strain is directly proportional to stress mechanically analogous to an ideal spring according to Hooke's Law. An elastomer is distinguished from a material that exhibits an elastic response in a way that elastomer can exhibit a large strain [1].

The elastomeric response to mechanical forces is highly dependent on the chemical structure and molecular architecture of elastomers. The stretching of an elastomer does not depend upon change in bond length or bond angle but upon rotation about bonds. As shown in Fig. 1a, an unstrained elastomer acquires a random coil confirmation. Once subjected to stress, the randomly oriented chains tend to uncoil into a linear patterned formation, thus showing additional strains (Fig. 1b). Therefore, high strain requires an elastomer to essentially be a polymer

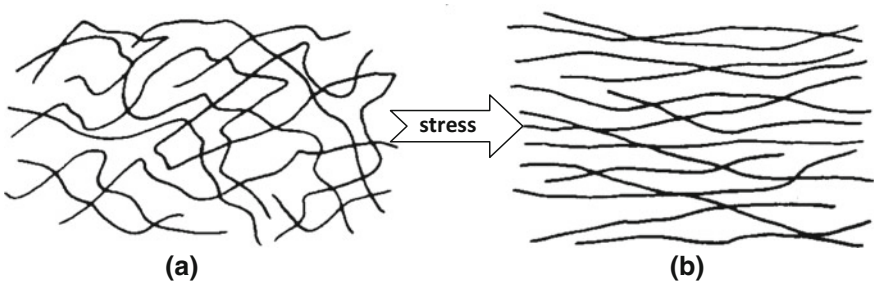

Fig. 1 **a** An unstrained elastomer with a random coiled structure and **b** an uncoiled elastomer under stress [1]

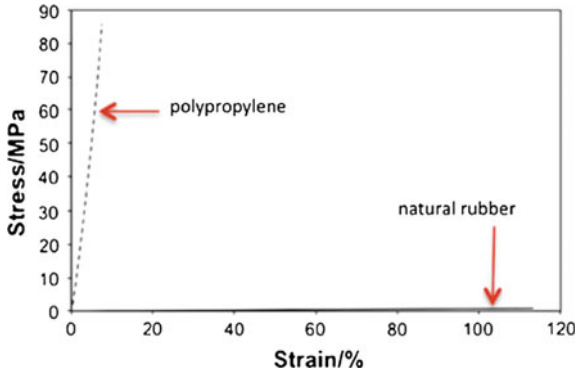

Fig. 2 Comparison of the elastic stress–strain curves of a thermoplastic polymer (*polypropylene*) and an elastomer (*rubber*) [2]

with a preferred high molar mass and long-chain structure. The limit to this elastic response in polymeric materials is when these long-chain molecules are in fully extended conformations with decrease in entropy. The system tends to favour high entropy state bounces back to coiled state. If you stretch it far enough, the chains will line up straight enough to crystallize which is avoided by reversible random coiling (Fig. 2).

In order to obtain reversibility and instant response, elastomers must have flexible chains with weak restraining intermolecular forces. Elastomers should have minimal hydrogen bonding or polar functional groups that contribute to intermolecular forces. Elastomers are unlikely to contain heavy and rigid groups such as benzene, bulky side-chains such as isopropyl which add stearic hindrance, polar groups such as ester and hydrogen bonding groups such as hydroxyl. Of course, not all amorphous polymers are elastomers. It depends on its glass transition temperature, T_g. This is the temperature above which a polymer becomes soft and pliable, and below which it becomes hard and glassy. Therefore, it is applicable to elastomers with T_g only at ambient temperatures.

The reversible elasticity of the elastomers is due to essential property called as "cross-linking". Cross-linking is the forming of covalent links between the different

polymer chains, joining them all into a single-networked molecule and forming a structure resembling a fish net. Chemical cross-linking prevents viscous flow and hence, creep formation in which an elastomer, once deformed, will remember and "relax" back to the deformed shape. Cross-linking makes it even harder to pull molecules out of their original positions, and so it bounces back even better when stretched. However, once cross-linked the unstrained shape of an elastomer hard to alter and the elastomer cannot be reprocessed or recycled. This permanence brought about by cross-linking and the needs to perform a cross-linking reaction on elastomers are undesirable and make their applications difficult. Elastomers are used in a variety of applications including gaskets, shoe heels, seals, bladders, pacifiers, medical prostheses and as the matrix for flexible composites, such as tires. While these materials can provide extraordinary chemical or thermal resistance sustain large deflections with little or no permanent deformation, elastomers can fail through fracture and fatigue processes. The answers to this dilemma is the use of thermosetting polymers using microcapsule based self-healing or thermoplastic elastomers in which chemical cross-linking is replaced by a network of physical cross-link [3].

Though elastomers have found versatile applications, the failures of commercial and industrial elastomer-based equipments have raised the immediate need for mutilation-tolerant materials. The tread separation failures of vehicular tires were caused by fatigue crack and resulted in propagation and complete tire failure, causing loss of property as well as human life. One possible way of preventing or mitigating such failures would be to incorporate a self-healing functionality into the elastomeric material. It offers unique development opportunities in the field of highly engineered materials, such as tires, for which safety, performance, and longer fatigue life are crucial factors [4].

When discussing healing of rubbers and elastomers, it involves the reformation of cross-links after a network has undergone breakage [5]. In addition to reformation of cross-links, rubbers have also been observed to bond to themselves through diffusion at elevated temperatures and pressures [6]. A reasonable approach is used to introduce self-healing behaviour by reacting commercially available bromobutyl rubber with various amines resulting in the formation of reversible ionic associates that exhibit physical cross-linking ability which facilitates the healing processes by temperature- or stress-induced rearrangements [4]. Therefore, further in this chapter "self-healing" material will be used to refer to a material if gets torn apart, when placed back into reasonable contact autonomically bridges the impairment and recovers majority of its properties and functions (Fig. 3).

2 Genesis and Mechanisms of Self-healing

Self-healing materials encompass a wide range of materials capable of restoring their functionality on damage. All living beings have innate property of self-healing which enable them to cope with all sorts of damage or injury they experience during

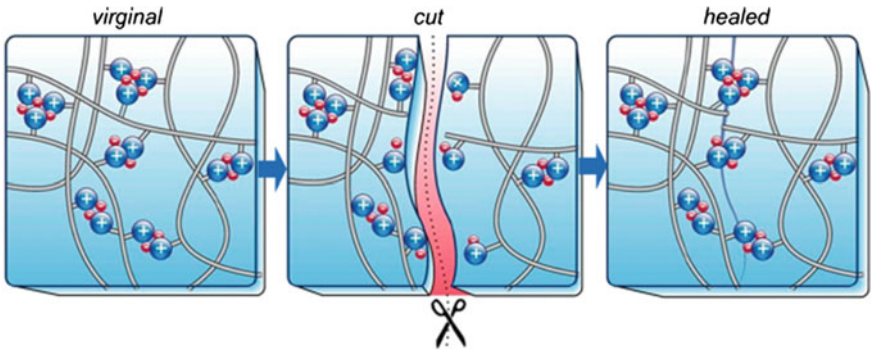

Fig. 3 Schematic representation of self-healing process in an ionic rubber network by reformation of reversible ionic associates [4]

their lifetime [7]. Inspired by nature, these materials are gaining interest [8]. In fact, natural elements, systems and processes are spontaneous and highly efficient as they have been developed and optimized through very slow evolutionary steps and constitute a continuous source of inspiration to create new artefacts [9]. Thus, skin cuts and wounds heal, broken bones heal, coagulating blood and even lost parts of living bodies can be replaced in some cases. For example, rhino's horn, when damaged, the credit of self-mending goes to a keratin-based resin, which seals scratches and wounds. Therefore, the healing prospects of living organisms and the repair tactics in natural materials is of great interest to scientists, engineers and technological designers seeking light weight structures with extended the working life and lower production costs. A clear shift from damage sustaining to damage repairing philosophy need to be followed.

The concept of self-healing is not naive to the world; for example, manufacturing transportation marvels like aircrafts, ships have been motivated from airborne and aquatic animals. Self-healing in natural systems in a unique and continuous process sometimes occurs stage-wise. Composite systems such as bones simply heal by remodelling themselves constantly through different stages such as detachment of damaged material, substitution by fresh material, removal of over-designed material and structures under stress are reinforced by supplementary material. All these steps are facilitated by specific cells entrapped in the bone tissues which act as strain sensors and track large deformations. Subsequently, signals are sent to cells responsible for removing or forming material (bone) [10]. For this reason only, a particular field of science called biomimetics (literally from Greek "imitation of life") evolved which studies and analyses biological structures, forms and functions in order to imitate the mechanisms and the connected principles of self-healing and transfer it to artificial materials and processes. Over the past few years, biomimetics has contributed to the development of several study fields like engineering, chemistry, physics and material science in one way or other [9].

Damage in general terms can be described as unwanted changes occurring in a system that hinders its properties and normal functioning. The understanding of the nature and the magnitudes of damage and of degradation processes is the key to design artificial self-healing functionalities for systems, structures and devices. The term damage does not necessarily imply a total loss of performance, but rather impairment in level of system operation from optimal. Hence, when both states of the system—original one and damaged one—are compared, the extent of damage can be deduced. Damage is typically a confined phenomenon around a crack or fracture, so the ultimate challenge lies in the timely detection of this damage before it spreads to all dimensions leading to final failure [11]. This can be achieved by drafting materials with properties such as damage detection and self-healing. Self-healing materials could be polymers, metals, ceramics and their composites that when damaged through thermal, mechanical, electrical, ballistic or other means have the capability to heal and refurbish or restore the impaired functionality of the material. This is a very valuable characteristic to design into a material since it effectively multiplies the service lifetime of the product and has desirable fiscal and social safety attributes.

With time, most materials (systems) become less dependable and lose their value, usefulness for the operation due to deterioration processes where defects grow and integrate to cause component and lastly system level damage (e.g. fatigue or corrosion damage accumulation). On a relatively short time scale, damage can also result from scheduled distinct events such as aircraft landing and from spontaneous events such as an impact. If this damage is allowed to propagate, the system operation reaches a point where it is no longer functional; this point is referred to failure. The main causes of degradation of materials may be summarized as:

(1) Harmful materials, substances and agents such as oxygen, oxidizing agents, water, salts, poisons, active materials and living biological bodies such as virus, bacteria, fungi, insects, animals, human beings and others,
(2) Environmental factors such as heat, visible light, external mechanical force, e.g. strong wind, radiation, pressure and precipitation, collapse of the adjacent structure may be due to natural calamity, a sudden impact and others.

Such deterioration (or damage) is in general a relentless and irreversible process, increasing exponentially with time until a certain critical limit is reached where either significantly repairing costs are high or a fatal failure is going to occur. Therefore, materials with increased lifetime and reliability can play critical role in systems and devices working in transportation, building, information transfer, medicine and strategic like military, space missions as well as in routine life.

In order to prevent such deterioration, the following response mechanisms are known.

2.1 Passive (Built-in Damage Prevention)

It is the method of using protection agents on the areas prone to deterioration, and this protection is short-lived, directly proportional to the concentration of the agent. It cannot repair by itself and hence no memory of the innate structure.

2.2 Active (Autonomous or Self-repair)

It involves direct attack on atoms and molecules of the material itself instead of protection agents. More the number of dented sites and more is the cumulative damage with time and at certain positions, more is the amount of repairing agents required. Moreover, the choice of repairing agent is controlled by the repair rate. A transfer of material is needed, and a memory of the original structure is preferable.

Presently, passive protection mechanisms are readily applicable and common for many different materials systems; therefore, they predominate in industries. However, such materials will always stay submissive, and therefore their lifespan and functionality is limited depending upon the quantity of protective additives and the intensity of their consumption. Therefore, improved and favourably active processes for the protection/repair of damaged materials—self-repairing-processes—were developed and need to be developed further.

All materials, natural or synthetic, have a tendency to degrade by natural or artificial causes. In the case of structural materials, the long-time degradation processes lead to microcracks that cause failure. Thus, repairing is indispensable to enhance dependability and lifetime of materials, in aerospace and automotive industry, IT and robotics, healthcare and pharma industries. Though the natural process like blood coalescence or repairing of cracked bones triggered the scientists to integrate the same theory into artificial materials but due to the complexity of the healing processes in natural materials, it is not fully achievable [12–15]. Jargons for self-repairing, such as autonomic-healing and autonomic-repairing are used. In most cases, incorporation of self-healing properties in man-made materials is not enough to perform the self-healing action. Based on these considerations, the repairing mechanisms of self-healing material systems can be of the following two types:

- **Autonomic (without any intervention)**: It is self-healing that occurs automatically without external trigger except the damage [16]. This means that it is fully self-instigated and requiring no outer intervention of any kind whatsoever [17].
- **Non-autonomic (needs human intervention or external triggering)**: This self-healing mechanism requires human action or outside prompting [18]. The material being partially self-contained has the healing capability, but an additional external stimulus such as thermal (heat) or light/electromagnetic

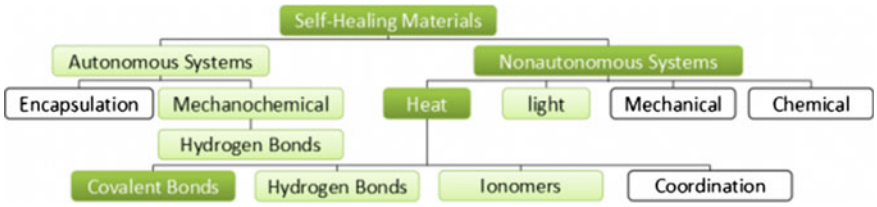

Fig. 4 Various mechanisms for autonomous and non-autonomous self-healing systems [20]

(UV radiation) is required for the healing to occur [17]. This can be represented through paints which self-heal when warmed up (for example, when exposed to the summer sun) [19] (Fig. 4).

3 Designing Strategies for Healing Capacity

Materials science, one of the most fascinating and challenging branches of knowledge, is a multidisciplinary science. The different types of materials such as plastics/polymers, paints/coatings, metals/alloys and ceramics/concrete have their own self-healing mechanisms depending on material microstructure. In understanding and designing materials with desirable properties, knowledge of their physics, chemistry and engineering aspects is necessary. Effort to design such novel and intelligent engineering materials with autonomous healing power have picked up considerably in recent years [21–23]. Healing is a three-step process, which is similar to that of a biological response. The first step involves triggering action immediately after the damage occurs. The second step is the quick transportation of materials to an affected region. The third step involves the chemical repair process [24]. This process is what differs in various self-healing materials and is achieved by using two approaches: extrinsic and intrinsic. In extrinsic systems, the healing agent is sequestered in microcapsules or vascular networks. The healing chemistries remain separated from the surrounding polymer and are released on the event of crack or damage. In intrinsic systems, the material has inherent capacity to restore its integrity that is triggered by damage or by an outside stimulus. It involves reversible cross-links and supramolecular interactions.

3.1 Release of Healing Agents

Liquid active agents, such as monomers, dyes, catalysts and hardeners entrapped into microcapsules, hollow fibres or channels, are embedded into polymeric systems during manufacturing stage. When there is a crack or any other damage, these

reservoirs are ruptured and the reactive agents are discharged into the cracks by capillary force where it solidifies on reacting with pre-dispersed catalysts and heals the crack. The propagation of cracks is the major driving force of this process. On the other hand, it requires the stress from the crack to be relieved of any kind of stress, which makes the task of designing such materials difficult. As this process does not need a manual or external intervention, except the damage, i.e. propagation of cracks, it is autonomic.

The following sections give an overview of different possibilities to explore this concept of designing self-healing materials.

3.1.1 Microcapsule Embedment

Microencapsulation is a process of entrapping micron-sized particles of solids, droplets of liquids, or gases in a tiny sphere which in turn isolates and protects them from the external environments [25–28]. It is carried out to form microcapsules which have two parts, namely the core and the shell. These microcapsules are inert as there is negligible reactivity of the shell to the core material. They may have spherical or irregular shapes and may vary in size ranging from nano- to microscale. Self-healing polymer composites are so designed to contain microcapsules enclosing healing agents or catalysts. Early literature [29, 30] suggests the use of microencapsulated healing agents in a polyester matrix to achieve a self-healing effect. But they were unsuccessful in producing practical self-healing materials. The earlier practical demonstration of self-healing materials was performed in 2001 by Prof. Scot White and his collaborators [31]. Self-healing capabilities were achieved by embedding microcapsules carrying healing agents into polymer matrix containing uniformly dispersed catalysts. The self-healing strategy used by them is shown in Fig. 5.

3.1.2 Capsule–Catalyst System

This process has been demonstrated with dicyclopentadiene (DCPD) as the liquid healing agent and Grubbs' catalyst (benzylidene-bis(tricyclohexylphosphine) dichlororuthenium) as an internal chemical trigger and dispersed them in an epoxy matrix. The monomer being relatively less expensive, highly durable and less viscous is advantageous. The low viscosity of the monomer helps it to flow into the crack plane. The microcapsules filled with DCPD release their content after mechanical damage and it then reacts with the Grubbs' catalyst dispersed in the epoxy resin to initiate a ring-opening metathesis polymerization (ROMP) [32, 33] and a highly cross-linked tough polycyclopentadiene is formed that seals the crack Fig. 6. The catalyst lowers the energy barrier of the polymerization reaction so that it can occur at room temperature. The authors have demonstrated that as much as 75% of the recovery of fracture toughness compared to the original specimen can be achieved [34].

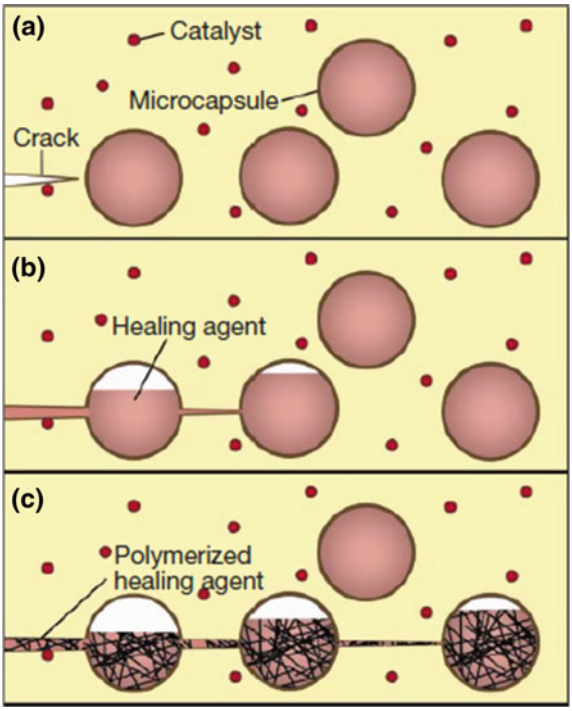

Fig. 5 Schematic representation of autonomic self-healing concept using embedded microcapsules containing healing agent in a polymer matrix [31]

Multicapsule System

The same group of scientists later used another approach in which catalyst was encapsulated instead of monomer healing agent [35]. Monomers such as hydroxyl-functionalized polydimethylsiloxane (HOPDMS) and polydiethyoxysilane (PDES) were added to vinyl ester matrix where they stay as microphase-separated droplets. The polyurethane microcapsules containing the catalyst di-*n*-dibutyltin dilaurate (DBTL) is then dispersed in the matrix (Figs. 5 and 6). Upon rupture of these capsules, the catalyst reacts with the monomer and polycondensation reaction of the monomers takes place (Fig. 7).

The critical factors that influence the microencapsulation-based self-healing approach to produce an effective self-healing material are summarized in Table 1.

Hollow Fibre Embedment

Self-healing approach using microcapsules is flawed by uncertainty in achieving complete and/or multiple healing as it has limited amount of healing agent and the

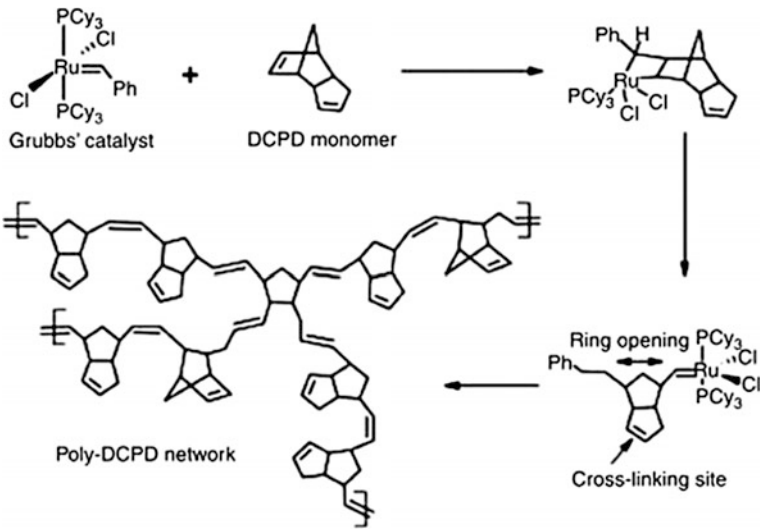

Fig. 6 Ring-opening metathesis polymerization of DCPD (permission requested [32])

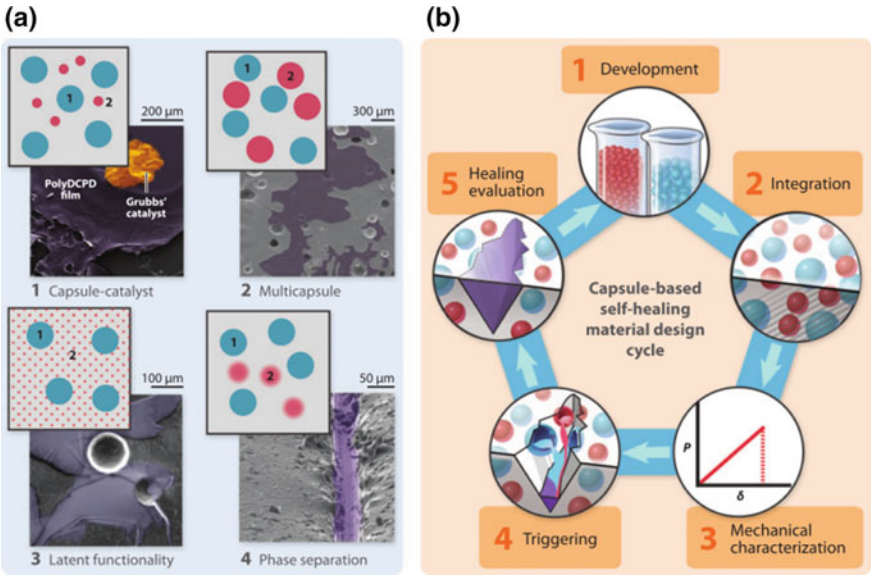

Fig. 7 **a** Capsule-based self-healing includes four main sequestration schemes. Materials with the sequestered components are labelled as 1 and 2. (*1*) Capsule–catalyst systems include an encapsulated healing agent and a dispersed catalyst phase, (*2*) multicapsule systems utilize two or more capsules that sequester separate components of the healing agents, (*3*) latent functionality systems make use of functional groups within the matrix phase that react with an encapsulated healing agent upon damage and release. (*4*) Phase-separated systems include at least one healing component that is phase-separated within the matrix, whereas other components may be encapsulated. **b** The design cycle for capsule-based self-healing materials composed of (*1*) development of encapsulation/separation technique, (*2*) capsule integration into the bulk material, (*3*) characterization of mechanical properties, (*4*) validation of damage triggering and release of healing agents and (*5*) evaluation of healing performance [16]

Table 1 Factors influencing the microencapsulation-based self-healing materials [36]

Parameters	Factors of influence
Micro capsules	Inertness towards the polymers shell
	Capsules lifetime
	Compatibility with the medium
	Weakness of the shell wall
	Proximity to the catalyst molecules
	Interfacial attraction strength between capsules and matrix
Monomers	Low viscosity
	Low volatility
Polymerization process	Rate of polymerization
	Stress relaxation
	Shrinkage
	Temperature
Catalysts	Solubility in monomer
	Dispersion
Coatings	Stability of properties upon incorporation of microcapsules
	Thickness
	Dispersion
	Processing
Healing effect	Rate of healing
	Repetitional

amount of healing agent left cannot be quantified. Manifold healing is only feasible when excess healing agent is available in the matrix after the first healing has occurred. Thus, to achieve multiple healing in composite materials, another type of reservoir that might be able to deliver larger amount of liquid healing agent was developed by Dry and coworkers [29, 37, 38]. However, the approach could not be practically successful. Later, large diameter capillaries were embedded into resins by Motuku et al., but the trials were unsuccessful as well [39]. Bleay et al. have used smaller hollow glass fibres (Hollex fibres) filled with resin as shown in the Fig. 8 [40]. Composites system formulated on the basis of these filled glass fibres were not of much success as the epoxy resins were highly viscous to be delivered into the crack and curing was also not good. Bond and coworkers later developed a process to optimize the production of hollow glass fillate [41] and used these fibres as the container for liquid healing agents and/or dyes [42–46]. These borosilicate glass fibres have diameter ranging from 30 to 100 μm with hollowness of 55%.

Bond and coworkers have employed a biomimetic approach of clot formation and fabricated composites with bleeding ability leading to polymerization and crack closure. Hollow fibres containing uncured resin or hardener (mixed with UV fluorescent dye for visual inspection) were prepared and piled to achieve a special layered-up (0°/90°) structure in the matrix (epoxy resin) in combination with

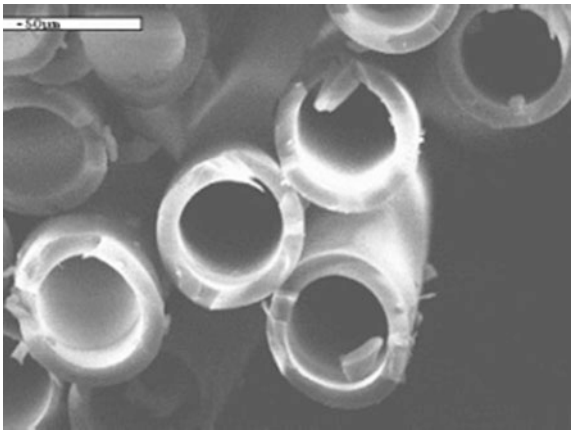

Fig. 8 Typical scanning electron micrographs of hollow glass fibres [47]. Copyright 2006.

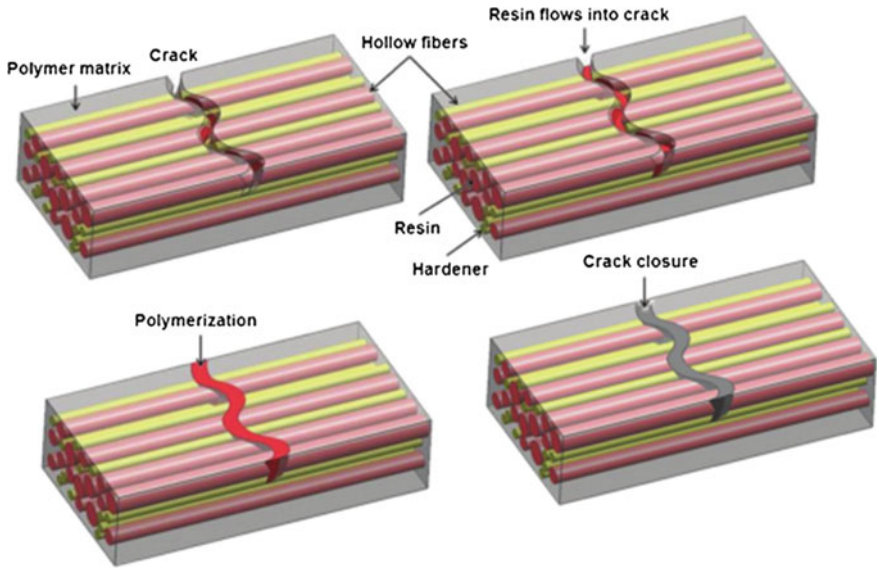

Fig. 9 Schematic representation of self-healing concept using hollow fibres [45]

conventional glass fibre/epoxy system. Hollow fibre-based self-healing strategy is shown in Fig. 9.

They have demonstrated that composite panels prepared using hollow fibres containing repairing agents can restore up to 97% of its initial flexural strength more than that achieved by microencapsulation method. The release and infiltration of fluorescent dye from fractured hollow fibres into the crack plane was also demonstrated. This approach of self-healing material design offers certain advantages, which are as follows:

- Higher volume of healing agent is available to repair damage which implies multiple cracks can be catered to;
- Different activation methods/types of resin can be used, hence greater ability to heal different failures;
- Visual inspection of the damaged site is feasible, which implies easier detection and confirmation of healing, thus improved efficiency;
- Hollow fibres can easily be mixed and tailored with the conventional reinforcing fibres, implies no change in structural design but can be functionally modified according to our need.

Besides the above advantages, this approach has the following disadvantages as well:

- Fibres must be broken to release the healing agent; compromising sensitivity.
- Low-viscosity resin must be used to facilitate fibre infiltration;
- Use of hollow glass fibres in carbon fibre-reinforced composites will lead to CTE (coefficient of thermal expansion) mismatch;
- Multistep fabrication is required making it cubersome.

3.1.3 Reversible Cross-links

Cross-linking, which is a permanent and irreversible process of polymeric materials, is done to achieve superior mechanical properties, such as high modulus, solvent resistance and high fracture strength which are conducive to any material. However, excessive cross-linking brings along brittleness and tendency to crack. As it is irreversible process, it adversely affects the re-fabrication and remoulding ability of polymers. One approach to these problems associated with cross-linked polymers is the introduction of reversible cross-links in polymeric systems [48–50]. The weak reversible interactions (weak metal-amine bonds or weak hydrogen bonds), in conjunction with a polymeric structure form a reversible network by cross-linking which will break under a sufficient mechanical stress. The weakest bond in the polymer structure is the polymerization or cross-linking bond of the Diels-Alder reaction adduct. While strong in comparison with other types of non-covalent chemical bonds, this is the first bond to break when the material is loaded to failure or heated above its transition temperature. However, because this bond is reversible, this is also the bond that reforms when the material is cooled below the transition temperature. Initial results on macrocracked neat polymer samples show excellent potential that near full recovery of original strength is possible. Moreover, healing may be carried out multiple times on the same broken bond [51]. However, an external trigger such as thermal, photo- or chemical activation is needed to achieve reversibility, and thereby the self-healing ability.

3.2 Supramolecular Polymers

The traditional polymerization is achieved due to the size and entanglement of long chains of monomers, held together by covalent bonds leading to the formation of conventional polymers. Recently, in contrast to this, assembly of low molar mass monomers by reversible non-covalent interactions to obtain polymer-like rheological or mechanical properties is being done, called as supramolecular polymers [52–55]. Supramolecular swollen polymer networks have received particular interest in self-healing materials as their behaviour can be tailored within the limits of highly elastic solid (steel like represented by spring) and low-viscous (represented by easy moving dashpot) solutions.

As non-covalent interactions can be easily broken and can be under thermodynamic equilibrium, this special class of macromolecular materials, that is, the so-called supramolecular polymers, shows additional features compared to usual polymers. These features include switchable environment-dependent properties, improved processing, and self-healing behaviour. In general, supramolecular polymers can be divided broadly into two categories, which are main-chain and side-chain types. Although non-covalent interactions hold, the backbone of the main-chain supramolecular polymers is held by non-covalent interactions, but side-chain supramolecular polymers are used to introduce modifications in conventional covalent polymers. These non-covalent main- or side-chain interactions are mechanically dynamic as the transient cross-links are under constant a dissociation/association equilibrium which in turn allows stress relaxation and benefits to the self-healing of the material.

Non-covalent forces that make up supramolecular polymers are metal–ligand interactions, π–π interactions, hydrophobic, electrostatic interactions and hydrogen bonding. Out of all these assembly forces, hydrogen bonding is the most preferable route to synthesize supramolecular polymers. In using hydrogen bonding, there are issues to find the right balance between the association constant and a reversible system. The higher the association constant, the lesser is the reversible interaction. In contrast, the lower the association constant, the better the reversibility, that is, smaller assemblies and poor mechanical properties.

Meijer and coworkers were the first to synthesize supramolecular polymers of ureidopyrimidone (Upy) by using quadruple hydrogen bonding non-covalent interactions with high degree of polymerization [56, 57]. The resulting material display mechanical properties similar to traditional polymers along with self-healing capacity. This discovery of using weak reversible hydrogen bonding interactions to produce supramolecular assemblies with high association constant and having polymeric properties makes this field an exciting area for materials research. The Upy compounds are cheap and can be incorporated into other polymeric systems to improve processability or other functionalities. This hydrogen bonded unit is further utilized in the chain extension of telechelic polysiloxanes, polyethers, polyesters to form side-chain type polymers. On the basis of the above discovery, a spin-off company from the Technical University of Eindhoven,

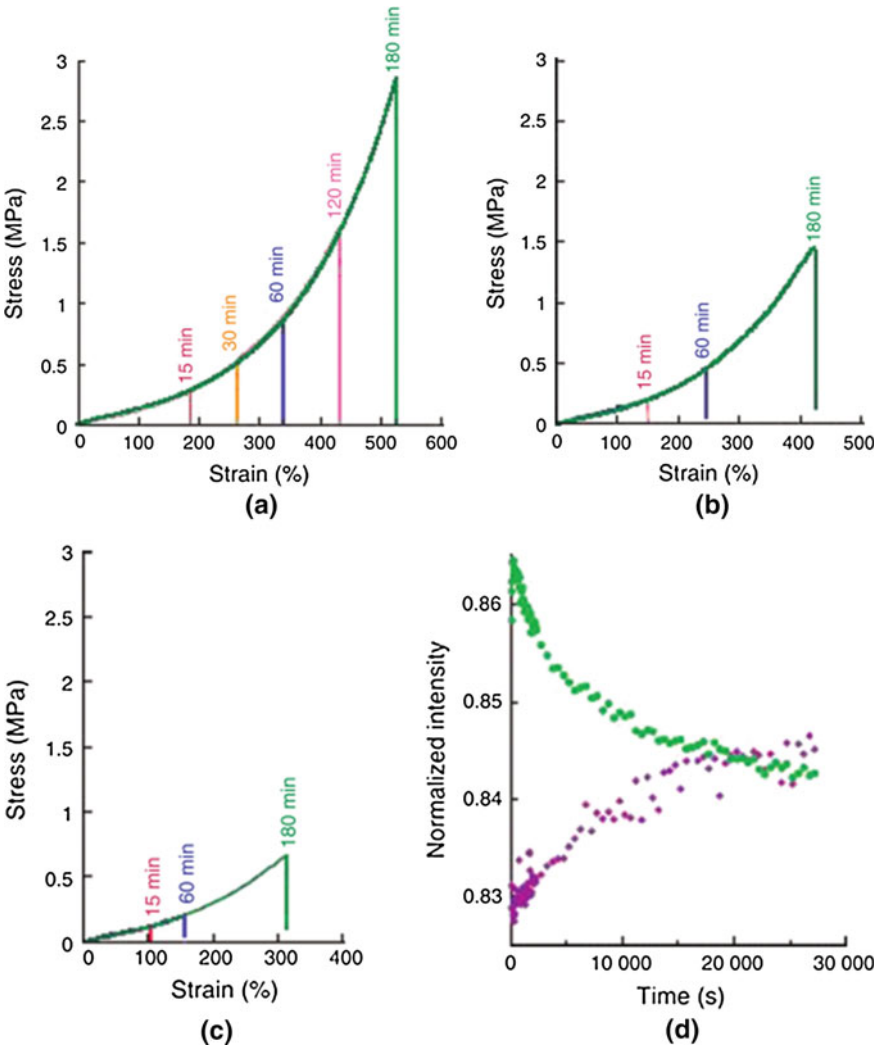

Fig. 10 Self-healing in rubbers at room temperature: **a** stress–strain behaviour measured at 40 °C after different healing times when the cut parts are brought into immediate contact at 20 °C, **b** stress–strain behaviour of mended samples measured at 40 °C; after keeping broken samples apart for 6 h and then mending done at 20 °C, **c** same as (**b**) with resting time between cutting and mending 18 h and mending at 20 °C. *Coloured vertical lines* in (**a**–**c**) correspond to elongation at breaking for given healing times. **d** Time-dependent infrared experiments. The spectra show decrease in the intensity at 1524 cm^{-1}, free N–H bending motions (*green*), increase in the intensity at 1561 cm^{-1}, associated N–H bending motions (*purple*) [59]. Copyright 2008. Permission requested from Nature

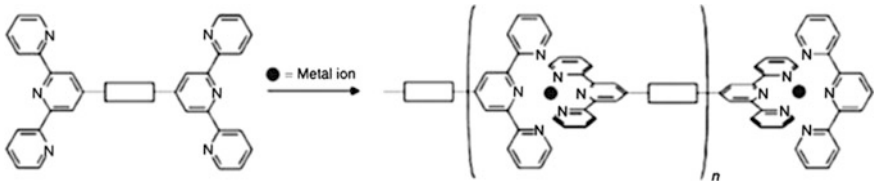

Fig. 11 An example of supramolecular polymer is bis-terpyridine–metal complex (charge and anions omitted) [61]. Copyright 2007. Reprinted with permission from American Chemical Society

SupraPolix BV, has already started exploring this field commercially [58]. Hybrid systems of supramolecular monomers and orthodox polymers were also developed. Cordier and team have recently published a very interesting piece of research that brings together supramolecular chemistry and polymer physics to develop self-healing rubbers [59]. They have used fatty diacids and triacids from renewable resources and subjected them to two-step synthetic routes to produce self-healing rubbers. In the first step, acid groups were condensed with excess of diethylene triamine, and in the second step, the condensed acid groups were made to react with urea. The resulting material shows both rubber-like characteristics as well as intrinsic self-healing capability. The prepared material can be repaired by simply bringing the two cut ends together at room temperature without the need of external heat. However, if the broken parts are kept for a longer period, they need to be hold together for longer period for self-mending and self-repairing as shown in Fig. 10.

Besides hydrogen bonding, another interaction has been looked over to design supramolecular polymers, which is metal–ligand interaction [60–62]. Metal complexes have the upper hand over other complexes due to its optical and photophysical properties. Moreover, different metal ions can be used to modulate its reversibility. Though bi-pyridine complexes are well known, it is the terpyridine-based metal–ligand complexes that are gaining increased attention as a new type of functional materials for example bis-terpyridine metal complex is shown in Fig. 11.

4 Applications

To commercialize a product in industries, the following major milestones need to be crossed:

- Idea generation (preliminary level)
- Laboratory implementation (product level)
- Scaling up of Pilot line (process level)
- Industrial applications (marketing level).

Currently, self-healing materials development is either in the preliminary or product level, and so these materials are yet to reach market profitably. Applications

of self-healing materials are expected to be very broad. In the future, it will have a massive impact on virtually all industries, from the automotive industry to the energy sector. The major applications being developed today are in automobile (windshield seal, wire/cable, gaskets, spoiler and fibre-reinforced soft touch surface for interior), building/construction (Public service buildings such as shops, restaurants and cafeterias; educational buildings such as schools and colleges; administrative buildings such as ministries and institutions building), medical devices (syringe, medical tubing, medical wrapping and packaging), mobile electronics (wire/cable, earplugs, cell phone), household appliance sector (sporting goods, footwear soles, toys and adhesives) and aerospace industries.

4.1 Civil Construction

The construction industries and contractors are looked upon for carrying out responsibilities like maintenance, monitoring and repair for life cycle of the infrastructures. The serviceability limit of these structures by most common cause of damage, i.e. cracks, can be overcome by crack control methodologies and that is where healing materials stand their applications [63]. Self-healing corrosion-resistant coatings could be beneficial for structural metallic components such as steel for achieving long-term service life with reduced maintenance cost. Structural materials like cement or concrete that can withstand extreme environments and harsh conditions will make it easier for designers to construct buildings in desert areas and polar conditions. Possibility of making buildings in space, planets or moon can be realized by having self-healing mechanisms in place.

4.2 Swelling Elastomer in Oil and Gas Industry

All elastomers are effected when it comes in contact with some chemical; most common is physical swelling. Swelling elastomers are a new breed of advanced polymers that swell upon interaction with fluids like water, oil or acid. Swelling occurs when oil or water reacts with one of the chemical ingredient of elastomer which controls its mechanical properties. Therefore, it results in change of geometry, density, hardness and other properties [64]. Water-swelling elastomers swell through the absorption of saline water following the mechanism of osmosis, while oil-swelling elastomers swell by the absorption of hydrocarbons through a diffusion process [65]. Swelling rate depends on the temperature, pressure, type of elastomer and its design and fluid composition. Swelling elastomers have replaced cement plugs in certain petroleum applications like zonal isolation where it has enhanced oil recovery tremendously. Swelling elastomer have found extensive applications where other materials fail to work like maintaining the profitability of old wells can be maintained, production from abandoned wells can be restarted, and production

from economics exploitation of inaccessible new reservoirs can be achieved economically. Swellable elastomer is an expanding and evolving technology with a huge potential. However, many challenges are still there to be overcome mainly how these elastomers deal with more extreme environments and conditions of high pressure and high temperature (HPHT) is still questionable. Highly acidic or highly saline and chemically more reactive aggressive reservoirs are also unexplored areas. Development of new swelling-elastomer materials and designing of improved and innovative applications is a need of the moment for the working envelope of HPHT and aggressive reservoirs.

4.3 Car Painting

The best example of initiating the application of laboratory-based materials to industries is done by companies such as Autonomic Materials or Akzo Nobel. More specifically, Akzo Nobel promotes a high gloss clear coat (Sikkens Autoclear LV Exclusive) for cars, which features self-healing properties when exposed to heat [66]. Nissan Motor Co. Ltd has commercialized world's first self-healing clear coat for car surfaces under the trade name of "Scratch Guard Coat" [67]. According to the company, this hydrophobic paint repairs scratches (arising from car washings, off-road driving, or fingernails, key marks, cleaning brushes, vandalism intentions) on coated car surfaces and is effective for a period of three years. This newly developed paint contains high elastic resins that prevent scratches reaching the inner layers of a painted car surface. Depending on the depth of the scratch and the temperature in the surrounding environment, the entire recovery occurs between 1 and 7 days. Another example in this category is the two-component polyurethane clear coats from Bayer Material Science (Fig. 8) [68]. The trade names of the raw materials used to formulate this coating are Desmodur and Desmophen. According to company sources (Fig. 12), this coating heals small scratches under the influence of heat (sunlight) and the trick employed to design such coatings is based on the use of dense polymer networks with flexible linkages.

4.4 Aerospace

The next industrial segment where applications of self-healing materials are foreseen is the aviation industry. Use of composites in aircrafts has grown significantly in the past years. Hollow fibres-reinforced composites are a possible solution to recover cracking or damages. Self-healing polymers have paved its way in space applications. A material that can heal itself is of great utility where access for manual repair is limited or impossible, as in a biological implant or a material that is launched into orbit in the solar system. It can extend lifetime of a satellite in orbit around earth, say twice, and would approximately decrease the cost of the mission

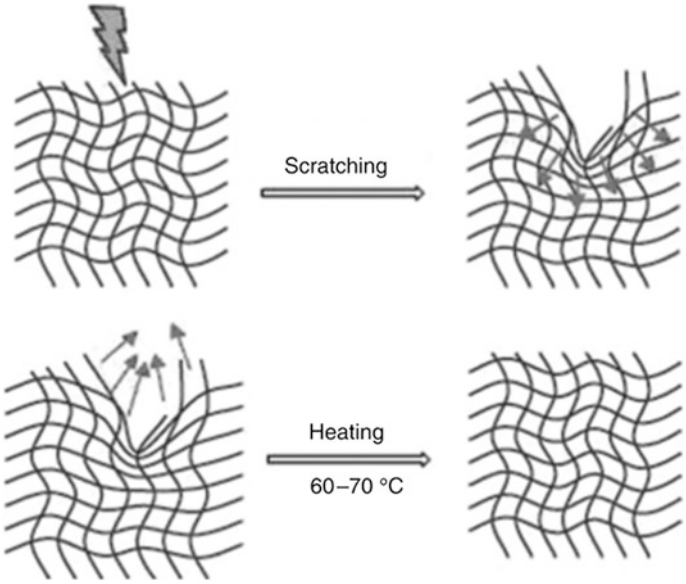

Fig. 12 Schematic representation of the reflow effect of self-healing clear coats when a scratched surface gets heat (adapted from a presentation [68] of Bayer Materials Science)

two times. Furthermore, the increase of a spacecraft lifetime will result in longer time missions to the destinations far away in the solar system, and maybe beyond. Incorporation of lighter self-healing polymer materials for constructing satellites instead of metal is a very cost-effective solution and will be able to deliver multiple satellites. Also it can avoid mishaps and help save valuable human lives by avoiding accidents due to material failures as had happened in Challenger (1986) and Columbia (2003) disasters. The extreme variation in temperatures and atmospheres makes space shuttles and vehicles very prone to failures, which can be troubleshot by allowing self-healing to occur in fabricating materials. Hence, safety of air and space craft can be improved by using self-healing components.

4.5 Military

Having safety armours, ballistic proof wear and body protection that could heal itself even during the combats will be beneficial for the armed forces. Additionally armoured vehicles, warships, jet fighters can benefit from fast self-disappearing holes in the skin of a tank, ship, or a plane, A prototype of such material already exists. DuPont's Surlyn shows good properties to heal after projectile hit damage.

4.6 Medical Dental/Artificial Body Replacements

Other areas of applications of self-healing materials are in medical segments. Nowadays, an artificial bone replacement can last up to 10–15 years. Development of good biocompatible self-healing composite materials may extend this time. Biocompatible self-healing composite may extend the service life of artificial bone, artificial teeth and soon. Another application will be in dentistry. In making artificial teeth and tooth-filling materials, self-healing would benefit their functional life time. All such material would be in big demand virtually independent of price.

5 Conclusion: Towards a New Generation of Self-healing Systems

Self-healing materials are actively under research across the world and in a century where maintenance and sustainability are emphasized, expectations of self-healing are becoming stronger. In order to develop a new generation of self-healing devices-smart structures, the following working areas need particular effort:

1. Development of tunable materials that can be targeted to any selected application. It is clear that dynamic bonds, such as H-bonds, bonds formed from Diels–Alder chemistry, disulfide bonds are common to a number of different polymeric systems. Therefore, a top-down approach is used to identify dynamic bonds that could be readily integrated into any number of polymeric systems and then this information is used to design a multipurpose self-healing material.
2. Development/design of intelligent materials with autonomic performance which includes self-diagnosis, self-control and self-healing; therefore, sensing elements need to be incorporated within structures/surfaces which are able to control the self-repair process in every aspect (signal transport, activation of the repair mechanism). It has been long time since efforts to provide such materials have been initiated, but the sensor function has to be further developed and extended with an active learning functionality, able to differentiate and to detect damage, to interpret the obtained information and to trigger/stimulate the repair action on demand. These sensor elements should be ideally structural parts of the system, and the working of the system should not be compromised.
3. In order to industrialize any material, its design should be kept simple and cost-effective. In order to achieve this, the reagents must be relatively cheap and stable and the design must be easy to reproduce, thereby avoiding the use of expensive or unstable catalysts and metal ions.
4. Development of new transport/repair mechanisms for different activation energies/materials and different circumstances (speed, temperature, amount of recovery). It can be made possible by utilization of quantum chemistry prediction methods to predict the energy (e.g. temperature) at which a dynamic

bond forms and breaks based on the chemical environment around the bonds. This is especially needed to widen the area of applications of self-healing systems to more materials and systems.

5. Finally, methods must be developed to test and characterize the structures/devices and to quantify the success of the self-repair action. Up till now, measurement of mechanical performance is the only method used to estimate the status of self-healed materials. However, since self-healing is not necessarily only connected to mechanical damage, some measure of the quality of the self-repair has to be developed.

If these requirements are met, then it will be possible to create truly smart structures, which sense their internal state and external environment and based on the information gained respond in a manner that fulfils their functional requirements. The primary advantage of moving towards smart structures technology is the potential cost benefit of condition-based maintenance strategies and the prospective life extension that may be achieved through in situ health monitoring.

References

1. Flory PJ (1953) Principles of polymer chemistry. Cornell University Press, Ithaca, pp 432–494
2. Shanks RA, Kong I (2013) General purpose elastomers: structure, chemistry, physics and performance, advanced structured materials, vol 11. Springer, Berlin Heidelberg, pp 11–45
3. Shanks R, Kong I (2012) Thermoplastic elastomers applied sciences. In tech, pp 137–154
4. Das A, Sallat A, Böhme F, Suckow M, Basu D, Wießner S, Stöckelhuber KW, Voit B, Heinrich G (2015) Ionic modification turns commercial rubber into a self-healing material. ACS Appl Mater Interfaces 7:20623–20630
5. Tobolsky AV (1960) Properties and structures of polymers, vol 47(149). Wiley, New York, 1–563
6. Ellul MD, Gent AN (1984) The role of molecular diffusion in the adhesion of elastomers. J Polym Sci 22:1953–1968
7. Castellucci M (2009) Resistive heating for self-healing materials based on ionomeric polymers. Thesis, Virginia Polytechnic Institute and State University
8. Trask RS, Williams HR, Bond IP (2007) Self-healing polymer composites: mimicking nature to enhance performance. Bioinsp Biomim 2:1–9
9. Ferrulli O (2013) Damage sensing and self-healing materials through microencapsulation process. Thesis, Politecnico Di Milano, pp 1–131
10. Fratzl P, Weinkamer R (2007) Hierarchical structure and repair of bone: deformation, remodeling, healing. Springer, Netherlands, pp 323–335
11. Zwaag S (2008) Self-healing materials, an alternative approach to 20 centuries of materials science. Springer Series in Materials Science, Springer Science+Business Media BV
12. Farrar CR, Worden K (2007) An introduction to structural health monitoring. Philos Trans R Soc A 365(1851):303–315
13. Ghosh SK (ed) (2009) Self-healing materials: fundamentals, design strategies and applications. Wiley-VCH, Weinheim
14. Harrington MJ, Speck O, Speck T, Wagner S, Weinkamer R (2015) Biological archetypes for self-healing materials, pp 1–38

15. Zwaag SVD (2007) Modeling of self-healing of skin tissue. Self healing materials. An alternative approach to 20 centuries of materials Science. Springer, Berlin, pp 1–18
16. Blaiszik BJ, Kramer SLB, Olugebefola SC, Moore JS, Sottos NR, White SR (2010) Self-healing polymers and composites. Ann Rev Mater Res 40:179–211
17. Wilson GO, Andersson HM, White SR, Sottos NR, Moore JS, Braun PV (2010) Self healing polymers, encyclopedia of polymer science and technology. Wiley, New York, p 2
18. Ghosh SK (2009) Self-healing materials: fundamentals, design strategies, and applications. Wiley VCH Verlag GmbH & Co. KGaA, Weinheim
19. Lutz A, De Graeve I, Terryn H (2013) Self-healing coatings and their electrochemical analysis, Research Group of Electrochemical and Surface Engineering
20. http://sandbox.softroboticstoolkit.com/book/self-healing-materials-0
21. Kessler MR (2007) Self-healing: a new paradigm in materials design. J Aerosp Eng 221 (4):479–495
22. White SR, Sottos NR, Geubelle PH, Moore JS, Kessler MR, Sriram SR, Brown EN, Viswanathan S (2001) Autonomic healing of polymer composites. Nature 409:794–797
23. Cordier P, Tournilhac F, Souli´e-Ziakovic C, Leibler L (2008) Self-healing and thermo reversible rubber from supramolecular assembly. Nature 451:977–980
24. Toohey KS, Sottos NR, Lewis JA, Moore JS, White SR (2007) Self-healing materials with microvascular networks. Nat Mater 6:581–585
25. Thies C (1987) Microencapsulation. In: Encyclopedia of polymer science and engineering, vol 9. Wiley, New York, pp 724–745
26. Benita S (2006) Microencapsulation: methods and industrial applications, 2nd edn. CRC Press, New York, p 158
27. Arshady R (1999) Microspheres, microcapsules and liposomes. Citrus Books, London
28. Ghosh SK (2006) Functional coatings by polymer microencapsulation. Wiley-VCH Verlag GmbH, Germany
29. Dry C (1996) Compos Struct 35:263–269
30. Jung D, Hegeman A, Sottos NR, Geubelle PH, White SR (1997) Self-healing composites using embedded microspheres. Am Soc Mech Eng Mater Div 80:265–275
31. White SR, Sottos NR, Geubelle PH, Moore JS, Kessler MR, Sriram SR, Brown EN, Viswanathan S (2001) Autonomic healing of polymer composites. Nature 409:794–797
32. Larin GE, Bernklau N, Kessler MR, DiCesare JC (2006) Rheokinetics of ring-opening metathesis polymerization of norbornene-based monomers intended for self-healing applications. Polym Eng Sci 46:1804–1811
33. Rule JD, Moore JS (2002) ROMP Reactivity of endo- and exo-Dicyclopentadiene. Macromolecules 35:7878–7882
34. Shansky E (2006) Synthesis and characterization of microcapsules for self-healing materials. Department of Chemistry, Indiana University, Bllomington, pp 515–546
35. Cho SH, Andersson HM, White SR, Sottos NR, Braun PV (2006) Polydimethylsiloxane-based self-healing materials. Adv Mater 18:997–1000
36. Tanasa F, Zanoaga M (2012) Self-healing materials—from design to specific applications. "Petru Poni" Institute of Macromolecular Chemistry, Iasi, Romania
37. Dry CM (1995) Adhesive liquid core optical fibers for crack detection and repairs in polymer and concrete matrices. Proc SPIE Int Soc Opt Eng 2444:410–413
38. Dry CM, McMillan W (1996) Crack and damage assessment in concrete and polymer matrices using liquids released internally from hollow optical fiber. Proc SPIE Int Soc Opt Eng 2718:448–451
39. Motuku M, Vaidya UK, Janowski GM (1999) Parametric studies on self-repairing approaches for resin infused composites subjected to low velocity impact. Smart Mater Struct 8:623–638
40. Bleay SM, Loader CB, Hawyes VJ, Humberstone L, Curtis V (2001) A smart repair system for polymer matrix composites. Compos A Appl Sci Manuf 32(12):1767–1776
41. Bond I, Foreman A, Hudd J (1999) Optimization of hollow glass fibers and their composites. Adv Compos Lett 8(4):181–189

42. Trask RS, Bond IP (2006) Biomimetic self-healing of advanced composite structures using hollow glass fibers. Smart Mater Struct 15:704–710
43. Pang JWC, Bond IP (2005) 'Bleeding composites'—damage detection and self-repair using a biomimetic approach. Compos A Appl Sci Manuf 36:183–188
44. Pang JWC, Bond IP (2005) A hollow fiber reinforced polymer composite encompassing self-healing and enhanced damage visibility. Compos Sci Technol 65:1791–1799
45. Williams HR, Trask RS, Bond IP (2006) Vascular self-healing composite sandwich structures. In: 15th US national congress of theoretical and applied mechanics, Boulder, CO, 25–31 June 2006
46. Williams GJ, Trask RS, Bond IP (2007) A self-healing carbon fiber reinforced polymer for aerospace applications. Compos A Appl Sci Manuf 38(6):1525–1532
47. Trask RS, Bond IP (2006) Biomimetic self-healing of advanced composite structures using hollow glass fibers. Smart Mater Struct 15(3):704–710
48. Adhikari B, De D, Maiti S (2000) Reclamation and recycling of waste rubber. Prog Polym Sci 25(7):909–948
49. Bergman SD, Wudl F (2008) Mendable polymers. J Mater Chem 18:41–62
50. Bergman SD, Wudl F (2007) Self-healing materials. An alternative approach to 20 centuries of materials science, vol 30(6). Springer, Berlin, pp 45–68
51. Nasser SN, Plaisted T, Starr A, Amirkhizi AV (2005) Multifunctional materials. In: Biomimetics: biologically inspired technologies. CRC Press, New York
52. Bouteiller L (2007) Assembly via hydrogen bonds of low molecular mass compounds into supramolecular polymers. Adv Polym Sci 207:79–112
53. Lehn JM (2002) Supramolecular polymer chemistry—scope and perspectives. Polym Int 51:825–839
54. Weck M (2007) Side-chain functionalized supramolecular polymers. Polym Int 56:453–460
55. Shimizu LS (2007) Perspectives on main-chain hydrogen bonded supramolecular polymers. Polym Int 56:444–452
56. Beijer FH, Sijbesma RP, Kooijman H, Spek AL, Meijer EW (1998) Strong dimerization of ureidopyrimidones via quadruple hydrogen bonding. J Am Chem Soc 120:6761
57. Ontjens S, Sijbesma SHM, van Genderen MHP, Meijer EW (2001) Selective formation of cyclic dimers in solutions of reversible supramolecular polymers. Macromolecules 34:3815
58. http://www.suprapolix.com/. Access year 2008
59. Cordier P, Tournilhac F, Soulie'-Ziakovic C, Leibler L (2008) Self-healing and thermoreversible rubber from supramolecular assembly. Nature 451:977–980
60. Andres PR, Schubert US (2004) New functional polymers and materials based on 2,2′:6′,2″-terpyridine metal complexes. Adv Mater 16(13):1043–1068
61. Hoogenboom R, Winter A, Marin V, Hofmeier H, Schubert US (2007) American chemical society proceedings
62. Ristenpart WD, Alesay IA, Saville DA (2007) electrically driven flow near a colloidal particle close to an electrode with a faradaic current. Langmuir 23(7):4071–4080
63. Ahn TH, Crack TK (2010) Self-healing behavior of cementitious composites incorporating mineral admixtures. J Adv Concrete Technol 8(2):171–186
64. Richard SM, Deepankar B, Suryanarayana PV (2004) Impact of thief zone identification and shut-off on water production in the Nimr field. Society of petroleum engineers paper
65. Herold BH, Edwards JE, Kujik RV, Froelich B, Marketz F, Welling RWF, Leuranguer C (2006) Evaluating expandable tubular zonal and swelling elastomer isolation using wireline ultrasonic measurements. Society of petroleum engineers paper
66. Guimard NK, Oehlenschlaeger KK, Zhou J, Hilf S, Schmidt FG, Kowollik CB (2012) Current trends in the field of self-healing materials. Macromol Chem Phys 213:131–143
67. http://www.nissanglobal.com/EN/TECHNOLOGY/INTRODUCTION/DETAILS/SGC/index.html. Access year 2008
68. http://www.research.bayer.com/edition%2016/Self%20healing%20automotive%20coating.aspx. Access year 2008

Nanocomposites for Extrinsic Self-healing Polymer Materials

Yongjing Wang, Duc Truong Pham and Chunqian Ji

Abstract Extrinsic self-healing composites are capable of automatic recovery when damaged, inspired by biological systems that are naturally able to heal themselves. Nanocomposites have been employed in the development of extrinsic self-healing composites to either improve the healing performances or reduce the adverse effects introduced by the embedded capsules or vessels. This chapter reviews the work on extrinsic self-healing composites and the role of nanocomposites in the field. It presents a summary of the various self-healing concepts that have been proposed over the past decade and a comparative analysis of healing mechanisms and fabrication techniques for building capsules and vascular networks. The use of nanocomposites is categorised into four groups based on their functions, indicating four research directions that can be greatly promoted by the introduction of nanocomposites. Based on the analysis, current key barriers and potential future works are highlighted.

Keywords Capsule-based · Vessel-based · Smart repair · Encapsulation · Sacrificial component · Structural reinforcement · Vascular networks

Contents

Y. Wang (✉) · D.T. Pham · C. Ji
Department of Mechanical Engineering, School of Engineering,
University of Birmingham, B15 2TT, Birmingham, UK
e-mail: YXW181@bham.ac.uk

D. Ponnamma et al. (eds.), *Smart Polymer Nanocomposites*,
Springer Series on Polymer and Composite Materials,
DOI 10.1007/978-3-319-50424-7_9

List of Abbreviations

ATRP	Atom transfer radical polymerisation
BNNTs	Boron nitride nanotubes
BTA	Benzotriazole
CE	Cyanate ester
CNFs	Carbon nanofibres
CNTs	Carbon nanotubes
DBTL	Di-n-butyltin dilaurate
DCPD	Dicyclopentadiene
DDS	Diaminodiphenylsulphone
DSC	Differential scanning calorimetry
EDA	Ethylenediamine
ENB	5-ethylidene-2-norbornene
EPA	Ethyl phenylacetate
G2	Grubbs' second-generation catalyst
GMA	Glycidyl methacrylate
HG1	Hoveyda–Grubbs' first-generation catalyst
HG2	Hoveyda–Grubbs' second-generation catalyst
HNTs	Halloysite nanotubes
HOPDMS	Hydroxyl end-functionalised poly(dimethylsiloxane)
IPDI	Isophorone diisocyanate
MBI	2-mercaptobenzimidazole
MBT	2-mercaptobenzothiazole
MMA	Methylmethacrylate
MUF	Melamine–urea-formaldehyde
ROMP	Ring-opening metathesis polymerisation
PAN	Poly(acrylonitrile)
PDADMAC	Poly(dimethyl diallyl ammonium chloride)
PDES	Poly(diethoxy siloxane)
PDMS	Poly(dimethylsiloxane)
PETMP	Pentaerythritol tetrakis(3-mercaptopropionate)
PEG	Poly(ethylene glycol)
PLA	Poly(lactic acid)
PS	Polystyrene
PSMA	Poly(styrene-maleic anhydride)
PSMA-b-PS	Poly(styrene-maleic anhydride)-block-polystyrene
PMF	Poly(melamine formaldehyde)

PMMA	Poly(methyl methacrylate)
PUF	Poly(urea-formaldehyde)
SEM	Scanning electron microscope
SWCNT	Single-wall carbon nanotubes
TEA	Triethanolamine
TFE	Trifluoroethanol
UF	Urea-formaldehyde

1 Introduction

Self-healing polymer materials can automatically restore their properties after damage. Through self-healing, it is expected to extend the material life and reduce the cost of maintenance. Self-healing composites can be categorised into extrinsic and intrinsic self-healing composites. Intrinsic self-healing composites heal through inherent reversibility of physical or chemical bonding [1]. Reversible mechanisms include the swelling and deflating of shape memory polymers [2] and the melting and solidification of thermoplastic materials [3]. In other words, the ability to recover in intrinsic self-healing composites is an inherent property of the materials themselves.

The healing ability in extrinsic self-healing composites is achieved using microstructures such as capsules and vessels embedded inside the composites. These microcapsules and microvessels are loaded with a special liquid which can flow to damaged areas and heal them. Once the composites are damaged, cracks cause microcapsules or microvessels to rupture and release the healing agents, which fill the cracks and solidify. The mechanical properties of the composites are restored as a result. This design was inspired by the bleeding and healing processes in nature. Compared with intrinsic self-healing composites, extrinsic self-healing composites have a wider application and can heal even when the damaged area is large [4, 5].

This chapter introduces extrinsic self-healing composites and the role and effect of nanocomposites in their development.

2 Extrinsic Self-healing Materials

2.1 Background

As mentioned above, when an extrinsic self-healing composite is damaged, cracks cause microstructures to rupture, releasing the healing agents stored inside. Based on the types of microstructures, extrinsic self-healing composites can be categorised into capsule-based self-healing composites and vessel-based self-healing composites.

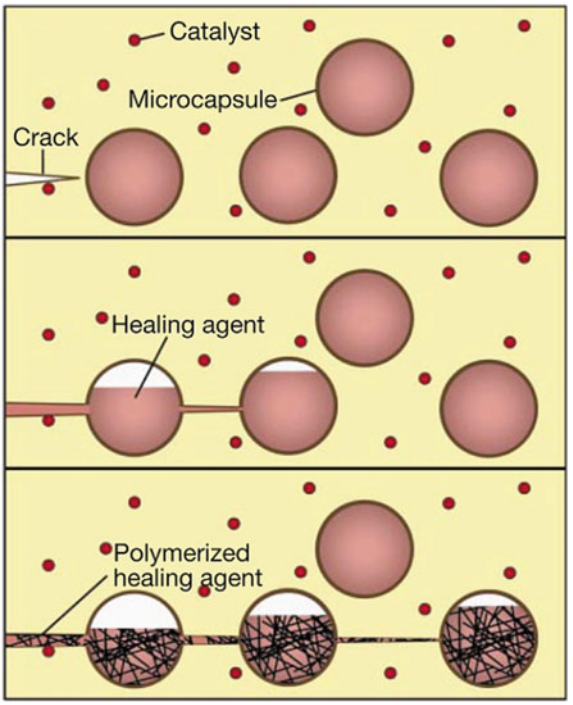

Fig. 1 Prototype of capsule-based self-healing composite [6]. Copyright 2001. Reproduced with permission from Nature Publishing Group

Capsule-based self-healing was first proposed in 2001 [6] (Fig. 1). In this prototype, a polymer matrix contains cell-like capsules containing dicyclopentadiene (DCPD) and Grubbs' catalyst. After damage, the composites recover through the ring-opening metathesis polymerisation (ROMP) of DCPD catalysed by Grubbs' catalyst. During ROMP process, the strained rings in monomers are open and reconnect to form long chains so that a mixture of cyclic olefin is converted to a polymeric material. Almost 75% toughness can be recovered in 48 h at room temperature as a result.

The development of vessel-based self-healing composites was first proposed in the 1990s, by using hollow glass tubes as one-dimensional vessels preloaded with an epoxy-based healing agent [7–9]. When the glass tubes ruptured, the loaded healing agent filled the damaged areas and solidified. A similar design based on hollow glass fibres can enable self-healing in fibre-reinforced composites [10]. Healing agents can also be mixed with UV fluorescent dye so that the 'bleeding process' could be observed [11]. The hollow fibres are not only a healing agent container but also a part of the reinforcing material (Fig. 2). However, the refilling of healing agents into hollow fibres as a special feature of vessel-based self-healing composites was difficult.

In 2007, the first vessel-based self-healing composite able to be refilled with healing agents was realised by Toohey et al., by embedding a three-dimensional vascular network inside materials [12]. The healing mechanism was also ROMP reaction of DCPD enabled by Grubbs' catalyst that has been used in capsule-based

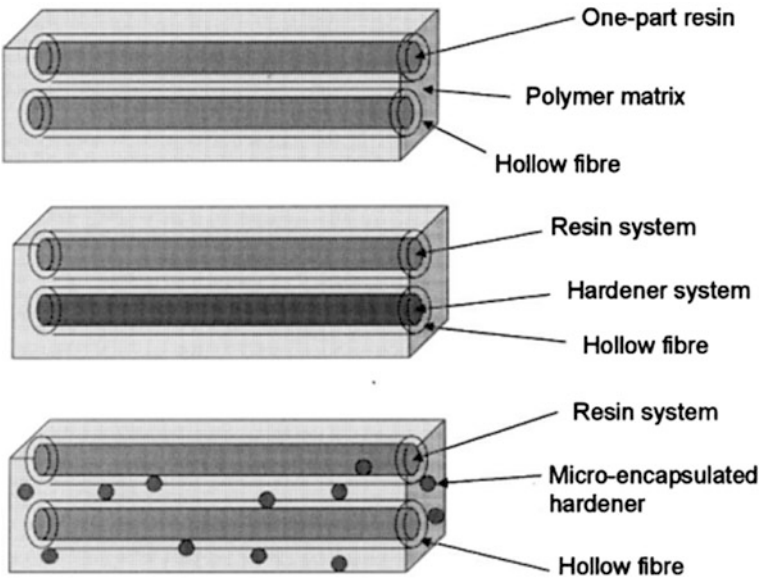

Fig. 2 Use of hollow fibres as vessels for self-healing composites [10]. Copyright 2001. Reproduced with permission from Elsevier

self-healing composites. The healing efficiency achieved as high as 70% in different healing cycles. Even though the healing efficiency was lower compared to that obtained in the capsule-based healing materials available then, it was the first time a self-healing composite capable of healing in multiple cycles was demonstrated (Fig. 3). Direct-write assembly of a fugitive organic ink was adopted to build sacrificial components that were incorporated in the host materials. The sacrificial parts were then heated, and the liquefied sacrificial material was removed to generate a hollow 3D architecture inside the host material.

Capsule-based and vessel-based self-healing composites have different healing performances. As the healing agents in capsules cannot be refilled, capsule-based self-healing composites can heal only if the damage is small or medium in extent. In comparison, as the vessels can be refilled externally and continuously, vessel-based self-healing composites are able to recover repeatedly from large-scale damages. This is the key advantage of vessel-based self-healing composites. However, the fabrication techniques for vessel-based self-healing composites are more complicated than those for capsule-based self-healing composites. First, the techniques to build interconnected three-dimensional vessels inside polymer composites are expensive and challenging. Second, vessel-based self-healing composites require healing agents able to flow inside vessels, limiting the types of healing agents that can be adopted. In fact, in the past two decades, work on extrinsic self-healing composites has focused on two main areas: healing agents and new fabrication techniques for microstructures. The development of new healing agents was to

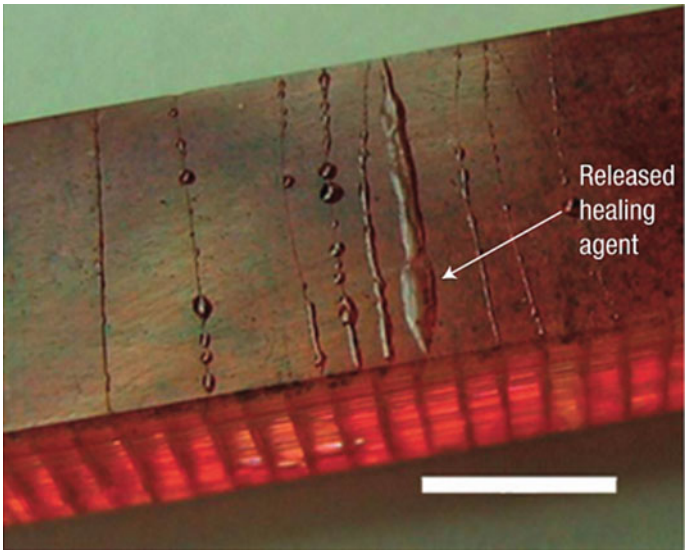

Fig. 3 Vessel-based self-healing composites are embedded with a three-dimensional vascular network [12]. Copyright 2007. Reproduced with permission from Nature Publishing Group

widen the range of healable host materials and to enhance the healing strength or healing rate. Research on new fabrication techniques was to improve the efficiency and reduce the cost of building strong 3D microstructures inside the host materials.

2.2 Capsule-Based Self-healing Composites

2.2.1 Healing Agent

In capsule-based self-healing composites, healing agent should be able to flow and be stored in the capsules. According to a recent review, capsule-based self-healing composites can be categorised into five groups [13]. These categories can be simplified into the four groups shown in Fig. 4.

For single capsules, the healing agent is a one-part liquid which can react with functional groups or particles dispersed or dissolved in a matrix. The reactions can even be triggered by light or heat. In phase-separated capsules, at least one component of healing agents sustains phase separation, and the other components are stored in capsules. The two fluids react when the liquids in capsules are released. In the all-in-one capsule system, all healing components are contained in one capsule, by either placing different components in different layers or using larger capsules to store smaller capsules loaded with different healing components. When the capsules

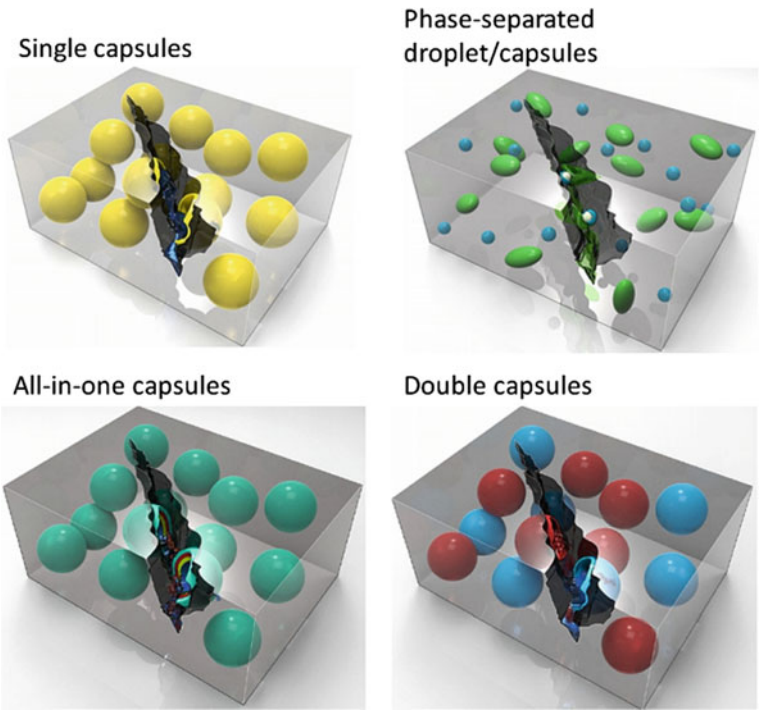

Fig. 4 Four types of capsule-based self-healing composites [13]. Copyright 2015. Reproduced with permission from Elsevier

are ruptured, various components contact and are subsequently polymerised without additional chemicals [13].

As most of the effort has been on developing new mechanisms to improve the healing efficiencies, tens of healing agents have been developed for various capsule-based self-healing composites. Table 1 gives a few typical examples. A more comprehensive list is available in the paper by Zhu et al. [13].

2.2.2 Fabrication Techniques

The fabrication of capsule-based self-healing composites normally involves two processes: healing agents encapsulation and the integration of capsules within the matrix material. Various encapsulation techniques widely employed in the food and pharmaceutical industries can be used for the encapsulation of healing agents.

Currently, in situ polymerisation in an oil-in-water emulsion is the most popular method of making capsules loaded with healing agents. Polymerisation of a shell monomer is carried out on the surface of a core material to form an isolating layer, as shown in Fig. 5. This method offers controllable shell thickness and

Table 1 Healing agents for capsule-based self-healing composites

Type	Materials to be healed	Encapsulated healing agent	Key substance outside the capsule dispersed in matrix	Healing conditions	Healing efficiency (%)	References
Single capsules	Epoxy resin	Solvent + epoxy monomer	Residual amines	Room temperature (RT), 24 h	100	[14]
		DCPD	Grubbs' catalyst	RT, 24 h	75	[6]
		Glycidyl methacrylate (GMA)	Residual amine	RT, 3 days	75–90	[15]
		Epoxy monomer	CuBr2(2-Melm)4	130 °C, 60 min; 140 °C, 30 min	111; 70	[16, 17]
	PMMA	Dibutylphthalate	N/A	RT, 72 h	100	[18]
Phase-separated capsules	Epoxy vinyl ester	DBTL solution	Phase-separated (HOPDMS + PDES)	Air, 50 °C, 24 h; water, 50 °C, 24 h	90; 25	[19]
Double capsules	Epoxy resin	Epoxy + amine	N/A	RT, 48 h; 50 °C, 24 h	91; 70	[20, 21]
		Epoxy + mercaptan + tertiary amine activator	N/A	RT, 24 h	≥100	[22]
	Polydimethylsiloxane (PDMS)	PDMS + Pt catalyst + PDMS copolymer	N/A	RT, 48 h	70–100	[23]
All-in-one capsules	PS	GMA-(PMMABr + CuBr/PMDETA)	N/A	RT, 48 h	100	[24]

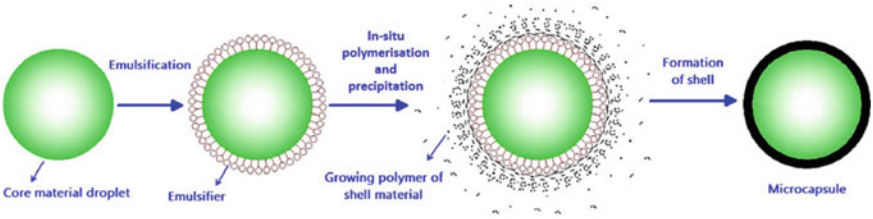

Fig. 5 Schematic diagram of the formation of capsules by in situ polymerisation [13]. Copyright 2015. Reproduced with permission from Elsevier

microcapsule size in the range 200 nm–1000 μm. In the work of Brown et al. [25], poly(urea-formaldehyde) (PUF) as a shell material was used to encapsulate DCPD healing agents, and the process of in situ polymerisation in an oil-in-water emulsion was presented in their paper in detail. Other materials have been employed to produce the shell of capsules including poly(melamine formaldehyde) (PMF) [26] and poly(methyl methacrylate) (PMMA) [27, 28] (Table 2).

Table 2 Summary of encapsulation techniques for capsule-based self-healing composites

Encapsulation techniques	Healing agent	Shell materials	Size (diameter; shell thickness)	References
In situ polymerisation	DCPD	PUF	10–1000 μm; 160–220 nm	[25]
	Epoxy monomer	PUF	30–70 μm; N/A	[17]
	Epoxy monomer and polythiol hardener	PMF	1–10 μm; 200 nm	[26]
	GMA	PMF	~190 μm; N/A	[15]
	Polyetheramine (hardener for epoxy)	PMMA	36–132 μm; 11.2–37.2 μm	[27]
	ENB	PMUF	113–122 μm; 700–900 nm	[35]
Interfacial polymerisation	Epoxy monomer	Ethylenediamine (EDA)	100 μm; 4–10 μm	[36]
	Amine	Rapid condensation of isocyanate with amine	26 ± 10 μm; N/A	[30]
	Isophorone diisocyanate (IPDI)	Polyurethane (PU)	40–400 μm; thickness to diameter ratio ~0.05	[37]
Miniemulsion polymerisation	Pentaerythritoltetrakis (3-mercaptopropionate) (PETMP)	A styrene–maleic anhydride copolymer (PSMA)	150–350 nm; N/A	[38]

Other techniques have also been employed to fabricate capsules to suit various material properties such as solubility and viscosity. Rule et al. [29] used wax to encapsulate Grubbs' catalyst by rapidly cooling hot and stirred wax mixed with the catalyst. Cho et al. [19] and McIlroy et al. [30] used interfacial polymerisation to encapsulate DBTL and amine for epoxy-based self-healing systems. Chen et al. [31] described the self-assembly of poly(acrylate amide) shell, containing polystyrene as core by atom transfer radical polymerisation (ATRP). Zhang et al. [32, 33] demonstrated a fabrication method to make etched glass bubbles as healing agent containers which would be more brittle and easy to rupture. Furthermore, the shell can also be formed of more than one kind of material. Jin et al. [34] created a two-layer capsule shell so that the thermal stability of the capsule can be improved without affecting the rupture performance. A summary of encapsulation techniques is given in Table 2. Methods that can be used to make nanometric capsules are further discussed in Sect. 2. More information about encapsulation techniques can be found in [13].

2.3 Vessel-Based Self-healing Composites

2.3.1 Healing Agent

Healing mechanisms for vessel-based self-healing composites are similar to those for capsule-based self-healing composites. ROMP reaction based on DCPD and Grubbs' catalyst was initially developed [12]. Toohey et al. also presented a two-part epoxy-based mechanism [39]. They were the first to build two isolated 3D vascular networks embedded in the same host materials, each containing a different liquid. A two-part polyurethane was used in a polymeric foam healing system [40]. Patrick et al. used a two-part epoxy for healing fibre-reinforced composites that have suffered delamination [41]. White et al. [42] developed a two-stage chemistry, involving a gel stage for gap-filling scaffolds and a polymer stage for the restoration of structural performance, so that a damaged area up to 35 mm in diameter on a PMMA specimen can be healed. To secure good fluidity and stability, the selection of healing agents for vessel-based self-healing composites is rigorous, and many new factors such as surface wettability and viscosity should be taken into consideration. Such a selection, in turn, affects the design and development of the vascular network.

2.3.2 Fabrication Techniques

Fabrication techniques for vessel-based self-healing composites aim to build or embed hollow vessels inside the host material. The vessels are required to have a small diameter and a high strength, as the introduction of hollow vessels may reduce the mechanical properties of the composites. However, it is beneficial to have a high coverage of vascular networks to increase the chance of releasing

healing agent when damaged. All these critical conditions set high demands on the fabrication techniques for vessel-based self-healing composites. In fact, this is what research into vessel-based self-healing composites has been concentrating on. In this section, popular fabrication methods are analysed and categorised.

Hollow Fibres

Installing tubes containing healing agents is one method to fabricate vascular self-healing fibre-reinforced composites [11, 43, 44], as shown in Fig. 6. The shell of the hollow fibres acts as an isolating layer between the matrix and the healing agent. The process of embedding hollow fibres in the host matrix is similar to that of a conventional fibre-reinforced material (i.e. covering fibres with uncured epoxy resins followed by curing). This simple fabrication procedure is one of the key advantages of this method. Mechanical tests also show that the mechanical effects of the hollow fibres on the host composite are small [45]. However, the design cannot yield interconnected networks and refilling is hard, which are the main drawbacks of using hollow fibres.

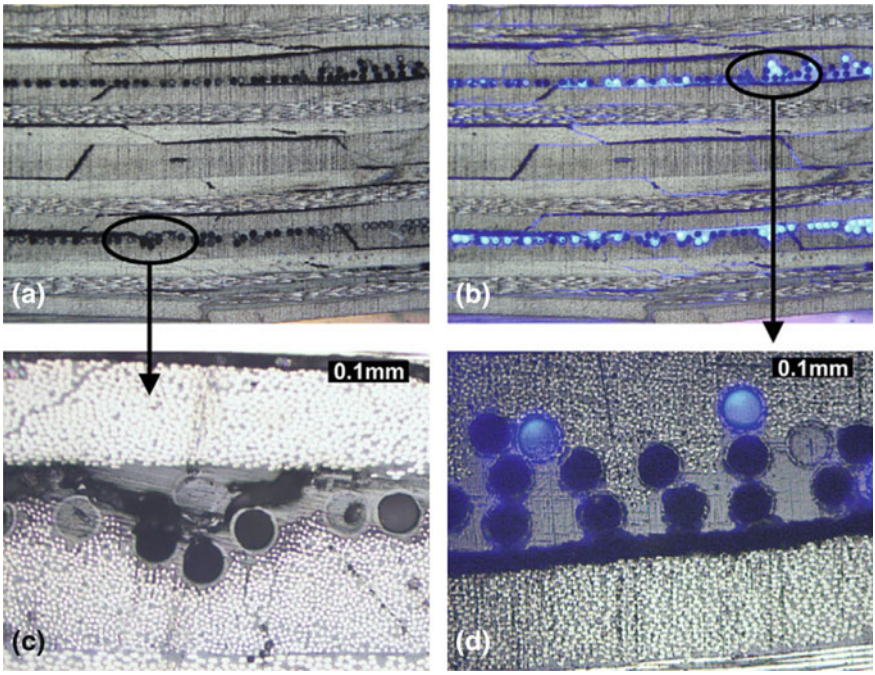

Fig. 6 **a** Distribution of cracks within laminate; **b** healing resin + fluorescent dye are released into the crack [46]. Copyright 2007. Reproduced with permission from Elsevier

Sacrificial Fibres/Scaffolds

Fabrication based on sacrificial fibres/scaffold is the most efficient method to produce three-dimensional hollow structures inside the polymer composites. Sacrificial fibres/scaffolds are formed of materials easy to remove, dissolve or degrade. After the sacrificial components have been integrated into the polymeric host material, and the host material is fully cured, the sacrificial fibres/scaffolds are removed manually or automatically by changing the surrounding conditions (e.g. increasing temperature) to liquefy or depolymerise the sacrificial components. This leaves a hollow microvascular network inside the host material. For example, to build single-line channels, straight steel wire [47] or nylon fibres [48] can be used to produce one-dimensional vessels. They can be removed easily by pulling out manually or using an external machine. To build complex 3D structures, the following methods can be adopted.

(i) *3D printing of sacrificial scaffolds*

Therriault et al. [49] and Lewis et al. [50] developed a 3D direct-write method to create sacrificial microvascular networks by using a fugitive ink. A robotic deposition apparatus was employed in a layerwise scheme to print paraffin-based organic ink in three dimensions, as shown in Fig. 7a. After the integration of the scaffold and the polymeric host material, the system was heated in a vacuum chamber to remove the melted sacrificial materials, leaving a hollow microvascular network inside. This technique produces vessels with a diameter ranging from 10 to 300 μm and a root-mean-square (rms) surface roughness of 13 ± 7 nm. It is possible to employ other fugitive inks, such as a composition of 60 wt% petroleum jelly and

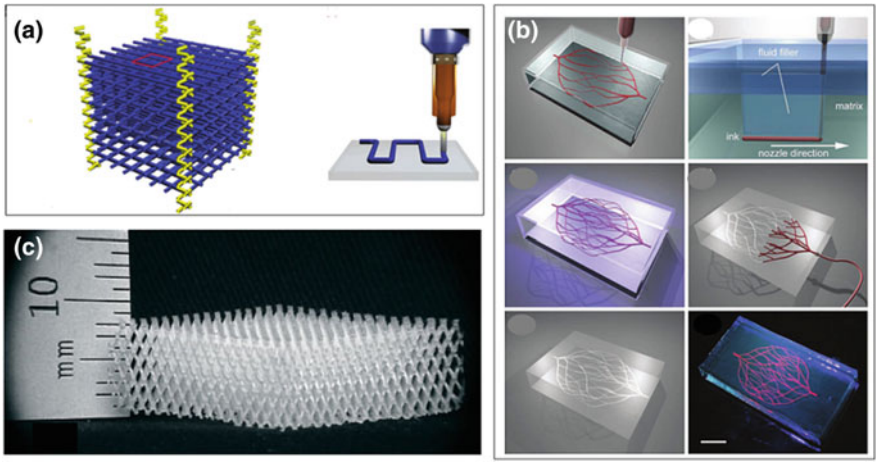

Fig. 7 Fabrication of Scaffolds. **a** 3D printing using nozzles [49]. Copyright 2003. Reproduced with permission from Nature Publishing Group. **b** 3D printing of a biomimicking pattern [55]. Copyright 2011. Reproduced with permission from John Wiley and Sons. **c** Self-propagated photopolymer [57]. Copyright 2007. Reproduced with permission from John Wiley and Sons

40 wt% microcrystalline wax [12]. The primary challenge in using this method is to remove the melted sacrificial materials from the vascular networks, as residues always exist when the vessel diameters are small, locking the liquids inside due to viscous force.

To solve this, poly(lactic acid) (PLA) is a good option for sacrificial materials as it leaves no residue after a thermal depolymerisation at high temperatures. 3D-printed PLA can be used to build sacrificial structures [51]. However, the high temperature needed to remove the sacrificial materials may harm the host material. Dong et al. [52] discovered a catalytic reaction system based on catalysts such as tin(II) oxalate that can improve the reaction rate of PLA depolymerisation from 1 wt%/h (weight percent per hour) to 25 wt%/h, decreasing the depolymerisation temperature to approximately 100 °C. The mixture of PLA and catalyst can also be 3D printed to form sacrificial structures [53].

In addition, the printing processes can be modified so that sacrificial materials in a biomimetic pattern similar to a leaf venation can be produced rather than simple uniform patterns [54, 55], as shown in Fig. 7b. The diameter of the network can be altered by changing the pressure inside the printing nozzle. Furthermore, Hansen et al. developed a multinozzle array to print multiple lines simultaneously to improve the printing efficiency [56].

Besides using nozzles, light-triggered solidification based on photopolymers can also be used to print sacrificial components. Jacobsen et al. [57, 58] fabricated interconnected photopolymer waveguides based on self-propagation and generated open-cellular microtruss structures (Fig. 7c). This technique was further developed to make metallic vascular networks [59] and bicontinuous fluid networks [60].

(ii) *Melt-spinning and Electrospinning*

Melt-spinning and electrospinning can generate sacrificial fibres from liquids, similar to the generation of cotton candy. The original equipment for melt-spinning sacrificial fibres was, in fact, a cotton candy machine [61]. In this work, the sugar fibres were placed in a Teflon mould with uncured PDMS. After curing, the sugar structure was dissolved away in a bath of water and ethanol, leaving a microchannel network inside the PDMS matrix, as shown in Fig. 8. A similar method was applied to form vascular networks inside gelatin by using shellac as sacrificial fibres. Shellac is a kind of natural material exhibits pH-sensitive solubility in aqueous solutions. Electrospinning can be used to produce similar sacrificial fibres. Gualandi et al. [62] employed electrospinning to produce Pullulan fibres as the sacrificial materials as they can be degraded when heated up to 250 °C.

(iii) *Replication of existing patterns*

Nature presents beautiful vascular networks such as leaf venations that can be replicated for producing vascular networks in self-healing composites. Soft lithography is a powerful tool for fabricating microfluidic networks [63], and this can also be applied to make vascular networks for self-healing material systems. Golden et al. [64] described a method using gelatin as a sacrificial material to form a hexagon beehive

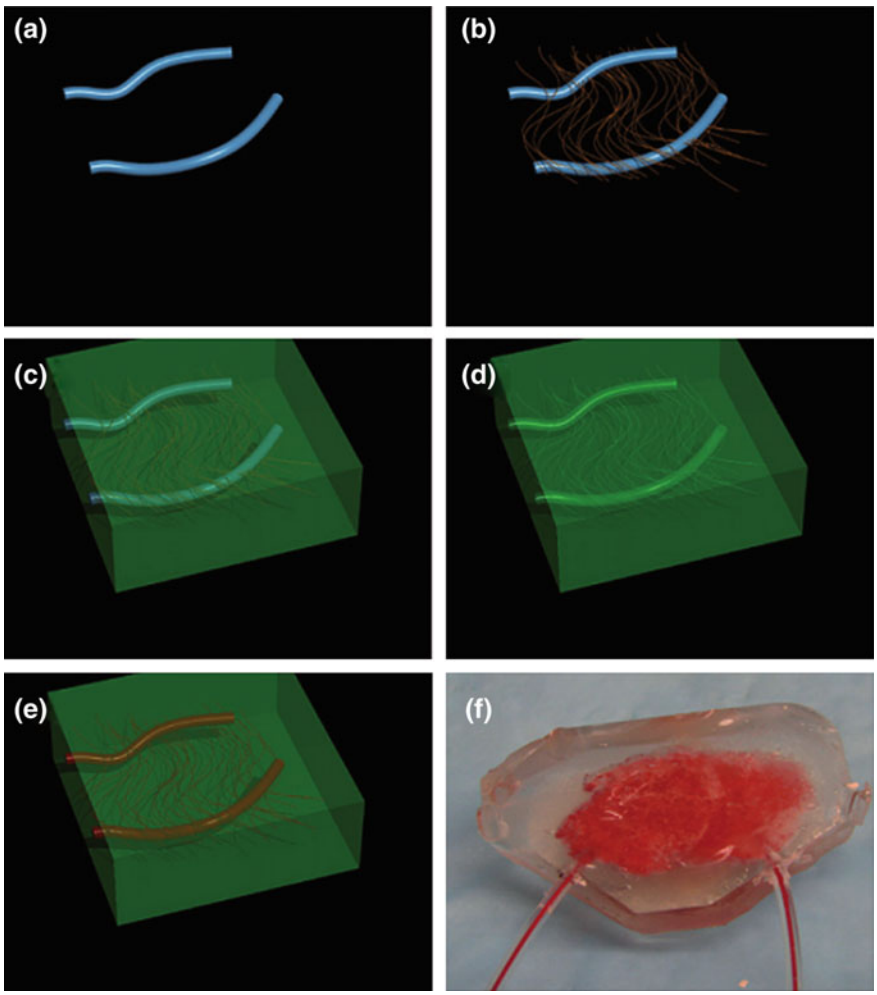

Fig. 8 Fabrication of vessels in PDMS matrix [61]. **a** Water-soluble materials are used to make large vessels; **b** water-soluble microfibres are used to make microvessels; **c** uncured polymer is poured to immerse the soluble structure; **d** a warm water bath was used to remove the soluble structure to generate hollow vascular networks in the matrix; **e** healing agents were injected into the vascular networks; **f** an example of a PDMS matrix embedded with vascular networks containing rat blood. Copyright 2009. Reproduced with permission from Royal Society of Chemistry

structure, as shown in Fig. 9. This method started with building the initial pattern of a vascular network followed by replicating the pattern using a substrate made of pre-oxidised PDMS, forming a 'negative' version of the pattern on the substrate. The gelatin was then used to fill up the cavity in the substrate. When the gelatin was cured, it was removed from the substrate and embedded in hydrogel, which was later given a heat treatment to remove molten gelatin. As a result, a microvascular network in the

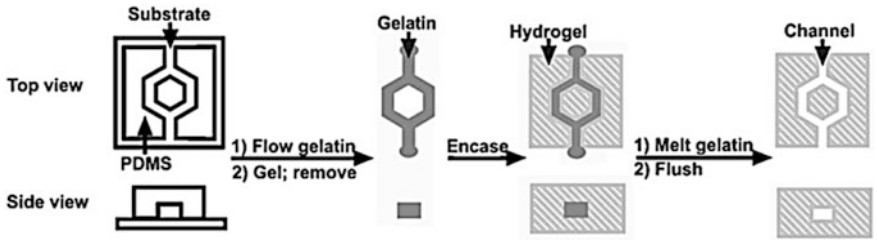

Fig. 9 Soft lithography for building microfluidics devices [64]. Copyright 2007. Reproduced with permission from Royal Society of Chemistry

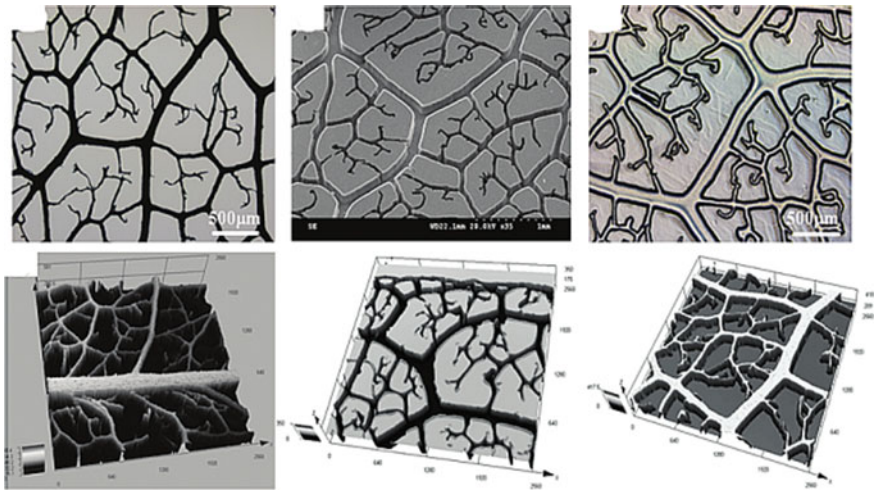

Fig. 10 Replication of a leaf venation [65]. Copyright 2013. Reproduced with permission from John Wiley and Sons

pattern was left inside the hydrogel, and the diameter of the vessels can be as small as 6 μm. Many suitable structures seen in natural systems can be replicated directly. He et al. [65] adopted a similar method to replicate a leaf venation to build interconnected vascular networks, as shown in Fig. 10.

In addition to hollow glass fibres and sacrificial fibres/scaffolds, other methods can also be used to produce vessels, but they are relatively less stable or efficient. For example, electrostatic discharge can be used to produce vessels with diameters ranging from 10 to 500 μm [66]. This is likely to be the most rapid fabrication method to build microvascular networks following natural designs (e.g. Murray's law). However, the generating process is not controllable, resulting in an uncertain quality of the network. The laser direct-write technique is another popular tool for fabricating channels in microfluidics devices [67]. Although lasers can be used to create very complex 2D patterns directly on polymeric materials, it is difficult to produce 3D structures. A summary of different fabrication techniques is given in Table 3.

Table 3 Features of fabrication techniques for vascular networks [4]

	1D hollow fibres	Sacrificial fibres/scaffold				Electrostatic discharge	Laser direct-write
		Straight wire/fibre	3D printing	Spinning	Replication		
1D vessels	Yes	Yes	Yes	Yes	Yes	Not predictable	Yes
2D vessels	No	No	Yes	Yes	Yes	Not predictable	Yes
3D vessels	No	No	Yes	Yes	Yes	Not predictable	No
Interconnection	No	No	Yes	Yes	Yes	Yes	Yes
Refill	Possible but difficult	Possible but difficult	Easy	Possible but difficult	Easy	Easy	Easy
Size	10–500 μm	10–500 μm	10–500 μm	5–300 μm	Depends on the pattern to be replicated	20–300 μm	Depends on the size of the laser beam
Fabrication time	Short	Short	Medium	Medium	Long	Short	Short
Large-scale fabrication	Yes	Yes	Possible but inefficient	Possible but inefficient	Yes	Yes	Possible but inefficient
Possibility of damage	Low	High	Low	Low	Low	High	Low
Surface roughness	Good	Good	Good	Good	Depends on the pattern to be replicated	Good	Bad

3 The Role of Nanocomposites in Extrinsic Self-healing Materials

The most popular definition of nanocomposites is that they are a solid combination of a bulk matrix and nanoscale fillers, for example, an epoxy matrix incorporating carbon nanofibers. Another definition is that they are composites on a nanoscale, such as nanocapsules or carbon nanotubes (CNTs), decorated with functional particles. Both definitions are adopted in this chapter.

The value of extrinsic self-healing composites relies on two fundamental factors: the healing performance and the effect of microstructures on mechanical properties. A perfect self-healing composite, which lies beyond current technology, is able to perform stable and highly efficient recovery whenever damage occurs, and the embedded microstructures do not weaken the mechanical properties of the overall structures. To ensure a good healing result, cracks must reach and break the microstructures and the amount of the released healing agents must be adequate to fill the cracks. This requires a high coverage of the capsules or vascular networks. However, this causes a large volume of voids, which reduces the mechanical properties of the composites. Thus, it becomes essential that microstructures should be small, and the pattern of the vessels or the strategy for capsules dispersion should be carefully designed. The need for new healing agents able to heal different types of host materials is also obvious. These requirements accelerate the introduction of nanocomposites into extrinsic self-healing composites. Based on the purpose of using nanocomposites, the role of nanocomposites can generally be categorised into four groups:

1. a healing agent carrier (e.g. nanocapsules);
2. an additive to alter the properties of host materials or healing agents;
3. nanocomposites as additives to activate or improve the chemical reactions in curing processes; and
4. nanocomposites used in the fabrication of capsules or vessels.

The following four sections introduce the four groups separately.

3.1 Nanocomposites as Healing Agent Carriers

A common method used to reduce the effects of capsules and vessels on the mechanical properties of host materials is to decrease their diameter. When the diameter is reduced to a nanoscale, healing agent carriers such as nanocapsules and nanovessels themselves become nanocomposites.

3.1.1 Nanotubes

A popular example of nanotubes that have been employed as healing agent carriers is CNTs [68]. Lanzara et al. analysed the dynamics of a fluid flowing out of a ruptured single-walled CNT to study the feasibility of using CNTs as a nanoreservoir. The study showed that when a single-walled CNT suffered a crack on its wall, organic liquids or healing agents stored inside the CNT could be released rapidly. In addition, as CNTs are endowed with excellent mechanical properties, the strength and toughness of host materials can be enhanced by the incorporation of CNTs. The result indicates the great potential of using CNT to develop stronger and lighter self-healing composites. However, techniques to embed healing agents inside the CNTs are yet to be developed, and so the feasibility of this approach has not been experimentally validated.

Halloysite is a naturally occurring two-layered aluminosilicate nanotube. The size of halloysite particles varies within 1–15 μm of length and 10–150 nm of inner diameter, depending on the deposits [69]. Melo et al. developed a procedure to fill nanotubes with dimethylsulphoxide (DMSO) and nitrobenzene as the healing agent [70]. The filled nanotubes were encapsulated using the layer-by-layer technique of oppositely charged polyelectrolytes to trap the solvent inside the structure, as shown in Fig. 11.

Abdullayev et al. [71] developed halloysite nanotubes (HNTs) containing corrosion inhibitors such as benzotriazole (BTA), 2-mercaptobenzimidazole (MBI) and 2-mercaptobenzothiazole (MBT) for self-healing paint used to coat copper. The nanotubes containing the inhibitors were achieved by mixing their saturated solutions in acetone with halloysite.

Halloysite can also be loaded with an antioxidant to resist ageing in styrene–butadiene rubber. Fu et al. developed halloysites loaded with antioxidant 4010NA by mixing halloysite with antioxidant acetone solution, followed by several cycles of vacuum treatment, washing and drying [72]. The dried antioxidant-loaded halloysite samples were milled to a fine powder and modified by silane coupling agent (KH570). KH570-modified halloysites were compounded with rubber using a two-roll mill at room temperature. It was found that filling styrene–butadiene rubber with the modified halloysite at 27 wt% allowed for a sustainable release of the antioxidant during nine months, extending material life.

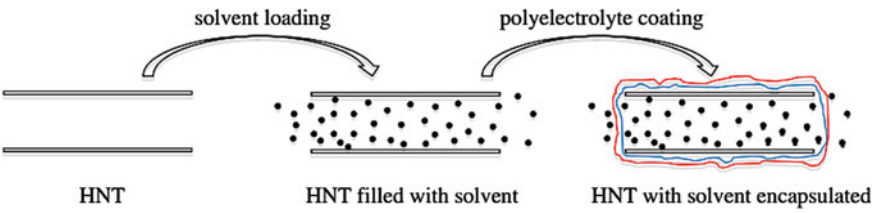

Fig. 11 Encapsulation of solvent into halloysite nanotubes [70]. Copyright 2014. Reproduced with permission from Taylor & Francis

The key advantage of using these nanotubes as healing agent carriers is that they do not reduce and can even improve the mechanical properties of host materials. However, they cannot store a large volume of healing agents and so can only be used to heal microscale or nanoscale damages.

3.1.2 Nanocapsules

In Situ Polymerisation

Nanocapsules is another example of nanocomposites being used as a healing agent carrier. Unlike capsules on a microscale where traditional encapsulation techniques based on in situ polymerisation are the most popular method (Fig. 5), nanocapsules are difficult to produce following conventional procedures. Blaiszik et al. developed a new method by combining a traditional method with a sonication technique to produce nanocapsules with a diameter as small as 220 nm [73]. For conventional encapsulation based on in situ polymerisation, a continuous stirring process is essential. During the stirring, Blaiszik et al. placed an ultrasonic homogenizer with a tapered 3.2 mm tip and a sonication horn of 750 W in the solution for 3 min at 40% intensity, as shown in Fig. 12. The result showed that the size of the capsules reduced from tens of micrometres to hundreds of nanometres.

Miniemulsion Polymerisation

To produce nanocapsules with diameters smaller than 200 nm, encapsulation techniques based on miniemulsion polymerisation can be used. Miniemulsions are a

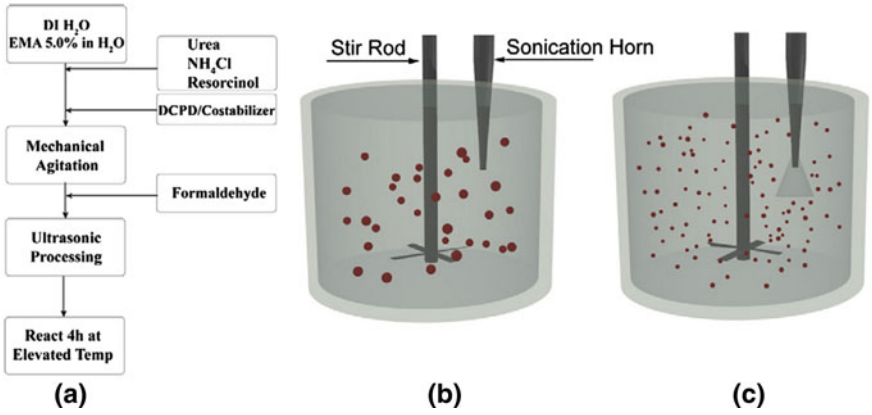

Fig. 12 Using sonication to assist the encapsulation of DCPD [73]. **a** Process flow chart; **b** schematic showing the emulsion prior to sonication; and **c** during sonication. Copyright 2008. Reproduced with permission from Elsevier

special case of emulsions obtained by a mixture containing two immiscible liquids stabilised by surfactants. They can be produced by using high-power ultrasound or high-pressure homogeniser [74]. As polymers can be synthesised in the dispersed phase of a miniemulsion system, micro-/nanocapsule shells formed at the interface of the droplets or in the continuous phase. This approach is referred to as miniemulsion polymerisation encapsulation [13].

The synthesis of nanocapsules containing liquid using miniemulsion polymerisation encapsulation with diameters as small as 60 nm was reported by Van den Dungen and Klumperman [38]. Nanocapsules (150–350 nm) were synthesised containing pentaerythritol tetrakis (3-mercaptopropionate) (PETMP) in the core and a styrene–maleic anhydride copolymer (PSMA) as a shell material. The nanocapsules were stabilised by the surfactant poly(styrene-maleic anhydride)-block-polystyrene (PSMA-b-PS) block copolymer via reaction with formaldehyde. Nanocapsules loaded with dinorbornene can also be synthesised through miniemulsion polymerisation of styrene (60–150 nm). The core–shell nanocapsules can be used in the fabrication of self-healing coatings [75], as PMF capsules containing the same thiol by using in situ polymerisation have been developed for self-healing in epoxy [22].

Such fabrication techniques can also produce nanocapsules with DCPD in the core and various functional groups [sulphonate, amine, carboxylic acid and poly (ethylene glycol) (PEG)] in the shell [76]. The hydrodynamic diameter of the nanocapsules can be as small as 290 nm. As ROMP of DCPD is a popular self-healing mechanism, this method exhibits the potential for self-healing composites. The interface of miniemulsion droplets as templates was also used to make silica nanocapsules for self-healing materials by the hydrolysis and condensation of alkoxysilanes, reported by Fickert et al. [76]. The silica shell contains healing agents including monomers and catalysts. And the size of the nanocapsules, the solid content of the dispersions and the thickness of the shells are controllable. Nanocapsules with diameters in the range 100–400 nm can be functionalised with thiol or amine groups.

In addition, miniemulsion techniques can be combined with the solvent evaporation method so that significant amount of healing agents can be encapsulated [77]. With the solvent evaporation method, both the polymer shell and the core are dissolved in a water-immiscible organic solvent that is volatile. Afterwards, the solution is added to an aqueous solution that contains a stabiliser. This creates droplets containing core material under stirring. The droplets harden gradually to create polymer microcapsules. Finally, evaporation at higher temperatures was conducted to remove the solvent from the droplets [13], as shown in Fig. 13. In the work of Zhao et al. [77], nanocapsules containing healing agent were formed when the solvent is evaporated from the miniemulsion. Various hydrophobic healing agents were encapsulated by a wide range of polymers, and the diameter was in the range 200–350 nm, as shown in Fig. 14.

Emulsion polymerisation encapsulation techniques can also be employed to produce larger capsules. Nanocapsules synthesised by a multistage emulsion

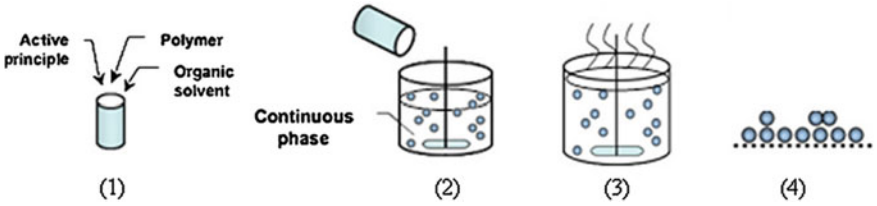

Fig. 13 Fabrication of microencapsulation by solvent evaporation [78]. *1* Dissolution; *2* emulsification of the dispersed phase in the continuous phase; *3* dispersed phase is transformed to solid particles and solvent evaporation; and *4* drying microspheres to remove the residual solvent. Copyright 2008. Reproduced with permission from Elsevier

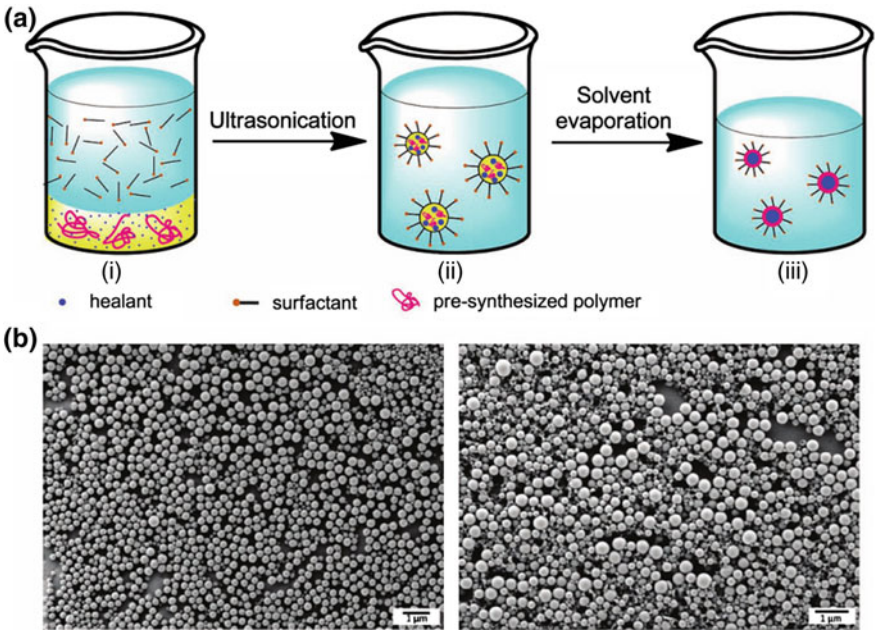

Fig. 14 **a** Fabrication of nanocapsules containing healant from miniemulsions using presynthesised polymers [77]. (*i*) Preparation of two immiscible phases, one containing healant and solvent, and the other one is the aqueous surfactant solution; (*ii*) miniemulsion droplets are formed by ultrasonic dispersion; (*iii*) nanocapsules were formed after the evaporation of the solvent. **b** SEM images of the fabricated nanocapsules. Copyright 2012. Reproduced with permission from John Wiley and Sons

polymerisation have been adopted to protect steel plate from corrosion [79, 80]. Nanocapsules with diameters of 400–450 nm containing triethanolamine (TEA), a corrosion inhibitor for zinc and steel, were fabricated. Polymeric nanocapsules were also produced that can contain six types of amine corrosion inhibitors 100–400 nm in diameter.

Interfacial Polymerisation

Interfacial polymerisation is similar to in situ polymerisation. However, the shell wall was formed by using the reactants from both the dispersed and the continuous phases [13]. Firstly, the core material is dispersed in a continuous phase containing one type of the predissolved monomer precursor for the shell material. Next, another monomer soluble in the dispersed phase is added. Polymerisation occurs at the aqueous–organic interface, generating microcapsules [13].

Cai et al. prepared urea-formaldehyde (UF) nanocapsules with a modified aliphatic amine (HB-1618) as a core material and the UF resin as shell material by interfacial polymerisation. The average diameter of unmodified and modified nanocapsules was 562 and 754 nm, respectively. Analysis of thermal stability and mechanical properties reflected that the introduction of KH560 significantly improved the tensile strength, elastic property and thermal stability. Scanning electron microscope (SEM) results indicated that the addition of KH560 led to excellent interfacial adhesion between the surface of the matrix and nanocapsules, thus improving the healing ability [81].

3.2 Nanocomposites as Additives to Improve the Properties of Healing Agents

The introduction of nanomaterials can significantly alter different properties of polymers such as mechanical and physical properties. There is much interest in modifying the properties of the host material or healing agent, for instance, increasing the strength of the cured healing agent. One possible way of doing this is to add nanoparticles into the healing agent.

Yan et al. [82] studied the effects of silicate-based nanoparticles on the mechanical properties of PDMS and revealed the interactions between the particles and the matrix. Its mechanical response to high-amplitude shear cycles and the recovery of the modulus in a long time were investigated. The results showed a significant hysteresis loop and pronounced stress softening (Mullins effect) during cyclic tests. It was found that the recovery at lower temperatures was much more pronounced compared to that at higher temperatures, given the same rest time, due to the reduced chain mobility at low temperatures. This property results in a material that can be significantly stiffer.

In addition to being a healing agent carrier, a halloysite can also be an additive for functional polymer composites. Abdullayev and Lvov [83] studied the effects of halloysite on mechanical properties of the PMMA bone cement and found the tensile and flexural strength were significantly improved.

Boron nitride nanotubes (BNNTs) have structures similar to CNTs and are endowed with excellent electrical and mechanical properties. They can be used in high-temperature applications as they are more resistant to oxidation. Thakur et al. [84] developed a simple and environment-friendly method for the functionalisation of BNNTs by using dopamine, a synthetic mimic of mussel adhesive proteins. Polymer nanocomposites containing BNNTs functionalised by pristine and dopamine were tested for mechanical and thermal properties. Compared to nanocomposites incorporating pristine BNNTs, the new functionalised BNNTs enable superior properties for the polymer nanocomposites.

To improve the epoxy-/glass fibre-laminated composites, ZrO_2 nanoparticles proved to be useful additives. Halder et al. incorporated ZrO_2 nanoparticles in glass fibre-reinforced composites and showed a strong improvement in tensile and flexural properties compared to that of the neat epoxy glass fibre composite [85]. A significant variation of tensile strength, stiffness and toughness of around 27, 62 and 110% was observed, and strength and modulus under bending were also enhanced to around 22 and 38%, respectively [85].

After nanoparticles are added, an external electrical field may be employed to align conductive nanoparticles to enhance the reinforcement strength further. Ladani et al. investigated the fracture energy and electrical conductivity of a thermoset epoxy polymer modified by the addition of aligned carbon nanofibres (CNFs) [86]. A liquid epoxy resin incorporating the CNFs was made by using a surfactant and a three-roll mill to achieve good dispersion. CNFs were aligned in an AC electric field and formed a head-to-head structure in epoxy with the majority (85%) of the CNFs lying within $\pm 15°$, as shown in Fig. 15. After the mixture had been cured, test results showed that the addition of 1.6 wt% of CNFs and the electric alignment increased the electrical conductivity by about seven orders of magnitude and the fracture energy by about 1600%. In addition to CNFs, CNTs can also be aligned by an electric field to enhance the strength or toughness of polymer composites [87, 88].

Graphene nanoplatelets can also be aligned using an AC electric field to promote the mechanical or electrical properties of epoxy composites. Wu et al. aligned graphene nanoplatelets that have an average thickness of 6–8 nm and an average diameter of 25 μm in epoxy resin by using an AC electric field with an amplitude of 25 V/mm and a frequency of 10 kHz [89], as shown in Fig. 16. It was found that alignment of the graphene nanoplatelets improved 7–8 orders of magnitude of the electrical conductivity, nearly 60% of the thermal conductivity and up to 900% of the mode I fracture toughness. Although this technique has yet to be experimentally tested in extrinsic self-healing composites, those results indicate that healing performances can potentially be greatly enhanced by incorporating healing agents with nanocomposite particles.

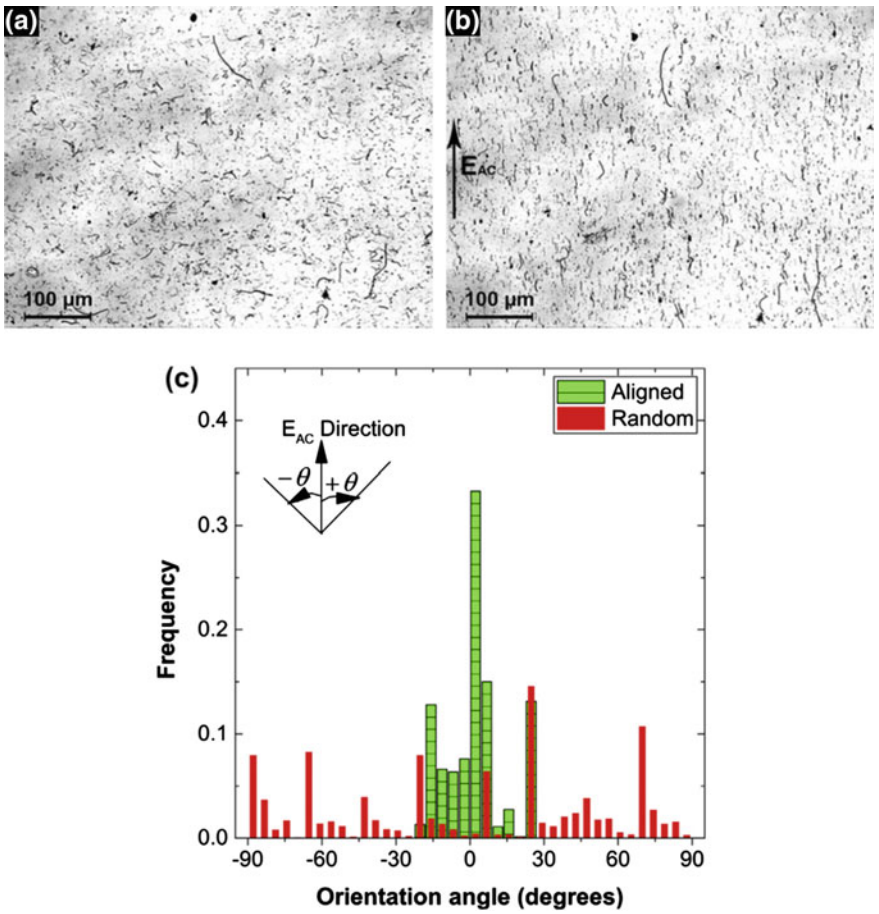

Fig. 15 Alignment of CNFs in an electric field **a** randomly oriented CNFs and **b** aligned CNFs, and the *arrow* indicates the direction of the field; **c** comparison of the angle distribution of randomly oriented CNFs and CNFs aligned in the electric field [86]. Copyright 2010. Available under a Creative Commons Attribution-Noncommercial License

3.3 Nanocomposites as Additives to Activate or Improve Chemical Reactions in Curing Processes

Once the healing agent is released from capsules or vessels, a catalyst or a hardener is usually needed to trigger or to accelerate the curing processes. A typical design is to disperse suitable nanoparticles in the host matrix and form a new nanocomposite in which healing agents can solidify. The most famous example is to disperse Grubbs' catalyst in an epoxy matrix to cure DCPD healing agents [6, 90]. In addition to Grubbs's catalyst, a number of other nanoparticles can also be used to trigger healing processes including tungsten chloride (WCl_6) [91], Grubbs'

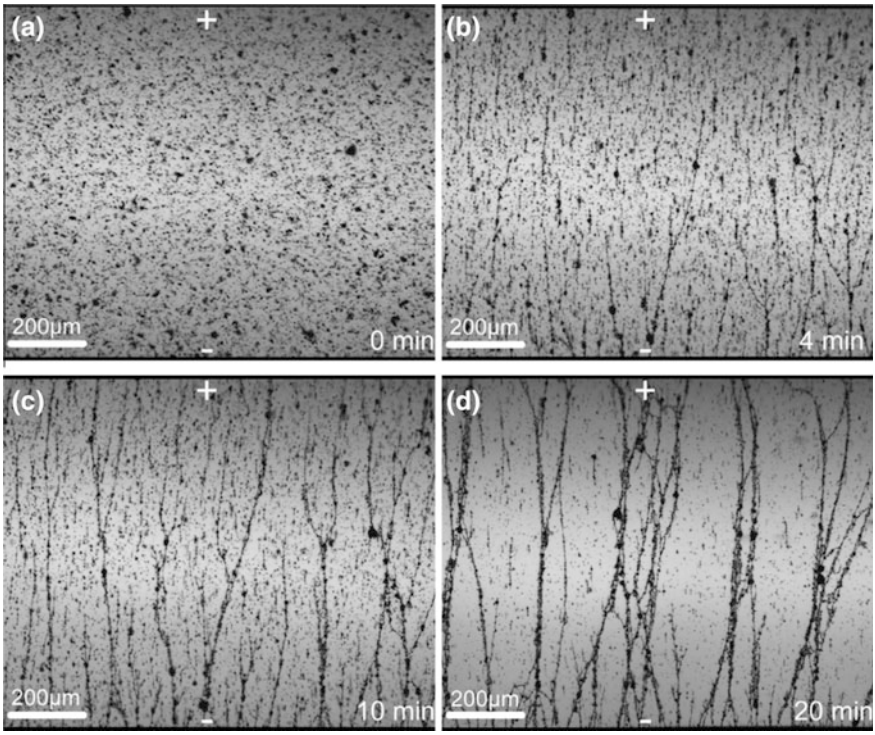

Fig. 16 Optical images of graphene nanoplatelets in epoxy resin aligned by an AC electric field [89]: **a** Randomly oriented graphene nanoplatelets; **b**, **c** and **d** after the field was applied for 4, 10 and 20 min, respectively. Copyright 2015. Available under a Creative Commons Attribution-Noncommercial License

second-generation catalyst (G2), Hoveyda–Grubbs' first-generation catalyst (HG1) and Hoveyda–Grubbs' second-generation catalyst (HG2) [92].

In addition to triggering chemical reactions in healing agents, nanoparticles can be used to accelerate reactions or to reduce polymerisation reaction temperatures. Yuan et al. [93] dispersed diamino diphenyl sulphone (DDS) particles in cyanate ester (CE) resin, an important high-temperature thermosetting polymer, to decrease the polymerisation reaction temperature, thus ensuring a low cure temperature. The DDS also served as a curing agent for epoxy resin healing agents.

Vertuccio et al. investigated the effects of carbon nanofillers, such as CNTs, short carbon fibres and graphene particles on the cure kinetic of an epoxy resin [94]. Kinetic analyses were carried out by dynamic and isothermal differential scanning calorimetry (DSC). It was found that the addition of one-dimensional fillers does not cause large differences in the curing kinetics compared to the unfilled ones. However, it was found that the activation energy is related to the secondary amine-epoxy reaction in the case of highly exfoliated graphite.

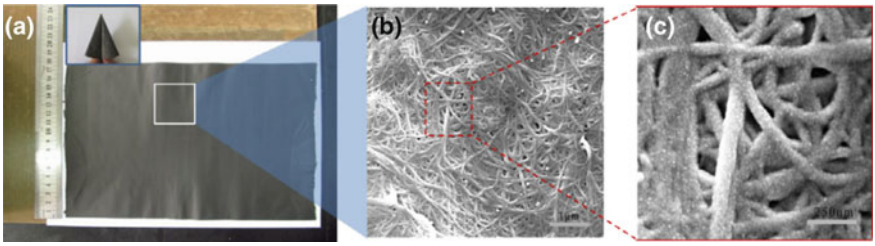

Fig. 17 **a** Dimensions digital pictures of as-prepared meso-/macropore carbon nanotube paper (CNP); the inset image is a plane using the resulting CNP to display the outstanding flexibility as ordinary paper. **b** FE-SEM image of the meso-/macropore CNP observed on the *top*. **c** Partially enlarged photograph of Fig. 17b [95]. Copyright 2014. Reproduced with permission from Elsevier

Healing processes in extrinsic self-healing composites place very stringent demands on healing conditions. For example, the healing agent is only active in a narrow temperature range, and the majority of healing agents require heat to accelerate the curing process. However, this heat treatment is often difficult to give in real applications. Zhang et al. developed a carbon nanotube paper, as shown in Fig. 17, that can be incorporated into fibre-reinforced composites. Once the paper is electrically charged, the composites generate internal heat to de-ice [95]. This method is valuable for self-healing composites as a similar mechanism can be used to accelerate healing. In addition, carbon nanotube paper also has various sensing properties and can be used as strain sensors [96].

3.4 Nanocomposites Used in the Fabrication of Capsules or Vessels

3.4.1 Fabrication of Capsules

Shell materials for capsules can be incorporated with nanoparticles to improve the capsule quality. Fereidoon et al. improved the morphology, thermal properties and water resistance of microcapsules by introducing either single-walled CNTs or aluminium oxide nanoparticles into the wall material, UF resin, as shown in Fig. 18 [97]. The microcapsules were synthesised via in situ polymerisation in an oil-in-water emulsion. After the emulsion had stabilised, formaldehyde mixed with the particles was added to the emulsion, which was then heated, cooled, rinsed, filtered and dried in sequence to produce the new capsules. Test results proved that the introduction of nanoparticles to the shell wall could reduce the surface roughness and size of the microcapsules, and the thermal stability was also improved.

Yang et al. developed microcapsules loaded with ethyl phenylacetate (EPA), and the PU/PMF shell walls were incorporated with silica nanoparticle [98], as shown in Fig. 19. SiO_2 nanoparticles can be absorbed at the interface between oil and water to stabilise the emulsions, and the size of the produced microcapsules can be altered

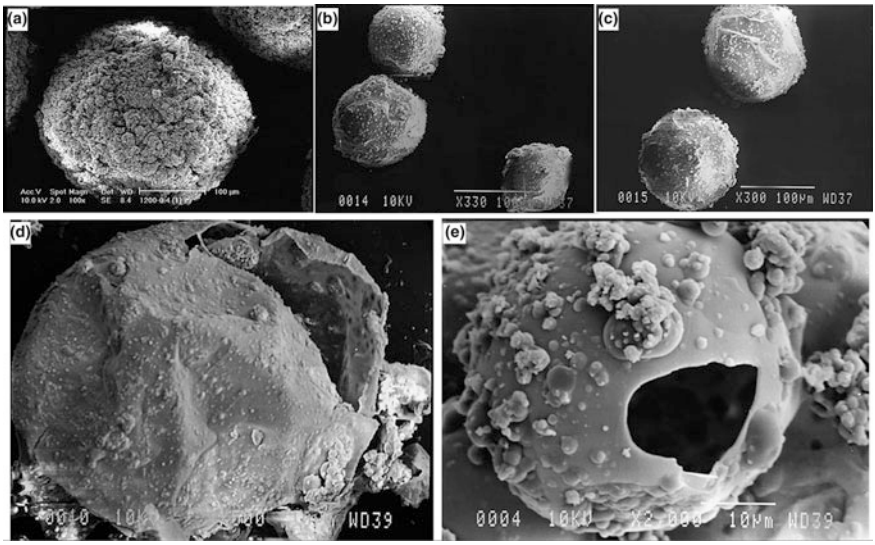

Fig. 18 SEM images of **a** traditional, **b** SWCNT-modified and **c** nanoalumina-modified microcapsules; wall thicknesses of **d** traditional and **e** modified microcapsules [97]. Copyright 2013. Reproduced with permission from Springer

depending on the concentration of SiO_2 nanoparticles [98]. The shell made of hybrid materials makes a rough exterior surface for capsules and promote their thermal conductivities and dispersion stability.

3.4.2 Fabrication of Vessels

Nanocomposites were employed in the fabrication of vessels. Using sacrificial fibres and scaffolds is the most important method of fabricating hollow vessels inside composites, but it has many challenges. One particular challenge was the way to remove sacrificial fibres and scaffolds from the cured polymer completely. Various materials, such as wax, were once used as the sacrificial materials as they can liquefy easily through heating. However, as previously stated, it is common for residues to block vessels. A few materials such as PLA that can be depolymerised at high temperatures showed great potential as sacrificial materials as they leave no residue once depolymerised. However, high depolymerisation temperatures—at around 280 °C in the case of PLA—can cause thermal damage to the host material. Dong et al. developed a method to reduce the depolymerisation temperature of PLA from 280 °C to around 180 °C, which is a tolerable temperature for a variety of epoxy resins which could be used for fibre-reinforced composites [52]. It was shown that tin(II) oxalate nanoparticles were the best catalyst able to reduce the depolymerisation temperature. To incorporate PLA fibres with the catalysts, a two-stage method was employed. First, the fibres were made to swell by using a

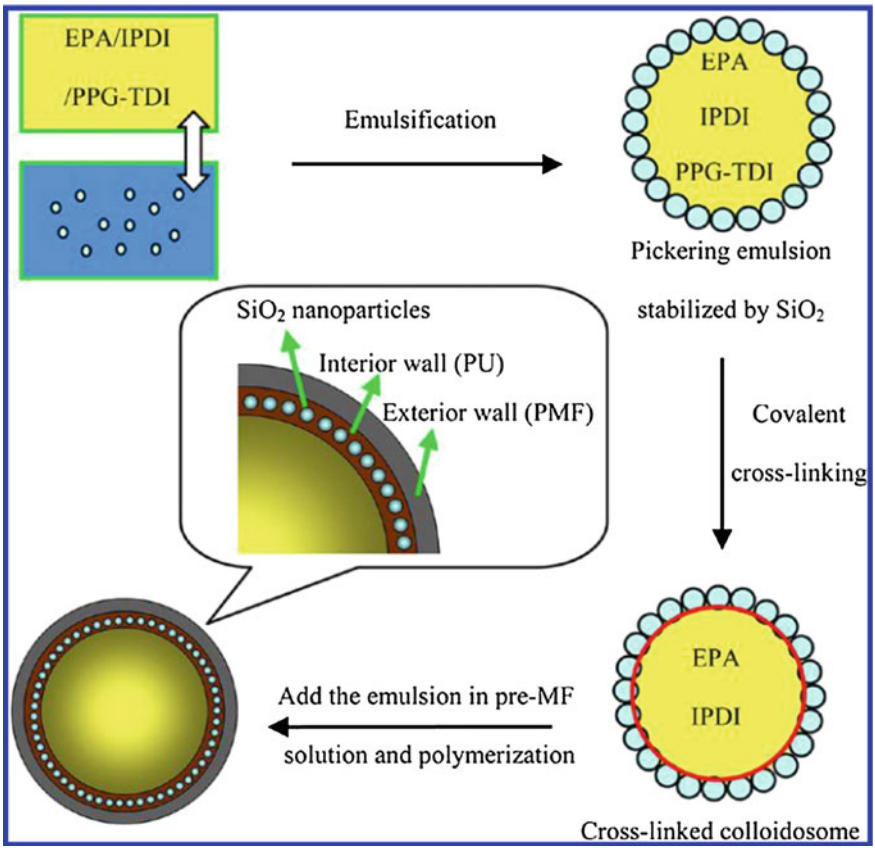

Fig. 19 Fabrication of microcapsules loaded with EPA with hybrid shell walls containing SiO_2 [98]. Copyright 2013. Reproduced with permission from American Chemical Society

mixture of the catalysts, trifluoroethanol (TFE) and water. After the catalysts had been dispersed in the swollen fibres, the solvent was evaporated, resulting in nanocomposites PLA incorporated with tin(II) oxalate, or PLA sacrificial fibres, as shown in Fig. 20. The fibres could be used to fabricate vessels in complex configurations inside polymer and fibre-reinforced composites [41, 53, 99].

In addition to tin(II) oxalate, Qu et al. showed another catalyst, zinc oxide nanoparticles, able to accelerate the hydrolytic degradation of PLA at temperatures well below its glass transition temperature [100]. It was reported that the activation energy for ZnO-catalysed PLA hydrolysis is about 38% lower than that of pure PLA hydrolysis. In addition to the new catalysts, the authors also demonstrated a new way to incorporate PLA with catalysts. PLA powders and the nanoparticles were premixed, and the mixture was passed through a twin-screw microcompounder. At a suitably high temperature, an extrusion/compounding process generates PLA fibres incorporating ZnO nanoparticles.

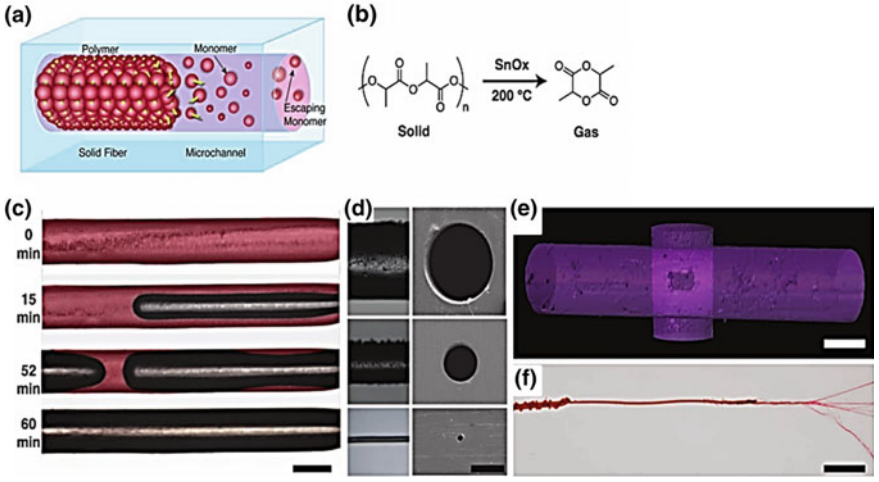

Fig. 20 Decomposition of PLA fibre. **a** Schematic of channel fabrication; **b** catalysed depolymerisation reaction of PLA fibre; **c** optical images showing the processing generating hollow vessels; **d** cross sections of vessels; **e** CT image of interconnecting vessels; **f** vascular branching [99]. Copyright 2011. Reproduced with permission from John Wiley and Sons

Nanocomposites can also be used for the structural reinforcement of microvascular networks. Olugebefola et al. showed a method to deposit HNTs onto the interior surface of hollow vessels [101], as illustrated in Fig. 21. Electrostatic layer-by-layer assembly was employed to deposit films containing HNTs onto the surfaces of a sacrificial scaffold [101]. After scaffold removal, halloysite was deposited onto the internal surface of the channels [101]. It is verified that the introduction of HNTs could reduce concentrations and improve mechanical performance, by using sensitive strain measurements on reinforced vessels.

To fabricate hollow vessels with nanometric diameters, Gualandi et al. proposed the use of electrospun nonwoven mats as sacrificial fibres to generate 3D interconnected vessels [62]. Pullulan was chosen as the sacrificial material due to its commercial availability, high solubility in water and good thermal stability. After removing the sacrificial materials by water immersion, hollow vessels with diameters as small as 280 nm were formed. Electrospinning technology makes it possible to produce core–shell fibres where the shell is made up of a strong material and the core can be a liquid healing agent. Therefore, this method could be used to encapsulate healing agents into nanofibres. Core–shell fibres, as shown in Fig. 22, are easy to produce. However, this method cannot build interconnected networks, and refilling is not possible. In this case, the material using core–shell fibres is more like an improved capsule-based self-healing material than a vessel-based self-healing material.

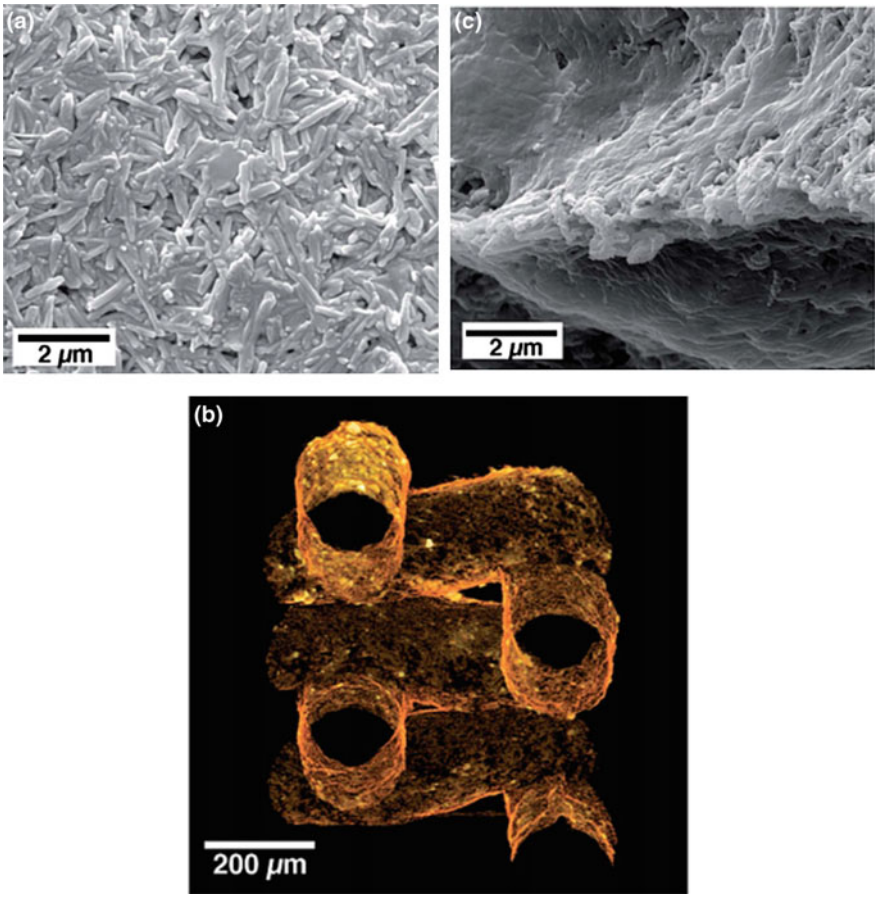

Fig. 21 **a** SEM image of the multilayer deposited onto the interior surface of the channel showing isotropic nanotube orientation. **b** MicroCT of halloysite nanotubes deposited onto the sacrificial scaffold. **c** SEM image of epoxy matrix embedded with interconnecting vessels deposited by the PDADMAC/halloysite multilayer [101]. Copyright 2013. Reproduced with permission from Royal Society of Chemistry

4 Challenges and Future Works

The introduction of nanocomposites into the research of extrinsic self-healing composites has brought many advantages as discussed in Sect. 3. However, self-healing composites have yet to be used in practical applications owing to uncertainties in their performances. One apparent uncertainty would be in the activation of healing processes. In both capsule-based and vessel-based self-healing composites, the healing agents are released once the capsules or vessels are damaged. When the composites are damaged but the cracks did not reach the capsules

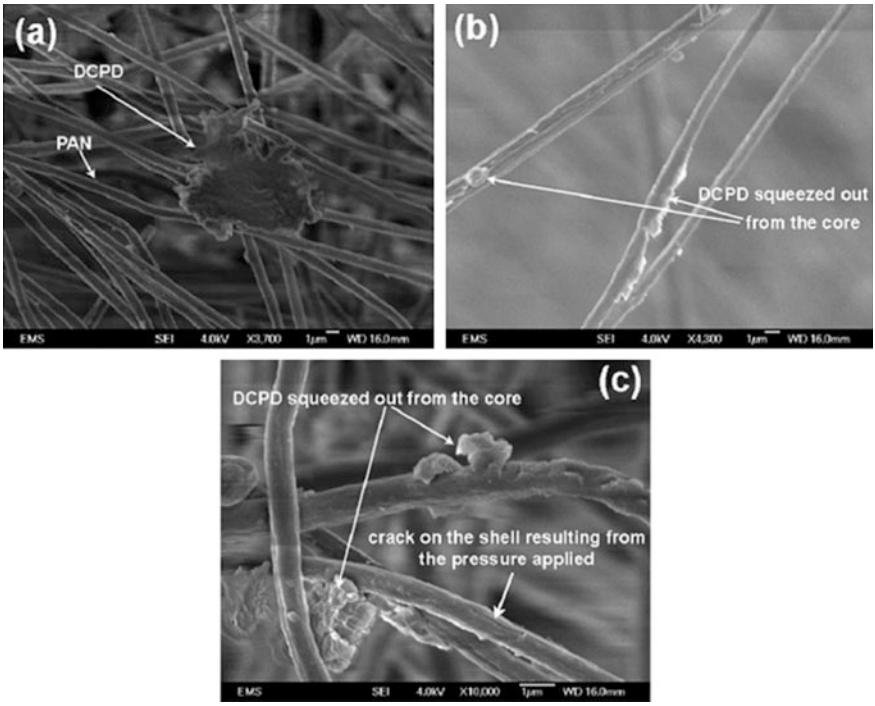

Fig. 22 SEM images of core–shell DCPD-PAN nanofibres [102]. **a**, **b** show healing agents releasing from the core; **c** shows a crack in the shell. Copyright 2012. Reproduced with permission from John Wiley and Sons

or vessels, the composites cannot heal at all. In order to increase the possibility of the activation, large volumes of capsules or vessels should be embedded into the host materials. However, the resulted voids can significantly reduce the strength of the composites. The dilemma could be a barrier in the practice of extrinsic self-healing composites.

Another important uncertainty is in healing capability embracing damage size and material type. For example, capsule-based self-healing composites can recover from microcracks, but they cannot be healed when the cracks are very big and deep, as the healing agents stored in capsules are not sufficient to fill all gaps. Regarding material type, a majority of extrinsic self-healing materials can recover only the matrix of their host materials. But the applications where self-healing composites have potential markets are those not easy to access or have very high maintenance costs, such as satellites, aeroplanes and offshore turbines. Structural composite materials containing more than one components have been widely adopted in the applications mentioned above. And when the materials are damaged, it is common that more than one types of the materials are fractured, and healing only the matrix is certainly not enough. Therefore, the development of self-healing composites with

high healing capability that can carry out an efficiency recovery regardless of damage size and material type is essential to the practical application.

In the future works, using nanocomposites in extrinsic self-healing composites to overcome those uncertainties is highly promising. As discussed in Sects. 3.1 and 3.4, nanocomposites could be used as carriers or in making stronger capsules and vessels, such as in [101], suggesting that the mechanical properties of host materials can be less reduced by the introduction of capsules or vessels. If more capsules or vessels could be embedded into host materials, the larger coverage could result in more consistent healing performances.

The most significant development that can be potentially accomplished by using nanocomposites is the autonomous recovery of multitype materials, as discussed in Sect. 3.2. The addition of nanocomposites in healing agents can not only alter the properties of healing agents but also be manipulated using electric fields or magnetic fields to fix other components in addition to the matrix [86]. For example, when carbon fibre composites are damaged, healing agents incorporating short carbon fibres are possible to fix the matrix and the structural carbon fibres simultaneously, using a suitable electric field to properly manipulate the short fibres.

Nanocomposites could also contribute to the recovery from large-scale damages. It has been reported that a special two-stage healing agent could be used to heal damages as big as 35 mm in diameter [42]. Since nanocomposites can be used to activate or improve the chemical reactions in the curing process, as discussed in Sect. 3.3, it is possible to use different nanocomposites to activate healing processes in different stages to seal even larger wounds.

5 Conclusion

This chapter has presented the development of extrinsic self-healing composites and the role of nanocomposites in relation to extrinsic self-healing materials. Nanoparticles such as CNTs and nanocapsules can be used as healing agent carriers as well as a structural reinforcement for host materials. After the incorporation of host materials or healing agents with nanocomposites, their mechanical properties can be improved and healing performance can be enhanced. The dispersion of nanoparticles in the host matrix can trigger or improve the curing of healing agents. The quality of capsules can be improved by adding nanoparticles to shell materials, and the depolymerisation temperature of sacrificial materials can be reduced by embedding sacrificial materials with suitable nanoparticles. Nanocomposites are promising in the future work as it shows potentials to overcome substantial uncertainties in the practice of self-healing composites.

References

1. Chen XX, Wudl F, Mal AK, Shen HB, Nutt SR (2003) New thermally remendable highly cross-linked polymeric materials. Macromolecules 36(6):1802–1807
2. Habault D, Zhang H, Zhao Y (2013) Light-triggered self-healing and shape-memory polymers. Chem Soc Rev 42(17):7244–7256
3. Selver E, Potluri P, Soutis C, Hogg P (2015) Healing potential of hybrid materials for structural composites. Compos Struct 122:57–66
4. Wang Y, Pham DT, Ji C (2015) Self-healing composites: a review. Cogent Eng 2 (1):1075686
5. Blaiszik BJ, Kramer SLB, Olugebefola SC, Moore JS, Sottos NR, White SR (2010) Self-healing polymers and composites. Annu Rev Mater Res 40(1):179–211
6. White SR, Sottos NR, Geubelle PH, Moore JS, Kessler MR, Sriram SR, Brown EN, Viswanathan S (2001) Autonomic healing of polymer composites. Nature 409(6822): 794–797
7. Dry C, McMillan W (1996) Three-part methylmethacrylate adhesive system as an internal delivery system for smart responsive concrete. Smart Mater Struct 5(3):297–300
8. Dry C (1996) Procedures developed for self-repair of polymer matrix composite materials. Compos Struct 35(3):263–269
9. Dry C, Sottos NR (1993) Passive smart self-repair in polymer matrix composite-materials. P Soc Photo-Opt Ins 1916:438–444
10. Bleay SM, Loader CB, Hawyes VJ, Humberstone L, Curtis PT (2001) A smart repair system for polymer matrix composites. Compos Part A-Appl Sci Manuf 32(12):1767–1776
11. Pang JWC, Bond IP (2005) A hollow fibre reinforced polymer composite encompassing self-healing and enhanced damage visibility. Compos Sci Technol 65(11–12):1791–1799
12. Toohey KS, Sottos NR, Lewis JA, Moore JS, White SR (2007) Self-healing materials with microvascular networks. Nat Mater 6(8):581–585
13. Zhu DY, Rong MZ, Zhang MQ (2015) Self-healing polymeric materials based on microencapsulated healing agents: from design to preparation. Prog Polym Sci 49–50: 175–220
14. Caruso MM, Blaiszik BJ, White SR, Sottos NR, Moore JS (2008) Full recovery of fracture toughness using a nontoxic solvent-based self-healing system. Adv Funct Mater 18 (13):1898–1904
15. Meng LM, Yuan YC, Rong MZ, Zhang MQ (2010) A dual mechanism single-component self-healing strategy for polymers. J Mater Chem 20(29):6030–6038
16. Yin T, Rong MZ, Zhang MQ, Zhao JQ (2009) Durability of self-healing woven glass fabric/epoxy composites. Smart Mater Struct 18(7):074001
17. Yin T, Rong MZ, Zhang MQ, Yang GC (2007) Self-healing epoxy composites—Preparation and effect of the healant consisting of microencapsulated epoxy and latent curing agent. Compos Sci Technol 67(2):201–212
18. Jackson AC, Bartelt JA, Braun PV (2011) Transparent self-healing polymers based on encapsulated plasticizers in a thermoplastic matrix. Adv Funct Mater 21(24):4705–4711
19. Cho SH, Andersson HM, White SR, Sottos NR, Braun PV (2006) Polydimethylsiloxane-based self-healing materials. Adv Mater 18(8):997–1000
20. Jin H, Mangun CL, Stradley DS, Moore JS, Sottos NR, White SR (2012) Self-healing thermoset using encapsulated epoxy-amine healing chemistry. Polymer 53(2):581–587
21. Zhang H, Wang P, Yang J (2014) Self-healing epoxy via epoxy–amine chemistry in dual hollow glass bubbles. Compos Sci Technol 94:23–29
22. Yuan YC, Rong MZ, Zhang MQ, Chen J, Yang GC, Li XM (2008) Self-healing polymeric materials using epoxy/mercaptan as the healant. Macromolecules 41(14):5197–5202
23. Keller MW, White SR, Sottos NR (2007) A self-healing poly(dimethyl siloxane) elastomer. Adv Funct Mater 17(14):2399–2404

24. Zhu DY, Wetzel B, Noll A, Rong MZ, Zhang MQ (2013) Thermo-molded self-healing thermoplastics containing multilayer microreactors. J Mater Chem A 1(24):7191–7198
25. Brown EN, Kessler MR, Sottos NR, White SR (2003) In situ poly(urea-formaldehyde) microencapsulation of dicyclopentadiene. J Microencapsul 20(6):719–730
26. Yuan YC, Rong MZ, Zhang MQ (2008) Preparation and characterization of microencapsulated polythiol. Polymer 49(10):2531–2541
27. Li Q, Mishra AK, Kim NH, Kuila T, K-t Lau, Lee JH (2013) Effects of processing conditions of poly(methylmethacrylate) encapsulated liquid curing agent on the properties of self-healing composites. Compos B Eng 49:6–15
28. Li Q, Siddaramaiah Kim NH, Hui D, Lee JH (2013) Effects of dual component microcapsules of resin and curing agent on the self-healing efficiency of epoxy. Compos Part B-Eng 55:79–85
29. Rule JD, Brown EN, Sottos NR, White SR, Moore JS (2005) Wax-protected catalyst microspheres for efficient self-healing materials. Adv Mater 17(2):205
30. McIlroy DA, Blaiszik BJ, Caruso MM, White SR, Moore JS, Sottos NR (2010) Microencapsulation of a reactive liquid-phase amine for self-healing epoxy composites. Macromolecules 43(4):1855–1859
31. Chen Y, Guan Z (2013) Self-assembly of core–shell nanoparticles for self-healing materials. Polym Chem 4(18):4885
32. Zhang H, Yang JL (2013) Etched glass bubbles as robust micro-containers for self-healing materials. J Mater Chem A 1(41):12715–12720
33. Zhang H, Wang PF, Yang JL (2014) Self-healing epoxy via epoxy-amine chemistry in dual hollow glass bubbles. Compos Sci Technol 94:23–29
34. Jin HH, Mangun CL, Griffin AS, Moore JS, Sottos NR, White SR (2014) Thermally stable autonomic healing in epoxy using a dual-microcapsule system. Adv Mater 26(2):282–287
35. Liu X, Sheng X, Lee JK, Kessler MR (2009) Synthesis and characterization of melamine-urea-formaldehyde microcapsules containing ENB-based self-healing agents. Macromol Mater Eng 294(6–7):389–395
36. Liu X, Zhang H, Wang J, Wang Z, Wang S (2012) Preparation of epoxy microcapsule based self-healing coatings and their behavior. Surf Coat Technol 206(23):4976–4980
37. Yang J, Keller MW, Moore JS, White SR, Sottos NR (2008) Microencapsulation of isocyanates for self-healing polymers. Macromolecules 41(24):9650–9655
38. van den Dungen ETA, Klumperman B (2010) Synthesis of liquid-filled nanocapsules via the miniemulsion technique. J Polym Sci, Part A: Polym Chem 48(22):5215–5230
39. Toohey KS, Hansen CJ, Lewis JA, White SR, Sottos NR (2009) Delivery of two-part self-healing chemistry via microvascular networks. Adv Funct Mater 19(9):1399–1405
40. Patrick JF, Sottos NR, White SR (2012) Microvascular based self-healing polymeric foam. Polymer 53(19):4231–4240
41. Patrick JF, Hart KR, Krull BP, Diesendruck CE, Moore JS, White SR, Sottos NR (2014) Continuous self-healing life cycle in vascularized structural composites. Adv Mater 26 (25):4302–4308
42. White SR, Moore JS, Sottos NR, Krull BP, Cruz WAS, Gergely RCR (2014) Restoration of large damage volumes in polymers. Science 344(6184):620–623
43. Trask RS, Bond IP (2006) Biomimetic self-healing of advanced composite structures using hollow glass fibres. Smart Mater Struct 15(3):704–710
44. Pang JWC, Bond IP (2005) 'Bleeding composites'—damage detection and self-repair using a biomimetic approach. Compos A Appl Sci Manuf 36(2):183–188
45. Kousourakis A, Mouritz AP (2010) The effect of self-healing hollow fibres on the mechanical properties of polymer composites. Smart Mater Struct 19(8):085021
46. Williams G, Trask R, Bond I (2007) A self-healing carbon fibre reinforced polymer for aerospace applications. Compos Part A Appl Sci Manuf 38(6):1525–1532
47. Norris CJ, Bond IP, Trask RS (2013) Healing of low-velocity impact damage in vascularised composites. Compos Part A Appl S 44:78–85

48. Hamilton AR, Sottos NR, White SR (2012) Pressurized vascular systems for self-healing materials. J R Soc Interface 9(70):1020–1028
49. Therriault D, White SR, Lewis JA (2003) Chaotic mixing in three-dimensional microvascular networks fabricated by direct-write assembly. Nat Mater 2(4):265–271
50. Lewis JA, Gratson GM (2004) Direct writing in three dimensions. Mater Today 7(7–8): 32–39
51. Guo SZ, Gosselin F, Guerin N, Lanouette AM, Heuzey MC, Therriault D (2013) Solvent-cast three-dimensional printing of multifunctional microsystems. Small 9(24):4118–4122
52. Dong HD, Esser-Kahn AP, Thakre PR, Patrick JF, Sottos NR, White SR, Moore JS (2012) Chemical treatment of poly(lactic acid) fibers to enhance the rate of thermal depolymerization. ACS Appl Mater Inter 4(2):503–509
53. Gergely RCR, Pety SJ, Krull BP, Patrick JF, Doan TQ, Coppola AM, Thakre PR, Sottos NR, Moore JS, White SR (2014) Multidimensional vascularized polymers using degradable sacrificial templates. Adv Funct Mater 25(7):1043–1052
54. Wu W, Hansen CJ, Aragon AM, Geubelle PH, White SR, Lewis JA (2010) Direct-write assembly of biomimetic microvascular networks for efficient fluid transport. Soft Matter 6 (4):739–742
55. Wu W, DeConinck A, Lewis JA (2011) Omnidirectional printing of 3D microvascular networks. Adv Mater 23(24):178–183
56. Hansen CJ, Saksena R, Kolesky DB, Vericella JJ, Kranz SJ, Muldowney GP, Christensen KT, Lewis JA (2013) High-throughput printing via microvascular multinozzle arrays. Adv Mater 25(1):96–102
57. Jacobsen AJ, Barvosa-Carter W, Nutt S (2007) Micro-scale truss structures formed from self-propagating photopolymer waveguides. Adv Mater 19(22):3892–3896
58. Jacobsen A, Kolodziejska J, Doty R, Fink K, Zhou C, Roper C, Carter W (2010) Interconnected self-propagating photopolymer waveguides: an alternative to stereolithography for rapid formation of lattice-based open-cellular materials. In: Twenty first annual international solid freeform fabrication symposium-an additive manufacturing conference
59. Schaedler T, Jacobsen A, Torrents A, Sorensen A, Lian J, Greer J, Valdevit L, Carter W (2011) Ultralight metallic microlattices. Science 334(6058):962–965
60. Roper CS, Schubert RC, Maloney KJ, Page D, Ro CJ, Yang SS, Jacobsen AJ (2015) Scalable 3D bicontinuous fluid networks: polymer heat exchangers toward artificial organs. Adv Mater 27(15):2479–2484
61. Bellan LM, Singh SP, Henderson PW, Porri TJ, Craighead HG, Spector JA (2009) Fabrication of an artificial 3-dimensional vascular network using sacrificial sugar structures. Soft Matter 5(7):1354–1357
62. Gualandi C, Zucchelli A, Osorio MF, Belcari J, Focarete ML (2013) Nanovascularization of polymer matrix: generation of nanochannels and nanotubes by sacrificial electrospun fibers. Nano Lett 13(11):5385–5390
63. Choi NW, Cabodi M, Held B, Gleghorn JP, Bonassar LJ, Stroock AD (2007) Microfluidic scaffolds for tissue engineering. Nat Mater 6(11):908–915
64. Golden AP, Tien J (2007) Fabrication of microfluidic hydrogels using molded gelatin as a sacrificial element. Lab Chip 7(6):720–725
65. He JK, Mao M, Liu YX, Shao JY, Jin ZM, Li DC (2013) Fabrication of nature-inspired microfluidic network for perfusable tissue constructs. Adv Healthc Mater 2(8):1108–1113
66. Huang J-H, Kim J, Agrawal N, Sudarsan AP, Maxim JE, Jayaraman A, Ugaz VM (2009) Rapid fabrication of bio-inspired 3D microfluidic vascular networks. Adv Mater 21 (35):3567–3571
67. Lim D, Kamotani Y, Cho B, Mazumder J, Takayama S (2003) Fabrication of microfluidic mixers and artificial vasculatures using a high-brightness diode-pumped Nd: YAG laser direct write method. Lab Chip 3(4):318–323
68. Lanzara G, Yoon Y, Liu H, Peng S, Lee WI (2009) Carbon nanotube reservoirs for self-healing materials. Nanotechnology 20(33):335704

69. Sauvant-Moynot V, Gonzalez S, Kittel J (2008) Self-healing coatings: an alternative route for anticorrosion protection. Prog Org Coat 63(3):307–315
70. Melo JDD, Barbosa APC, Costa MCB, de Melo GN (2014) Encapsulation of solvent into halloysite nanotubes to promote self-healing ability in polymers. Adv Compos Mater 23(5–6):507–519
71. Abdullayev E, Abbasov V, Tursunbayeva A, Portnov V, Ibrahimov H, Mukhtarova G, Lvov Y (2013) Self-healing coatings based on halloysite clay polymer composites for protection of copper alloys. Acs Appl Mater Inter 5(10):4464–4471
72. Fu Y, Zhao D, Yao P, Wang W, Zhang L, Lvov Y (2015) Highly aging-resistant elastomers doped with antioxidant-loaded clay nanotubes. ACS Appl Mater Inter 7(15):8156–8165
73. Blaiszik BJ, Sottos NR, White SR (2008) Nanocapsules for self-healing materials. Compos Sci Technol 68(3–4):978–986
74. Crespy D, Landfester K (2010) Miniemulsion polymerization as a versatile tool for the synthesis of functionalized polymers. Beilstein J Org Chem 6:1132–1148
75. Hoyle CE, Lee TY, Roper T (2004) Thiol–enes: Chemistry of the past with promise for the future. J Polym Sci Part A Polym Chem 42(21):5301–5338
76. Fickert J, Makowski M, Kappl M, Landfester K, Crespy D (2012) Efficient encapsulation of self-healing agents in polymer nanocontainers functionalized by orthogonal reactions. Macromolecules 45(16):6324–6332
77. Zhao Y, Fickert J, Landfester K, Crespy D (2012) Encapsulation of self-healing agents in polymer nanocapsules. Small 8(19):2954–2958
78. Li M, Rouaud O, Poncelet D (2008) Microencapsulation by solvent evaporation: state of the art for process engineering approaches. Int J Pharm 363(1–2):26–39
79. Choi H, Song YK, Kim KY, Park JM (2012) Encapsulation of triethanolamine as organic corrosion inhibitor into nanoparticles and its active corrosion protection for steel sheets. Surf Coat Technol 206(8–9):2354–2362
80. Choi H, Kim KY, Park JM (2013) Encapsulation of aliphatic amines into nanoparticles for self-healing corrosion protection of steel sheets. Prog Org Coat 76(10):1316–1324
81. Cai XL, Fu DT, Qu AL (2014) Effects of surface modification on properties of nanocapsules for self-healing materials. Plast Rubber Compos 43(5):161–165
82. Yan L, Dillard DA, West RL, Rubis KJ, Gordon GV (2012) Strain rate and temperature dependence of a nanoparticle-filled poly(dimethylsiloxane) undergoing shear deformation. J Polym Sci Part B Polym Phys 50(13):929–937
83. Abdullayev E, Lvov Y (2013) Halloysite clay nanotubes as a ceramic "skeleton" for functional biopolymer composites with sustained drug release. J Mater Chem B 1(23):2894–2903
84. Thakur VK, Yan J, Lin M-F, Zhi C, Golberg D, Bando Y, Sim R, Lee PS (2012) Novel polymer nanocomposites from bioinspired green aqueous functionalization of BNNTs. Polym Chem 3(4):962–969
85. Halder S, Ahemad S, Das S, Wang J (2015) Epoxy/glass fiber laminated composites integrated with amino functionalized ZrO_2 for advanced structural applications. ACS Appl Mater Inter 8(3):1695–1706
86. Ladani RB, Wu S, Kinloch AJ, Ghorbani K, Zhang J, Mouritz AP, Wang CH (2015) Improving the toughness and electrical conductivity of epoxy nanocomposites by using aligned carbon nanofibres. Compos Sci Technol 117:146–158
87. Martin CA, Sandler JKW, Windle AH, Schwarz MK, Bauhofer W, Schulte K, Shaffer MSP (2005) Electric field-induced aligned multi-wall carbon nanotube networks in epoxy composites. Polymer 46(3):877–886
88. Xie X-L, Mai Y-W, Zhou X-P (2005) Dispersion and alignment of carbon nanotubes in polymer matrix: a review. Mater Sci Eng R Reports 49(4):89–112
89. Wu S, Ladani RB, Zhang J, Bafekrpour E, Ghorbani K, Mouritz AP, Kinloch AJ, Wang CH (2015) Aligning multilayer graphene flakes with an external electric field to improve multifunctional properties of epoxy nanocomposites. Carbon 94:607–618

90. Kessler MR, White SR (2001) Self-activated healing of delamination damage in woven composites. Compos Part A Appl S 32(5):683–699. doi:10.1016/S1359-835x(00)00149-4
91. Kamphaus JM, Rule JD, Moore JS, Sottos NR, White SR (2008) A new self-healing epoxy with tungsten (VI) chloride catalyst. J R Soc Interface 5(18):95–103
92. Raimondo M, Guadagno L (2013) Healing efficiency of epoxy-based materials for structural applications. Polym Compos 34(9):1525–1532
93. Yuan L, Huang S, Gu A, Liang G, Chen F, Hu Y, Nutt S (2013) A cyanate ester/microcapsule system with low cure temperature and self-healing capacity. Compos Sci Technol 87:111–117
94. Vertuccio L, Russo S, Raimondo M, Lafdi K, Guadagno L (2015) Influence of carbon nanofillers on the curing kinetics of epoxy-amine resin. RSC Adv 5(110):90437–90450
95. Chu HT, Zhang ZC, Liu YJ, Leng JS (2014) Self-heating fiber reinforced polymer composite using meso/macropore carbon nanotube paper and its application in deicing. Carbon 66: 154–163
96. Zhang ZC, Chu HT, Wang KW, Liu YJ, Leng JS (2013) Multifunctional carbon nano-paper composite. In: Fourth international conference on smart materials and nanotechnology in engineering, 8793
97. Fereidoon A, Ghorbanzadeh Ahangari M, Jahanshahi M (2013) Effect of nanoparticles on the morphology and thermal properties of self-healing poly(urea-formaldehyde) microcapsules. J Polym Res 20(6):1–8
98. Yang Y, Wei Z, Wang C, Tong Z (2013) Versatile fabrication of nanocomposite microcapsules with controlled shell thickness and low permeability. ACS Appl Mater Inter 5 (7):2495–2502
99. Esser-Kahn AP, Thakre PR, Dong H, Patrick JF, Vlasko-Vlasov VK, Sottos NR, Moore JS, White SR (2011) Three-dimensional microvascular fiber-reinforced composites. Adv Mater 23(32):3654–3658
100. Qu M, Tu HL, Amarante M, Song YQ, Zhu SS (2014) Zinc oxide nanoparticles catalyze rapid hydrolysis of poly(lactic acid) at low temperatures. J Appl Polym Sci 131(11)
101. Olugebefola SC, Hamilton AR, Fairfield DJ, Sottos NR, White SR (2014) Structural reinforcement of microvascular networks using electrostatic layer-by-layer assembly with halloysite nanotubes. Soft Matter 10(4):544–548
102. Wu XF, Rahman A, Zhou ZP, Pelot DD, Sinha-Ray S, Chen B, Payne S, Yarin AL (2013) Electrospinning core-shell nanofibers for interfacial toughening and self-healing of carbon-fiber/epoxy composites. J Appl Polym Sci 129(3):1383–1393

A Brief Overview of Shape Memory Effect in Thermoplastic Polymers

M. Imran Khan, M.M. Zagho and R.A. Shakoor

Abstract Like shape memory alloys (SMAs) and shape memory ceramics, some polymers also exhibit shape memory effect. The polymeric materials demonstrating shape memory effect are commonly referred to as shape memory polymers (SMPs), intelligent or adaptive polymers. These SMPs have the ability to respond to an external stimulus such as heat, magnetism, electricity, light, moisture, pH and some specific chemicals. SMPs possess many advantages over SMAs and shape memory ceramics, i.e., better shape memory effect, lower density, biodegradability, easier processing, better control on recovery behavior, programmability and lower cost. Many different kinds of polymers can exhibit shape memory behavior, and more than twenty types of SMPs have already been reported in the literature. Interestingly, the shape memory behavior in SMPs mainly depends on the glass transition temperature of the polymer. SMPs are attractive materials for research, both for academia and industry, mainly because of their potential usage in, i.e., smart textiles, active aircraft equipment, biomedical instruments, smart electronic apparatuses, space deployable structures, actuators and smart self-healing systems. SMPs can be categorized into thermoset SMPs (chemically crosslinked) and thermoplastic SMPs (physically crosslinked). SMPs can be further subcategorized into linear polymers, branched polymers or a polymer complex. Thermoplastic SMPs are important class of polymeric-based shape memory materials. In this class of SMPs, two phase morphology is the main cause of the thermally induced shape memory effect. One phase causes the physical crosslinking, and the other phase behaves as a molecular switch. Linear thermoplastic SMPs are the most important

M. Imran Khan
Faculty of Materials Science and Chemical Engineering, GIK Institute of Science and Technology KPK, Topi, Swabi, Pakistan

M.M. Zagho · R.A. Shakoor (✉)
Center for Advanced Materials (CAM), Qatar University, 2713 Doha, Qatar
e-mail: shakoor@qu.edu.qa

D. Ponnamma et al. (eds.), *Smart Polymer Nanocomposites*,
Springer Series on Polymer and Composite Materials,
DOI 10.1007/978-3-319-50424-7_10

members of the group of thermoplastic SMPs. The linear thermoplastic SMPs can be further subdivided into the categories of block copolymers and high molecular weight polymers. However, the block copolymers have emerged as relatively more important class of linear thermoplastic SMPs. Polyurethanes and polyether esters are important examples of block copolymers. The current chapter focuses on the development, characterization and applications of thermoplastic SMPs and presents a comprehensive review of the recent advancements made in the area of thermoplastic SMPs.

Keywords Shape recovery · Thermoplastics · Crystalline polymers · Fabrication methods · Shape memory composites

Contents

1 Introduction

Shape memory polymers (SMPs) can memorize a particular shape and can recover to the original permanent shape upon heating. Today the shape memory polymers (SMPs) are an important subclass of smart materials and offer an attractive set of properties. The mostly used form of external stimuli responsible for triggering the shape recovery is heat, but various other forms of external stimuli may be utilized as the recovery initiators. According to the literature, the first official use of the term SMP can be linked to the development of the polynorbornene-based SMP by CDF Chimie Company (France) in 1984 [1].

Despite the long history of SMP, the phenomenon of polymer SME had remained little known and the scientific paper in this area had been rather limited until 1990s. Along this time frame, the discovery of segmented polyurethane SMP by Mitsubishi Heavy Industries Ltd. stimulated significant interests in SMPs, presumably due to the versatility of urethane chemistry that allows easy structural tuning and the industrial significance of polyurethane. For the same reasons, research on shape memory polyurethanes has remained quite active even today, despite many different SMPs that have since been discovered. Historically, the advancement of the SMP field has been closely associated with its practical potential. As such, the lack of excitement and research activities in the early days of SMPs can be attributed to the limited applications envisioned for such materials [2].

In 2002, Lendlein et al. demonstrated that SMP could be used as self-tightening suture for minimally invasive surgery [3].

2 Shape Memory Effect in Polymers

The simplest form of SME in polymers is given in Fig. 1. The temperature of SMP is first increased to a deformation temperature. This causes material softening and the modulus of the material drops. Next, a load is applied by keeping the SMP at the deformation temperature. Then, the SMP is cooled down while keeping the applied load intact. When the applied load is removed, the temporary deformed shape becomes fixed. When in a stress-free condition, the SMP is heated again to a recovery temperature which restores the original shape [2].

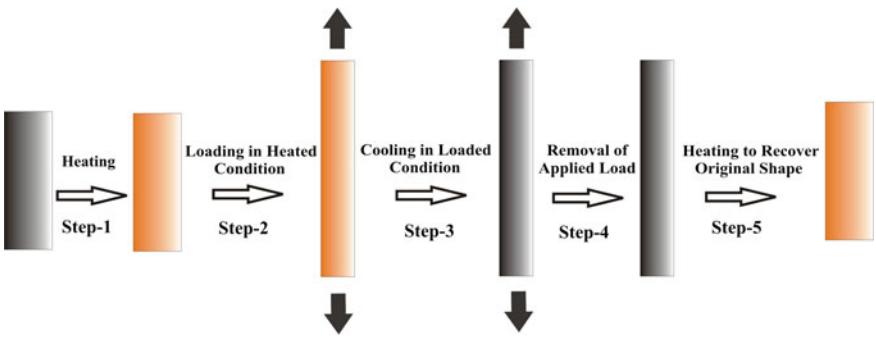

Fig. 1 A general shape memory mechanism in SMPs

3 Shape Memory Mechanism in SMPs

In metallic materials, generally the SME is based upon a reversible phase transformation between two crystalline phases, i.e., the low-temperature martensitic phase (or daughter phase) and the high-temperature austenitic phase (or parent phase). In case of polymers, the SME is an entropy-based phenomenon. In a permanent macroscopic shape, the molecular chains of an SMP adopt certain configurations with the highest entropy. When the temperature is changed above the T_{trans}, the chain mobility is enhanced. Upon loading, the chain configurations are significantly changed. This causes a decrease in entropy along with macroscopic shape change. Upon cooling the SMP below T_{trans}, the lower entropy state (or the temporary changed shape) is kinetically trapped due to the freezing of the molecular chains. This results in the macroscopic shape fixation. When the load is removed and the SMP is reheated above T_{trans}, the molecular mobility comes in action again and helps the molecular chains to return to their highest entropy state. This is the recovery of the permanent shape.

SMPs can exhibit dual SME, triple SME and multi-SME. The above-mentioned SME is dual SME as one temporary shape and one permanent shape are involved in each shape memory cycle. The abilities of an SMP to fix and recover shapes can be defined as shape fixity (R_{f}) and shape recovery (R_{r}) as given below [2]:

$$R_{\text{f}} = \left(\varepsilon_y - \varepsilon_x\right) / \left(\varepsilon_y \,\text{load} - \varepsilon_x\right) \tag{1}$$

$$R_{\text{r}} = \left(\varepsilon_y - \varepsilon_x \,\text{rec}\right) / \left(\varepsilon_y - \varepsilon_x\right) \tag{2}$$

where $\varepsilon_{y\ \text{load}}$ is the maximum strain under load, ε_y and ε_x are the fixed strains after cooling and load removal and $\varepsilon_{x\ \text{rec}}$ is the strain after recovery. SMPs may also be evaluated by the recovery speed (or strain recovery rate). The instantaneous recovery speed V_{r}, for instance, is defined as the time (t) derivative of strain.

$$V_{\text{r}} = (\partial\varepsilon/\partial t)\, 100\% \tag{3}$$

There are two essential conditions for a SMP to exhibit dual SME: (1) a reversible thermal transformation that induces temporary shape fixing and recovery and (2) a crosslinked molecular chain network which is responsible for permanent shape. Generally the polymers are intrinsically viscoelastic materials and most (if not all) polymers fulfill the first requirement.

The nature of crosslinking (the second condition) can be of two types, chemical and physical. In the absence of crosslinking, the deformation force causes a long-range chain slippage in a polymer at temperature above its transformation temperature which can be observed as a macroscopic permanent deformation. Although this process changes the macroscopic shape of the polymer, it does not change the molecular chain configuration, or in other words the entropy does not change. This is the reason that the shape memory effect is absent in the polymers

where crosslinking is not present. For an ideal shape memory effect, total stoppage of long-range molecular chain slippage is a prime requirement. Generally the chemically crosslinked SMP systems exhibit this kind of behavior [2].

The T_{trans} of a SMP is a temperature range which can coincide with the glass transition temperature (T_g) or melting temperature (T_m) of SMP. It is an important parameter in the initial design of an SMP. The T_{trans} is dependent on SMPs chemistry, its structure, and processing and programming parameters [4–6].

The physically crosslinked SMPs mainly comprise of two microstructural regions, the high- and low-temperature transition phases which serve as the physically crosslinked regions and the shape memory transition regions, respectively. In case of ultrahigh molecular weight polymers, the presence of extensive chain entanglements can also serve as the physical crosslinks. There is another fact that the physical crosslinks do not exist universally in polymers, no matter what type of physical crosslinks they are. On the other hand, the chemical crosslinks can be generally introduced into any polymers by general methods, i.e., e-beam radiation. It is also worth mentioning that most of the polymers can be converted into dual-shape memory polymers by chemical crosslinking [2].

Both the physically and chemically crosslinked polymers have large elastic strains above either T_g (amorphous cases) or T_m (crystalline cases) of the bulk material (strain up to more than 200% can be observed). Generally the SMPs are of low cost, low density, and possess biocompatibility. Another advantage that can be offered by many SMPs is their biodegradability [7].

SMPs and SMAs are used in distinct applications mainly because of their fundamental differences in their shape memory mechanism, mechanical and shape memory properties, viscoelastic properties and optical properties. A comparison of the different characteristics of SMPs and SMAs is summarized in Table 1.

Table 1 A general comparison of SMAs and SMPs [7]

Characteristic	SMPs	SMAs
Density (g cm^{-3})	0.9–1.1	6–8
Processing conditions	<200 °C, low pressure	High temperature (>1000 °C) and high pressure required
Cost	<$10 per lb	≈$250 per lb
Biocompatibility and biodegradability	Can be biocompatible and/or biodegradable	Some are biocompatible (i.e., nitinol), not biodegradable
Stress generated during recovery (MPa)	1–3	150–300
Young's modulus at $T < T_{tran}$ (GPa)	0.01–3	83 (NiTi)
Young's modulus at $T > T_{tran}$ (GPa)	$(0.1–10) \times 10^{-3}$	28–41
Stress required for deformation (MPa)	1–3	50–200
Corrosion performance	Excellent	Excellent

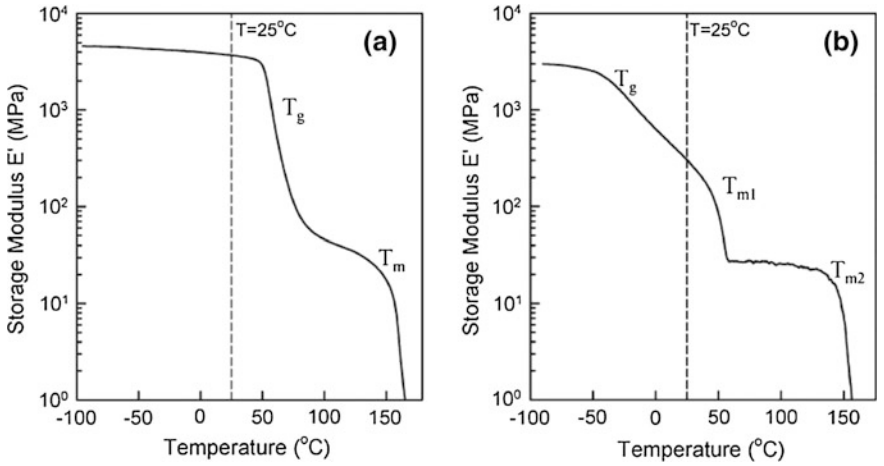

Fig. 2 Definition of two types of shape memory polymers with different shape fixing and shape recovery mechanisms depicted as a function of their dynamic mechanical behavior. **a** Physically crosslinked thermoplastics and **b** physically crosslinked block copolymers [7]

C. Liu et al. have categorized the SMPs into four broad categories based upon their differences in fixing mechanism and origin of "permanent" shape elasticity. Those categories are (1) chemically crosslinked glassy thermosets; (2) chemically crosslinked semicrystalline rubbers; (3) physically crosslinked thermoplastics; and (4) physically crosslinked block copolymers [7]. In this chapter, our focus is on the last two categories and Fig. 2 gives the definition of these two categories of shape memory polymers with different shape fixing and shape recovery mechanisms shown as a function of their mechanical behavior.

4 Physically CrossLinked Thermoplastics (or Physically CrossLinked Glassy Copolymers)

Thermosets are less attractive than thermoplastics in a sense that their processing is relatively difficult and is not repeatable as in case of thermoplastics. Same is the case with SMPs. Easy processing is considered to be an important issue for their further technological advancement. A list of physically crosslinked thermoplastic along with some important information is given in Table 2 [7].

The thermoplastic SMPs can be processed by conventional thermoplastic technology because of their rheological properties.

In physically crosslinked thermoplastic SMPs, rigid amorphous domains in thermoplastics can serve as physical crosslinks and can help to develop shape memory effect mainly in the form of phase-separated block copolymers.

Table 2 Physically crosslinked thermoplastic along with some important information

Materials	Hard segments	Soft segments	References
Aramid/PCL	Aramid	PCL or poly-THF	[8]
PVDF/PVAc blends	PVDF crystals	PVDF/PVAc amorphous regions	[9, 10]
PE-co-PMCP	Polyethylene	Poly (methylene-1,3-cyclopentane)	[11]
PET-co-PEO	PET crystals	PEO crystals	[12–14]
PS–TPB	Polystyrene	Polybutadiene	[15, 16]
Poly (ketone-co-alcohol)	Microcrystalline segments	Amorphous polyketone E-P/CO	[17]
PLAGC multiblock copolymer	PLLA crystalline domain	Copolymer amorphous	[18]
PCL-b-ODX	ODX(oligo (p-dioxanone) diol)	PCL	[19]
PA–PCL	Polyamide (nylon 6/6,6)	Polycaprolactone	[20]
PE-co-Nylon 6	Nylon 6	PE	[20, 21]
POSS–PN block copolymer	POSS domain	PN	[22, 23]
Poly(1-hexadecene)-co-PP	PP crystals	PHD crystals	[24]
POSS telechelic	POSS domain	PEG	[25, 26]
PLA/PVAc blends	PLA crystals	PLA/PVAc amorphous region	[27, 28]

A well-known example of physically crosslinked thermoplastics is a miscible blend of thermoplastic polyurethane and phenoxy resin. Here the soft segment of the polyurethane is polycaprolactone (PCL). A single glass transition (T_g > RT) is formed in this system which is dependent upon the ratio between the PCL segments and phenoxy resin [29].

The soft domain shows sharp and tunable glass transition temperatures in some block copolymers and polyurethanes which is good for shape memory behavior in these SMPs [29, 30].

Some semicrystalline homopolymers or melt-miscible polymer blends are also the members of this category that are compatible in the molten and amorphous states, but have at least one semicrystalline component [27]. In these, the crystals serve as hard domains and the composition-dependent T_g of the amorphous region act as the transition temperature. For these miscible blends, the glass transition temperature of the amorphous phase and the work output during shape recovery are strongly dependent upon blend composition.

Liu et al. have reported two miscible blend systems: poly(vinyl acetate) (PVAc) with poly(lactic acid) (PLA) and PVAc or PMMA with poly(vinylidene fluoride) (PVDF) [27, 31]. Their findings show that both the systems are melt miscible for all blend ratios, with the PVAc and PMMA being almost 100% amorphous. PLA and PVDF each show a semicrystalline nature with a degree of crystallinity of about

50%. The T_g of the amorphous phase serve as a transition temperature and can be tailored between the T_g values of the two homopolymers.

Alternate physical crosslinking techniques, i.e., hydrogen bonding or ionic clusters, can also help to set the network within the hard domains [32, 33]. Ionomers can show a strong behavior in setting a network and can give the elasticity values very similar to that of the chemically crosslinked materials [34]. But it is also a fact that pure ionomer-based shape memory polymers have not been reported so far. Another option is the hydrophilic oligomers which can be used to construct multiblock shape memory copolymers with better properties [7]. For these materials, moisture can also be used to activate shape recovery effect [34, 35]. It is also reported that the techniques like electrospinning can also be used to produce shape memory fibers mainly because of the easy processing nature of this class [36].

5 Physically CrossLinked Semicrystalline Block Copolymers as Shape Memory Polymers

There is another class of SMPs in which the soft domains of some block copolymers crystallize. In these SMPs, instead of their T_g values, their T_m values act as shape memory transformation temperatures. Multiblock polyurethane with PEO as soft domain is an example of this class [37]. The permanent shape of SMPs belonging to this class can be reprocessed by thermal processing techniques above 100 °C, when both the domains start flowing. A possible disadvantage of this class is the creep of the so-called hard microdomains under the applied stress during the temporary shape setting near their T_g which negatively affects the %age of recoverable strain in these materials [7].

Polyurethane-based SMPs have many technological advantages. Their room temperature stiffness, transformation temperatures and other shape memory properties are strongly dependent upon composition and easily controllable. Also they can easily form porous structures, i.e., foams. Conventionally, polyurethane-based SMPs are multiblock copolymers which consist of alternating oligomeric sequences of hard and soft domains. In these SMPs, the physical crosslinks are formed by the hard segments because of hydrogen bonding, polar interaction or crystallization. These crosslinks can withstand the high temperatures without being destroyed. The soft segment gives a thermally reversible phase, and the secondary shape is dependent upon the crystallization of these soft segments [7].

In these materials, the hard and soft domains show phase separation mainly due to the thermodynamic incompatibility of the two domains. By varying the soft domain component, using different diisocyanates, and diol or diamine as chain extender, various properties of these materials can be changed [38–40] as shown in Table 3.

Table 3 List of physically crosslinked polyurethane multiblock copolymers which exhibit shape memory effect

Chain extenders	Soft segments	Diisocyanate	References
1,4-BD	Poly(tetramethylene glycol) (PTMG)	MDI	[41]
BEBP or BHBP	PCL diol	MDI	[42]
1,4-BD	Poly(tetramethylene oxide) glycol (PTMO)	MDI	[43]
1,4-BD	PCL diol	MDI	[44, 45]
BD + DMPA	PCL diol, 2000, 4000, 8000 Da	MDI	[46]
DHBP	PCL diol, 4000 Da	HDI	[47]
1,6-HD	HDI–1,2-BD	4,4′-MDI	[48]
1,4-Butanediol	Poly(ethylene adipate), 300, 600, 1000 Da	MDI	[49]
4,4′-Dihydroxybiphenyl (DHBP)	PCL blend with phenoxy resin or PVC	Hexamethylene diisocyanate (HDI)	[29, 30]

6 Synthesis of Thermoplastic Shape Memory Polymers

Shape memory polymers (SMPs) can be synthesized by various conventional techniques including profile extrusion, fiber spinning and film casting. These techniques are briefly described as follows:

6.1 Profile Extrusion

Extrusion method is considered as one of the most conventional techniques to prepare SMPs. This process includes polymer blending with fillers using twin-screw extruder for certain time at certain temperature depending upon the melting point of the used polymer. The filler content can be varied to control the mechanical and thermal properties of the composites. After filler mixing, the samples are injection molded at fixed temperature for a certain time. The molded materials are cut to prepare samples for studying mechanical properties and shape memory effect. As an example, Yan et al. [50] introduced polylactide-based copolyester (PLAE) and its nanocomposites with glass temperature below body temperature for smart punctual plugs applications. PLAE was mixed melted with modified SiO_2 nanoparticles using Haake Rheomix 100 extruder. The samples were then injection molded at 160 °C employing pressure of 400 bar. The mold temperature was set at 50 °C, and the pressure was held for 30 s.

6.2 Fiber Spinning

In the last years, researchers paid great attention for electrospinning due to its ability to produce fibers in the range of 2 nm to several micrometers through applying electrical forces. Electrospinning is the most used method to prepare fibers with larger surface area than that formulated by conventional spinning procedures. This technique consists of spinneret, high voltage power supply and grounded collected plates. There are two standard sets of electrospinning which are horizontal and vertical sets. The SMP solution is charged and accelerated the opposite charged collector. Moreover, the electrical repulsive forces exceed the feeble surface tension of the polymer solution at certain DC voltage. Electrified jet is obtained and ejected from the Tylor cone tip, and the solvent is evaporated leaving SMPs nanofibers [51, 52]. For example, Alhazov et al. [53] prepared TPU nanofibers composed of clusters of hard segments connected by amorphous tie chains by dissolving TPU in DMF and THF. The TPU solution was electrospun with 0.9 mL/h flow rate and an electrostatic field of 1.2 kV/cm. The ambient temperature during electrospinning process was 21 °C, and in addition, the collector was placed at a distance of 12 cm from the needle spinneret and with a tangential velocity of 6 m/s.

6.3 Film Casting

SMPs can be fabricated utilizing solution method. This method is useful in dispersing the filler homogenously in the polymer gallery. In this process, the polymer is dissolved first in solvent at certain temperature. The filler particles are distributed in a solvent, and the composites are prepared by adding the filler suspension to the dissolved polymer solution. The composite can be prepared using different filler loadings on the final composite material. A continuous stirring at fixed temperature for certain time is ensured during the synthesis process. The mixture is then left to dry in a mold having appropriate dimensions at certain temperature. The produced composite samples are then cut or grind to obtain the samples of desired size and shapes. For instance, TPU films were fabricated by casting the TPU solution onto a 40×40 mm^2 Teflon mold with 2 mm depth [53]. Then, the films were completely dried in air overnight. The produced films were removed from the Teflon mold and then left to dry in vacuum for 2 h.

Furthermore, Saralegi [54] synthesized TPU bionanocomposites by in situ polymerization with various cellulose nanocrystals (CNCs) in THF medium. This sort of bionanocomposites introduces a good candidate for shape memory applications. The freeze-dried CNCs were re-dispersed in THF solution to avoid CNCs agglomerates. The pre-polymer was produced by reacting HDI with CO_2 in the presence of dispersed CNCs in THF at 100 °C for 6 h. Finally, 1,3-propanediol was added and the mixture was stirred at 100 °C for 2 h before curing and casting on a Teflon mold. The mixture was then left to dry at 60 °C for 48 h under vacuum to attain thin films.

7 Recent Advancements in Thermoplastic SMPs and Composites

7.1 Thermoplastic SMPs

Among physically crosslinked block copolymer-based SMPs, thermoplastic segmented polyurethanes are well known for their shape memory effect and other interesting properties [43–46]. Conventionally, polyurethanes are phase-separated multiblock copolymers which contain two types of regions, i.e., hard and soft segments. X. Gu et al. have used a slightly different approach and reported a family of hard block-free multiblock thermoplastic polyurethane (TPU)-based SMPs consisting of poly(å-caprolactone) (PCL) and poly(ethylene glycol) (PEG). They achieved high degrees of molecular chain entanglements mainly because of higher molecular weight. They claimed that the molecular chain entanglements play the role of physical crosslinks in this system which is different than the conventional physically crosslinked SMPs. This entanglement slows the stress relaxation and suspends the flow above the melting temperatures of the soft blocks. This allows the sufficient elastic deformation for shape fixing purpose. The authors claimed large recoverable strains and fast actuation in this material which make these SMPs attractive for applications especially in the field of medical devices [55].

P.T. Mather and coscientists have reported many research reports describing a series of advanced and novel multiblock polyurethane copolymers for various shape memory applications. They used POSS hybrid monomer as hard domains and various polyols, (amorphous or semicrystalline), as soft domains. According to them, these materials may also be modified to be biocompatible and biodegradable [26, 40, 56–58].

Biodegradable and biocompatible polyurethane-based SMPs have attracted significant research interest in the recent years especially due to their potential applications in biomedical field [59–62]. Y. Wangat et al. have reported a novel poly(urethane-urea) shape memory polymer (PUU SMP) which was synthesized from poly(D,L-lactic acid) (PDLLA) diols, hexamethylene diisocyanate (HDI) and butanediamine (BDA). They claimed that the response temperature for shape memory of PDLLA–PUU SMP is mainly dependent on the glass transition temperature. According to their research, this polymer exhibits an excellent shape memory behavior, i.e., an approximately 100% ratio of the shape memory fixation and 98% ratio of the shape memory recovery. They also claimed the biocompatible and biodegradable nature of the same material with a T_g which is very near to the human body temperature [63].

The most common type of SMP developed mainly for biomedical applications is thermoplastic polyurethane (TPU) [64, 65]. Many research groups have reported that the mechanical and shape memory properties of TPUs can be improved by modifying the chemistry of the polymer. For example, the use of ethylene diamine chain extenders and ionomers plays an important role in improving the strength and modulus in TPUs [66, 67]. Some other chemical modifications of TPUs include the

modification of the hard and soft domains, crosslinking and usage of SBS, PCL, PLA and PLLA components [68–73]. Mixing of polylactic acid (PLA) with TPU is a very effective way to improve its mechanical properties without changing its chemistry [74]. Addition of PLA is reported to increase the shape memory properties, tensile strength and toughness of TPU [75–78].

J.J. Song et al. have recently developed biocompatible TPU-/PLA-based SMP blends and claimed to achieve significantly higher actuation forces as compared to that of existing materials. They also reported that the shape fixity ratio increases with increasing PLA composition and programming temperature and the shape recovery ratio remains independent of the programming temperature. They also observed that the T_{trans} of the TPU/PLA blends increases with increasing programming temperature, and its range becomes wider with the increasing TPU content. The optimum values were found in case of 80/20 and 65/35 TPU/PLA blends which were programmed at 70 °C for generating the highest recovery force. According to their claim the above-mentioned TPU/PLA SMP blend actuators can be further developed for a number of biomedical applications such as artificial muscles [78].

L. Xue et al. have reported the design and synthesis of PCTBVs block copolymers which contain hyper-branched three-arm PCL as soft segment (switch) and microbial polyester PHBV as crystallizable hard segment and claimed a significant increase in yield. The two segments were developed for the first time for the development of a biodegradable SMP with improved performance mainly for biomedical applications. The developed PCTBVs showed desired thermal properties with a T_m of 39–40 °C of the soft segment suitable for thermal switching at body temperature and a T_m of 142 °C of the hard segment suitable for the stabilization of permanent. The developed PCTBVs exhibited ductile nature, and their mechanical properties were adjustable by changing the block ratio. According to their research results, the hyper-branched PCL segment proved to be much better as compared to the linear PCL-based segment which ultimately increased the value of R_f. Similarly the use of novel microbial polyester PHBV hard segment significantly improved the value of R_r. On the basis of the results of this research effort, the authors claimed to successfully develop a biodegradable and non-cytotoxic block copolymer (PCTBV-25) SMP with a capability of thermal switching at body temperature which could be useful as fast self-expandable stent or stent cover [79].

7.2 *Thermoplastic Shape Memory Composites and Blends*

Park et al. [80] investigated the influence of graphene content on the performance of thermoplastic shape memory polyurethane (SPU) using different composite fabrication procedures. They realized that the graphene loading controls the shape recovery, IR absorption, electrical conductivity and the compatibility of SPU blends. In addition, it was observed that SPU synthesized by aromatic 4,4′-diphenylmethane diisocyanate (MSPU) exhibits better compatibility than SPU synthesized with

hexamethylene diisocyanate (HSPU). This behavior may be attributed to the aromatic nature of MSPU structures. The homogenous dispersion of graphene particles improved the crystallization and shape recovery of MSPU composites while that were diminished in case of HSPU blends. Owing to the higher conductivity of graphene/MSPU blends, the shape recovery by resistive heating of this sort of composites was better than that of graphene/HSPU blends. The modification of graphene with methanol develops the conductivity, resistive heating efficiency and compatibility of the as-prepared blends. The graphene segments disturbed the hydrogen bonds between the hard segments and the dense filling of SPU blends. At high graphene loadings, this behavior offset the reinforcing influence of graphene. Moreover, the IR absorption bands of modified graphene with methanol were developed and modified graphene was more operative than pristine graphene for shape recovery performance activated by IR heating. PVA/SWCNTs composite fibers show improved mechanical energy to rupture the fiber composite at 20 wt% of SWCNTs [81]. These composites were fabricated by mixing surfactant-stabilized SWCNTs with PVA solution to produce composite fibers with high toughness. The shape recovery of the prepared composites was higher than that of the conventional polymers. It was also observed that high stresses were required to deform the fibers at low deformation temperature (T_d). At higher T_d, the fibers became softer and can be deformed easily. The prepared fibers show good shape fixity ratios and recovered to its original shape after heating. The maximum stress generated by theses fibers was approximately 150 MPa which is close to the stress generated by shape memory metallic alloys (0.5 $\pm$ 0.25 GPa) [82–85]. High surge in the temperature more than 100 K was needed to attain moderate shape recovery standards around 50%, but the broad T_g of this composite was a disadvantage for the shape recovery performance. Poly(rac-lactide)/β-tricalcium phosphate (PDLLA/β-TCP) nanocomposites are desirable biostructures for tissue engineering applications [86]. This sort of composites can be synthesized by dissolving PDLLA in $CHCl_2$ and mixed with β–TCP solution in ethanol then evaporating the solvent to obtain some floccules of PDLLA/β-TCP nanocomposites at the bottom of the beaker. Then, the floccules were dried at 30 °C under vacuum and press-molded at 105 °C. The shape memory effect of pure PDLLA and PDLLA/β-TCP nanocomposites with different β-TCP concentrations was studied using the bending test before and after immersing in buffer saline solution with pH of 7.4 at 37 °C. Dramatic change in the shape memory performance was noticed between the pure PDLLA and PDLLA/β-TCP nanocomposites. It was found that the shape recovery ratio of PDLLA/β-TCP nanocomposites was higher than that of pure PDLLA at the same degradation time. This may be related to the change in the crystal phases of β-TCP and also the chains fission in PDLLA matrix during the degradation procedure. Due to the plasticizer effect, the T_g was declined owing to new inorganic phases formation [87, 88]. The rise in the shape recovery ratio can be contributed to the presence of $Ca_2P_2O_7$ and $CaHPO_4$ species after 21-day degradation. These species produce dynamical constrains to the LLDPA galleries [89]. Furthermore, the shape memory characteristics of PDLLA/β-TCP nanocomposites became undesirable with increasing the degradation time because of the

dissolution degradation of the inorganic phases of the PDLLA/β-TCP nanocomposites as well as the polymer chains fission. Polyvinylidene fluoride (PVDF)/acrylic copolymer (ACP) blends with measured composition ratios and crystallization conditions show excellent shape memory characteristics which addressed by You et al. [90]. In addition, You et al. [91] studied the impact of cold crystallization temperature on the shape memory performance and the crystal structure for 50:50 PVDF/ACP blend. They noted that the quenched sample has amorphous structure with low glass temperature. The glass temperature of this blend was enhanced due to inducing the crystallization of PVDF from the miscible amorphous PVDF/ACP phase after annealing at temperature higher than T_g. Furthermore, low annealing temperature leads to formation of tiny crystals while large PVDF spherulites were produced after high annealing temperature. It is noteworthy to mention that PVDF/ACP blends with tiny crystals exhibit unique characteristics such as good recovery ratios and excellent shape fixity.

8 Applications of Thermoplastic SMPs

It is desirable to design and synthesize materials for various advanced engineering and other applications. Shape memory alloys are used in many technical applications such as actuators, sensors and transducers. However, they show clear drawbacks such as limited recoverable deformation as well as high cost and toxicity. The shape memory effect in polymers is temperature sensitive, representing desired requirements for practical uses in different fields. This is so because different polymers exhibit different glass temperatures and melting temperatures [92]. In the last decades, many applications were developed because of the unique characteristics of thermoplastic shape memory polymers. Some important applications of these polymers are represented in more detail in this section.

8.1 Thermoplastic Polyurethanes (TPUs)

In case of SMPs, the SME can be utilized on surfaces in the form of polymer films/coatings as well as in bulk form where the SMP is able to change its overall bulk shape. SMPs have a significant number of identified and unidentified industrial applications, biomedical applications as well as applications in aerospace [93]. SMPs have some distinct advantages over other types of shape memory materials such as shape memory alloys (SMA) and shape memory ceramics. They possess low density, low cost, high elastic deformation, simpler manufacturing routes, tunable transition temperature, and their potential biocompatible and biodegradable properties [2].

It is noteworthy to mention that TPUs are utilized in a wide range of industries owing to their excellent biocompatibility and physical characteristics. Their range

of applications includes rollers systems, biomedical products and automobiles [94]. Because of light weight, low cost, high tunable morphology and good strain recovery properties, PUs are considered as smart materials [95, 96]. Nanofillers have been incorporated to PU-based shape memory systems to enhance the properties of TPUs [97]. For instance, CNTs were incorporated to improve electrical conductivity and to prepare electrically actuated shape memory PU/CNT composites [98]. PU/CNT shape memory systems are suitable for many applications ranging from frozen food packaging to medical instruments.

The discovery of thermoplastic shape memory polyurethane was a major breakthrough in the development of thermoplastic-based SMPs. Many commercial applications were identified for these materials instantly, i.e., as safety tag or as self-deploying chair [99, 100].

SMPs have very attractive set of properties for biomedical applications mainly due to their excellent biocompatibility and biodegradability [7, 101]. Despite the fact that SMPs are attractive for a number of biomedical applications, due to their low recovery force they have not been considered as viable candidates for actuators type of applications [2]. Some of the advanced biomedical applications of SMPs which have already been reported in the literature are blood clot removal devices, biodegradable self-tightening sutures, expandable catheters, biodegradable surgical staples and self-expanding foams in cardiovascular stents [102–107].

Thermoplastic polyurethane (TPU) is a very well-known SMP mainly because of its suitable nature for biomedical applications [108, 109]. Ahmad et al. have developed PU-based SMP for pressure bandage applications which is capable of generating the required recovery stresses within a range of 0.0026–0.006 MPa [110].

Biodegradable SMP-based implants offer an attractive set of multifunctions, such as shape memory effect at body temperature to initiate the shape change after the placement of implant into the human body for minimally invasive surgery, and biodegradability which saves patients especially the older ones from a second round of surgery for implant removal [111].

8.2 Poly(ε-Caprolactone) (PCL)

Poly(ε-caprolactone) (PCL) is widely used in medicine as it is a biodegradable, bioresorbable and biocompatible aliphatic polyester which is non-toxic for living creatures. Moreover, PCL is utilized in the manufacture of containers for sustained drug release, artificial bones and artificial skin owing to its excellent permeability and biodegradability [112, 113]. PCL decomposes by enzymatic reactions in physiological conditions inside the human body as it has low melting point (60 °C). Because of its salient advantages, PCL is incorporated into segmented polyurethane to modify the shape memory property. Radiotherapy patient immobilization, orthopedic splinting, prosthetic socket cone production and reconstructive surgery splinting utilize low-temperature polyurethanes with PCL-based soft segments

(PCL/TPU) [114, 115]. At the same time, there is large waste produced from orthopedics splints using PCL/TPU which is disposed of to landfill [116].

8.3 Nylon 12

The growth in the usage of thermoplastic elastomers (TPEs) is developed every year as it can be recycled easily after being used. Nylon 12 is one of the most common polymers designed for TPEs production. Because of the unique properties of nylon 12 such as high chemical and abrasion resistances as well as high toughness, it is widely utilized in many applications such as manufacture of electronic equipment, machinery, information industries and automobiles [116]. As aforesaid, TPEs with a thermally triggered shape memory effect were fabricated by Choi et al. [117]. They mixed semicrystalline maleated polyolefin elastomer (mPOE) with nylon 12 at 200 °C. The unique characteristic associated with this sort of TPEs is used for sports shields, toys and ergonomic grips.

9 Conclusion

Thermoplastic shape memory polymers and their variations, i.e., composites, represent an important class of advanced shape memory materials. A significant demand of these materials is expected to arise in future for various engineering and biomedical applications which require a thorough understanding and in-depth knowledge of shape memory mechanisms in these materials and the controlling factors which mainly control the required properties of these materials. This chapter gives an overview of the thermoplastic shape memory polymers, and readers are referred to the original research papers enlisted in reference list for an in-depth view.

References

1. Ratna D, Karger-Kocsis J (2008) Recent advances in shape memory polymers and composites: a review. J Mater Sci 43:254–269
2. Xie T (2011) Recent advances in polymer shape memory. Polymer 52:4985–5000
3. Lendlein A, Langer R (2002) Biodegradable, elastic shape-memory polymers for potential biomedical applications. Science 296:1673–1676
4. Lendlein A, Kelch S (2002) Shape-memory polymers. Angew Chem Int Ed 41:2034–2057
5. Hu J, Zhu Y, Huang H, Lu J (2012) Recent advances in shape–memory polymers: structure, mechanism, functionality, modeling and applications. Prog Polym Sci 37:1720–1763
6. Song JJ, Chang HH, Naguib HE (2015) Design and characterization of biocompatible shape memory polymer (SMP) blend foams with a dynamic porous structure. Polymer 56:82–92

7. Liu C, Qin H, Mather PT (2007) Review of progress in shape-memory polymers. J Mater Chem 17:1543–1558
8. Kraft A, Rabani G (2004) Thermally induced shape-memory effect in segmented copolymers containing polycaprolactone soft segments and aramid hard segments. Polym Mater Sci Eng 90:41–42
9. Campo CJ, Mather PT (2005) PVDF: PMMA shape memory blends: effect of short carbon fiber addition. Polym Mater Sci Eng 93:933
10. Mather PT, Liu C (2004) Shape memory blends. US Patent 20040122174 A1
11. Jeong HM, Song JH, Chi KW, Kim I, Kim KT (2002) Shape memory effect of poly (methylene-1, 3-cyclopentane) and its copolymer with polyethylene. Polym Int 51(4):275–280
12. Luo X, Zhang X, Wang M, Ma D, Xu M, Li F (1997) Thermally stimulated shape-memory behavior of ethylene oxide-ethylene terephthalate segmented copolymer. J Appl Polym Sci 64(12):2433–2440
13. Wang M, Luo X, Ma D (1998) Dynamic mechanical behavior in the ethylene terephthalate-ethylene oxide copolymer with long soft segment as a shape memory material. Eur Polymer J 34(1):1–5
14. Wang M, Zhang L (1999) Recovery as a measure of oriented crystalline structure in poly (ether ester) s based on poly (ethylene oxide) and poly (ethylene terephthalate) used as shape memory polymers. J Polym Sci, Part B: Polym Phys 37(2):101–112
15. Kitahara SN, Nigata N (1991) 'Novel crosslinked polymer having shape memorizing property, method of its use, and molded article having shape memory', US Patent US 5043396 A
16. Ikematsu TK, Kishimoto Y, Miyamoto K (1990) Shape memory polymer resin, resin composition and shape-memorizing molded product therefrom. Eur. Pat., EP 374961 A2
17. Perez-Foullerat D, Hild S, Muecke A, Rieger B (2004) Synthesis and properties of poly (ketone-co-alcohol) materials: shape memory thermoplastic elastomers by control of the glass transition process. Macromol Chem Phys 205(3):374–382
18. Min C, Cui W, Bei J, Wang S (2005) Biodegradable shape-memory polymer—polylactide-co-poly (glycolide-co-caprolactone) multiblock copolymer. Polym Adv Technol 16(8):608–615
19. Langer RS, Lendlein A (2003) Biodegradable shape memory polymeric sutures. World Pat., WO 2003088818 A2
20. Lee HY, Jeong HM, Lee JS, Kim BK (2000) Study on the shape memory polyamides. Synthesis and thermomechanical properties of polycaprolactone-polyamide block copolymer. Polym J 32(1):23–28
21. Li F, Chen Y, Zhu W, Zhang X, Xu M (1998) Shape memory effect of polyethylene/nylon 6 graft copolymers. Polymer 39(26):6929–6934
22. Jeon HG, Mather PT, Haddad TS (2000) Shape memory and nanostructure in poly (norbornyl-POSS) copolymers. Polym Int 49(5):453–457
23. Mather PT, Jeon HG, Haddad TS (2000) Strain recovery in POSS hybrid thermoplastic. Polym Prepr Am Chem Soc Div Polym Chem 41:528–529
24. Jeong HM, Lee SH, Cho KJ, Jeong YT, Kang KK, Oh JK (2002) Thermal and mechanical properties of the polymers synthesized by the sequential polymerization of propylene and 1-hexadecene. J Appl Polym Sci 84(9):1709–1715
25. Mather PT, Kim BS, Ge Q, Liu C (2004) Synthesis of nonionic telechelic polymers incorporating polyhedral oligosilsesquioxane and uses thereof. US. Pat. 2004024098
26. Mather PT, Kim BS, Ge Q, Liu C (2004) Preparation and uses of nonionic telechelic polymers incorporating polyhedral oligosilsesquioxane (POSS). World Pat. 2004011525
27. Liu C, Mather PT (2003) Proceedings of the annual technical conference—society of plastics engineers, 61st (Vol. 2), Society of Plastics Engineers, Brookfield, CT, USA, 1962–1966
28. Mather PT, Liu C (2004) Shape memory blends. US Pat., 20040122174 A1
29. Jeong HM, Ahn BK, Kim BK (2001) Miscibility and shape memory effect of thermoplastic polyurethane blends with phenoxy resin. Eur Polymer J 37(11):2245–2252

30. Jeong HM, Song JH, Lee SY, Kim BK (2001) Miscibility and shape memory property of poly (vinyl chloride)/thermoplastic polyurethane blends. J Mater Sci 36(22):5457–5463
31. Rousseau IA (2008) Challenges of shape memory polymers: a review of the progress toward overcoming SMP's limitations. Polym Eng Sci 48(11):2075–2089
32. Kim BK, Lee SY, Lee JS, Baek SH, Choi YJ, Lee JO, Xu M (1998) Polyurethane ionomers having shape memory effects. Polymer 39(13):2803–2808
33. Li F, Chen Y, Zhu W, Zhang X, Xu M (1998) Shape memory effect of polyethylene/nylon 6 graft copolymers. Polymer 39(26):6929–6934
34. Weiss RAF, Fitzgerald JJ, Kim D (1991) Viscoelastic behavior of lightly sulfonated polystyrene ionomers. Macromolecules 24(5):1071–1076
35. Yang B, Huang WM, Li C, Li L (2006) Effects of moisture on the thermomechanical properties of a polyurethane shape memory. Polymer 47:1348–1356
36. Cha DI, Kim HY, Lee KH, Jung YC, Cho JW, Chun BC (2005) Electrospun nonwovens of shape-memory polyurethane block copolymers. J Appl Polym Sci 96:460–465
37. Korley LTJ, Pate BD, Thomas EL, Hammond PT (2006) Effect of the degree of soft and hard segment ordering on the morphology and mechanical behavior of semicrystalline segmented polyurethanes. Polymer 47:3073
38. Christenson EM, Anderson JM, Hiltner A, Baer E (2005) Relationship between nanoscale deformation processes and elastic behavior of polyurethane elastomers. Polymer 46:11744–11754
39. Park JS, Chung YC, Do Lee S, Cho JW, Chun BC (2008) Shape memory effects of polyurethane block copolymers cross-linked by celite. Fibers Polym 9(6):661–666
40. He Y, Xie D, Zhang X (2014) The structure, microphase-separated morphology, and property of polyurethanes and polyureas. J Mater Sci 49(21):7339–7352
41. Lee BSC, Chun BC, Chung YC, Sul KI, Cho JW (2001) Structure and thermomechanical properties of polyurethane block copolymers with shape memory effect. Macromolecules 34(18):6431–6437
42. Jeong HM, Lee JB, Lee SY, Kim BK (2000) Shape memory polyurethane containing mesogenic moiety. J Mater Sci 35:279–283
43. Lin JR, Chen LW (1998) Study on shape-memory behavior of polyether-based polyurethanes. II. Influence of soft-segment molecular weight. J Appl Polym Sci 69:1575–1586
44. Li F, Qi L, Yang J, Xu M, Luo X, Ma D (2000) Polyurethane/conducting carbon black composites: structure, electric conductivity, strain recovery behavior, and their relationships. J Appl Polym Sci 75:68–77
45. Li F, Hou J, Zhu W, Zhang X, Xu M, Luo X, Ma D, Kim BK (1996) Crystallinity and morphology of segmented polyurethanes with different soft-segment length. J Appl Polym Sci 62:631–638
46. Kim BK, Lee SY, Lee JS, Baek SH, Choi YJ, Lee JO, Xu M (1998) Polyurethane ionomers having shape memory effects. Polymer 39:2803–2808
47. Jeong HM, Kim BK, Choi YJ (1999) Synthesis and properties of thermotropic liquid crystalline polyurethane elastomers. Polymer 41:1849–1855
48. Kim BKS, Young J, Seong C, Jeong M, Han M (2000) Shape-memory behavior of segmented polyurethanes with an amorphous reversible phase: The effect of block length and content. J Polym Sci Part B Polym Phys 38:2652–2657
49. Takahashi T, Hayashi N, Hayashi S (1996) Structure and properties of shape-memory polyurethane block copolymers. J Appl Polym Sci 60(7):1061–1069
50. Yan B, Gu S, Zhang Y (2013) Polylactide-based thermoplastic shape memory polymer nanocomposites. Eur Polymer J 49(2):366–378
51. Taylor GI (1969) Electrically driven jets. Proc R Soc Lond A Math Phys Sci 313:453–475
52. Adomaviciute E, Rimvydas M (2007) The influence of applied voltage on poly (vinyl alcohol) (PVA) nanofibre diameter. Fibers Text East Eur 15:64–65
53. Alhazov D, Gradys A, Sajkiewicz P, Arinstein A, Zussman E (2013) Thermo-mechanical behavior of electrospun thermoplastic polyurethane nanofibers. Eur Polymer J 49:3851–3856

54. Saralegi A, Gonzalez ML, Valea A, Eceiza A, Corcuera MA (2014) The role of cellulose nanocrystals in the improvement of castor oil based segmented thermoplastic polyurethane shape-memory properties. Compos Sci Technol 92:27–33
55. Gu X, Mather PT (2012) Entanglement-based shape memory polyurethanes: synthesis and characterization. Polymer 53:5924–5934
56. Wu J, Ge Q, Burke KA, Mather PT (2005) Crystallization of POSS in a PEG-based multiblock polyurethane architecture: toward a hybrid hydrogel. Mater Res Soc Proc 847 EE10.2-6
57. Mather PT, Qin H, Wu J, Bobiak J (2006) 'POSS-based polyurethanes: from degradable polymers to hydrogels', Medical Polymers 2006, International Conference Focusing on Polymers used in the Medical Industry, 5th, Cologne, Germany, RAPRA, Shrewsbury, UK, 2006, 5/1–5/9
58. Qin H, Mather PT (2009) Combined one-way and two-way shape memory in a glass-forming nematic network. Macromolecules 41:273–280
59. Lendlein A, Langer R (2002) Biodegradable, elastic shape-memory polymers for potential biomedical applications. Science 296:1673–1676
60. Alteheld A, Feng Y, Kelch S, Lendlein A (2005) Biodegradable, amorphous copolyester-urethane networks having shape-memory properties. Angew Chem Int Ed 44:1188–1192
61. Wang WS, Ping P, Chen XS, Jing XB (2006) Polylactide-based polyurethane and its shape-memory behavior. Eur Polym J 142:1240–1249
62. Meng QH, Hu JL, Zhu Y, Lu J, Liu Y (2007) Polycaprolactone-based shape memory segmented polyurethane fiber. J Appl Polym Sci 106:2515–2523
63. Wang Y, Li Y, Luo Y, Huang M, Liang Z (2009) Synthesis and characterization of a novel biodegradable thermoplastic shape memory polymer. Mater Lett 63(3):347–349
64. Yakacki CM, Shandas R, Lanning C, Rech B, Eckstein A, Gall K (2007) Unconstrained recovery characterization of shape-memory polymer networks for cardiovascular applications. Biomaterials 28(14):2255–2263
65. Lendlein A, Behl M, Hiebl B, Wischke C (2010) Shape-memory polymers as a technology platform for biomedical applications. Expert Rev Med Devices 7(3):357–379
66. Chun BC, Cho TK, Chung YC (2006) Enhanced mechanical and shape memory properties of polyurethane block copolymers chain-extended by ethylene diamine. Eur Polym J 42:3367–3373
67. Gurunathan T, Chepuri RKR, Narayan R, Raju KVSN (2013) Polyurethane conductive blends and composites: synthesis and applications perspective. J Mater Sci 48(1):67–80
68. Zhang H, Wang H, Zhong W, Du Q (2009) A novel type of shape memory polymer blend and the shape memory mechanism. Polymer 50(6):1596–1601
69. Ajili SH, Ebrahimi NG, Soleimani M (2009) Polyurethane/polycaprolactane blend with shape memory effect as a proposed material for cardiovascular implants. Acta Biomater 5 (5):1519–1530
70. Peponi L, Navarro-Baena I, Sonseca A, Gimenez E, Marcos-Fernandez A, Kenny JM (2013) Synthesis and characterization of PCL–PLLA polyurethane with shape memory behavior. Eur Polym J 49(4):893–903
71. Wang W, Ping P, Chen X, Jing X (2006) Polylactide-based polyurethane and its shapememory behavior. Eur Polym J. 42:1240–1249
72. Lee SH, Kim JW, Kim BK (2004) Shape memory polyurethanes having crosslinks in soft and hard segments. Smart Mater Struct 13:1345–1350
73. Yang JH, Chun BC, Chung YC, Cho JH (2003) Comparison of thermal mechanical properties and shape memory effect of polyurethane block copolymers with planar or bent shape of hard segment. Polymer 44:3251–3258
74. Juikham S (2011) Design and characterization of novel blends of poly(lactic acid). Ph.D. dissertation. Birmingham, England: Department of Chemical Engineering and Applied Chemistry, Aston University

75. Song J, Srivastava I, Kowalski J, Naguib HE (2014) Fabrication and characterization of a foamed polylactic acid (PLA)/thermoplastic polyurethane (TPU) shape memory polymer (SMP) blend for biomedical and clinical applications. Paper No. 9058-11. SPIE Smart Structures/NDE 2014, San Diego, CA, USA
76. Feng F, Ye L (2010) Morphologies and mechanical properties of polylactide/ thermoplastic polyurethane elastomer blends. J Appl Polym Sci 119:2778–2783
77. Lai SM, Lan YC (2013) Shape memory properties of melt-blended polylactic acid (PLA)/ thermoplastic polyurethane (TPU) bio-based blends. J Polym Res 20(5):1–8
78. Song JJ, Chang HH, Naguib HE (2015) Biocompatible shape memory polymer actuators with high force capabilities. Eur Polym J 67:186–198
79. Xue L, Dai S, Li Z (2010) Biodegradable shape-memory block co-polymers for fast self-expandable stents. Biomaterials 31(32):8132–8140
80. Park JH, Dao TD, Lee H, Jeong HM, Kim BK (2014) Properties of graphene/shape memory thermoplastic polyurethane composites actuating by various methods. Materials 7(3):1520–1538
81. Miaudet P, Derre A, Maugey M, Zakri C, Piccione PM, Inoubli R, Poulin P (2007) Shape and temperature memory of nanocomposites with broadened glass transition. Science 318 (5854):1294–1296
82. Humbeeck JV (2001) Shape memory alloys: a material and a technology. Adv Eng Mater 3 (11):837–850
83. Kornbluh RD, Pelrine R, Pei Q, Heydt R, Stanford S, Oh S, Eckerle J (2002) Electroelastomers: applications of dielectric elastomer transducers for actuation, generation, and smart structures. In SPIE's 9th annual international symposium on smart structures and materials international society for optics and photonics, pp 254–270
84. Patoor E, Lagoudas DC, Entchev PB, Brinson LC, Gao X (2006) Shape memory alloys, part I: general properties and modeling of single crystals. Mech Mater 38(5):391–429
85. Lagoudas DC, Entchev PB, Popov P, Patoor E, Brinson LC, Gao X (2006) Shape memory alloys, Part II: modeling of polycrystals. Mech Mater 38(5):430–462
86. Hench LL, Polak JM (2002) Third-generation biomedical materials. Science 295(5557):1014–1017
87. Choi D, Kumta PN (2007) Mechano-chemical synthesis and characterization of nanostructured β-TCP powder. Mater Sci Eng C 27(3):377–381
88. Yang B, Huang WM, Li C, Chor JH (2005) Effects of moisture on the glass transition temperature of polyurethane shape memory polymer filled with nano-carbon powder. Eur Polym J 41(5):1123–1128
89. Prokop A, Jubel A, Hahn U (2005) A comparative radiological assessment of polylactide pins over 3 years in vivo. Biomaterials 26(19):4129–4138
90. You J, Dong W, Zhao L, Cao X, Qiu J, Sheng W, Li Y (2012) Crystal orientation behavior and shape-memory performance of poly (vinylidene fluoride)/acrylic copolymer blends. J Phys Chem B 116(4):1256–1264
91. You J, Fu H, Dong W, Zhao L, Cao X, Li Y (2012) Shape memory performance of thermoplastic polyvinylidene fluoride/acrylic copolymer blends physically cross-linked by tiny crystals. ACS Appl Mater Interfaces 4(9):4825–4831
92. Tobushi H, Shimada D, Hayashi S, Endo M (2003) Shape fixity and shape recovery of polyurethane shape-memory polymer foams. Proc I MECH E Part L J Mater Des Appl 217(2):135–143
93. Hagera MD, Bodea S, Webera C, Schubert US (2015) Shape memory polymers: past, present and future developments. Prog Polym Sci 49:3–33
94. Petrovic´ ZS, Ferguson J (1991) Polyurethane elastomers. Prog Polym Sci 16(5):695–836
95. Kim BK, Lee SY, Xu M (1996) Polyurethane having shape memory effects. Polymer 37:5781–5793
96. Huang WM, Yang B, Zhao Y, Ding Z (2010) Thermo-moisture responsive polyurethane shape-memory polymer and composites: a review. J Mater Chem 20(17):3367–3381

97. Razzaq MY, Anhalt M, Frormann L, Weidenfeller B (2007) Thermal, electrical and magnetic studies of magnetite filled polyurethane shape memory polymers. Mater Sci Eng A 444(1):227–235
98. Sahoo NG, Jung YC, Yoo HJ, Cho JW (2007) Influence of carbon nanotubes and polypyrrole on the thermal, mechanical and electroactive shape-memory properties of polyurethane nanocomposites. Compos Sci Technol 67(9):1920–1929
99. Anonymous TPU Newsletter March 2012. www.bayer-materialscience.com, 2012
100. Marcus Fairs Memories of the future by Carl de Smet. www.dezeen.com/2012/10/25/noumenon-by-carl-de-smet/, 2012
101. Behl M, Razzaq MY, Lendlein A (2010) Multifunctional shape-memory polymers. Adv Mater 22(31):3388–3410
102. Behl M, Lendlein A (2007) Shape-memory polymers. Mater Today 10(4):20–28
103. Small W IV, Singhal P, Wilson TS, Maitland DJ (2010) Biomedical applications of thermally activated shape memory polymers. J Mater Chem 20(17):3356–3366
104. Lendlein A, Behl M, Hiebl B, Wischke C (2010) Shape-memory polymers as a technology platform for biomedical applications. Expert Rev Med Devices 7(3):357–379
105. Lendlein A, Langer R (2002) Biodegradable, elastic shape-memory polymers for potential biomedical applications. Science 296(5573):1673–1676
106. Mather PT, Luo X, Rousseau IA (2009) Shape memory polymer research. Annu Rev Mater Res 39:445–471
107. Small W IV, Buckley PR, Maitland DJ (2007) Shape memory polymer stent with expandable foam: a new concept for endovascular embolization of fusiform aneurysms. IEEE Trans Biomed Eng 54(6):1157–1160
108. Chang LC, Read TA (1951) Plastic deformation and diffusion less phase changes in metals-the gold-cadmium beta-phase. Trans Am Inst Min Metall Eng 191(1):47–52
109. Buehler WJ, Gilfrich JV, Wiley RC (1963) Effect of low-temperature phase changes on the mechanical properties of alloys near composition TiNi. J Appl Phys 34(5):1475–1477
110. Ahmad M, Luo J, Miraftab M (2012) Feasibility study of polyurethane shape-memory polymer actuators for pressure bandage application Sci Technol. Adv Mater 13:1–7
111. Yoshida M, Langer R, Lendlein A, Lahann J (2006) From advanced biomedical coatings to multi-functionalized biomaterials. J Macromol Sci part C Polym Rev 46(4):347–375
112. Temtema M, Casimiro T, Manob J F, Ricardo A A (2007) Preparation of membranes with polysulfone/ polycaprolactone blends using a high pressure cell specially designed for a CO_2-assisted phase inversion. J Supercrit Fluids 43:542–548
113. Rhee SH (2004) Bone-like apatite-forming ability and mechanical properties of poly (ε-caprolactone)/silica hybrid as a function of poly(ε-caprolactone) content. Biomaterials 25(7–8):1167–1175
114. United States Patent 4784123. Orthopedic/Orthotic Splint Materials, 1988
115. United States Patent 6595937. Bent Splint and Method of Manufacturing the Same, 2003
116. Jankauskaitė V, Macijauskas G, Lygaitis R (2008) Polyethylene terephthalate waste recycling and application possibilities: a review. Mater Sci (Medžiagotyra) 14(2):119–127
117. Choi MC, Jung J Y, Chang YW (2014) Shape memory thermoplastic elastomer from maleated polyolefin elastomer and nylon 12 blends, Polym Bull 71:625–635

Shape Memory Materials from Epoxy Matrix Composites

Loredana Santo and Fabrizio Quadrini

Abstract Recent advances in shape memory materials from epoxy matrix composites are discussed. Shape memory polymers and their composites (SMPs and SMPCs) belong to a new class of smart materials which can have interesting applications as expandable/deployable structures and light actuators. In particular, SMPCs have typical properties of composites and in addition shape memory properties. SMP matrices or the integration of parts made of SMPs can give such functionality to the composite materials and structures. In the case of integration, SMPC laminate or sandwich can be manufactured. The laminate can be obtained by adding a shape memory layer of powder between the two composite skins, the composite sandwich by applying flexible composite skins over a shape memory foam core. As shape memory materials, SMPCs can react to specific external stimulus changing their configuration and then remember the original shape. Considering the low weight, the shape reconfiguration, and recovery force, the SMPCs are expected to have great potential applications in many engineering fields. This chapter highlights some recent progress in manufacturing, characterization, and future possible applications.

Keywords Shape memory polymer composites (SMPC) · Epoxy matrix composites · Expandable/deployable structures

Contents

L. Santo (✉) · F. Quadrini
Department of Industrial Engineering, University of Rome "Tor Vergata",
Via del Politecnico 1, 00133 Rome, Italy
e-mail: loredana.santo@uniroma2.it

D. Ponnamma et al. (eds.), *Smart Polymer Nanocomposites*,
Springer Series on Polymer and Composite Materials,
DOI 10.1007/978-3-319-50424-7_11

1 Introduction

1.1 What Are SMP Materials?

SMPs are innovative materials that possess the capability of responding to specific external stimulus changing their configuration and then remember the original shape. The stimulus can be heat, electricity, light, magnetic field, water, and solvent. For heat-induced SMPs, the shape memory effect is observed by performing a typical thermomechanical cycle. The possibility to change the configuration mainly depends on the material state that switches from glassy state to rubbery state when the temperature reaches a characteristic value (the glass transition temperature (T_g) or melting transition temperature (T_m) based on the nature of the polymer configuration) that can be labeled transition temperature (T_{trans}) [1]. The chemical nature of the material is fundamental for obtaining this behavior, but also the morphology together with the applied processing and programming [2].

Figure 1 schematically shows an example of typical thermomechanical behavior of SMP.

In detail, the process of shape recovery can be divided into different steps: (1) manufacturing step of the initial shape of the SMP; (2) heating and deforming step (T above T_{trans}), deforming the SMP in a new configuration; (3) cooling and storing step, reducing the temperature (below T_{trans}) maintaining the applied deforming force, and finally removing it and storing the part; and (4) reheating step, increasing the temperature above T_{rans} in order to recover the original shape. In particular, in the case of Fig. 1, the SMP is packed in a new configuration (for SMP

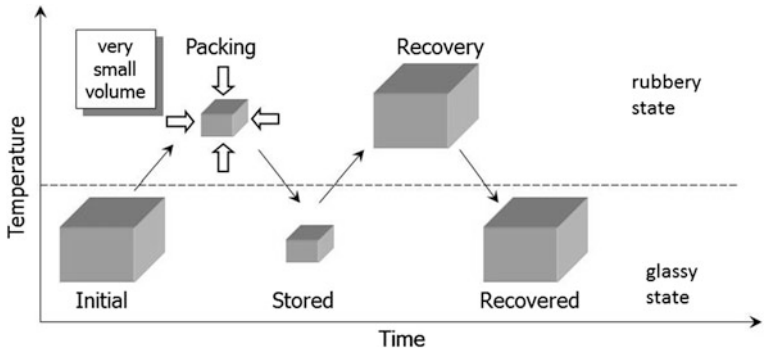

Fig. 1 Schematic representation of thermomechanical cycle for SMP [3]. Copyright 2016. Reproduced with permission from Elsevier

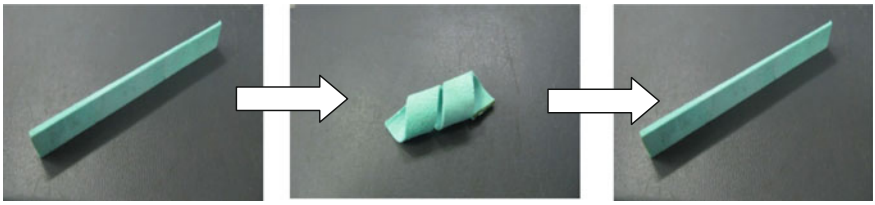

Fig. 2 The initial, stored, and final configuration of a SMP sheet

foams or deployable SMP), and subsequently, the initial configuration can be recovered [3].

Figure 2 shows an example of SMP material: a sheet of epoxy foam (2 mm thick) in three different configurations (initial, stored, and final). It is so possible to give a new configuration and finally to recover the initial geometry by means of a thermomechanical cycle.

SMPs have numerous advantages over shape memory alloys, resulting in potential substitutes for lightness, low cost, high shape recovery, easy manufacturing, good biocompatibility, and larger recoverable strains, and their physical (e.g., transition temperature) and mechanical properties can be adapted by small changes in chemical composition and structure [2].

Thermosets and thermoplastics can be used, but considering the comparison between chemically cross-linked thermosets and physically cross-linked thermoplastics, it shows that the former SMPs are better candidate for future structural applications. In fact, the advantages of thermoset SMPs include excellent shape fixity and recovery ratio, higher transition temperature, and better thermal and chemical stability.

However, SMP generally has some limitations, such as low deformation stiffness and low recovery stress. Therefore, SMPCs have been developed in many practical applications in order to overcome these deficiencies [1].

The SMPCs can have higher strength, higher stiffness, and special characteristics determined by what fillers are added which can offer further advantages over SMPs [1, 4]. SMPCs can exhibit novel properties significantly different from their pure counterparts, so that they can be suitable for more applications.

In general, shape memory properties can be given to composite materials and structures by using SMP matrices or integrating parts made of SMPs [5–7]. Shape memory composite structures can be also produced by joining composite shells with shape memory foams.

For the first time, a SMPC laminate was also tested in a space mission on board the BION-M1 capsule through the Soyuz-2 launch vehicle with the aim to study its behavior in microgravity for future applications (Ribes_Foam2 Experiment, April 20, 2013) [8–10]. The experiment is the second in microgravity, and it follows the experiment IFOAM on SMP foams, Mission Shuttle STS-134 (May, 2011) [11, 12]. The experiment Ribes_Foam2 has shown the ability of composites to

recover their shape in microgravity. In the case of small and light parts, the effect of microgravity is negligible if compared with recovery forces, but it strongly affects the performances of heating devices and has to be taken into account for designing actuators or self-deployable structures in future space applications.

2 SMC from Epoxy Matrix

SMCs from epoxy matrix have been extensively studied by the authors. They can be produced in different ways, by using SMP matrices, by integrating parts made of SMPs, or by assembling SMP elements [5]. Moreover, SMP nanocomposite can be also obtained by adding nanofillers in the shape memory matrix [13]. In the case of integration, SMP laminate can be obtained by adding a shape memory layer in the form of powder between the two composite skins, or flexible composite skins can be applied over a shape memory foam core obtaining composite sandwich. In several works [14–19], the outer skins are made of thermosetting carbon fiber-reinforced (CFR) prepregs, whereas the shape memory interlayer is a thermosetting epoxy resin in the form of powder or foam. Figure 3 shows some examples for producing SMC and the raw materials.

2.1 Shape Memory Composite with a Bulk SMP Interlayer

In the previous works of the authors, commercial materials are generally used for the fabrication of prototypes of SMC with a bulk SMP interlayer. The composite layers is carbon/epoxy prepreg (HexPly® M49/42%/200T2X2/CHS-3K, nominal epoxy resin content of 42 wt%, nominal area weight of 200 g/m^2, thickness of

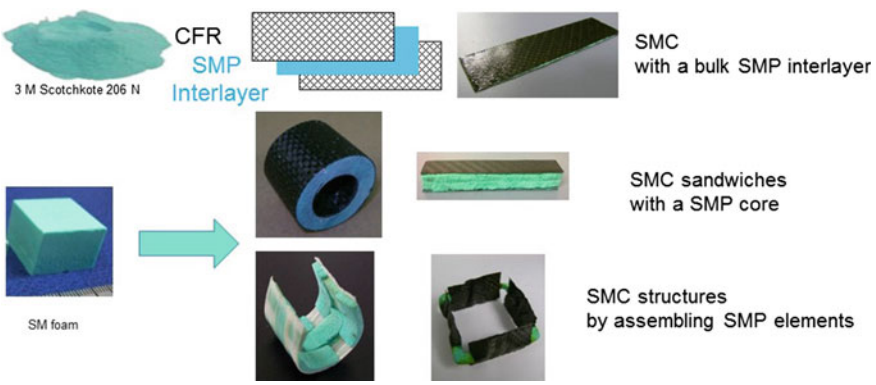

Fig. 3 Examples of producing SMC

0.35 mm), while the SMP interlayer is an epoxy resin 3M Scotchkote 206 N. The prototypes are formed by hot pressing in a hydro-pneumatic press (by ATS FAAR). The applied pressure is 1.3 MPa, the molding temperature is 150 °C, and the holding time is 15 min. In the case of powder deposition, it is generally limited to specific zones located within the folding lines of the deploying structures.

The procedure of fabrication of the SMPC samples is quite simple: A layer of 100 μm of uncured SMP powder is poured over a prepreg sheet (properly cut) on a spaced position where the hinge is intended to be for the deploying phase; afterward, the assembly is covered with another prepreg sheet. The SMPC is placed between two sheets of thermoplastic film (used for mold release) and finally molded together.

2.1.1 Examples of SMPC

Figure 4 shows some prototypes for space applications realized by using this methodology, in particular a prototype of solar sail, a self-deploying cross, a prototype of de-orbiting sail, and a prototype of solar panel.

Instead, Fig. 5 shows in detail the different phases for the fabrication of a composite panel for the deploying of a solar panel. In this case, four aluminum plates were applied to simulate the panels.

After the fabrication, the memorizing step is necessary to give the new configuration.

The behavior of the SMPC structure is relatively complex because of the presence of 2 epoxy systems with different glass transition temperatures. In the examined case, the transition range is comparable, and consequently, 150 °C is considered as a good temperature for the material softening and recovery, while higher temperatures could lead to degradation. A hot air gun is used for the material heating and appropriate tools for giving the new geometry.

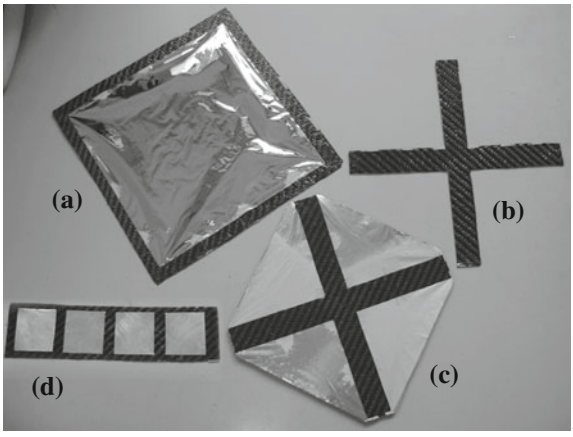

Fig. 4 Molded composite structures **a** prototype of solar sail, **b** self-deploying cross, **c** prototype of de-orbiting sail, and **d** prototype of solar panel

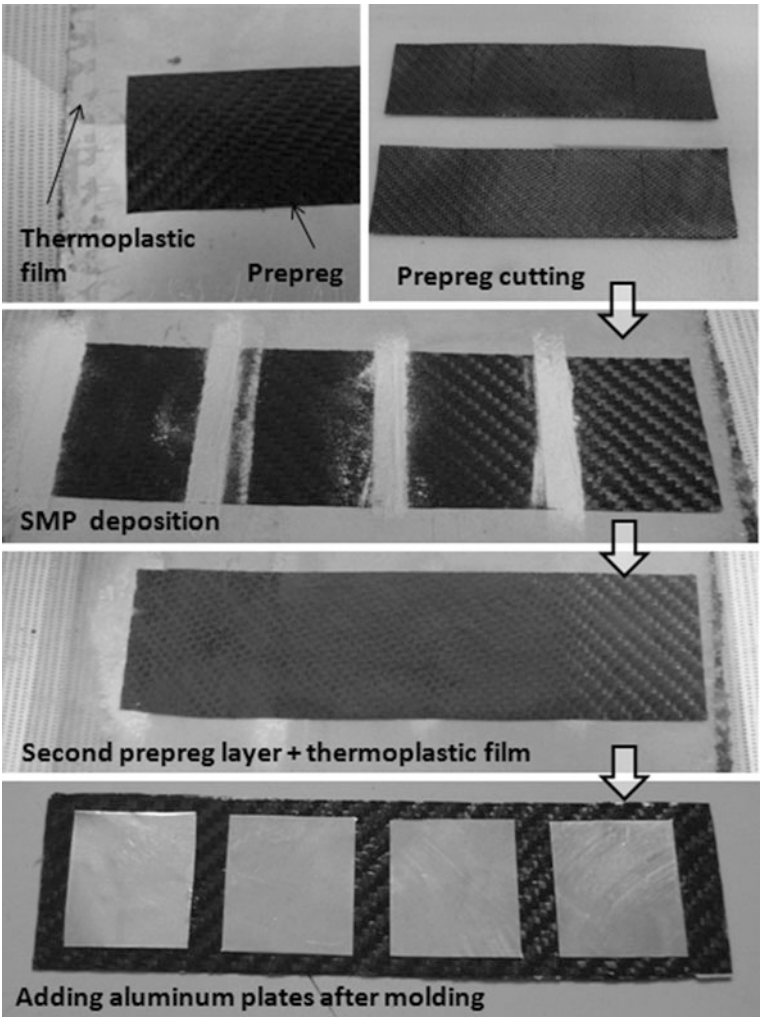

Fig. 5 Fabrication of the composite panel for the deploying of a solar panel

Figure 6 shows the memorized configuration of the prototypes of Fig. 4, whereas Figs. 7 and 8 report the details of the recovery tests by using a hot gun for heating.

The time for the shape recovery is short in comparison with SMP [10]. In particular, 140 s are necessary for the recovery of the SMPC frame, 35 s for the panel, 40 s for the cross, and 85 s for the cross with sail, respectively. The time is also strictly related to the heating source.

The initial geometry is fully recovered; no damage is visible during and after the memory stage, while the residual stiffness could be evaluated.

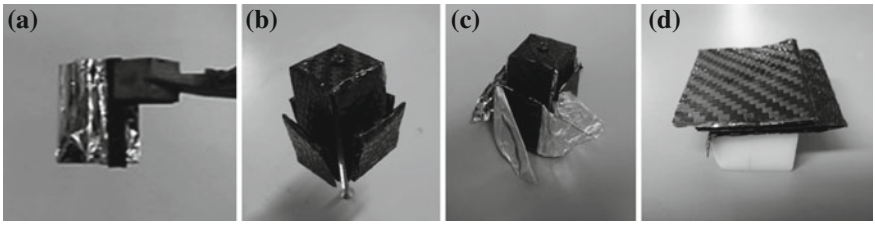

Fig. 6 Memorized configuration of the composite structures: **a** solar sail, **b** self-deploying cross, **c** de-orbiting sail, and **d** solar panel

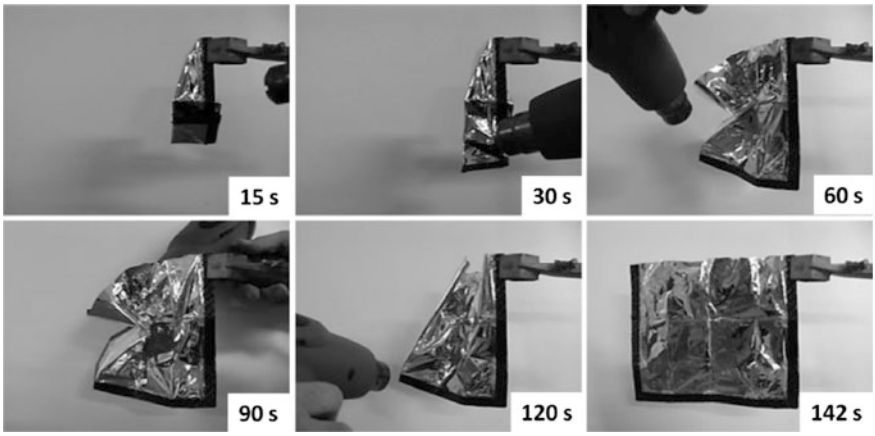

Fig. 7 Details of the prototype of the SMC frame recovery stage

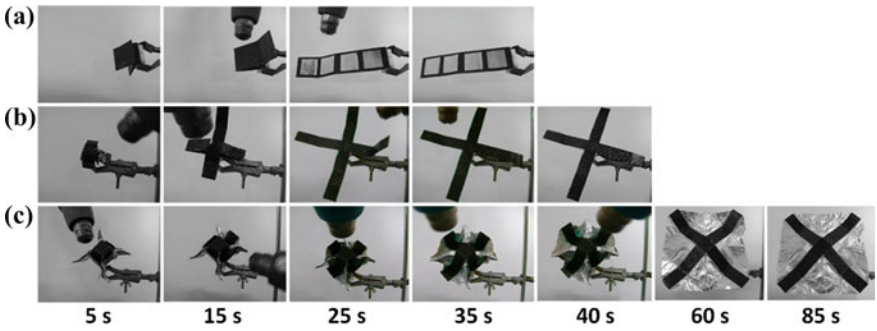

Fig. 8 Details of the recovery tests of **a** the panel, **b** the cross, and **c** the cross with the sail

In [19], a multipart structure is studied, a de-orbiting dual sail for satellite applications. The dual-sail configuration deploying on the opposite sides of a micro-sat is schematically reported in Fig. 9. As in the previous works, the SMC

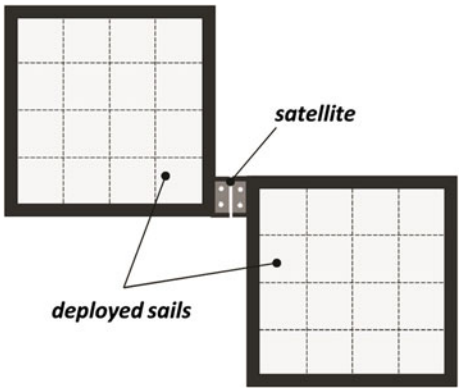

Fig. 9 Dual-sail configuration deploying on the opposite sides of a micro-sat [19]. Copyright 2016. Reproduced with permission from ASME

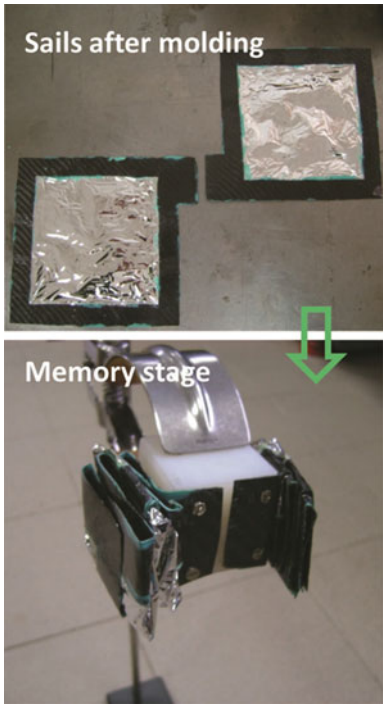

Fig. 10 Composite structures before and after the memory step [19]. Copyright 2016. Reproduced with permission from ASME

structures were produced in the opened shape and subsequently memorized in the closed configuration (see Fig. 10). The initial deployed configuration is always recovered by heating the prototype. The closed configuration increases the packing efficiency of large structures for space orbiting systems. In this case, the shape memory properties were provided only to folding zones and memory–recovery cycles have been performed to test SMC performances. As result, the configuration

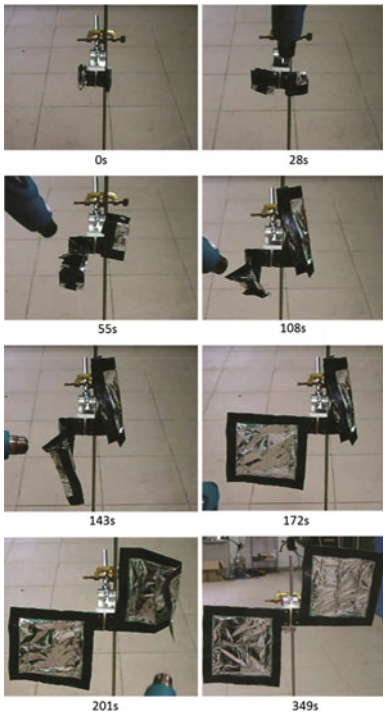

Fig. 11 Details of the shape memory tests of the dual-sail configuration [19]. Copyright 2016. Reproduced with permission from ASME

can successfully self-deploy following the desired design constraints and recovering the original flatness without noticeable defects, as shown in Fig. 11. A time of 349 s is necessary for the full recovery of the initial shape.

Other interesting configurations of SMPCs are composite hands [16]. They can be manufactured with the same methodology, but they are produced in the closed-hand configuration and subsequently opened in the memorizing step. In this case, due to heating, composites tended to recover the initial closed configuration, allowing to grab small objects. This could be interesting for space debris capture. Figure 12 shows an example of composite hands after the memory step and in the final configuration.

2.1.2 Monitoring of the Shape Recovery

In future final application, higher sizes are expected for the parts and local heating could be easily embedded to control the shape recovery and to avoid the heating of the entire structure. In the space environment, the recovery could be obtained by solar irradiation, but further studies are necessary to reach such result.

Moreover, a monitoring of the recovery can be performed by fiber optic sensor devices. In [17], the strain history of a prepreg carbon fiber system, cured with a

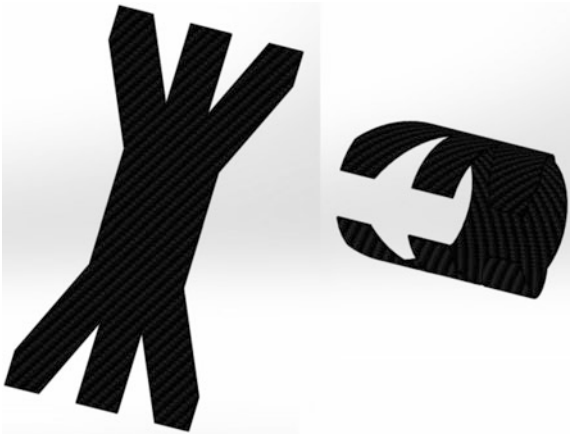

Fig. 12 Example of composite hand: after the memory step (*left*) and in the final configuration (*right*)

Table 1 Thickness of the samples

Sample	Thickness (mm)
Sample 1	0.56 ± 0.05
Sample 2	0.91 ± 0.05
Sample 3	1.24 ± 0.05

shape memory polymer (SMP) interlayer, has been monitored through a fiber Bragg grating (FBG). Optic fiber arrangement was optimized to avoid unwanted breakings, whereas strains were limited by fiber collapsing, i.e., within nominal 2% of deformation. Dynamic information about shape recovery has given fundamental insights about strain evolution during time as well as its spatial distribution.

The first results suggest that the fiber should be embedded inside the layers, and attention should be paid to the adhesive choice because it can lead to fiber release during heating. The use of the so-called ribbon tape (or smart patch) technique that ensures a stronger surface coupling can be performed. Experimental results also suggest that the design and manufacture of specific jig and tools are necessary to face the SMPC handling and their governing (i.e., the reset of its shape) so as to improve the test reliability.

2.1.3 Multilayered SMPC

Another aspect to evaluate is the influence of the layers' number on the shape memory properties. In [15], three composite plates of 100 × 30 mm^2 were produced by means of a layer structure. The composite structure was produced alternating CFR prepreg layers to uncured epoxy powder layers of about 100 μm thick. Table 1 reports the thickness of the samples.

The study is therefore extended to multilayers. In particular, the study of the differences in the load explicated by the layer during the shape recovery of percentage and time of recovery of the composites as a function of layers number was

Fig. 13 SMC with five layers in the deformed V-shape

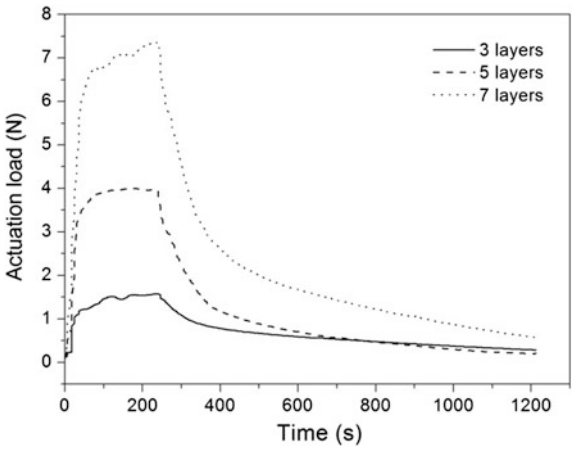

Fig. 14 Actuation load as a function of time for different layers

carried out. The actuation load and the shape recovery percentage were measured after a V-shape memorizing step of the composites by bending test. Figure 13 shows the SMC sample with five layers in deformed V-shape.

Experimental results have shown that such structures can successfully recover their original shape regardless of the number of layers without noticeable damages [15]. Figure 14 shows the actuation load as a function of the time for different layers. A maximum load of about 1.5, 4, and 7.5 N was reached for 1, 3, and 5 layers, respectively.

As expected, actuation loads increase with the increasing layers, but the trend is not linear.

An exponential curve has been found [15]. This has to be taken into account for the structure design.

2.1.4 Shape Recovery by Irradiation

Generally, heating has been obtained by a hot gun or in a furnace, but the chance to recover the shape of SMC structures by irradiation can be of fundamental

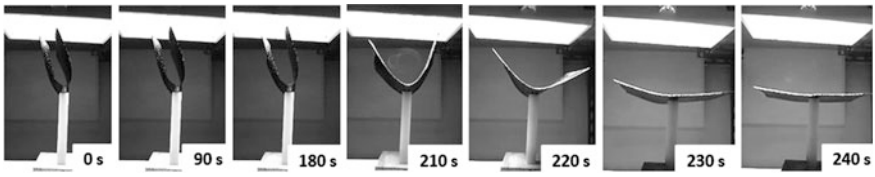

Fig. 15 Recovery sequences of the SMPC panel by using a 500 W halogen lamp, distance of 95 mm

importance for space applications. In [18], a first step in this direction has been taken. The recovery step of different configurations was achieved by irradiation of two different lamps (infrared and halogen). The first experimental evidences suggest, as expected, that the lamp power and the distance from the irradiating source are crucial to obtain a complete recovery of the shape, to avoid poor performance of the final SMC structure and for the success of the deployment. In particular, good results have been obtained using a 500 W halogen lamp at a distance of about 95 mm from the SMC memorized structure (samples of $150 \times 150 \times 1$ mm^3). A complete recovery of the complex shape configuration has been achieved using these parameters, without noticeable damages (see Fig. 15). For shape recovery time reduction, it seems to be important that the SMC bending regions are directly exposed to the irradiating source. Moreover, the effect of using only radiating lamps and the study of radiations' consequences on SMC structures should be deepened in further studies.

2.2 Shape Memory Composite Sandwiches with a SMP Core

Shape memory composite sandwiches with a SMP core can be obtained by using composite skins made with carbon fiber-reinforced (CFR) prepregs and SMP foam as core [5, 20].

The core material can be a shape memory epoxy foam [12], and the composite skin can consist of two-layer unidirectional thermoplastic composite (glass-filled polypropylene) or thin carbon fiber laminates or prepreg. In the case of unidirectional thermoplastic composite [7], skins were joined to the core by hot compression without any adhesive. The result was a very good adhesion. Shape memory tests revealed the ability of the SMC structures to recover the initial shape even after significant damage.

In [20], skins made of thin carbon fiber laminates and SMP foam core were used for obtaining SMC sandwiches with self-healing properties for the marine field. Self-healing is the ability of the composite to fix the damage occurred after impact, mainly in the case of matrix failure [21]. Self-healing reflexive composite structures, originally developed for application in unmanned aerial vehicles, have been adapted to function in a marine environment [22]. Reflexive structures combine

healable resin, structural health monitoring, and integrated autonomous repair for increased survivability in composite vehicles and structures. Adapting this proven reflexive solution to marine environments involved the development of a marine-compatible resin and the optimization of signal parameters for structural health monitoring functionality underwater.

In the previous studies, it has been shown that SMCs have good self-repairing properties at least in terms of shape recovery [5], and a further development is the integration of the additional self-healing function. This function can be obtained, for example, by mixing small hollow microspheres in the foam core: These spheres can be filled with a resin precursor and a catalyzer. In the case of an impact, the SMC structure could be dramatically deformed with cracks and delamination: This energy would also break the microspheres, making contact between uncured resin and catalyzer. If the SMC structure is locally heated, e.g., by means of a hot air gun, the shape is recovered using SMP and cracks are partially closed using the resin polymerization.

For this purpose, prototypes have been made: Two-ply composite skins were produced by molding with a hot parallel plate press at low pressure (1.5 bar), a plate temperature of 150 °C, and a molding time of 20 min. A thermoplastic film was used as mold release. In the case of the epoxy foam, the sizes were 90 × 15 mm^2, while the laminate thickness was about 0.4 mm. Shape memory composite skins were also produced by placing a 150 μm SMP interlayer between the two plies in order to obtain SMC skins. During lamination, the SMP resin was placed on the first prepreg layer in the shape of uncured resin, and subsequently, the second prepreg layer was placed on the first one. Figure 16 shows an example of SMC sandwiches with an epoxy foam core.

The skin–core joining was achieved by means of the same resin powder which was already used for shape memory cores and interlayers. The adhesion was achieved after placing the resin powder at the interfaces and curing at 150 °C for 5 min at low pressure (0.5 bar). The final thickness of the adhesive interface was estimated to be about 100 μm. Final size of CF/epoxy sandwiches was 90 × 15 mm^2 with a thickness about 14 mm.

After production, the sandwich samples have been tested in bending up to failure and subsequently recovered by using a hot air gun. Such samples were recovered after coating the failure zone with a small amount of uncured epoxy resin, in liquid state. That was a method to simulate the self-healing function. Subsequently, bending tests have been repeated to evaluate the residual properties of composite sandwiches. Figures 17, 18, and 19 show some experimental results.

In detail, Fig. 17 shows the setup for bending test and the failure of SMC sandwiches after the bending test; Fig. 18 reports bending curves of CF/epoxy

Fig. 16 SMC sandwiches with epoxy foam core

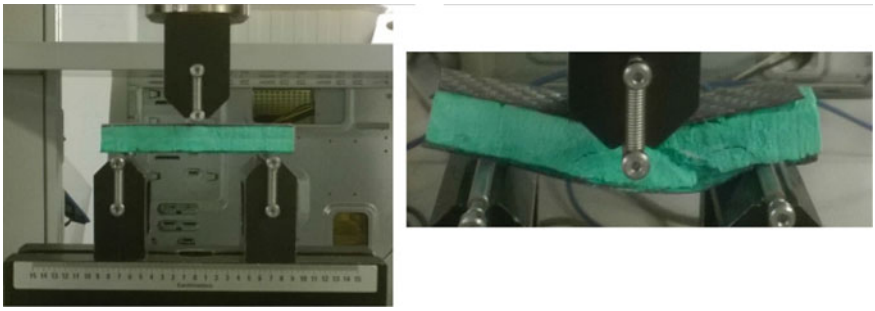

Fig. 17 Bending test (*left*) and failure of SMC sandwiches with epoxy foam core (*right*) [3]. Copyright 2016. Reproduced with permission from Elsevier

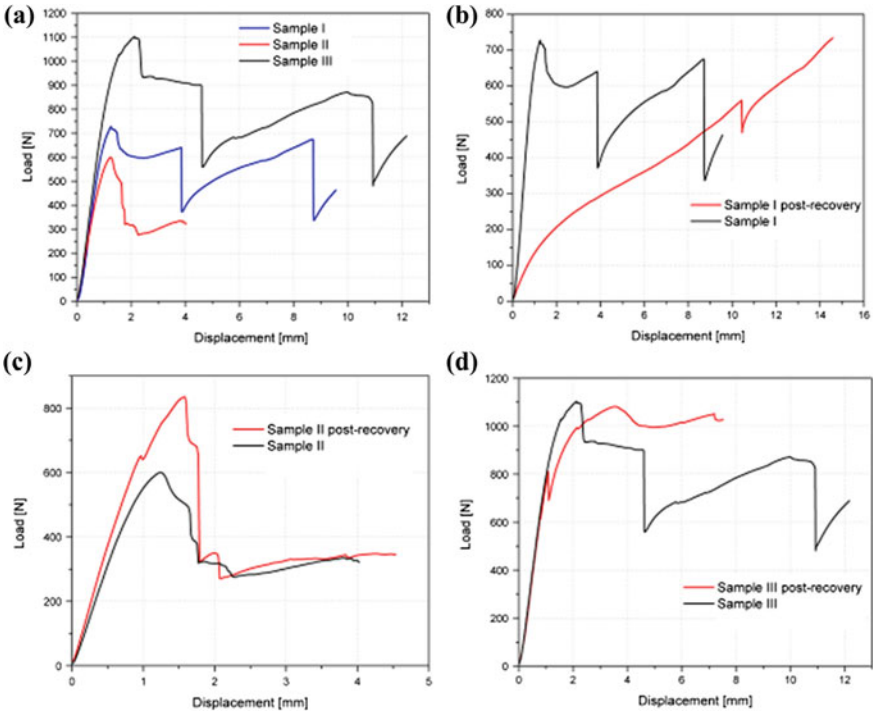

Fig. 18 Bending curves of CF/epoxy sandwiches: **a** initial tests on sandwiches without (Sample I and Sample II) and with (Sample III) SMC skins; **b–d** bending tests before and after recovery for Sample I (without self-healing function), Sample II (with self-healing function), and Sample III (with self-healing function and SMC skins), respectively

sandwiches before (damage) and after (post-recovery) shape recovery in the absence and presence of the self-healing function; and Fig. 19 shows the shape recovery of CF/epoxy sandwiches.

The shape recovery and the effect of self-healing function are well evident. In order to quantify this effect, Table 2 reports stiffness data extracted from bending curves of all the sandwiches before and after recovery. Residual stiffness after recovery is a simple way to measure the efficiency of shape recovery and self-healing. Strength could be used as well, but several failure mechanisms were observed during tests and it is difficult to make a comparison.

CF/epoxy sandwiches showed good stiffness because of the higher core density and properties. On the other hand, the foam core was sensitive to cracks under bending.

Due to this fact, very low residual stiffness was measured in the sample without the self-healing function (19%) after recovery. Moreover, the effect of the self-healing function is significant. In the case of using SMC skins, a 90% of residual stiffness was observed. In the sample with the healing function but without the SMC skins, the residual stiffness was even higher than the initial one (+26%).

The first results are interesting and seem to confirm the validity of this approach. Sandwich structures are therefore particularly appropriate for producing SMC

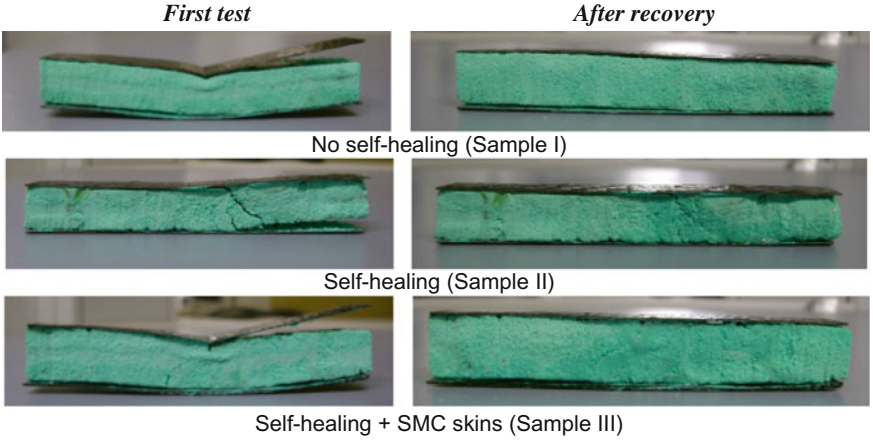

Fig. 19 Shape recovery of CF/epoxy sandwiches [3]. Copyright 2016. Reproduced with permission from Elsevier

Table 2 Stiffness of SMC sandwiches before and after recovery [3]

Sandwich Type	Details	Initial stiffness (N/mm)	Stiffness after recovery (N/mm)
CF/Epoxy	No healing	664.4	124.8
CF/Epoxy	Healing	493.3	623.0
CF/Epoxy	Healing + SMC skins	797.9	720.3

Copyright 2016. Reproduced with permission from Elsevier

structures with self-healing properties because of the possibility of using shape memory foams for core. In the study, only commercial materials have been used with the evidence of high residual properties after shape and damage recoveries. It has also been shown that it is possible to concentrate the shape memory behavior only in the foam core, leaving the composite skins made of traditional materials.

3 Perspective for the Field

Considering the low weight, the shape reconfiguration, and recovery force of SMPCs, they are expected to have great potential applications in many engineering fields.

In particular, SMPCs from epoxy matrix are expected to develop and have great potential applications mainly in aerospace in the near future; significant research works are focusing on the design and evaluation of SMPC components such as foldable SMPC truss booms, SMPC hinges to actuate solar array deployment, systems for antenna, mirror and reflector deployment, and systems for debris capture and opening of solar sail for microsatellite de-orbiting. Moreover, a morphing vehicle concept is developed by using both SMPs and SMPCs [23]. First experiments in microgravity have been carried out, and the results are promising.

In space applications, microgravity and space environment play a significant role in the deployment phase, and for this reason, other space missions will be necessary to evaluate the feasibility after ground tests, in particular for large and complex composite structures.

Moreover, solar radiation could be used for the shape recovery, but material aging and damage cannot be neglected for a potential application.

Interesting applications of SMPCs from epoxy matrix could be also for the marine field, by using a SMP core with self-healing properties in sandwich structures for self-repairing of boats or marine structures after impact.

In any case, extensive studies are needed on the relationship between the structure of SMPC and properties of the material, and requirements of specific applications. Moreover, a study on the multiple-step and two-way shape memory effect is at its initial state [23, 24] and of great interest for the applications.

Finally, based on all the advantages of SMPCs, previously stated, there is no doubt that SMPCs are expected to become one of the leading roles in the field of smart materials and they will be materials for future engineering applications.

4 Conclusion

In this chapter, some results on shape memory materials from epoxy matrix composites are discussed. The aspects of manufacturing, shape recovery, and mechanical characterization are mainly analyzed. The primary scope is to spread the knowledge about the capabilities of these smart materials and the future challenge

for their applications mainly in the aerospace field. Other important aspects regarding chemistry and physical behavior could be considered and can be found in specific literature.

Acknowledgements Authors are grateful to Dr. Antonio Accettura for the help in the development of SMPC structures for aerospace and to Mr Gennaro De Vita and Mr Gianni Palomba for their technical support.

References

1. Liu Y, Du H, Liu L, Leng J (2014) Shape memory polymers and their composites in aerospace applications: a review. Smart Mater Struct 23:023001 (22 pp)
2. Lendlein A, Kelch S (2002) Shape-memory polymers. Angew Chem Int Edn 41:2034–2057
3. Santo L (2016) Shape memory polymer foams. Prog Aerospace Sci 81:60–65
4. Ratna D, Karger-Kocsis J (2008) Recent advances in shape memory polymers and composites: a review. J Mater Sci 43:254–269
5. Quadrini F (2014) Polymer matrix composites with shape memory properties. Adv Mater Res 783–786:2509–2516
6. Santo L, Quadrini F, Accettura A, Villadei W (2014) Shape memory composites for self-deployable structures in aerospace applications. Procedia Eng 88C:42–47
7. Santo L, Quadrini F, De Chiffre L (2013) Forming of shape memory composite structures. Key Eng Mater 554–557:1930–1937
8. Santo L, Quadrini F, Ganga PL, Zolesi V (2015) Mission BION-M1: results of Ribes/Foam2 experiment on shape memory polymer foams and composites. Aerosp Sci Technol 40: 109–114
9. Santo L, Quadrini F, Villadei W, Mascetti G, Zolesi V (2015) Shape memory epoxy foams and composites: Ribes_foam2 experiment on spacecraft "Bion-m1" and future perspective. Procedia Eng 104:50–56
10. Quadrini F, Santo L, Squeo EA (2012) Shape memory epoxy foams for space applications. Mater Lett 69:20–23
11. Santo L, Quadrini F, Squeo EA, Dolce F, Mascetti G, Bertolotto D, Villadei W, Ganga PL, Zolesi V (2012) Behavior of shape memory epoxy foams in microgravity: experimental results of STS-134 mission. Microgravity Sci Technol 24:287–296
12. Santo L (2014) Recent developments in the field of shape memory epoxy foams. Mater Sci Forum 783–786:2523–2530
13. Quadrini F, Santo L, Squeo EA (2012) Solid-state foaming of nano-clay-filled thermoset foams with shape memory properties. Polym-Plast Technol Eng 51:560–567
14. Accettura AG, Santo L, Quadrini F (2012) Space mission opportunities using shape memory composites. In: Proceedings of "63rd international astronautical congress" IAC 2012, Naples, Italy
15. Santo L, Quadrini F, Bellisario D (2016) Multilayered composite plates with shape memory properties. Key Eng Mater 699:1–7
16. Quadrini F, Tedde GM, Santo L (2015) Shape memory composite hands for space applications. In: ASME 2015 international manufacturing science and engineering conference, MSEC 2015, vol 1, Charlotte, United States, 8 June 2015–12 June 2015; Code 115672
17. Quadrini F, Santo L, Ciminello M, Concilio A, Volponi R, Spena P (2016) Shape memory polymeric composites sensing by optic fibre bragg gratings: a very first approach. In: Proceedings of times of polymers (TOP) & composites, Ischia, Italy, 19–23 June 2016
18. Santo L, Bellisario D, Quadrini F (in press) Shape recovery of polymeric matrix composites by irradiation. Adv Mater Res 879:1645–1650

19. Santo L, Quadrini F, Bellisario D, Accettura AG (2016) Conceptual prototypes of composite structures for aerospace. In: Proceedings of the ASME 2016 international manufacturing science and engineering conference, MSEC2016, Blacksburg, Virginia, USA, 27 June–1 July 2016
20. Santo L, Quadrini F (2015) Shape memory composite sandwich with self-healing properties for marine applications. In: Proceedings of 20th international conference on composite materials, Copenhagen, 19–24th July 2015
21. Gupta N, Paramsothy M (2014) Metal-and polymer-matrix composites: functional lightweight materials for high-performance structures. JOM 66:862–865
22. Meents EP, Barnell TJ, Cable KM, Margraf TW, Havens E (2009) Self-healing reflexive composite structures for marine environments. In: Proceedings of international SAMPE symposium and exhibition, vol 54, 16 p, Baltimore, MD, United States, 18–21 May, Code 79037
23. Leng JS, Lan X, Liu YJ, Du SY (2011) Shape memory polymers and their composites: stimulus methods and applications. Prog Mater Sci 56:1077–1135
24. Meng Q, Hu J (2009) A review of shape memory polymer composites and blends. Compos A 40:1661–1672

Shape Memory Behavior of Conducting Polymer Nanocomposites

Deepalekshmi Ponnamma, Yara Mohamed Hany El-Gawady, Mariappan Rajan, Solleti Goutham, Kalagadda Venkateswara Rao and Mariam Al-Ali Al-Maadeed

Abstract The remarkable advances in the area of shape memory devices during the past few decades have triggered wide applications in numerous areas ranging from aerospace to household products and from civil engineering to biomedical fields. Shape memory metals, alloys, polymers, and composites are mainly used in fabricating many useful products; more significance is given to the polymers and its composites due to their lightweight, low cost, easy processability, and large strain. The electroactivity and the electrical conductivity of polymer composites are also correlated with this shape memory behavior. The current chapter is specifically prepared to address the various electrically conducting polymers and their composites applied in shape memory devices. A brief introduction to shape memory effect, conducting polymers, and the composite fabrication, followed by discussion about the conducting additives and applicability of conducting composites in shape memory, is provided in this chapter. It will also provide a review of the up-to-date information on this specific topic of conducting composites in shape memory, and the challenges need to be solved for their potential future advancement.

Keywords Electroactivity · Conductivity · Nanomaterials · Shape recovery

D. Ponnamma (✉) · Y.M.H. El-Gawady
Center for Advanced Materials, Qatar University, P.O. Box 2713, Doha, Qatar
e-mail: lekshmi_deepa@yahoo.com

M. Rajan
Biomaterials in Medicinal Chemistry Laboratory, Department of Natural Products Chemistry, School of Chemistry, Madurai Kamaraj University, Madurai 21, Tamil Nadu, India

S. Goutham · K. Venkateswara Rao
Centre for Nano Science and Technology, Institute of Science and Technology, Jawaharlal Nehru Technological University Hyderabad, Kukatpally 500085, Hyderabad, India

M.A.-A. Al-Maadeed
Materials Science and Technology Program, Qatar University, PO Box 2713, Doha, Qatar

D. Ponnamma et al. (eds.), *Smart Polymer Nanocomposites*,
Springer Series on Polymer and Composite Materials,
DOI 10.1007/978-3-319-50424-7_12

Contents

1 Introduction

Stimuli-responsive materials change their mechanical, electrical, optical, thermal, and surface properties along with their shape when specific environmental conditions are applied on the samples [1]. Shape memory polymers (SMPs) belong to this class of stimuli-responsive materials capable of recovering their permanent initial appearance on exposure to any stimulus such as heat, humidity, pH, and magnetic/electric field, from their temporary deformed shape [2]. In order to possess shape memory effect, a polymer should possess a stable network and ability to undergo reversible switching transition [1]. Though certain polymers possess good shape memory behavior, low mechanical strength and shape recovery stress are observed as their major disadvantages. Filler particles of various dimensions and their polymer composites can improve the shape memory and physicomechanical properties [1].

The most general way of attaining shape memory is by thermal stimulation in which direct heating is applied to accomplish shape deformation [3]. But since direct heating can be not appropriate in all cases, other stimuli alternatives such as magnetic field, electric charge, light, and water are employed to achieve shape recovery. Among these various means of stimuli, electrical stimulation stands most interesting due to its remote controllability, uniform heating profile, and convenient manipulation. However, many polymers are insulating in nature, transferring them to conducting materials, either by the addition of conducting filler particles or by addition of conducting polymers, and are very important to execute the electroactive shape memory effect. Such shape recovery effect is known as the electroactive shape memory. In the case of conducting filler-reinforced composites, the fillers enhance the thermal conductivity of the base polymer and facilitate fast transfer of the induced Joule heating and thus improve the recovery speed [4, 5]. Electroactive shape memory and its influence on the conducting filler particle concentration were reported by Du et al. in their research works [3, 6]. They have used multi-walled carbon nanotubes (MWCNTs) as the filler and the polyvinyl alcohol (PVA) as the

base polymer and achieved good shape recovery at higher concentrations of MWCNT.

Electrically conducting plastic materials are called inherently conducting polymers [7]. These organic polymers exhibit high electrical conductivity similar to metallic or semiconducting materials, but their mechanical properties are lower when compared to other commercial polymers. By tuning the synthesis and dispersion methods, the electrical properties are often improved. Polypyrroles (PPy), polyanilines (PANIs), polyphenylenes, polyacetylenes, poly(p-phenylene vinylene), etc., are some types of such conducting polymers in which the conjugated p-orbitals are responsible for the conductivity. The electrochemical doping/dedoping within the polymers can cause the variation in their properties. Such electrochemical redox processes occurring inside the polymer can cause a reversible/simultaneous swelling and contraction which can lead to actuation and thus are useful in organic microelectromechanical systems and artificial muscles [7]. Electroactive shape memory of the polypyrrole/polyurethane block copolymer prepared by the chemical oxidative polymerization was reported for its use in actuators [8].

By the preparation of nanostructured conducting materials, monofunctional devices can improve multifunctional systems [9] that can be tailored for different applications. Recent studies on applying high-resolution three-dimensional shape memory structures in constructing flexible electronic devices through commercial stereolithography evidence good correlation between the electrical conductivity of the polymer and the significant shape memory effect [10]. Many conducting polymer nanocomposites report shape recovery property independent of its electrical resistivity and filler networks. In these cases, the recovery often triggered by light, temperature, or water stimulus is due to the associated structural confirmation of the polymer nanocomposite. In this chapter, the aim is to review the recent developments in shape memory behavior of conducting polymers and polymer nanocomposites, in addition to keeping an eye on electroactive shape recovery process. Overall, the main purpose is to bring out the influence of electrical conductivity of the materials as well as the electrical stimulus in the shape recovery of polymer nanocomposites.

2 Basics of Shape Memory

The process of shape memory is cyclic and contains two major steps: (i) programing process in which the sample is deformed to a temporary shape (B) from its original permanent shape (A) and (ii) recovery process in which the sample comes back to the original shape (A) by an external stimulus. Both these steps can be repeated in many subsequent cycles with various temporary shapes. When compared to shape memory alloys, the SMP exhibits shorter time intervals between the steps and higher deformation rate [11].

A typical shape memory response cycle is shown in Fig. 1 in terms of thermal response and is supposed to have the following steps [12]: In the first step, the

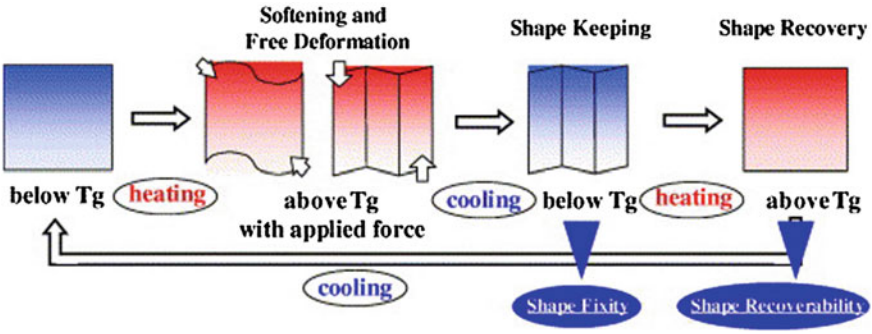

Fig. 1 Schematic representation of the shape memory effect [12]. Copyright 2007. Reprinted with the permission from Elsevier Ltd.

polymer is fixed to have its original shape by proper fabrication methods. During the second step, the SMP is heated above its thermal transition temperature, which can be either the glass transition (T_g) or melting (T_m). This deforms the material, and with the proper cooling or by applying any external force, the temporary shape of the SMP is preserved. This shape fixity is followed by the last step of shape recovery by which the SMP recovers its permanent original shape when thermally triggered above the T_g [13].

The reason for this shape switching is rather complex, and many reports have come out substantiating the exact mechanism of this molecular level transformation. Within the SMP, the stable structure is made of crystalline phase, chemical cross-linking, molecule entanglement, or interpenetrated networks. The various mechanisms responsible for shape memory recovery of a typical SMP can be vitrification/glass transition, crystallization/melting transition, liquid crystal anisotropic/isotropic transition, supramolecular association/disassociation, and reversible molecule cross-linking [1]. The typical mechanism occurring within a SMP is shown in Fig. 2. The reversible switching reactions are also shown here.

The quantitative estimation of shape memory behavior is very necessary in technological applications. This is usually done by two parameters: shape/strain fixity rate, $R_{f,}$ and the shape/strain recovery rate, R_r. In addition to this, the time intervals between the cycles, quantity of stimulus needed, switching temperature T_{switch} in thermal stimulation, etc., are also significant. The shape fixity is defined as the ability of a material to fix the mechanical deformation (denoted as ε_m) given to it and thus to keep its temporary deformed shape (denoted as $\varepsilon_u(N)$) for N number of cycles, whereas the shape recovery measures the ability of the material to retain the permanent shape (denoted as $\varepsilon_p(N)$) after applying a small triggering stimulus. The strain change is $\varepsilon_m - \varepsilon_p(N)$, during shape memory and $\varepsilon_m - \varepsilon_p(N-1)$, during programming. The R_f and R_r are, respectively, calculated by the following Eqs. (1) and (2). The values should be 100% ideally.

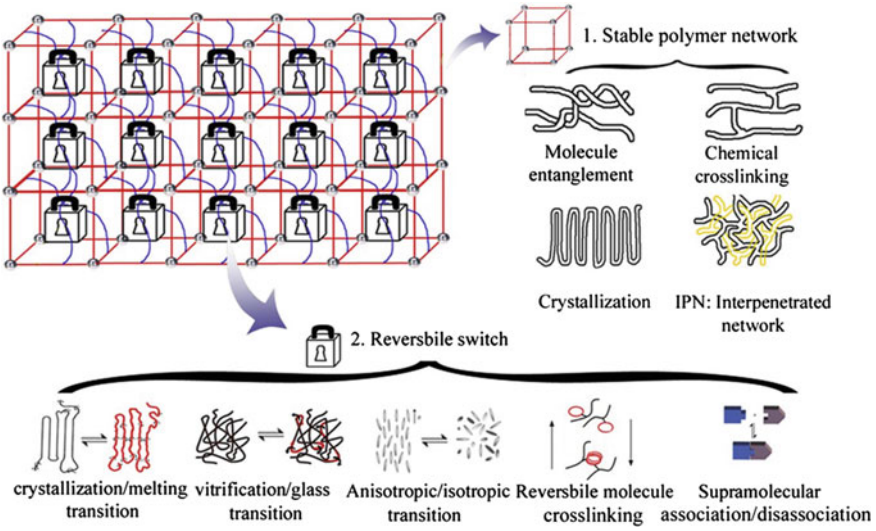

Fig. 2 Various molecular structures of SMPs [1]. Copyright 2013. Reprinted with the permission from Elsevier Ltd.

For a given cycle number N,
The shape fixity ratio

$$R_f(N) = \frac{\varepsilon_u(N) - \varepsilon_p(N-1)}{\varepsilon_m - \varepsilon_p(N-1)} \tag{1}$$

And the shape recovery ratio

$$R_r(N) = \frac{\varepsilon_u(N) - \varepsilon_p(N)}{\varepsilon_u(N) - \varepsilon_p(N-1)} \tag{2}$$

where $\varepsilon_u(N)$ is the unloading strain in the cycle number N, and $\varepsilon_p(N)$ and $\varepsilon_p(N-1)$ were residual strain in the cycle number N and $N-1$.

In their review of shape memory polymers, Behl et al. explain the practical mode of testing the shape memory. This is shown in Fig. 3 as a typical stress-controlled programming cycle. For testing, the sample is clamped to a tensile testing equipment and elongated to ε_m, given as in Step 1. Now, the molecular switches within the SMP are opened by proper external way of deformation. For thermally induced shape memory, the sample is heated above its transition temperature, while in the case of photoinduced and electricity-induced shape memory, the sample is irradiated with light of appropriate wavelength or kept under suitable electrical field of known strength, respectively. This cleaves the bonds within the SMP, and under a constant stress of σ_m, the material fixes its temporary shape by closing the molecular switches (Step 2 in the figure). In thermally induced shape memory, the

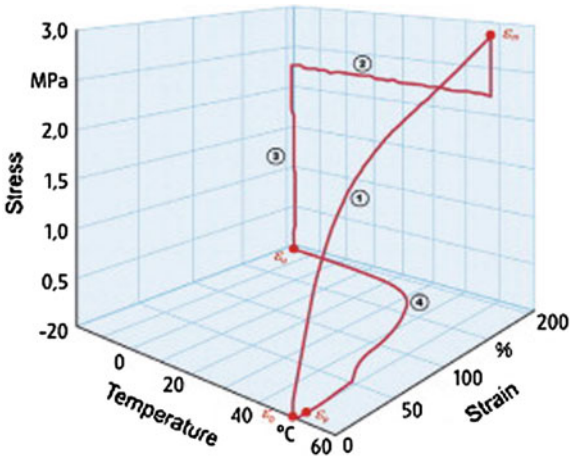

Fig. 3 Typical stress–strain–temperature diagram (first cycle) for a thermoplastic SMP with a thermally induced shape memory effect. Step 1 is strain controlled, while Steps 2–4 to the beginning of the next cycle are stress controlled [11]. Copyright 2007. Reprinted under creative commons license

closing of switches occurs by cooling, whereas in photoinduced and electroinduced shape memory, this is, respectively, done by irradiating with another wavelength or changing the electrical field to another strength. Now, in Step 3, the material reaches to a stress-free condition by reducing its strain. In the last Step 4, the stress maintains constant, molecular switches open up again, and the sample contracts and achieves its permanent shape [11].

3 Synthesis Methods

3.1 Conducting Polymers

A large number of conducting polymers are used in many of the industrial applications such as electronics, photonics, lithography, and optical devices. The main types of such polymers and their applications are tabulated in Table 1.

With the advancement of molecular electronics, conducting polymers have significant demands [14] and these polymers are synthesized by many routes. PANIs are often synthesized by in situ polymerization of aniline, which is very simple and cost-effective [15]. A cost-effective way to synthesize many conducting polymers with respect to their application is well explained by Gurunathan et al. in their review article. This electrochemical synthesis was first established for polypyrrole, and many semiconducting polymers can be synthesized from their monomers such as aniline, indole, thiophene, carbazole, furan, azulene, and pyrene [14]. In this synthesis, both oxidative and reductive polymerizations are possible. The advantage of electrochemical polymerization over the chemical oxidation is particularly when the synthesized polymer has use in making electrodes, sensors, and other electronic applications [16]. Electrochemical copolymerization of polythiophene derivative to fabricate biosensor was also reported [17].

Table 1 Applications of conducting polymers in device [14]

	Device application
PANI and substituted PANI	(1) Electrochromic display (2) Photolithography (3) Rechargeable battery (4) Electrochemical capacitors (5) Corrosion inhibitors (6) Sensors
PPy and substituted PPy	(1) Electrochromic display (2) Lightweight battery (3) Sensors (4) Solar energy cells
Polythiophene and substituted polythiophene	(1) Electroluminescence (2) Electrochemical capacitors (3) Cathode materials for battery (4) Microlithography (5) Corrosion inhibitors
Poly-p-phenylene (PPP) p-phenylene vinylene (PPV)	(1) Electroluminescence (2) Photoconductors (3) Solar energy cells (4) Laser materials

3.2 Nanoparticles and Polymer Nanocomposites

Nanoparticles are prepared via different routes depending on the type of the material, dimension required, and application. All general methods of preparation such as arc discharge method, laser ablation, and chemical vapor deposition for CNTs as well as the top-down and bottom-up processes for graphene are extensively reported in the two reviews published [18, 19] by our group. Many nanoparticles are synthesized also by means of hydrothermal method, colloidal processes, self-assembling reactions, solvothermal reactions, pyrolysis, sol–gel processes, etc. Though a large number of methods are available, more attention will be focused on simple and low-cost processes that can lead to high yields. The usual problems associated with the synthesized particles are their high tendency of coalescence and agglomeration. To reduce the agglomeration, surface functionalization methods, use of compatibilizers/surfactants/ionic liquids, etc., are employed too.

The major synthesis methods of polymer nanocomposites include melt blending, solution mixing, and in situ polymerization. In melt blending and solution mixing, the polymers and fillers are mixed together in different experimental conditions, whereas the monomer is polymerized in the presence of nanofillers in the in situ polymerization method to ensure maximum level of reinforcement. Table 2 represents some of the preparation methods of polymer nanocomposites with their possible applications.

Table 2 Preparation methods of various polymer nanocomposites

Polymer	Filler	Synthesis method	Applications	References
PANI	CNT	In situ polymerization	Sensors and magnetic shielding	[20]
PPy	CNT	In situ polymerization	Sensors and magnetic shielding	[20]
Polysiloxanes	Carbazole	Blending	Components of photovoltaic devices Electrophotographic photoreceptors Photorefractive materials	[21]
PANI	$CaCO_3$	In situ polymerization and solution mixing	Anticorrosion	[22]
Polyethylene	MWCNTs	Solution mixing followed by sintering	Better electrical and mechanical properties	[23]
PVDF	f-G (functionalized graphene)	Solution mixing	Improving electrical conductivity	[24]
Epoxy	Partially reduced GO	In situ polymerization at 250 °C	Higher thermal conductivity	[25]
TPU (thermoplastic polyurethane)	TRG (thermally reduced graphene)	In situ polymerization	Better electrical conductivity and magnetic shielding	[26]
Epoxy	Ag	In situ photochemical method	Higher K and dielectric constant	[27]
Polyfuran (PFu)	Poly (2-iodoaniline) P2IAn	Polymerization	Higher conductivity and magnetic susceptibility	[28]
PANI	ZnO	In situ polymerization	Higher optical properties	[29]
PANI	ZnO	in situ polymerization	Photoconductivity	[30]

4 Shape Memory Effects in Conducting Polymer Composites

4.1 Conducting Polymers and Its Composites

Conducting polymers and its composites are extensively studied for shape memory behavior. The topic can be subdivided to two categories: (i) shape memory behavior of usual polymers containing conducting polymers as fillers and (ii) shape memory behavior observed for conducting polymers and its composites.

Aranguren et al. [31] reported that PANI (conducting polymer) was grafted on the surface of cellulose nanocrystals and then used as a reinforcement to identify the shape memory property of polyurethane (PU). Here, the recovery ratio decreased with increasing the amount of the rigid particles (filler particles were added in 2, 4, and 10 wt%), whereas the fixity was increased [31]. Similar methods of preparation were followed by Auad et al. [32] as they obtained a recovery between 63 and 78% for all PU samples containing various PANI–cellulose nanofibrils doped filler up to the fourth cycle of thermal shape recovery. For the samples containing 2% of the PANI–cellulose nanofibrils, the shape fixity was >90% for all cycles, whereas for the sample with 4% PANI–cellulose nanofibril, the fixity decreased for certain cycles. This is attributed to the interaction of the hard segments of PU with PANI–CNC leading to some morphological disruptions [32]. Figure 4 shows shape recovery behavior for the PU and its composite containing PANI–cellulose hybrid nanomaterial. As reported, the first cycle behaves differently due to the rearrangement of domain morphology at high temperature during first deformation. However, during the subsequent cycles, the property becomes repeatable. Up to fourth cycle, all samples show a recovery between 63 and 78% if the actual strain happening in the sample following the first cycle is considered, and the calculated recovery can be >85%. However, more useful properties will be achieved if the

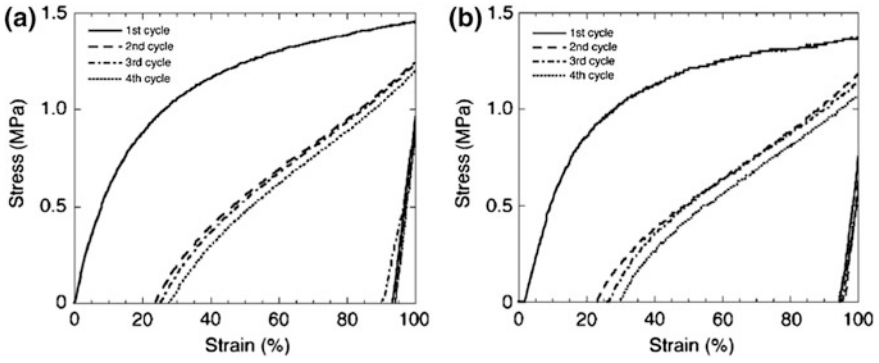

Fig. 4 Plots of thermomechanical tensile response of **a** neat PU and **b** PU containing 2 wt% PANI–cellulose nanofibril composite [32]. Copyright 2011. Reprinted with the permission from Wiley

PANI–cellulose nanofibrils are redoped after synthesis or during mixing with PU since the solvent employed may cause partial dedoping of PANI.

Similar composites containing PU as the base matrix and PANI-coated cellulose nanofibers were reported by Casado et al. as well [33]. In their work, they have obtained both the recovery and fixity properties, respectively, above 60 and 94% for all composites containing different concentrations of PANI and PANI–cellulose nanocrystals. In addition, the cycling process does not affect the shape fixity and recovery ratio of the PU, though the recovery stress decreases with the increase in cycle. For the PANI composites, the recovery ratio decreases with cycling as well as with the increase in filler concentration, whereas the fixity was not affected. For the PANI–cellulose composites, the recovery ratio was lower than the matrix and a minimum is observed at 1% concentration. The electrical conductivity of the PANI–cellulose composites was higher than that of PANI composites due to enhanced interactions between the two nanoparticles. But because the electrical percolation of fibers through PU was not achieved, good conduction levels were not reached.

The conducting polymer, polythiophene, also improved the shape recovery of PU when both polymers are made into form of a blend [34]. This recent investigation showed that 80–92% shape recovery was observed for all PU/polythiophene blends and its composites containing various concentrations of amine-functionalized MWCNTs. The recovery of this particular composite is well demonstrated in Fig. 5.

The maximum shape recovery of 92% observed for the MWCNT blend composite is attributed to the high stored energy due to the fine dispersion of nanotubes in the blend. The shape recovery was tested by varying the polythiophene concentration from 0.3 to 1 wt%, and an increasing trend was noticed due to the increase in crystallinity. In addition to the crystallinity influence, the high electrical conductivity and mechanical properties due to modified MWCNT addition are also responsible for the good shape recovery in blend nanocomposite.

4.2 Conducting Fillers in Shape Memory

Conducting fillers such as carbon nanoparticles, fullerenes, carbon nanotubes (CNTs), graphene derivatives, and metal nanoparticles are added to various polymers to develop composites exhibiting good shape memory. The influence of CNT concentration and deformation temperature on the shape fixity and shape recovery ratio of epoxy composites was reported by Zhong et al. [35]. The samples were deformed at different temperatures, and the shape fixity was calculated based on the sample deformations. The results obtained are shown in Fig. 6. When deformed at 100 and 150 °C, the samples are in rubbery state and the deformation happens due to the conformational rotation of the network chains and all deformations are frozen by vitrification, whereas at 25 °C, the sample is at glassy state, and other than the conformational chain rotation, the deformation of C–C bonds and angles also occur

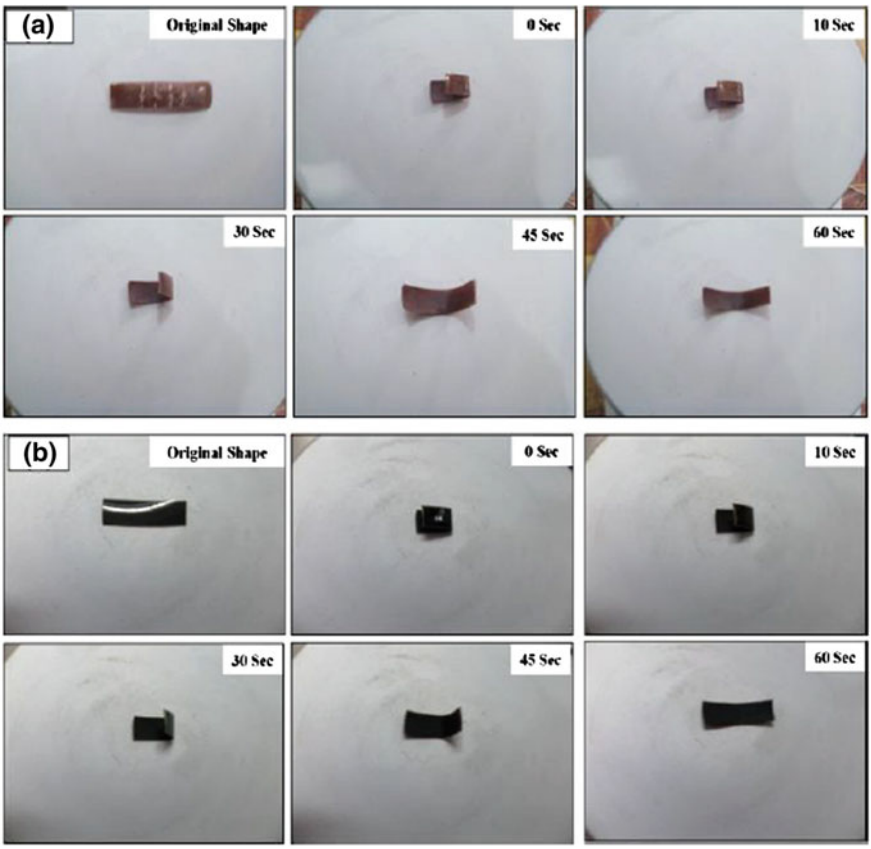

Fig. 5 Shape recovery of **a** PU/polythiophene containing 1 wt% of polythiophene **b** PU/1% polythiophene blend containing 3 wt% amine-functionalized MWCNT heated at 60 °C [34]. Copyright 2016. Reprinted under creative commons attribution license

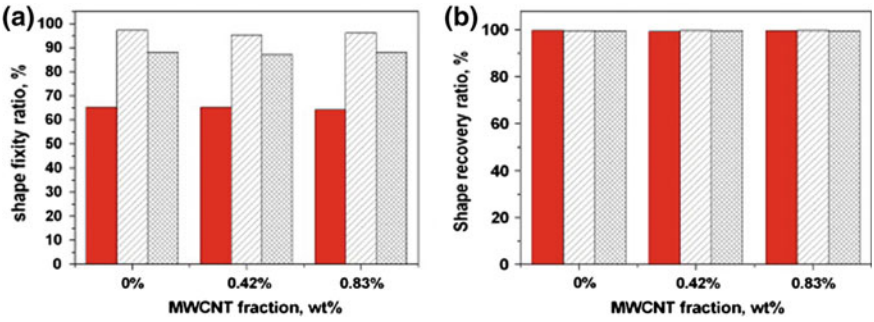

Fig. 6 The dependence of shape memory effects on the deformation temperature and weight percent of CNTs. (25 °C; 100 °C; 150 °C) [35]. Copyright 2013. Reprinted with the permission from Elsevier Ltd.

leading to poor shape fixity ratio. The results also indicate that the shape memory effect is little influenced by the CNT addition and change is mainly from the temperature-dependent characteristics of the polymer [35]. Moreover, the reinforcement of CNT becomes maximum at a specific temperature at which proper stiffness and good conformational motion of polymer chains are achieved.

CNTs prepared from carbon fibers by vapor growing were added to PU, and the composite specimens were tested for static tensile and thermomechanical cycle tests [12]. The stress at the maximum strain and the residual strain was increased when vapor-grown carbon fiber (VGCF) concentration added to PU was increased (1.7, 3.3, and 5 wt%) . During the first cycle, the strain recovery ratio was 80% for the PU/CNT composite and decreased with VGCF addition, whereas for the second cycle, it became 90% and subsequently increased to 95% at more number of cycles. This training effect for the shape memory polymer was well reported before as well [36, 37]. At 3.3 wt% VGCF weight fraction, the nanocomposite showed about twice recovery stress than the neat polymer. Thus, other than the shape memory application, the reported material is proposed to have sensibility to temperature as well. In another work, the CNTs were electrically induced into aligned chains in a polymer/carbon black composite where the CNTs serve as long-distance conductive channels capable of bridging the CB aggregations [38]. The electrical resistivity for the synthesized polymer composites containing chained CNTs was lowered 100 times when compared with composites containing randomly distributed CNTs. Such shape memory composites were actuated by very low electrical power.

Smart shape memory materials based on graphene and graphitic derivatives have recently attracted wider attention [39–43]. The shape recovery of the thermally responsive epoxy nanocomposite containing 0.1% of graphene was better compared to the neat polymer due to its lower cross-link density [44]. The graphene dispersion can strongly affect the shape memory property, and the poorly distributed graphene often hinders the crystallinity of the base polymers like PU [45]. The graphene modified with methanol enhanced the compatibility with PU, thus enhancing the shape recovery. However, such composites showed lower conductivity and thus the resistive heating efficiency. The three-dimensional shape memory behaviors for the polyimide and its composites with graphene are shown in Fig. 7 [46]. Here, glass transition temperature was used as the triggering temperature. Graphene addition has reduced the viscous deformation of the polyimide from 5 to 3% and enhanced the strain recovery rate from 89 to 96%.

By chemical oxidation–reduction method, uniform graphene distribution was achieved in epoxy polymer and high recovery stress and recovery time were obtained for all composites containing graphene from 0.5 to 2% [47]. Hybrid nanocomposites containing graphene and metal particles were also reported to be used as shape memory. For instance, synergic combination of thermally exfoliated reduced graphene oxide and the Iron(III) acetylacetonate nanoparticles was added to PU, and the ultra-fast shape recovery along with high thermal conductivity and mechanical property enables it to design magnetoresponsive shape memory polymers for multifunction applications [48]. For graphene oxide-filled PVA

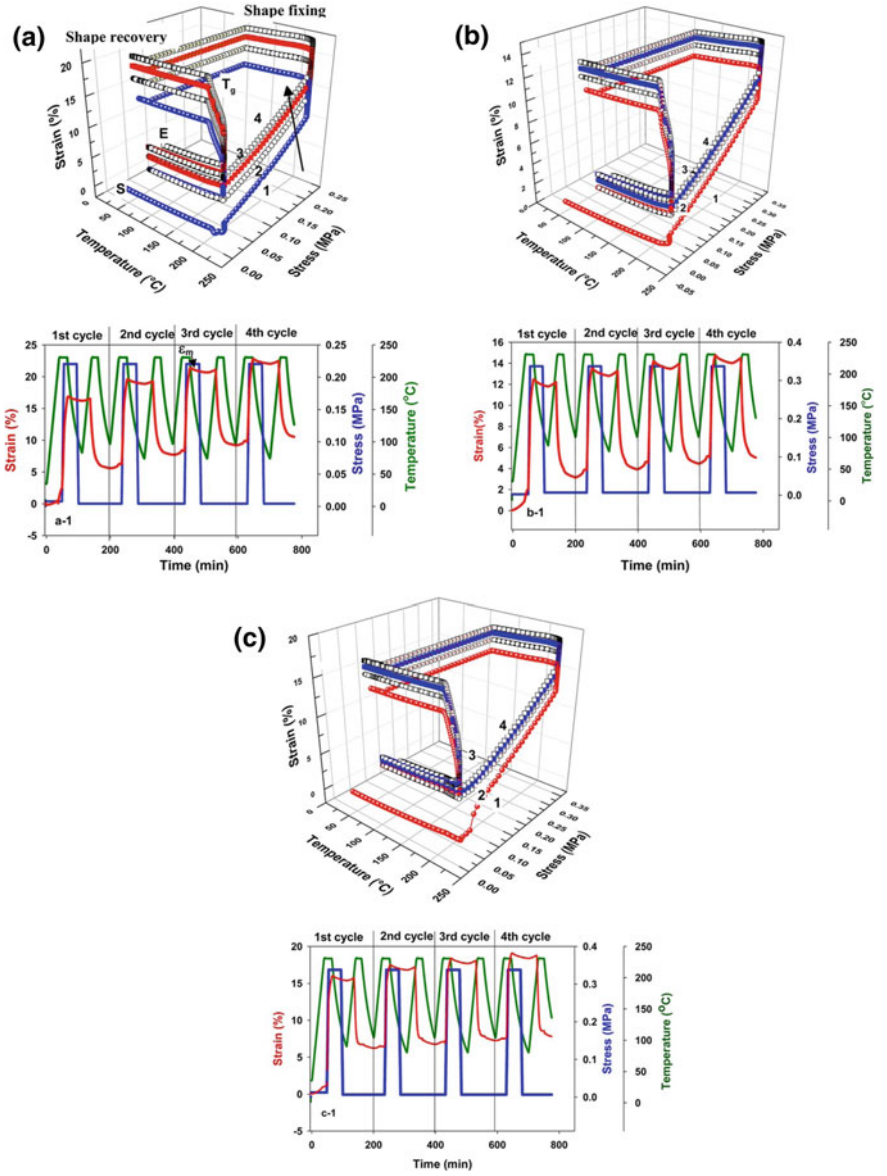

Fig. 7 **a** Three-dimensional shape memory stress–strain–temperature data of **a** neat polyimide, **b** 0.5 wt% polyimide graphene nanocomposite, and **c** 1 wt% polyimide graphene nanocomposite. Two-dimensional demonstration of change of strain and stress, with temperature and time **a-1** neat polyimide, **b-1** 0.5 wt% polyimide graphene nanocomposite, **c-1** 1 wt% polyimide graphene nanocomposite [46]. Copyright 2012. Reprinted with the permission from American Chemical Society

composites, water-induced shape recovery was also observed [49] due to the decrease in T_g and the polymer chain stiffness.

The thermoresponsive shape recovery of styrene-based shape memory polymers containing Ni (nickel) particles is reported by Lan et al. [50]. During preparation of the composite, an external magnetic field is applied so that perfectly aligned Ni chains are formed within the material. This causes the electrical resistivity of the samples to decrease and allows 80–85% recovery while Joule heating. However, the complete recovery in short time interval is still need to be investigated for the thermosetting styrene-based composite. Electrically conducting epoxy composites containing CNTs are reported recently by Liu et al. [51]. At 0.75% concentration of MWCNT, the recovery rate and all the mechanical properties were found to be enhanced. The material showed good cyclic stability.

4.3 *Electroactive Shape Memory*

The electroactive shape memory effect is observed when electrical field is applied to the composites for programming. The most important requirement of a sample to show the electroactive shape memory is the sample conductivity. As a stimulus, electricity enables resistive actuation of shape memory polymers containing conductive fillers. Such electrical triggering avoids external heating and enhances the technological potential of materials [52]. The review by Liu et al. [52] illustrates different polymer composites useful in electroactive shape memory. The composites include polymer reinforced with CNTs, electromagnetic fillers, metal particles, and their hybrid combinations.

The surface temperature change occurring in the polycaprolactone composite containing polyethylene glycol-modified MWCNT composites at various applied voltages along with shape recovery images is shown in the Fig. 8 [53]. The electroactive shape memory is compared with thermoactive effect showing a faster recovery in the latter case. The less recovery for electrical stimulus is due to the

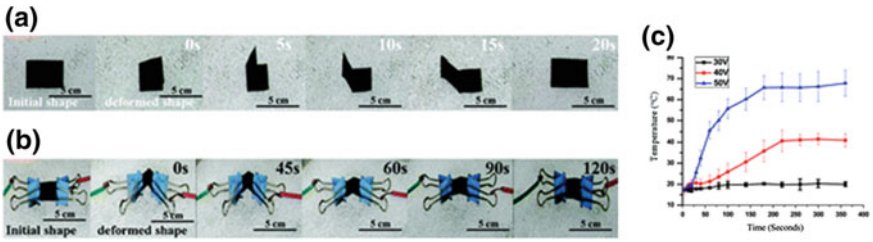

Fig. 8 Photographs showing shape recovery process of the cPCL/PEG-M samples **a** in the hot water at 55 °C and **b** in the supplied voltage 60 V and **c** temperature changes of the composites used as a function of decayed time when a constant voltage was applied to the samples [53]. Copyright 2010. Reprinted with the permission from American Chemical Society

slow heat loss and faster thermal transfer. However, the electroactive shape memory showed noticeable change when the sample is subjected to biodegradation. Comparing with the thermal stimulation (recovery ratio decreased by 22%), the electroactive method decreased the shape recovery ratio by 90% in 4 weeks of biodegradation. This can be attributed to the separation of the functionalized nanotube network within the polymer chains and thus loss in electrical conductivity. The effect of biodegradation and cytotoxicity confirms the material applicability in biomedical field.

Conducting PPy was added to PU block polymer by chemical oxidative polymerization method [8], and the shape recovery property was studied. At 6–20 wt% concentration of PPy, the conductivity of the composites was obtained in the order of 10^{-2} S/cm. The composite was deformed by heating above the transition temperature of 40–45 °C, and a good recovery of 80–90% was observed for the composite containing 20 wt% of PPy in 25 s when electrically triggered at 40 V. But for the composite containing 10 wt% of PPy, the recovery time was little higher (30 s). This substantiates the requirement of good electrical conductivity and minimum extent of elongation at break other than the high crystallinity of soft segments to show electroactive shape memory effect compared to thermally induced shape recovery.

Electroactive shape memory of the conducting PPy–MWCNT–PU composite synthesized by the chemical oxidative in situ polymerization of pyrrole in a surface layer of PU–MWCNT film was reported by Sahoo et al. [54]. The room temperature conductivity of the obtained composite was very high (about 0.098 S/cm), and by thermal heating, the sample was deformed. With the application of 25 V, the sample was recovered by 90–96% of its original shape in 20 s. They have also investigated the effect of applied voltage on surface temperature [55]. At less than 15 V, the sample was not able to be heated above the transition temperature. When the voltage was above 20 V, the surface temperature increased with time, and at 25 V, the sample was heated above 45 °C in 10 s. The authors confirmed that high degree of crystallinity for the soft segments as well as both high electrical conductivity and mechanical properties is the major requirements to achieve electroactive shape memory compared to thermomechanical shape memory effect.

In another study, the surface-modified MWCNT was added to PU/polylactic acid (PLA) by melt blending method, and the resultant composite was tested for the shape memory at 40 V [56]. In 5 s, about 95% of the deformed structure is recovered for both modified and unmodified CNT-filled PU/PLA blends. However, complete recovery of the modified CNT-filled sample took place in 15 s, but for the unmodified CNT-filled sample, 40 s was taken. By increasing the number of cycles, the recovery ratio decreased for both modified and unmodified nanocomposites. This is due to the molecular segment orientation in the direction of external force and thus the formation of frozen-in crystals on repeated cycling. The less deformation recovery ratio for the modified CNT-filled PU/PLA nanocomposite is caused by the rise in crystallization percentage. By electrical resistive Joule heating, the actuation of a shape recovery polymer filled with conducting porous carbon nanofiber paper is reported by Lu et al. [57]. The usual problems associated with the

shape memory property such as electrical resistive heating due to high-quantity filler, high voltage applied, and the inferior recovery effect were solved in their report by using carbon nanofibers and the styrene-based shape memory polymer matrix. With 1.2 g carbon nanofiber and a voltage of 12 V, complete shape recovery was achieved within 140 s. The final composite has good electroactive response as well as relatively better shape memory compared to all polymer composites containing conductive fillers.

Electric field-triggered shape recovery of the surface-functionalized MWCNT (5%)-filled PU at a constant voltage of 40 V was monitored, and complete recovery of the thermally deformed sample was achieved within 10 s [58]. The electrical conductivity in the order of 10^{-3} S cm^{-1} for the surface-modified MWCNT composites at 5 wt% was lower than that of the untreated MWCNT; however, it exhibited electroactive shape recovery with an energy conversion efficiency of 10.4% as well as improved mechanical properties. Nanodiamond in various percentages (ranging from 1 to 10 wt%) was added to PU to investigate the electroactive shape memory. The deformed sample in liquid nitrogen recovered 95% of its original shape in 40 s at a voltage of 40 V. Here, the authors have compared two synthesis methods—solution mixing and melt blending, and the latter showed comparatively lower recovery due to less conducting nature of the sample [59].

A synergic combination of carbon nanofiber and a few layer graphene (FLG) in the form of buckypaper was made, and the electrical actuation and optimization of temperature distribution of a typical shape memory polymer composite were tested by coating with the FLG/carbon nanofiber buckypaper [60]. The graphene enhanced the electrical conductivity, and the carbon nanofiber bridges the gaps among FLGs, thus again adding to the conductivity value. Electroactive shape memory was also reported by Liu et al. [61] in their developed polymer-infused conductive carbon scaffolds using reduced CNT and graphene compound aerogel as a scaffold and epoxy resin as a matrix. The 3D networks within the aerogel increase the conductivity (16 S m^{-1}) and make the material low dense (6 mg mL^{-1}). When such aerogels are added to epoxy matrix, the resultant composite displayed conductivity of 5.2 S m^{-1}, and other than shape memory device, the composite can be applied in designing electromagnetic shielding, actuators, and thermal sensors.

Epoxy resin is also strengthened by carbon nanofiber, and the final composite exhibited good shape recovery and the capability of high-speed electrical actuation [62]. Figure 9 shows the electroactive shape recovery of the composite. The sample conductivity of about 30.5 S/m was observed due to the large level of interconnections between carbon nanofibers and the negligible concentration (no free ends) of conducting nanofiber termini. The complete shape recovery in 2.1 s, at 20 V, is shown in Fig. 9a. Dramatically, faster recovery is observed with the increase in DC voltage as shown in Fig. 9b and is also in accordance with the standard sigmoidal function. The induction and recovery time as a function of applied voltage (Fig. 9c) show the significance of voltage in regulating the shape fixity and recovery. It is found that at 15 V, both induction and recovery time were the minimum.

Electrically triggered shape memory has been precisely controlled by achieving a quasi-state shape between the permanent and temporary shapes upon adjusting the

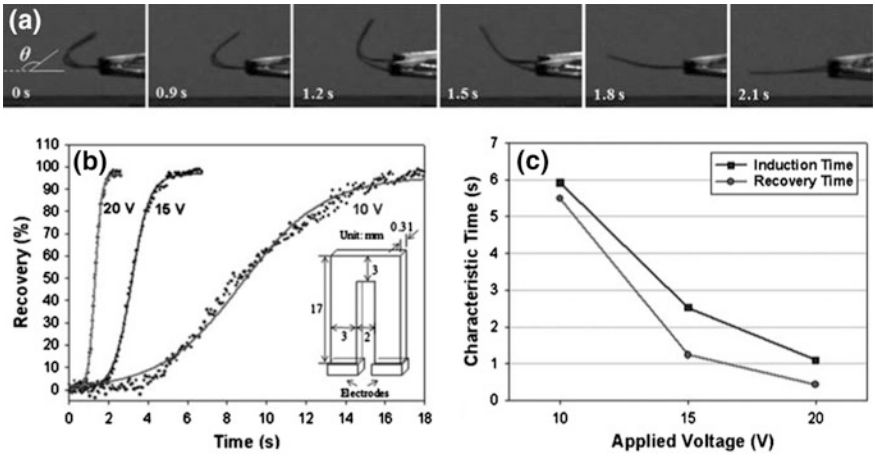

Fig. 9 Electroactive shape recovery of epoxy/carbon nanofiber nanocomposites. The sample has a "P"-shaped geometry, as in (**b**) *inset*. **a** Presents time-resolved photographs showing the fast recovery of the nanocomposite under 20 V DC voltage. **b** Shows the recovery profiles under 20, 15, and 10 V. The voltage was applied at time "0" for all the samples. The *solid lines* are fit curves using a three-parameter sigmoidal function. **c** Plots the induction and recovery times for the three voltages studied [62]. Copyright 2010. Reprinted with the permission from Royal Society of Chemistry

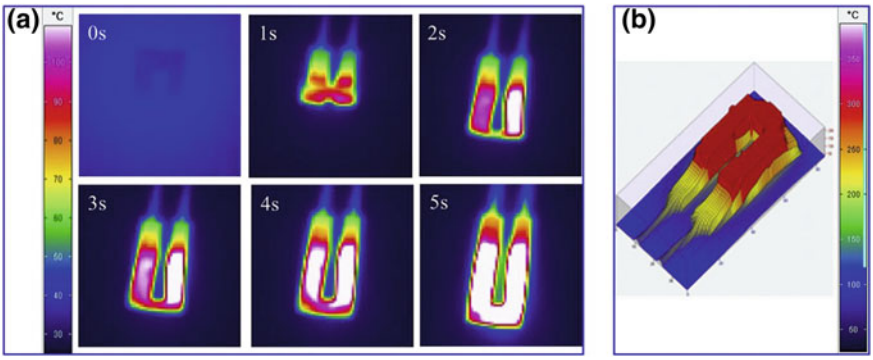

Fig. 10 Infrared thermal images of reduced graphene oxide paper/epoxy-based shape memory composite under 6 V **a** 2D surface temperature distribution of shape recovery photographs and **b** 3D surface temperature distribution photograph at 5 s [64]. Copyright 2015. Reprinted with the permission from Elsevier Ltd.

electrical energy input by Liang et al. [63]. They have investigated the synergistic effect of carbon nanofiber and carbon nanofiber paper on the shape recovery of epoxy polymer and successfully come up with faster, accurate, and repeatable recovery. Using the same base epoxy polymer, good electrical actuation was achieved with the incorporation of reduced graphene oxide paper as well [64]. For the composite, complete shape recovery was noticed at 6 V within 5 s.

Figure 10 shows the shape recovery and the surface temperature distributions monitored for the sample through an infrared thermal camera. As shown in Fig. 10a, the temperature increases to 102.39 °C with an increased temperature of 74.8 °C compared to the temperature at 1 s. The temperature increase is above T_g, and the uniform distribution of temperature is observed by the maximum red color in Fig. 10b. This also proves the uniform electric heating performance of the composite sample. They have also observed that the shape recovery time at 4 V is about 5 times higher than that at 6 V, good energy efficiency at lower voltages. The lower recovery time at higher voltage is attributed to the high entropy achieved at higher voltages (temperature).

Combination of in situ generated silver nanoparticles, carbon black, and carbon nanofibers was used to reinforce epoxy matrix [65]. For neat epoxy, the resistivity was about 10^{16} Ω cm, whereas with 4 wt% carbon black, the value became 10^{3} Ω cm. Both carbon black and nanofiber reduced the glass transition temperature of the matrix, and above T_g, the surface temperature of carbon black nanocomposite was rapidly increased, with proper voltage. While carbon black reduced the stiffness and yield properties of epoxy, silver nanoparticles improved the flexural yield stress. In the final composite, silver particles stabilized the surface temperature at higher voltages and prevented the thermal degradation of the sample.

Functionalized CNTs decorated with Cu (copper) particles were reported to enhance the shape recovery of PLA composites [66]. A solution dispersion

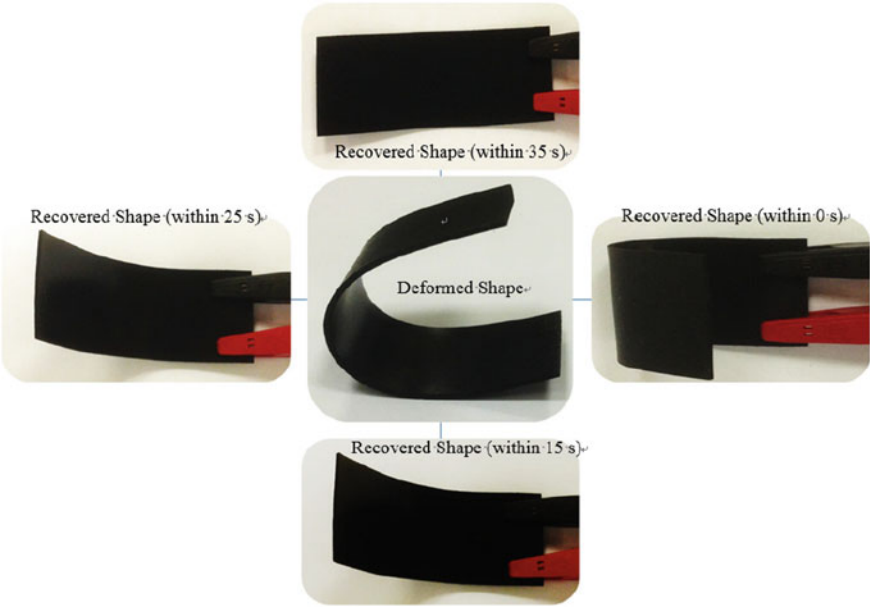

Fig. 11 Electroactive shape recovery behavior of the Cu-CNT dispersed PLA/epoxidized soybean oil nanocomposite (Cu-CNTs content of 2 wt%) at a DC voltage of 40 V [66]. Copyright 2015. Reprinted under creative commons attribution license

blending followed by solvent casting was applied to prepare the composite containing 1–3 wt% of Cu-CNT and PLA/epoxidized soybean oil in 9:1 ratio. The sample was deformed to U-shape by heating them in hot water and then electrically triggered at 40 V (Fig. 11). Composite containing 2 wt% of the filler exhibited a prompt recovery in 35 s due to more efficient and fast heat conduction though the composite. At 2 wt%, maximum filler dispersion decreased the polymer–filler interfacial contact electrical resistance and enhanced the electrical conductivity. This caused faster transfer of electrons within the composite, and thus, the Joule heating during electrical actuation is dominated.

Very recently, the advantages of 3D porous CNT were effectively utilized to achieve faster electrical actuation [67]. At 0.2 wt% of CNT, electrical conductivity of 1.29 S/cm was obtained for the composite. The nanocomposite recovered its shape in 21 s when triggered by a voltage of 7.5 V. At 10 V, the recovery time was reduced to 10 s. In addition to the experimental results, theoretical simulations were also done using the finite element method to investigate the Joule heating and thermal transport process.

5 Conclusion

Shape recovery of a typical polymer nanocomposite can be arranged through the modification of the structure of the material. Examples of modifications include chain conformations within the polymer, dispersion of the nanoparticles, and their orientation [68]. Various conducting polymer composites have proved their significance in attaining good shape recovery. In this chapter, we review some of the developments in this particular area of conducting composites in shape recovery. Also, we discuss the basics of shape memory and the shape recovery of the conducting polymers, fillers, and their composites. Electrically triggered or electroactive shape memory are also presented. The chapter explains composites possessing conductivity and the role of electrical conductivity in shape memory.

Acknowledgment This publication was made possible by NPRP grant 6-282-2-119 from the Qatar National Research Fund (a member of Qatar Foundation). The statements made herein are solely the responsibility of the authors.

References

1. Meng H, Li G (2013) A review of stimuli-responsive shape memory polymer composites. Polymer 54:2199–2221
2. Vechambre C, Buleon A, Chaunier L, Gauthier C, Lourdin D (2011) Understanding the mechanisms involved in shape memory starch: macromolecular orientation. Stress recovery and molecular mobility. Macromolecules 44(23):9384–9389

3. Du FP, Ye EZ, Yang W, Shen TH, Tang CY, Xie XL, Zhou XP, Law WC (2015) Electroactive shape memory polymer based on optimized multi-walled carbon nanotubes/polyvinyl alcohol nanocomposites. Compos B 68:170–175
4. Lau KT, Wong TT, Leng JS, Hui D, Rhee KY (2013) Property enhancement of polymer based composites at cryogenic environment by using tailored carbon nanotubes. Compos Part B 54:41–43
5. Jiang Q, Wang X, Zhu YT, Hui D, Qiu YP (2014) Mechanical, electrical and thermal properties of aligned carbon nanotube/polyimide composites. Compos Part B 56:408–412
6. Du FP, Ye EZ, Tang CY, Ng SP, Zhou XP, Xie XL (2013) Microstructure and shape memory effect of acidic carbon nanotubes reinforced polyvinyl alcohol nanocomposites. J Appl Polym Sci 129(3):1299–1305
7. Higgins MJ, Grosse W, Wagner K, Molino PJ, Wallace GG (2011) Reversible shape memory of nanoscale deformations in inherently conducting polymers without reprogramming. J Phys Chem B 115:3371–3378
8. Sahoo NG, JungYC Goo NS, Cho JW (2005) Conducting shape memory polyurethane-polypyrrole composites for an electroactive actuator. Macromol Mater Eng 290:1049–1055
9. Rana S, Kim SD, Cho JW (2013) Conducting core-sheath nanofibers for electroactive shape-memory applications. Polym Adv Technol 24:609–614
10. Zarek M, Layani M, Cooperstein I, Sachyani E, Cohn D, Magdassi S (2015) 3D Printing of shape memory polymers for flexible electronic devices. Adv Mater 28(22):4449–4454
11. Behl M, Lendlein A (2007) Shape-memory polymers. Mater Today 10(4):20–28
12. Ni QQ, Zhang C, Fu Y, Dai G, Kimura T (2007) Shape memory effect and mechanical properties of carbon nanotube/shape memory polymer nanocomposites. Compos Struct 81 (2):176–184
13. Leng J, Lan X, Liu Y, Du S (2011) Shape-memory polymers and their composites: stimulus methods and applications. Prog Mater Sci 56:1077–1135
14. Gurunathan K, Vadivel Murugan A, Marimuthu R, Mulik UP, Amalnerkar DP (1991) Electrochemically synthesized conducting polymeric materials for applications towards technology in electronics, optoelectronics and energy storage devices. Mater Chem Phys 61:173–191
15. Sadasivuni KK, Ponnamma D, Kasak P, Krupa I, Al-Maadeed MASA (2014) Designing dual phase sensing materials from polyaniline filled styrene–isoprene–styrene composites. Mater Chem Phys 147(3):1029–1036
16. Inzelt G (2008) Chemical and electrochemical syntheses of conducting polymers. In: Conducting polymers, a new era in electrochemistry. Springer, Berlin
17. Kesik M, Akbulut H, Söylemez S et al (2014) Synthesis and characterization of conducting polymers containing polypeptide and ferrocene side chains as ethanol biosensors. Polym Chem 5:6295–6306
18. Sadasivuni KK, Ponnamma D, Thomas S, Grohens Y (2014) Evolution from graphite to graphene elastomer composites. Prog Polym Sci 39(4):749–780
19. Ponnamma D, Sadasivuni KK, Grohens Y, Guo Q, Thomas S (2014) Carbon nanotube based elastomer composites–an approach towards multifunctional materials. J Mat Chem C 2 (40):8446–8485
20. Peng C, Zhang S, Jewell D, Chen GZ (2008) Carbon nanotube and conducting polymer composites for supercapacitors. Prog Nat Sci 18:777–788
21. Riaz U, Ashraf SM (2013) Conductive polymer composites and blends: recent trends. In: Thomas S, Shanks R, Chandrasekharakurup S (eds) Nanostructured polymer blends. Elsevier, Amsterdam
22. Balint R, Cassidy NJ, Cartmell SH (2014) Conductive polymers: Towards a smart biomaterial for tissue engineering. Actabiomaterialia 10:2341–2353
23. Olad A, Rashidzadeh A (2008) Preparation and characterization of polyaniline/$CaCO_3$ composite and its application as anticorrosive coating on iron. Iran J Chem Eng 5(2):45–54

24. Mierczynska A, Mayne-L'Hermite M, Boiteux G, Jeszk JK (2007) Electrical and mechanical properties of carbon nanotube/ ultrahigh-molecular-weight polyethylene composites prepared by a filler prelocalization method. J Appl Polym Sci 105(1):158–168
25. Eswaraiah V, Sankaranarayanan V, Ramaprabhu S (2011) Functionalized graphene–PVDF foam composites for EMI shielding. Macromol Mater Eng 296(10):894–898
26. Kim H, Abdala AA, Macosko CW (2010) Graphene/polymer nanocomposites. Macromolecules 43:6515–6530
27. Lu J, Moon KS, Wong CP (2008) Silver/polymer nanocomposite as a high-k polymer matrix for dielectric composites with improved dielectric performance. J Mater Chem 18:4821–4826
28. Gök A, Sarı B, Talu M (2003) Synthesis and characterization of novel polyfuran/poly (2-iodoaniline) conducting composite. J Appl Polym Sci 89(10):2823–2830
29. Ahmed F, Kumar S, Arshi N, Anwar MS, Su-Yeon L, Kil GS, Park DW, Koo BH, Lee CG (2011) Preparation and characterizations of polyaniline (PANI)/ZnO nanocomposites film using solution casting method. Thin Solid Films 519(23):8375–8378
30. Thomas D, Simon SA, Sadasivuni KK, Ponnamma D, Yaser AA, Cabibihan JJ, Vijayalakshmi KA (2016) Microtron irradiation induced tuning of band gap and photoresponse of Al-ZnO thin films synthesized by mSILAR. J Electron Mat 1–7
31. Marcovich NE, Auad ML, Bellesi NE, Nutt SR, Aranguren MI (2006) Cellulose micro/nanocrystals reinforced polyurethane. J Mater Res 21(04):870–881
32. Auad ML, Richardson T, Orts WJ, Medeiros ES, Mattoso LHC, Mosiewicki MA, Marcovich NE, Aranguren MI (2011) Polyaniline modified cellulose nanofibrils as reinforcement of a smart polyurethane. Polym Int 60(5):743–750
33. Casado UM, Quintanilla RM, Aranguren MI, Marcovich NE (2012) Composite films based on shape memory polyurethanes and nanostructured polyaniline or cellulose–polyaniline particles. Synth Met 162(17–18):1654–1664
34. Sattar R, Kausar A, Siddiq M (2016) Influence of conducting polymer on mechanical, thermal and shape memory properties of polyurethane/polythiophene blends and nanocomposites. Adv Mater Lett 7(4):282–288
35. Li H, Zhong Z, Meng J, Xian G (2013) The reinforcement efficiency of carbon nanotubes/shape memory polymer nanocomposites. Compos B Eng 44(1):508–516
36. Tobushi H, Hayahi S, Ikai A, Hara H, Miwa N (1996) Shape fixity and shape recoverability in a film of shape memory polymer of the polyurethane series. Trans Jpn Soc Mech Eng A 62:1291–1298
37. Ohki T, Ni QQ, Ohsako N, Iwamoto M (2004) Mechanical and shape memory behavior of composites with shape memory polymer. Compos A 35:1065–1073
38. Yu K, Zhang Z, Liu Y, Leng J (2011) Carbon nanotube chains in a shape memory polymer/carbon black composite: to significantly reduce the electrical resistivity. Appl Phys Lett 98:074102
39. Li C, Qiu L, Zhang B, Li D, Liu CY (2016) Robust vacuum-/air-dried graphene aerogels and fast recoverable shape-memory hybrid foams. Adv Mater 28(7):1510–1516
40. Das R, Banerjee SL, Kundu PP (2016) Fabrication and characterization of in situ graphene oxide reinforced high-performance shape memory polymeric nanocomposites from vegetable oil. RSC Adv 33:27648–27658
41. Kashif M, Chang YW (2015) Supramolecular hydrogen-bonded polyolefin elastomer/modified graphene nanocomposites with near infrared responsive shape memory and healing properties. Eur Polymer J 66:273–281
42. Taherzadeh M, Baghani M, Baniassadi M, Abrinia K, Safdari M (2016) Modeling and homogenization of shape memory polymer nanocomposites. Compos B Eng 91:36–43
43. Zhao Q, Qi HJ, Xie T (2015) Recent progress in shape memory polymer: new behavior, enabling materials, and mechanistic understanding. Prog Polym Sci 49:79–120
44. Williams T, Meador M, Miller S, Scheiman D (2011) Effect of graphene addition on shape memory behavior of epoxy resins. NASA technical reports

45. Park JH, Dao TD, Lee HI, Jeong HM, Kim BK (2014) Properties of graphene/shape memory thermoplastic polyurethane composites actuating by various methods. Materials 7(3): 1520–1538
46. Yoonessi M, Shi Y, Scheiman DA, Lebron-Colon M, Tigelaar DM, Weiss RA, Meador MA (2012) Graphene polyimide nanocomposites; thermal, mechanical, and high-temperature shape memory effects. ACS Nano 6(9):7644–7655
47. Zhao LM, Feng X, Li YF, Mi XJ (2014) Shape memory effect and mechanical properties of graphene/epoxy composites. Polym Sci Ser A 56(5):640–645
48. Lee SH, Jung JH, Oh IK (2014) 3D networked graphene-ferromagnetic hybrids for fast shape memory polymers with enhanced mechanical stiffness and thermal conductivity. Small 10 (19):3880–3886
49. Qi X, Yao X, Deng S, Zhou T, Fu Q (2014) Water-induced shape memory effect of graphene oxide reinforced polyvinyl alcohol nanocomposites. J Mater Chem A 2:2240–2249
50. Lan X, Liu Y, Leng J (2009) Electrically conductive shape-memory polymer filled with Ni powder chains. Proc SPIE 7287:72871S
51. Liu Y, Zhao J, Zhao L, Li W, Zhang H, Zhang Z (2016) High performance shape memory epoxy/carbon nanotube nanocomposites. ACS Appl Mater Interfaces 8:311–320
52. Liu Y, Lv H, Lan X, Leng J, Du S (2009) Review of electro-active shape-memory polymer composite. Compos Sci Technol 69:2064–2068
53. Xiao Y, Zhou S, Wang L, Gong T (2010) Electro-active shape memory properties of poly (ε-caprolactone)/functionalized multiwalled carbon nanotube nanocomposite. ACS Appl Mater Interfaces 2(12):3506–3514
54. Sahoo NG, Jung YC, Cho JW (2007) Electroactive shape memory effect of polyurethane composites filled with carbon nanotubes and conducting polymer. Mater Manuf Processes 22 (4):419–423
55. Sahoo NG, Jung YC, Yoo HJ, Cho JW (2007) Influence of carbon nanotubes and polypyrrole on the thermal, mechanical and electroactive shape-memory properties of polyurethane nanocomposites. Compos Sci Technol 67(9):1920–1929
56. Mohan R, Ryu SH, Shanmugharaj AM (2013) Thermal, mechanical and electroactive shape memory properties of polyurethane (PU)/poly (lactic acid) (PLA)/CNT nanocomposites. Eur Polymer J 49(11):3492–3500
57. Lu H, Liu Y, Gou J, Leng J, Du S (2010) Electroactive shape-memory polymer nanocomposites incorporating carbon nanofiber paper. Int J Smart Nano Mat 1(1):2–12
58. Cho JW, Kim JW, Jung YC, Goo NS (2005) Electroactive shape-memory polyurethane composites incorporating carbon nanotubes. Macromol Rapid Commun 26(5):412–416
59. Kausar A (2015) Effect of nanofiller dispersion on morphology, mechanical and conducting properties of electroactive shape memory Poly(urethane-urea)/functional nanodiamond composite. Adv Mat Sci 15(4):46
60. Lu H, Gou J (2012) Study on 3-D high conductive graphene buckypaper for electrical actuation of shape memory polymer. Nanosci Nanotechnol Lett 4(12):1155–1159
61. Liu X, Li H, Zeng Q, Zhang Y, Kang H, Duan H, Guo Y, Liu H (2015) Electro-active shape memory composites enhanced by flexible carbon nanotube/graphene aerogels. J Mater Chem A 3:11641–11649
62. Luo X, Mather PT (2010) Conductive shape memory nanocomposites for high speed electrical actuation. Soft Matter 6:2146–2149
63. Liang F, Sivilli R, Gou J, Xu Y, Mabbott B (2013) Electrical actuation and shape recovery control of shape-memory polymer nanocomposites. Int J Smart Nano Mat 4(3):167–178
64. Wang W, Liu D, Liu Y, Leng J, Bhattacharyya D (2015) Electrical actuation properties of reduced graphene oxide paper/epoxy-based shape memory composites. Compos Sci Technol 106:20–24
65. Dorigato A, Giusti G, Bondioli F, Pegoretti A (2013) Electrically conductive epoxy nanocomposites containing carbonaceous fillers and in-situ generated silver nanoparticles. eXPRESS Polym Lett 7(8):673–682

66. Alam J, Khan A, Alam M, Mohan R (2015) Electroactive shape memory property of a Cu-decorated CNT dispersed PLA/ESO nanocomposite. Materials 7:6391–6400
67. Zhou G, Zhang H, Xu S, Gui X, Wei H, Leng J, Koratkar N, Zhong J (2016) Fast triggering of shape memory polymers using an embedded carbon nanotube sponge network. Sci Rep 6:24148
68. Ponnamma D, Sadasivuni KK, Strankowski M, Moldenaers P, Thomas S, Grohens Y (2013) Interrelated shape memory and Payne effect in polyurethane/graphene oxide nanocomposites. RSC Adv 3(36):16068–16079

Functional Nanomaterials for Transparent Electrodes

Bananakere Nanjegowda Chandrashekar, A.S. Smitha, K. Jagadish, Namratha, S. Srikantaswamy, B.E. Kumara Swamy, Kishor Kumar Sadasivuni, S. Krishnaveni, K. Byrappa and Chun Cheng

Abstract In recent years, extensive progress has been made in the development of primary and applied aspects of fabrication of transparent conductive electrodes especially in flexible, stretchable, low-cost, and lightweight electrode materials for the enhancement of energy generation devices. Fabrication of high-performance transparent conductive flexible plastic is necessary for industrial-scale manufacturing with an extensive range of applications. Transparent electrodes (TE's) are optically transparent to visible light and are electrically conductive. These qualities are important for

B.N. Chandrashekar and A.S. Smitha both have equal contribution.

B.N. Chandrashekar · C. Cheng (✉)
Department of Materials Science and Engineering, Shenzhen Key Laboratory of Nanoimprint Technology, South University of Science and Technology, Shenzhen 518055, People's Republic of China
e-mail: chengc@sustc.edu.cn

B.N. Chandrashekar (✉) · K. Jagadish · Namratha · S. Srikantaswamy · K. Byrappa (✉)
Center for Materials Science and Technology, Vijnana Bhavan, University of Mysore, Manasagangothri, Mysuru 570006, India
e-mail: chandrashekarbn1984@gmail.com

K. Byrappa
e-mail: kbyrappa@gmail.com

S. Krishnaveni
Department of Studies in Physics, University of Mysore, Mysuru, India

A.S. Smitha · S. Krishnaveni
Department of Electronics, Yuvaraja's College, University of Mysore, Manasagangothri, Mysuru 570006, India

B.E. Kumara Swamy
Department of P.G. Studies and Research in Industrial Chemistry, Kuvempu University, Shankaraghatta, 577 451 Shimoga, Karnataka, India

K.K. Sadasivuni
Department of Mechanical and Industrial Engineering, Qatar University, P.O. Box 2713, Doha, Qatar

D. Ponnamma et al. (eds.), *Smart Polymer Nanocomposites*,
Springer Series on Polymer and Composite Materials,
DOI 10.1007/978-3-319-50424-7_13

many renewable energy conversion processes. As transparent electrodes, they are widely used in industry, especially in optoelectronic devices. TE's are essential components for touch panels, organic photovoltaic (OPV) cells, liquid crystal displays (LCDs), and organic light-emitting diodes (OLEDs). Functionalized nanomaterials having the characteristic properties such as flexible, stretchable, and lightweight-based TE's are promising substitutes for commonly used indium tin oxide (ITO)-based TE's for future flexible optoelectronic devices. This chapter broadly summarizes recent developments in the fabrication, properties, modification, patterning, and integration of functionalized nanomaterials for the applications of optoelectronic devices. Their challenges and potential applications, such as in touch panels, optoelectronic devices, liquid crystal displays, and photovoltaic cells, are discussed in detail. Despite many challenges, nanomaterials such as carbon nanotube and graphene TE's have exhibited various applications in optoelectronic devices and some commercially available products such as touch panels of smartphones. An account of recent developments in the fabrication, performance, and significant opportunities for the industrially used transparent conductive electrode, followed by a brief introduction, is provided.

Keywords Transparent electrode · Graphene · Carbon nanotube · Optoelectronic devices

Contents

1 Introduction

Today, the demand for transparent screens is enormous and growing rapidly. The touch-screen-based electronics have changed human life to a greater extent. From the beginning, electronics follows the Moore's law, i.e., smaller electronic elements based on the semiconducting materials such as silicon. Currently, the frontier of electronics mainly depends on the large-scale microchip industries that cost billions of dollars. However, there are some approaches to improve the current technologies from hybrid functional nanomaterials. Perhaps, the most interesting among these new directions lightweight, small, portable electronic devices such as smart tablets and wearable devices have become widespread in everyday life. Large-area power sources such as solar cells and rechargeable batteries will be required for a long-time operation, and a significant demand for large is for transparent displays. Thus, flexible and transparent device components are a key technology for the development of future portable devices that could be folded and placed in a pocket and then opened out at the time of use, such as a newspaper or magazine. Many electronic devices are manufactured on transparent, conductive substrates; such devices include displays and solar cells. The most commonly used transparent conductive substrates are doped metallic oxide glass, and indium tin oxide (ITO) glass is used most frequently. However, present electronic devices are heavy and cannot be folded, because of the heavy and brittle nature of ITO glasses [1–4].

Meanwhile, from the application point of view, flexibility is one of the additional requirements for transparent conductive films [TCFs]. The main material used in TCF on a commercial scale is the tin-doped indium oxide (ITO) layer showing lowest resistivity, which is a prevailing material in flat-panel displays. Nowadays, vacuum process is frequently used to deposit ITO films. However, this process requires costly equipment and can cause the release of material waste. Furthermore, ITO films are too brittle to be used in flexible devices and exempted their use in flexible devices [5]. Apart from that, indium is a scarce material, causing fluctuations in ITO costs [6]. Due to these reasons, there is a delay in the new production and innovation of TCFs based on ITO materials. The advanced markets are desired for curved screens and flexible transparent conductive materials having optoelectronic performance which can be fabricated easily at low cost on plastic substrates. Thus, the disadvantages of ITO prompted several efforts in discovering substitute materials to use in electrically conductive, transparent, flexible materials such as carbon-based nanomaterials, zinc oxide (ZnO)-based transparent-conducting oxides [11–13], graphene [9, 10] and nanotubes [7, 8]), nanowire grids [18, 19], metal microgrids [16, 17], noble metals (Au, Ag) [14, 15], and graphene–silver nanowire (NW) hybrids [20]. The noble metals exhibit flexibility, stretchability, transmittance, and superior conductivity but these are uncompetitive for low-cost transparent conductor's devices due to expensive and their abundance.

Recent reports suggest the similar performance for noble metal NWs to ITO; for instance, the Ag NWs showed high transparency with low sheet resistance (R_s) higher than the performance of ITO [21]. Spin coating or vacuum transfer processes

were practiced to deposit Ag NWs on flexible substrates [16, 22, 23]. But the mass production of Ag-based optoelectronic devices is often hindered by the high cost of this material. Copper (Cu) is another candidate for TCFs due to its high intrinsic conductivity and Cu NWs can replace ITO and Ag NWs. In addition, Cu is abundant and less expensive with only 6% less conductivity when compared to silver [24]. The high electric conductivity and high optical transmittance are reported for Cu NW films [25–27]. Though the Cu NWs have much significance, their easiness to get oxidized at ambient conditions affects the stability and needs to be improved. The carbon-based nanomaterials such as graphene and carbon nanotubes (CNTs) also did not show relatively higher optoelectronic performance compared to ITO [28, 29]. But they have all special properties required to fabricate the miniaturized electronics. The advantageous properties of using graphene as a transparent electrode are important when approaching realistic applications [30–39]. The prospective applications of graphene as electrodes in an extensive range of devices including light-emitting diodes [35–37], touch screens [33], organic memories [31], organic solar cells [38, 39], field-effect transistors [30], molecular junction devices [32], and liquid crystal displays [34] have been reported. However, graphene films need to be further modified to ensure such applications, via synthesis [40–43], tuning of their work functions [44, 45], transfer [46, 47], and doping [33, 48, 49]. In this chapter, we report recent research progress on functional nanomaterials as promising conductive transparent materials. Finally, it covers the functional nanomaterial synthesis, methods to fabricate TCFs, and their wide range of applications based on the optoelectronic properties.

2 Functional Materials

Since the discovery of nanomaterials, its unusual properties have been exploring the vast applications in electronic industry. The synthesis, purification, and analysis of nanomaterials have an important role on their properties. Currently, researcher has been motivated into the enhancement of mechanical, thermal, optical, and electrical properties of nanomaterials and their composite films. Very recently, researchers are involving in searching alternative material for the replacement of ITO as a transparent electrode. Few functional materials such as silver nanowires, copper nanowires, carbon nanotube, and graphene are possessing good flexibility and transparency, which paved their way to fabricate the flexible and transparent electrodes. These unique nanomaterials show excellent elastic modulus and yield strength, irrespective of their relative electrical conductivity as compared to the standard ITO films. Moreover, it can be easily dispersed in common solvents by simple ways. Hence, simpler and lower-cost techniques can be applied to fabricate the thin-film electrodes. In addition, solution-based processing method is compatible with roll-to-roll coating techniques, which enhance to produce a large-scale industrial production of transparent electrodes. Two-dimensional (2D) carbon allotrope graphene becomes novel kind with a unique band structure, excellent thermal,

mechanical, and electrical properties [50]. Besides, high electron mobility and high transmittance of graphene is a well-known property [50, 51]. Transparent electrodes of graphene have much interest in research nowadays, and there have been much efforts to utilize this terrific property [52]. In the transparent electrode fabrication, several methods have been reported [53] and synthesis of graphene is the most important issue. Currently, chemical vapor deposition (CVD) techniques have been documented as the most promising method for the preparation of flexible transparent electrode. But multilayer graphene films are necessary for electrodes, with high resistance value fabricated by complicated multiple growth and transfer processes [51]. For the achievement of outstanding electrical and optical properties of transparent flexible electrodes, combination of graphene with other conducting material is necessary [54]. Combination of CVD-grown graphene with microstructure of metal has been reported. For instance, Ag nanowires and graphene combination has been reported for the fabrication of flexible transparent electrode [55]. The difficulty of distribution of Ag NWs on film limits its additional developments. Thus, the hybrid electrodes reduce the resistance in one side and improve the flexibility on the other side. High in-plane electrical conductivity, easy and low-cost processing, and high mechanical compliance demonstrate potential applications for flexible electrodes. Flexibility of transparent electrode materials can be enhanced by combining with elastomeric polymer substrates, such as polydimethylsiloxane, poly(ethylene terephthalate) and polyimide to fabricate highly stretchable and flexible electrodes.

3 Metal Wire-Based Transparent Conductive Films

3.1 Synthesis of Copper Nanowires (CuNWs)

Vacuum thermal decomposition [56], chemical vapor deposition [57], and electro-spinning [58] methods were used for Cu NWs synthesis. In the last decades, hydrothermal synthesis [59], reduction of a precursor solution [60], and catalytic synthesis [61] are mostly used to synthesize NWs including chemical solution methods (CSMs). CSMs have become favorable advantages such as the feasibility of large-scale production, larger choice of precursors, and the conditions of the solvents and reactions over other methods. Synthesis of Cu NW at low temperature by CSMs at ambient conditions is easier than vacuum-vapor processes in terms of scaling-up and commercialization. Using reducing agent, metal ions transform into metal atoms and a capping agent was utilize to bring metal atoms into the NWs in all CSMs.

3.2 Fabrication of Cu NW Thin Films

Copper nanowires should be deposited on a substrate to manufacture TCFs that can be potentially replacing the dominant transparent conductor. The methods adopted to

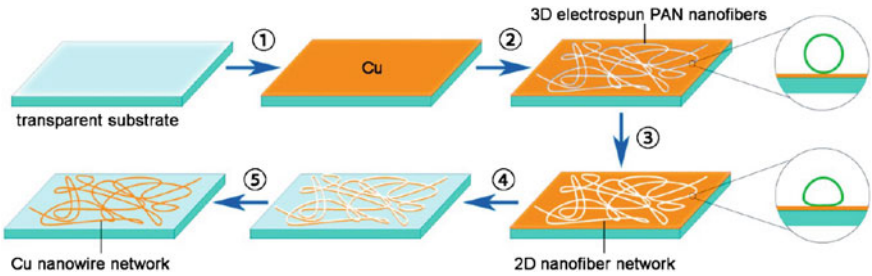

Fig. 1 Scheme of copper nanowire network electrode fabrication. (*1*) Electron-beam deposition of a copper film on the transparent substrate. (*2*) Electrospin PAN nanofibers on the copper-covered substrate. (*3*) Solvent vapor annealing. The insets show the schematic fiber cross-sectional shapes before and after solvent vapor annealing. (*4*) Metal etching. (*5*) Removal of PAN fibers by dissolution [64]. Copyright 2014. Reproduced with permission from American Chemical Society

obtain thin films regardless of the types of materials are reported by many groups such as vacuum filtration [62, 63], spin coating [64–66], Meyer rod coating [67], nitrocellulose-based ink printing [68, 69], drop-spray coating [70, 71], and vacuum filtration and spray deposition [72]. Generally, the fabricated TCFs show high sheet resistance value due to contact resistance (R_s) between NWs. However, solving this sheet resistance problem is the major challenge for the researchers, and different methods to reduce contact resistance to attain lower R_s values of nanowire networks have been suggested. He et al. [64] reported that Cu NW electrodes fabricated using electrospun fibers to get an excellent mechanical and transparency properties of material. We can understand from Fig. 1 that metal NW connected completely as a pattern which leads to creating high-conductivity networks using electrospun nanofiber fabrication method. In virtue of the superior results compared to the performance of ITO along with the low cost and possibility of mass production, replacement of ITO-based devices with metal NWs is believed to happen in the near future. Reduction of R_s using ultrafast plasmonic nanoscale welding was developed using a polarized laser under ambient conditions. Initially the formation of percolation networks for the NWs on different substrates follows laser irradiation due to the plasmonic effect laser-induced heat at the junctions of each NW generated. As a result, the NW junctions were welded together and resulted in the R_s of Cu NW. TCFs can be reduced significantly [62]. NW alignment is responsible for the improvement of the electrical performance of NW TCFs. Kang et al. [73] fabricated transparent electrodes using Ag NWs (Fig. 2) by developing capillary printing technique. The solution of Ag NW was deposited and spread to produce uniformly aligned NWs by controlling the nanochannels. The conductivity and transmittance of the film improved the lower percolation threshold of aligned NWs, even though processing was applied for the alignment of Ag NW and Cu NWs. In addition, optothermal heating [74], thermal annealing [75], and mechanical pressing [76, 77] reported progressing electrical performance of silver nanowire electrodes, and it can be applied to copper nanowire electrodes as well. However, the point to be considered is the easiness of Cu to

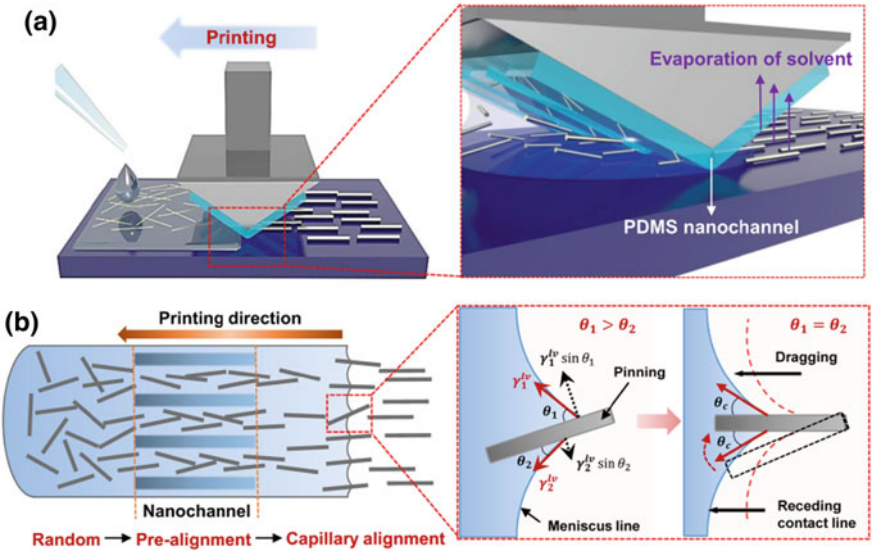

Fig. 2 Solution-printed highly aligned Ag nanowire (NW) arrays: **a** Schematic of the capillary printing process using a nanopatterned polydimethylsiloxane (PDMS) stamp to produce highly aligned NW arrays; **b** Schematic showing the alignment process during capillary printing of unidirectional NW arrays. The solvent-evaporation-induced capillary force produces highly aligned networks by dragging confined NWs at the solid–liquid–vapor contact line. [73]. Copyright 2015. Reproduced with permission from American Chemical Society

oxidation. In contrast, still there are a lot of improvements need to become to use Cu NWs as flexible transparent and conductive films.

3.3 Applications of CuNWs

The replacement of ITO films in various optoelectronic devices is investigated by using excellent performance of transparent and electrically conductive Cu NW. Therefore, they have probable application in various optoelectronic devices such as solar cells [68], OLEDs [78], sensors [79], and touch screens [62]. Zhu et al. [62] designed a CuNW based TCF's for the wide range of optoelectronic applications. The electrical and optical properties of TCFs can be different for each application. For example, R_s value of touch screens requires 50–100 Ω/m^2 and more than 85% transmittance, whereas for solar cells, R_s value can be below 20 Ω/m^2 and needs more than 90% transmittance [80]. Figure 3a shows the excellent mechanical durability of Cu NWs surrounded on the surface of a transparent glass fabric-reinforced plastic from the cyclic bending tests. Both oxidation and thermal stability tests for long term were done for the material, and consistent electrical performance was seen even after 15 days (Fig. 3b). These results along with it more

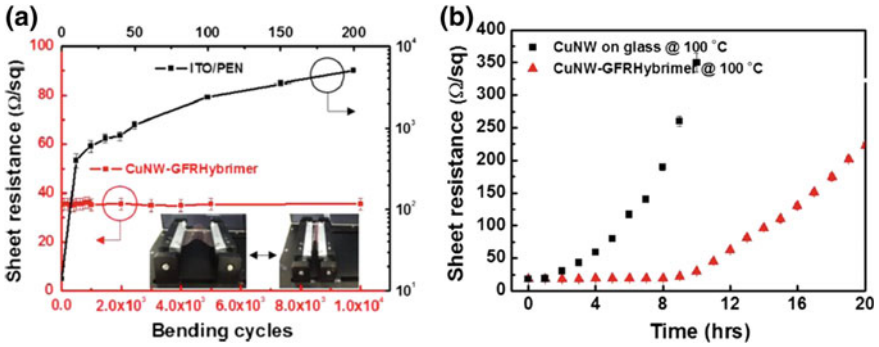

Fig. 3 **a** Bending test results of a CuNW_GFRHybrimer film (Rsh = 35 Ω sq^{-1}) and a reference ITO/PEN film (Rsh = 15 Ω sq^{-1}). Top and right axes are for the ITO/PEN (the inset represents the experimental setup for the bending test; bending radius is 5 mm). **b** A plot of sheet resistance versus annealing period for the CuNW_GFRHybrimer film at 100 °C, respectively [72]. Copyright 2014. Reproduced with permission from American Chemical Society

abundance compared to In or Ag make Cu NWs a promising material for the sustainable and efficient production of transparent conductors.

3.4 Synthesis of Ag NWs

Synthesis of Ag NWs was carried out using a one-step polyol method [81], from two solutions—about 1.0 g $AgNO_3$/40 mL ethylene glycol at room temperature and 0.8 g polyvinylpyrrolidone (PVP) (Mw = 360,000)/in 50 mL ethylene glycol at 60 °C with stirring rate at 300 rpm. Later the prepared dissolution was mixed with 13.6 g of $FeCl_3$ solution (600 µmol L^{-1} in ethylene glycol) and the mixture was, and stirred with magnetic bead at 300 rpm at room temperature for the duration of 3 min. The mixture was heated at the temperature 110 °C without stirring for the duration of 12 h. Finally, the acetone was added to the solution at 1:4 volume ratio to get AgNWs precipitate for the subsequent steps.

AgNW precipitate mixed with ethanol at a ratio of 1:15 to control the thickness of PVP nanolayer by stirring the mixture at 150 rpm for 15 min at room temperature, followed by the centrifugation at 3000 rpm for the duration of 3 min; after centrifugation, the supernatant was removed and the remaining residual precipitate was dispersed in the ethanol solution and washed repeatedly. The repetition of washing procedure applied one cycle of ethanol washing (E1) and followed by twice (E2), thrice (E3), or four times (E4) to obtain different AgNWs. Then deionized (DI) water was added to E4-AgNWs and mixed at either 25 or 90 °C, with stirring at 150 rpm for 15 min, to obtain W25-AgNWs and W90-AgNWs. Meanwhile, dimethylformamide (DMF) mixed with E4-AgNWs at either 25 or 140 °C, keeping the conditions of stirring as the same to form D25-AgNWs and D140-AgNWs. Both the resultant solutions of AgNW ink in DI water and DMF were centrifuged at 3000 rpm

for the duration of 3 min to obtain AgNW precipitate. However, these three solvents on PET were different; then, the AgNWs were finally dispersed in methanol for film coating. All these AgNW inks were at 1.2 wt% concentration.

3.5 Preparation of Ag NWs Thin Films

High-transparency Ag NW thin-film preparation on polyethylene terephthalate (PET) has been demonstrated by Cui et al. For this, 2.7 mg/mL concentrated Ag NW ink in methanol was used as shown in Fig. 4a. The stable dispersion of AgNWs ink solution is found up to the duration of 3 months at room temperature. After some period, nanowires stick each other gradually to form irreversible clumps. Sonication of Ag inks with a bath sonicator for 10–30 s to accomplish uniform, agglomeration-free films. Figure 4b explains the easily scaled-up coating of Ag NW films using the Meyer rod setup for a laboratory scale using slot die [76]. The Ag NW ink of 200 μL was dropped on a 120-μm-thick PET substrate to the transparent conductive film and the solution was either pulled or rolled using Meyer rod (RD Specialist Inc.) by leaving a uniform, thin layer of Ag NW ink on the substrate with a 4–60 μm wet thickness. The thickness of liquid is mainly determined by the rod wire distribution, i.e., the wire diameter and the spacing. Then the infrared lamp was used to dry and wet coating of Ag NW on PET, and uniform heat was supplied to avoid agglomeration or coffee rings [82]. Controlled drying is a critical parameter for achieving a uniform film coating [83]. Figure 4c shows an 8 in. × 8-in. uniform coating of Ag NWs on a PET substrate. Finally, methanol leads to the best uniform coating than other different solvents, such as ethylene glycol (EG) and ethanol. For the process of tuning the ink viscosity for uniform coatings, AgNWs ink concentration is having major role. Because of the mechanical force, the wet coating easily moves around if the ink is diluted. Sheet conductance is improved by annealing process which serves in two steps; initially, film was dried at 65 °C and made to complete dry at 120 °C in an oven. Usually, ink concentration and the Meyer rod size determine the film thickness. Figure 4d shows a silver nanowire film coating on PET substrate with a sheet resistance of 50 Ω/m^2.

3.6 Optoelectrical Properties of AgNWs

For the applications of optoelectronic devices, transparent AgNW electrodes must meet certain mechanical requirements [76] and chemical properties to certify device stability during and after the fabrication process. The film adhesion to the substrate will measure using the mechanical tape test. Without encapsulated, AgNW electrode shows a large resistance increase after performing the tape test (finger pressure was applied). This tape test reported that the AgNWs have poor mechanical adhesion to the plastic substrate [84]. Recently, ZF Liu et al. designed the AgNWs-based

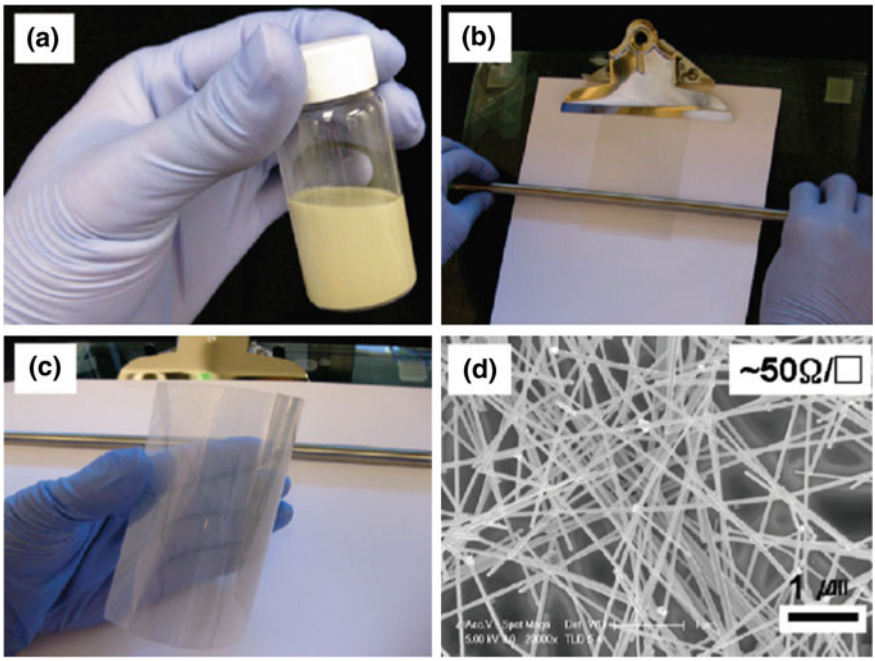

Fig. 4 **a** Ag NW ink in ethanol solvent with a concentration of 2.7 mg/mL. **b** Meyer rod coating setup for scalable AgNW coating on plastic substrate. The PET plastic substrate is put on a flat glass plate and a Meyer rod is pulled over the ink and substrate, which leaves a uniform layer of Ag NW ink with thicknesses ranging from 4 to 60 μm. **c** Finished Ag NW film coating on PET substrate. The Ag NW coating looks uniform over the entire substrate shown in the figure. **d** A SEM image of Ag NW coating shown in panel **c**. The sheet resistance is $\sim 50\ \Omega/m^2$ [76]. Copyright 2010. Reproduced with permission from American Chemical Society

transparent conductive film by encapsulating the AgNW between PET/EVA and graphene for the higher efficiency [84]. The flattening and fusion of NW junctions enable excellent optical and electrical properties of NW network electrodes. The bridging effect between AgNWs and graphene domains also facilitates the electrical conduction of the hybrid film. Encapsulated graphene/CuNT/EVA/PET hybrid films exhibit excellent optoelectronic properties (94% optical transmittance at 550 nm with sheet resistance of $\sim 8\ \Omega\ sq^{-1}$), shown in Fig. 5a. The encapsulated graphene/AgNWs/EVA/PET films also show outstanding performance with 90% optical transmittance (550 nm) at 22 Ω/m and 84% at 10 Ω/m, superior to other transparent electrodes based on AgNWs or CuNWs, ITO, pristine CVD graphene, chemical-doped CVD graphene, and carbon nanotubes. Figure 5b shows the sheet resistance of the encapsulated graphene/NWs/EVA/PET films tuned by varying the number density of NWs. For pure AgNW film whose number density is larger than a percolation critical density, Nc, continuous NW network can be formed, and electrons can percolate across this NW network. Hence, if the number density of AgNWs is larger than Nc, then the conductance is dominated by the relatively high

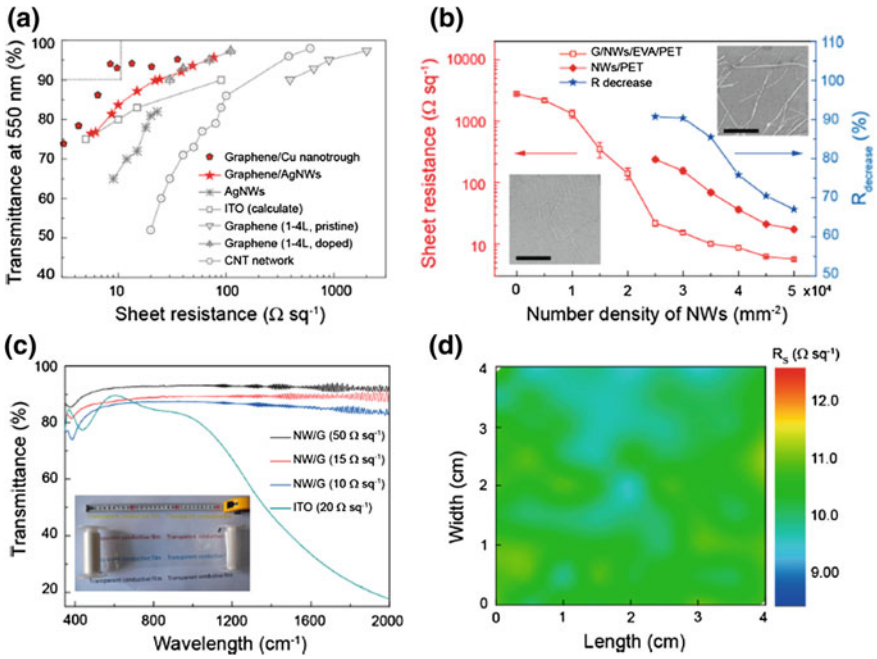

Fig. 5 Graphene and metal nanowire hybrid films as transparent, conductive electrodes. **a** Sheet resistance versus optical transmission (at 550 nm) for the hybrid film of graphene and AgNWs or Cu nanotrough. The performances of AgNWs, ITO, pristine graphene, HNO_3-doped graphene, and CNTs are shown for comparison. Note that the measured transmittance mentioned does not include the absorption and reflectance from the substrate. **b** Sheet resistance versus number density of AgNWs for pure AgNW film and graphene/AgNW hybrid film. (Inset) SEM image of hybrid films with different nanowire densities, *scale bar* 1 μm. **c** UV–vis–NIR spectra of graphene/AgNW hybrid films with different sheet resistance, showing a flat spectrum for broad wavelength range and much better near-infrared transmittance than a commercial ITO electrode. **d** A 2D mapping image of the sheet resistance for a graphene/AgNW hybrid film with the size of 4 × 4 cm^2, showing considerable uniformity of conductivity [84]. Copyright 2015. Reproduced with permission from American Chemical Society

conductive AgNW networks, rather than graphene (Fig. 5b). Note that in this number density region, the encapsulated AgNW film shows 60–90% decrease in sheet resistance than the random pure AgNWs networks with the same NW number densities, which is presumably due to the graphene conduction channel and the decrease of the inter-nanowire contact resistance due to the fusion of wire-to-wire junction in the hot lamination process as discussed above. When the number density of AgNWs is smaller than Nc (Fig. 5b), the conductivity of encapsulated AgNW film is mostly dominated by the graphene channel. Moreover, the encapsulated film possesses lower resistance than pristine graphene because the AgNWs act as additional conduction channels across graphene grain boundaries to bridge graphene domains [85]. In addition to the outstanding electrical property, Fig. 5c shows the encapsulated graphene/AgNWs/EVA/PET film demonstrates a flat, high

transmittance in a broad, wide spectrum from 400 to 2000 nm, much better than the commercial ITO electrode that is opaque in the near-infrared region. Wideband flat spectra of the transparent electrode are used for many optoelectronic devices such as near-infrared sensors and may improve the efficiency of the solar cell by using light energy in the near-infrared region [86]. Production yield controllability and high uniformity in the conductivity of transparent electrode are critical for the practical applications. Figure 5d shows a sheet resistance distribution of an encapsulated graphene/AgNWs/EVA/PET film with the area of 4×4 cm^2 was tested at the interval of 0.5×0.5 cm^2 exhibit a mean value of 10.3 Ω sq^{-1} and a standard deviation of 0.4 Ω sq^{-1}, which evidence a reasonably high electrical homogeneity. The homogeneity of conductivity is due to the optimized coating conditions of NWs and the usage of graphene. Coated AgNWs film on the substrate is a conductive mesh with many holes. The porous structure within the AgNWs network is occupied by graphene, allowing the charge transport across the original nonconductive open space, which greatly improves the electrical homogeneity [87]. Corrosion resistance is a main problem for metal NWs-based transparent conductive electrodes because the chemically unstable and the ease of oxidation may hinder the practical applications as transparent electrodes. Surface modification of AgNW and CuNW films is necessary to significantly improve their performance. It has been reported that graphene is chemically inert [88] and can be used for corrosion-inhibiting coating for metallic nanostructures that are susceptible to atmospheric corrosion.

4 Carbon Nanotube-Based Transparent Conductive Films

4.1 Single-Walled Carbon Nanotube

Due to their unique 1D arrangement, excellent mechanical, electronic, and thermal properties, single-walled carbon nanotubes' (SWCNTs) research from decades attracting considerable scientific interest which constructs them with great potential in many applications. A stable and uniform dispersion of SWCNTs in different solvents is a fundamental condition to accomplish many of these promising applications [89]. The adjacent van der Waals interactions between SWCNTs ($\sim$500 eV μm^{-1}) and exceptionally high aspect ratio (typically >1000) encompass a strong tendency to form large bundles, which strictly limits their properties and applications in many fields [90]. The three foremost strategies such as covalent functionalization [90], noncovalent functionalization, [91], and solvent exfoliation [92] have been figured out to disperse SWCNTs in aqueous and commonly used organic solvents with some advantages and disadvantages. Noncovalent functionalization by adsorption and covering of some additives such as DNA, surfactants, polymers, and peptides are regarded as most capable for the dispersion of SWCNTs without worsening their intrinsic properties. Removing these additives is very difficult, which results in additional electrical resistance at inter-tube junctions [93]. Covalent chemical functionalization modifies the sp^2 carbon skeleton of SWCNTs

to a certain degree without additives to a certain degree, thus inevitably altering their intrinsic properties [90]. The utilization of this potential SWCNT for several applications without any external additives. The dispersion of SWCNTs are highly preferred to achieve excellent properties.

4.2 *Basic Principle and Preparation of SWCNT Dispersion*

Cheng et al. [89] proposed an idea about the preparation of SWCNT dispersion, based on the fact that a few carbonaceous by-products (CBs) such as carbon nanoparticles, amorphous carbon, and carbonaceous fragments are formed during SWCNT synthesis [94]. These by-products are amorphous with less crystallinity, but more chemically reactive and show low thermal stability compared to high-quality SWCNTs [94]. Due to the reactivity difference between such particles and SWCNTs, it is possible to use selective functionalization methods for CBs by keeping the CNTs unaffected. This is proved by Green et al. by means of nitric acid functionalization through which –COOH groups are attached on CBs surfaces rather than SWCNTs side walls [95]. In another report, Huang et al. demonstrated the use of GO as surfactant to distribute MWCNTs and graphite in water due to its amphiphilicity [96]. When the CBs are functionalized with –COOH groups, these also become amphiphilic and play the same role as surfactants in the dispersion of SWCNTs. Figure 6 shows schematic representation of the preparation of soluble SWCNTs. Floating catalyst chemical vapor deposition (FCCVD) was used for the synthesis of SWCNTs [97] and purified by refluxing in 37% HCl to remove Fe catalyst nanoparticles at some extent. The resultant as-purified SWCNTs are present as big bundles (usually 10–50 nm in diameter) with few carbonaceous substances firmly attached on their outer surface (Fig. 6a). It is reported that SWCNT bundles can be intercalated, disentangled, and dissolved in superacids such as oleum/chlorosulphonic acid [90]. In additive-free SWCNTs synthesis [89], the as-purified SWCNT was selectively oxidized by oleum intercalation and nitric acid treatment to obtain the soluble SWCNTs. The oleum intercalation treatment

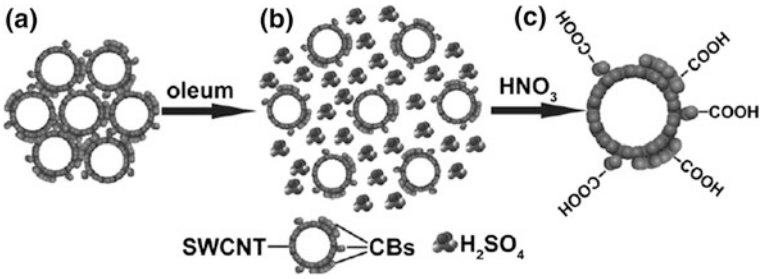

Fig. 6 Schematic of the preparation of soluble SWCNTs: **a** tightly bundled SWCNTs, **b** oleum intercalated SWCNT bundle, and **c** a soluble SWCNT [89]. Copyright 2011. Reproduced with permission from Wiley-VCH

decreases the interaction between adjacent SWCNTs and allows SWCNT bundles to swell. Figure 6b shows the channels for oxidizing agents to infiltrate the bundles and expose the CBs. With the controlled oxidation conditions, this treatment helps to maintain the structural integrity and high intrinsic electrical conductivity of the SWCNTs, while the CBs can be functionalized with COOH groups. Figure 6c shows the presence of SWCNTs containing functionalized CBs attached on their surface, making the formed structure an amphiphilic surfactant with hydrophobic carbon network on one end and hydrophilic COOH groups at the other end, and this helps the SWCNTs soluble in solvents.

4.3 Fabrication and Characterization of SWCNT TCFs

Stable and uniform dispersion of SWCNTs without altering their intrinsic properties and exclusive of external additives are the main key factors for many applications. TCFs are important apparatus in many electronic devices including organic light-emitting diodes, flat-panel displays, touch screens, and photovoltaic cells [98]. The fabrication of TCFs by SWCNT with high flexibility and good electrical conductivity has received much notice in recent years due to their impending for replacing indium tin oxides as transparent electrodes. Fabrication of TCFs by Hui-Ming Cheng group using the additive-free dispersed SWCNTs was demonstrated. A similar method was investigated by Wu et al. [98] for the fabrication of SWCNT TCFs on a glass or quartz substrate. Functionalized CBs were eliminated from as-prepared SWCNT TCFs by short-time heat treatment method. Therefore, the sheet resistance of the heat-treated SWCNT TCFs becomes 180 Ω sq^{-1} with 80% transmittance at 550 nm and the color changes to faint yellow due to the oxidation of residual Fe nanoparticles, which can be easily removed by immersion in HCl. In subsequent HCl treatment, there was an increase in transmittance (82%) and a decrease in sheet resistance (147 Ω sq^{-1}) which is attributed to slight HCl doping of the SWCNTs [99]. A noticeable difference from the soluble SWCNTs is that the agglomerated CBs, and effective removal of metal nanoparticles, preservation of SWCNTs, and functionalized CBs certainly exist in the soluble sample form, and their chemical and thermal stability is lower. The electrical conductivity of the SWCNT networks was improved by usual and effective method of chemical doping [100]. Optical and SEM images of HNO_3-doped TCFs are shown in Fig. 7a, b, which demonstrate a uniform and clear SWCNT network. For the HNO_3-doped TCFs, sheet resistance becomes 76 Ω sq^{-1} and the transmittance is 82%. Figure 7c shows the thickness dependence of the sheet resistance and transmittance. The AFM images to measure the thickness of the SWCNT films are shown in Fig. 7c. A sheet resistance of 48, 76, and 133 Ω sq^{-1} and respective 73, 82, and 90% optical transmittance were observed for the 62-, 35-, and 20-nm-thick SWCNT TCFs. The performance of TCFs fabricated from different materials is determined by using the ratio of direct current conductivity (σDC) to the optical conductivity (σOP) [101, 102]. It is reported that a higher value of σDC/σOP indicates an

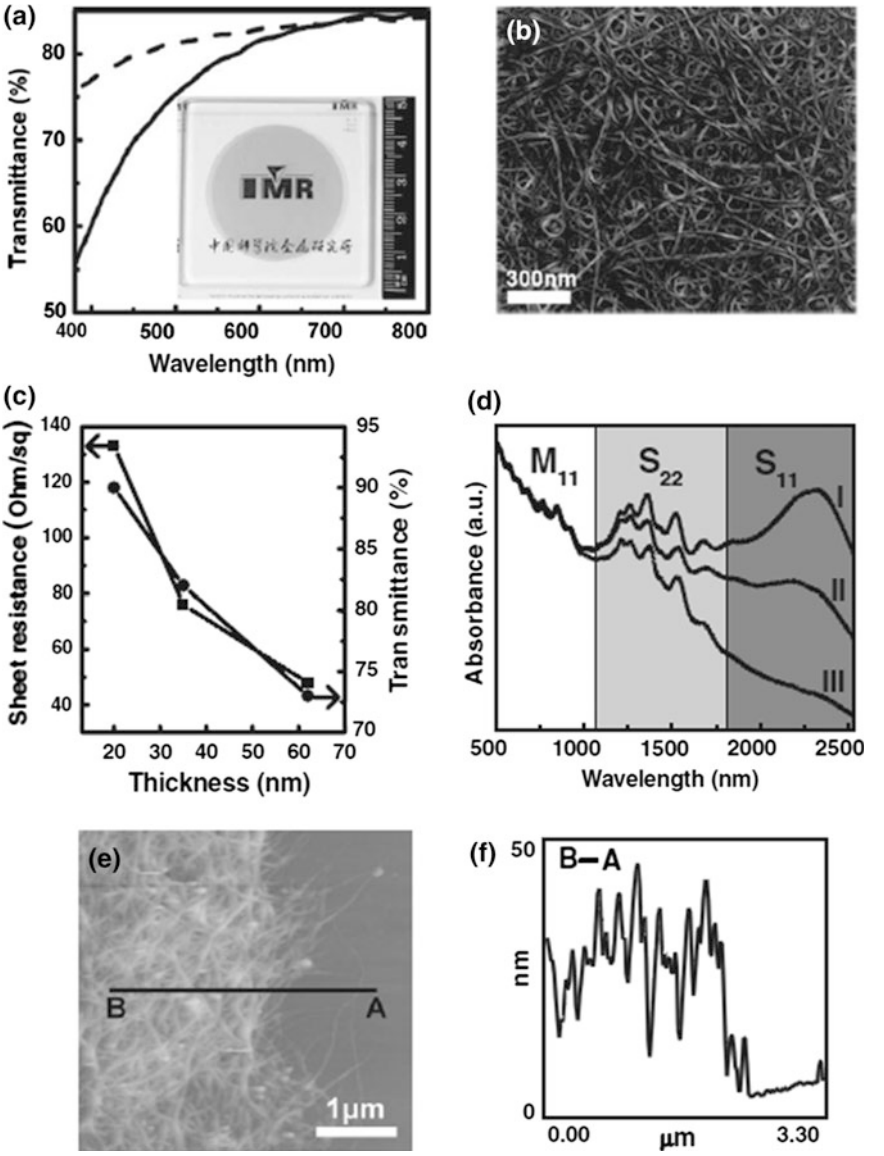

Fig. 7 **a** Transmittance spectra of the SWCNT TCFs before (*solid line*) and after (*dash line*) HCl immersion. Inset: an optical image of HNO_3-doped TCFs on a quartz substrate. **b** A SEM image of SWCNT TCF. **c** Sheet resistance and optical transmittance performance of SWCNT TCFs with different thicknesses. **d** Optical absorption spectra of the SWCNT films: (*I*) heat treated, (*II*) HCl-doped, and (*III*) HNO_3-doped TCFs. **e** AFM image of a transferred SWCNT film on a silicon wafer. **f** Height profile along line AB in (**e**) showing a film thickness of $\sim$35 nm [89]. Copyright 2011. Reproduced with permission from Wiley-VCH

improved performance of TCFs. Compared to other SWCNT TCFs, additive-free SWCNT dispersion exhibits better performance [89].

5 Graphene-Based Transparent Conductive Films

Graphene, the two-dimensional sheet of C atoms, is widely used as an advanced carbon nanomaterial, since from its discovery in 2004 through the scotch tape peeling [103]. Following this mechanical exfoliation from graphite, highly ordered ideal graphene sheets of high Young's modulus (1 Tpa), large surface areas (2630 $m^2\ g^{-1}$), high thermal conductivity (5000 W m K^{-1}), high electron mobility ($2.5 \times 10^5\ cm^2\ V^{-1}\ s^{-1}$), and utmost chemical durability are expected [104]. The analysis of transport properties of large-area graphene grown on SiC, Cu, and many other substrates in addition to the chemical modification of graphene reports its use in fabricating new energy materials. An improved method for the preparation of graphene from Hummer's method to CVD still remains challenging. The advanced method for synthesis of graphene will be important for industrial large-scale production of graphene as well as the fabrication of flexible devices. However, the efficiency and performance of graphene-based devices depend on the proper production methods for this material. For instance, the flake size and high edge to surface ratio highly required for fuel cells and batteries are controlled by high-volume liquid-phase exfoliation method. Following this method, storage capacity also can be improved by regulating the functionalization. Large-area growth through CVD produces material with high structural and electronic quality for the preparation of transparent conducting electrodes for displays and touch screens, and is being evaluated for photovoltaic applications. Bilayered graphene growth by CVD is the research direction to overcome the sheet resistance problem of the microscale crystalline monolayer graphene, less mature, and needs further development. While many transfer techniques have been developed successfully and required optimization of development on green transfer is desired. CVD and solution-based processes for the preparation of large-area graphene film, which have large applications and show one order of magnitude less resistance than graphene films of solution processed, give high-performance electronic instruments and transparent electrode. If the graphene materials are used as transparent electrodes, they should have low sheet resistance and high transmittance on a large scale. Graphene films synthesized by CVD using Cu foil show relatively higher uniformity than stacked graphene flakes produced by reduced graphene oxide. However, the graphene synthesized by CVD method is preferable than other methods and also reduced graphene oxide synthesized by solution processing method, which is cost-effective to obtain films of large graphene area. Therefore, graphene films created by these two methods are actively used as transparent electrodes for various device applications. Finally, graphene growth on the insulating substrate, high-quality graphene on a metal substrate, and transfer techniques are remaining as the big challenge for the industrial scale.

5.1 Industrial Production of Graphene Synthesis by Roll-to-Roll CVD Method

5.1.1 Roll-to-Roll Large-Area Graphene Growth

In 2015, the ZF Liu group demonstrated a roll-to-roll low-pressure chemical vapor deposition was used for the growth of large-area graphene on industrial copper foil [105]. The polycrystalline copper foil (99.9% purity, 18-μm thickness, 1-μm roughness) was fixed between two rollers within the furnace tube. When the furnace temperature reaches 980 °C, under 50 sccm H_2 flow, the sample was annealed for 30 min without changing the gas flow. Graphene growth was carried out under a gas mixture of 10 sccm of CH_4 and 50 sccm of H_2 for 30 min, and the Cu foil is rolled up at a constant speed from the supplying roller to the receiving roller by the winders. Cold water circulation in the receiving roller cools the graphene grown on Cu and a similar process were repeated on the reused Cu.

5.1.2 Roll-to-Roll Lamination and Delamination for Graphene Transfer

Generally, graphene films grown on copper substrates could find excellent interesting many possible applications after deposited on transparent and flexible plastic such as PET/EVA [105]. For the past several years, traditional graphene transfer fails to achieve clean transfer; recently, ZF Liu group demonstrated green transfer [105] for the industrial-scale applications. Large area of graphene grown on copper foil was hot laminated with ethylene vinyl acetate (EVA, 50 μm thickness)—precoated with polyethylene terephthalate (PET, 75 μm thickness) using a SG 330-SCL lamination machine to design a Cu/graphene/EVA/PET stacked structure [105]. A container with a specific set of rolling systems in hot DI water was used as the delamination machine [105]. While the Cu/graphene/EVA/PET film was fixed on the middle roller, both Cu and graphene/EVA/PET were fixed to the two opposite rollers at the ends. Cu/graphene/EVA/PET stacked structure was separated after immersing into the hot water ($\sim$50 °C) for 2 min.

5.2 Optoelectronic Properties

Simultaneous controlling of optical and electrical properties of graphene films is critical for transparent conductive film applications with unique requirements. Both optical and electrical properties can be regulated by carefully controlling the thickness of the graphene film. This will affect the sheet resistance and transmissions properties of the films. An efficient transparent conductor should have low absorption of visible light and high electrical conductivity. The quantitative

performance of transparent conductors is defined as the ratio between electrical conductivity σ and the visible absorption coefficient α and the value directly indicates the performance [106]. If the value of σ/α is more, the performance of transparent conductors is more (Eq. 1).

$$\sigma/\alpha = -1/R_s \ln(T + R) \tag{1}$$

where R_s is the sheet resistance in Ω/m^2, T is the total visible transmission, and R is the total visible reflectance. When the transfer reaction completed, the structural changes of graphene/EVA/PET plastic were analyzed by SEM (Fig. 8a, b). The images obtained from SEM show islands of bilayer domain in continuous monolayer of graphene, in which films of graphene were developed on copper [105]. The films were uniform without cracks, and during the transfer process, there was negligible stress-induced damage. This is attributed to the strong adhesive effect between the graphene and the thermoplastic EVA supporting layer. The roll-to-roll green transfer involves a direct delamination in hot DI water without using any chemicals. This etching-free green method will not introduce any ionic contamination such as Fe^{3+} if $FeCl_3$ is used as an etchant of copper. Furthermore, copper can be completely removed from the surface of graphene/EVE/PET. In support of clean transfer, Fig. 8c illustrates the full XPS spectra for as-transferred graphene/EVA/PET plastic. The predominant peaks at 284.5 and 530 eV, respectively, correspond to C1s and O2s (sp^2 C of graphene and the oxygen in EVA). In Fig. 8d, the graphene/EVA/PET shows negligible Cu peak between 930 and 960 eV, which indicates the efficiency of the chemical etchant-free method to transfer clean graphene from Cu substrate onto the plastics. In Fig. 8e, an optical transmittance of ~97.5% is shown for graphene deposited on EVA/PET, suggesting the graphene as monolayer. Using the four-point probe method, sheet resistance of the material is also measured (Fig. 8f) and uniform distribution is observed over the 3 × 4 cm graphene/EVA/PET film. For the undoped graphene film, the sheet resistance was around 5.2 kΩ/m^2. Good optical and electrical properties of this particular graphene/EVA/PET film demonstrate its applicability in transparent electronic device.

5.3 *Applications of Graphene as Transparent Conductive Electrodes*

5.3.1 Touch Screen

There are many modes of touch-screen technologies such as capacitive, surface capacitance, projected capacitance, resistive, and surface acoustic wave [107, 108]. Out of those, resistive and capacitive are the mostly practiced and require a sheet resistance of 300–1500 Ω/m^2 at 86–90% transparency. Recently, Bae et al. [33] fabricated the centimeter-sized graphene films with the abovementioned conditions and successfully incorporated transparent electrodes with large-size graphene films

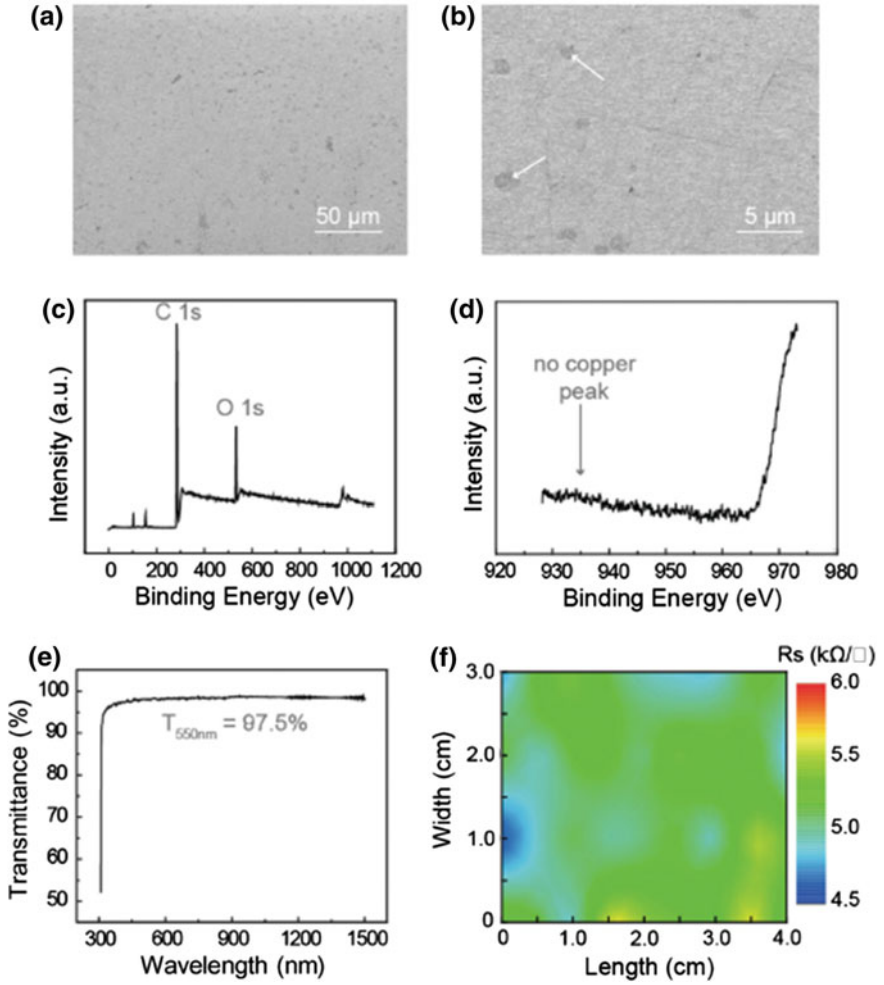

Fig. 8 Characterization of graphene/EVA/PET film. **a**, **b** SEM images of graphene/EVA/PET in low magnification and high magnification, respectively. **c**, **d** XPS broad spectra and fine spectra of graphene/EVA/PET film, respectively. **e** Typical UV–vis–NIR spectrum of graphene/EVA/PET film. **f** Distribution of sheet resistance of graphene/EVA/PET film with the size of 4 cm × 3 cm [105]. Copyright 2015. Reproduced with permission from Wiley-VCH

into touch-screen panel devices (Fig. 9). In particular, they were able to achieve 30-inch graphene film on copper foil using CVD method and transferred onto the PET for the touch-screen application. Through the film, 90% of light will pass and had very low electrical resistance than ITO which consists of standard transparent conductor. The incorporation of graphene-outperformed ITO into display of real touch screen will increase the performance. ITO has applied in touch screens, which used for record signatures in credit card purchasing. The touch screen made up by

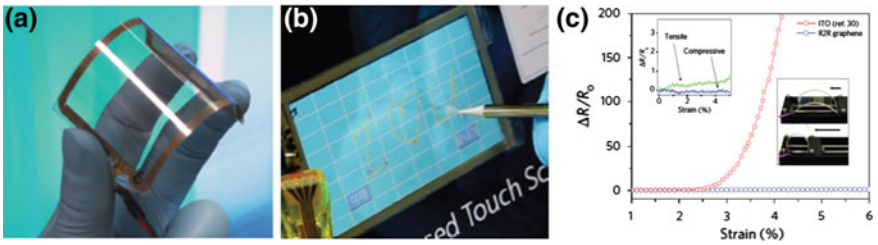

Fig. 9 **a** An assembled graphene/PET touch panel showing outstanding flexibility. **b** A graphene-based touch-screen panel connected to a computer with control software. **c** Electromechanical properties of graphene-based touch-screen devices compared with ITO/PET electrodes under tensile strain. The inset shows the resistance change with compressive and tensile strain applied to the upper and lower graphene/PET panels, respectively [33]. Copyright 2010. Reproduced with permission from Nature Publishing Group

using graphene could handle twice as more strain as conventional ITO-based devices. Figure 9c shows the electromechanical properties of graphene/PET touch-screen panels [33]. Under 2–3% strain, the touch panel of ITO will breaks easily, but with the help of printed silver electrodes graphene-based panel restricted the break up to 6% strain.

5.3.2 Liquid Crystal Displays

Liquid crystals that are having light-modulating properties are used as displays in many electronic devices such as liquid crystal displays (LCD). Droplets of liquid crystals (LC) of micrometer-sized thin film which consist of polymers of optically transparent placed within pores of polymers. The light passes through the LC polymer will scatter and generate a milky film. If the ordinary refractive index of LC polymer is equal to transparent host polymer, the advantages of electric field result in transparent state [109]. When LCDs have potential to switch from translucent to opaque states, the advantages of LCDs will be wide in the field of computer displays, TV screens, instrument displays, and displays of aircraft cockpit. The major role of conductive transparent films in LCD instrument is to serve as pixel and common electrodes. Generally, low sheet resistance of 30–300 Ω/m^2 and high transparency of 87–90% are required for LCDs [110]. Comparable performance with ITO electrode has been reported for an LCD based on 6 nm thick thermally reduced graphene oxide film [110, 111]. A schematic diagram of a mechanically exfoliated monolayer graphene-based LCD fabrication method is shown in Fig. 10a [112]. Figure 10b–f shows the transmission of graphene-based LCD changes under both the white and monochromatic light, and the threshold voltage of the graphene-based LCD was around 0.9 V_{rms}. The absence of negative effect of graphene on the LCD alignment is marked by the uniform change in graphene-electrode area. Contrast ratio (between maximum transmission

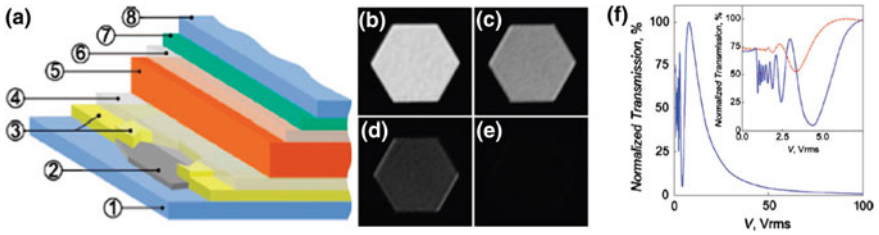

Fig. 10 **a** Schematic diagram of our liquid crystal devices with typical layer thicknesses in brackets: *1* glass (1 mm); *2* graphene; *3* Cr/Au contact surrounding graphene flake (5 nm Cr + 50 nm Au); *4* alignment layer (polyvinyl alcohol) (40 nm); *5* liquid crystal (20 μm); *6* alignment layer (40 nm); *7* ITO (150 nm); *8* glass (1 mm). The graphene flake is surrounded by a nontransparent Cr/Au contact. **b**–**e** Optical micrographs of one of our liquid crystal devices using green light (505 nm, *f* 23 nm) with different voltages applied across the cell: (**b**) *V*, 8 Vrms; (**c**) *V*, 13 Vrms; (**d**) *V*, 22 Vrms; (**e**) *V*, 100 Vrms. Overall image width is 30 μm. The central hexagonal window is covered by graphene, surrounded by the opaque Cr/Au electrode. **f** Light transmission through the LCD as a function of the voltage applied across the cell. Inset: the same at low voltages. *Solid blue curve* in green light (505 nm); *dashed red curve* in white light [112]. Copyright 2008. Reproduced with permission from American Chemical Society

and the transmission at 100 V_{rms} across the cell) was better than 100 under white-light illumination. The graphene-based cell with excellent performance can be effectively used as transparent electrode for ICDs. Usually the glass with ITO served as transparent conductive film in which it can generate electric field across the LCD. However, the properties such as instability and less flexibility will be avoided for the development of fabrication of flexible and transparent electronic devices. Diffusion of ions into active medium and chemical stability of metal oxide are the most important issues for ITO-based LC devices and photonic devices. Degradation of active medium by oxidation process which introduced by ITO [113] and breakdown will take place at lower voltage. And also, in LCDs, the applied electric field [114] will be screened by injected ions which can be trapped in alignment layer. Therefore, these problems easily decreased using graphene and thereby the stability of graphene reduces the ion diffusion order [112].

5.3.3 Solar Cells

Transparent conductive films are fundamental for the fabrication and working of many solar cells. Several organic and inorganic solar cells based on graphene are reported for their applications, e.g., dye-sensitized solar cells [115], hybrid ZnO/poly(3-hexylthiophene) (P3HT) solar cells [117], organic bulk-heterojunction (BHJ) photovoltaic cells [116], Si Schottky junction solar cells [118], and InGaN p–i–n solar cells [119]. Low-cost, high-transparency flexibility, and low resistance are the main keywords associated with graphene to be used for the fabrication of graphene-based photovoltaic device applications. The driving force of designing a graphene-based solar cell has been the huge potential of the technology to enable

high-throughput production of cheap solar cells. Arco et al. [120] have demonstrated graphene-based highly flexible organic solar cells (OSCs). However, separation of the photogenerated electron–hole pairs and transferring the separated charge carriers to the electrodes are considered to be the major challenges for the successful implementation of these solar cells. The surface functionalization and post-treatment of the graphene-based materials have shown very well controllable surface as well as, interfacial properties and tailored work functions for the high performance of the solar cells [121, 122]. The organic solar cell contains two conductors, which can produce the electric field in the organic layer. The incident light on organic layer was caused to excitation of electron from LUMO to HOMO by leaving holes and forming excitons. The excited pairs will be separated by the potential because of the different work function, and it can pull the electron toward cathode and holes toward the anode. Charge carriers can be transported easily by the development of additional functional layer. Graphene films synthesized by CVD method are used as conductive and transparent electrode, by using thin layer of titanium suboxide (TiO_x)—the electrodes applied successfully in OSCs (Fig. 11a) [38]. First, the glass substrate coated with graphene film acts as an anode and also the graphene layer spin coated with thin layer of PEDOT:PSS. The spin coating of BHI composite of P3HT and [6] -phenyl-C61, and butyric acid ester [PCDM] was coated on graphene with PEDOT:PSS layer to form photoactive layer. A thin film of TiO_X was also spin coated for some devices. At last, thermally evaporated aluminum was used as cathode (Fig. 11b). CVD-grown graphene at different temperature was studied for the power conversion efficiency (PCE) of the graphene electrode in OSCs, and PCE of $\sim$1.3% was found at 1000 °C-grown graphene films. After the insertion of TiO_X layer as hole-blocking layer, the PCE of $\sim$2.6% was considerably improved (Fig. 11c, d). TiO_X layer acts as an optical spacer and facilitating better transport of charge carriers to each electrode as a hole-blocking layer [123, 124] which increased photogenerated charge carriers density and the PCE for graphene/ITO—photovoltaic devices [123, 124]. As a result, the TiO_X layer decreased the cathode photoactive layer contact resistance due to dipole formation [125]. Hence, the PCE is the major factor in evaluating the performance of solar cells. To date, graphene-based OSCs PCE values have been reported to be in the range of 0.08–2.60% [126], much lower than OSCs using conventional ITO electrodes (8.37%) [127]. This necessitates the improvement in PCE of graphene-based OSCs for the commercialized OSCs.

5.3.4 Triboelectric Nanogenerator

Nowadays, triboelectricity was studied intensively by applying in power-generating device, to convert mechanical energy into electrical energy [105]. Triboelectricity has advantage over the other familiar method, here the device made up of graphene/EVA/PET film, by the method of large-scale roll-to-roll fabrication; it has advantages such as good conductor, high transparency, and high uniformity; and these electrodes are also applicable to optoelectronic device fabrications. Peng et al.

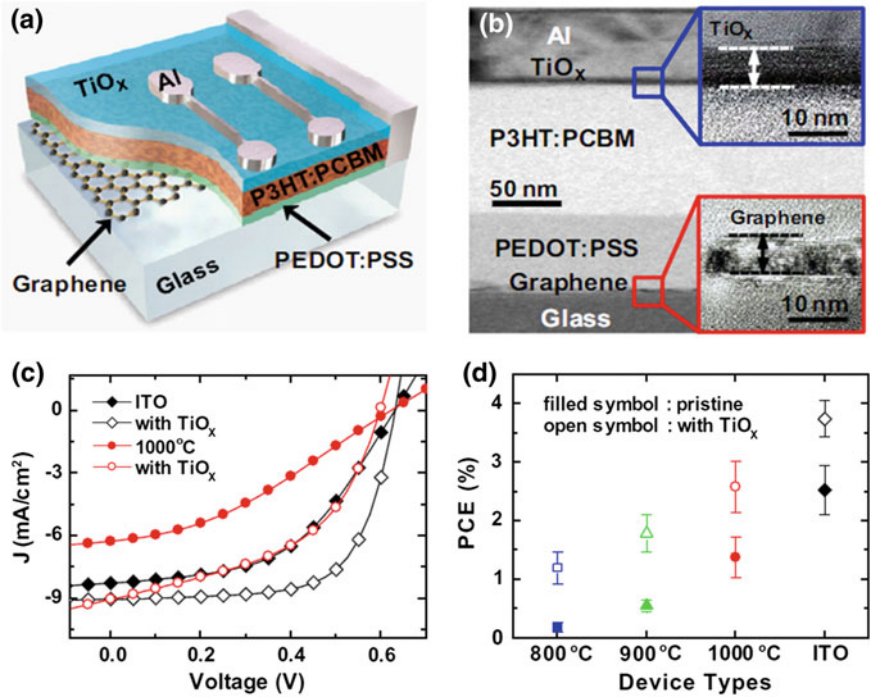

Fig. 11 **a** Schematic diagram of a photovoltaic device structure with graphene electrodes and a hole-blocking TiO_X layer. **b** TEM cross-sectional image of a photovoltaic device. The insets show high-resolution TEM images near the TiO_X layer (*top*) and near the graphene films (*bottom*). **c** J–V curves of photovoltaic devices with 1000 °C-grown graphene electrodes (*circles*) and with ITO electrodes (*diamonds*). The *curves* without the TiO_X layer (*filled symbols*) are compared to those with the TiO_X layer (*open symbols*). **d** Comparison of the PCEs used for graphene-electrode photovoltaic devices with those used for ITO-electrode photovoltaic devices with TiO_X layers and without TiO_X layers (*pristine*). The types of devices are indicated on the *x*-axis (800, 900 and 1000 °C: graphene-electrode devices; ITO: ITO-electrode devices) [38]. Copyright 2010. Reproduced with permission from Elsevier Ltd.

showed the applications in flexible and transparent triboelectric nanogenerator (TENG).

TENG mainly consists of two layers and the schematic diagram of TENG of graphene/EVA/PET is shown in Fig. 12a. The upper layer is made up of graphene/EVA/PET; here graphene layer acts as electrode and also acts as friction layer of TENG. Here we can also note that CVD-grown graphene has wrinkles and ripples, which can prepare and validate on the plastic substrate by our RGT process. From triboelectric effect, we can generate significant amounts of friction and surface charge, and these create the wrinkles and ripples, which make graphene more suitable for the high-output voltage applications.

The micro-pyramid-patterned PDMS lower layer transferred to friction layer of graphene/EVA/PET. Arch-shaped TENG fabricated by dielectric layer of PDMS

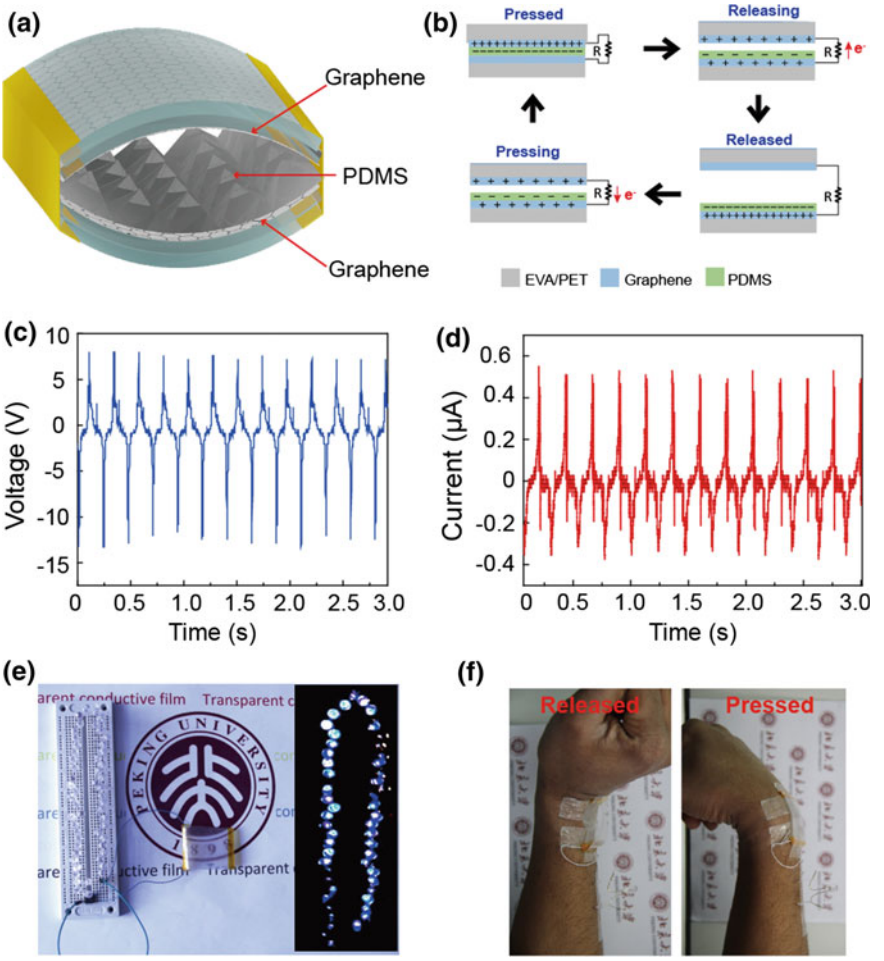

Fig. 12 Triboelectric nanogenerator device based on graphene/EVA/PET electrode. **a** Schematic diagram of graphene/EVA/PET-based triboelectric nanogenerator. **b** Working mechanism of the triboelectric nanogenerator. **c**, **d** Output voltage and current measured under a vertical compressive force, respectively. **e** Photograph of the graphene/EVA/PET electrode-based transparent and flexible triboelectric nanogenerator. Inset photograph shows that 56 LED bulbs were lightened up by the nanogenerator. **f** Photograph of the nanogenerator fixed at a wrist to harvest mechanical energy [105]. Copyright 2015. Reproduced with permission from Wiley-VCH

and electrode of graphene/EVA/PET. The bent shape of graphene/EVA/PET easily turned to arch shape in which by releasing the pressure TENG regains its original position. The air voids between PDMS and graphene in the two layers of 0.5 mm space increase the strength of dipole moment and capacitance of the system in the process of mechanical deformation. Figure 12b illustrates the working principles of the arch-shaped TNG and its mechanism of coupling of contact electrification and

electrostatic induction. The device is in neutral state and initially, there was no charge on the surfaces of both the electrodes. When device is pressed or contracted by using vibrator, the positive and negative charges are generated on graphene and PDMS films, respectively, when they are in full contact [128]. The produced triboelectric charges and opposite polarities are equally balanced; in this condition, there is no electron flows between the electrodes.

After deformation started, the opposite triboelectric charges separate along with the air gap which generates the dipole moment—it is the driven force for electron flow from bottom graphene electrode to upper graphene electrode, when PDMS and graphene films reach maximum separation than the flow of electron lost. If the device is pressed again, the dipole moment disappears and as a result the reverse flow of electrons in electrode occurs. Both the surfaces are in pressed state until the generated electrostatic induction produces the output signals. If the irrational frequency is 4.3 Hz, the maximum output voltage and current signal are up to 22 V and 0.9 μA, respectively (Figs. 5d and 12c). In this way, high electrical energy can be generative in a tiny TENG device with the size of 3 cm × 4 cm; the energy liberated from this device can glow up to 56 commercial blue LED lamps connected in a series and is shown in Fig. 12e. This TENG device can be operated by wrist movement (Fig. 12f). The above explanations can be concluded that importance of TENG device is that it is potential as wearable for accumulate energy from human movements.

6 Conclusion

The promising next-generation conducting materials such as graphene, silver nanowire, carbon nanotube, and copper nanowire are with the tendency to substitute commercial electrode materials such as ITO (less abundant) in optical and electrical devices. Regarding the practical applications, the properties including flexibility, high optical transparency, low sheet resistance and superior mechanical properties of metal nanowires (CuNWs and AgNWs), CNTs, and graphene have attracted a great interest. The products of these materials have also been demonstrated in wide-range areas such as LEDs, LCDs, touch screen, and triboelectric nanogenerators (energy-harvesting nanogenerators). CuNWs, AgNWs, CNT, and graphene films produce components smart technologies for flexible and transparent electronic gadgets due to their combination of the transparency, conductivity, and mechanical flexibility. With regard to easy large-scale manufacturing technique, roll-to-roll synthesis of CVD-grown graphene and green methods has been shown to be encouraging for the industrial-scale method to prepare transparent electrodes in flexible and transparent devices. In the near future, it is important to realize to overcome the key issues; however, further research should be focused at an optimizing the synthesis, techniques to fabricate conductive thin film, improvement of conductivity by doping, and cost of final product. The key challenges such as low-cost processing and eco-friendly method will require continued innovative

research and development. Currently, there have been huge numbers of reports on electrical and optical device applications of graphene. We anticipate that future scientific research will include the incorporation of graphene-based hybrid optically transparent material to help achieve the future-generation transparent and flexible electronics in many areas.

References

1. Lee JY, Connor ST, Cui Y, Peumans P (2008) Solution-processed metal nanowire mesh transparent electrodes. Nano Lett 8:689–692
2. Ellmer K (2012) Past achievements and future challenges in the development of optically transparent electrodes. Nat Photonics 6:809–817
3. Layani M, Kamyshnya A, Magdassi S (2014) Transparent conductors composed of nanomaterials. Nanoscale 6:5581–5591
4. Cheng T, Zhang Y, Lai W-Y, Huang W (2015) Stretchable thin-film electrodes for flexible electronics with high deformability and stretchability. Adv Mater 27:3349–3376
5. Gordon RG (2000) Criteria for choosing transparent conductors. MRS Bull 25:52–57
6. Rathmell AR, Bergin SM, Hua YL, Li ZY, Wiley BJ (2010) The growth mechanism of copper nanowires and their properties in flexible, transparent conducting films. Adv Mater 22:3558–3563
7. Ding ZQ, Zhu YP, Branford-White C, Sun K, Um-I-Zahra S, Quan J, Nie HL, Zhu LM (2014) Self-assembled transparent conductive composite films of carboxylated multi-walled carbon nanotubes/poly(vinyl alcohol) electrospun nanofiber mats. Mater Lett 128:310–313
8. McCarthy MA, Liu B, Donoghue EP, Kravchenko I, Kim DY, So F, Rinzler AG (2011) Low-voltage, low-power, organic light-emitting transistors for active matrix displays. Science 332:570–573
9. Sagar RUR, Zhang XZ, Xiong CY, Yu Y (2014) Semiconducting amorphous carbon thin films for transparent conducting electrodes. Carbon 76:64–70
10. Kim KS, Zhao Y, Jang H, Lee SY, Kim JM, Kim KS, Ahn JH, Kim P, Choi JY, Hong BH (2009) Large-scale pattern growth of graphene films for stretchable transparent electrodes. Nature 457:706–710
11. Girtan M, Vlad A, Mallet R, Bodea MA, Pedarnig JD, Stanculescu A, Mardare D, Leontie L, Antohe S (2013) On the properties of aluminium doped zinc oxide thin films deposited on plastic substrates from ceramic targets. Appl Surf Sci 274:306–313
12. Chen T–H, Chen T–Y (2015) Effects of annealing temperature on properties of Ti-Ga-doped ZnO films deposited on flexible substrates. Nanomaterials 5:1831–1839
13. Lee D, Pan H, Ko SH, Park HK, Kim E (2012) Grigoropoulos, C.P. Non-vacuum, single-step conductive transparent ZnO patterning by ultra-short pulsed laser annealing of solution-deposited nanoparticles. Appl Phys A 107:161–171
14. De S, Higgins TM, Lyons PE, Doherty EM, Nirmalraj PN, Blau WJ, Boland JJ, Coleman JN (2009) Silver nanowire networks as flexible, transparent, conducting films: Extremely high DC to optical conductivity ratios. ACS Nano 3:1767–1774
15. Zhang YY, Ronning F, Gofryk K, Mara NA, Haberkorn N, Zou GF, Wang HY, Lee JH, Bauer E, McCleskey TM, Burell AK, Civale L, Zhu YT, Jia Q (2012) Aligned carbon nanotubes sandwiched in epitaxial NbC film for enhanced superconductivity. Nanoscale 4:2268–2271
16. Lee D, Paeng D, Park HK, Grigoropoulos CP (2014) Vacuum-free, maskless patterning of Ni electrodes by laser reductive sintering of NiO nanoparticle ink and its application to transparent conductors. ACS Nano 8:9807–9814

17. Liu YK, Sie YY, Liu CA, Lee MT (2015) A novel laser direct writing system integrated with A & F XXY alignment platform for rapid fabrication of flexible electronics. Smart Sci 3:87–91
18. Ge ZB, Wu ST (2008) Nanowire grid polarizer for energy efficient and wide-view liquid crystal displays. Appl Phys Lett 93:121104 (5 pages)
19. Kim SH, Park JD, Lee KD (2006) Fabrication of a nano-wire grid polarizer for brightness enhancement in liquid crystal display. Nanotechnology 17:4436–4438
20. Lee MS, Lee K, Kim SY, Lee H, Park J, Choi KH, Kim HK, Kim DG, Lee DY, Nam S, Park J-U (2013) High-performance, transparent, and stretchable electrodes using graphene-metal nanowire hybrid structures. Nano Lett 13:2814–2821
21. Song M, You DS, Lim K, Park S, Jung S, Kim CS, Kim DH, Kim DG, Kim JK, Park J, Kang Y-C, Heo J, Jin S-H, Park JH, Kang J-W (2013) Highly efficient and bendable organic solar cells with solution-processed silver nanowire electrodes. Adv Funct Mater 23:4177–4184
22. Yao HF, Sun JL, Liu W, Sun HS (2007) Effect of a magnetic field on the preparation of silver nanowires using solid electrolyte thin films. J Mater Sci Technol 23:39–42
23. Eom H, Lee J, Pichitpajongkit A, Amjadi M, Jeong JH, Lee E, Lee JY, Park I (2014) Ag@Ni core-shell nanowire network for robust transparent electrodes against oxidation and sulfurization. Small 10:4171–4181
24. Jewell S, Kimball S (2014) Mineral commodity summaries. US Geological Survey, Reston, VA, USA
25. Cui F, Yu Y, Dou LT, Sun JW, Yang Q, Schildknecht C, Schierle-Arndt K, Yang PD (2015) Synthesis of ultrathin copper nanowires using tris(trimethylsilyl)silane for high-performance and low-haze transparent conductors. Nano Lett 15:7610–7615
26. Ye SR, Rathmell AR, Stewart IE, Ha YC, Wilson AR, Chen ZF, Wiley BJ (2014) A rapid synthesis of high aspect ratio copper nanowires for high-performance transparent conducting films. Chem Commun 50:2562–2564
27. Han S, Hong S, Ham J, Yeo J, Lee J, Kang B, Lee P, Kwon J, Lee SS, Yang MY, Ko SH (2014) Fast plasmonic laser nanowelding for a Cu-nanowire percolation network for flexible transparent conductors and stretchable electronics. Adv Mater 26:5808–5814
28. Arnold MS, Stupp SI, Hersam MC (2005) Enrichment of single-walled carbon nanotubes by diameter in density gradients. Nano Lett 5:713–718
29. Spitalsky Z, Tasis D, Papagelis K, Galiotis C (2010) Carbon nanotube-polymer composites: chemistry, processing, mechanical and electrical properties. Prog Polym Sci 35:357–401
30. Lee S, Jo G, Kang S-J, Wang G, Choe M, Park W, Kim D-Y, Kahng YH, Lee T (2011) Enhanced charge injection in pentacene field-effect transistors with graphene electrodes. Adv Mater 23:100–105
31. Ji Y, Lee S, Cho B, Song S, Lee T (2011) Flexible organic memory devices with multilayer graphene electrodes. ACS Nano 5:5995–6000
32. Wang G, Kim Y, Choe M, Kim T-W, Lee T (2011) A new approach for molecular electronic junctions with a multilayer graphene electrode. Adv Mater 23:755–760
33. Bae S, Kim H, Lee Y, Xu X, Park J-S, Zheng Y, Balakrishnan J, Lei T, Kim HR, Song YI, Kim Y-J, Kim KS, Özyilmaz B, Jong-Hyun Ahn J-H, Hong BH, Iijima S (2010) Roll-to-roll production of 30-inch graphene films for transparent electrodes. Nat Nanotechnol 5:574–578
34. Blake P, Brimicombe PD, Nair RR, Booth TJ, Jiang D, Schedin F, Ponomarenko LA, Morozov SV, Gleeson HF, Hill EW, Geim AK, Novoselov KS (2008) Graphene-based liquid crystal device. Nano Lett 8:1704–1708
35. Jo G, Choe M, Cho C-Y, Kim JH, Park W, Lee S, Hong W-K, Kim T-W, Park S-J, Hong BH, Kahng YH, Lee T (2010) Large-scale patterned multi-layer graphene films as transparent conducting electrodes for GaN light-emitting diodes. Nanotechnology 21:175201–175206
36. Wu J, Agrawal M, Becerril HA, Bao Z, Liu Z, Chen Y, Peumans P (2010) Organic light-emitting diodes on solution-processed graphene transparent electrodes. ACS Nano 4:43–48

37. Lee JM, Choung JW, Yi J, Lee DH, Samal M, Yi DK, Lee C-H, Yi G-C, Paik U, Rogers JA, Park WI (2010) Vertical pillar-superlattice array and graphene hybrid light emitting diodes. Nano Lett 10:2783–2788
38. Choe M, Lee BH, Jo G, Park J, Park W, Lee S, Hong W-K, Seong M-J, Kahng YH, Lee K, Lee T (2010) Efficient bulk-heterojunction photovoltaic cells with transparent multi-layer graphene electrodes. Org Electron 11:1864–1869
39. Wang X, Zhi L, Mullen K (2008) Transparent, conductive graphene electrodes for dye-sensitized solar cells. Nano Lett 8:323–327
40. Li X, Magnuson CW, Venugopal A, An J, Suk JW, Han B, Borysiak M, Cai W, Velamakanni A, Zhu Y, Fu L, Vogel EM, Voelkl E, Colombo L, Ruoff RS (2010) Graphene films with large domain size by a two-step chemical vapor deposition process. Nano Lett 10:4328–4334
41. Thiele S, Reina A, Healey P, Kedzierski J, Wyatt P, Hsu P-L, Keast C, Schaefer J, Kong J (2010) Engineering polycrystalline Ni films to improve thickness uniformity of the chemical-vapor-deposition-grown graphene films. Nanotechnology 21:015601(1)–015601(9)
42. Wei D, Liu Y (2010) Controllable synthesis of graphene and its applications. Adv Mater 22:3225–3241
43. Kahng YH, Lee S, Choe M, Jo G, Park W, Yoon J, Hong W-K, Cho C-H, Lee B H, Lee T (2011) A study of graphene films synthesized on nickel substrates: existence and origin of small-base-area peaks. Nanotechnology 22:045706 (9 pp)
44. Kim KK, Reina A, Shi Y, Park H, Li L-J, Lee Y H, Kong J (2010) Enhancing the conductivity of transparent graphene films via doping. Nanotechnology 21:285205 (6 pp)
45. Guo B, Fang L, Zhang B, Gong JR (2011) Graphene doping: a review. Insci J 1:80–89
46. Jo G, Na S-I, Oh S-H, Lee S, Kim T-S, Wang G, Choe M, Park W, Yoon J, Kim D-Y, Kahng YH, Lee T (2010) Tuning of a graphene-electrode work function to enhance the efficiency of organic bulk heterojunction photovoltaic cells with an inverted structure. Appl Phys Lett 97:213301–213303
47. Shi Y, Kim KK, Reina A, Hofmann M, Li L-J, Kong J (2010) Work function engineering of graphene electrode via chemical doping. ACS Nano 4:2689–2694
48. Lee Y, Bae S, Jang H, Jang S, Zhu S-E, Sim SH, Song YI, Hong BH, Ahn J-H (2010) Wafer-scale synthesis and transfer of graphene films. Nano Lett 10:490–493
49. Li X, Zhu Y, Cai W, Borysiak M, Han B, Chen D, Piner RD, Colombo L, Ruoff RS (2009) Transfer of large-area graphene films for high-performance transparent conductive electrodes. Nano Lett 9:4359–4363
50. Ghosh S, Calizo I, Teweldebrhan D, Pokatilov EP, Nika DL, Balandin AA, Bao W, Miao F, Lau CN (2008) Extremely high thermal conductivity of graphene: prospects for thermal management applications in nanoelectronic circuits. Appl Phys Lett 92:151911
51. Ponnamma D, Sadasivuni KK, Wan C, Thomas S, AlMa'adeed MA (eds) (2016) Flexible and stretchable electronic composites. Springer, Berlin
52. Pang S, Hernandez Y, Feng X, Müllen K (2011) Graphene as transparent electrode material for organic electronics. Adv Mater 23:2779–2795
53. Guo CX, Guai GH, Li CM (2011) Graphene based materials: enhancing solar energy harvesting. Adv Energy Mater 1:448–452
54. Zhu Y, Sun Z, Yan Z, Jin Z, Tour JM (2011) Rational design of hybrid graphene films for high-performance transparent electrodes. ACS Nano 5:6472–6479
55. Liu Y, Chang Q, Huang L (2013) Transparent, flexible conducting graphene hybrid films with a subpercolating network of silver nanowires. J Mater Chem C 1:2970–2974
56. Choi H, Park SH (2004) Seedless growth of free-standing copper nanowires by chemical vapor deposition. J Am Chem Soc 126:6248–6249
57. Haase D, Hampel S, Leonhardt A, Thomas J, Mattern N, Buchner B (2007) Facile one-step-synthesis of carbon wrapped copper nanowires by thermal decomposition of copper (II)-acetylacetonate. Surf Coat Technol 201:9184–9188
58. Khalil A, Hashaikeh R, Jouiad M (2014) Synthesis and morphology analysis of electrospun copper nanowires. J Mater Sci 49:3052–3065

59. Zang WL, Li P, Fu YM, Xing LL, Xue XY (2015) Hydrothermal synthesis of Co-ZnO nanowire array and its application as piezo-driven self-powered humidity sensor with high sensitivity and repeatability. RSC Adv 5:84343–84349
60. Xu P, Chen WZ, Wang Q, Zhu TS, Wu MJ, Qiao JL, Chen ZW, Zhang JJ (2015) Effects of transition metal precursors (Co, Fe, Cu, Mn, or Ni) on pyrolyzed carbon supported metal-aminopyrine electrocatalysts for oxygen reduction reaction. RSC Adv 5:6195–6206
61. Panciera F, Chou YC, Reuter MC, Zakharov D, Stach EA, Hofmann S, Ross FM (2015) Synthesis of nanostructures in nanowires using sequential catalyst reactions. Nat Mater 14:820–825
62. Zhu Z, Mankowski T, Balakrishnan K, Shikoh AS, Touati F, Benammar MA, Mansuripur M, Falco CM (2015) Ultrahigh aspect ratio copper-nanowire-based hybrid transparent conductive electrodes with PEDOT:PSS and reduced graphene oxide exhibiting reduced surface roughness and improved stability. ACS Appl Mater Interfaces 7: 16223–16230
63. Guo H, Lin N, Chen Y, Wang Z, Xie Q, Zheng T, Gao N, Li S, Kang J, Cai D, Peng D-L (2013) Copper nanowires as fully transparent conductive electrodes. Sci Rep 3:2323 (1–8)
64. He T, Xie A, Reneker DH, Zhu YA (2014) tough and high-performance transparent electrode from a scalable and transfer-free method. ACS Nano 8:4782–4789
65. Chen TG, Huang BY, Liu HW, Huang YY, Pan HT, Meng HF, Yu PC (2012) Flexible silver nanowire meshes for high-efficiency microtextured organic-silicon hybrid photovoltaics. ACS Appl Mater Interfaces 4:6849–6856
66. Chung CH, Song TB, Bob B, Zhu R, Duan HS, Yang Y (2012) Silver nanowire composite window layers for fully solution-deposited thin-film photovoltaic devices. Adv Mater 24:5499–5504
67. Hsun-Chen Chu H-C, Yen-Chen Chang Y-C, Yow Lin Y, Shu-Hao Chang S-H, Wei-Chung Chang W C, Li G-A, Tuan H-Y (2016) Spray-deposited large-area copper nanowire transparent conductive electrodes and their uses for touch screen applications. ACS Appl Mater Interfaces 8:13009–13017
68. Stewart IE, Rathmell AR, Yan L, Ye SR, Flowers PF, You W, Wiley BJ (2014) Solution-processed copper-nickel nanowire anodes for organic solar cells. Nanoscale 6:5980–5988
69. Li SJ, Chen YY, Huang LJ, Pan DC (2014) Large-scale synthesis of well-dispersed copper nanowires in an electric pressure cooker and their application in transparent and conductive networks. Inorg Chem 53:4440–4444
70. Akter T, Kim WS (2012) Reversibly stretchable transparent conductive coatings of spray-deposited silver nanowires. ACS Appl Mater Interfaces 4:1855–1859
71. Celle C, Mayousse C, Moreau E, Basti H, Carella A, Simonato JP (2012) Highly flexible transparent film heaters based on random networks of silver nanowires. Nano Res 5:427–433
72. Im H-G, Jung S-H, Jin J, Lee D, Lee J, Lee D, Lee J-Y, Kim I-D, Bae B-S (2014) Flexible transparent conducting hybrid film using a surface-embedded copper nanowire network: a highly oxidation-resistant copper nanowire electrode for flexible optoelectronics. ACS Nano 8:10973–10979
73. Kang S, Kim T, Cho S, Lee Y, Choe A, Walker B, Ko SJ, Kim JY, Ko H (2015) Capillary printing of highly aligned silver nanowire transparent electrodes for high-performance optoelectronic devices. Nano Lett 15:7933–7942
74. Garnett EC, Cai WS, Cha JJ, Mahmood F, Connor ST, Christoforo MG, Cui Y, McGehee MD, Brongersma ML (2012) Self-limited plasmonic welding of silver nanowire junctions. Nat Mater 11:241–248
75. Langley DP, Lagrange M, Giusti G, Jiménez C, Bréchet Y, Nguyen ND, Bellet D (2012) Metallic nanowire networks: effects of thermal annealing on electrical resistance. Nanoscale 6:13535–13543
76. Hu LB, Kim HS, Lee JY, Peumans P, Cui Y (2010) Scalable coating and properties of transparent, flexible, silver nanowire electrodes. ACS Nano 4:2955–2963

77. Tokuno T, Nogi M, Karakawa M, Jiu JT, Nge TT, Aso Y, Suganuma K (2011) Fabrication of silver nanowire transparent electrodes at room temperature. Nano Res 4:1215–1222
78. Song JZ, Li JH, Xu JY, Zeng HB (2014) Superstable transparent conductive Cu@Cu4Ni nanowire elastomer composites against oxidation, bending, stretching, and twisting for flexible and stretchable optoelectronics. Nano Lett 14:6298–6305
79. Stortini AM, Moretto LM, Mardegan A, Ongaro M, Ugo P (2015) Arrays of copper nanowire electrodes: preparation, characterization and application as nitrate sensor. Sens Actuators B 207:186–192
80. Rowell MW, McGehee MD (2011) Transparent electrode requirements for thin film solar cell modules. Energy Environ Sci 4:131–134
81. Wang J, Jiu J, Araki T, Nogi M, Sugahara T, Nagao S, Koga H, He P, Suganuma K (2015) Silver nanowire electrodes: conductivity improvement without post-treatment and application in capacitive pressure sensors. Nano-Micro Lett 7:51–58
82. Liu C-H, Yu X (2011) Silver nanowire-based transparent, flexible, and conductive thin film, Nanoscale Res Lett 6:75 (1–8)
83. Gutoff EB, Cohen ED (2006) Coating and drying defects: troubleshooting operating problems. Wiley, New York
84. Deng B, Hsu P-C, Chen G, Chandrashekar BN, Liao L, Ayitimuda Z, Wu J, Guo Y, Lin L, Zhou Y, Aisijiang M, Xie Q, Cui Y, Liu Z, Peng H (2015) Roll-to-roll encapsulation of metal nanowires between graphene and plastic substrate for high-performance flexible transparent electrodes. Nano Lett 15:4206–4213
85. Jeong CW, Nair P, Khan M, Lundstrom M, Alam MA (2011) Prospects for nanowire-doped polycrystalline graphene films for ultratransparent, highly conductive electrodes. Nano Lett 11:5020–5025
86. Peng H, Dang W, Cao J, Chen Y, Wu D, Zheng W, Li H, Shen Z-X, Liu Z (2012) Topological insulator nanostructures for near infrared transparent flexible electrodes. Nat Chem 4:281
87. An BW, Hyun BG, Kim S-Y, Kim M, Lee M-S, Lee K, Koo JB, Chu HY, Bae B-S, Park J-U (2014) Stretchable and transparent electrodes using hybrid structures of graphene-metal nanotrough networks with high performances and ultimate uniformity. Nano Lett 14: 6322–6328
88. Novoselov KS, Falko VI, Colombo L, Gellert PR, Schwab MG, Kim K (2012) A roadmap for graphene. Nature 490:192–200
89. Liu W-B, Pei S, Du J, Liu B, Gao L, Su Y, Liu C, Cheng H-M (2011) Additive-free dispersion of single-walled carbon nanotubes and its application for transparent conductive films. Adv Funct Mater 21:2330–2337
90. Chen Z, Kobashi K, Rauwald U, Booker R, Fan H, Hwang W-F, Tour JM (2006) Soluble ultra-short single-walled carbon nanotubes. J Am Chem Soc 128:10568–10571
91. Asada Y, Miyata Y, Ohno Y, Kitaura R, Sugai T, Mizutani T, Shinohara H (2010) High-performance thin-film transistors with DNA-assisted solution processing of isolated single-walled carbon nanotubes. Adv Mater 22:2698–2701
92. Coleman JN (2009) Liquid-phase exfoliation of nanotubes and graphene. Adv Funct Mater 19:3680–3695
93. Wang Y, Di CA, Liu YQ, Kajiura H, Ye SH, Cao LC, Wei DC, Zhang HL, Li YM, Noda K (2008) Optimizing single-walled carbon nanotube films for applications in electroluminescent devices. Adv Mater 20:4442–4449
94. Dillon AC, Gennett T, Jones KM, Alleman JL, Parilla PA, Heben MJ (1999) A simple and complete purification of single-walled carbon nanotube materials. Adv Mater 11:1354
95. Salzmann CG, Llewellyn SA, Tobias G, Ward MAH, Huh Y, Green MLH (2007) The role of carboxylated carbonaceous fragments in the functionalization and spectroscopy of a single-walled carbon-nanotube material. Adv Mater 19:883–887
96. Kim J, Cote LJ, Kim F, Yuan W, Shull KR, Huang J (2010) Graphene oxide sheets at interfaces. J Am Chem Soc 132:8180–8186

97. Liu Q, Ren W, Chen ZG, Wang DW, Liu B, Yu B, Li F, Cong H, Cheng HM (2008) Diameter-selective growth of single-walled carbon nanotubes with high quality by floating catalyst method. ACS Nano 2:1722–1728
98. Wu ZC, Chen ZH, Du X, Logan JM, Sippel J, Nikolou M, Kamaras K, Reynolds JR, Tanner DB, Hebard AF, Rinzler AG (2004) Transparent, conductive carbon nanotube films. Science 305:1273–1276
99. Graupner R, Abraham J, Vencelova A, Seyller T, Hennrich F, Kappes MM, Hirsch A, Ley L (2003) Doping of single-walled carbon nanotube bundles by Brønsted acids. Phys Chem Chem Phys 5:5472–5476
100. Geng HZ, Kim KK, Song C, Xuyen NT, Kim SM, Park KA, Lee DS, An KH, Lee YS, Chang Y, Lee YJ, Choi JY, Benayad A, Lee YH (2008) Doping and de-doping of carbon nanotube transparent conducting films by dispersant and chemical treatment. J Mater Chem 18:1261–1266
101. Hu L, Hecht DS, Gruner G (2004) Percolation in transparent and conducting carbon nanotube networks. Nano Lett 4:2513–2517
102. Chen JH, Jang C, Xiao S, Ishigami M, Fuhrer MS (2008) Intrinsic and extrinsic performance limits of graphene devices on SiO_2. Nat Nanotech 3:206–209
103. Novoselov KS, Geim AK, Morozov SV, Jiang D, Zhang Y, Dubonos SV, Grigorieva IV, FirsovA A (2004) Electric field effect in atomically thin carbon films. Science 306:666–669
104. Chabot V, Higgins D, Yu A, Xiao X, Chena Z, Zhang J (2014) A review of graphene and graphene oxide sponge: material synthesis and applications to energy and the environment. Energy Environ Sci 7:1564–1596
105. Chandrashekar BN, Deng B, Smitha AS, Chen Y, Tan C, Zhang H, Peng H, Liu Z (2015) Roll-to-roll green transfer of CVD graphene onto plastic for transparent and flexible triboelectric nanogenerator. Adv Mater 27:5210–5216
106. Jo G, Choe M, Lee S, Park W, Kahng YH, Lee T (2012) The application of graphene as electrodes in electrical and optical devices. Nanotechnology 23:112001 (19 pp)
107. Bonaccorso F, Sun Z, Hasan T, Ferrari AC (2010) Graphene photonics and optoelectronics. Nat Photon 4:611–622
108. Sadasivuni KK, Kafy A, Zhai L, Ko H-U, Mun S, Kim J (2015) Transparent and flexible cellulose nanocrystal/reduced graphene oxide film for proximity sensing. Small 11: 994–1002
109. Sheraw CD, Zhou L, Huang JR, Gundlach DJ, Jackson TN, Kane MG, Hill IG, Hammond MS, Campi J, Greening BK, Francl J, West J (2002) Organic thin-film transistor-driven polymer-dispersed liquid crystal displays on flexible polymeric substrates. Appl Phys Lett 80:1088–1090
110. Nordendorf G, Kasdorf O, Kitzerow HS, Liang Y, Feng X, Muellen K (2010) Liquid crystal addressing by graphene electrodes made from graphene oxide. Jpn J Appl Phys 49:100206-1–100206-3
111. Reshak AH, Shahimin MM, Juhari N, Suppiah S (2013) Electrical behaviour of MEH-PPV based diode and transistor. Prog Biophys Mol Biol 113:289–294
112. Yuan J, Luna A, Neri W, Zakri C, Schilling T, Colin A, Poulin P (2015) Graphene liquid crystal retarded percolation for new high-k materials. Nat Commun 6:8700 (1–8)
113. Scott JC, Kaufman JH, Brock PJ, DiPietro R, Salem J, Goitia JA (1996) Degradation and failure of MEH-PPV light-emitting diodes. J Appl Phys 79:2745–2752
114. Bremer M, Naemura S, Tarumi K (1998) Model of ion solvation in liquid crystal cells. Jpn J Appl Phys 37:L88
115. Roy-Mayhew JD, Aksay IA (2014) Graphene materials and their use in dye-sensitized solar cells. Chem Rev 114:6323–6348
116. Li SS, Tu KH, Lin CC, Chen CW, Chhowalla M (2010) Solution-processable graphene oxide as an efficient hole transport layer in polymer solar cells. ACS Nano 4:3169–3174
117. Yin Z, Wu S, Zhou X, Huang X, Zhang Q, Boey F, Zhang H (2010) Electrochemical deposition of ZnO nanorods on transparent reduced graphene oxide electrodes for hybrid solar cells. Small 2:307–312

118. Li X, Zhu H, Wang K, Cao A, Wei J, Li C, Jia Y, Li Z, Li X, Wu D (2010) Graphene-on-silicon Schottky junction solar cells. Adv Mater 22:2743–2748
119. Shim J-P, Choe M, Jeon S-R, Seo D, Lee T, Lee D-S (2011) InGaN-based p–i–n solar cells with graphene electrodes. Appl Phys Express 4:052302–052302–052302–052303
120. Arco LGD, Zhang Y, Schlenker CW, Ryu K, Thompson ME, Zhou C (2010) Continuous, highly flexible, and transparent graphene films by chemical vapor deposition for organic photovoltaics. ACS Nano 4:2865–2873
121. Huang J-H, Fang J-H, Liu C-C, Chu C-W (2011) Effective work function modulation of graphene/carbon nanotube composite films as transparent cathodes for organic optoelectronics. ACS Nano 5:6262–6271
122. Kim JK, Kim SJ, Park MJ, Bae S, Cho S-P, Du QG, Wang DH, Park JH, Hong BH (2014) Surface-engineered graphene quantum dots incorporated into polymer layers for high performance organic photovoltaics. Sci Rep 5:14276
123. Roy A, Park SH, Cowan S, Tong MH, Cho S, Lee K, Heeger AJ (2009) An inverted organic solar cell with an ultrathin Ca electron transporting layer and MoO_3 hole-transporting layer. Appl Phys Lett 95:153304–153309
124. Kim JY, Lee K, Coates NE, Moses D, Nguyen T-Q, Dante M, Heeger AJ (2007) Efficient tandem polymer solar cells fabricated by all-solution processing. Science 317:222–225
125. Cho S, Seo JH, Lee K, Heeger AJ (2009) Enhanced performance of fullerene n-channel field-effect transistors with titanium sub-oxide injection layer. Adv Funct Mater 19: 1459–1464
126. Wan X, Long G, Huang L, Chen Y (2011) Graphene—a promising material for organic photovoltaic cells. Adv Mater 23:5342–5358
127. He Z, Zhong C, Huang X, Wong W, Wu H, Chen L, Su S, Cao Y (2011) Simultaneous enhancement of open-circuit voltage, short-circuit current density, and fill factor in polymer solar cells. Adv Mater 23:4636–4643
128. Fan FR, Lin L, Zhu G, Wu WZ, Zhang R, Wang ZL (2012) Transparent triboelectric nanogenerators and self-powered pressure sensors based on micropatterned plastic films. Nano Lett 12:3109–3114

Biodegradable Nanocomposites for Energy Harvesting, Self-healing, and Shape Memory

Deepu Thomas, John-John Cabibihan, Sasi Kumar, S.K. Khadheer Pasha, Dipankar Mandal, Meena Laad, Bal Chandra Yadav, S.I. Patil, Anil Ghule, Payal Mazumdar, Sunita Rattan and Kishor Kumar Sadasivuni

Abstract This review aims to survey the rapidly expanding field of energy harvesting, self-healing, and shape-memory biodegradable composites by reviewing the major successful autonomic designs developed over the last decade. We have discussed the characterization of the composite and dispersion of the filler by different methods such as grafting, chemical modifications. Also, we have highlighted the recent work on polymers and blends, hydrogels of biocomposites and their controllable approach for adjusting desired properties. In addition to above,

D. Thomas (✉)
Research and Development Centre, Bharathiar University, Coimbatore 641046, India
e-mail: deepuskariankal@gmail.com

J.-J. Cabibihan · K.K. Sadasivuni
Mechanical and Industrial Engineering Department, Qatar University,
P.O. Box 2713, Doha, Qatar
e-mail: kishor_kumars@yahoo.com

S. Kumar
Chemistry Division, School of Advanced Sciences, VIT University,
Vellore 632014, Tamil Nadu, India

S.K. Khadheer Pasha
Sensors Laboratory, School of Advanced Sciences, VIT University,
Vellore 632014, Tamil Nadu, India

D. Mandal
Organic Nano-Piezoelectric Device Laboratory, Department of Physics,
Jadavpur University, Kolkata 700032, India

M. Laad
Symbiosis Institute of Technology (SIT), Symbiosis International University (SIU),
Lavale, Pune, Maharashtra, India

B.C. Yadav
Nanomaterials and Sensors Research Laboratory, Department of Applied Physics,
Babasaheb Bhimrao Ambedkar University, Lucknow 226025, Uttar Pradesh, India

S.I. Patil
Department of Physics, University of Pune, Pune-7, India

D. Ponnamma et al. (eds.), *Smart Polymer Nanocomposites*,
Springer Series on Polymer and Composite Materials,
DOI 10.1007/978-3-319-50424-7_14

the design considerations critical to the successful integration of these components in the commercial applications have been discussed. These materials have huge demand in the development of robust modeling and design tools based on a fundamental understanding of the complex and time-variant properties of the material and mechanization structure in diverse environments. The potential directions for future advancement in this field are also discussed.

Keywords Biocomposites · Nanogenerators · Biodegradable · Shape recovery

Contents

1 Introduction

Biodegradable materials based on bio polymers are the real solutions for the majority of current environmental problems. The biopolymers originating from the renewable biomass help to maintain a sustainable nature. Other than the biomass, the source of biopolymers can be microorganisms, petrochemical sources, and/or synthetic polymerization processes. The biodegradable materials decompose to water and CO_2 under aerobic conditions whereas under anaerobic conditions, methane will forme as an additional product. These materials are capable of substituting many petroleum-based products in technology and industry as well as it allow the reuse of the composte after their use [1]. Very recently, biocompatible electronic devices, operated inside the human body for a prolonged period without pain, has been removed by disintegrating it without any surgery. In this context, the time controlled, biodegradable nanogenerators for such implanted electronic devices will be of great interest. Many biological molecules such as proteins, polysaccharides, and deoxyribonucleases are investigated for their application in mechanical energy generation/piezoelectricity.

The extended lifetime, renewability, scalability, no recharging methods, etc., make piezoelectric power harvesting the most sustainable way of energy genera-

A. Ghule
Department of Chemistry, Shivaji University, Kolhapur 416004, Maharashtra, India

P. Mazumdar · S. Rattan
Amity Institute of Applied Sciences, Amity University Uttar Pradesh, Noida 201301, India

tion. This mechanical energy harvesting is much effective in building the self-powered systems, military monitoring devices, remote weather station, wireless sensors, and biomedical implants [2]. The main advantage of this energy harvesting method is its applicability in many fields where mechanical energy exists.

Nanogenerators based on the silk fibroin composites containing biocompatible ferroelectric materials are reported. The transparent silk fibroin is also used to develop transistors and many photonic devices. Wood is also studied for its piezoelectric performance on account of the monoclinic symmetry and uniaxial orientation of cellulose crystallites in the wood fibers. However, the piezoelectric modulus of wood is about 5% of a quartz crystal. The seashells are also reported for their piezoelectric and ferroelectric properties. Macrofiber composites (MFC) made up of PZT fibers embedded in epoxy resin shows good piezoelectric behavior. This material is lightweight, and its increased actuation strain energy density and robust construction make them useful in automotive, aerospace, and other industrial applications [3, 4].

The shape recovery by various stimulations [5–11] (for instance, magnetic-active effect, water-active effect, electroactive effect, and photoactive effect [12]) has tremendous applications in many industries [13–16]. In biomedical fields, safety and poor degradability often limits the use of conventional shape-memory polymers, in this context, biodegradable polymers have to be explored. PLA/HA composites are reported for their excellent shape recovery [17, 18].

Biodegradable electronic devices made of natural and synthetic materials [19–21] can transform electronically active permanent implantable biomedical devices into temporary components [22–25], by avoiding risks of chronic implants [26]. Polypyrrole/lignin composites are reported for such application due to the redox reactivity of the quinone groups in lignin and the high electrical conductivity of doped Ppy (σPpy/lignin ~ 30 s cm^{-1}) [27]. However, the organic electrolytes of poor biocompatibility and toxic electrode materials cause many problems for implementation and clinical adoption. Recently, melanin pigments are also suggested as anode materials for aqueous Na^+ energy storage devices [21]. The lightweight and low-cost electroactive polymers (EAPs) change their shape with an applied electric field, and useful in artificial muscles and other smart electronic devices [28, 29]. Electrostrictive EAP is reported for its actuator application [30] and thus can be useful in energy harvesting from environmental sources, such as human movements [31].

Mechanical damage on microscopic level is a serious issue which needs periodic inspection and maintenance [32]. Self-healing materials solve this issue by responding to microcracks through certain active phases within the material and by proper repairing mechanism [33]. The self-healing process extends the durability and sustainability of developed materials. The biopolymer chitosan notable for its low toxicity, biocompatibility, and biodegradability [34, 35] is known for its self-healing properties. Here, the sunlight triggers the healing mechanism through the reaction of chitosan molecules with split oxetane rings from a ring-shaped molecule and polyurethane paint [36]. The self-healing ability of nanofibers containing embedded healing agents also prevent microcracking and delamination [37–41]. Numerous investigation on self-healing process [42], the chemistry

involved in it [43], biomimicing [44] the healing additives, and external stimuli to initiate healing [45] were the subjects of major study.

Many shape-memory polymers (SMPs) are applied in orthodontic wires, pipe couplings vascular stents, vibration dampers, and actuators [13, 46]. PLA/PCL/EC-bp biocomposites made by solution casting demonstrate good thermomechanical and shape-memory properties [13, 47–50]. Usually, the SMP retains its shape by releasing the stress while changing its temperature (by cooling/heating) [48, 51, 52]. Biodegradable SMPs will be a useful device for the minimall invasive surgery [13, 14, 53, 54], temporary devices [55, 56], and scaffolding devices [13]. Zheng et al. reported the shape-memory behavior of poly(D,L-lactide) (PDLLA)/hydroxyapatite (HA) composites [18]. PLLA is another biopolymer exhibiting good shape recovery [57–62]. Shape-memory properties investigated by cyclic thermomechanical study under stress/strain-controlled state and its quantification were the subject of study of Sauter et al. [63].

2 Biodegradable Composites for Energy Harvesting

Kim et al. [64] synthesized a polyvinylpyrrolidone (PVP) composite made of Ag nanowires, silk solution (30 wt%), and a few nanoparticles ($BaTiO_3$, $ZnSnO_3$, etc.). The biodegradable property of the silk fibroin film were controlled by glycerol. A nanogenerator was designed based on this composite as shown in Fig. 1a. It consists of a one-dimensional Al wire at the inner side and an Al sheet at the outer. An output voltage of 1.8 V and an output current density of 0.1 $\mu A/cm^2$ are obtained which were similar in performance with film nanogenerator. The whole work suggests a promising application of robust textile nanogenerator in future smart textiles.

An electrostrictive polymer composite was used to make energy harvesting devices by Eddiai et al. [65]. Figure 2 shows the schematic representation of the developed sample (Fig. 2a) and the equivalent electric circuit for the electric impedance of a vibrating polymer (Fig. 2b). Here, CP represents the capacitance of the clamped polymer, $RP(\omega)$, the resistance attributed to the dielectric losses and conduction (both parameters are functions of the relaxation frequency) and I_{ac} is the current. An electrical load, R, is also connected in series with the polymer, and P is the power harvested on this load, $P = RI^2$ (I, the current due to mechanical–electrical conversion).

The power versus the electric load R is shown in Fig. 3, and the measurements are correlated with modeling. This illustrates the influence of strain ($S = 2\%$, $S = 4\%$, and $S = 6.5\%$ at 6 Hz) on the piezoelectric coefficient using FFT analysis for a given electric field (13 MV/m). It is established that an optimal load resistance near 75 MΩ exists in addition to the linear dependence of the harvested power and the strain amplitude. Also, the change in mechanical parameters causes slight increase in the optimal load.

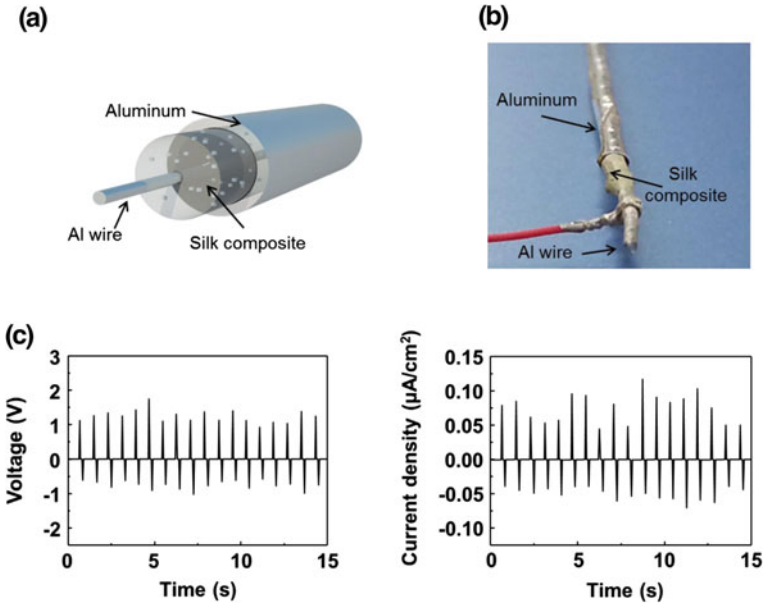

Fig. 1 **a** Schematic image and **b** a photograph of silk fibroin-based composite-type wire generator which consists of aluminum wire, silk fibroin composite layer, and aluminum electrode **c** output voltage and current density of the wire generator [64]. Copyright 2015. Reproduced with permission from Elsevier Ltd

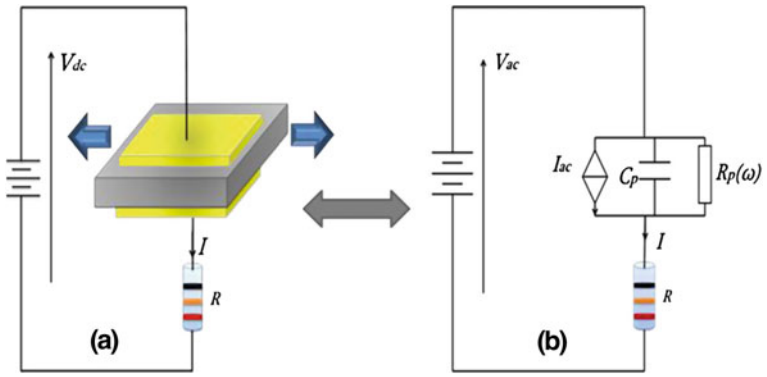

Fig. 2 **a** A schematic of the sample, **b** the equivalent electric circuit of an electrostrictive polymer [65]. Copyright 2016. Reproduced with permission from John Wiley and Sons

Schnepp and coworkers determined the shear piezoelectric constants $-d_{14} = d_{25}$ for anisotropic nanorods with uniaxial symmetry. By investigating the properties of optically active polymers and polypeptides, it is suggested that the piezoelectricity is due to the internal rotation of dipoles. Biodegradable and optically active PLA

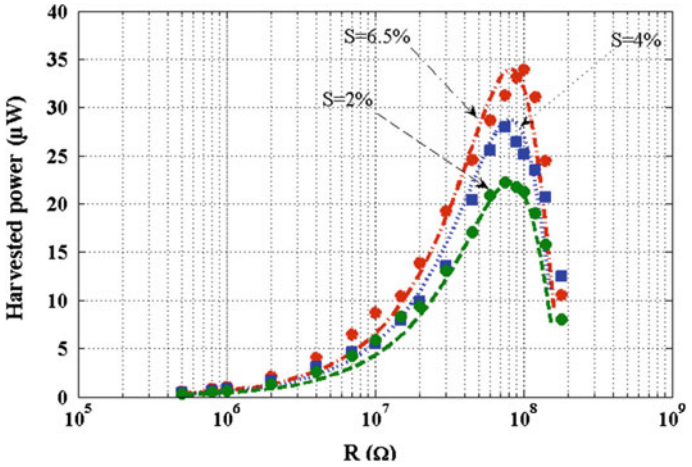

Fig. 3 The harvested power under different strain amplitude values at f_e = 1 Hz and f_m = 6 Hz for a constant electric field of E_{dc} = 13 MV/m [65]. Copyright 2016. Reproduced with permission from John Wiley and Sons

was tested by elongation, and a value of $d_{14} = -10$ pC/N was obtained. The poled films of submicron-thick aliphatic polyurea also exhibited pyro- and piezoelectric effects. In that case, a piezoelectric constant of d_{31} = 10 pC/N was observed (up to 200 °C) [66].

In an oscillating field of maximum amplitude 2 V, the needle-like crystals expand and contract as evidenced from the piezoresponse force microscopy (Fig. 4). In response to the applied AC voltage, the nanorods show a uniform out-of-plane response (solid bright region of Fig. 4a). The corresponding topographic image given in Fig. 4b further evidences the uniform perpendicular crystal deflection. Figure 4c indicate the phase shift increase with increasing AC voltage, again confirming piezoresponsive nature of the nanorods over the entire applied voltage range. This was in accordance with the piezobehavior of a single-crystalline ZnO. Similar investigations carried out on aragonite structure did not show any piezoresponse.

Investigation of piezoelectric nature was done by various techniques such as dual-AC resonance tracking (DART), piezoresponse force microscope (vector-PFM), and switching spectroscopy PFM (SS-PFM). Strong piezoresponse along the direction perpendicular to the platelet surface (close to local polarization direction of intracrystalline biopolymers) was observed by vector-PFM technique whereas strong piezoresponse for the interlamellar biopolymer is exhibited at a parallel direction to the platelet surface. It is also established that the biopolymers in nacre have similar ferroelectric hysteresis loops as polyvinylidene fluoride (PVDF) and useful in energy storage applications [68].

Cellulose is another piezoelectric material, especially in its nanocrystalline form [69, 70]. The chemical treatments on cellulose can enhance the piezoelectric

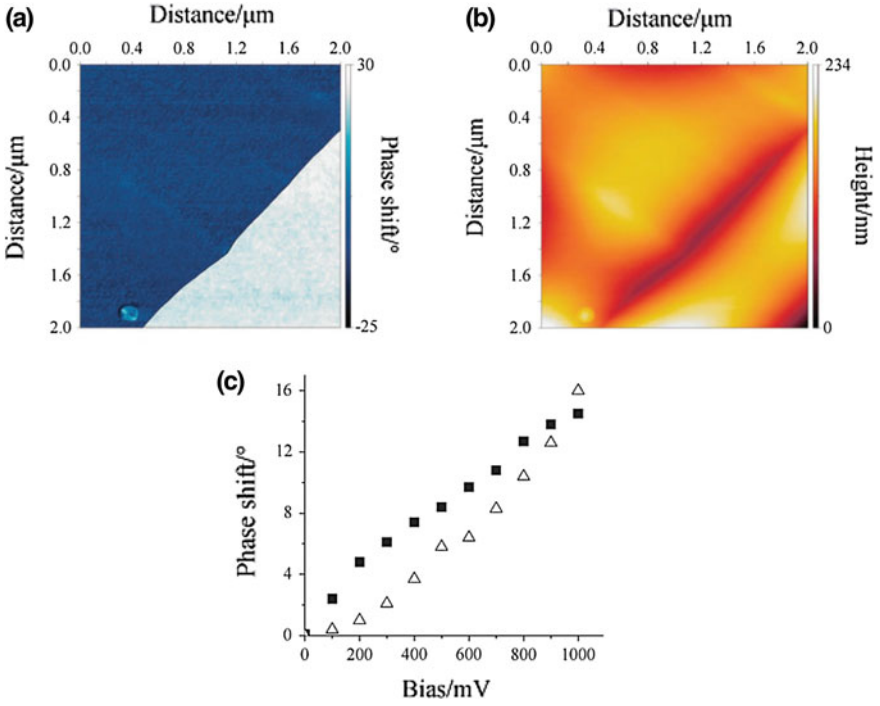

Fig. 4 **a** Out-of-plane piezoresponse image (*perpendicular deflection*), showing two distinct out-of-phase regions (*blue* and *white domains*) and **b** corresponding topographic image for a single langasite nanorod. **c** Plot of the phase shift against varying AC voltage in the out-of-plane direction for the langasite sample (') and a piezoelectric ZnO control (*n*) [67]. Copyright 2010. Reproduced with permission from Royal Society of Chemistry

modulus, whereas gamma-ray irradiation has little effect on it. In wood, the piezoelectric polarization can be effectively utilized in checking the shock velocity. It is also reported that the piezoelectric modulus of polymethyl-glutamate thin film is twice or thrice higher than quartz crystal. Similar performance and sensitivity are obtained for two microphones: one, the ordinary dynamic microphones; the other made of polymethyl-glutamate film. Piezoelectric property is also shown by bone, silk, tendon, cellulose acetate, and synthetic polypeptides. Collagen fibers inside the bone and tendon produce piezoelectric polarization inside the living body upon mechanically energy [69].

The piezoelectric property of cellulose paper was further increased by stretching method with different wet-drawing ratios. In addition to the piezoelectric charge constant, the Young's modulus also depends on the drawing ratio and the direction of nanofibrils. Without drawing, the paper showed a piezoelectric charge constant of 0.41 pC/N, and with drawing, it became 5.2 pC/N. At 45° alignment, the charge constant was its maximum, 7.3 pC/N, and this was 18 times higher than that at 90° alignment. In another study, the nanocrystalline cellulose (CNCs) films were tested

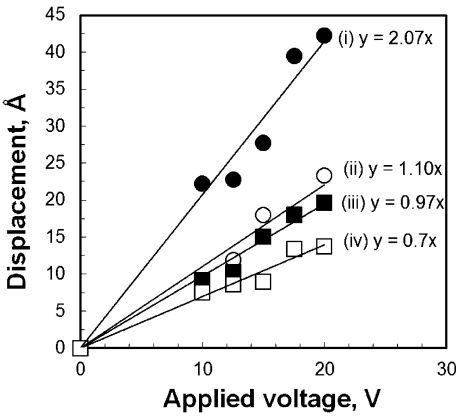

Fig. 5 Vertical displacement of CNC films subject to externally applied electric fields. Included are results for films produced under four different conditions during electric field-assisted shear. The films with the higher degree of alignment produced a higher piezoelectric response, as indicated by the *slopes* of the profiles. The displacements and voltages are both peak-to-peak values [71]. Copyright 2009. Reproduced with permission from Elsevier Ltd

for their polarization gradients and strain mechanics using contact mode atomic force microscopy. The collective asymmetric crystalline structure of CNC causes a good piezoelectric response, in terms of the effective shear piezoelectric constant (d_{25}) which was 2.1 Å/V, similar to a piezoelectric metal oxide reference film [71] (Fig. 5).

Various CNC films with different degrees of particle alignment were analyzed for the piezoelectricity. An average value was calculated for several repetitive measurements for a given voltage. The applied voltage and the measured effective displacement are found to be linear. CNC films with partial alignment showed a piezoelectric constant of 0.97 Å/V (at 800 V/cm, 45 Hz), and a similar value, 1.10 Å/V, at 400 V/cm and 200 Hz. The degree of alignment for these two films was 42 and 46%, respectively. When the frequency is high (2 kHz), high particle rotation is expected, but low field strength at this stage (100 V/cm) will not be sufficient for the effective particle polarization.

The main criterion for a CNC to be piezoelectric is its high-level orientation, and electric fields at different strengths are usually applied to achieve this criterion. The piezoelectric measurement using a contact mode AFM is schematically represented in Fig. 6. The conducting diamond tips avoid sample-tip electrostatic interaction, and the measurements were done at 23 °C and 50% relative humidity. By knowing the slope of the measured tip displacement at the applied voltage, the piezoelectric constant was calculated. The peak-to-peak voltage was changed by 2.5 V with a maximum of 20 V.

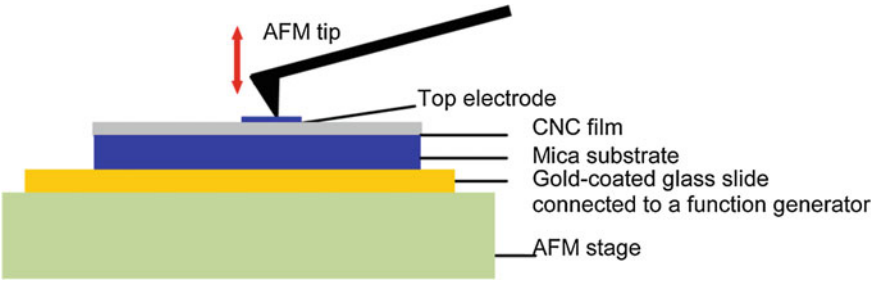

Fig. 6 Schematic illustration of the AFM system used to measure the displacement of CNC films in contact with an AFM diamond tip and under given applied voltages (10 Hz frequency) [71]. Copyright 2012. Reproduced with permission from American Chemical Society

3 Biodegradable Composites for Self-healing

The general mechanism of self-healing can be divided into the following four categories: (i) self-healing by crack-filling adhesion, (ii) self-healing by diffusion, (iii) self-healing by bond reformation, and (iv) self-healing by virgin property strengthening in response to stress. Out of all these mechanisms, the one by crack-filling adhesion is the most significant and well-investigated type.

Bisphosphonate groups and calcium phosphate nanoparticles are non-covalently cross-linked in HABP.CaP and showed excellent self-healing behavior greater than that in covalently cross-linked hyaluronan hydrogels. The recovery is observed for HABP.CaP hybrids in <5 s (Fig. 7a), but in the case of its covalently cross-linked analog (with same amount of CaP), HA.CaP, the healing was not seen. The self-healing property is also quantified by measuring the storage and loss modulus of both covalently cross-linked (HA + CaP) and non-covalently cross-linked (HABP.CaP) nanocomposites under various strains of 1 and 1000% (Fig. 7b).

Spoljaric et al. synthesized hydrogels from NFC filled PVA–borax system and observed good self-healing as illustrated in Fig. 8. The main reason behind this effect is due to the hydrogen bonds present within the hydrogels which are readily able to break and reform. However, the use of such hydrogels is limited and mostly the self-healing process relies on pH, heat, or other external stimulus. Another significant point to be noted is its ability to reform in the absence of external stimulus. This can be attributed to the free −OH groups present in its structure that can cause formation of hydrogen bonds as well as the sufficient polymer chain mobility.

Completely autonomic, biomimetic, and efficient self-healing devices will definitely change the current biomedical scenario and favors the invention of advanced equipment in many industrial applications. Self-healable and biodegradable polymeric composites can be good alternatives in orthopedic fixation due to their appropriate stiffness, high strength, and strength retention.

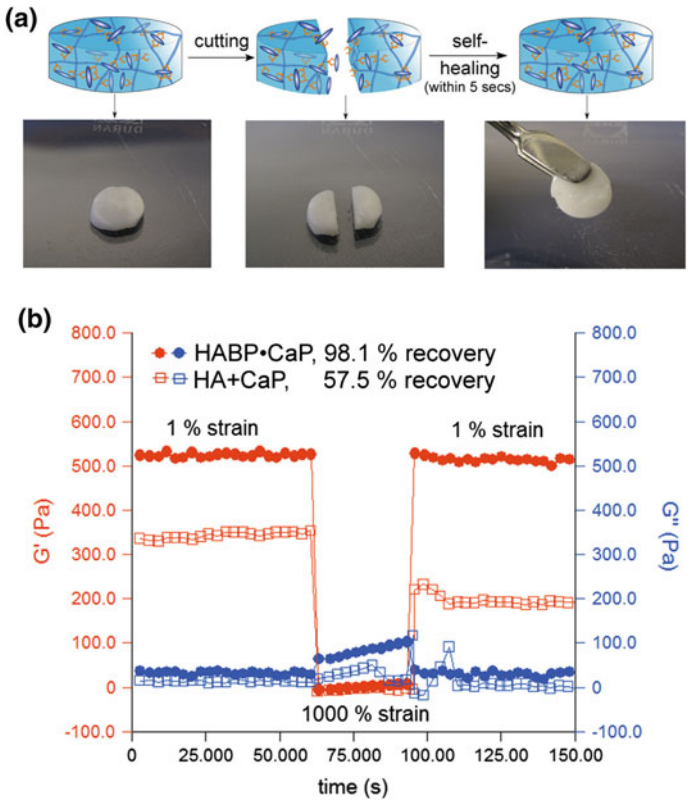

Fig. 7 Self-healing behavior of non-covalently cross-linked HABP.CaP hybrid nanocomposites containing 2 w/v% hyaluronan-bisphosphonate (DSBP = 8.1%) and 6 w/v% CaP nanoparticles. **a** Schematic illustration and photographs of self-healing after failure induced by cutting. **b** Recovery of non-covalently cross-linked HABP.CaP and covalently cross-linked HA + CaP hydrogels after sequential shear strains of 1, 1000 and 1% [72]. Copyright 2014. Reproduced with permission from Elsevier Ltd

4 Biodegradable Composites for Shape Memory

The key characteristics of a polymer to be a typical SMP are the presence of a stable network and the possibility of a reversible switching transition [74]. Examples for these stable networks include chemical cross-linking, molecule entanglement, crystallization, and interpenetrating network. [8, 74–80]. Large number of biodegradable polymers such as poly(ε-caprolactone), poly(D,L-lactide), poly(*p*-dioxanone)epoly(ε-caprolactone) copolymer, poly(ethylene glycol) monomethylether-monomethacrylate (PEGMA) also show shape recovery. Chen et al. developed a biodegradable material from chitosan cross-linked epoxy composite and explained its water-sensitive shape recovery [81, 82]. In another study, Luo et al. also reported water-active shape-memory material from cellulose

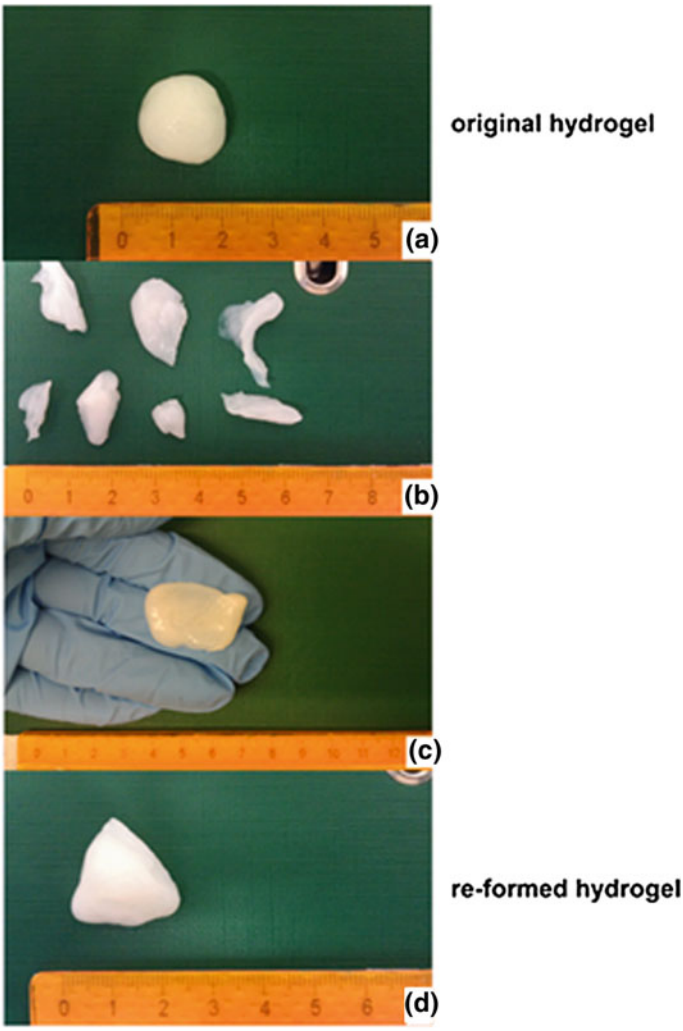

Fig. 8 Malleability and "reformability" of NFC–PVA–borax hydrogels (PVA:borax ratio 5:1, NFC concentration 50 wt%): **a** the original hydrogel, **b** fracturing the hydrogel into several pieces, **c** molding the pieces into a single material by hand, **d** the "reformed" single, continuous hydrogel [73]. Copyright 2014. Reproduced with permission from Elsevier Ltd

nanowhisker/SMPU nanocomposites [83]. Many water-active materials are synthesized from the hydrophilic Cellulose nano-whiskers. In such materials, the deformed cellulose nanowhisker/SMP composite recovers its shape, when exposed to water stimulant, due to the change in enthalpy elasticity of the polymer network. If a typical shape-memory polymer has well-separated thermal transitions, that can exhibit MSME after multiple-step programming stages. Another filler used to

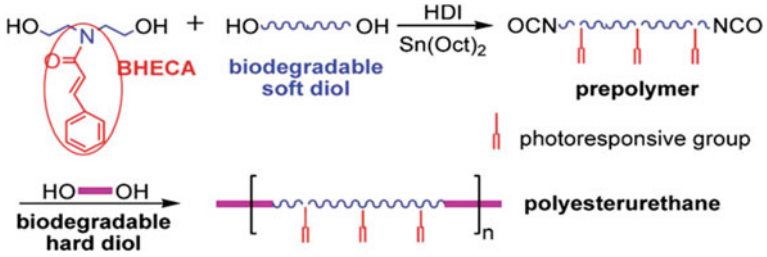

Fig. 9 Synthesis of biodegradable multiblock polyesterurethane containing pendant photoactive cinnamamide groups from biodegradable soft diol (polycaprolactone diol), biodegradable hard diol (poly-(L-lactic acid) diol), and *N*,*N*-bis(2-hydroxyethyl) cinnamamide (BHECA) [9]. Copyright 2011. Reproduced with permission from American Chemical Society

synthesize biodegradable SMP is polyhedral oligomeric silsesquioxanes (POSS) [84–89].

Figure 9 represents a reversible photodimerization-based SMP made of *N*,*N*-bis (2-hydroxyethyl) cinnamamide (BHECA) in which the cinnamamide moieties undergo the photodimerization process. Lendlein et al. [9] also synthesized similar photoresponsive polymers with cinnamic acid and cinnamylidene acetic acid terminal as the photoreversible switches.

The shape-memory property of PCL-based composites is mainly due to the polymer's entropic elasticity upon heating. The neat PCL shows the property depending only on ambient heat whereas the PCL composites containing Fe_3O_4 nanoparticles alternating magnetic field induces heating. This is due to the Brownian and Néel relaxation losses happening in Fe_3O_4 which is transferred to heat. The shape recovery of PCL in hot water and that of PCL/Fe_3O_4 in an alternating magnetic field is shown in Fig. 10. The recovery for the helicoidal *c*-PCL/Fe_3O_4 system in hot water took place in about 30 s whereas the same specimen took 130 s when inductively heated in the alternating magnetic field. This proved the better reactivity of the composite to hot water when compared with the magnetic field due to the slower heat loss and faster thermal transfer taking place in hot water. Faster recovery can be achieved by increasing the frequency and by using a heat shield for specimens when inductively heated [91].

Figure 11 well demonstrates the shape-memory property of PDLLA/HA composites at different times. Here, the shape recovery was achieved upon heating the specimen to 70 °C. Original shape is achieved at 60th second itself; however, complete recovery is observed at the 100th second. The reason for shape recovery of the PDLLA/HA composite is attributed to the crystalline nature of calcium phosphate particles and amorphous nature of PDLLA polymer. When these two components are mixed, the stationary phase and reversible phase come together, which is an essential condition for shape-memory effect.

The variation of shape recovery with respect to temperature for the PDLLA/HA composites are represented in Fig. 12. When the recovery temperature changed from 70 to 76 °C, the recovery time starts to stabilize. Moreover, starting from the

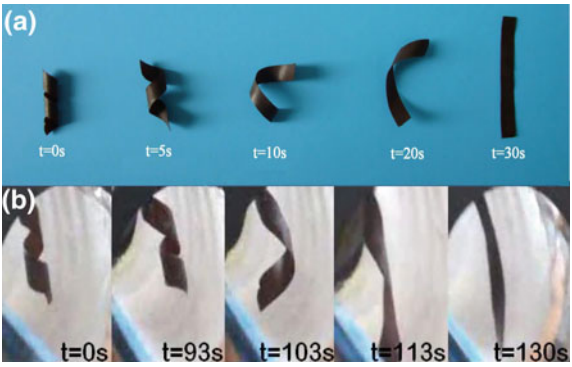

Fig. 10 Series of deploying helicoidal photograph **a** in hot water and **b** in an alternating magnetic field. The composites with 15 wt% Fe_3O_4 and 2.5 wt% BPO were selected to finish taking shape-recovery photographs when the specimens were responsive to 55 °C hot water and an alternating magnetic field with a frequency of 20 kHz and a field strength of 6.8 kA m^{-1} [90]. Copyright 2009. Reproduced with permission from IOP Science

onset of 76 °C, the recovery time little decreased [92]. Copyright 2015. Reproduced with permission from Elsevier Ltd.

Meng et al. investigated the shape-memory behavior of PLLA composites as illustrated in Fig. 13. With 50 and 100% maximum deformation strain, good recovery is reported (Fig. 13a, b). There is a different trend when subsequent cycles are tested, this can be due to the molecular reorganization taking place because of the crystallization, molecule orientation, and/or breakage of weak points during deformation. However, the remaining cycles after the first one, show similar and stable stress–strain behaviors. At 200% maximum deformation strain (Fig. 13c), the PLLA loses its shape recovery in addition to the increase in irrecoverable deformation with increasing testing cycles. The reason for this observation is attributed to the crystallinity loss of PLLA with large deformation strain. This points out that PLLA is not suitable for those shape-memory applications at large deformations. Based on this result, the author's synthesized chitosan/PLLA and checked the shape memory at a maximum deformation strain of 100%.

Shape-memory property of chitosan/PLLA biocomposite containing different concentrations of chitosan is well demonstrated in Fig. 14. For the experiment, composite wires are fabricated by melt blending at 160 °C. The wires are further cooled to normal room temperature to attain the permanent straight shape. The wires became soft, when they were kept in hot water at 65 °C. Now the samples were folded and cooled in air at room temperature. Thus, the deformed shape was fixed and after 2-min time, the folded wires memorize its original shape when triggered by keeping again in hot water at 65 °C. Quick shape recovery was observed for the composites containing lower amounts of chitosan; however, for the samples containing higher concentrations of chitosan, complete shape recovery is not observed. Thus, it is concluded that chitosan has a negative effect in shape-memory property of PLLA.

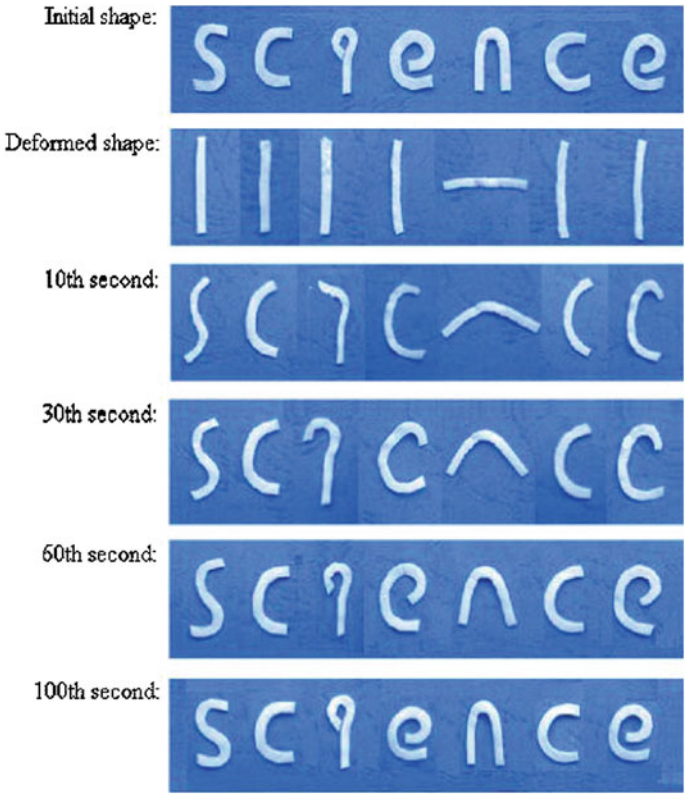

Fig. 11 The photographs showing the process of shape-memory recovery of "science" word made of PDLLA/HA composite taken with digital camera [18]. Copyright 2006. Reproduced with permission from Elsevier Ltd

In another study by Tsujimoto et al., shape-recovery property of polyESO/PCLs composites were studied. Here, the melting/recrystallization of PCL acts as a switching transition between the shape-memory/recovery effect and good recovery was observed for 50/50 wt% composite sample. For this specific composite, original shape was recovered after 25 s at 80 °C. It is also established that the recovery time completely depends on the operating temperature and component ratio of the samples. The major driving force for the recovery is elastic force generated in the ESO-based network polymer during deformation in additional to the PCL crystallinity. First, the PCL components melt causing the polyESO/PCL sample to deform. Cooling proceeds with the melt crystallization of PCL and fixes the shape with the internal stress of ESO-based network polymer. When the sample is reheated above the PCL melting temperature, polymer chain mobility enhances and the sample returns to original shape by the entropy elasticity of the ESO-based network polymer [93].

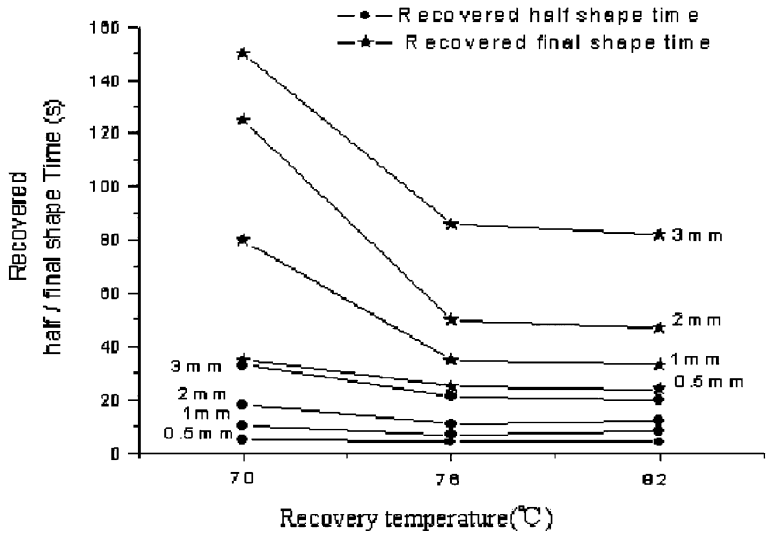

Fig. 12 Recovery time of different recovery temperatures of poly(D,L-lactide)/hydroxyapatite composites. Weight ratio: 2.5; thickness: 0.5, 1, 2, 3 mm. [18]. Copyright 2006. Reproduced with permission from Elsevier Ltd

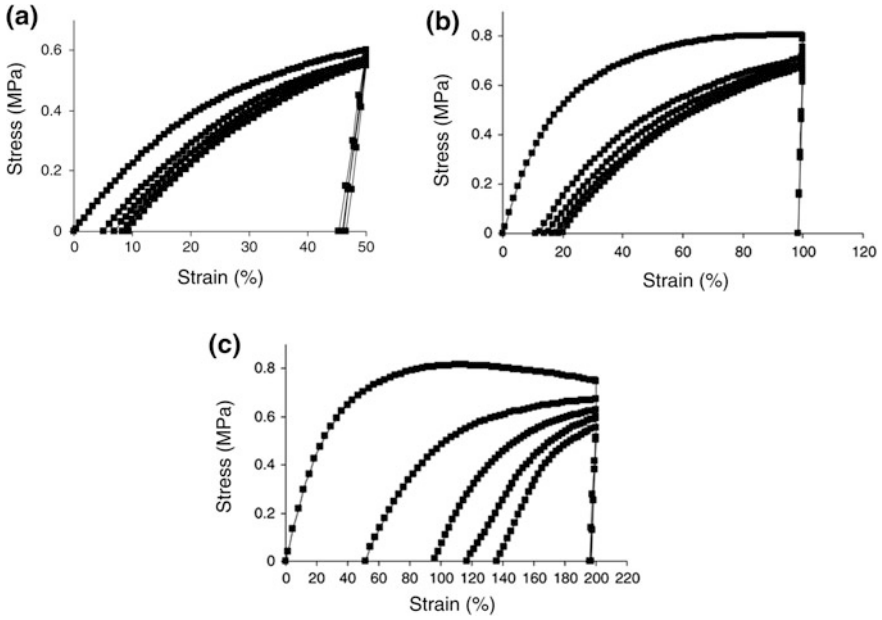

Fig. 13 The influence of deformation strain on the thermomechanical cyclic tensile curves of the PLLA. **a** 50%, **b** 100%, **c** 200% [92]. Copyright 2009. Reproduced with permission from Springer

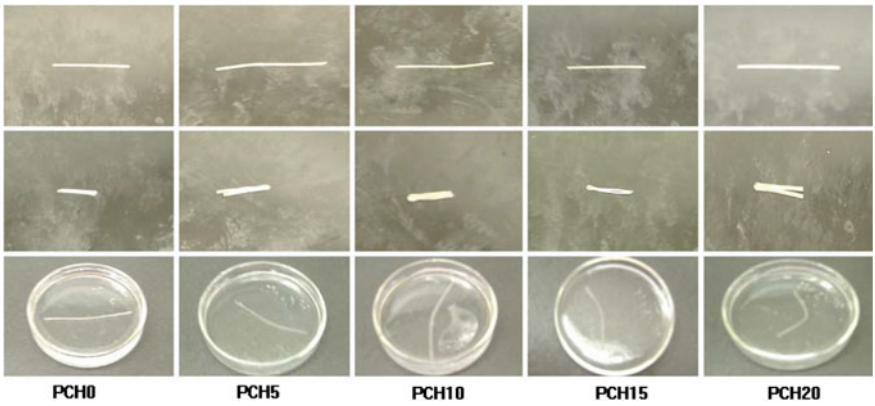

Fig. 14 The shape-memory effect of the chitosan/PLLA (*from top to bottom*: permanent shape, deformed shape, and recovered shape) [92]. Copyright 2009. Reproduced with permission from Springer

The main areas of useful applications of biodegradable shape-memory composites include biomedical devices, remote active medical instruments, deployable space structures, energy, textiles, engineering structures, bionics engineering, electronic engineering, civil engineering, dry/wet adhesives and fasteners, and household products. The biodegradable polyester-based SMPs are widely used in fabricating surgical sutures, catheters, and stents [94].

5 Limitations, Challenges, and Conclusions

Cost-effective and environmental friendly materials are the need of the hour, and the main properties discussed in this chapter—piezoelectricity, self-healing, and shape memory—contribute a major part to the development of bioelectronics. However, the situation is not that much clear to immediately change the current scenario. A lot of progress has to be made to make the synthesized materials in laboratories technologically feasible, economically affordable, and environmentally suitable. Energy harvesters based on PZT composite are capable of fabricating with low cost, low maintenance charges, and in the increased operational temperature range provided these devices have longer lifetime compared to batteries. The suitability of the energy harvester at different vibration sources has to be ensured for better efficiency. For self-healing devices, other than economic feasibility, long-term healability must also be well studied. In shape memory, triggering by external stimulus such as electric and magnetic fields (other than thermal), and maintaining recovery temperature at ambient temperature (near 37 °C) stands as the significant challenges. Usually blending with polymers of low melting point, addition of specific nanoparticles, etc., is practiced to solve these issues. A few

biopolymers exhibiting shape memory cannot work under large deformation strains. As new materials, lot of progress also to be made in its design process. Usual problems associated with polymer nanocomposites such as maintaining good interfacial interaction and homogeneous composite fabrication are also to be considered.

In summary, this chapter aims in providing a brief survey about the various biopolymers and its composites useful in smart applications such as self-healing, energy generation, and shape memory. A few biodegradable composites were reported for converting mechanical vibrations to useful electrical energy without compromising its robustness, flexibility, and longer life. Electrostrictive polymers are also proved their ability in harvesting power from low-frequency vibrations. Cross-linking and modification of nanocomposites enhanced the shape recovery, and other than the thermal triggering magnetic/electric field was also practiced in some composites. In other words, the conventional metals- and alloys-based devices can be replaced largely by polymer based products with high efficiency, lightweight, and low cost. Nanoparticles even in very low concentration improve the mechanical properties and recovery stress of the polymer. The shape recovery of a typical composite also depends on the concentration of component polymers, strain rates, and triggering conditions. Thus, we believe that the future is going to be really "smart" with these novel biodegradable materials.

Acknowledgments This publication was made possible by the support of an NPRP grant from the Qatar National Research Fund (NPRP 7-673-2-251). The statements made herein are solely the responsibility of the authors.

References

1. Sodano HA, Inman DJ, Parck G (2005) Comparison of piezoelectric energy harvesting devices for recharging batteries. J Intell Mater Struct 16:799–807
2. Ren K, Liu Y, Hofmann H, Zhang QM (2007) An active energy harvesting scheme with an electroactive polymer. Appl Phys Lett 91(13):132910
3. Wilkie W, High J, Mirick P, Fox R, Little B, Bryant R, Hellbaum R, Jalink A (2000) Low-cost piezocomposite actuator for structural control applications. Proceedings of the SPIE's 7th international symposium on smart structures and materials, Newport Beach, California
4. High JW, Wilkie WK (2003) Piezoelectric macro-fiber composite actuator and method for making same. US Patent 6629341
5. Ionov L (2010) Actively-moving materials based on stimuli-responsive polymers. J Mater Chem 20:3382–3390
6. Behl M, Lendlein A (2007) Actively moving polymers. Soft Matter 3:58–67
7. Lendlein A, Kelch S (2002) Shape-memory polymers. Angew Chem Int Ed 41:2034–2057
8. Liu C, Qin H, Mather PT (2007) Review of progress in shape-memory polymers. J Mater Chem 17:1543–1558
9. Lendlein A, Jiang H, Junger O, Langer R (2005) Light-induced shape memory polymer. Nature 434:879–882

10. Jiang H, Kelch S, Lendlein A (2006) Polymers move in response to light. Adv Mater 18:1471–1475
11. Huang WM, Yang B, An L, Li C, Chan YS (2005) Water-driven programmable polyurethane shape memory polymer: demonstration and mechanism. Appl Phys Lett 86:114105
12. Yoo HJ, Jung YC, Sahoo NG, Cho JW (2006) Polyurethane-carbon nanotube nanocomposites prepared by in-situ polymerization with electroactive shape memory. J Macromol Sci Phys 4:441–451
13. Lendlein A, Langer R (2002) Biodegradable, elastic shape-memory polymers for potential biomedical applications. Science 296:1673–1676
14. Metcalfe A, Desfaits AC, Salazkin I, Yahia LH, Sokolowski WM, Raymond J (2003) Cold hibernated elastic memory foams for endovascular interventions. Biomaterials 24:491–497
15. Sokolowski W, Metcalfe A, Hayashi S, Yahia LH, Raymond J (2007) Medical applications of shape memory polymers. Biomed Mater 2:S23
16. Yakacki CM, Shandas R, Safranski D, Ortega AM, Sassaman K, Gall K (2008) Strong, tailored, biocompatible shape-memory polymer networks. Biomed Mater 18:2428–2435
17. Zhou SB, Zheng XT, Yu XJ (2007) Hydrogen bonding interaction of poly (D,L-lactide)/hydroxyapatite nanocomposites. Chem Mater 2:247–253
18. Zheng X, Zhou S, Li X, Weng J (2006) Shape memory properties of poly(D,L-lactide)/hydroxyapatite composites. Biomaterials 27:4288–4295
19. Bettinger CJ, Bao Z (2010) Organic thin-film transistors fabricated on resorbable biomaterial substrates. Adv Mater 22(5):651–655
20. Siegel AC, Phillips ST, Dickey MD, Lu N, Suo Z, Whitesides GM (2009) Foldable printed circuit boards on paper substrates. Adv Funct Mater 20(1):28–35
21. Bettinger CJ, Bruggeman JP, Misra A, Borenstein JT, Langer R (2009) Biocompatibility of biodegradable semiconducting melanin films for nerve tissue engineering. Biomaterials 30 (17):3050–3057
22. Meredith P, Bettinger CJ, Irimia-Vladu M, Mostert AB, Schwenn PE (2013) Electronic and optoelectronic materials and devices inspired by nature. Rep Prog Phys 76(3):034501
23. Irimia-Vladu M, Głowacki ED, Troshin PA, Schwabegger G, Leonat L, Susarova DK, Krystal O, Ullah M, Kanbur Y, Bodea MA, Razumov VF (2012) Indigo—from jeans to semiconductors: indigo—a natural pigment for high performance ambipolar organic field effect transistors and circuits. Adv Mater 24(3):321
24. Irimia-Vladu M, Troshin PA, Reisinger M, Shmygleva L, Kanbur Y, Schwabegger G, Bodea M, Schwödiauer R, Mumyatov A, Fergus JW, Razumov VF (2010) Edible electronics: biocompatible and biodegradable materials for organic field-effect transistors. Adv Funct Mater 20(23):4017
25. Irimia-Vladu M, Troshin PA, Reisinger M, Shmygleva L, Kanbur Y, Schwabegger G, Bodea M, Schwödiauer R, Mumyatov A, Fergus JW, Razumov VF (2010) Biocompatible and biodegradable materials for organic field-effect transistors. Adv Funct Mater 20(23):4069–4076
26. Hwang S-W, Kim DH, Tao H, Kim TI, Kim S, Yu KJ, Panilaitis B, Jeong JW, Song JK, Omenetto FG, Rogers J (2013) Materials and fabrication processes for transient and bioresorbable high-performance electronics. Adv Funct Mater 23(33):4087–4093
27. Yang C, Liu P (2009) Water-dispersed conductive polypyrroles doped with lignosulfonate and the weak temperature dependence of electrical conductivity. Ind Eng Chem Res 48 (21):9498–9503
28. Pelrine RE, Kornbluk RD, Joseph JP (1998) Electrostriction of polymer dielectrics with compliant electrodes as a means of actuation. Sens Actuators, A 64:77–85
29. Bar-Cohen Y (2001) Electroactive polymer (EAP) actuator as artificial muscles. SPIE publication, Washington, DC
30. Petit L, Guifard B, Seveyrat L, Guyomar D (2008) Actuating abilities of electroactive carbon nanopowder/polyurethane composite films. Sens Actuators, A 148:105–110

31. Lebrun L, Guyomar D, Guiffard B, Cottinet P-J, Putson C (2009) The Characterisation of the harvesting capabilities of an electrostrictive polymer composite. Sens Actuators, A 153:251–257
32. van der Zwaag S (ed) (2007) Self-healing materials: an alternative approach to 20 centuries of materials science, vol 100. Springer, Dordrecht, The Netherlands
33. Yuan YC, Yin T, Rong MZ, Zhang MQ (2008) Self-healing in polymers and polymer composites. Concepts, realization and outlook: a review. Express Polym Lett 2(4): 238–250
34. Peniche C, Argüelles-Monal W, Goycoolea FM (2008) Chitin and chitosan: major sources, properties and applications. Monomers, polymers and composites from renewable resources. Elsevier, Amsterdam, The Netherlands, pp 517–542
35. Rabea EI, Badawy MET, Stevens CV, Smagghe G, Steurbaut W (2003) Chitosan as antimicrobial agent: applications and mode of action. Biomacromolecules 4(6):1457–1465
36. Trask RS, Williams HR, Bond IP (2007) Self-healing polymer composites: mimicking nature to enhance performance. Bioinspiration and Biomimetics 2(1):P1–P9
37. Chen B, Payne S, Yarin AL (2012) Electrospinning core—shell nanofibers for interfacial toughening and self-healing of carbon-fiber/epoxy composites. J Appl Polym Sci 129 (3):1383–1393
38. Lee MW, An S, Lee C, Liou M, Yarin AL, Yoon SS (2014) Self-healing transparent core—shell nanofiber coatings for anti-corrosive protection. J Mater Chem A 2(19):7045–7053
39. Lee MW, An S, Lee C, Liou M, Yarin AL, Yoon SS (2014) Hybrid self-healing matrix using core—shell nanofibers and capsuleless microdroplets. ACS Appl Mater Interfaces 6:10461–10468
40. Sinha-Ray S, Pelot DD, Zhou ZP, Rahman A, Wub XF, Yarin AL (2012) Encapsulation of self-healing materials by coelectrospinning, emulsion electrospinning, solution blowing and intercalation. J Mater Chem 22:9138–9146
41. Wu XF, Yarin AL (2013) Recent progress in interfacial toughening and damage self-healing of polymer composites based on electrospun and solution-blown nanofibers: an overview. J Appl Polym Sci 129:2225–2237
42. Wu DY, Meure S, Solomon D (2008) Self-healing polymeric materials: a review of recent developments. Prog Polym Sci 33:479–522
43. Williams KA, Dreyer DR, Bielawski CW (2008) The underlying chemistry of self-healing materials. MRS Bull 33:759–765
44. Trask RS, Williams HR, Bond IP (2007) Self-healing polymer composite: mimicking nature to enhance performance. Bioinsp Biomim 2:1–9
45. van der Zwaag S, van Dijk NH, Jonkers HM, Mookhoek SD, Sloof WG (2009) Self-healing behaviour in man-made engineering materials: bioinspired but taking into account their intrinsic character. Philos Trans R Soc A 367A:1689–1704
46. Samra K, Galaev IY, Mattiasson B (2000) Thermosensitive, reversibly cross-linking gels with a shape "memory". Angew Chem Int Ed 39:2364–2367
47. Hu Z, Zhang X, Li Y (1995) Synthesis and application of modulated polymer gels. Science 269:525–527
48. Liu GQ, Ding XB, Cao YP, Zheng ZH, Peng YX (2004) Shape memory of hydrogen-bonded polymer network/poly (ethylene glycol) complexes. Macromolecules 37(6):2228–2232
49. Osada Y, Matsuda A (1995) Shape memory in hydrogels. Nature 376:219–221
50. Beloshenko VA, Varyukhin VN, Voznyak YV (2005) Electrical properties of carbon-containing epoxy compositions under shape memory effect realization. Compos A 36:65–70
51. Kitahara S, Nagata N (1991) Cross-linked polymer having shape memorizing property, method of its use and molded article having shape memory. US Patent 5043396
52. Yang B, Huang WM, Li C, Li L, Chor JH (2005) Qualitative separation of the effects of carbon nano-powder and moisture on the glass transition temperature of polyurethane shape memory polymer. Scripta Mater 53:105–107
53. Anderson DG, Burdick JA, Langer R (2004) Smart biomaterials. Science 305:1923–1924

54. Langer R, Tirrell DA (2004) Designing materials for biology and medicine. Nature 428:487–492
55. Lendlein A, Schmidt AM, Langer R (2001) AB-polymer networks based on oligo (e-caprolactone) segments showing shape-memory properties. PNAS 98(3):842–847
56. Lendlein A, Schmidt AM, Schroeter M, Langer R (2005) Shape-memory polymer networks from Oligo (e-caprolactone) Dimethacrylates. J Polym Sci A 43:1369–1381
57. Lu X, Sun Z, Cai W (2007) Structure and shape memory effects of poly(L-lactide) and its copolymers. Physica Scripta T:T129. Second international symposium on functional materials, pp 231–235
58. Lu X, Cai W, Zhao L (2005) Study on the shape memory behavior of poly(L-lactide). Mater Sci Forum 475–479(III). PRICM 5: the fifth pacific rim international conference on advanced materials and processing, pp 2399–2402
59. Shikinami Y (2001) Shape memory biodegradable and absorbable material. US Patent 6281262 B1
60. Jordan G (2008) Balloon geometry for delivery and deployment of shape memory polymer stent with flares. US Patent 20080132988
61. Moaddeb S, Shaolian SM, Shaoulian E, Rhee R, Anderson SC (2007) Shape memory devices and methods for reshaping heart anatomy. US Patent 7285087
62. Mather PT, Liu C, Campo CJ (2007) Blends of amorphous and semicrystalline polymers having shape memory properties. US Patent 7208550
63. Sauter T, Heuchel M, Kratz K, Lendlein A (2013) Quantifying the shape-memory effect of polymers by cyclic thermomechanical tests. Polym Rev 53:6–40
64. Kim KN, Chun J, Chae SA, Ahn CW, Kim IW, Kim SW, Wang ZL, Baik JM (2015) Silk fibroin-based biodegradable piezoelectric composite nanogenerators using lead-free ferroelectric nanoparticles. Nano Energy 14:87–94
65. Eddiai A, Meddad M, Mazroui M, Boughale Y, Idiri M, Khanfer R, Rguitie M (2016) Strain effects on an electrostrictive polymer composite for power harvesting: experiments and modeling. Polym Adv Technol 27:677–684
66. Fukada E (1995) Piezoelectricity of biopolymers. Biorheology 32(6):593–609
67. Schnepp Z, Mitchells J, Mann S, Hall SR (2010) Biopolymer-mediated synthesis of anisotropic piezoelectric nanorods. Chem Commun 46:4887–4889
68. Li T, Zeng K (2013) Nanoscale piezoelectric and ferroelectric behaviors of seashell by piezoresponse force microscopy. J Appl Phys 113:187202
69. Fukada E (1968) Piezoelectricity as a fundamental property of wood. Wood Sci Technol 2 (4):299–307
70. Kim JH, Yun S, Kim JH, Kim J (2009) Fabrication of piezoelectric cellulose paper and audio application. J Bionic Eng 6:18–21
71. Csoka L, Hoeger IC, Rojas OJ, Peszlen I, Pawlak JJ, Peralta PN (2012) Piezoelectric effect of cellulose nanocrystals thin films. ACS Macro Lett 1:867–870
72. Nejadnik MR, Yang X, Bongio M, Alghamdi HS, van den Beucken JJJP, Huysmans MC, Jansen JA, Hilborn J, Ossipov D, Leeuwenburgh SCG (2014) Self-healing hybrid nanocomposites consisting of bisphosphonated hyaluronan and calcium phosphate nanoparticles. Biomaterials 35:6918–6929
73. Spoljaric S, Salminen A, Dang Luong N, Seppälä J (2014) Stable, self-healing hydrogels from nanofibrillated cellulose, poly(vinyl alcohol) and borax via reversible crosslinking. Eur Polym J 56:105–117
74. Meng H, Li G (2013) A review of stimuli-responsive shape memory polymer composites. Polymer 54:2199–2221
75. Hu JL, Mondal S (2005) Structural characterization and mass transfer properties of segmented polyurethane: influence of block length of hydrophilic segments. Polym Int 54:764–771
76. Hu JL, Yang Zh, Ji FL, Liu YQ (2005) Crosslinked polyurethanes with shape memory properties. Polym Int 54:854–859
77. Beloshenko VA, Varyukhin VN, Voznyak YV (2005) The shape memory effect in polymers. Russ Chem Rev 74:265–283

78. Voit W, Ware T, Dasari RR, Smith P, Danz L, Simon D, Barlow S, Marder SR, Gall K (2010) High-strain shape-memory polymers. Adv Funct Mater 20:162–171
79. Zhang S, Yu Z, Govender T, Luo H, Li B (2008) A novel supramolecular shape memory material based on partial α-CD–PEG inclusion complex. Polymer 49:3205–3210
80. Yu Z, Liu Y, Fan M, Meng X, Li B, Zhang S (2010) Effects of solvent, casting temperature, and guest/host stoichiometries on the properties of shape memory material based on partial α-CD-PEG inclusion complex. J Polym Sci Part B: Polym Phys 48:951–957
81. Behl M, Lendlein A (2007) Shape-memory polymers. Mater Today 10:20–28
82. Chen MC, Tsai HW, Chang Y, Lai WY, Mi FL, Liu CT, Wong HS, Sung HW (2007) Rapidly self-expandable polymeric stents with a shape-memory property. Biomacromolecules 8:2774–2780
83. Luo H, Hu J, Zhu Y, Zhang S, Fan Y, Ye G (2012) Achieving shape memory: reversible behaviors of cellulose–PU blends in wet–dry cycles. J Appl Polym Sci 125:657–665
84. Ishida K, Hortensius R, Luo X, Mather PT (2012) Soft bacterial polyester-based shape memory nanocomposites featuring reconfigurable nanostructure. J Polym Sci Part B: Polym Phys 50:387–393
85. Xu J, Song J (2010) High performance shape memory polymer networks based on rigid nanoparticle cores. Proc Natl Acad Sci 107:7652–7657
86. Filion TM, Xu J, Prasad ML, Song J (2011) In vivo tissue responses to thermal-responsive shape memory polymer nanocomposites. Biomaterials 32:985–991
87. Lee KM, Knight PT, Chung T, Mather PT (2008) Polycaprolactone—POSS chemical/physical double networks. Macromolecules 41:4730–4738
88. Alvarado-Tenorio B, Romo-Uribe A, Mather PT (2011) Microstructure and phase behavior of POSS/PCL shape memory nanocomposites. Macromolecules 44:5682–5692
89. Bothe M, Mya KY, MLin JE, Yeo CC, Lu XH, He C, Pretsch T (2012) Triple-shape properties of star-shaped POSS-polycaprolactone polyurethane networks. Soft Matter 8: 965–972
90. Yu X, Zhou S, Zheng X, Guo T, Xiao Y, Song B (2009) A biodegradable shape-memory nanocomposite with excellent magnetism sensitivity. Nanotechnology 20:235702 (9 pp)
91. Shen T, Liang L, Lu M (2011) Novel biodegradable shape memory composites based on PLA and PCL crosslinked by polyisocyanate. International conference on agricultural and biosystems engineering, advances in biomedical engineering, vols 1–2
92. Meng Q, Hu J, Ho K, Ji F, Chen S (2009) The shape memory properties of biodegradable, chitosan/poly(L-lactide) composites. J Polym Environ 17:212–224
93. Tsujimoto T, Takayama T, Uyama H (2015) Biodegradable shape memory polymeric material from epoxidized soybean oil and polycaprolactone. Polymer 7:2165–2174
94. Wei X, Liu J (2008) Power sources and electrical recharging strategies for implantable medical devices. Front Energy Power Eng Chin 2(1):1–13